[This page is intentionally left blank]

CATALYTIC CONSEQUENCES OF INNER- AND OUTER-SPHERE INTERACTIONS AT THE SOLID-LIQUID INTERFACE IN ZEOLITES

BY

DANIEL THOMAS BREGANTE

DISSERTATION

Submitted in partial fulfillment of the requirements
for the degree of Doctor of Philosophy in Chemical Engineering
in the Graduate College of the
University of Illinois at Urbana-Champaign, 2020

Urbana, Illinois

Doctoral Committee:

Associate Professor David W. Flaherty, Chair
Professor Catherine J. Murphy
Professor Baron G. Peters
Assistant Professor Damien Guironnet

[This page is intentionally left blank]

ABSTRACT

Catalytic transformations at solid-liquid interfaces are inherently complex, as they require considerations for adsorption, desorption, molecular rearrangement, charger transfer, and dispersive interactions, but also involve interactions mediated by the solvating molecules. The rational design of improved systems for a desired transformation, require that each of these types of processes and interactions be accounted for. Colloquially, interactions among surface intermediates bound *directly* to an active site are referred to as "inner-sphere" interactions, while those involving molecules within the second shell are known as "outer-sphere" interactions. This dissertation explores both inner- and outer-sphere interactions that influence the stability of catalytically relevant surface species within zeolite catalysts.

We use a combination of *experimental* synthetic, kinetic, spectroscopic, and thermodynamic tools and analyses to develop quantitative structure-activity relationships to describe how orthogonal changes to the catalytic system result in large charges in activity and selectivity during alkene epoxidation. We developed a proposed series of elementary steps to describe alkene epoxidation with hydrogen peroxide over early transition metals substituted into zeolite frameworks. First, this model was used to show that apparent activation enthalpies linearly scale with functional measures of Lewis acid strength (i.e., inner-sphere interactions) and explain how changing the active site identity could result in 10^6- and 10^2-fold increases in rates and selectivities among groups 4 and 5 metals. Second, outer-sphere, dispersive interactions among pore walls and reactive species are shown to persist within liquid-phase catalysis, which show how titanium within the *BEA framework (Ti-BEA) catalyzes styrene epoxidation with rates 5-times greater than these same atoms supported on mesoporous silica. Third, the presence of hydrophilic surface functions in a Ti-BEA catalyst nucleate confined H_2O clusters that differ significantly in physical and chemical properties from bulk H_2O. These H_2O structures reorganize to accommodate the formation of surface intermediates (e.g., transition states) that lead to large increases in excess entropy and lower the free energy of the aggregate complex and increase rates by a factor of 100. Finally, we discuss how lateral inner-sphere interactions among surface intermediates bound to a single active site can be mediated by the presence and size of a surrounding pore and can ultimately lead to differences in rates spanning an order of magnitude. Collectively, this dissertation lays the foundation to measure and interpret complex inner- and outer-sphere interactions within microporous materials and will aid in the rational design of improved materials.

ACKNOWLEDGEMENTS

First and foremost, I want to thank my advisor, David Flaherty, for his support and guidance throughout my Ph.D. He has done a tremendous job with keeping me motivated, supporting my ideas, and giving insightful advice at every turn. Thanks, Dave for everything. I really appreciate all you've done.

Next, I want to thank my parents and family for being so supportive. Whether it's my weekly conversations with my parents or just everyone being their supportive selves during holidays when I'd return home, it always helped me put everything in perspective and keep going.

I've had the pleasure of getting to know pretty much every person to join Dave's group or go through it. I'll always think back fondly to my first year when it was just us five graduate students, Neil, Andy, Megan, Pranjali, and myself. I've developed a strong bond with every one of them. From working out regularly with Andy and Neil to the late nights in lab with Megan and Pranjali. It was a joy to work with all of you. I've also gotten to know the classes since. I've gotten to know many of the student who have come since, Jason, Yao, Abinaya, Claudia, Tom, Zeynep, Chris, Devinda, David, and Ohsung, many of whom are close friends. I'm glad to have gotten to meet all of you and look forward to all of the things you accomplish. I hope the group keeps their weekly lunch tradition and that someone will pick up my mannerism of peering over someone's shoulder at a random plot and say "looks good." The future of the lab is in good hands with you all.

I've been very lucky to get to work with four *outstanding* undergraduates during my time at UIUC: Jun, Ami, Rebecca, and Alayna. Thanks to all of you for helping me grow as a mentor. Best of luck in what comes next for each of you.

I couldn't have done it with all of my friends I've made and kept up with during my Ph.D. I always looked forward to our weekly lunches with the now-old people group: Dylan, Mai, Carl, Shekhar, and Will. Thanks to my friends who I've kept in touch with from Union City: Panan, Sarah, and Alison and from Berkeley: Cameron, Yuji, Effie, David, and Josh. A special thanks to Valerie for helping me get through the early stages of my Ph.D. when I was still figuring everything out. Special thanks also to Zeynep who's helped keep me motivated and put things into perspective. I appreciate you all.

I'd like to commend the ChBE department and the School of Chemical Sciences at UIUC. I've gotten to know so many of the faculty and staff and each has made a great impression on me.

Special thanks to Xiao Su, Cathy Murphy, and Damien Guironnet, who have met with me several times over the last few years and offered their advice on a variety of things. Thanks also to all the faculty – Profs. Kenis, Higdon, Su, Shukla, Guironnet, Yang, Diao, Rodriguez-Lopez, Gewirth, Sing, Schroeder, and Seebauer – who were able to participate in my mock interview. A special thanks to my thesis committee members, Damien Guironnet, Cathy Murphy, and Baron Peters. I appreciate all of you.

Thanks to all of my collaborators I've gotten to work with during my Ph.D.: Raj, Justin, Chris, Michael, Laura, Matt, Diwakar, Gina, Nick, Alex, Brandon, Connie, Taka, Hongbo, Arian, Yangsik, and Damin. It's been my pleasure getting to know you and I hope to catch up with each of you at some point in the future.

I apologize to anyone I might've missed. Know that if we've interacted during my Ph.D., you're a big part of my success.

I was supported by a Samuel W. Parr Fellowship and a Dissertation Completion Fellowship, both through the University of Illinois, and a National Defense Science and Engineering Graduate (NDSEG) Fellowship through the Army Research Office with the Department of Defense. This work was carried out, in part, at the Frederick Seitz Materials Research Laboratory Central Research Facilities, School of Chemical Sciences NMR Laboratory, and the School of Chemical Sciences Microanalysis Laboratory. This work was supported through several research grants from the U.S. Army Research Office (W911NF-16-1-0128 and W911NF-181-0100) and the U.S. Department of Energy (DE-SC0020224).

To My Parents, Family, and Friends

TABLE OF CONTENTS

CHAPTER ONE

Introduction

1.1 Zeolites for Liquid-Phase Catalysis

Zeolites are microporous, crystalline forms of silica (SiO_2) that are ubiquitous in the fields of catalysis[1-2] and separations.[3-4] Lewis acidic zeolites possess tetrahedral sites that are substituted by early transition- or base-metal heteroatoms of similar or higher valence (e.g., Ti^{4+}, Sn^{4+}, Nb^{5+}, Ta^{5+}, W^{6+}, …) than silicon. These materials have attracted significant interest from both industry[5-6] and academia[7-10] due to their ability to differentiate between reactants based upon their shape and size. This allure stems from the topological and morphological diversity of the microporous voids within zeolites (0.4 – 1.3 nm), which can tuned to increase reaction rates and selectivities through stabilizing interactions between the surrounding pore walls with reactive intermediates through dispersive interactions (e.g., van der Waals forces; Scheme, 1.1).[11-13]

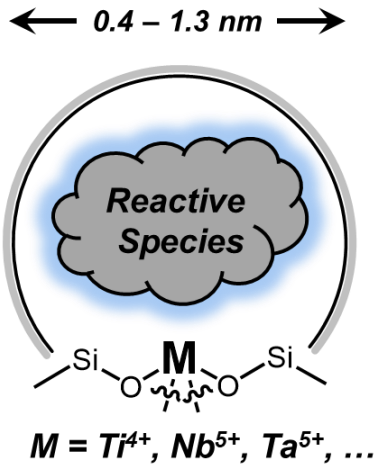

Scheme 1.1. A heteroatom (M) substituted zeolite that contains a reactive species stabilized through dispersive interactions (blue glow) with the surrounding pore walls.

Historically, the design of zeolites for specific catalytic transformations have relied on empirical observations regarding similarities between reactant molecules and the structure-directing agents that are used to crystallize the solid materials. Over the last decade, however, a renaissance of research activity has emerged, devoted to the rational design of new zeolite structures to stabilize specific intermediates.[2, 14] For example, computational and experimental methods[7, 15] can independently probe the effects of acid strength and confinement within zeolite

materials to quantify their contributions to the rate and equilibrium constants among a series of elementary steps. The ways in which these (non-)specific interactions can be used to stabilize specific reactive species along a reaction coordinate are well documented and understood when the surrounding pores are largely vacant (e.g., during gas-phase catalysis);[7, 16-17] yet, are poorly understood when the zeolite pores contain liquid-like densities of molecules that surround intermediates and influence their thermodynamic stability.

Catalysis at solid-liquid interfaces formed between solvent mixtures and the surface of a heterogeneous solid possesses all the complexities of catalysis at gas-solid interfaces; yet, are further convoluted by interactions that are mediated by the solvent molecules.[18-19] Both classes of reactions (both liquid- and gas-phase) involve, adsorption, charge transfer, and molecular rearrangement processes that depend intimately on the electronic and dispersive interactions among reactive intermediates and active sites. Interactions among ligands or reactive intermediates within the first-coordination shell encompass inherently fast, short-range electron transfer and molecular rearrangement are known as "inner-sphere" interactions. Historically, heterogeneous catalysis research studying inner-sphere interactions have focused on methods to modify the active site through metal-support interactions, active site identity and speciation, and formation of inter-metallic compounds, to name a few. There is a large amount of inherent ambiguity when these changes are made, as they can induce changes to the catalytic system (e.g., differences in confinement, mechanism) that may obviate differences associated predominantly with changes in the electronic properties of the active site.

The presence of a liquid phase, however, introduces additional specific interactions among solvent molecules, catalyst surfaces, and reactive species that can lead to changes in rates and selectivities by orders of magnitude. Complex, multi-body interactions between reactive species and molecules outside of the first-coordination sphere are colloquially referred to as "outer-sphere" effects. Intuition for the effects of inner- and outer-sphere interactions on chemical reactions have been developed in organic chemistry and homogeneous catalysis; however, these principles are less frequently invoked in the rational design of heterogeneous catalysts. Consequently, a quantitative understanding for how these effects influence heterogeneous catalysis could have an enormous technological impact and influence on the field of reaction engineering.

Specific interactions (e.g., hydrogen bonds) among transition states, solvent molecules, and surfaces are much weaker than covalent and ionic bonds formed between reactive intermediates

and active sites. The collective effects of these interactions, however, can nucleate extended solvent structures that surround active sites and influence catalysis. Catalysis within zeolites are especially sensitive to inner- and outer-sphere interactions mediated by solvent molecules, because the confining environments that surround active site are similar in size to solvation shells (0.5 – 1 nm) which may further influence the structure and dynamics of reactive species. Zeolite catalysts provide an ideal platform to study the effects of inner- and outer-sphere interactions at the solid-liquid interface for several reasons:

1. The crystalline nature of zeolite catalysts provides a greater uniformity in the structure and nature of active sites than transition metals grafted onto an amorphous support.
2. Zeolites can be synthesized to control the proximity of polar surface functions to active sites and control the structure of solvent molecules localized near active sites.
3. The confined active sites require that solvation shells surrounding reactive species change drastically upon molecular rearrangement during catalysis.
4. The micropores of zeolites introduces finite size effects into the solvent structures because these molecules cannot adapt the same equilibrium structures formed in the bulk.

There have been significant experimental[20-23] and computational[23-26] efforts to understand how solvent molecules structure themselves within zeolites; however, many of these studies focus primarily on aqueous systems and often do not involve a catalytic reaction. For example, Siepmann and coworkers have used molecular dynamics simulations to show how water (H_2O) molecules form two-dimensional chains at high pressures within H-ZSM-5 (i.e., Zeolite MFI) and can influence the selective adsorption of alcohols from water-alcohol mixtures.[25, 27] The ways in which these H_2O and alcohol structure within zeolites *restructure* around surface intermediates and influence catalysis, however, is not known.

Solvent molecules within zeolites form distinct structures that differ significantly from the bulk and must reorganize to accommodate intermediates and transition states as reactions proceed, which contributes to changes in the free energy of activation and reaction with each elementary step along a reaction coordinate. The influence of solvent structure and reorganization on catalysis depends intimately on the identity of the solvent, size of the surrounding pore, and reaction studied. Much of this thesis focuses on understanding how H_2O structures within an acetonitrile (CH_3CN)

solvent influence catalysis; however, there are many additional avenues of study, some of which will be outlined in Chapter 10.

Many catalytic reactions (e.g., alkene epoxidation,[28-32] glucose isomerization,[22, 33-34] Baeyer-Villiger oxidation[35]) at surfaces respond sensitively to the presence of H_2O, proximate hydroxyl groups, and hydrogen bonding. The catalytic consequences of H_2O and the associated hydrogen-bonded networks it forms are significant within the micropores of zeolite catalysts, which either preclude the formation of H_2O clusters when surfaces are non-polar and hydrophobic or nucleate these same structures when pore walls contain polar, hydrogen-bonding functions. Within the context of zeolite catalysis, the densities of isolated silanol groups (SiOH) and of silanol nests ($(SiOH)_4$) within the material are known to have drastic effects on the adsorption properties and intrapore condensation of small molecules (e.g., H_2O,[36-39] CH_3OH,[33, 39] C_2H_5OH[24, 37]). Once stabilized within the pores, these species influence the stability of co-adsorbates, reactive intermediates, and transition states through specific intermolecular interactions, such as hydrogen bonds. Unfortunately, the catalytic contributions of silanol groups and the networks of H_2O (or other solvents) they stabilize are not clear due to concomitant changes in other properties of the catalysts and reaction systems in previous investigations. Evidently, the field of heterogeneous catalysis would benefit from the development of quantitative structure-activity relationships (QSAR) that guide how inner- and outer-sphere interactions, specifically involving solvent structures surrounding active sites, may be used to tune the stability of reactive species in zeolites. The development of QSARs that aid in the design of new catalytic systems, however, requires a probe reaction that is sensitive to the inner- and outer-sphere interactions within zeolites.

1.2 Alkene Epoxidation Catalysis to Probe Interactions at the Solid-Liquid Interface

Nearly 10 billion kilograms of propylene oxide (PO) are produced every year.[40] In 2015 alone, the chlorohydrin process used 5.2 billion kilograms of chlorine (Cl_2) and 3.7 billion kilograms of alkali hydroxides (e.g., $Ca(OH)_2$) to produce PO.[41-44] Many other current methods for epoxidations also rely on the use of Cl_2, which produces a slew of toxic and caustic by-products, or the use of stoichiometric amounts of organic peroxides or peracids (e.g., *tert*-butylhydroperoxide), which generates co-products that must be regenerated.[41] Hydrogen peroxide (H_2O_2) can replace the use of Cl_2-alkali hydroxides and organic oxidants entirely in epoxidations and oxidations, and eliminate the concomitant formation of hazardous co-products.[5] One of the

few industrial catalysts that use H_2O_2 for oxidations is titanium silicalite-1 (TS-1), which was first synthesized in the late 1970's,[45] and has since been adopted industrially for the H_2O_2-mediated oxidation of phenol (> 10 M kg yr^{-1}), ammoxidation of cyclohexanone (> 60 M kg yr^{-1}), and epoxidation of propylene to PO (> 300 M kg yr^{-1}).[46] Despite success in these industrial processes, Cl_2 and other environmentally-impactful oxidants continue to be used in other chemistries as a result of the higher cost of H_2O_2-mediated epoxidations, due in part to non-productive H_2O_2 decomposition, the limited substrate scope of the MFI framework (pore diameter ~0.5 nm), and the lack of clear design rules for similar heterogeneous epoxidation catalysts.[46]

Monomeric metal centers and small oligomers of metal oxides (e.g., Al,[47-48] Ti,[49-52] Zr,[51, 53] Nb,[54-56] and Ta[57-59]) activate H_2O_2 and catalyze alkene epoxidations. Several computational studies have probed the effects of transition metal atom substitution into zeolite frameworks on the "strength" of the corresponding Lewis and Brønsted acids and correlated these changes to predicted reactivity predominantly for biomass conversion or the isomerization of glucose.[60-63] For example, Boronat *et al.* used quantum chemical calculations to infer that the high relative reactivity of Ti-BEA zeolites for 1-octene epoxidation, relative to Zr- and Sn-substituted analogues, stems from the lower energy of its lowest unoccupied molecular orbital. Experimentally, Thornburg *et al.* showed that atomically disperse groups 4 and 5 metal atoms grafted onto mesoporous SiO_2 catalyze cyclohexene epoxidation with H_2O_2, where the rates of epoxidation increased monotonically with the electronegativity of the metal atom.[51] Despite the decades of work on alkene epoxidation, we have not found any investigations in the open literature that correlate measured barriers for epoxidation (for reactivity) and H_2O_2 decomposition (for selectivity) to physicochemical properties of the catalyst to develop *experimentally-validated* QSARs that can drive the design and synthesis of improved materials.

Rates of alkene epoxidation over Ti-bearing silicates depend strongly on the size of the confining void (i.e., the identity of the zeotype support) and the solvent used for reaction. The use of TS-1 for propylene epoxidation is often phenomenologically attributed to the stabilization of propylene and titanium hydroperoxide (Ti-OOH) reactive intermediates within the pores of MFI.[64-65] As such, the use of other zeotype supports (e.g., BEA,[30, 66] FAU,[67] SBA-15[68]) for alkene epoxidations are often motivated by the small pores of TS-1 and the need to develop materials that can react with a greater diversity (i.e., larger) of alkenes. The effects of pore size can indeed impart a sieving effect, where bulky alkenes may not be able to enter pores and react; however, the

topological nature of the interior voids can solvate and stabilize specific intermediates through van der Waals forces between the surface intermediates that form during catalysis and the surrounding pore walls. These effects are well studied and documented in gas-phase catalysis;[7, 13] yet, are less common in liquid-phase oxidation catalysis, as the presence of solvent molecules adds layers of complexity to the system and the changes in free energy of active intermediates do not only reflect dispersive interactions with the surrounding void.

The presence, structure, and proximity of solvent molecules to Lewis acid active sites influence measured rates and selectivities. Specifically, the role of hydrogen bonding among adventitious H_2O molecules within Ti-based silicate catalysts on alkene epoxidation has been debated for decades. Seminal studies on epoxidation within titanium silicalite-1 (TS-1) reported that the hydrophobic nature of pristine TS-1 gives greater yields of epoxide products with respect to hydrophilic titanium silicates (e.g., Ti-BEA, TiO_2-SiO_2), which was attributed to an increase in the concentration of the alkene substrate near active Ti active sites.[29-30, 69] These findings laid the foundation for a plethora of work on liquid-phase oxidations that sought to relate changes in hydrophilicity to measured catalysis.[69-71] The differences in reactivity among TS-1 and other silicates, however, may be related to changes in the extent of confinement of reactive intermediates in the different porous environments. Relating changes in rates and selectivities to changes in hydrophilicity among different materials is difficult because experimental observations may reflect convoluted effects from confinement, mass transfer restrictions, and even differences in mechanism. Consequently, the catalysis community has not reached a consensus on the effects of H_2O structure and proximity on liquid-phase epoxidation catalysis.

This research aims to examine how inner- and outer-sphere interactions at the solid-liquid interface in Lewis acid zeolites affect the stability of surface intermediates and, by extension, measured rates and selectivities. Through this, we ultimately develop a quantitative understanding of the catalytic consequences that result from changing specific facets of the reaction environment. Turnover rates, within the context of transition state theory, depend on the change in Gibbs free energy for the transition states relative to an apparent reference state. In this framework, measured catalytic rates are represented by the apparent Gibbs free energy of activation ($\Delta G_{App.}{}^{\ddagger}$; Fig. 1.1), which can be represented as

$$\Delta G_{App.}{}^{\ddagger} = \Delta G_{Intrinsic.}{}^{\ddagger} + G_{Excess} \tag{1.1}$$

where $\Delta G_{Intrinsic}^{\ddagger}$ is the *intrinsic* free energy of activation and ΔG_{Excess} represents the *excess* free energy that encompasses inner- and outer-sphere interactions among reactive species and its solvation spheres. Values of ΔG_{Excess} describe how the thermodynamic stability of reactive intermediates depend on the extent of electron transfer between reactive ligands and active sites, solvent reorganization associated with confined solvent structures, and the dispersive interactions with the surrounding environment, among other effects. This dissertation lays a foundation for how to quantitatively determine how ΔG_{Excess} changes as a result of specific changes to the catalytic system and how this information can be used to rationally design improved catalysts.

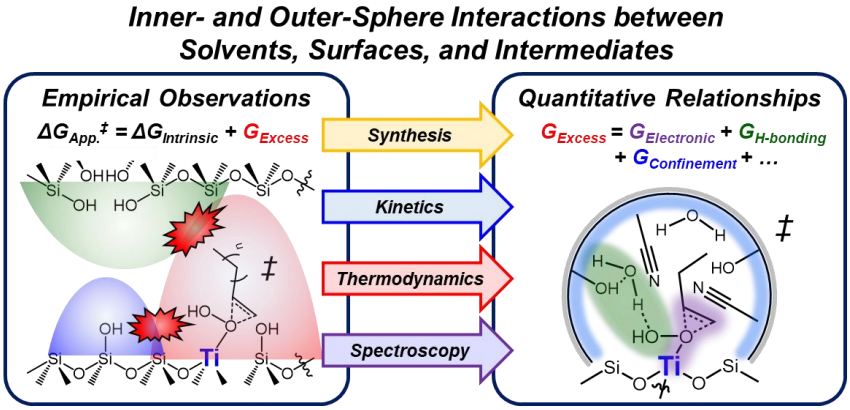

Figure 1.1. Apparent Gibbs free energies of activation are the sum of an *intrinsic* and *excess* free energy contribution. Excess free energies can be deconvoluted into specific interactions that stem from the electronic properties of the active site, hydrogen-bonding interactions among solvent molecules, and confinement through a combination of precise synthetic methods, intrinsic kinetic measurements, thermodynamic analysis, and *in situ* spectroscopic techniques.

Chapter 2 details how the series of elementary steps (i.e., the mechanism) that describes alkene epoxidation over early transition metal substituted zeolites was determined through mechanistic interpretations of kinetic measurements obtained at various reaction conditions (e.g., reactant and product concentrations). The identity of reactive species was probed by *in situ* UV-vis and infrared spectroscopy to show that reactive metal peroxide and hydroperoxide intermediates form upon H_2O_2 activation. Chapters 3 and 4 show that alkene epoxidation (and thiophene sulfoxidation) depends strongly on the identity of the active metal atom. Groups 4 and 5 metals (i.e., Ti, Zr, Hf, Nb, and Ta) substituted into *BEA all activate H_2O_2 to form metal hydroperoxide and peroxide intermediates, which react through nearly identical mechanisms to oxidize an alkene or thiophene. Measured rates and selectivities increase by factors of 100,000 and

100-fold when the identity of the active metal is change from Hf to Ti and depend exponentially on the functional Lewis acid strength of the reactive metal center. The role of confinement within *hydrophilic* microporous and mesoporous materials is explored in chapters 5 and 6, where changes in apparent activation enthalpies for epoxidation are shown to correlate with the adsorption enthalpies for the alkene into the various porous environments. This shows that epoxidation reactions over a given metal ion possess a single *intrinsic* activation enthalpy, that does not depend on the physicochemical properties of the active site. Chapters 7 and 8 provide synthetic, kinetic, thermodynamic, and spectroscopic evidence for how confined H_2O clusters within titanium substituted *BEA depend on the shape and size of the void surrounding active sites. Specifically, confined H_2O form small structures that differ significantly from bulk H_2O, which is owed to the loss of three-dimensional order associated with the surrounding pores. These structures reorganize in response to the formation of reactive intermediates during epoxidation catalysis. As a consequence, hydrophilic pores nucleate these structures of H_2O near Ti active sites and yield rates of epoxidation that are 100-fold greater than hydrophobic analogues. Inner-sphere interactions among multiple surface intermediates that are bound to a single active site are quantified in Chapter 9. Epoxidation reactions with H_2O_2, *t*-butyl hydrogen peroxide, or cumene hydroperoxide in Ti-BEA and Ti grafted onto SBA-15 show that the micropores of *BEA essentially act as an enormous non-innocent ligand that mediates the interactions among reactive species. The work discussed in this dissertation is intended to guide future researchers in how to design experiments and systems to explore how inner- and outer-sphere interactions at solid-liquid interfaces affect intermediates critical to the fields of separations and catalysis. Finally, Chapter 10 offers my concluding remarks along with several avenues of study for epoxidations within Lewis acid zeotype catalysts.

CHAPTER TWO

Kinetic and Spectroscopic Evidence for Reaction Pathways and Intermediates for Alkene Epoxidation Over Nb-Substituted *BEA[I]

Abstract

The selective epoxidation of alkenes with hydrogen peroxide (H_2O_2) over transition metal substituted zeolites is less environmentally impactful than epoxidation schemes that use chlorinated or organic oxidants. The structure and reactivity of reactive intermediates derived from H_2O_2 and the mechanism for alkene epoxidation on such materials are debated. Here, cyclohexene oxide formation and H_2O_2 decomposition rates (measured as functions of reactant and product concentrations) and in situ infrared (IR) and UV-vis spectroscopy are used to probe the intervening elementary steps for cyclohexene (C_6H_{10}) epoxidation and the identity of the reactive intermediates on a Nb-BEA catalyst. IR and UV-vis spectra acquired in situ show that the reactive intermediates are predominantly superoxide species (Nb^{4+}-$(O_2)^-$; observed also by X-ray photoelectron spectroscopy), which form by the irreversible activation of H_2O_2 over Nb centers. Similar M-(O_2)* (M= Ti or Ta) intermediates were previously assumed to form via reversible processes; however, in situ IR and UV-vis measurements directly show that Nb^{4+}-$(O_2)^-$ forms irreversibly in both H_2O and acetonitrile. Activation enthalpies ($\Delta H^{\ddagger}$) for C_6H_{10} epoxidation are 27 kJ mol^{-1} higher than for H_2O_2 decomposition, while activation entropies ($\Delta S^{\ddagger}$) for epoxidation are 56 J mol^{-1} K^{-1} lower than for H_2O_2. These comparisons show that the selectivities for epoxidation, via primary reaction pathways, increase with increasing reaction temperatures. Collectively, these results provide a self-consistent mechanism for C_6H_{10} epoxidation that is also in agreement with previously published data. These findings will aid the rational design and study of alternative metal oxide catalysts for alkene oxidation reactions.

[I]This chapter has been adapted from the following publication:
Bregante, D.T.; Priyadarshini, P.; Flaherty, D.W.; "Kinetic and Spectroscopic Evidence for Reaction Pathways and Intermediates for Alkene Epoxidation on Nb in *BEA"
Journal of Catalysis, **2017**, *348*, 75-89.

2.1 Introduction

Epoxides are important precursors for the synthesis of epoxy resins, plastics, and complex molecules used to manufacture aircraft hulls, perfumes, and pharmaceuticals.[72-74] Currently, epoxides are produced primarily by the reaction of alkenes with stoichiometric amounts of organic peroxy compounds[75] or through chlorohydrin intermediates followed by strong alkaline treatments to form oxiranes.[76-77] These processes generate stoichiometric amounts of corrosive organic acids and alcohols[78] or chloride salts,[76] respectively, that require subsequent energy-intensive separation, waste-treatment, and regeneration.[79-80] More environmentally benign oxidants should be used; however, the costs of "green" oxidants that generate less waste are generally greater and the product selectivities may be lower than Cl-mediated pathways.[81-82] Hydrogen peroxide (H_2O_2) is one such oxidant whose use only byproduct in epoxidation reactions is water (H_2O), which is easily separated from organic product streams by liquid-liquid extraction.[83-84] Currently, the high relative cost of H_2O_2 (to that of Cl-based oxidizers) requires catalysts that selectively activate and utilize H_2O_2 for alkene epoxidation while minimizing non-productive H_2O_2 decomposition (i.e., $2H_2O_2 \rightarrow O_2 + 2H_2O$) and epoxide decomposition.

Isolated metal centers and small oligomers of early transition metal oxides (e.g., Al^{3+},[47-48] Ti^{4+},[78, 85-87] Zr^{4+},[51, 53] Ta^{5+},[58-59, 88] and Nb^{5+})[55-56] catalyze the epoxidation of alkenes with H_2O_2. Isolated Nb atoms grafted onto silica give greater rates and selectivities for alkene epoxidation compared to isolated Ti centers as well those of other group 4 and 5 metals (i.e., Zr, Hf, V, and Ta) on silica, which was attributed to differences between the Lewis acidity (estimated from the ionic character of the M-O bond) of the different metal atoms.[51] Zeolite frameworks can stabilize relatively high loadings of isolated transition metal atoms,[49, 89-92] which in some cases, are believed to possess higher turnover rates and selectivities than their oligomeric- and bulk-oxide counterparts. For example, Ti centers in titanium silicalite-1 (TS-1) activate H_2O_2 to form intermediates that epoxidize propylene in one of few industrially practiced H_2O_2-based oxidation reactions.[65, 93-94] TS-1, however, possesses relatively small diameter pores (~ 5.5 Å, due to the MFI framework),[95] which hinders the diffusion of larger alkenes (e.g., cyclooctene, limonene, etc.)[28, 65] to Ti centers within the pores. Larger pore zeolite frameworks, such as the beta (*BEA) polymorph, possess pores with diameters of ~ 7 Å,[95] which broadens the range of potential substrates for epoxidations.[96] Post-synthetic modification of *BEA and other zeolites provides a facile method to synthesize transition metal substituted catalysts using commercially-available zeolites as

precursors,[89-90, 96-97] which enables studies of how the elemental identity of isolated metal centers in similar coordination environments affects catalysis. As such, the mechanism of alkene epoxidation on transition metal substituted *BEA (M-BEA) must be established before such periodic trends can be understood.

Here, we combine catalytic rate measurements with in situ UV-vis and Fourier transform-infrared (FTIR) spectroscopy to determine the mechanism for cyclohexene epoxidation and the structure and reactivity of relevant reaction intermediates on Nb-BEA. In situ UV-vis and IR spectroscopy show Nb-bound superoxide (Nb-$(O_2)^-$) and hydroperoxide/peroxide (Nb-OOH and Nb-$(O_2)^{2-}$) intermediates form by irreversible activation of H_2O_2 at Nb atoms, which conflicts with proposed mechanisms for alkene epoxidation on similar catalysts (i.e., TS-1,[98] Ta-SBA-15,[57-58] and Ta-SiO_2)[59, 88] that assume reversible (and quasi-equilibrated) H_2O_2 activation. X-ray photoelectron spectroscopy of H_2O_2-activated Nb-BEA confirms the presence of Nb-$(O_2)^-$ surface species by showing that Nb atoms shift from a 5+ to 4+ oxidation state when activated with H_2O_2. A combination of transient in situ UV-vis and FTIR measurements demonstrate that the Nb-$(O_2)^-$ specie is the active oxidizing intermediate for epoxidation and possesses a rate constant for epoxidation that is a factor of $2 \cdot 10^4$ larger than that for Nb-OOH/Nb-$(O_2)^{2-}$.

Turnover rates were measured as functions of the concentrations of C_6H_{10} (0.01 – 5 M), H_2O_2 (0.5 – 5 mM), and cyclohexene oxide ($C_6H_{10}O$, 1 – 5 mM). Formation rates of $C_6H_{10}O$ increase in proportion to $[C_6H_{10}]$ but become constant at high $[C_6H_{10}]$ values. The rate of epoxidation is independent of $[H_2O_2]$ when $[C_6H_{10}]$ is low but becomes proportional to $[H_2O_2]$ at high $[C_6H_{10}]$. These results reflect the competitive adsorption of H_2O_2- and C_6H_{10}-derived species, which results in a change in the most abundant reactive intermediate (MARI) on Nb-sites. Upon formation of Nb-$(O_2)^-$, the intermediate reacts either with C_6H_{10} or H_2O_2 to form the epoxidation (i.e., cyclohexene oxide) or decomposition products (i.e., H_2O and O_2), respectively. Measured activation enthalpies ($\Delta H^{\ddagger}$) for epoxidation (72 kJ mol^{-1}) and H_2O_2 decomposition (45 kJ mol^{-1}) show that decomposition is enthalpically favorable, whereas activation entropies ($\Delta S^{\ddagger}$, -35 J mol^{-1} K^{-1} for $C_6H_{10}O$ formation and -91 J mol^{-1} K^{-1} for H_2O_2 decomposition) suggest that epoxidation is entropically favorable. Collectively, these data provide insight to the identity of the reactive surface species responsible for epoxidations and the mechanism for this reaction on transition metal substituted zeolites, which is needed to understand the underlying chemical reasons that lead

to significant differences in rates and selectivities that reflect the elemental identity of the transition metal atoms that facilitate oxidation reactions.

2.2 Materials and Methods

2.2.1 Synthesis of Nb-BEA Catalysts

Niobium-substituted zeolite catalysts were prepared by the post-synthetic modification of commercial zeolite beta.[89-90] Commercial *BEA (Zeolyst, Si:Al ~ 12.5, NH_4^+ cation, Al-BEA) was dealuminated by treatment with concentrated HNO_3 (Macron Chemicals, 69 – 70 wt. %, 20 cm^3 per gram of zeolite) at reflux (448 K) for 20 h. Slurries of Al-BEA and HNO_3 are initially a dark brown color, but the color of these suspensions change to a light tan after four hours at reflux. The dealuminated zeolite (Si-BEA, Si:Al > 1200 determined by inductively couple plasma – optical emission spectroscopy) was then recovered by filtration and washed with concentrated HNO_3 (10 cm^3 g^{-1}) followed by deionized (DI) water (17.8 MΩ, 20 cm^3 g^{-1}). The wet recovered Si-BEA solids were dried in an oven within ambient air for 18 hours at 423 K. The dried solids were then heated to 823 K at 5 K min^{-1} and held at 823 K for 6 hours in flowing dry air (Airgas, Ultra-zero grade, 100 cm^3 min^{-1}) with the intent to remove residual volatiles from the Si-BEA. Nb atoms were incorporated into the framework by liquid-phase adsorption (LPA), which involved stirring Si-BEA in a 0.35 – 3.5 mM solution of $NbCl_5$ (Sigma-Aldrich, 99%, 50 cm^3 g^{-1}) in isopropyl alcohol (VWR Analytical, >99.5%) for 6 hours at 343 K. Volatiles were then removed in vacuo at 6.6 kPa for 30 minutes followed by washing with 75 cm^3 g^{-1} DI water with the intent to remove any residual $NbCl_5$ not exchanged into defects within the framework. The recovered solids were heated to 723 K at 5 K min^{-1} and held at 723 K for 4 hours in flowing dry air (Airgas, Ultra-zero grade, 100 cm^3 min^{-1}) to yield a white powder. Nb-substituted zeolites are referred to as Nb_X-BEA where the subscript denotes the final wt. % of Nb (0.15 – 5.0 wt. %), which was controlled by changing the concentrations of $NbCl_5$ and Si-BEA in the LPA solution.

A 10 wt. % Nb-SiO_2 (Nb_{10}-SiO_2) catalyst was prepared by incipient wetness impregnation of washed SiO_2 (1 g, Sigma-Aldrich, Davisil 646, 35–60 mesh) with 1.2 cm^3 of 0.9 M $NbCl_5$ dissolved in isopropyl alcohol. The catalyst was dried under ambient conditions for 4 h by ramping to 823 K (5 K min^{-1}) for 6 hours under flowing dry air (Airgas, Ultra-zero grade, 100 cm^3 min^{-1}).

2.2.2 Catalyst Characterization

Catalyst metal loadings were quantified using inductively coupled plasma optical emission spectroscopy (ICP-OES, PerkinElmer 2000DV), calibrated against known dilution standards. The reported Nb_x-BEA subscript corresponds to values measured by ICP-OES.

Catalyst crystallinity was confirmed by powder X-ray diffraction (p-XRD). X-ray diffractograms were obtained using a powder X-ray diffractometer (Siemens/Bruker D-5000) with Cu K-α radiation (0.15418 nm) using a step size of 0.02° at 1° min^{-1} in an ambient atmosphere. X-ray diffractograms for commercial NH_4^+-BEA, the dealuminated Si-BEA, and prepared Nb-BEA catalysts are effectively indistinguishable (Figure A1). These comparisons show that the post-synthetic modification method does not affect the crystalline structure of the zeolites, and that framework crystallinity is maintained.

Diffuse reflectance UV-vis (DRUV-vis) spectra were measured from 700 to 175 nm using a spectrophotometer (Agilent, CARY 5) equipped with a diffuse-reflectance accessory (Harrick Cricket®). Spectra were recorded in absolute reflectance (R) mode at ambient pressure and temperature. Magnesium oxide powder (MgO, Sigma Aldrich, 99.995% trace metals basis) was used to collect a total reflectance spectrum for use as a baseline for Kubelka-Munk pseudo absorbances (Fig. A2). Nb-BEA and Nb-SiO_2 samples were ground with MgO (10% sample by weight) prior to measurement. Optical band gaps (E_g) were calculated from the x-intercept of the linear portion of a Tauc plot (Fig. A3).[51, 99] Table 2.1 summarizes the optical band edges of Nb-BEA, Nb_{10}-SiO_2, bulk Nb_2O_5,[100] and calixarene-assisted Nb grafted onto silica (Calix-$Nb_{1.7}$-SiO_2).[51] Nb_{10}-SiO_2 has a band edge (3.7 eV) that is similar to that of bulk Nb_2O_5 (3.4 eV),[100] which indicates that this material contains metal-oxide clusters with bulk-like electronic properties and sizes of at least several nanometers. All Nb-BEA catalysts have band edge energies (4.2 eV) that are much larger than that of bulk Nb_2O_5 and similar to those previously reported (4.0 eV) for isolated atoms grafted onto mesoporous silica.[51] The similarity between the band gaps for $Nb_{0.7}$-BEA and $Nb_{1.5}$-BEA strongly suggests that Nb atoms are incorporated into the zeolite framework as single isolated sites (i.e., the samples contain immeasurable extents of Nb-O-Nb connectivity). If the Nb atoms were not incorporated into the zeolite framework, but rather forming small clusters, the NbO_x clusters would become larger with increasing loadings, which would result in a decreasing band gap. Additionally, Fig. A2 shows the Kubelka-Munk absorbance as a function of wavelength for $Nb_{0.7}$-BEA, $Nb_{1.5}$-BEA, and Nb_{10}-SiO_2. Both Nb-BEA samples show no distinct

absorbance feature beyond ~300 nm, which suggests that no extra-framework Nb^{5+} species exist either as bulk or oligomeric niobia-like phases.[89, 101]

Table 2.1. Optical band edges and wavelengths of maximum absorption obtained from diffuse-reflectance UV-vis spectroscopy Nb-based catalysts.

Sample	Band Edge (eV)	Maximum Absorption (nm)
Bulk Nb_2O_5	3.4[100]	-
$Nb_{10.0}$-SiO_2	3.7	265
Calix-$Nb_{1.7}$-SiO_2	4.0[51]	240
$Nb_{0.7}$-BEA	4.2	255
$Nb_{1.5}$-BEA	4.2	255

Solid-state magic angle spinning-nuclear magnetic resonance (MAS NMR) spectroscopy was performed on a spectrometer (Varian, Unity Inova 300 MHz) equipped with a 4 mm MAS probe (Varian-Chemagnetics, double resonance APEX HX). Approximately 36.4 mg of $Nb_{1.5}$-BEA was packed into a 4 mm zirconia rotor, which was spun at 10 kHz in the spectrometer for MAS-NMR. Powdered octakis(dimethylsilyloxy)silsesquioxane (Q_8M_8) was used for pulse calibration and ^{29}Si chemical shift referencing (Q_8M_8 has a chemical shift of 11.45 ppm, relative to the primary standard, tetramethylsilane at 0 ppm). ^{1}H direct polarization (DP-MAS NMR) was performed with a 10 sec recycle delay with the averaging of 32 scans. $^{1}H \rightarrow ^{29}Si$ cross polarization (CP-MAS NMR) was performed with a 5 sec recycle delay using a 8 ms contact time with the averaging of 6000 scans. ^{29}Si DP-MAS NMR was performed with a 10 sec recycle delay with the averaging of 6000 scans. ^{93}Nb MAS NMR experiments were unsuccessful due to low signal to noise levels even with 69,000 scans with a 1 sec recycle delay.

Figure A4 shows ^{1}H MAS-NMR spectra for $Nb_{1.5}$-BEA. The lack of a distinct feature located at 5.4 ppm is consistent with the incorporation of Nb atoms into silanol pockets during post-synthetic modification.[101] Figure A5a shows the ^{29}Si DP-MAS NMR spectra for $Nb_{1.5}$-BEA, which shows three distinct features at -102, -112, and -115 ppm. The feature at -102 ppm is attributed to Si atoms in a $Si(OH)(OSi)_3$ environment,[101-103] while the features at -112 and -115 ppm are assigned to Si atoms in a $Si(OM)_4$ environment, where M = Si or Nb, which are similar to features seen in Nb-BEA,[101] Ta-BEA,[103] and Zr-BEA.[102] Figure A5b shows the $^{1}H \rightarrow ^{29}Si$ CP-

MAS NMR spectra with an 8 ms contact time, which is used to selectively enhance the excitation of Si atoms that are near ^{1}H atoms. Figure A5b clearly shows the enhancement of the feature located at -102 ppm during cross polarization, which confirms the assignment of this feature to $Si(OH)(OSi)_3$ atoms. In short, the appearance of the -112 and -115 ppm features in Fig. A5a suggest that the Nb atoms are incorporated into the framework as there are two distinct type of Q4 Si atoms (i.e., $Si(OM)_4$), and these features are similar to those observed in related framework-substituted *BEA (i.e., Nb-BEA,[101] Ta-BEA,[103] and Zr-BEA).[102]

Nb-atom incorporation was also characterized by attenuated total reflectance IR spectroscopy (ATR-IR, Bruker Alpha). $Nb_{1.5}$-BEA and Si-BEA samples (~10 mg) were pressed onto a diamond ATR-IR internal reflection element and IR spectra were recorded (32 scans, 2 cm^{-1} resolution) at ambient conditions. Figure A6a shows IR spectra for Si-BEA and $Nb_{1.5}$-BEA samples just after heating to 823 K for 6 h in flowing air (100 cm^3 min^{-1}, Praxair, Ultra-zero grade), both of which exhibit absorbance features centered at 1234, 1075, and 803 cm^{-1}, which correspond to the SiO_4 internal tetrahedral stretch, the ν_{as}(Si-O), and the ν_s(Si-O) features, respectively.[104] $Nb_{1.5}$-BEA also possesses an additional feature in the ATR-IR spectra that is centered at 950 cm^{-1} (Fig. A6c), which corresponds to ν(Si-O-Nb).[10, 101] Additionally, extra-framework Nb atoms would result in a distinct absorbance feature at ~835 cm^{-1} which is assigned to ν_s(O-Nb-O) of oligomeric or polymeric niobia.[105] Figure A6d shows the difference spectra for $Nb_{10.0}$-SiO_2 with respect to SiO_2, and possesses a distinct absorbance feature at 831 cm^{-1}, which suggests that $Nb_{10.0}$-SiO_2 contained oligomeric or bulk-like clusters of niobia on the surface. Notably, the lack of an additional IR absorbance feature (Fig. A6c) near 835 cm^{-1} suggests that these Nb-BEA samples do not contain oligomeric or bulk forms of NbO_x. These data, in conjunction with DRUV-vis and solid-state NMR, strongly suggest that Nb atoms have been incorporated into the *BEA framework and that no extra-framework Nb^{5+} is formed after the post-synthetic modification of *BEA.

The presence of Lewis acid sites was characterized by the FTIR spectroscopy of deuterated acetonitrile (CD_3CN, Cambridge Isotope Laboratories, 99.8% D atom)[106-107] coordinated to $Nb_{1.5}$-BEA and Si-BEA using a custom-made transmission cell, the design of which was described previously.[108] The transmission cell was mounted within an FTIR spectrometer (Bruker, Tensor 37) equipped with a liquid-N_2 cooled HgCeTe detector. Catalysts were pressed into self-supporting wafers (~80 mg) and placed within the stainless-steel cell, which was equipped with CaF_2 windows and connected to a gas manifold by gas-transfer lines that were heated to 423 K via electrical

heating tape (Omega, FGH Series). The catalyst temperature was measured using a K-type thermocouple (Omega) located within the cell. Catalysts were heated to 423 K at 10 K min^{-1} and held at 423 K for 1.5 h under flowing He (50 cm^3 min^{-1}, Airgas, Ultra High Purity) to remove H_2O and then allowed to cool to 298 K. Liquid CD_3CN (1 μL min^{-1}) was fed via a syringe pump (Legato 100, KD Scientific) and vaporized inside the heated gas-transfer lines into a stream of flowing He (50 cm^3 min^{-1}) to generate a mixture (1.2 kPa CD_3CN, 100 kPa He). Each catalyst was then contacted with the CD_3CN/He stream until reaching the saturation coverage of CD_3CN (determined by constant absorbance intensities in FTIR spectra, ~15 min) at which point the CD_3CN flow was stopped. The sample was then heated at 10 K min^{-1} to increasing temperatures in 20 K increments to a maximum temperature of 423 K, and steady-state FTIR spectra (128 scans, 1 cm^{-1} resolution) were acquired continuously.

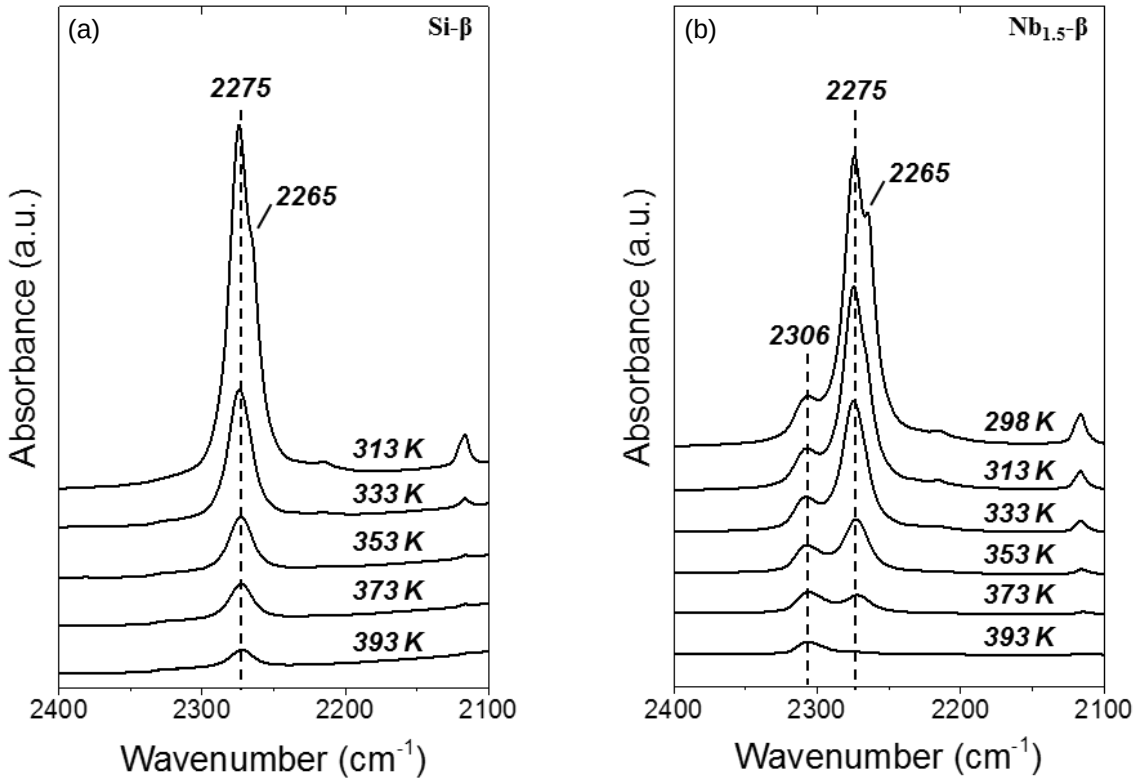

Figure 2.1. Infrared spectra of adsorbed CD_3CN on the (a) Si-BEA and (b) $Nb_{1.5}$-BEA samples at the indicated temperatures within a steam of flowing He (101 kPa). Prior to the acquisition of these spectra, the samples were saturated with CD_3CN at 298 K (1.2 kPa CD_3CN, 100 kPa He, 50 cm^3 min^{-1}), after which CD_3CN flow was stopped.

Figure 2.1 shows representative FTIR spectra for CD_3CN adsorbed on Si-BEA (Fig. 2.1a) and $Nb_{1.5}$-BEA (Fig. 2.1b). Absorption features between 2260 – 2340 cm^{-1} correspond to the $\nu(C\equiv N)$ mode, while the band near 2115 cm^{-1} arises from the $\delta_s(CD_3)$ mode.[107] The absorbance peak located at 2275 cm^{-1} (Fig. 2.1a) is associated with CD_3CN hydrogen bonded to silanol groups located within the zeolite, while the shoulder located at 2265 cm^{-1} is attributed to physisorbed CD_3CN, which weakly interacts with the pore walls.[107] As the temperature of the Si-BEA sample increases, hydrogen-bonded CD_3CN species (2275 cm^{-1}) persist on the surface, while the physisorbed CD_3CN (2265 cm^{-1}) desorb. Spectra of CD_3CN on $Nb_{1.5}$-BEA (Fig. 2.1b, 298 K) largely resemble those of Si-BEA but possess an additional absorption feature at 2306 cm^{-1} that can be attributed to Lewis acid sites associated with adsorption on Nb atoms, similar to CD_3CN features on Sn-BEA.[106] Yet these spectra on $Nb_{1.5}$-BEA show only a single new feature, in contrast to FTIR spectra of CD_3CN on Sn-BEA, which show features at both 2308 and 2316 cm^{-1} and reflect the presence of both open and closed Lewis acid sites.[106] Consequently, we conclude that $Nb_{1.5}$-BEA possesses predominantly one type of Lewis acid site, because additional types of Lewis acid sites would result in multiple absorbance peaks in the 2300 cm^{-1} region.[12] These results (Fig. 2.1) taken together with NMR spectra (Fig. A4 and A5) strongly suggest that the Lewis acid sites are Nb-atoms tetra-coordinated within the zeolite framework.[12]

The UV-vis (Fig. A2 and A3), solid-state NMR (Fig. A4 and A5), and ATR-IR (Fig. A6) data show that Nb atoms are incorporated into the *BEA framework and do not exist as extra-framework bulk or oligomeric niobia. Additionally, the IR spectra of adsorbed CD_3CN (Fig. 2.1b) show a single absorbance feature associated with Lewis acidic sites. It is possible that multiple types of Nb sites exist in Nb-BEA, that have similar IR absorption features for adsorbed CD_3CN and also possess similar heats of adsorption that preclude their detection; however, this seems to be unlikely due to the significant shift in wavenumbers (2308 and 2316 cm^{-1}) and different heats of adsorption seen in Sn-BEA for open and closed sites.[106] These Lewis acid sites are most likely to be Nb atoms tetra-coordinated to the framework of BEA and to possess a single pendant –OH (i.e., $Nb(OSi)_4(OH)$) based on the characterization here, together with previous results that combined experiments (i.e., solid-state NMR, powder XRD, UV-vis, XPS, and IR spectroscopy) and theory (i.e., ab initio DFT calculations) to show that the most energetically stable form of Nb in Nb-BEA is the $Nb(OSi)_4(OH)$ unit.[89, 101]

X-ray photoelectron spectroscopy (XPS) measurements were used to measure the oxidation state of Nb atoms in $Nb_{5.0}$-BEA and H_2O_2-activated $Nb_{5.0}$-BEA and were performed on a Kratos AXIS Ultra spectrometer with a monochromatic Al-Kα (1486.6 eV) X-ray source. High-resolution spectra were collected with 40 eV pass energy, and the binding-energy scales were referenced with respect to the aliphatic C 1s absorbance feature at 284.8 eV. Peak fittings were done in CasaXPS© via the method of Shirley.

2.2.3 Epoxide Formation and H_2O_2 Consumption Rate Measurements

Reaction rates for epoxidation were measured using a batch reactor (100 cm^3, three-neck round bottom flask) equipped with a reflux condenser to minimize evaporative losses. For typical reaction conditions, the reactor was filled with a solvent mixture of ~30 cm^3 acetonitrile (CH_3CN, Macron Chemicals, >99.8%) and 30 μL benzene (Sigma-Aldrich, thiophene free, >99%) as an internal standard. The reagents, C_6H_{10} (Sigma-Aldrich, >99%) or cis-stilbene (Sigma-Aldrich, >96%) and H_2O_2 (Fischer Chemicals, 30 wt. % in H_2O), were added and the reaction mixture was heated to the desired temperature (303 – 333 K) while stirring at 450 rpm. The epoxidation of C_6H_{10} was initiated by introducing ~30 mg of the Nb-BEA catalyst. Small aliquots (~300 μL) were extracted through a 0.22 μm filter (GS-Tek, PVDF filter) to remove suspended catalyst, and thus quench C_6H_{10} epoxidation and H_2O_2 decomposition. All reactants and solvents used were miscible under the conditions tested in this study. The concentrations of $C_6H_{10}O$ and other potential reaction products (e.g., cyclohexane diol and cyclohexanol) were determined as a function of time with a gas chromatograph (HP-5890 Series A) equipped with a non-polar dimethylpolysiloxane capillary column (Agilent, HP-1, 30 m length, 1.05 μm) and a flame ionization detector. All species were identified and response factors were calculated using calibrated mixtures of known standards. The change in the concentration of H_2O_2 was determined by colorimetric titrations using a solution of Cu-based indicator (12 mM neocuproine (Sigma-Aldrich, >98%); 8.3 mM $CuSO_4$ (Fisher Chemicals, >98.6%); 25% v/v ethanol (Decon Laboratories Inc., 100%).[109-110] The concentrations of H_2O_2 in each aliquot was determined from the absorbance at 454 nm, measured using a visible-light spectrophotometer (Spectronic, 20 Genesys), and by comparison to calibrated standards. In all reported data, the selectivity towards $C_6H_{10}O$ formation was >99% (e.g., no common byproducts were detected, such as cyclohexanol or cyclohexane diol) upon reaction of C_6H_{10} with H_2O_2 over Nb-BEA. The carbon balance closed to within 98% for all reactions reported, which

shows all significant reaction products were detected. The calculated uncertainties for all turnover rate measurements are less than 7%, as determined by comparison of repeated measurements.

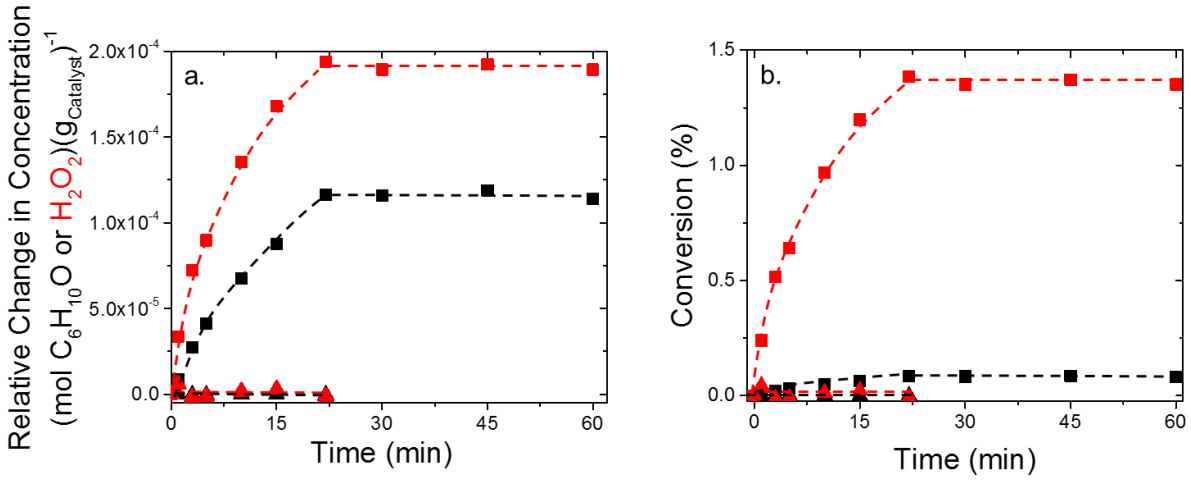

Figure 2.2. Concentration profiles for the formation of $C_6H_{10}O$ (black) and for the consumption of H_2O_2 (red) as a function of time expressed as (a) "Relative Change in Concentration" (given in mol $C_6H_{10}O$ or H_2O $(g_{cat})^{-1}$) for direct comparison between catalysts, as there is no Nb present in Si-BEA, and (b) conversion of C_6H_{10} or H_2O_2 (10 mM C_6H_{10}, 1 mM H_2O_2, $Nb_{1.5}$-BEA (■) or Si-BEA (▲) in CH_3CN, 313 K) with hot filtration at 22 minutes. Lines are intended to guide the eye.

Control experiments were performed using Si-BEA and $Nb_{1.5}$-BEA to demonstrate that the metal centers contained within the zeolite were responsible for C_6H_{10} epoxidation and H_2O_2 consumption. Figure 2.2 shows that turnover numbers (TON) for C_6H_{10} epoxidation and H_2O_2 consumption are undetectable on Si-BEA but increase with time on $Nb_{1.5}$-BEA, which shows that the Nb atoms in the framework catalyze epoxidation and H_2O_2 conversion. The values of the TON become constant (i.e., turnover rates are zero) after hot filtration, suggesting that Nb-atoms do not leach into solution and homogeneously catalyze epoxidation. Additionally, ICP-OES analyses of the reaction solution (after 1 h of reaction) and of the spent $Nb_{1.5}$-BEA show no discernible changes in the Nb content of either the liquid phase or the solid catalyst. The ICP-OES analysis performed has an experimental error of ± 0.01 wt. %, which correlates to a sensitivity of <1 % of the total Nb content of the catalyst. Turnover rates reported in all subsequent sections were obtained in the linear region (i.e., first 5 min) of alkene epoxidation at differential conversion (i.e., <5% conversion of C_6H_{10} and H_2O_2).

Reported rates of C_6H_{10} epoxidation and H_2O_2 consumption were measured in the absence of mass-transfer limitations. To ensure that the Madon-Boudart criterion[111] was satisfied, reactions

were performed with Nb-BEA catalysts with different metal loadings (0.15 – 1.5 wt. % Nb) at constant H_2O_2 concentrations over a range of C_6H_{10} concentrations (Section A2, Fig. A8). Epoxidation turnover rates did not depend on the Nb content over this range of weight loadings, which shows that intra-pellet mass-transfer limitations were insignificant. Reported turnover rates and kinetic analyses are taken from experiments using $Nb_{1.5}$-BEA.

2.2.4 Activation of Nb-BEA with H_2O_2 for XPS Analysis

$Nb_{5.0}$-BEA (200 mg) was combined with a mixture of 2.5 cm^3 CH_3CN and 2.5 cm^3 H_2O_2 (30 wt. % in H_2O) to produce H_2O_2-activated $Nb_{5.0}$-BEA for XPS analysis of the Nb oxidation states. The $Nb_{5.0}$-BEA changed from bleached white to pale yellow in color upon addition of the H_2O_2-CH_3CN mixture. This slurry was then heated to 333 K for 1 h with the intent of reacting all of the Nb active sites with H_2O_2 in solution. The slurry was then dried under dynamic vacuum (5.3 kPa) at 333 K for 30 minutes followed by static vacuum (0.02 kPa) for 12 hours, which gave the final H_2O_2-activated $Nb_{5.0}$-BEA material (light yellow solid).

2.2.5 In Situ UV-Vis and IR Spectroscopy

In situ UV-vis spectroscopy was used to measure the reactivity of the different intermediates for epoxidation on Nb-BEA. $Nb_{0.3}$-BEA samples were pressed into 7 mm diameter self-supporting pellets (~5 mg) and loaded into a custom-built UV-vis liquid flow cell. Reactant and solvent solutions were introduced using a high-performance liquid chromatography (HPLC) pump (Waters, 515), and UV-vis spectra were collected using a 45-degree reflection probe (Avantes, solarization-resistant fibers) attached to an AvaFast fiber-optic spectrometer (Avantes 2048) with a compact deuterium-halogen light source (Avantes, 200 – 1700 nm). The $Nb_{0.3}$-BEA samples were activated by flowing (1 cm^3 min^{-1}) a solution of H_2O_2 in CH_3CN (0.1 M H_2O_2, 0.4 M H_2O) over the pellet at 313 K until the absorbance features at ~320 nm were unchanging (~15 min). A H_2O_2-free solution of CH_3CN (0.4 M H_2O) then flowed through the reactor (1 cm^3 min^{-1}) to remove all liquid-phase and weakly adsorbed H_2O_2 from the system at 313 K. This treatment did not attenuate the UV-vis absorbance features, which shows that the surface species on H_2O_2-activated $Nb_{0.3}$-BEA were stable at 313 K under pure CH_3CN. The reactivity of the surface intermediates on $Nb_{0.3}$-BEA was measured by continuously acquiring UV-vis spectra (600 msec integration time, co-adding 100 scans per spectrum) while flowing a solution of C_6H_{10} in CH_3CN

(0.1 M C_6H_{10}, 0.4 M H_2O), similar to that used for rate measurements in the batch reactor. Reference spectra for all experiments were obtained using a $Nb_{0.3}$-BEA pellet within a flowing CH_3CN solution (0.4 M H_2O) at 313 K. Peak smoothing, background subtraction, and spectral deconvolution were performed in OriginPro® (Section A3.1 for example spectra).

In situ attenuated total reflectance infrared (ATR-IR) spectroscopy was used to characterize the vibrational structure and chemical stability of the intermediates formed upon exposing Nb-BEA to H_2O_2. Untreated $Nb_{1.5}$-BEA was deposited onto a ZnSe cylindrical internal reflection element (IRE, International Crystal Labs) by dip coating. Briefly, 100 mg of $Nb_{1.5}$-BEA were suspended in ~10 cm^3 of CH_3OH (Macron Chemicals, anhydrous) and the IRE was dipped into the suspension and subsequently dried at ambient temperature to retain the powdered catalyst on the IRE. A series of 10 cycles were typically used to accumulate a thin layer of $Nb_{1.5}$-BEA. The catalyst-coated IRE was then loaded into a customized ATR flow cell (Axiom TNL-120) equipped with two liquid inlets and one outlet with a cell volume of 40 μL. The ATR cell was mounted within the sample compartment of a FTIR spectrometer (Bruker Vertex 70, RapidScan) and liquid streams were introduced at controlled flowrates using two high-pressure piston pumps (SSI Series 1), which were controlled using LabView™. Background scans were obtained at steady state under pure flowing DI H_2O at 333 K after loading the ATR cell. Transient FTIR spectra showing changes upon introducing H_2O_2 were obtained while flowing aqueous H_2O_2 (0.03 M H_2O_2 in DI H_2O, 0.5 cm^3 min^{-1}) over the $Nb_{1.5}$-BEA coated IRE for 2.5 h at 333 K. Subsequently, a stream of pure DI H_2O was pumped through the cell at 0.5 cm^3 min^{-1} for 1 h. Reported FTIR spectra for these experiments are the average of 1000 scans taken at a resolution of 4 cm^{-1} and were acquired every 66 seconds. Deconvolution of steady-state FTIR spectra were performed in OriginPro® by fixing the centers of the known framework vibrations attributed to the BEA framework of $Nb_{1.5}$-BEA (950 cm^{-1}, 1090 cm^{-1})[10, 101, 104, 112-113] and fitting the residual absorbance features with Gaussian functions.

Modulation excitation spectroscopy (MES) is a powerful technique, in which a periodic stimulation is applied to the system while acquiring spectra as a function of time. The time domain response is then converted to a phase domain response, and the spectral changes that occur at the frequency of the applied stimulation are extracted using a phase sensitive detection (PSD) method described by the following equation:

$$A_k(\varphi_k^{PSD}) = \frac{2}{T}\int_0^T A(t)\, sin(k\omega t + \varphi_k^{PSD})dt \quad (2.1)$$

where *A(t)* and $A_k(\varphi_k^{PSD})$ are time- and phase- domain response of the active species respectively, T is the length of a time period, ω is the demodulation index and φ_k^{PSD} is the user defined phase demodulation angle. The application of the MES-PSD technique to FTIR spectra of intermediates on catalytic surfaces greatly increases the signal to noise ratio, suppresses the spectral contributions of static (i.e., spectator) species, and reveals high quality spectra containing contributions only of intermediates that change with respect to our applied stimulus (i.e., changing reactant concentrations).[114]

MES-PSD was used with ATR-IR to confirm that the predominant surface intermediates that form upon exposing $Nb_{1.5}$-BEA to aqueous H_2O_2 solutions (vide supra) are, in fact, active species for the epoxidation of alkenes. MES-PSD experiments were performed by sinusoidally modulating the flowrates of two liquid streams (0.065 M H_2O_2 in CH_3CN, and 0.1 M C_6H_{10} in CH_3CN) from 0 to 0.5 $cm^3\ min^{-1}$ with a period of 0.5 h (which approximately corresponds to the turnover rate for epoxidation at these conditions), while maintaining a total flowrate of 0.5 $cm^3\ min^{-1}$. Spectra (128 scans, 4 cm^{-1}) were acquired every 8.5 s over 3 h. Flowrates were sinusoidally modulated and controlled on the two piston pumps through use of a LabView program that changes the set point of the pump in a step-wise manner every 0.5 s to approximate a sine wave with the desired frequency. Verification of sinusoidal reactant modulation was done by monitoring and absorbance feature at 1630 cm^{-1}, that is assigned to the ν_2 bending mode of H_2O,[115] as a function of phase angle (Fig. A9) because H_2O was only present in the H_2O_2-containing stream. The recorded time domain spectra were resampled to a single period, and subsequently the spectra of the active species were extracted by PSD using equation 2.1. Details of the analysis method are described in Section A4.1.

2.3 Results and Discussion

2.3.1 Spectroscopic Evidence for an Irreversibly Formed Active Intermediates on Nb

Metal-bound oxygen intermediates (i.e., superoxide (M-$(O_2)^-$), peroxide (M-$(O_2)^{2-}$), and hydroperoxide (M-OOH)), have been implicated in the epoxidation of alkenes (e.g., propylene, cyclohexene, allylic alcohol) on metal-oxide catalysts (e.g., Ta-SBA-15,[58] TS-1,[116-117] and peroxoniobate ionic liquids).[118] The primary distinction between superoxide and peroxide species

is the charge of the $-O_2$ moiety bound to the metal (i.e., superoxide ($-O_2^-$) and peroxide ($-O_2)^{2-}$), and is, therefore, reflected in the oxidation state of the metal center (e.g., Ti^{3+}-$(O_2)^-$ vs. Ti^{4+}-$(O_2)^{2-}$; or Nb^{4+}-$(O_2)^-$ vs. Nb^{5+}-$(O_2)^{2-}$).[119-120] Zecchina[121] and Frei[116] used combinations of IR, Raman, and UV-vis spectroscopy to show that reactive Ti^{4+}-$(O_2)^{2-}$ and/or Ti^{4+}-OOH species form by activation of H_2O_2 on TS-1. However, Ratnasamy et al. used in situ electron paramagnetic resonance (EPR) spectroscopy and determined that a paramagnetic Ti-superoxo (Ti^{3+}-$(O_2)^-$) species is created on TS-1 upon activation of H_2O_2 and is active and selective for the epoxidation of allylic alcohol,[50] and the exact identity of the reactive intermediate on TS-1 (specifically the Ti^{4+}-OOH or Ti^{3+}-$(O_2)^-$)[119-120, 122-123] is still debated. Similar types of hydroperoxo, peroxo, and superoxo species (i.e., Nb^{5+}-OOH, Nb^{5+}-$(O_2)^{2-}$, or Nb^{4+}-$(O_2)^-$) likely form when H_2O_2 reacts with Nb-BEA, and the vibrational structure, electronic transitions, and oxidation states, of the reactive complexes may be determined with the combination of FTIR, UV-vis, and x-ray photoelectron spectroscopy.

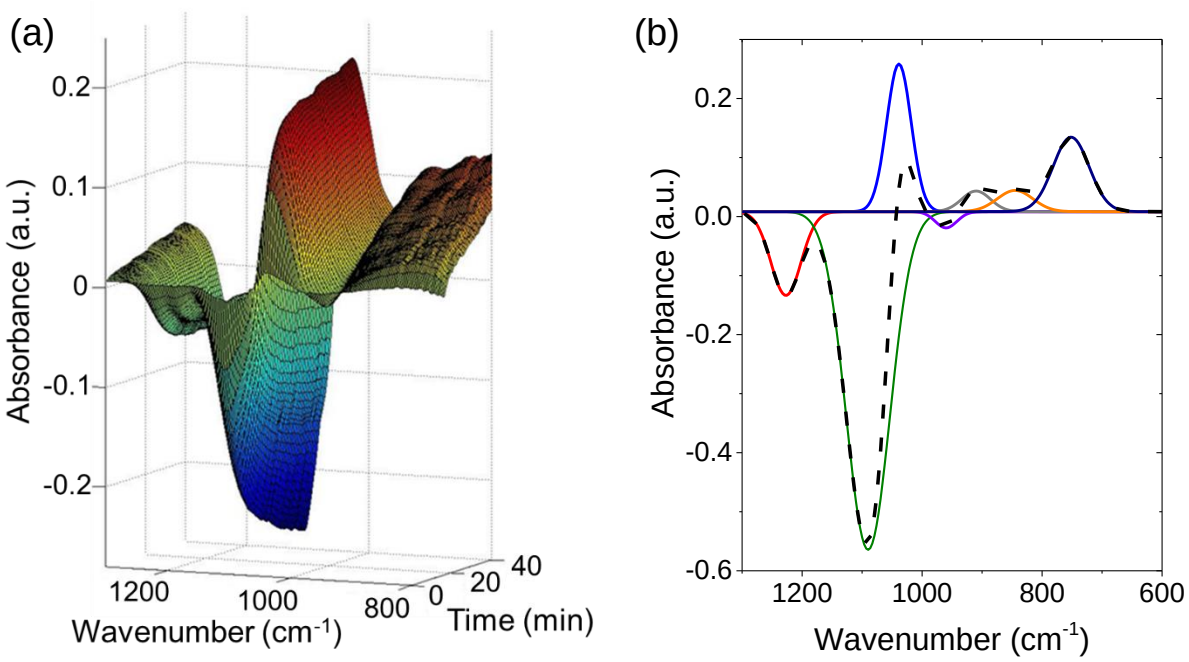

Figure 2.3. In situ FTIR spectra obtained upon exposing $Nb_{1.5}$-BEA to H_2O_2 (0.03 M H_2O_2 in CH_3CN, 0.5 cm^3 min^{-1}, 333 K) showing, (a) changes in the infrared spectra of Nb-BEA upon first contact with flowing H_2O_2, and (b) deconvoluted FTIR spectrum obtained at steady-state after flowing H_2O_2 for 2 h. Vibrational frequencies and peak assignments are given in Table 2.2.

Table 2.2. Observed Vibrational Frequencies and Mode Assignments for the Deconvoluted FTIR Spectrum in Figure 2.3b.

Vibrational Frequency (cm^{-1})	Vibrational Assignment	Parent Species
750	Libration[115]	Water
845	ν(O-O)[122, 124]	Nb^{5+}-OOH/ Nb^{5+}-$(O_2)^{2-}$
915	Internal tetrahedral – asymmetric stretch[104]	*BEA Framework
950	ν(Si-O-Nb)[10, 101]	Nb-BEA
1040	ν(O-O)[124-126]	Nb^{4+}-$(O_2)^{-}$
1090	Internal tetrahedral – asymmetric stretch[10, 104, 112-113]	*BEA Framework
1230	Internal tetrahedral – asymmetric stretch[10, 104, 112-113]	*BEA Framework

Figure 2.3 shows FTIR spectra obtained upon exposing $Nb_{1.5}$-BEA to a flowing solution of H_2O_2 (0.03 M H_2O_2 in CH_3CN, 0.5 cm^3 min^{-1}, 333 K). Figure 2.3a shows that several new absorption features appear (i.e., 1040 cm^{-1}, 845 cm^{-1}, and 915 cm^{-1}), while existing absorption features attenuate (i.e., 950 cm^{-1}, 1090 cm^{-1}, and 1230 cm^{-1}) when $Nb_{1.5}$-BEA contacts H_2O_2, and Figure 2.3b shows a representative steady-state FTIR spectrum acquired ~2 h after initiating the flow of H_2O_2. The steady-state spectrum (Fig. 2.3b) is comprised of seven individual components, which are listed in Table 2.2 along with the corresponding vibrational assignments. The negative absorbance features at 1090 and 1230 cm^{-1} and the positive feature at 915 cm^{-1} are attributed to the quenching and stimulation, respectively, of internal framework tetrahedral Si-O vibrational modes in the *BEA framework.[10, 104, 112-113] The absorbance feature at 750 cm^{-1} corresponds to the libration band of liquid-phase H_2O.[115] The absorbance peak observed at 845 cm^{-1} closely matches previously reported features at 837 cm^{-1} (Ti^{4+}-OOH/Ti^{4+}-$(O_2)^{2-}$ moieties on TS-1)[116, 123] and in the range of 850-888 cm^{-1} (Nb^{5+}-OOH and Nb^{5+}-$(O_2)^{2-}$) species on niobate ionic liquids[118] and bulk niobia,[124] respectively. Consequently, we attribute this feature to Nb^{5+}-OOH/Nb^{5+}-$(O_2)^{2-}$ intermediate(s). The feature at 1040 cm^{-1} resembles that previously attributed to superoxide (O_2^-)

moieties bound to Nb-centers of bulk Nb_2O_5.[124] The formation of Nb^{5+}-$(O_2)^{2-}$ and Nb^{4+}-$(O_2)^-$ species must occur concomitantly with the cleavage of an Nb-O-Si linkage shown by the formation of the negative feature at 950 cm^{-1}.[101] Additionally, Corma[125] and Wan[126] observed spectral features with similar wavenumber (900 – 1150 cm^{-1}) upon activating O_2 over CeO_2-based catalysts, which form superoxide species bound to differently coordinated metal cations (e.g., defect sites). Thus, the peak at 1040 cm^{-1} likely corresponds to an Nb^{4+}-$(O_2)^-$ (i.e., Nb-superoxide) intermediate. Finally, all of the spectral features (Table 2.2) persist when H_2O contacts the IRE (Fig. A10) after activation of H_2O_2 at 333 K, which shows that the Nb^{4+}-$(O_2)^-$ and Nb^{5+}-OOH/Nb^{5+}-$(O_2)^{2-}$ intermediates form irreversibly and do not spontaneously decompose in the presence of H_2O. This finding is also in agreement with results from DRUV-vis spectroscopy, discussed below, which are used to further identify and test the stability of these intermediates. The isomerization between hydroperoxide, peroxide, and superoxide intermediates has been proposed over TS-1 catalysts,[121-122] which suggests that interconversion between Nb^{5+}-OOH, Nb^{5+}-$(O_2)^{2-}$, and Nb^{4+}-$(O_2)^-$ species may also occur upon the irreversible activation of H_2O_2 (Scheme 2.1). For the purpose of brevity, Nb^{4+}-$(O_2)^-$ will be referred to as Nb^{4+}-(O_2) while Nb^{5+}-OOH and Nb^{5+}-$(O_2)^{2-}$ will be collectively referred to as Nb^{5+}-(O_2).

X-ray photoelectron spectroscopy (XPS) was used to determine the oxidation state of Nb in both untreated and H_2O_2-activated (Section 2.2.4) $Nb_{5.0}$-BEA samples in order to verify the presence of Nb^{4+} species (i.e., Nb^{4+}-(O_2)). Figure 2.4a shows the XPS spectra for untreated $Nb_{5.0}$-BEA in the Nb 3d region (200 – 220 eV), which possesses a doublet with absorbance peaks centered at 210.6 and 208.0 eV that correspond to Nb^{5+} $3d_{3/2}$ and $3d_{5/2}$, respectively.[127-128] These features shift to lower binding energies when the $Nb_{5.0}$-BEA sample has been treated with H_2O_2 (details given in section 2.2.4). The peak energies of the H_2O_2-treated $Nb_{5.0}$-BEA are 209.7 and 207.0 eV, which resemble reported values for Nb^{4+},[127] and is consistent with the presence of the proposed Nb^{4+}-(O_2) species. Under ultra-high vacuum conditions (i.e., 10^{-9} Torr), the preferred state of the H_2O_2-activated Nb-BEA is Nb^{4+}-(O_2), because the lack of free protons favors the formation of the superoxo species, as shown for H_2O_2-activated TS-1.[50]

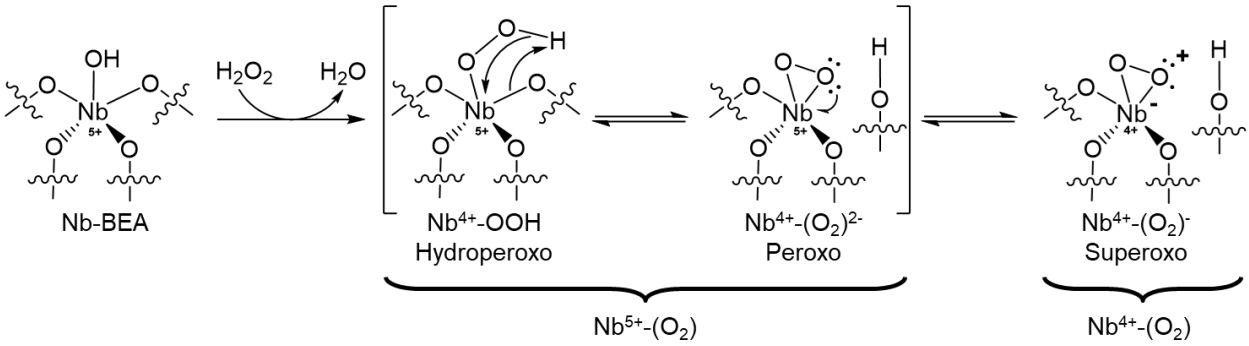

Scheme 2.1. Activation of H_2O_2 to form Nb^{5+}-OOH with the interconversion of Nb^{5+}-OOH, Nb^{5+}-$(O_2)^{2-}$, and Nb^{4+}-$(O_2)^{-}$. The oxidation state of each Nb center is depicted beneath the atom.

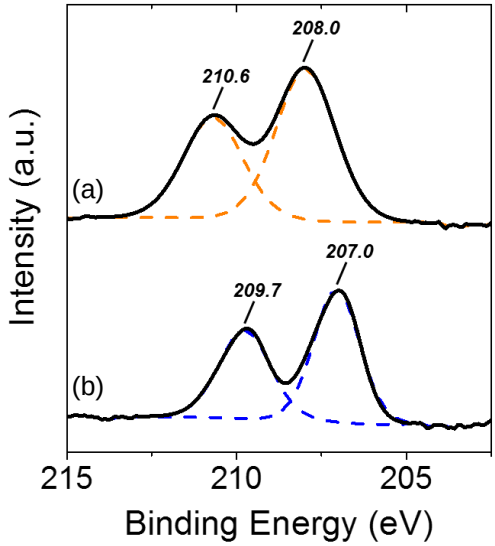

Figure 2.4. X-ray photoelectron spectra of the Nb 3d region with peak fittings (dashed lines) for (a) untreated $Nb_{5.0}$-BEA and (b) H_2O_2-treated $Nb_{5.0}$-BEA. The peak fittings from the different oxidation states are color-coded for clarity: Nb^{4+} (blue) and Nb^{5+} (orange). Spectra are referenced to an aliphatic C 1s feature at 284.8 eV. The H_2O_2 treatment procedure is described in section 2.2.4.

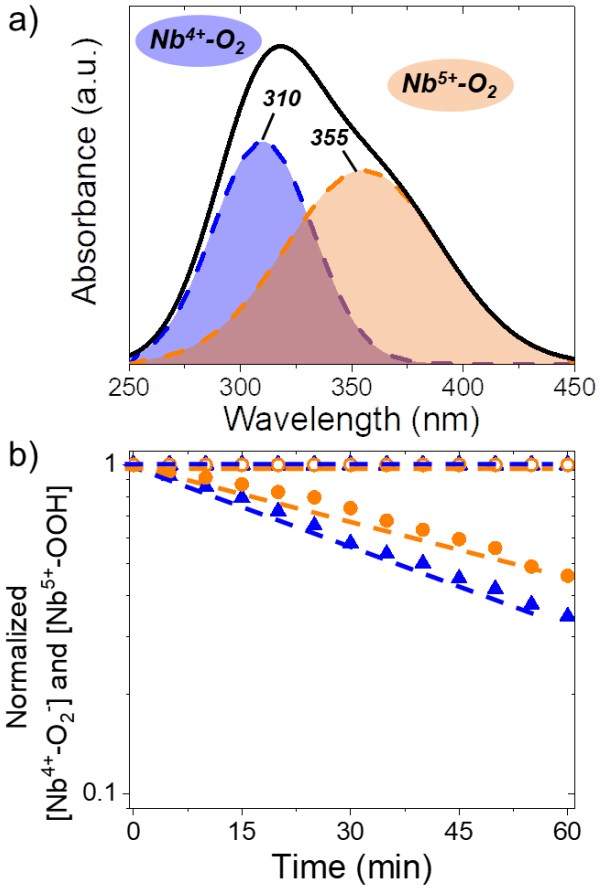

Figure 2.5. (a) UV-vis spectra of H_2O_2-treated $Nb_{0.3}$-BEA in flowing CH_3CN (0.4 M H_2O) at 348 K (black), and deconvoluted peaks (dashed) centered at 301 (blue) and 365 nm (orange); and (b) changes in the normalized coverages of [Nb^{4+}-(O_2)] (330 nm, ▲) and [Nb^{5+}-(O_2)] (370 nm, ●) as a function of time after contact with C_6H_{10} in CH_3CN (0.1 M C_6H_{10}, 0.4 M H_2O, 1 cm^3 min^{-1}, closed symbols) or pure DI H_2O (1 cm^3 min^{-1}, open symbols) at 313 K. Dashed lines are intended to guide the eye.

The surface intermediates (i.e., Nb^{4+}-(O_2) and Nb^{5+}-(O_2)) generated by reacting $Nb_{0.3}$-BEA with H_2O_2 appear as distinct absorption features in in situ DRUV-vis spectroscopy. Figure 2.5a shows a UV-vis spectrum of H_2O_2-treated $Nb_{0.3}$-BEA (section 2.2.5), which contains two distinct absorbance bands at 310 and 355 nm that are assigned to Nb^{4+}-(O_2) and Nb^{5+}-(O_2) moieties, respectively.[122, 124] Figure 2.5b shows that the normalized intensities of the Nb^{4+}-(O_2) (310 nm) and Nb^{5+}-(O_2) (355 nm) features decrease with an exponential dependence on time when the H_2O_2-treated $Nb_{0.3}$-BEA contacts a flowing solution of C_6H_{10} in CH_3CN (0.1 M C_6H_{10}, 0.4 M H_2O, 1 cm^3 min^{-1}). However, Figure 2.5b shows also that neither the 310 or 355 nm absorbance feature change noticeably even after one hr of contact with a flowing stream of pure DI H_2O (1 cm^3 min^{-}

[1]), which demonstrates further that these intermediates (i.e., Nb^{4+}-(O_2) or Nb^{5+}-(O_2)) form irreversibly. These data, along with steady-state IR spectra obtained under a flow of H_2O (Fig. A10), strongly suggest that Nb-BEA activates H_2O_2 irreversibly to form both Nb^{4+}-(O_2) and Nb^{5+}-(O_2) intermediates, in contrast to proposed mechanisms on similar Ti- and Ta-based catalysts, where H_2O_2 activation is proposed to occur reversibly (and often in a quasi-equilibrated fashion).[58-59, 88, 98]

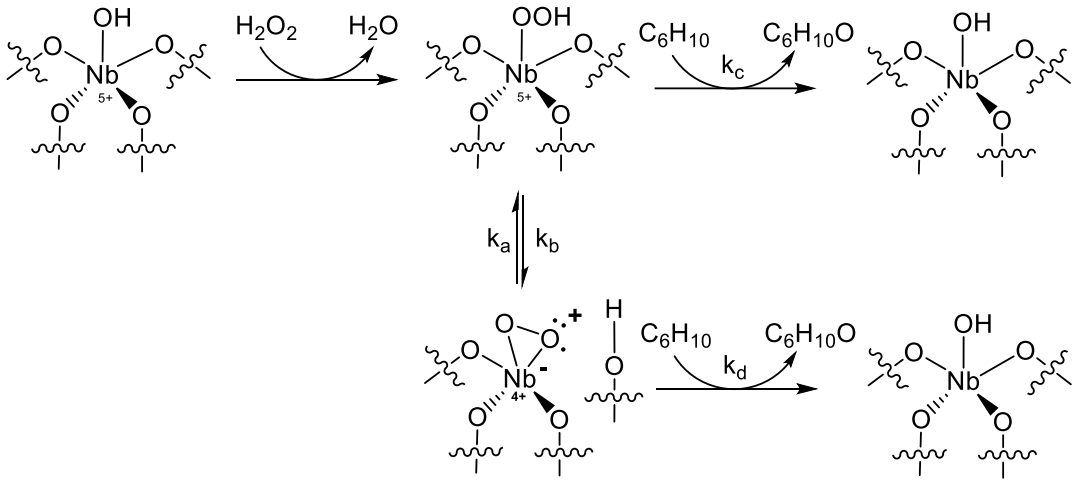

Scheme 2.2. Formation and consumption of active species on Nb-BEA. Nb^{5+}-(O_2) (Nb^{5+}-OOH shown) and Nb^{4+}-(O_2) form upon reaction of H_2O_2 with Nb-BEA, and these species interconvert, and may be consumed by reaction with C_6H_{10}. Formation of Nb^{5+}-(O_2) and Nb^{4+}-(O_2) occurs during the activation of H_2O_2 over $Nb_{0.3}$-BEA by flow of H_2O_2 in CH_3CN (Section 2.2.5).

The intensity of these two UV-vis features (Fig. 2.5a, 310 and 355 nm, normalized by their initial intensities) attenuate with an exponential dependence on time at different rates when H_2O_2-treated $Nb_{0.3}$-BEA contacts a solution of C_6H_{10} in CH_3CN (0.1 M C_6H_{10}, 0.4 M H_2O, 1 cm^3 min^{-1}), and the differences in the rates of consumption of these species reflect the nature of the elementary steps that consume Nb^{4+}-(O_2) and Nb^{5+}-(O_2) (Scheme 2.2). Nb^{4+}-(O_2) and Nb^{5+}-(O_2) species may be consumed by reaction with C_6H_{10}, but these species may also interconvert during the course of the reaction, as shown in Schemes 2.1 and 2.2.[121] Consequently, the change in coverage of Nb^{4+}-(O_2) and Nb^{5+}-(O_2) depends on the summed rates of formation and consumption of each species, which take the forms of:

$$\frac{d[Nb^{4+}-(O_2)]}{dt} = k_a[Nb^{5+}-(O_2)] - k_b[Nb^{4+}-(O_2)] - k_d[Nb^{4+}-(O_2)][C_6H_{10}] \quad (2.2)$$

$$\frac{d[Nb^{5+}-(O_2)]}{dt} = k_b[Nb^{4+}-(O_2)] - k_a[Nb^{5+}-(O_2)] - k_c[Nb^{5+}-(O_2)][C_6H_{10}] \quad (2.3)$$

where $[Nb^{4+}\text{-}(O_2)^-]$ and $[Nb^{5+}\text{-}(O_2)]$ represents the coverage of $Nb^{4+}\text{-}(O_2)$ and $Nb^{5+}\text{-}(O_2)$, $[C_6H_{10}]$ is the concentration of C_6H_{10}, k_a is the rate constant for the interconversion of $Nb^{5+}\text{-}(O_2)$ to $Nb^{4+}\text{-}(O_2)$, k_b is the rate constant for the interconversion of $Nb^{4+}\text{-}(O_2)$ to $Nb^{5+}\text{-}(O_2)$, and k_c and k_d are the rate constants for the epoxidation of C_6H_{10} with $Nb^{5+}\text{-}(O_2)$ and $Nb^{4+}\text{-}(O_2)$, respectively. Pseudo first-order kinetics are assumed for the reaction of $Nb^{5+}\text{-}(O_2)$ and $Nb^{4+}\text{-}(O_2)$ with C_6H_{10}, and $[C_6H_{10}]$ is constant because C_6H_{10} flows continuously through the reactor and conversion of C_6H_{10} is negligible. MATLAB™ is used to numerically solve these two coupled differential equations (equations 2.2 and 2.3), while iteratively optimizing the rate constants (i.e., k_i) to fit the experimental data (Section A3.2). Table 2.3 shows the optimized rate constants for Scheme 2.2. The value of k_d is calculated to be ~$2 \cdot 10^4$ times that of k_c, which shows directly that $Nb^{4+}\text{-}(O_2)$ is the reactive species that is responsible for all observed epoxidation rates and that this species is more than four orders of magnitude more reactive than the $Nb^{5+}\text{-}(O_2)$ species. The consumption of $Nb^{5+}\text{-}(O_2)$ is, therefore, attributed to its interconversion to reform additional $Nb^{4+}\text{-}(O_2)$ throughout the course of the reaction (i.e., value of k_b significantly greater than k_a). Collectively, these data show that both $Nb^{4+}\text{-}(O_2)$ and $Nb^{5+}\text{-}(O_2)$ are formed upon activation of H_2O_2, but only $Nb^{4+}\text{-}(O_2)$ participates directly in the epoxidation of C_6H_{10}, while $Nb^{5+}\text{-}(O_2)$ simply interconverts to partially replenish $Nb^{4+}\text{-}(O_2)$ during reaction.

Table 2.3. Numerically optimized rate constants k_i for the interconversion of $Nb^{5+}\text{-}(O_2)$ and $Nb^{4+}\text{-}(O_2)$ and reaction with C_6H_{10} (Scheme 2.2). See Section A3.2 for a complete description of the procedure used to optimize parameters and fit the experimental data.

k_i	Numerically Optimized Value (min^{-1})
k_a	$2.3 \cdot 10^{-4}$
k_b	$2.0 \cdot 10^{-2}$
k_c	$1.3 \cdot 10^{-5}$
k_d	$2.7 \cdot 10^{-1}$

Modulation excitation spectroscopy (MES) experiments were employed to support the conclusion that Nb^{4+}-(O_2) is the active intermediate for the epoxidation of C_6H_{10}. The flow rates H_2O_2 and cyclohexene in CH_3CN (Section 2.2.5) were modulated sinusoidally with the intent to periodically populate the catalyst surface with the active species (i.e., Nb^{4+}-(O_2) and Nb^{5+}-(O_2)) and subsequently consume these species by cyclohexene epoxidation. Figure 2.6a displays phase domain spectra (obtained by resampling all spectra into a single period, converting to the phase domain, and employing phase sensitive detection, see Section A4.1), that show only the active surface species whose coverages change at frequencies comparable to the modulation (i.e., contributions from spectator species are suppressed). Figure 2.6 shows a broad feature at 864 cm^{-1} that is assigned to ν(C-C) of a C_6 ring of either C_6H_{10} or $C_6H_{10}O$.[129] Notably, this broad 864 cm^{-1} feature is perfectly out of phase (i.e., 180º phase shift) with the absorbance feature corresponding to the active Nb^{4+}-(O_2) intermediate (1024 cm^{-1}, Fig. 2.6b), which supports the conclusion that Nb^{4+}-(O_2) species are consumed by reaction with C_6H_{10}, which is followed by the replacement of Nb^{4+}-(O_2) with C_6H_{10} or $C_6H_{10}O$ as the MARI on the catalyst surface. Unfortunately, the spectroscopic feature at 845 cm^{-1} attributed to Nb^{5+}-(O_2) (Fig. 2.3b, Nb^{5+}-(O_2)) is overwhelmed by the broad feature at 864 cm^{-1}, which precludes clear analysis of how the coverage of Nb^{5+}-(O_2) species vary with the changes in the concentrations of C_6H_{10} and H_2O_2. However, the previous analysis of the in situ UV-vis spectra (Figure 2.5, Table 2.3) shows already that the Nb^{5+}-(O_2) intermediates do not directly participate in epoxidation reactions. In summary, the combined in situ FTIR and UV-vis data (Figures 2.3, 2.5-2.6) suggest that H_2O_2-activation over $Nb_{1.5}$-BEA occurs irreversibly and that Nb^{4+}-(O_2) (and not Nb^{5+}-(O_2)) is the active intermediate for C_6H_{10} epoxidation upon activation of H_2O_2 by Nb-BEA.

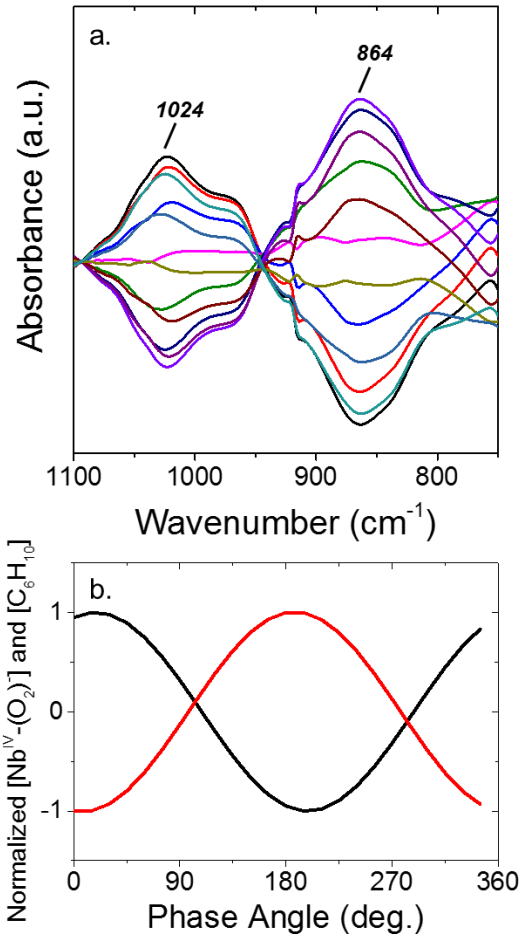

Figure 2.6. (a) Phase-angle resolved in situ FTIR spectra showing spectral contributions of active surface species for C_6H_{10} epoxidation on $Nb_{1.5}$-BEA, and (b) Normalized Nb^{4+}-$(O_2)^-$ (1024 cm^{-1}, black) and C_6H_{10} (864 cm^{-1}, red) IR-feature absorbances as a function of phase angle. Spectra were obtained while sinusoidally modulating the flowrates of C_6H_{10} (0.1 M C_6H_{10} in CH_3CN) and H_2O_2 (0.065 H_2O_2 in CH_3CN) solutions (0.5 cm^3 total volumetric flowrate, 333 K, Section 2.5). Lines correspond to FTIR spectra obtained at 30° increments of the demodulation phase angle.

The conclusion that Nb^{4+}-(O_2) is the active species for alkene epoxidation is not immediately intuitive, because superoxide species are typically though to be one electron oxidants (or even reductants) and not two-electron ($2e^-$) oxidants. In order for Nb-(O_2) to undergo a $2e^-$ oxidation (e.g., alkene epoxidation), the process must involve concomitant oxidation of the Nb-metal center from Nb^{4+} to Nb^{5+} and the reformation of a Nb-O-Si framework bond. Similar processes have been proposed to occur through a biradical, stepwise reaction on homogeneous vanadium complexes,[130-131] and Nb-$(O_2)^-$ superoxide species may react in an analogous manner (Scheme S2.2). The epoxidation of cis-stilbene provides one method to test this hypothesis and to

determine whether the epoxidation reaction proceeds through a concerted reaction or by a stepwise reaction, which would be consistent with the participation of Nb^{4+}-(O_2) as the active intermediate.[132] The reaction of cis-stilbene with $Nb_{1.5}$-BEA (0.01 M cis-stilbene, 0.01 M H_2O_2, in CH_3CN, 323 K) produces nearly equimolar quantities of cis- and trans-stilbene oxides (the exact ratio of cis- to trans-stilbene oxide is equal to 0.96). This equimolar ratio suggests that alkene epoxidation over Nb-BEA occurs through the biradical stepwise mechanism (e.g., Scheme A2), which provides sufficient time for the coordinated alkene intermediate to isomerize about the central C=C bond prior to oxirane cyclization. Collectively, these spectroscopic data and product selectivities provide compelling evidence that H_2O_2 irreversibly activates over Nb-BEA to form a pool of Nb^{5+}-(O_2) and Nb^{4+}-(O_2) species that interconvert, and that from this pool, Nb^{4+}-(O_2) species participate directly in the epoxidation of alkenes by a biradical, stepwise reaction pathway (Scheme A2).

2.3.2 Dependence of Turnover Rates on Reactant Concentrations and Mechanistic Interpretation

Figure 2.7a shows turnover rates for the formation of $C_6H_{10}O$ as a function of [C_6H_{10}] (0.01 – 5 M C_6H_{10}, 1 mM H_2O_2, 313 K) over $Nb_{1.5}$-BEA, and Figure 2.7b shows turnover rates for $C_6H_{10}O$ formation as a function of [H_2O_2] (0.5 – 5 mM H_2O_2, 0.05 and 3 M C_6H_{10}, 313 K). Rates of epoxidation depend linearly on [C_6H_{10}] and do not change with [H_2O_2] (0.5 – 5 mM, 5 mM C_6H_{10}) at low [C_6H_{10}] (0.01 – 0.1 M C_6H_{10}), which suggests that the active sites are saturated with an H_2O_2-derived intermediate, such as adsorbed H_2O_2 or Nb^{4+}-(O_2)/Nb^{4+}-(O_2) (section 2.3.1). Rates of epoxidation become independent of [C_6H_{10}] as [C_6H_{10}] increases further (0.1 – 5 M C_6H_{10}), and this change indicates that the identity of the MARI changes to a C_6H_{10}-derived intermediate (e.g., C_6H_{10} or $C_6H_{10}O$). This is likely due to the increasing amount of C_6H_{10}-derived species (i.e., C_6H_{10} or $C_6H_{10}O$) occupying additional Nb active sites which decreases the number of sites that exist as the active Nb^{4+}-$(O_2)^-$ species. Additionally, Figure 2.7b shows the turnover rates become proportional to [H_2O_2] (0.5 – 3 mM) at higher [C_6H_{10}] (3 M), which is consistent with a change in the MARI from an H_2O_2-derived intermediate to a C_6H_{10}-derived MARI. Figure 2.7a shows that the rate of epoxidation depends inversely on the $C_6H_{10}O$ concentration (1 – 5 mM) within this same range of [C_6H_{10}] (3 M) and [H_2O_2] (1 mM), which implies that $C_6H_{10}O$ binds strongly to the active site and inhibits rates.

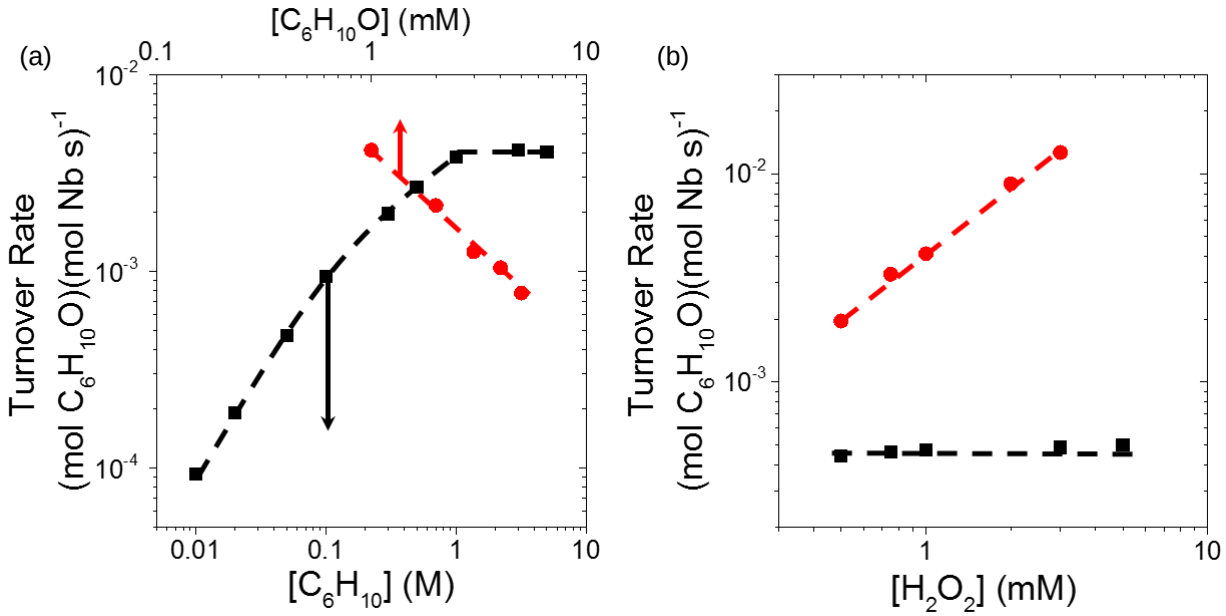

Figure 2.7. Turnover rates for the formation of $C_6H_{10}O$ as a function of (a) $[C_6H_{10}]$ (■, 1 mM H_2O_2, $Nb_{1.5}$-BEA, 313 K) and $[C_6H_{10}O]$ (●, 3 M C_6H_{10}, 1 mM H_2O_2, $Nb_{1.5}$-BEA, balance CH_3CN to 30 cm^3, 313 K) and (b) as a function of $[H_2O_2]$ (50 mM C_6H_{10} (■) or 3 M C_6H_{10} (●), $Nb_{1.5}$-BEA, 313 K). Error bars omitted for clarity, and lines are intended to guide the eye.

Previously proposed mechanisms for alkene epoxidation on metal-oxide catalysts (i.e., TS-1[98] and Ta-SBA-15)[58-59] assume that steps for the adsorption of the alkene, H_2O_2, epoxide, and the formation of the reactive intermediate (e.g., M-OOH or M-$(O_2)^-$) are quasi-equilibrated (QE) and that the epoxidation of the alkene by the M-(O_2) species is the sole kinetically relevant (KR) step. Such mechanisms give rate expressions (Section A5 contains the rate expressions based on these previous models) that predict epoxide formation rates that do not depend on $[H_2O_2]$ and increase linearly with $[C_6H_{10}]$ at low $[C_6H_{10}]$ (equation A10), and that reaction rates become constant with $[C_6H_{10}]$ but proportional to $[H_2O_2]$ at greater $[C_6H_{10}]$ (equation A11). The previously described mechanisms and rate expressions for cyclohexene and cyclooctene epoxidation on TS-1[98] and Ta-SiO_2[58-59] are consistent with the rate data shown here (Figs. 2.7a and 2.7b) as a function of $[H_2O_2]$ and $[C_6H_{10}]$, but fail to predict the dependence on $[C_6H_{10}O]$. These previous studies did not report changes in rates as a function of the epoxide concentration. Several aspects of the previously proposed mechanisms are inconsistent with the results shown in this article (and perhaps with chemical intuition). The in situ FTIR and UV-vis spectra show that neither the Nb^{4+}-(O_2) or the Nb^{5+}-(O_2) species decompose or reform H_2O_2 in the presence of H_2O (Section 2.3.1), which

demonstrate that these intermediates form irreversibly (Scheme 2.3, step 3) when H_2O_2 reacts with the metal center (e.g., Nb). Notably, these results disagree with previous assumptions that M-(O_2) species form on Ti- and Ta-based catalysts by QE processes.[58-59, 98] Chemical intuition also suggests that H_2O_2 is not likely to reform from the Nb^{4+}-(O_2) and Si-OH groups (created by hydroperoxidolysis of the Nb-O bond) when the sample is hydrated (Scheme 2.3, reverse step 3), because the formation of H_2O_2 from H_2O and the surface function is most likely endothermic and thermodynamically disfavored under these conditions. Therefore, the mechanism shown below (Scheme 2.3) differs from previous proposals in a few significant ways.

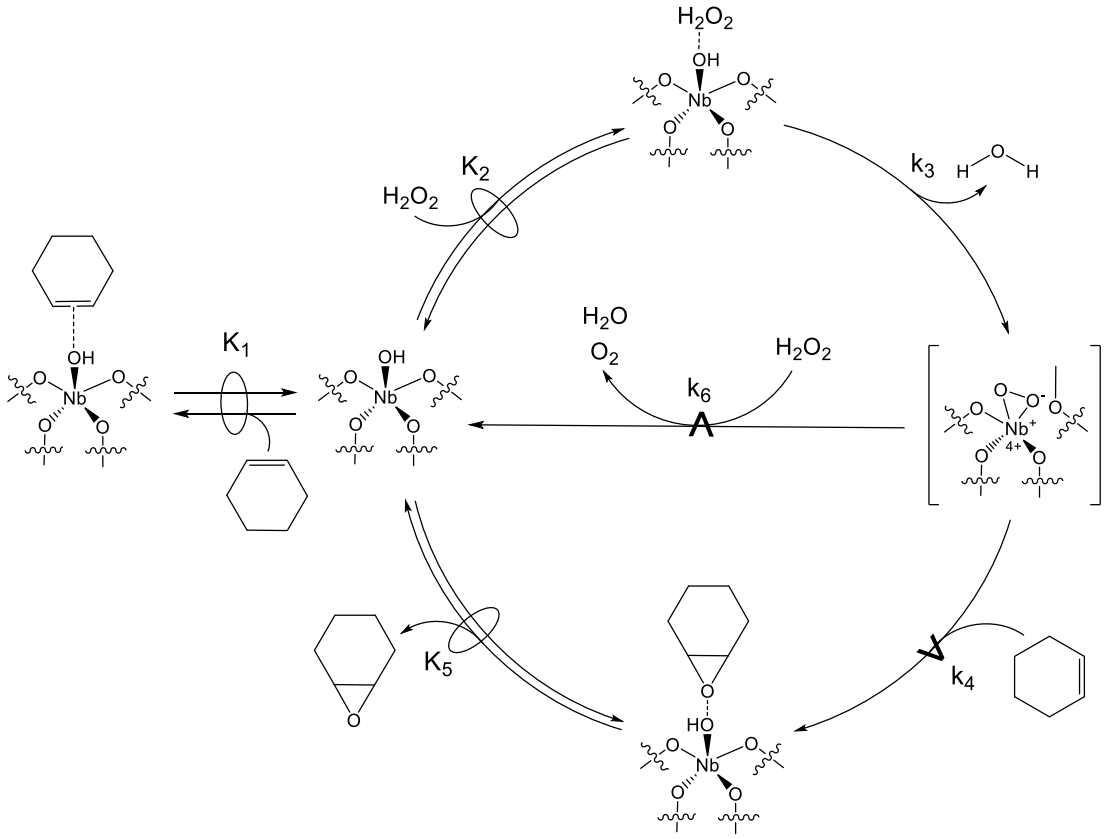

Scheme 2.3. Proposed mechanism for cyclohexene epoxidation with H_2O_2 over Nb-BEA. subscripts for rate constants or equilibrium constants (k_x or K_x, respectively) denote the number of the elementary step. The proposal for an active Nb^{4+}-(O_2) intermediate is supported by XPS (Fig. 2.4) and time-resolved in situ FTIR (Fig. 2.3 and 2.6) and UV-vis spectroscopy (Fig. 2.5).

Scheme 2.3 depicts our proposed mechanism for the epoxidation of C_6H_{10} with H_2O_2 over Nb-BEA. This scheme includes quasi-equilibrated adsorption and desorption of C_6H_{10} (step 1), H_2O_2 (step 2), and $C_6H_{10}O$ (step 5), and the irreversible formation of Nb^{4+}-(O_2) (step 3). The

epoxidation of C_6H_{10} (step 4) and the bimolecular decomposition of H_2O_2 (step 6) occur in kinetically relevant, irreversible steps that involve Nb^{4+}-(O_2) and C_6H_{10} or H_2O_2 co-reactants, respectively. A Langmuir-Hinshelwood mechanism seems unlikely because the average distance between adjacent Nb atoms (2.64 nm)[133] is too large for interaction between adsorbates.[134-135] Scheme 2.3 suggests net $C_6H_{10}O$ formation rates (r_E) that depend on the number of Nb^{4+}-(O_2) intermediates and the concentration of C_6H_{10} in solution as:

$$r_E = k_4[C_6H_{10}] \cdot [Nb^{4+} - (O_2)] \tag{2.4}$$

where [Nb^{4+}-(O_2)] is the number of Nb^{4+}-(O_2) species and k_4 is the rate constant for the epoxidation of C_6H_{10} with Nb^{4+}-(O_2). Application of the pseudo-steady state hypothesis (PSSH) to the number of Nb^{4+}-(O_2) complexes yields the following rate expression:

$$\frac{r_E}{[L]} = \frac{k_3 k_4 K_2 [C_6H_{10}] \cdot [H_2O_2] \cdot [*]}{(k_4[C_6H_{10}] + k_6[H_2O_2])} \tag{2.5}$$

where k_x and K_x are the rate and equilibrium constants, respectively, for each step x (Scheme 2.3) and [*] is the number of available Nb-OH moieties (i.e., active sites) that can bind and react with species in solution (or weakly associate with silica near the active site). An expression for $[*]$ is given from the sum of all likely surface intermediates:

$$[L] = [*] + [C_6H_{10}\,*] + [H_2O_2\,*] + [Nb - (O_2)] + [C_6H_{10}O\,*] \tag{2.6}$$

where $[L]$ is the total number of active sites, [Nb-(O_2)] is the pool of Nb^{4+}-(O_2) and Nb^{5+}-(O_2) species, and $[C_6H_{10}\,*]$, $[H_2O_2\,*]$, and $[C_6H_{10}O\,*]$ are the number of adsorbed C_6H_{10}, H_2O_2, and $C_6H_{10}O$ species, respectively. Equation 2.6 can then be re-stated in terms of the rate and equilibrium constants as well as the liquid-phase reactant concentrations by application of the PSSH to each specie:

$$[L] = \left([*] + K_1[C_6H_{10}] \cdot [*] + K_2[H_2O_2] \cdot [*] + \frac{k_3 K_2 [H_2O_2] \cdot [*]}{(k_4[C_6H_{10}] + k_6[H_2O_2])} + K_5[C_6H_{10}O] \cdot [*]\right) \tag{2.7}$$

The combination of equations 2.5 and 2.7 yield a complete rate expression for $C_6H_{10}O$ formation:

$$\frac{r_E}{[L]} = \frac{k_3 k_4 K_2 [C_6H_{10}] \cdot [H_2O_2]}{(k_4[C_6H_{10}] + k_6[H_2O_2])\left(1 + K_1[C_6H_{10}] + K_2[H_2O_2] + \frac{k_3 K_2 [H_2O_2]}{(k_4[C_6H_{10}] + k_6[H_2O_2])} + K_5[C_6H_{10}O]\right)} \quad (2.8)$$

The form of this full rate equation simplifies in the limit when active sites become saturated with H_2O_2-derived intermediates (i.e., Nb^{4+}-(O_2)/Nb^{5+}-(O_2) are the MARI) as is expected in the limit of low $[C_6H_{10}]$:$[H_2O_2]$ reactant ratios:

$$\frac{r_E}{[L]} = k_4[C_6H_{10}] \quad (2.9)$$

Equation 2.9 is consistent with the $C_6H_{10}O$ formation rates that increase in proportion to $[C_6H_{10}]$ at low $[C_6H_{10}]$ (Figure 2.7a, 0.01 – 0.1 M C_6H_{10}), and which do not depend on $[H_2O_2]$ (Figure 2.8b, 0.5 – 5 mM H_2O_2, 5 mM C_6H_{10}). Turnover rates for epoxidation depend inversely on $[C_6H_{10}O]$ at high $[C_6H_{10}]$, because adsorbed $C_6H_{10}O$ becomes the MARI at values of $[C_6H_{10}]$ greater than 0.5 M. Intuitively, $C_6H_{10}O$ becomes the MARI at high $[C_6H_{10}]$ only when small amounts of epoxide (present as a reagent contaminant, or upon initial formation of $C_6H_{10}O$) are present. In this limit, equation 2.8 simplifies to:

$$\frac{r_E}{[L]} = \frac{k_3 k_4 K_2 [C_6H_{10}][H_2O_2]}{(k_4[C_6H_{10}] + k_6[H_2O_2])[C_6H_{10}O]} \quad (2.10)$$

The denominator in equation 2.10 shows that the rate of epoxidation when adsorbed $C_6H_{10}O$ is the MARI depends on the propensity of Nb-$(O_2)^-$ to epoxidize C_6H_{10} ($k_4[C_6H_{10}]$) relative to decompose by reaction with H_2O_2 ($k_6[H_2O_2]$).

2.3.3 Mechanistic Interpretation for H_2O_2 Decomposition over Nb-BEA

Control experiments show that in the absence of Nb-BEA, no H_2O_2 decomposition is observed after 4 h at 333 K (data not shown). Values of $[H_2O_2]$, however, decrease steadily with time when H_2O_2 contacts Nb-BEA. The unimolecular decomposition of H_2O_2 via a Nb^{4+}-(O_2) intermediate cannot account for H_2O_2 consumption, because FTIR (Fig. A10) and UV-vis spectra (Fig. 2.5b) show that the Nb^{4+}-(O_2) species are stable over multiple hours when they are isolated

from liquid-phase C_6H_{10} and H_2O_2. Therefore, H_2O_2 decomposition likely occurs through a bimolecular reaction between Nb^{4+}-(O_2) and a liquid-phase H_2O_2 molecule.[59] The rate of this reaction follows the form:

$$r_D = k_6[H_2O_2] \cdot [Nb^{4+} - (O_2)] \tag{2.11}$$

where r_D is the rate of H_2O_2 consumption via decomposition over Nb-BEA and k_6 is the rate constant for the bimolecular reaction between Nb^{4+}-(O_2) and a H_2O_2 molecule in solution. The expression for total H_2O_2 consumption is obtained from the sum of equations 2.4 and 2.11 to yield:

$$r_{H_2O_2} = k_4[C_6H_{10}] \cdot [Nb^{IV} - (O_2)] + k_6[H_2O_2] \cdot [Nb^{4+} - (O_2)] \tag{2.12}$$

where $r_{H_2O_2}$ is the rate of total H_2O_2 consumption through epoxidation and decomposition processes. Application of the PSSH to Nb^{4+}-(O_2) (Section 2.3.2, algebraic manipulation omitted) allows equation 2.12 to be restated in terms of liquid concentrations as:

$$\frac{r_{H_2O_2}}{[L]} = \frac{k_3K_2[H_2O_2]}{\left(1+K_1[C_6H_{10}]+K_2[H_2O_2]+\frac{k_3K_2[H_2O_2]}{(k_4[C_6H_{10}]+k_6[H_2O_2])}+K_5[C_6H_{10}O]\right)} \tag{2.13}$$

Equation 2.13 shows that the rate of H_2O_2 consumption depends only on the rate of C_6H_{10} epoxidation ($k_4[C_6H_{10}]$) or H_2O_2 decomposition ($k_6[H_2O_2]$) when surfaces are saturated with Nb^{4+}-(O_2). For all other identities of the MARI, H_2O_2 consumption is controlled by the rate of H_2O_2 activation at the reactive Nb-centers. This shows that the H_2O_2 selectivity for epoxidation can be controlled by reaction at conditions which solely maximize the turnover rate for $C_6H_{10}O$ formation.

2.3.4 H_2O_2 Selectivity for Epoxidation and Mechanistic Implications

The selective use of H_2O_2 for epoxidations is a necessary economic consideration before a catalyst can be adapted for industrial epoxidation chemistries, and consequently requires the ratio of the rates for epoxidation to H_2O_2 consumption (i.e., $r_E/r_{H_2O_2}$) to approach unity (i.e., 100%

selectivity). From the combination of equations 2.8 and 2.13, the ratio of the rate of $C_6H_{10}O$ formation to that for H_2O_2 consumption (Fig. A11) yields the following expression:

$$\alpha = \frac{r_E}{r_{H_2O_2}} = \frac{k_4[C_6H_{10}]}{k_4[C_6H_{10}]+k_6[H_2O_2]} \tag{2.14}$$

Equation 2.14 may be linearized, with respect to inverse $[C_6H_{10}]$, by taking the inverse of α to give:

$$\alpha^{-1} = \frac{r_{H_2O_2}}{r_E} = 1 + \frac{k_6[H_2O_2]}{k_4[C_6H_{10}]} \tag{2.15}$$

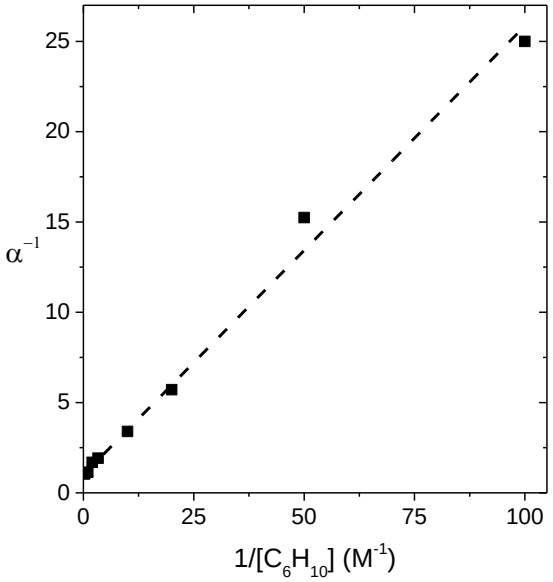

Figure 2.8. Ratio of total H_2O_2 consumption to $C_6H_{10}O$ formation as a function of inverse C_6H_{10} concentration on $Nb_{1.5}$-BEA (1 mM H_2O_2, 313 K). Dashed line represents linear fit to equation 2.15 with an r^2 of 0.995.

Figure 2.8 shows values of α^{-1} as a function of inverse $[C_6H_{10}]$ (1 mM $[H_2O_2]$, 313 K). The value of the slope (found to be 0.25) shows that $k_4[C_6H_{10}] >> k_6[H_2O_2]$ at high $[C_6H_{10}]$ (1 – 5

M), which indicates that in the limit of high $[C_6H_{10}]$:$[H_2O_2]$, equation 2.10 can be approximated as follows:

$$\frac{r_E}{[L]} = \frac{k_3 K_2 [H_2O_2]}{[C_6H_{10}O]} \tag{2.16}$$

which qualitatively agrees with the trends observed in Figures 2.7a (i.e., $r_E \sim [C_6H_{10}]^0 \cdot [C_6H_{10}O]^{-1}$) and 2.7b ($r_E \sim [H_2O_2]^1$) when $[C_6H_{10}]$:$[H_2O_2]$ reactant ratios are large. Overall, the proposed mechanism (Scheme 2.3) agrees with the spectroscopic observations in Figures 2.3 – 2.6 and the rate data presented in Figures 2.7 and 2.8.

2.3.5 Epoxidation and Decomposition Activation Enthalpies ($\Delta H^{\ddagger}$) and Entropies ($\Delta S^{\ddagger}$)

Transition-state theory (TST) provides a theoretical foundation to relate the stability of a reference state (e.g., the most abundant reactive intermediate) to an activated complex that facilitates the reaction (i.e., the transition state).[75, 136] Here, the values of apparent activation enthalpies ($\Delta H^{\ddagger}$) and entropies ($\Delta S^{\ddagger}$) can be used to compare the relative stability of the transition states that selectively activate H_2O_2 and epoxidize an alkene to those that facilitate non-selective H_2O_2 decomposition. TST, in conjunction with our proposed mechanism (Scheme 2.3), proposes that the reactant species (e.g., Nb^{4+}-(O_2) and C_6H_{10}) exist in equilibrium with the transition state (i.e., Nb^{4+}-(O_2)-$C_6H_{10}^{\ddagger}$) for the elementary step for epoxidation (i.e., Scheme 2.3, step 4) [110].

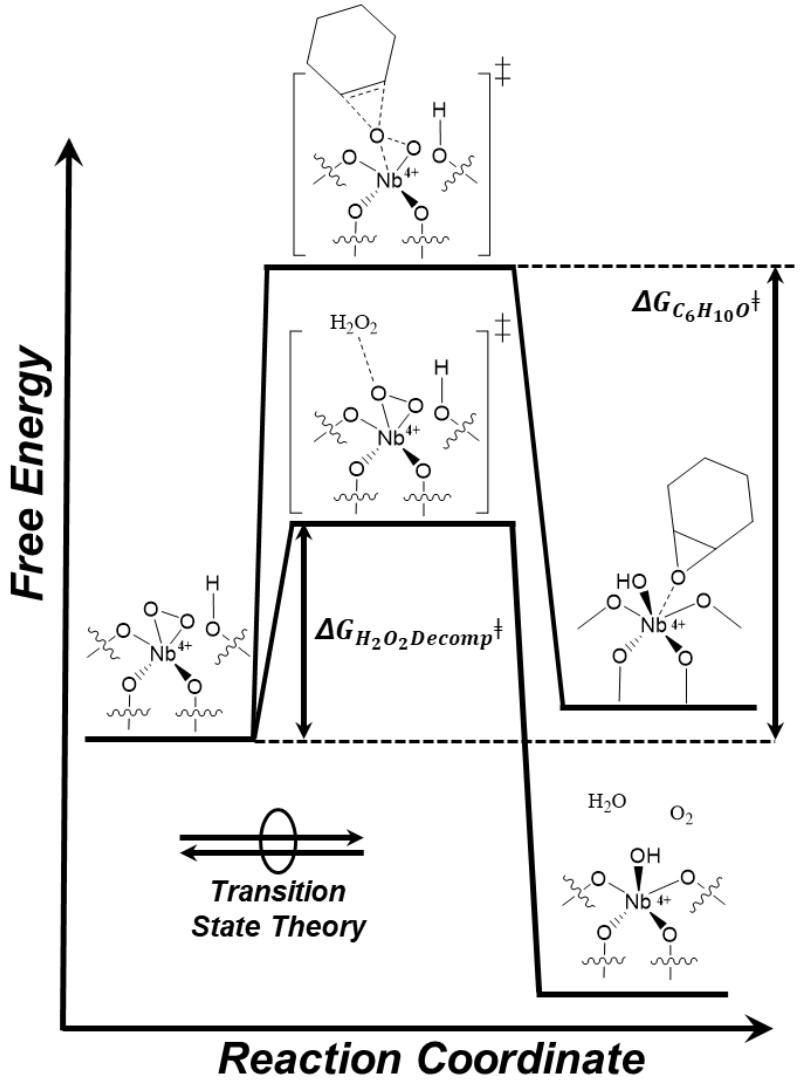

Scheme 2.4. Thermochemical cycle depicting changes in free energy in the reaction sequence shown in Scheme 2.3, which forms transition states for epoxide formation and H_2O_2 decomposition through reaction with Nb^{4+}-(O_2).

The combined equilibria are expressed as:

$$Nb^{4+} - (O_2) + C_6H_{10} \overset{K^{\ddagger}_E}{\rightleftharpoons} [Nb - (O_2) - C_6H_{10}{}^{\ddagger}] \tag{2.17}$$

$$Nb^{4+} - (O_2) + H_2O_2 \overset{K^{\ddagger}_D}{\rightleftharpoons} [Nb - (O_2) - H_2O_2{}^{\ddagger}] \tag{2.18}$$

where $K^{\ddagger}_E$ and $K^{\ddagger}_D$ are the transition state equilibrium constants for $C_6H_{10}O$ formation and H_2O_2 decomposition, respectively. Expression of the rate of epoxidation and H_2O_2 decomposition in terms of the number of transition states (i.e., $[Nb^{4+}\text{-}(O_2)\text{-}C_6H_{10}{}^{\ddagger}]$ or $[Nb^{4+}\text{-}(O_2)\text{-}H_2O_2{}^{\ddagger}]$), yields:

$$\frac{r_E}{[L]} = \frac{k_B T}{h}\left[Nb^{4+} - (O_2) - C_6H_{10}{}^{\ddagger}\right] \tag{2.19}$$

$$\frac{r_D}{[L]} = \frac{k_B T}{h}\left[Nb^{4+} - (O_2) - H_2O_2{}^{\ddagger}\right] \tag{2.20}$$

where T is the temperature in Kelvin, and k_B and h are Boltzmann's and Planck's constant, respectively. When the rates of reaction are measured on $Nb^{4+}\text{-}(O_2)/Nb^{5+}\text{-}(O_2)$ saturated surfaces, the equations 2.19 and 2.20 may be expressed in terms of reactant concentrations and transition-state equilibrium constants:

$$\frac{r_E}{[L]} = \frac{k_B T}{h} K_E^{\ddagger}[C_6H_{10}] \tag{2.21}$$

$$\frac{r_D}{[L]} = \frac{k_B T}{h} K_D^{\ddagger}[H_2O_2] \tag{2.22}$$

which allows the values of $K^{\ddagger}_E$ and $K^{\ddagger}_D$ to be determined by measuring the turnover rates for each reaction pathway at a given temperature. Values of $K^{\ddagger}_x$ may be expressed in terms of the apparent free energy change of activation ($\Delta G^{\ddagger}$), and subsequently $\Delta H^{\ddagger}$ and $\Delta S^{\ddagger}$

$$K_x^{\ddagger} = e^{-\Delta G_x^{\ddagger}/RT} = e^{-\Delta H_x^{\ddagger}/RT} e^{\Delta S_x^{\ddagger}/R} \tag{23}$$

where R is the ideal gas constant and the subscript x indicates that the associated variable corresponds to the formation of product x (i.e., epoxidation (E) for $C_6H_{10}O$ and decomposition (D) for H_2O). Figure A12 shows measured values for $K^{\ddagger}_E$ and $K^{\ddagger}_D$ as functions of inverse temperature, which are used to determine experimental values for $\Delta H^{\ddagger}_E$, $\Delta H^{\ddagger}_D$, $\Delta S^{\ddagger}_E$, and $\Delta S^{\ddagger}_D$ by combining equations 2.21 – 2.23.

Table 2.4. Catalyst Activation Enthalpies and Entropies for C_6H_{10} Epoxidation and H_2O_2 Decomposition on a Nb^{4+}-(O_2)/Nb^{5+}-(O_2) Covered Surface.[a]

Catalyst	$\Delta H^{\ddagger}_E$ (kJ mol^{-1})	$\Delta S^{\ddagger}_E$ (J mol^{-1} K^{-1})	$\Delta H^{\ddagger}_D$ (kJ mol^{-1})	$\Delta S^{\ddagger}_D$ (J mol^{-1} K^{-1})
$Nb_{1.5}$-BEA	72 ± 3	-35 ± 21	45 ± 2	-91 ± 30

[a]Activation enthalpies and entropies were calculated from measured transition-state equilibrium constants ($K^{\ddagger}$, Figure A12) and equation 2.23. Error in activation enthalpies and entropies was estimated by the linear regression analysis performed to fit the Eyring equation to the data in Fig. A12.

Table 2.4 shows values of $\Delta H^{\ddagger}_E$, $\Delta H^{\ddagger}_D$, $\Delta S^{\ddagger}_E$, and $\Delta S^{\ddagger}_D$ for Nb-BEA calculated from $K^{\ddagger}_E$ and $K^{\ddagger}_D$ (Fig. A12, equations 2.21 and 2.22). $\Delta H^{\ddagger}$ values for epoxidation (72 kJ mol^{-1}) are 27 kJ mol^{-1} higher than for H_2O_2 decomposition (45 kJ mol^{-1}), which show that H_2O_2 decomposition is enthalpically favored to that of C_6H_{10} epoxidation. Alternatively, $\Delta S^{\ddagger}$ values for H_2O_2 decomposition (-91 J mol^{-1} K^{-1}) are significantly more negative than for C_6H_{10} epoxidation (-35 J mol^{-1} K^{-1}), which makes epoxidation entropically favored in comparison to H_2O_2 decomposition. Interestingly, epoxidation is entropically favored over H_2O_2 decomposition, which suggests H_2O_2 selectivity is maximized by running the reaction at higher temperatures. This finding is not immediately intuitive as H_2O_2 and H_2O_2-derived intermediates are generally thought to decompose rapidly (in comparison to many other species) at elevated temperatures. Besides the non-intuitive differences in $\Delta H^{\ddagger}$, the selectivities for H_2O_2 to epoxidize C_6H_{10} reflect the ratio of the concentrations of the co-reactants (i.e., H_2O_2 or C_6H_{10}) for these bimolecular pathways, because the fate of the Nb^{4+}-(O_2) depends on the likelihood that this reactive intermediate first encounter liquid-phase C_6H_{10} or H_2O_2.

2.4 Conclusions

Ex situ XPS and in situ UV-vis and FTIR spectra reveal two types of metal-bound oxygen species (i.e., Nb^{4+}-(O_2) and Nb^{5+}-(O_2)) that form upon the irreversible activation of H_2O_2 over Nb-BEA. Time-resolved UV-vis spectra acquired in situ reveal that Nb^{4+}-(O_2) (i.e., superoxide) species is responsible for alkene epoxidation, which is further confirmed by the isomeric distribution (cis:trans ~ 1) of the epoxide products from reaction with cis-stilbene. Collectively, these data, when combined with the observed dependencies of reaction rates on C_6H_{10}, H_2O_2, and $C_6H_{10}O$ provide a complete mechanistic understanding of alkene epoxidation over Nb-BEA that

is consistent with an Eley-Rideal mechanism and indicate that the reactive form of oxygen (i.e., Nb^{4+}-(O_2)) forms irreversibly under reaction conditions. Additionally, this mechanism also accurately describes the dependence of epoxidation rates on reactant concentrations observed in previous studies on similar Ti- and Ta-based catalysts, which had assumed the quasi-equilibrated formation of the reactive intermediate. Calculated values of $\Delta H^{\ddagger}$ and $\Delta S^{\ddagger}$ for $C_6H_{10}O$ formation and H_2O_2 decomposition demonstrate that epoxide formation is enthalpically disfavored, which suggests that H_2O_2 selectivity towards epoxidation is maximized at higher temperatures. Overall, these results can aid in the rational design of increasingly selective catalysts for alkene epoxidation with H_2O_2 and provide methods to probe other metals to observe possible periodic trends in reactivity.

CHAPTER THREE

Periodic Trends in Alkene Epoxidation over Groups 4 and 5 Framework-Substituted Zeolites[II]

Abstract

Group 4 and 5 framework substituted zeolites have been used for alkene epoxidation reactions for decades, yet the underlying properties that determine the selectivities and turnover rates of these catalysts have not yet been elucidated. Here, a combination of kinetic, thermodynamic, and *in situ* spectroscopic measurements show that when group 4 (i.e., Ti, Zr, and Hf) or 5 (i.e., Nb and Ta) transition metals are substituted into zeolite *BEA, the metals that form stronger Lewis acids give greater selectivities and rates for the desired epoxidation pathway and present smaller enthalpic barriers for both epoxidation and H_2O_2 decomposition reactions. *In situ* UV-vis spectroscopy shows that these group 4 and 5 materials activate H_2O_2 to form pools of hydroperoxide, peroxide, and superoxide intermediates. Time-resolved UV-vis measurements and the isomeric distributions of stilbene epoxidation products demonstrate that the active species for epoxidations on group 4 and 5 transition metals are only M-OOH/-$(O_2)^{2-}$ and M-$(O_2)^{-}$ species, respectively. Mechanistic interpretations of kinetic data suggest that these group 4 and 5 materials catalyze cyclohexene epoxidation and H_2O_2 decomposition through largely identical Eley-Rideal mechanisms that involve the irreversible activation of coordinated H_2O_2 followed by reaction with an alkene or H_2O_2. Epoxidation rates and selectivities vary over five- and two-orders of magnitude, respectively, among these catalysts and depend exponentially on the energy for ligand-to-metal charge transfer (LMCT) and the functional Lewis acid strength of the metal centers. Together these observations show that more electrophilic active-oxygen species (i.e., lower energy LMCT) are more reactive and selective for epoxidations of electron-rich alkenes and explain why Ti-based catalysts have been identified as the most active among early transition metals for these reactions. Further, H_2O_2 decomposition possesses a weaker dependence on Lewis acidity than epoxidation, which suggests that the design of catalysts with increased Lewis acid strength will simultaneously increase the reactivity and selectivity of alkene epoxidation.

[II]This chapter has been adapted from the following publication:
Bregante, D.T.; Flaherty, D.W.; "Periodic Trends in Alkene Epoxidation over Group IV and V Framework Substituted Zeolite Catalysts: A Kinetic and Spectroscopic Study"
Journal of the American Chemical Society, **2017**, *139*, 6888 – 6898.

3.1 Introduction

Small-molecule oxidations are among the most important and well-studied reactions in synthetic chemistry.[137] Alkene epoxidation is of particular importance, as epoxides (e.g., propylene oxide, styrene oxide, etc.) are important precursors and monomers for the production of pharmaceuticals and epoxy resins.[72-73, 82] Despite the importance of epoxides, current production methods typically involve the use of hazardous organic-peroxide oxidants[82] or caustic-waste producing Cl-containing processes (e.g., the chlorohydrin process).[77] Molecular oxygen (O_2) is utilized for the epoxidation of ethylene (C_2H_4) to form ethylene oxide (EO) over promoted Ag catalysts.[138-141] However, selectivities for C_2H_4 epoxidation with O_2 reach 90 %, while 5 – 10 % of C_2H_4 is over oxidized to form massive amounts of CO_2 annually (1.5 – 3 Mton yr^{-1}),[138] which contributes to global climate change.[142] Furthermore, supported Ag catalysts tend to oxidize allylic positions within hydrocarbons, which prevents the use of these catalysts and O_2 for the epoxidation of molecules larger than C_2H_4.[138]

Hydrogen peroxide (H_2O_2) is a green oxidant that can selectively epoxidize alkenes and may replace more environmentally impactful oxidants. Currently, one of the few industrial processes that utilizes H_2O_2 for alkene epoxidation is the hydrogen peroxide – propylene oxide process,[82, 143] which couples the anthraquinone auto-oxidation process with a propylene epoxidation facility that catalyzes propylene epoxidations with a microporous titanium silicate zeolite catalyst (TS-1).[144-145] TS-1 gives acceptable H_2O_2 selectivities (80 – 95 %) for propylene epoxidation;[146] however, it is not obvious how other early-transition metal substituted zeolites may perform in epoxidations. Additionally, the differences of epoxidation rates and selectivities between Ti- and other early transition metal atoms in zeolite frameworks are not experimentally demonstrated in the open literature and neither are the reasons for such potential differences. Consequently, there are few proven guiding principles for the synthesis of improved microporous catalysts for epoxidations.

Group 4 and 5 metals grafted onto SiO_2 or incorporated into tetrahedral sites within zeolite frameworks effectively activate H_2O_2 and epoxidize alkenes.[51, 58, 82, 96, 147-151] Monomeric Nb atoms in the *BEA zeolite framework (Nb-BEA) irreversibly activate H_2O_2 to form superoxide intermediates (i.e., Nb-$(O_2)^-$) that selectively epoxidize alkenes. Alternatively, Ti atoms within TS-1 activate H_2O_2 to form Ti-OOH species, which are thought to be active for alkene epoxidation.[50, 65, 116] Several computational studies probed the effects of transition metal atom substitution into

zeolite frameworks on the Lewis and Brønsted acid strengths and correlated these changes to predicted reactivity predominantly for biomass conversion or the isomerization of glucose.[60-63] Most relevant to this work, Boronat *et al.* used quantum chemical calculations to relate the LUMO energy of the transition metal atoms Ti, Zr, and Sn within the framework of zeolite *BEA to the measured rates of octene epoxidation and attributed the relatively high reactivity of Ti-BEA to a LUMO energy that is lower than those of Zr- and Sn-BEA.[152] Experimentally, Notestein and coworkers found that the initial rates of cyclohexene epoxidation over group IV and V metals grafted onto silica correlate with the Pauling electronegativity of these metals.[51] In summary, the Lewis acidity of these heterogeneous atomically-isolated catalysts has been hypothesized to determine the ability of such species to activate H_2O_2 and the manner by which the activated complex reacts with an alkene.[151-157] Interestingly, these trends disagree with a significant body of work on group 7 and 8 (e.g., Mn and Fe) homogeneous complexes (e.g., porphyrin- and Schiff-base complexes), for which greater electron densities on the metal centers increase oxidation rates by facilitating the formation of M=O species via heterolytic cleavage of the O-O bond of H_2O_2.[82, 158] Connections between the Lewis acid strength of metal-substituted zeolites and epoxidation rates and selectivities have been hypothesized to exist for nearly two decades.[51, 152, 156-157] However, to the best of our knowledge, no investigations have correlated barriers for epoxidation and H_2O_2 decomposition (i.e., to infer selectivity) to *experimentally* determined descriptors of the strength of the Lewis acid sites or to the electronic structure of the reactive surface intermediates for epoxidation. Furthermore, no studies have compared the identities and relative reactivities of the active hydroperoxo and superoxo intermediates for epoxidation or the ways in which their electronic structures reflect the chemical properties of the transition metal heteroatom on these group 5 and 5 metal substituted zeolite catalysts.

Here, we incorporate group 4 (i.e., Ti, Zr, and Hf) and 5 (i.e., Nb, and Ta) metal atoms into the framework of zeolite *BEA (M-BEA) and use reaction rates measured as a function of the reactant concentrations to show that these M-BEA catalysts catalyze H_2O_2 decomposition and cyclohexene (C_6H_{10}) epoxidation through an identical mechanism that varies only in the structure of the active oxidant. H_2O_2 activates irreversibly to form dioxygen intermediates (M-(O_2)), such as M-$(O_2)^-$ or M-OOH/-$(O_2)^{2-}$, which subsequently react with C_6H_{10} through an Eley-Rideal mechanism to form cyclohexene oxide ($C_6H_{10}O$) or with H_2O_2 to decompose. *In situ* UV-vis measurements and the distributions of isomeric products from *Z*-stilbene epoxidation demonstrate

that only M-$(O_2)^-$ species participate directly in epoxidation on group 5 Lewis acid sites, whereas only M-OOH/-$(O_2)^{2-}$ intermediates react to form epoxides on group 4 Lewis acid sites. Reaction rates and selectivities depend exponentially on the extent of electron exchange between these active intermediates and the metal centers, as shown by the energy of the ligand-to-metal charge transfer (LMCT) bands. The thermodynamic strengths of the Lewis acidic metal centers were quantified from adsorption isobars for deuterated acetonitrile and compared to activation enthalpies ($\Delta H^{\ddagger}$) for both pathways. These comparisons show that stronger Lewis acids possess *both* lower $\Delta H^{\ddagger}$ (i.e., increased reactivity) and higher selectivities for the epoxidation of C_6H_{10} by M-(O_2) intermediates. Collectively, these results demonstrate that the rates for catalytic epoxidation on these M-BEA materials (and likely that in other zeolite frameworks) directly reflect the strength of the Lewis acid site and elucidate the reasons for observed selectivity trends on similar group 4 and 5 heterogeneous catalysts.

3.2 Materials and Methods

3.2.1 Catalyst Synthesis

Group 4 and 5 transition metal atoms were incorporated into tetrahedral positions of the *BEA framework by either solid-state[49] (Zr and Hf) or liquid-phase[33, 101] (Nb, Ta, and Ti) metal-atom incorporation of dealuminated *BEA following previously published procedures. In short, commercial *BEA (Zeolyst, Si:Al ~ 12.5, NH_4^+ cation) was contacted with concentrated HNO_3 (Macron Chemicals, 69-70 wt. %, 20 cm^3 HNO_3 $g_{zeolite}^{-1}$) at reflux (448 K) for 20 h with the intent to remove Al atoms from the framework to produce solvated $Al(NO_3)_3$. Afterwards, the solids were recovered by filtration and washed first with concentrated HNO_3 and then with deionized H_2O (17.8 MΩ). The recovered solids were then heated to 823 K at 5 K min^{-1} under flowing dry air (100 cm^3 min^{-1}, Airgas, Ultra-zero grade) with the intent to remove residual volatiles and any organic species and to produce Si-BEA (Si:Al > 1200, determined by ICP-OES).

Ti atoms were incorporated into the framework by liquid-phase incorporation (LPI),[33, 101] which involved stirring Si-BEA in dichloromethane (DCM, Fisher Chemicals, Certified ACS Stabilized, 15 cm^3 DCM $g_{zeolite}^{-1}$) under an argon atmosphere using standard schlenk technique. An appropriate amount of $TiCl_4$ (Sigma-Aldrich, 99.9%) was added dropwise to the stirring suspension of Si-BEA in DCM and brought to reflux (323 K) for 3 hours. Notably, $TiCl_4$ and will violently react with moisture in air to release HCl and should be handled carefully in an inert

atmosphere. After ca. 30 minutes at reflux, the color of the suspension turned from bleached white to tan.

Nb and Ta atoms were also incorporated into the framework by LPI,[33, 101] which involved stirring Si-BEA in isopropanol (IPA, Fisher Chemicals, 15 cm^3 IPA $g_{zeolite}^{-1}$) under an ambient atmosphere. An appropriate amount of $NbCl_5$ (Sigma-Aldrich, 99.9%) or $TaCl_5$ (Sigma-Aldrich, 99%) dissolved in IPA was added to the stirring suspension of Si-BEA in IPA and heated to 333 K for 3 hours. Notably, $NbCl_5$ dissolved in IPA is bright yellow, and maintains this color for a short time (ca. 10 min) upon addition of Si-BEA, after which the color of the suspension turns white.

For Ti-, Nb-, and Ta-samples, the solvent (i.e., DCM or IPA) was removed *in vacuo* (via rotovap), and the recovered solids were heated to 823 K at 5 K min^{-1} for 6 h in flowing dry air (100 cm^3 cm^{-1}, Airgas, Ultra-zero grade). The heat-treated solids possessed a bleached white color.

Hf- and Zr-incorporated *BEA materials were synthesized via solid-state ion exchange.[49] In brief, Si-BEA was intimately ground with an appropriate amount of $Hf(OEt)_4$ (Alfa-Aesar, 99.9 %) or $Zr(OEt)_4$ (Alfa-Aesar, 99 %) to yield a homogeneous solid mixture. The solids were then heated to 823 K at 2 K min^{-1} for 6 h in flowing air (100 cm^3 min^{-1}, Airgas, Ultra-zero grade), with the intent to melt the Zr- and $Hf(OEt)_4$ and provide ample time for these species to diffuse into the SiOH pockets within the Si-BEA crystals prior to decomposition. This process results in Zr- or Hf-BEA, the colors of which are bleached white and light gray, respectively. This solid-state synthesis method can potentially produce extra-framework species (e.g., oligomeric ZrO_x or HfO_x species); however, characterization results (shown below) suggest the fraction of Zr- and Hf-atoms that exist outside the framework are insignificant. Furthermore, the kinetic analysis (Sections 3.3.2 and B2) and correlations reported here rely only on how rates change with a function of reactant concentrations and temperature, such that an error in the site count would be systematically applied and would not alter any conclusions.

3.2.2 Catalyst Characterization

The transition metal content of each M-BEA content was determined by inductively coupled plasma-optical emission spectroscopy (ICP-OES, PerkinElmer 2000DV), which was calibrated against known dilution standards. For M_x-BEA, the subscript refers to the number of metal atoms per unit cell of the *BEA framework, quantified by ICP-OES. For all kinetic and in

situ spectroscopic measurements (Sections 2.3 and 2.4), samples of M-BEA were prepared to result in 0.6 – 1 (M atoms)(unit cell)$^{-1}$ (i.e., Si/M ratios > 60). Consequently, statistical arguments show that the M-atoms are well separated from one another and that catalysts will contain only a very small fraction of M-O-M linkages, which is supported also by other characterization methods described below. Furthermore, the post-synthetic modification of Al-BEA only replaced approximately 1 in 5 Al atoms, which leaves ~4 silanol nests (unit cell)$^{-1}$. This suggests that all M-BEA used in this study are highly hydrophilic, rather than hydrophobic (as is the case in defect-free M-BEA materials).[159]

Catalyst crystallinity was confirmed by powder X-ray diffraction (p-XRD). X-ray diffractograms were obtained on a Siemens/Bruker D5000 diffractometer with Cu K-α radiation (0.15418 nm) using a step size of 0.02º, taken at 1º min^{-1}, under ambient conditions. The similarities between the x-ray diffractograms (Fig. B1) show that the *BEA framework remains intact after dealumination and metal incorporation for all M-BEA samples.

Band edges (E_g) were determined by analysis of diffuse reflectance UV-vis spectra of the bare M-BEA materials (Fig. B2). Total reflectance spectra were measured at ambient conditions with a UV-vis-NIR spectrophotometer (Agilent CARY 5) equipped with a diffuse reflectance accessory (Harrick cricket®). Magnesium oxide (MgO, Sigma Aldrich, 99.995% trace metals basis) was used as a background for all spectra obtained. Samples were prepared by intimately combining M-BEA (~10 mg) with MgO (~100 mg) using a pestle and mortar. Values of E_g were determined from the x-intercept of the linear portion of the corresponding Tauc plots for each material (Fig. B2b).[99] The relatively large value of the band edges (Table 3.1) for all of the materials (and absence of shoulders towards lower energies) further suggests that transition metal atoms within each of these materials are highly disperse and contain little to no oligomeric or bulk metal-oxide phases.[147]

The incorporation of the transition metal atoms into the *BEA framework was confirmed by vibrational spectra of each sample obtained by attenuated total reflectance IR (ATR-IR) spectroscopy. Samples (~10 mg) were pressed onto the diamond internal reflection element of an ATR-IR instrument (Bruker Alpha) and spectra were recorded at ambient conditions (Fig. B3, 32 scans, 2 cm^{-1} resolution). Figure B3a shows the normalized IR spectra for all M-BEA, all of which possess nearly identical spectra within the framework stretching region. Figure B3b shows the difference spectra for group 4 and 5 catalysts with respect to that of Si-BEA, and are all normalized

to the well-documented ν(Si-O-M)[104] feature at 960 cm^{-1}, for clarity. The appearance of this feature at ca. 960 cm^{-1} (ν(Si-O-M)) on all M-BEA shows that the transition metal atoms are incorporated into the *BEA framework upon post-synthetic modification.

The presence of Lewis acid sites was characterized by the IR spectra of adsorbed deuterated acetonitrile (CD_3CN, Cambridge Isotope Laboratories, 99.8% D atom),[106-107] coordinated to M-BEA using a custom-made transmission cell coupled to an FTIR spectrometer (Bruker, Tensor 37) equipped with a liquid-N_2-cooled HgCdTe detector.[108] Catalysts were pressed into self-supporting wafers (~60 mg) and placed within the stainless-steel cell, which was equipped with CaF_2 windows and connected to a gas manifold by gas-transfer lines that were heated to 423 K via electrical heating tape (Omega, FGH Series). Catalysts were first heated to 423 K (10 K min^{-1}) and held for 1.5 h under flowing He (50 cm^3 min^{-1}, Airgas Ultra High Purity), with the intent to remove any residual H_2O and other volatiles that may have adsorbed during catalyst storage. CD_3CN was fed via a syringe pump (KD Scientific, Legato 100) at 1 μL min^{-1} and vaporized inside the heated gas-transfer lines into a stream of flowing He (50 cm^3 min^{-1}, Airgas, 99.999%) to produce a stream containing 1.0 kPa CD_3CN. IR spectra (Fig. B4) of adsorbed CD_3CN were obtained by flowing the CD_3CN/He stream over the sample for 15 minutes. The flow of CD_3CN was then stopped and the sample was heated at 10 K min^{-1} to a final temperature of 423 K while FTIR spectra (128 scans, 1 cm^{-1} resolution) were continuously recorded.

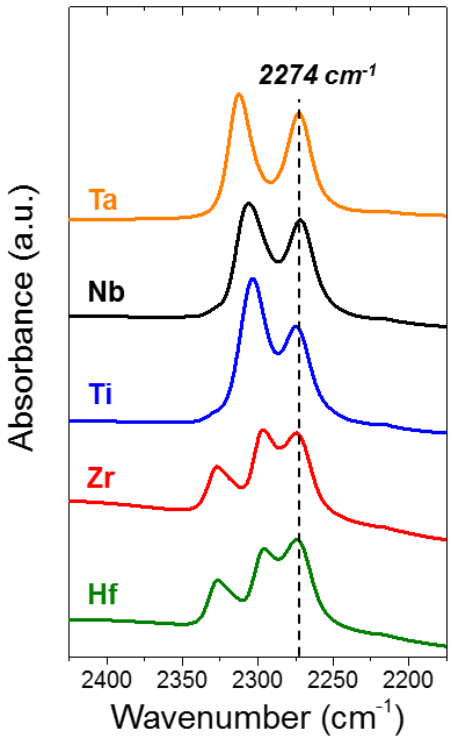

Figure 3.1. Infrared spectra of CD_3CN bound to Lewis acid, Brønsted acid, and silanol sites on M-BEA catalysts including $Ti_{1.0}$- (blue), $Zr_{1.0}$- (red), $Hf_{1.0}$- (green), $Nb_{0.2}$- (black), and $Ta_{0.6}$-BEA (orange). Spectra are normalized to ν(C≡N) of silanol-bound CD_3CN (2274 cm^{-1}) and were acquired in flowing He (50 cm^3 min^{-1}, ~373 K) to monitor the desorption of CD_3CN after saturation.

Figure 3.1 shows FTIR spectra for adsorbed CD_3CN on all M-BEA during the desorption of CD_3CN in flowing He (50 cm^3 min^{-1}, ~333 K) after saturation of CD_3CN to visualize relevant CD_3CN IR features. All M-BEA possess an absorbance feature at ~2274 cm^{-1}, which corresponds to ν(C≡N) of CD_3CN coordinated to SiOH functionalities within the *BEA framework. Ti-, Nb-, and Ta-BEA each possess a single additional feature at 2302, 2306, and 2312 cm^{-1}, respectively, which is assigned to ν(C≡N) of Lewis-acid bound CD_3CN.[159] Both Zr- and Hf-BEA possess two additional features at 2326 cm^{-1} and 2296 cm^{-1}. Of these two features, the peaks at 2296 cm^{-1} are assigned to CD_3CN coordinated to the Lewis acidic Zr and Hf atoms in the *BEA framework, based on recent reports for Zr-BEA.[160] Finally, CD_3CN bound to Brønsted acid sites on H-exchanged USY[161] has been observed at 2332 cm^{-1}; therefore, the features at 2326 cm^{-1} on Zr- and Hf-BEA may be attributed to CD_3CN coordinated to Brønsted acid sites (e.g., $(SiO)_3Zr(OH)$), as Zr-BEA is known to contain Brønsted acid sites at open Zr sites in the framework.[162] Notably, the features at 2326 and 2296 cm^{-1} in Zr- and Hf-BEA do not correspond to remaining Lewis or

Brønsted acidic Al atoms in the framework[159] as these features are not observed in the purely Si-BEA starting material (Fig. B4), nor are they attributed to bulk or oligomeric extraframework metal oxide clusters.[107]

The presence and ratio of open versus closed sites has been shown to influence the reactivity of similar M-BEA catalysts. For example, the rates for the conversion of ethanol to butadiene on Zr-BEA has been shown to be proportional to the number of open Zr sites on a series of materials (as detected by FTIR of adsorbed CO at 100 K),[163] which suggests that butadiene forms primarily on open sites. Gounder and coworkers have used the FTIR spectra of adsorbed CD_3CN to show that Sn-BEA made by both post-synthetic modification and hydrothermal syntheses contain significant amounts of both open and closed sites, which suggests that it is extremely difficult to synthesize materials that contain solely one type of site.[159] Thus, the M-BEA materials in this study likely contain a mixture of open and closed sites. However, the relationships developed within this work seek to correlate the experimentally observed reactivity (e.g., quantified by values of the $\Delta H^{\ddagger}$ which do not depend on the number of sites) of these materials with a functional descriptor of the Lewis acid strength, rather than compare within each material the reactivity of open versus closed sites. Future studies will explore how changes in the prevalence of open or closed sites (e.g., manipulated using hydrothermal synthesis versus post-synthetic modification methods) affect the Lewis acid strength, reactivity, and selectivity of a given group 4 or 5 metal in the framework of these zeolitic materials

To obtain functional measures of the Lewis acid strength, the enthalpies for adsorption of CD_3CN to Lewis acid sites (ΔH_{CD_3CN}) were determined by monitoring the absorbance value of the ν(C≡N) feature as a function of inverse temperature (at a constant partial pressure of CD_3CN (Fig. B5, ~1.2 kPa CD_3CN, 373 – 423 K). The coverage of Lewis-acid bound CD_3CN is proportional to the intensity of the ν(C≡N) feature in the absorbance spectra, and the heat of adsorption for CD_3CN onto Lewis-acid sites on each of the M-BEA materials is calculated by the method of van't Hoff (Fig. B5). Table 1 summarizes the experimentally determined values of ΔH_{CD_3CN} for all M-BEA catalysts.

Overall, the results from p-XRD, diffuse reflectance UV-vis spectroscopy, and IR spectra of M_x-BEA and adsorbed CD_3CN show that the *BEA framework is intact after post-synthetic modification; very little, if any, oligomeric or bulk metal oxide is present; metal atoms are

incorporated into the framework; and quantify Lewis-acid strength, respectively (SI, Section S1; Table 3.1; Fig. 3.1 and B1 – B5).

Table 3.1. Heats of adsorption for CD_3CN coordinated to Lewis acidic framework metal atoms and band edge energies (measured via DR UV-vis) for $Nb_{0.6}$-, $Ta_{0.6}$-, $Ti_{1.0}$-, $Zr_{1.0}$-, and $Hf_{1.0}$-BEA.

Sample	ΔH_{CD_3CN} (kJ mol^{-1})	Band Edge (eV)
$Nb_{0.6}$-BEA	-22 ± 2	4.2
$Ta_{0.6}$- BEA	-17 ± 1	4.8
$Ti_{1.0}$- BEA	-31 ± 2	4.0
$Zr_{1.0}$- BEA	-14 ± 1	5.6
$Hf_{1.0}$- BEA	-13 ± 1	5.7

3.2.3 Measurements of Reaction Rates and Selectivities

Rates for cyclohexene (C_6H_{10}) epoxidation and H_2O_2 decomposition were measured within batch reactors (100 cm^3, three-neck round bottom flask) equipped with reflux condensers to minimize evaporative losses. Appropriate amounts of C_6H_{10} (Sigma-Aldrich, 99%) or *cis*-stilbene (Sigma-Aldrich, >96 %) and H_2O_2 (Fischer Chemicals, 30 wt. % in H_2O) were added to a solution of acetonitrile (CH_3CN, Macron Chemicals, >99.8%) and benzene (for use as an internal standard, Sigma-Aldrich, thiophene free, >99%) and heated to the desired temperature (303 – 348 K) while stirring at 600 rpm. Epoxidation and H_2O_2 decomposition was initiated by adding the M-BEA catalyst. Small aliquots (~300 μL) of the reaction solution were extracted as a function of time through a 0.22 μm syringe filter (with the intent to remove suspended catalyst and quench epoxidation and H_2O_2 decomposition). The hydrocarbon and oxygenate concentrations within these aliquots were quantified via a gas chromatograph (HP-5890, Series A) equipped with a flame-ionization detector. All species were identified and calibration factors were quantified using standards of known concentration. The H_2O_2 concentration of each aliquot was determined by colorimetric titration using an aqueous solution of $CuSO_4$ (8.3 mM, Fisher Chemicals, >98.6%), neocuproine (12 mM, Sigma-Aldrich, >98%), and ethanol (25% v/v, Decon Laboratories Inc., 100%). The concentration of H_2O_2 was quantified from comparison of the absorbance at 454 nm to calibrated standards, measured using a visible-light spectrophotometer (Spectronic, 20 Genesys). Test reactions (0.01 M C_6H_{10}, 1 mM H_2O_2, 313 K) with Si-BEA reveal that no reaction

(i.e., C_6H_{10} epoxidation or H_2O_2 decomposition) occurs in the absence of the metal atoms. In all reported data, the carbon balance closed within 98% and the standard uncertainty for measured reaction rates was < 7%. Rates for the conversion of C_6H_{10} and H_2O_2 on the five M-BEA were measured as functions of $[H_2O_2]$, $[C_6H_{10}]$, and $[C_6H_{10}O]$, and all reported results were obtained at differential conversion (i.e., < 5% conversion of limiting reagent).

Reported rates were measured in the absence of intra-pellet mass-transfer limitations, as shown by satisfying the Madon-Boudart criterion for Ti-BEA (i.e., the M-BEA catalyst with the greatest turnover rates) by performing reactions under identical conditions with catalysts containing different metal loadings (see Appendix B, Section B1.2).[111] Over the metal loadings tested, the epoxidation turnover rates did not depend on the metal content, which demonstrates that concentration gradients do not exist within the reactor or within the M-BEA particles. Additionally, all catalysts tested are of similar metal loadings (group 4 ~ 1 (M atom)(unit cell)-1; group 5 ~ 0.6 (M atom)(unit cell)-1).

3.2.4 In Situ UV-Vis Spectroscopy

In situ UV-vis spectroscopy was used to identify the intermediates formed upon H_2O_2 activation and determine which of these species were directly responsible for alkene epoxidation. M-BEA samples were pressed into 7 mm diameter pellets (~5 mg) and loaded into a custom-built UV-vis liquid flow cell equipped with cartridge heaters for temperature control. UV-vis spectra (100 scans, 600 ms integration time) were collected using a 45-degree diffuse reflection probe (Avantes, solarization-resistant fibers) connected to a fiber-optic spectrometer (Avantes, AvaFast 2048) with a compact deuterium-halogen light source (Avantes, AvaLight-DHc). Reactant and solvent solutions were introduced via a high-performance liquid chromatography pump (Waters, 515). A CH_3CN solution (0.4 M H_2O, 1 cm^3 min^{-1}) flowed over the samples at 313 K for 1 h and the corresponding UV-vis spectra for each M-BEA was used as the background for all measurements. The M-BEA samples were activated with H_2O_2 by switching the flow to a solution of H_2O_2 in CH_3CN (0.1 M H_2O_2, 0.4 M H_2O, 1 cm^3 min^{-1}) at 313 K until the UV-vis spectra became constant (i.e., implying a constant coverage of surface intermediates). Pure CH_3CN (1 cm^3 min^{-1}) was then flowed over the samples at 313 K for 10 min to remove residual H_2O_2. The reactivity of the surface intermediates was determined by continuously acquiring UV-vis spectra while flowing a solution of C_6H_{10} in CH_3CN (0.1 M C_6H_{10}, 0.4 M H_2O, 1 cm^3 min^{-1}) and by

mathematically modeling the rates of peak attenuation (see Appendix B, Section B2). Notably, separate experiments showed that the UV-vis absorbance features on the H_2O_2-activated M-BEA did not change or attenuate (for a period of 2 h) under a flowing stream of CH_3CN (0.4 M H_2O, 1 cm^3 min^{-1}) or pure H_2O (1 cm^3 min^{-1}, 17.8 MΩ) at 313 K. Processes for peak smoothing, background subtraction, and peak fitting were performed within OriginPro® and are described in Appendix B (Section B2).

3.3 Results and Discussion

3.3.1 Identifying Active Oxygen Intermediates for Epoxidation

Metal-bound superoxide (M-$(O_2)^-$),[122] peroxide (M-$(O_2)^{2-}$),[50, 58, 149] and hydroperoxide (M-OOH)[50, 59, 65, 85, 116, 118] intermediates have been proposed as the active intermediates for alkene epoxidation on group 4 and 5 catalysts grafted onto SiO_2 and incorporated into zeolite frameworks. However, published results disagree over the exact identity of the reactive intermediate on these solid catalysts. The activation of H_2O_2 on group 4 (i.e., Ti, Zr, and Hf) and 5 (i.e., Nb and Ta) transition metal atoms incorporated into the *BEA framework (M-BEA) likely forms a pool of superoxide, peroxide, and hydroperoxide intermediates, where these complexes may be characterized by their electronic transitions (e.g., ligand-to-metal charge transfer) via UV-vis spectroscopy.

UV-vis spectra of H_2O_2-activated M-BEA acquired in situ (Fig. 2, 0.1 M H_2O_2, 0.4 M H_2O, in CH_3CN, 1 cm^3 min^{-1}, 313 K) show that all M-BEA materials possess overlapping absorbance features (Fig. B8), whose intensities are proportional to the relative surface coverage of these species. Similar overlapping features exist on TS-1,[50, 120, 164] Nb-BEA, and bulk Nb_2O_5,[124] where the lower energy (higher wavelength (λ)) features are known to correspond to M-OOH/M-$(O_2)^{2-}$ species while the higher energy (lower λ) peaks are assigned to the M-$(O_2)^-$ species.[50, 122, 124, 165] As such, we systematically assign the higher λ features in Ta-, Zr-, and Hf-BEA to the M-OOH/-$(O_2)^{2-}$ species and the lower λ feature to M-$(O_2)^-$.

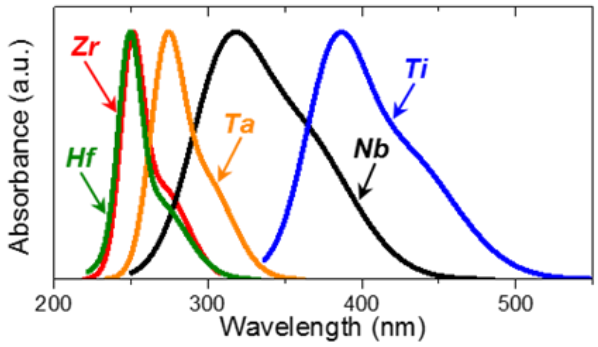

Figure 3.2. UV-vis spectra of H_2O_2-activated (Section 2.4) M-BEA catalysts including $Hf_{1.0}$- (green), $Zr_{1.0}$- (red), $Ta_{0.6}$- (orange), $Nb_{0.2}$- (black), and $Ti_{1.0}$-BEA (blue). Spectra were acquired in situ in flowing H_2O_2 in CH_3CN (0.1 M H_2O_2, 0.4 M H_2O, 1 cm^3 min^{-1}) at 313 K.

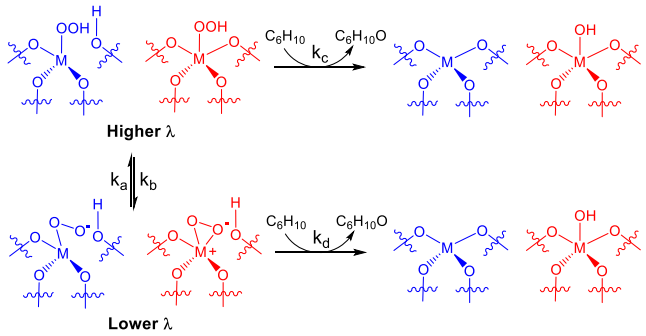

Scheme 3.1. Interconversion and consumption of M-OOH/M-$(O_2)^{2-}$ (M-OOH) shown) and M-$(O_2)^-$ species upon reaction with C_6H_{10}. Color coding is for clarity: Group 4 (Ti, Zr, and Hf, blue) and 5 (Nb and Ta, red).

Scheme 3.1 shows the possible reaction of both the M-OOH/-$(O_2)^{2-}$ and M-$(O_2)^-$ intermediates with C_6H_{10}, where the differences in the rates of consumption of these species in the presence of C_6H_{10} will reflect the relative reactivity of these intermediates. However, to accurately estimate values of rate constants for the reaction of dioxygen species with C_6H_{10} (i.e., k_c and k_d), the analysis must account for the interconversion of these species via reversible isomerization and charge transfer processes (Section B2.3 discusses how the interconversion of the two intermediates is accounted for during the transient kinetic analysis).[121]

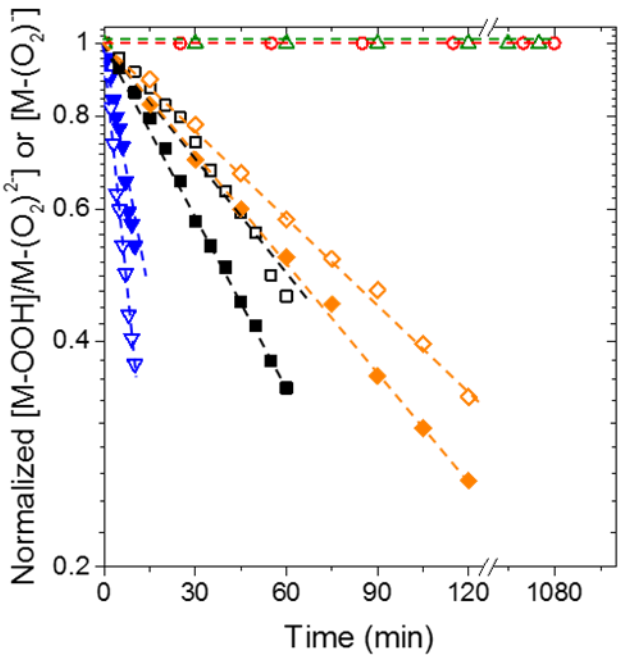

Figure 3.3. Change in the normalized surface coverage of M-OOH/M-$(O_2)^{2-}$ (open symbols) and M-$(O_2)^{-}$ (closed symbols) species as a function of time for $Ti_{1.0}$- (▼), $Zr_{1.0}$- (●), $Hf_{1.0}$- (▲), $Nb_{0.2}$- (■), and $Ta_{0.6}$-BEA (♦). UV-vis spectra were acquired in situ upon flowing C_6H_{10} in CH_3CN (0.1 M C_6H_{10}, 0.4 M H_2O, 1 cm^3 min^{-1}) over H_2O_2-activated samples (Section 3.2.4) at 313 K. Closed symbols for $Zr_{1.0}$- and $Hf_{1.0}$-BEA coincide with the open symbols. Note that the Y-axis is shown on a logarithmic scale.

The UV-vis absorbance features for species on Ti-, Nb-, and Ta-BEA attenuate exponentially with time upon exposure to flowing C_6H_{10} (0.1 M C_6H_{10}, 0.4 M H_2O, in CH_3CN, 313 K). Figure 3.3 shows the change in the normalized surface coverages of these species as a function of time and indicates clearly that specific intermediates are more reactive than others on a given M-BEA catalyst. Specifically, the number of Ti-OOH/-$(O_2)^{2-}$ species diminish at a faster rate than those for Ti-$(O_2)^{-}$, while the opposite is observed for Nb- and Ta-BEA. Table 3.2 shows rate constants for the reaction between M-$(O_2)^{-}$ or M-OOH/-$(O_2)^{2-}$ intermediates and C_6H_{10} (Scheme 3.1) on each catalyst that are calculated from the change in the normalized intensity of the corresponding spectral features for each species (Fig. 3.3), during the reaction of H_2O_2-activated M-BEA with flowing C_6H_{10} at conditions similar to those for rate measurements (Section B2.3). The calculated rate constants (Tables 3.2 and B2) for epoxidation by M-$(O_2)^{-}$ on Nb- and Ta-BEA are $2 \cdot 10^4$ and 32 times larger than for epoxidation by M-OOH/-$(O_2)^{2-}$, respectively, which suggests that superoxide species are the active intermediates for epoxidation on group V substituents in the *BEA. However, for Ti-BEA, the rate constant for the consumption of Ti-

OOH/-$(O_2)^{2-}$ (i.e., k_c) is larger than that for Ti-$(O_2)^-$ (i.e., k_d) by a factor of 170. This difference shows that the Ti-OOH/-$(O_2)^{2-}$ species are primarily responsible for alkene epoxidation on Ti-BEA, which agrees with the intermediates proposed for epoxidation reactions on TS-1.[65, 116, 120-121, 123] The attenuation of the UV-vis absorbance features for Zr- and Hf-BEA were negligible on the time scale of the experiment, which corresponds to rate constants for epoxidation with these intermediates of $<10^{-6}$ s^{-1} and is consistent with kinetic measurements for these materials (i.e., the rates of reaction for Zr- and Hf-BEA are a factor of $\sim10^5$ less than Ti-BEA at comparable conditions; Fig. 3.5). The values of k_c and k_d could not be determined on Zr-BEA and Hf-BEA, because the attenuation rates were immeasurable, however, the identities of the H_2O_2-derived intermediates responsible for epoxidation on these materials was determined using an alternative method, described next.

Epoxidation reactions with *Z*-stilbene were used to support the identifications of the active intermediates derived from the in situ UV-vis measurements. Alkene epoxidations that involve M-OOH/-$(O_2)^{2-}$ species occur through a concerted mechanism, where oxygen-atom transfer from the active intermediate to the alkene occurs in a single step and, thus, prevents stereochemical rearrangement (e.g., C-C bond rotation).[65, 82, 119] Such epoxidations result in the nearly exclusive formation of *Z*-stilbene oxide. Epoxidations that use M-$(O_2)^-$ intermediates, however, react through a biradical mechanism that allows nearly unhindered rotation about the C=C bond, and therefore, gives distributions of epoxide products that contain comparable amounts of *E*- and *Z*-stilbene oxide isomers.[130-131] Table 3.2 shows that group IV (i.e., Ti, Zr, and Hf) catalysts preferentially form *Z*-stilbene oxide, while group V (i.e., Nb and Ta) produce nearly equal amounts of *Z*- and *E*-stilbene oxide. The microporous nature of these materials does not introduce artifacts in the analysis or the interpretation of these isomer distributions. The disparity in the *Z:E* ratio of stilbene oxide between group IV and V metals (Table 3.2), suggests that the pore geometry has minimal, if any, effect on the distribution of products. An in situ UV-vis experiment was performed on H_2O_2-activated Ti-BEA (Fig. B9) to determine if *Z*-stilbene was able to diffuse into the *BEA framework and react with all Ti-atoms within the bulk. The absorbance features for both M-OOH/-$(O_2)^{2-}$ and M-$(O_2)^-$ attenuated exponentially and indicate that ~95% of the intermediates were consumed, which strongly suggests that the *Z*-stilbene is able to fully access the pores of M-BEA and react. Consequently, the *E*- and *Z*-stilbene oxide isomers form by reactions that occur on the same sites and with the same intermediates that facilitate C_6H_{10} epoxidation and not on a subset of sites on

the exterior surface of the catalyst particles. These product isomer distributions, in conjunction with in situ UV-vis measurements (Fig. 3.3) and the calculated rate constants (Table 3.2), strongly suggest that the reactive intermediate(s) responsible for alkene epoxidation on group 4 (i.e., Ti, Zr, and Hf) catalysts are the M-OOH/-$(O_2)^{2-}$ species, while group 5 (i.e., Nb and Ta) materials react through a M-$(O_2)^-$ intermediate.

Table 3.2. Evidence for the Direct Involvement of Specific Intermediates in Alkene Epoxidation: Rate constants for the epoxidation of C_6H_{10} and *Z:E* (*cis:trans*) stilbene oxide product ratios for the epoxidation of *Z*-stilbene

Sample	k_c (s^{-1})	k_d (s^{-1})	*Z:E* ratio
$Ti_{1.0}$-BEA	$2.9 \cdot 10^{-2}$	$1.7 \cdot 10^{-4}$	9.2
$Nb_{0.2}$-BEA	$2.2 \cdot 10^{-7}$	$4.5 \cdot 10^{-3}$	1.0
$Ta_{0.6}$- BEA	$1.0 \cdot 10^{-4}$	$3.3 \cdot 10^{-3}$	1.0
$Zr_{1.0}$- BEA	$< 10^{-6}$	$< 10^{-6}$	7.1
$Hf_{1.0}$- BEA	$< 10^{-6}$	$< 10^{-6}$	6.3

3.3.2 Mechanistic Interpretations of Epoxidation Kinetics

Figure 3.4a shows turnover rates for the formation of cyclohexene oxide ($C_6H_{10}O$) as a function of [C_6H_{10}] (10^{-4} – 5 M) at constant [H_2O_2] over all M-BEA, while Fig. 3.4b shows turnover rates for $C_6H_{10}O$ formation as a function of [H_2O_2] at constant [C_6H_{10}], and Fig 3.4c shows $C_6H_{10}O$ formation rates as a function of [$C_6H_{10}O$] at constant [H_2O_2] and [C_6H_{10}]. In all cases, rates of epoxidation depend linearly on [C_6H_{10}] (Fig. 3.4a) and do not depend on [H_2O_2] (Fig. 3.4b) at relatively low [C_6H_{10}]:[H_2O_2], which suggests that the active sites are saturated with a H_2O_2-derived intermediate at these conditions. As [C_6H_{10}]:[H_2O_2] reactant ratios increase, the rate of epoxidation eventually becomes independent of [C_6H_{10}] (Fig.3. 4a), proportional to [H_2O_2] (Fig. 3.4b, Ti-, Nb-, and Ta-BEA), and inversely proportional to [$C_6H_{10}O$] (Fig. 3.4c). This change suggests that the identity of the most abundant surface intermediate (MASI) changes to a C_6H_{10}-derived intermediate (e.g., most likely $C_6H_{10}O$). Conceptually, this occurs because C_6H_{10} and its derivatives displace H_2O_2-derived species from the metal centers at high values of [C_6H_{10}]. Notably, the effect of [$C_6H_{10}O$] on epoxidation turnover rates on Zr- and Hf-BEA (comparable to

Fig. 3.4c) could not be measured because catalytic turnover rates at high [C_6H_{10}] (>1 M) were obscured by non-catalytic C_6H_{10} oxidation rates (i.e., homogeneous reactions).

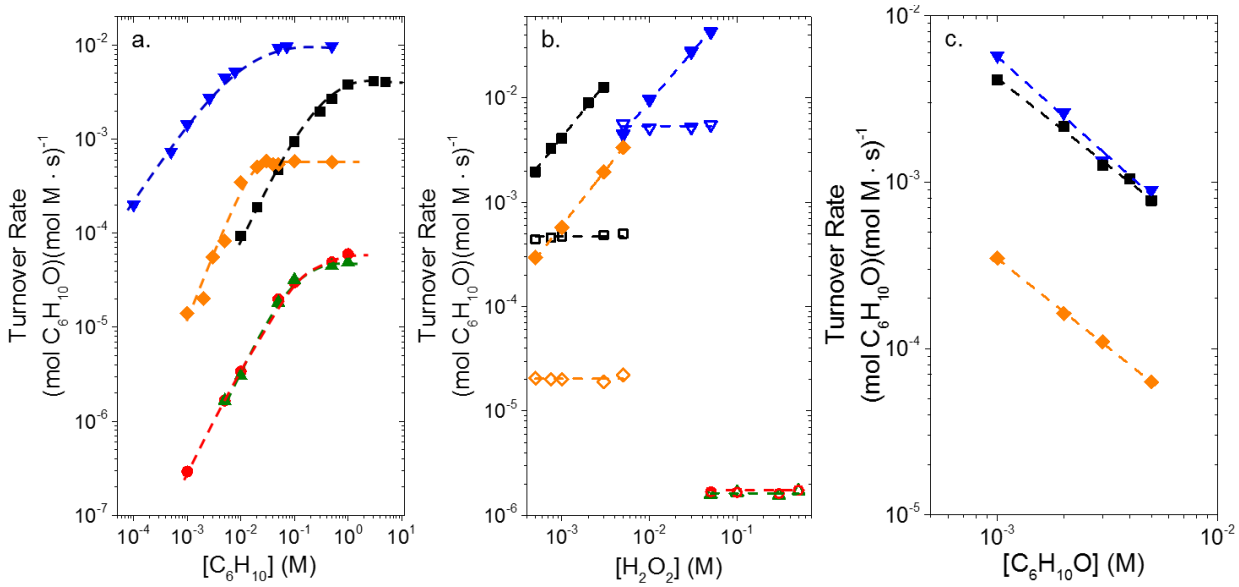

Figure 3.4. Turnover rates for the formation of $C_6H_{10}O$ as a function of (a) C_6H_{10} over $Nb_{0.6}$-BEA (■, 1 mM H_2O_2, 313 K), $Ta_{0.6}$-BEA (♦, 1 mM H_2O_2, 313 K), $Ti_{1.0}$-BEA (▼, 0.01 M H_2O_2, 313 K), $Zr_{1.0}$-BEA (●, 0.1 M H_2O_2, 323 K), and $Hf_{1.0}$-BEA (▲, 0.1 M H_2O_2, 323 K), (b) H_2O_2 over $Nb_{0.6}$-BEA (□, 0.05 M C_6H_{10}, ■, 3 M C_6H_{10}, 313 K), $Ta_{0.6}$-BEA (◊, 2 mM C_6H_{10}, ♦, 0.5 M C_6H_{10}, 313 K), $Ti_{1.0}$-BEA (▽, 0.05 M C_6H_{10}, ▼, 0.5 M C_6H_{10}, 313 K), $Zr_{1.0}$-BEA (○, 5 mM C_6H_{10}, 323 K), and $Hf_{1.0}$-BEA (△, 5 mM C_6H_{10}, 323 K), and (c) $C_6H_{10}O$ over $Nb_{0.6}$-BEA (■, 3 M C_6H_{10}, 1 mM H_2O_2, 313 K), $Ta_{0.6}$-BEA (♦, 0.5 M C_6H_{10}, 1 mM H_2O_2, 313 K), $Ti_{1.0}$-BEA (▼, 0.5 M C_6H_{10}, 0.01 M H_2O_2, 313 K) Dashed lines are intended to guide the eye.

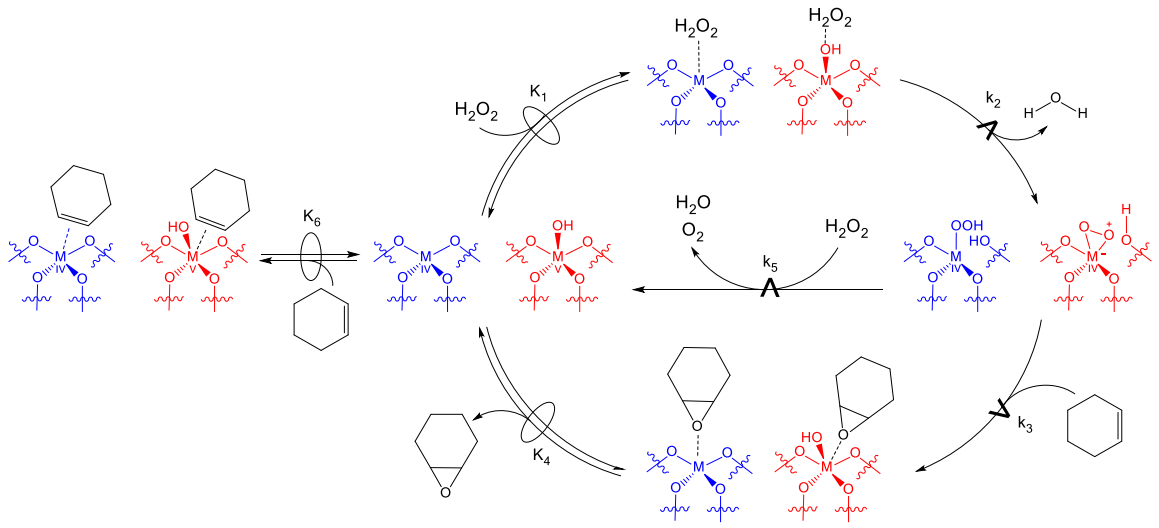

Scheme 3.2. Proposed mechanism for the epoxidation of C_6H_{10} with H_2O_2 over group 4 (Ti, Zr, and Hf, M-OOH shown, blue) and group 5 (Nb and Ta, red) M-BEA. The symbol ⇄ represents a quasi-equilibrated step, while → represents a kinetically relevant step. Note, the unoccupied metal atoms are meant to be representations of an empty site, rather than suggest all metal atoms exist as closed sites, as both open and closed sites likely exist in these materials (see characterization results, Section 3.2.2).

Scheme 3.2 shows a series of elementary steps that account for the measured effects of $[C_6H_{10}]$ (Fig. 3.4a), $[H_2O_2]$ (Fig. 3.4b), and $[C_6H_{10}O]$ (Fig. 4c) on both rates of C_6H_{10} epoxidation and of H_2O_2 decomposition (H_2O_2 decomposition rate expression is derived in SI, section N3.2). The catalytic cycle for epoxidation involves the quasi-equilibrated adsorption of H_2O_2 (step 1),[58, 111] followed by the irreversible activation of H_2O_2 (step 2) to form a pool of M-$(O_2)^-$ and M-OOH/-$(O_2)^{2-}$ active intermediates (referred to collectively as M-(O_2)).[82, 116-117, 121] Among these species, either M-OOH/-$(O_2)^{2-}$ or M-$(O_2)^-$ then reacts with C_6H_{10} (depending on the metal identity, Section 3.3.1) via an Eley-Rideal mechanism to form $C_6H_{10}O$ (step 3), which desorbs (step 4). The M-(O_2) species may also decompose nonproductively by reaction with H_2O_2 (step 5). Measured C_6H_{10} epoxidation rates represent the kinetically relevant reaction of the active form of the oxidizing surface intermediate with a C_6H_{10} molecule:

$$r_E = k_3[M - O_2][C_6H_{10}] \tag{3.1}$$

where r_E is the rate of C_6H_{10} epoxidation, [M-(O_2)] is the number of the M-OOH/-$(O_2)^{2-}$ (group 4) or M-$(O_2)^-$ (group 5) species and k_x is the rate constant for step x in Scheme 3.2. Application of the

pseudo-steady state hypothesis to the M-(O_2) intermediates, in combination with a site balance to account for all surface species (full derivation in Appendix B; Section B3.1), provides:

$$\frac{r_E}{[L]} = \frac{\frac{k_2 k_3 K_1 [C_6H_{10}][H_2O_2]}{(k_3[C_6H_{10}]+k_5[H_2O_2])}}{\beta} \tag{3.2}$$

where [L] is the total number of M atoms (i.e., active sites) present during reaction, and BEA describes the sum of terms representing all potential surface intermediates:

$$\beta = 1 + K_6[C_6H_{10}] + K_1[H_2O_2] + \frac{k_2 K_1 [H_2O_2]}{(k_3[C_6H_{10}]+k_5[H_2O_2])} + K_4[C_6H_{10}O] \tag{3.3}$$

Here, K_x is the equilibrium constant for each step *x*, such that the five terms in *BEA* correspond to the number of sites occupied by CH_3CN (i.e., the solvent), C_6H_{10}, H_2O_2, -(O_2) species, and $C_6H_{10}O$, respectively. At high $[H_2O_2]$:$[C_6H_{10}]$ reactant ratios (e.g., 10 for Ti-BEA), M-(O_2) species become MASI, which is shown by epoxidation rates that increase linearly with $[C_6H_{10}]$ and do not depend on $[H_2O_2]$ (Fig. 3.4). In this limit, equation 3.2 simplifies to the form:

$$\frac{r_E}{[L]} = k_3[C_6H_{10}] \tag{3.4}$$

which is consistent with the measured dependence of r_E on the reactant concentrations (Fig. 3.4). Similarly, at lower ratios of $[H_2O_2]$:$[C_6H_{10}]$, the reaction product ($C_6H_{10}O$) becomes the MASI as indicated by epoxidation rates that are independent of $[C_6H_{10}]$ and proportional to $[H_2O_2]$ (Fig. 3.4b), but also inversely dependent on $[C_6H_{10}O]$ (Fig. 3.4c, observed on Ti-, Nb-, and Ta-BEA). When $C_6H_{10}O$ is the MASI, the rate of epoxidation is much greater than the rate of H_2O_2 decomposition (i.e., $k_3[C_6H_{10}] >> k_5[H_2O_2]$; Section B3.2), and, equation 3.2 simplifies to yield:

$$\frac{r_E}{[L]} = \frac{k_2 K_1 [H_2O_2]}{k_5 K_4 [C_6H_{10}O]} \tag{3.5}$$

Notably the form of equation 3.5 matches the ways in which r_E changes with variations in $[C_6H_{1o}]$ and $[H_2O_2]$ as well as $[C_6H_{10}O]$.

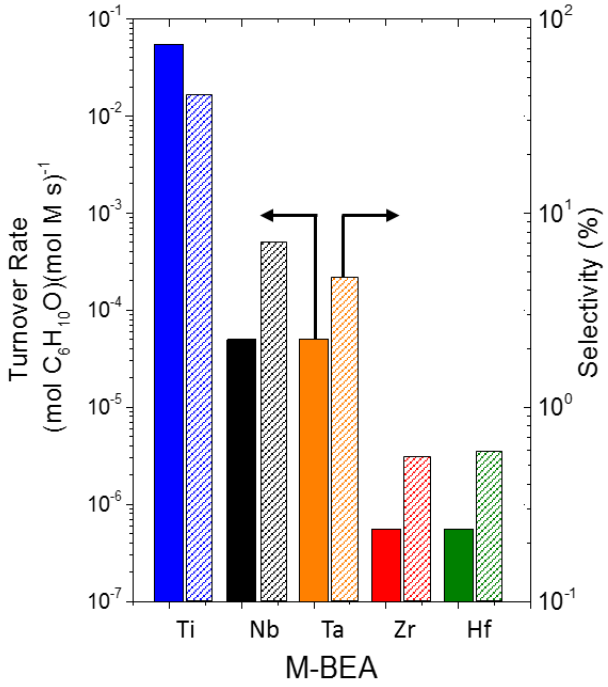

Figure 3.5. Turnover rates for the formation of $C_6H_{10}O$ (solid) and H_2O_2 selectivities (taken as the ratio of the turnover rate for $C_6H_{10}O$ formation to total H_2O_2 consumption, striped) for $Ti_{1.0}$-BEA (blue), $Nb_{0.6}$-BEA (black), $Ta_{0.6}$-BEA (orange), $Zr_{1.0}$-BEA (red), and $Hf_{1.0}$-BEA (green) (5 mM C_6H_{10}, 5 mM H_2O_2, at 313 K).

Figure 3.5 shows that these M-BEA catalysts all have very different turnover rates and selectivities (i.e., productive use of H_2O_2) at standardized conditions (5 mM C_6H_{10}, 5 mM H_2O_2, 313 K). For example, Ti-BEA gives turnover rates that are a factor of 10^5 (i.e., 100,000) times greater and selectivities that are 60 times greater than those on Zr-BEA (one element down group IV), while changing the metal from Nb to Ta results in minimal changes in rates and selectivities. Epoxidation rates depend on $[C_6H_{10}]$, $[H_2O_2]$, and $[C_6H_{10}O]$ in similar ways on all M-BEA, which strongly suggests that these materials catalyze alkene epoxidation with H_2O_2 through the common mechanism shown in Scheme 3.2. The reasons for such large differences in turnover rates and selectivities and the disparity between group 4 and 5 catalysts must be related to consequential differences in the electronic structure and reactivity of the involved intermediates. Moreover, these differences must produce activation barriers for epoxidation and H_2O_2 decomposition that depend on both the elemental identity and the details of how these transition metal atoms are coordinated within the *BEA framework. Revealing the reasons for these differences requires both quantitative measurements of the activation barriers and methods to probe the chemical properties of the active

sites and the electronic structure of the reactive intermediates that bind to these sites. To make equitable comparisons among activation barriers for epoxidation and H_2O_2 decomposition reactions, all M-BEA materials must be evaluated within the same kinetic regime (i.e., at comparable surface coverages, MASI).

Table 3.3. Activation enthalpies and entropies for C_6H_{10} epoxidation ($\Delta H^{\ddagger}_E$ and $\Delta S^{\ddagger}_E$) and H_2O_2 decomposition ($\Delta H^{\ddagger}_D$ and $\Delta S^{\ddagger}_D$) over M-BEA catalysts, measured on M-(O_2) saturated sites.

Sample	$\Delta H^{\ddagger}_E$ (kJ mol^{-1})	$\Delta S^{\ddagger}_E$ (J mol^{-1} K^{-1})	$\Delta H^{\ddagger}_D$ (kJ mol^{-1})	$\Delta S^{\ddagger}_D$ (J mol^{-1} K^{-1})
$Nb_{0.6}$-BEA	72 ± 5	-35 ± 21	45 ± 5	-91 ± 30
$Ta_{0.6}$-BEA	86 ± 6	-19 ± 11	56 ± 5	-61 ± 25
$Ti_{1.0}$-BEA	43 ± 5	-53 ± 30	31 ± 10	-104 ± 40
$Zr_{1.0}$-BEA	91 ± 10	-31 ± 9	65 ± 8	-55 ± 25
$Hf_{1.0}$-BEA	93 ± 7	-26 ± 8	64 ± 6	-77 ± 21

Table 3.3 shows activation enthalpies ($\Delta H^{\ddagger}$) and entropies ($\Delta S^{\ddagger}$) for both C_6H_{10} epoxidation ($\Delta H^{\ddagger}_E$ and $\Delta S^{\ddagger}_E$) and H_2O_2 decomposition ($\Delta H^{\ddagger}_D$ and $\Delta S^{\ddagger}_D$) obtained on M-(O_2) saturated surfaces (i.e., where rates are proportional to [C_6H_{10}] and independent of [H_2O_2] in Fig. 3.4) by operating at high [H_2O_2]:[C_6H_{10}] reactant ratios and by measuring rates of reaction as a function of inverse temperature (Section B3.3, Fig. B11). Notably, values of $\Delta S^{\ddagger}_E$ and $\Delta S^{\ddagger}_D$ do not change systematically with the identity of the metal, because these activation entropies largely reflect the loss of translational entropy that results from the coordination of either C_6H_{10} or H_2O_2 to the activated catalyst for epoxidation and H_2O_2 decomposition pathways, respectively. Table 3.3 shows that values of $\Delta H^{\ddagger}$ are much smaller for Ti-BEA (the catalyst with the greatest turnover rates), somewhat larger for Nb- and Ta-BEA, and ~50 kJ mol^{-1} greater on Zr- and Hf-BEA (the catalysts with the lowest turnover rates). Although these active site structures are similar in coordination (among Ti-, Hf-, and Zr-BEA), clearly the 10^5-fold difference in rates (Fig. 3.5) and 50 kJ mol^{-1} change in $\Delta H^{\ddagger}_E$ must reflect some intrinsic property of the metal atom, how the metal coordinates to the framework, and properties of the M-(O_2) species (i.e., active intermediate).

Previous studies have attempted to relate the reactivity of site-isolated group 4 and 5 metal atoms grafted onto mesoporous SiO_2 to the Pauling electronegativity (E_x, where x represents the elemental identity) of the metal.[51, 166-167] Values of $\Delta H^{\ddagger}$ and E_x among the different M-BEA catalysts appear to correlate linearly for Nb-, Ta-, Zr-, and Hf-BEA and $\Delta H^{\ddagger}$ values decrease with

increasing electronegativity (Fig. B12); however, the values of $\Delta H^{\ddagger}$ for both reactions (i.e., C_6H_{10} epoxidation and H_2O_2 decomposition) on Ti-BEA are grossly overestimated (by 40 kJ mol^{-1}) by this trend. The fact that E_x values alone are not enough to predict reactivity is not surprising, because the electronic structure of the metal sites and their Lewis acid strength should reflect, in part, their coordination environment within the zeolite framework. This same consideration also indicates that the E_x of the metal atoms should not be an accurate predictor for the properties of the active oxidizing intermediates (i.e., M-OOH/-$(O_2)^{2-}$ for group 4 or M-$(O_2)^{-}$ for group 5). Therefore, a complete understanding of the role that metal identity has for epoxidation with H_2O_2 requires a direct measurement of Lewis acid strength of the metal centers (as it exists in the zeolite framework) and the electronic structure of the reactive intermediate (acquired in situ).

3.3.3 Importance of Lewis Acid Strength and Electronic Structure on Alkene Epoxidation

The enthalpy of adsorption of CD_3CN (ΔH_{CD_3CN}) to Lewis acid sites provides a direct and quantitative measure of the Lewis acid strength for all M-BEA. Values of ΔH_{CD_3CN} were determined by van't Hoff analysis of CD_3CN adsorption isobars as a function of inverse temperature (Fig. B5, Table 3.1). These measurements were acquired using transmission infrared (IR) spectroscopy to quantify the change in the coverage of CD_3CN at individual Lewis acid sites (Section 3.2.2) by monitoring the intensity of the specific ν(C≡N) feature of interest within the range of 2295 – 2320 cm^{-1}. This approach distinguishes between the amounts of CD_3CN adsorbed by physisorption to the zeolite framework, coordination to surface silanol groups, and strong chemisorption to Lewis acid sites, because each adsorption mode produces a distinct ν(C≡N) absorbance feature in the IR spectra (Fig. B4).[106, 156] Consequently, IR spectroscopy allows measurements of ΔH_{CD3CN} at distinct Lewis acid sites, while conventional calorimetric methods would give ensemble averaged values that would lack specificity for CD_3CN molecules adsorbed to Lewis acid sites.

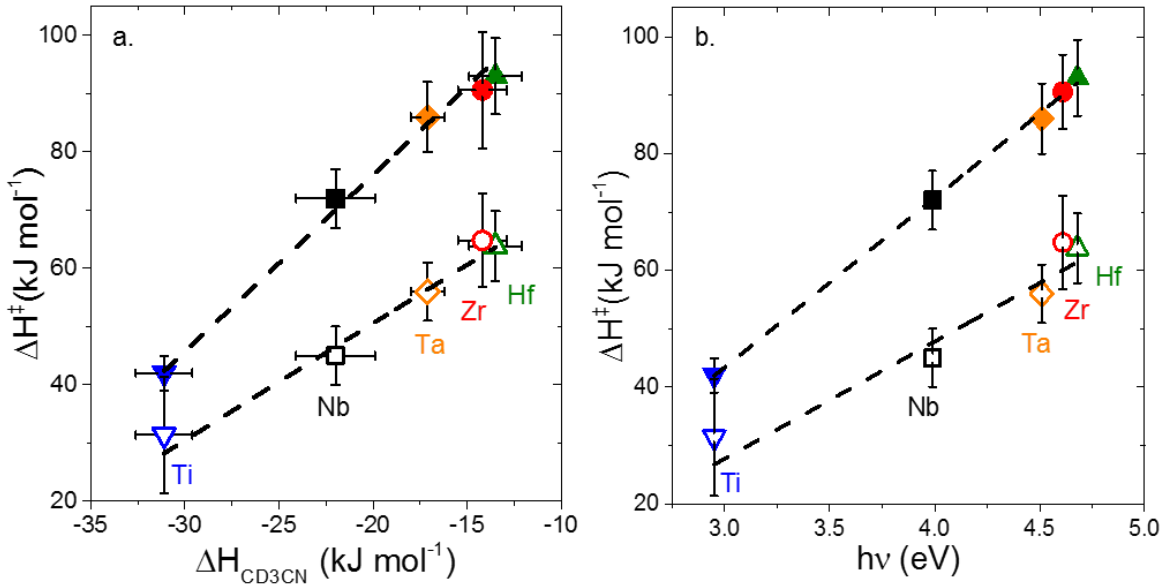

Figure 3.6. Comparisons between activation enthalpies for C_6H_{10} epoxidation ($\Delta H^{\ddagger}_E$, solid symbols) and H_2O_2 decomposition ($\Delta H^{\ddagger}_D$, open symbols)for M-(O_2) saturated surfaces of M-BEA catalysts and measured (a) heats of adsorption for acetonitrile to the active sites (ΔH_{CD_3CN}; Table 1) and (b) ligand-to-metal charge transfer (LMCT) energies (Table B1) of the specific reactive intermediate identified on each catalyst for Ti-BEA (▼), Nb-BEA (■), Ta-BEA (♦), Zr-BEA (●), and Hf-BEA (▲). Dashed lines represent linear fits.

Figure 3.6a shows that values of $\Delta H^{\ddagger}_E$ and $\Delta H^{\ddagger}_D$ depend linearly on ΔH_{CD_3CN} for all M-BEA catalysts, which strongly suggests that stronger Lewis acids (i.e., more negative ΔH_{CD_3CN}) possess lower activation enthalpies for both C_6H_{10} epoxidation and H_2O_2 decomposition. These trends show that stronger Lewis acid sites give greater turnover rates (Figs. 3.4 – 3.6), lower $\Delta H^{\ddagger}$ values (Table 3.3), and greater selectivities for epoxidation (Fig. 3.5), because strong acids pull electron density away from the $-(O_2)^-$ or -OOH/$-(O_2)^{2-}$ moiety, making these oxidants more electrophilic and reactive. Consequently, these surface species are more reactive towards electron-rich functions of C_6H_{10} (i.e., the C=C) and H_2O_2 (i.e., the lone pairs of O).[75] The phenomena observed here was alluded to by Boronat *et al.*, who predicted that among Lewis acidic metal atoms within the *BEA framework those with a lower-energy LUMO would give greater rates for the epoxidation of alkenes.[152] Additionally, these experimentally determined descriptors of the Lewis acid strength (i.e., ΔH_{CD_3CN}) and the electronic structure of the reactive intermediate (i.e.,

LMCT energy, discussed below; Fig. 3.6b) also show the reasons for the large differences in selectivity for H_2O_2 use in the epoxidations (discussed next). To the best of our knowledge, these data provide the first clear link between both the turnover rates and selectivities of M-BEA catalysts for epoxidation that span multiple groups in the periodic table and show how these catalytic properties depend on the Lewis acid strength of the active sites and also the electronic structure of the reactive species that are formed.

Furthermore, the difference in the slopes for $\Delta H^{\ddagger}_{E}$ (~3) and $\Delta H^{\ddagger}_{D}$ (~2) as a function of ΔH_{CD3CN}, show that the most electrophilic M-(O_2) intermediates give the greatest selectivities for epoxidation (Fig. 3.5), which is industrially desirable. Figure 3.5 shows that H_2O_2 selectivities increase by nearly a factor of 60 at these conditions when the framework metal atom changes from Hf (~0.5 %) to Ti (38%). Note that different reaction conditions are used to optimize the H_2O_2 selectivity on the most selective material (e.g., selectivities exceeding 95% for Ti-BEA at high [C_6H_{10}]:[H_2O_2]). For all M-BEA, C_6H_{10} epoxidation (Section 3.3.2) and H_2O_2 decomposition (Section B3.2) occur through an Eley-Rideal mechanism between C_6H_{10} or H_2O_2 with the active M-(O_2) intermediate,[59] which when combined with the observed dependencies of $\Delta H^{\ddagger}_{E}$ and $\Delta H^{\ddagger}_{D}$ on ΔH_{CD_3CN} suggests that there is a stronger interaction of C_6H_{10} with the M-(O_2) specie than H_2O_2 in the transition state. This trends differs from previously proposed O-O bond homolysis mechanism for H_2O_2 decomposition over TS-1,[64, 164] where increasing Lewis acid strength was thought to decrease H_2O_2 decomposition rates by pulling electron density from the –(O_2) moiety and, thus, decreases the propensity for O-O bond cleavage. The data and conclusions here (i.e., Fig. 3.6, more electrophilic intermediates yield greater epoxidation rates) are consistent with the prior observation that epoxidation turnover rates increase with the electron richness of the alkene (e.g., allyl alcohol > allyl chloride > 1-hexene).[65, 82] Importantly, here the electronic structure of the active site was modified (and by extension the structure and form of the reactive dioxygen intermediate that is active for epoxidation) by changing the identity of the transition metal substituent, whereas, the earlier studies manipulated rates by changing the structure of the reactant.

Figure 3.6b shows that $\Delta H^{\ddagger}_{E}$ and $\Delta H^{\ddagger}_{D}$ also increase linearly with the energy for LMCT (assessed by UV-vis) for the active intermediate (i.e., specifically M-$(O_2)^-$ species for group 5 and M-OOH/-$(O_2)^{2-}$ for group 4, Fig. 3.2 and B8) on all M-BEA. Higher LMCT energies reflect weaker Lewis acid sites, because these catalysts have a lower tendency to pull electron density towards the metal nuclei. As such, electronic transitions in weaker Lewis acids (e.g., Hf) require higher-

energy photons, as the electrons have the preference to reside on the -OOH/-$(O_2)^{2-}$ or –$(O_2)^-$ moiety. Conversely, a strong Lewis acid (i.e., Ti) has the tendency to pull electron density to the metal center, resulting in a lower energy LMCT as there is a smaller energetic preference for the electrons to reside on the -OOH/-$(O_2)^{2-}$ or -$(O_2)^-$. These differences correlate with the $\Delta H^{\ddagger}_E$ and $\Delta H^{\ddagger}_D$ values and show that the M-O_2 species with the greatest degree of electrophilicity are the most reactive and selective for alkene epoxidation.

Table 3.1 (Section 3.2.2) contains ΔH_{CD_3CN} values for each M-BEA catalyst and Fig. B13 shows that Lewis acid strength (quantified by the value of ΔH_{CD_3CN}) appears to correlate linearly with the values of E_{Nb}, E_{Ta}, E_{Zr} and E_{Hf}, but E_{Ti} deviates sharply from this trend. Recently, Román *et al*. measured the chemical shifts of ^{15}N within labeled pyridine coordinated to defect-less M-BEA materials (using MAS-NMR) and correlated these shifts to the Mulliken electronegativities (χ_x, where x is the metal identity) and calculated (via DFT methods) metal-pyridine bond dissociation energies.[168] Figure B14 shows ΔH_{CD_3CN} plotted as a function of χ_x and suggests that there is no obvious relationship between the measured Lewis acid strength and χ_x. The discrepancies in the relationship between Lewis acidity and Pauling/Mulliken electronegativity likely reflects differences in coordination environment of the metal center. For example, group 5 metals (i.e., Nb and Ta) are penta-coordinated in *BEA with typically four -O-Si bonds to the framework and an appendage -OH group (i.e., closed sites),[89, 103] while group 4 metals (i.e., Ti, Zr, and Hf) are tetra-coordinated and exist with four framework -O-Si bonds (i.e., closed sites) or three framework bonds and a terminal -OH (i.e., open sites).[91, 96, 107] Consequently, the reactivity of elements within the same group may correlate with E_x or χ_x; however, more meaningful comparisons that extend across the periodic-table and which capture potential variations in the coordination of the metal to the zeolite framework require more direct measurements of the properties of the active sites and active intermediates that exist in the catalyst, such as those presented here.

The structure-function relationships elucidated here (Fig. 3.6) for group 4 and 5 transition metal atoms within a zeolite framework directly oppose the widely-accepted electronic relationships described for homogeneous porphyrin and Schiff-base catalysts.[82, 158] These homogeneous complexes are generally constructed to result in increased electron density at the metal center (generally Fe or Mn) to facilitate homolysis of the M-OOH species and yield active oxo (M=O) or oxene (M^+=O) intermediates. In contrast, epoxidation rates and selectivities of these

group IV and V catalysts increase exponentially with Lewis acid strength, while increased electron density (as is beneficial to porphyrin and Schiff-base complexes) on the metal centers would lead to lower epoxidation rates and selectivities.

3.4 Conclusions

In situ UV-vis spectroscopy shows that group 4 (i.e., Ti, Zr, and Hf) and 5 (i.e., Nb and Ta) metal atoms incorporated into the *BEA zeolite framework activate H_2O_2 to form a pool of hydroperoxide, peroxide, and superoxide intermediates. Time resolved UV-vis spectra acquired *in situ* during reaction of H_2O_2-activated materials with C_6H_{1o} show that group 4 metals react primarily through M-OOH/M-$(O_2)^{2-}$ (i.e., hydroperoxide/peroxide) intermediates, while M-$(O_2)^{-}$ (i.e. superoxide) complexes are the active intermediates on group 5 metals, which are further confirmed by the isomeric distributions of the epoxide products detected from reaction with *Z*-stilbene. The dependencies of turnover rates on reactant and product concentrations, show that these group 4 and 5 catalysts all irreversibly activate H_2O_2 to form a pool of M-(O_2) intermediates that react with C_6H_{10} or H_2O_2 via an Eley-Rideal mechanism to form $C_6H_{10}O$ or H_2O_2-decomposition products, respectively. Correlation of activation enthalpies for epoxidation and H_2O_2 decomposition to CD_3CN adsorption enthalpies reveal that stronger Lewis acids give greater turnover rates and selectivities towards alkene epoxidation. Additionally, activation enthalpies depend strongly on the energy of the LMCT band of the reactive intermediate for each M-BEA, which suggests that metals that more easily pull electron density from the bound-dioxygen intermediates result in a more electrophilic, reactive, and selective intermediates. As such, the design of catalysts with metal centers that are stronger Lewis acids can give both greater reactivity for alkene epoxidation and also greater selectivity and yield for these epoxidations on the basis of H_2O_2.

CHAPTER FOUR

Catalytic Thiophene Oxidation over Groups 4 and 5 Framework-Substituted Zeolites: Role of Metal Lewis Acidity and Solvent Lewis Basicity[III]

Abstract

Group 4 (Ti and Zr) and 5 (Nb and Ta) atoms substituted into the *BEA zeolite framework (M-BEA) irreversibly activate hydrogen peroxide (H_2O_2) and form pools of metal-hydroperoxide (M-OOH) and peroxide (M-(η^2-O_2)) intermediates active for the oxidation of 2,5-dimethylthiophene (C_6H_8S), a model reactant representative of organosulfur species in fossil reserves and chemical weapons. Sequential oxidation pathways convert C_6H_8S into 2,5-dimethylthiophene oxide (C_6H_8SO) and subsequently into 2,5-dimethylthiophene dioxide by oxidative dearomatization. Oxidation rates measured as functions of reactant concentrations together with in situ UV-vis spectra show that all M-BEA activate H_2O_2 to form pools of M-OOH and M-(η^2-O_2), which then react with either C_6H_8S or H_2O_2 to form the sulfoxide or to decompose into H_2O and O_2, respectively. Turnover rates for C_6H_8S oxidation and H_2O_2 decomposition both increase exponentially with the electron affinity of the active site, which is quantitatively probed via the adsorption enthalpy for deuterated acetonitrile to active sites. C_6H_8S oxidation rates depend also on the nucleophilicity of the solvent used, and rates decrease in the order acetonitrile > *p*-dioxane ~ acetone > ethanol ~ methanol. In situ UV-vis spectra show that highly nucleophilic solvent molecules compete effectively for active sites, inhibit H_2O_2 activation and formation of reactive M-OOH and M-(η^2-O_2) species, and give lower turnover rates. Consequently, this work shows that turnover rates for sulfoxidation are highest when highly electrophilic active sites (i.e., stronger Lewis acids) are paired with weakly nucleophilic solvents, which can guide the design of increasingly productive catalytic systems for sulfide oxidation.

[III]This chapter has been adapted from the following publication:
Bregante, D.T.; Patel, A.Y.; Johnson, A.M.; Flaherty, D.W.; "Catalytic Thiophene Oxidation by Groups 4 and 5 Framework-Substituted Zeolites with Hydrogen Peroxide: Mechanistic and Spectroscopic Evidence for the Effects of Metal Lewis Acidity and Solvent Lewis Basicity"
Journal of Catalysis, **2018**, *364*, 415 – 425.

4.1 Introduction

Fossil fuel reserves and chemical warfare agent stockpiles contain potentially harmful organosulfur compounds (OSCs) that must be captured and sequestered by adsorption or deactivated by chemical or catalytic methods. These compounds threaten human and environmental health,[142] because they are toxic in their native form but also because they form noxious species (i.e., SO_x) upon combustion. Crude fossil fuels contain up to 5 wt. % OSCs,[169] which must be reduced below 15 ppm (i.e., <0.015 wt. %) to comply with environmental regulations for diesel fuels in many countries.[170] Furthermore, the sulfur contents of hydrocarbon feedstocks impact environmental pollution[171] but also the corrosion of equipment[172] and the reactivity of catalysts in down-stream processes.[173] OSCs are frequently removed from fossil fuels by hydrodesulfurization (HDS), which reduces OSCs using molecular hydrogen to liberate hydrogen sulfide (H_2S)[174-177] that is captured by chemical separations (i.e., absorption) or treatment (to form elemental sulfur).[178] Aromatic sulfur compounds (e.g., thiophenes) comprise the vast majority of OSCs within fossil fuel reserves.[169] Yet, many HDS catalysts (e.g., $CoMoS/Al_2O_3$) give low rates for the hydrodesulfurization of hindered thiophenes (e.g., 4,6-dimethyldibenzothiophene) because the steric bulk surrounding the sulfide moiety hinders coordination to the catalyst surface.[179-180] Consequently, reduction of these compounds requires long residence times and harsh process conditions (e.g., high temperatures, high H_2 pressures) that leads also to undesirable hydrogenolysis reactions that reduce fuel quality.[181-182]

Alternatively, oxidative desulfurization (ODS) can chemically abate the OSCs that are present in crude fuels without cleaving C-C bonds in long-chain hydrocarbons.[82] Oxidation of the sulfide moiety in thiophenes using environmentally benign oxidants, such as hydrogen peroxide (H_2O_2), produces less-toxic sulfoxide or sulfone products that are easily sequestered and analogous oxidations of many chemical warfare agents eliminates their bioactivity.[183] Multiple articles have reported the synthesis and evaluation of titanium silicalite (TS-1),[82, 184-187] titania-silicates (TiO_2-SiO_2),[188-190] Ti-BEA,[187, 191-194] and other Ti-based catalysts[195-196] for the oxidation of thiophenes. For example, Li and coworkers have shown that both TS-1[185] and Au/TS-1[184] catalysts oxidize more than 80% of the thiophene present (100 – 1000 ppm) in fluid catalytic cracking gasoline and model fuel mixtures (e.g., octane) using H_2O_2 in batch reactors (0.5 – 4 h; 333 K). Recently, other compositions of material, such as Ca^{2+}-doped MoO_3/Al_2O,[197] and Zr-incorporated UiO-66,[198] have been synthesized and shown to oxidize at least 90% of substituted dibenzothiophenes (e.g.,

dimethyldibenzothiophene; 400 – 500 ppm) within model fuel streams (e.g., octane) using short reaction times (<30 min; 328 – 333 K). Thornburg *et al*. have recently shown that niobium silicates (Nb-SiO_2) efficiently oxidize thioanisole and possess nearly perfect selectivity toward the formation of the corresponding sulfone.[190] The Nb-SiO_2 catalysts are also significantly more active for thioanisole oxidation than Ti- and Zr-SiO_2 at 318 K, which exhibit initial turnover rates of 9.0, 7.9, and 2.3 min^{-1}, respectively.[190] These trends differ markedly different from those for epoxidation catalysis on similar materials, where rates of cyclohexene and styrene epoxidation are greatest for Ti-incorporated BEA and Ti-SiO_2, followed by the Nb analogues.[11, 54, 147, 199] Currently, the reasons for the differences in thiophene oxidation rates and selectivities are unknown but may be related to changes in the mechanism for oxidation or to differences in the electronic structure and coordination of the active sites. Overall, the literature lacks a detailed mechanism for the oxidation of substituted thiophenes or guiding principles for the design of improved groups 4 and 5 catalytic systems for sulfoxidation chemistry.

Here, we seek to explain how and why rates and selectivities for the oxidation of 2,5-dimethylthiophene (C_6H_8S) depend on the intrinsic properties of active sites formed by substituting group 4 or 5 transition metal atoms into the framework of zeolite *BEA (M-BEA). A combination of reaction rates measured as a function of the reactant concentrations, in conjunction with spectroscopic measurements acquired in situ, show that all M-BEA activate H_2O_2 and oxidize C_6H_8S through a series of equivalent elementary steps that utilize similar reactive species. Comparisons of turnover rates for C_6H_8S oxidation within different solvents show that conversion rates depend exponentially on the nucleophilicity of the solvent mixture, which is quantified using the Mayr nucleophilicity scale. UV-vis spectra of Ti-BEA contacted by H_2O_2 solutions in these different solvent mixtures show a concomitant decrease in the number of M-(O_2) intermediates and C_6H_8S oxidation rates, which suggests that competitive adsorption of these Lewis basic solvents to the Lewis acidic metal centers contributes to the decrease in rates. These comparisons show that thiophene oxidation depends sensitively on the Lewis acid-base interactions between the active sites and the solvent molecules. Finally, reaction rates for C_6H_8S oxidation and H_2O_2 decomposition increase with a similar functional dependence on the electron affinity of the active sites, which are quantitatively compared using the adsorption enthalpy of deuterated acetonitrile to Lewis acid sites. Consequently, the design of catalytic systems that maximize the electron

affinity of the group 4 or 5 metal center and utilize weakly Lewis basic solvent system give greater turnover rates for ODS without sacrificing the selective use of the costly oxidant, H_2O_2.

4.2 Materials and Methods

4.2.1 Reagents

The regents used in the synthesis and characterization of M-BEA were NH_4^+-exchanged Al-BEA (Zeolyst, CP814E), HNO_3 (Macron Chemicals, 69-70%), H_2O (17.8 MΩ cm), $TiCl_4$ (Sigma, 99%), $NbCl_5$ (Sigma, 99.9%), $TaCl_5$ (Sigma, 99%), $Zr(OEt)_4$ (Alfa-Aesar, 99%), dichloromethane (Fisher Chemicals, ACS stabilized), isopropanol (Fisher Chemicals), magnesium oxide (MgO; Sigma, 99.995%), deuterated acetonitrile (CD_3CN; Cambridge Isotopes, 99.8% D atom), He (Airgas, Ultra-zero grade), and air (Airgas, Ultra-zero grade) and were used as received.

The reagents used in kinetic and in situ UV-vis spectroscopic measurements were 2,5-dimethylthiophene (C_6H_8S; Sigma, >99%), H_2O_2 (Fisher Scientific, 30 wt. % in H_2O), benzene (Sigma, 99%, thiophene free), acetonitrile (CH_3CN; Macron Chemicals, 99.8%), copper sulfate ($CuSO_4$; Fisher Chemcials, >98.6%), neocuproine (Sigma-Aldrich, >98%), ethanol (C_2H_5OH; Decon Laboratory, 200 proof), *p*-dioxane ($C_4H_8O_2$; Avantor, ACS Reagent), dimethylsulfoxide ($(CH_3)_2SO$; Macron Chemicals, ACS grade), tetrahydrofuran (C_4H_8O; Sigma, ACS grade), acetone ($(CH_3)_2CO$; Sigma, ACS Reagent), decane ($C_{10}H_{22}$; Sigma, >99%), methanol (CH_3OH; Macron, ACS grade), and He (Airgas, Ultra-zero grade) and were used as received.

4.2.2 Synthesis and Characterization of M-BEA

Ti-, Nb-, and Ta-BEA catalysts were synthesized by the post-synthetic modification of NH_4^+-BEA, while Zr-BEA was prepared by solid-state ion exchange of NH_4^+-BEA[49, 54, 96, 101, 103, 199] and is detailed in our previous reports.[11, 54, 199] In short, NH_4^+-BEA was dealuminated by reflux in HNO_3 (20 mL g^{-1}) to produce Si-BEA (Si:Al >1400, determined by EDXRF). Ti-, Nb-, and Ta-BEA were synthesized by refluxing an appropriate amount of Si-BEA with the corresponding metal chloride (e.g., $TiCl_4$) in either dichloromethane (for Ti) or isopropanol (for Nb and Ta). Solids were then recovered by rotary evaporation. Zr-BEA was produced by grinding Si-BEA with an appropriate amount of $Zr(OEt)_4$ to form an intimate mixture. In all cases, recovered solids were treated in flowing air (100 cm^3 min^{-1}) and were heated to 823 K at 2 K min^{-1} for 6 h, which produced bright white solids.

The metal contents (Table 4.1) of the M-BEA catalysts were quantified using energy dispersive X-ray fluorescence (EDXRF) spectroscopy. Briefly, 30 – 40 mg of sample was loaded into a polypropylene sample holder (1 cm diameter) that was sealed with ultralene film. These were then loaded into a spectrometer (Shimadzu, EDX-7000), whose sample chamber compartment was purged with He. One hundred scans were taken from 0 – 30 keV and the relative intensities of the fluorescence features for each element was used to determine the percent by mass of each element present.

The crystallinity of the M-BEA materials and differences in framework bond lengths before and after post-synthetic modification were determined using powder X-ray diffraction. Samples were finely ground and loaded (~60 mg) onto a polycarbonate holder, which was mounted into a diffractometer (Siemens/Bruker, D5000) with Cu Kα radiation (0.15418 nm). All X-ray diffractograms (Figure C1) were collected under ambient conditions. X-ray diffractograms were smoothed using a finite fourier transform with 10 points of fitting and the highest intensity was used to determine the positions of peak centers.

Optical band edge energies (E_g) were determined by extrapolation of the linear portion of the corresponding Tauc plot calculated from diffuse reflectance UV-vis spectra (Figure C2). M-BEA samples were intimately combined in a 1:10 by weight ratio with MgO prior to analysis. Total reflectance spectra were collected at ambient conditions on a UV-vis-NIR spectrophotometer (Agilent, CARY 5) using pure MgO as a background.

The heat of adsorption for CD_3CN bound to the cationic framework transition metal atoms (ΔH_{CD_3CN}) is used as a quantitative measure of the difference in electron affinity between the Lewis acid sites of the M-BEA catalysts. Values of ΔH_{CD_3CN} were determined using van't Hoff analysis of the coverage of CD_3CN, which was determined using infrared spectra. Catalysts were pressed into self-supporting wafers (~70 mg) and loaded into a custom-built transmission cell using CaF_2 windows,[200] which was placed into a spectrometer (Bruker, Tensor 37) and connected to a gas manifold. M-BEA pellets were first heated to 423 K at 10 K min^{-1} and held for 1.5 h under flowing He (50 cm^3 min^{-1}) with the intent to desorb water and other volatile species present. A background spectrum (128 scans, 4 cm^{-1} resolution) was then recorded in flowing He (50 cm^3 min^{-1}). CD_3CN (1.6 uL min^{-1}) was then introduced via a syringe pump (KD Scientific, Legato 100) and vaporized in flowing He within the gas-transfer lines to produce a mixture containing 1.5 kPa CD_3CN in He.

ΔH_{CD_3CN} were measured by measuring the change in the peak area for ν(C≡N) of CD_3CN bound to Lewis acid sites as a function of inverse temperature (1.5 kPa CD_3CN, 100 kPa He; Figure C3).

4.2.3 Kinetics of Thiophene Oxidation and H_2O_2 Decomposition

Rates for C_6H_8S oxidation and H_2O_2 decomposition were measured within batch reactors (100 cm^3, three-neck round-bottom flasks). C_6H_8S and H_2O_2 were added to a solution of CH_3CN (or other solvent) and benzene (used as an internal standard for chromatographic analysis) and heated to the desired temperature (303 – 348 K) while stirring at 700 rpm. M-BEA catalysts were added to initiate the reaction and small aliquots of the reaction solution were extracted as a function of time through a 0.22 μm syringe filter that removed suspended catalyst, which prevented further reaction. The concentrations of the organic components within these aliquots were quantified via a GC equipped with a flame ionization detector (HP, 5890). The concentration of H_2O_2 in each aliquot was measured by colorimetric titration using an aqueous solution of $CuSO_4$ (8.3 mM), neocuproine (12 mM), and ethanol (25% v/v). The concentration of H_2O_2 was calculated by comparison of the absorbance at 454 nm to calibrated standards, measured using a visible-light spectrophotometer (Spectronic, 20 Genesys). The product of triply-oxidized C_6H_8S (i.e., $C_6H_8SO_3$) was determining using high-resolution electron ionization mass spectrometry. Briefly, liquid samples were injected into a gas chromatograph (Agilent, 7890) and resolved chromatographic features were ionized in a mass spectrometer (Waters, GCT Premier) using electron ionization techniques to determine the relevant mass-to-charge (m/z^+) ratios. In all reported data, the carbon balance closed within 95% and the standard uncertainty for measured reaction rates was <10%.

Rates for the conversion of C_6H_8S and H_2O_2 were measured as functions of reactant concentrations, and all reported results were obtained at differential conversion (i.e., <5% conversion of the limiting reagent). Reported turnover rates on Ti-BEA, which provides the greatest turnover rates among the materials reported here, do not change with the loading of Ti atoms within the *BEA framework (section C1.2), which satisfies the Madon-Boudart criterion.[111] Consequently, concentration gradients within the catalyst particles and artifacts due to mass transfer are negligible under the conditions of this investigation.

4.2.4 In Situ UV-Vis Spectroscopy

M-BEA samples were pressed into 7 mm diameter self-supporting pellets and loaded into a custom-built liquid flow cell equipped with cartridge heaters for temperature control. UV-vis spectra were obtained in situ using a 45º diffuse-reflectance probe (Avantes, solarization-resistant fibers) connected to a modular fiber-optic spectrometer (Avantes, AvaFast 2048) with a compact deuterium-halogen light source (Avantes, AvaLight-DHc). Liquid solutions were introduced using a high-performance liquid chromatography pump (Waters, 515). Background spectra were collected after flowing CH_3CN (1 cm^3 min^{-1}) over the samples for 1 h at 313 K prior to changing the liquid reservoir to vary the reaction conditions. Between switching solvents, the Ti-(O_2) intermediates were removed by flowing a solution of C_6H_8S in CH_3CN (0.01 M; 1 cm^3 min^{-1}) for 2 h at 333 K. Processes for peak smoothing are described in section C2.

4.3 Results and Discussion

4.3.1 Catalyst Characterization

X-ray diffractograms (XRD) for all M-BEA catalysts (Figure C1a) shows that all materials are *BEA-type zeolites and that the post-synthetic modifications did not significantly alter the zeolite structure.[159] Comparisons between the X-ray diffractograms for the dealuminated *BEA and M-BEA materials (Figure C1b, Ti, Zr, Nb, and Ta metal loadings of 1.2, 2.4, 1.5, and 3.0 wt. %, respectively) show that the diffraction peak assigned to the d_{302} spacing[201] shifts from 22.52º for dealuminated *BEA to lower values (22.42 – 22.45º) following treatments intended to substitute Ti, Zr, Nb, and Ta atoms into the framework. The observed shifts match prior reports[101, 202-203] and reflect an expansion of the *BEA lattice, which confirms that the transition metal ions (e.g., Zr^{4+} or Nb^{5+}) occupy tetrahedral sites following the synthesis methods used here.[204]

Table 4.1 summarizes the weight loading of transition metal atoms in the M-BEA catalysts used for kinetic measurements, as measured by energy dispersive X-ray fluorescence (EDXRF). For Ti-, Nb-, and Ta-materials, M-BEA were made to result in ~0.1 (M atom)(unit cell)$^{-1}$ on average (i.e., Si/M ratios >500), with the intent to form predominantly equivalent M-atom sites and to minimize intraparticle concentration gradients. Zr-BEA was synthesized with a lower Si/Zr ratio (i.e., higher metal loading) that results in ~1 (M atom)(unit cell)$^{-1}$ in order to accurately measure the kinetics behind C_6H_8S ODS on this catalyst (Section 4.2.3), because the turnover rates measured were very low. In all cases, the post synthetic modification results in M-BEA catalysts

with many residual silanol nests (i.e., $(SiOH)_4$ groups), because only a small fraction of the Al atoms in the parent Al-BEA were replaced. These high silanol densities lead to highly hydrophilic materials, the catalytic properties of which may differ from analogous structures with hydrophobic pores, such as those synthesized within fluoride media.[159]

In all cases, M-BEA materials possess a single prominent UV-vis absorbance feature (e.g., at 230 nm for Ta-BEA; Fig. C2) that correspond to a charge transfer from the 2p orbitals of oxygen to the valence orbitals of the transition metal (i.e., Ti, Nb, Ta, or Zr) in the *BEA framework [205]. The relatively large band gaps (Table 4.1) and absence of other observable features shoulders at higher wavelengths strongly suggests that the transition metal atoms within each M-BEA are highly disperse and that these materials contain little, if any, oligomeric or bulk oxide phases.[51]

Figure 4.1 shows infrared (IR) spectra of CD_3CN adsorbed on all M-BEA materials. All spectra of CD_3CN adsorbed on M-BEA catalysts show contain an absorbance feature at ~2274 cm^{-1} attributed to the ν(C≡N) of CD_3CN bound to SiOH groups within the *BEA framework.[11, 49, 54, 159, 199] Ti-, Nb-, and Ta-BEA possess also additional peaks at 2302, 2306, and 2312 cm^{-1}, respectively, which correspond to the ν(C≡N) mode of CD_3CN bound to these Lewis acidic metal centers.[49, 199] In addition to the peak at ~2274 cm^{-1}, Zr-BEA possesses a second feature at 2296 cm^{-1} assigned to CD_3CN bound to Lewis acid sites and a third peak attributed to CD_3CN coordinate to Brønsted acidic open sites (i.e., $(SiO)_3Zr(OH)$).[96, 161, 199] Adsorption enthalpies for CD_3CN bound to Lewis acidic metal atoms (ΔH_{CD_3CN}) in the M-BEA framework were used to quantify differences in the electron affinity of these active sites, which serves as a descriptor for Lewis acid strength. Notably, measured values of ΔH_{CD_3CN} likely represents the intrinsic adsorption enthalpy for CD_3CN to the Lewis acidic metal atom, as the solvation of CH_3CN within the micropores of siliceous MFI results in a heat of adsorption of ~60 kJ mol^{-1}. Table 4.1 summarizes values of ΔH_{CD_3CN} for all M-BEA and shows that Ti atoms in *BEA have the greatest electron affinity, followed by Nb, Ta, and Zr, which matches our previous report.[199] These comparisons suggest that the transition metal atoms within *BEA are electronically equivalent, as ΔH_{CD_3CN} is independent of metal loading (e.g., Ti-BEA with a Ti loading of 0.14 wt.% and 1.2 wt.% each possess values of ΔH_{CD_3CN} of -31 ± 2).[199]

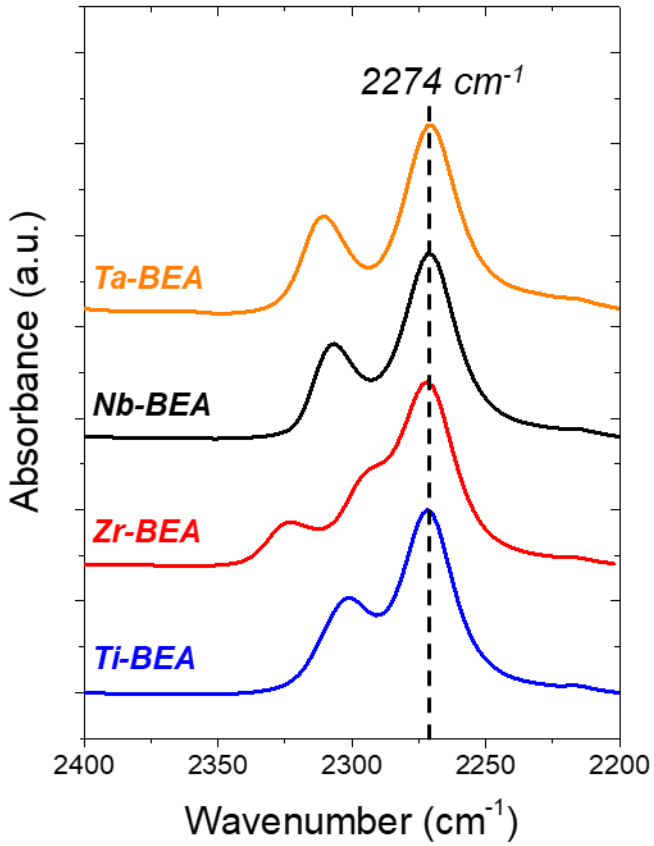

Figure 4.1. Infrared spectra of CD_3CN bound to Ti-BEA (blue), Zr-BEA (red), Nb-BEA (black), and Ta-BEA (orange). Spectra were normalized to intensity of the ν(C≡N) mode of CD_3CN bound to silanol sites (2274 cm^{-1}) and were collected in flowing CD_3CN He (1.5 kPa CD_3CN, ~443 K).

Table 4.1. Band Edge Energies, Silicon-to-Metal Ratios, Metal Loadings, Silicon-to-Aluminum Ratios, and Heats of Adsorption for CD_3CN Coordinated to Lewis Acidic Metal Atoms for M-BEA catalysts used for Catalytic Rate Measurements (Sections 4.3.2 – 4.3.4)

Sample	Band Edge (eV)[a]	Si:M Ratio[b]	Weight loading (wt. %)	Si:Al Ratio[b]	ΔH_{CD_3CN} (kJ mol^{-1})[c]
Ti-BEA	4.2	550	0.14	>1400	-31 ± 2
Zr-BEA	5.3	60	2.4	>1400	-12 ± 1
Nb-BEA	4.0	690	0.22	>1400	-20 ± 2
Ta-BEA	4.6	570	0.53	>1400	-16 ± 2

[a]Measured by diffuse reflectance UV-vis spectroscopy; [b]Measured by energy dispersive X-ray fluorescence spectroscopy; [c]Determined using van't Hoff analysis of infrared spectra

Collectively, these data suggest that the post-synthetic modification of the commercially-available Al-BEA does not significantly change the structure of the *BEA framework, successfully

incorporates group 4 and 5 metal atoms into the framework of *BEA, and that the electron affinities (i.e., ΔH_{CD_3CN}) differ with elemental identity.

4.3.2 Reaction Pathways for 2,5-dimethylthiophene Oxidation

Figure 4.2a shows the selectivity towards primary, secondary, and tertiary oxidation products as a function of 2,5-dimethylthiophene (C_6H_8S) conversion during the reaction of C_6H_8S with H_2O_2 over Ti-BEA (0.005 M C_6H_8S, 0.05 M H_2O_2, 313 K). The oxide (C_6H_8SO), 2,5-dimethylthiophene dioxide ($C_6H_8SO_2$), and $C_6H_8SO_3$ (e.g., epoxidized $C_6H_8SO_2$) as a function of C_6H_8S conversion over Ti-BEA (0.005 M C_6H_8S, 0.05 M H_2O_2, 313 K). As the conversion of C_6H_8S approaches zero, the selectivity towards 2,5-dimethylthiophene oxide (C_6H_8SO) nears 100%, which shows that C_6H_8SO is the sole primary product of C_6H_8S oxidation. The selectivity to 2,5-dimethylthiophene dioxide ($C_6H_8SO_2$) becomes detectable when the conversion exceeds 5% and reaches a maximum at ~40% conversion, which indicates that this sulfone forms by a secondary reaction. Selectivities to both the sulfoxide and sulfone products decrease as the C_6H_8S conversion increases, because tertiary reaction pathways also consume $C_6H_8SO_2$ to form the resultant 2,5-dimethylthiophene dioxide epoxide (i.e., $C_6H_8SO_3$; identified by mass spectrometry; m/z^+ = 160.0141) from oxidation of the C=C bonds within the thiophenic ring.

The selectivity patterns and reaction pathways of C_6H_8S oxidation differ markedly from oxidations of related sulfides (e.g., thioanisole) in which non-aromatic sulfide moieties readily oxidize to form the corresponding sulfone on Ti-based catalysts.[206] Specifically, singly-oxidized thiophenes (i.e., the corresponding sulfoxide) resist further oxidation.[75] Estimates using group additivity indicate that the reaction enthalpy for the oxidation of C_6H_8SO to $C_6H_8SO_2$ is 37 ± 6 kJ mol^{-1} less exothermic than the initial sulfoxidation of C_6H_8S, because the second oxidation breaks the aromaticity of the ring.[207] Consequently, linear free energy relationships would suggest that barriers for oxidation of the sulfoxide would be greater than those for the thiophene, which is consistent with the change in selectivities with C_6H_8S conversion (Figure 4.2a). The H_2O_2-mediated oxidation of C_6H_8S on Nb- and Ta-BEA catalysts shows similar product selectivity patterns (Figure C6), which suggests that C_6H_8S reacts through identical reaction pathways that first form C_6H_8SO, which undergoes dearomative oxidation to form $C_6H_8SO_2$ and then $C_6H_8SO_3$ on all M-BEA. Figure 4.2b shows the selectivity towards each of the two pathways for H_2O_2 consumption, thiophene oxidation and bimolecular H_2O_2 decomposition, as a function C_6H_8S

conversion over Ti-BEA. H_2O_2 selectivities for thiophene oxidation remain constant (0.29 ± 0.06) at all values of C_6H_8S conversion. The H_2O_2 selectivities are nearly constant because the MASI changes throughout the course of the reaction due to competitive adsorption, which inhibits reaction rates of both C_6H_8S oxidation and H_2O decomposition pathways similarly.

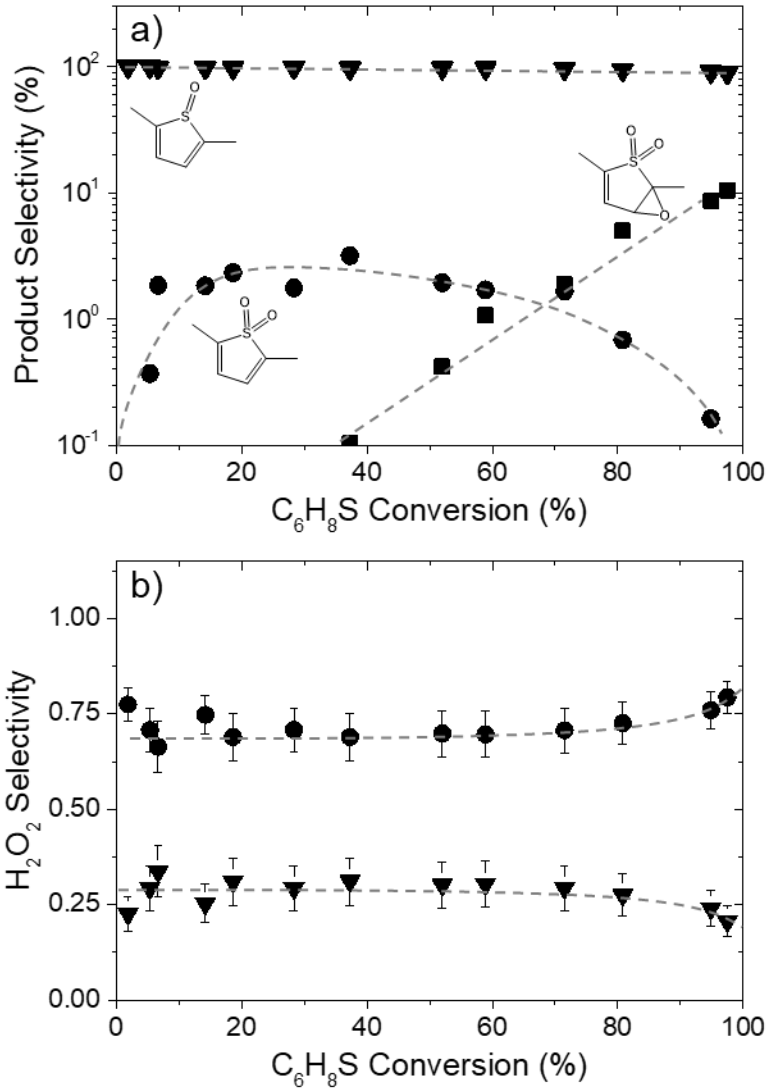

Figure 4.2. (a) Product selectivity towards C_6H_8SO (▼), $C_6H_8SO_2$ (●), and oxidized $C_6H_8SO_2$ (■); and (b) selectivity for the consumption of H_2O_2 by oxidation reactions (▼) and H_2O_2 decomposition (●) as a function of C_6H_8S conversion (5 mM C_6H_8S, 0.05 M H_2O_2, 313 K) over Ti-BEA. Dashed curves are intended to guide the eye.

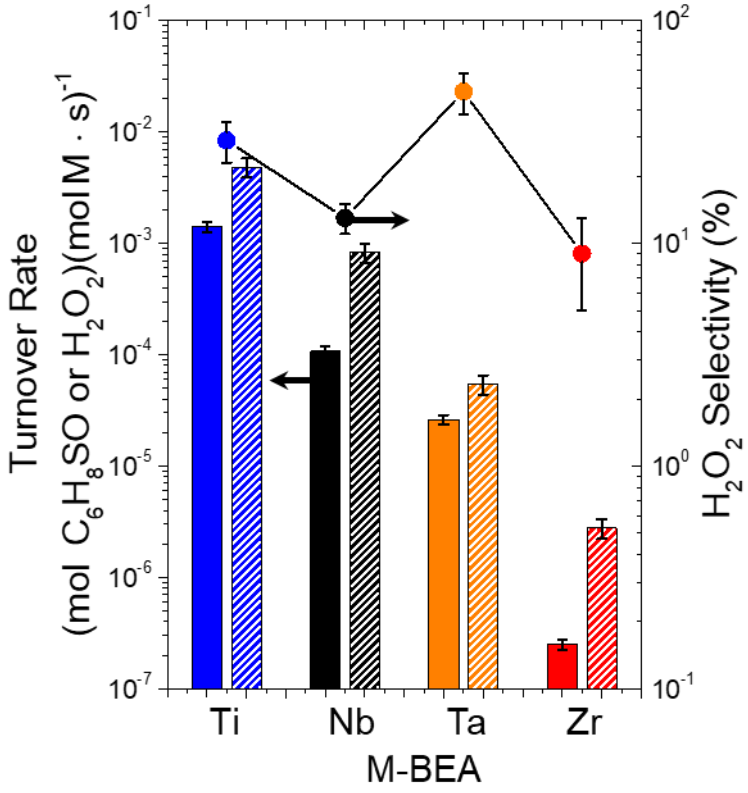

Figure 4.3. Turnover rates for the formation of C_6H_8SO (solid bars), H_2O_2 decomposition (striped bars), and selectivities for H_2O_2 use in C_6H_8S oxidation (●, taken as a ratio of the turnover rate for C_6H_8SO formation to total H_2O_2 consumption, 0.01 M C_6H_8S, 0.01 M H_2O_2, 313 K) in CH_3CN as a function of metal identity in M-BEA.

Figure 4.3 shows the turnover rates for C_6H_8S oxidation and H_2O_2 decomposition at differential conversion over all M-BEA catalysts at a standard set of conditions (0.01 M C_6H_8S, 0.01 M H_2O_2, 313 K). The rates of C_6H_8S oxidation and H_2O_2 decomposition vary significantly among the different M-BEA catalysts: Ti-BEA possesses rates for both pathways that are ~$3.5 \cdot 10^4$ times greater than those for Zr-BEA. Interestingly, the values of C_6H_8S oxidation and H_2O_2 decomposition rates tend to differ by similar amounts between the different metals; however, H_2O_2 selectivity does not follow the same trend as the turnover rates for C_6H_8S oxidation, as Ta-BEA possesses the highest selectivities at this set of conditions (~49%). Notably, Ta-BEA converts

C_6H_8SO to $C_6H_8SO_2$ at lower C_6H_8S conversions than Ti-BEA (e.g., 10% versus 2% selectivity towards $C_6H_8SO_2$ for Ta-BEA and Ti-BEA, respectively at 20% C_6H_8S conversion; Figure C6). These large differences in turnover rates and the lack of concomitant variance in H_2O_2 selectivities among these M-BEA catalysts clearly reflect some combination of differences between the specific surface species (i.e., most abundant surface intermediate) during C_6H_8S oxidation, the energetic barriers for each reaction pathway, or an intrinsic property of the active sites among the M-BEA catalyst, which are investigated in the following sections.

4.3.3 Kinetics and Mechanistic Interpretation of Oxidation Kinetics

Figure 4.4 shows initial turnover rates for the oxidation of C_6H_8S as a function of the concentrations of C_6H_8S, H_2O_2, and dimethylsulfoxide ($(CH_3)_2SO$; $(CH_3)_2SO$ was used as a model sulfoxide to measure the dependence of turnover rates on the concentration of initial sulfoxide product, because sufficiently pure samples of C_6H_8SO were not available) on Ti-, Nb-, Ta, and Zr-BEA catalysts. On these materials, relatively low ratios of the concentrations of C_6H_8S to that of H_2O_2 (e.g., $[C_6H_8S]:[H_2O_2] < 1$ on Ti-BEA) result in rates of C_6H_8S oxidation that increase linearly with $[C_6H_8S]$ and are not functions of $[H_2O_2]$, which suggests that active sites are saturated with H_2O_2-derived species under these conditions. As the $[C_6H_8S]$ increases further at constant $[H_2O_2]$, the rate of oxidation becomes independent of $[C_6H_8S]$, proportional to $[H_2O_2]$, and inversely proportional to $[(CH_3)_2SO]$, which shows that the most abundant surface intermediate (MASI) becomes a species formed from C_6H_8S (e.g., C_6H_8SO).[208]

Scheme 4.1 shows a series of elementary steps that account for the measured effects of $[C_6H_8S]$, $[H_2O_2]$, and $[(CH_3)_2SO]$ on sulfoxidation turnover rates across all M-BEA catalysts. The catalytic cycle for C_6H_8S oxidation involves the quasi-equilibrated adsorption of C_6H_8S (step 1) and H_2O_2 (step 2), followed by the irreversible activation of H_2O_2 (step 3) to form a pool of M-OOH and M-(η^2-O_2) intermediates,[11, 54, 199] which are collectively denoted as M-(O_2). The active M-(O_2) species react with C_6H_8S (step 4) or C_6H_8SO (step 7) to form the corresponding sulfoxide or sulfone product, respectively, which then desorb (steps 6 and 8). Alternatively, the active M-(O_2) intermediates may decompose non-productively by reaction with liquid-phase H_2O_2 (step 5) [164]. Notably, the rate dependencies for this sulfoxidation on $[C_6H_8S]$ and $[H_2O_2]$ are analogous to the functional form of epoxidation rates on the concentrations of cyclohexene[199] and styrene[11] on M-BEA catalysts.

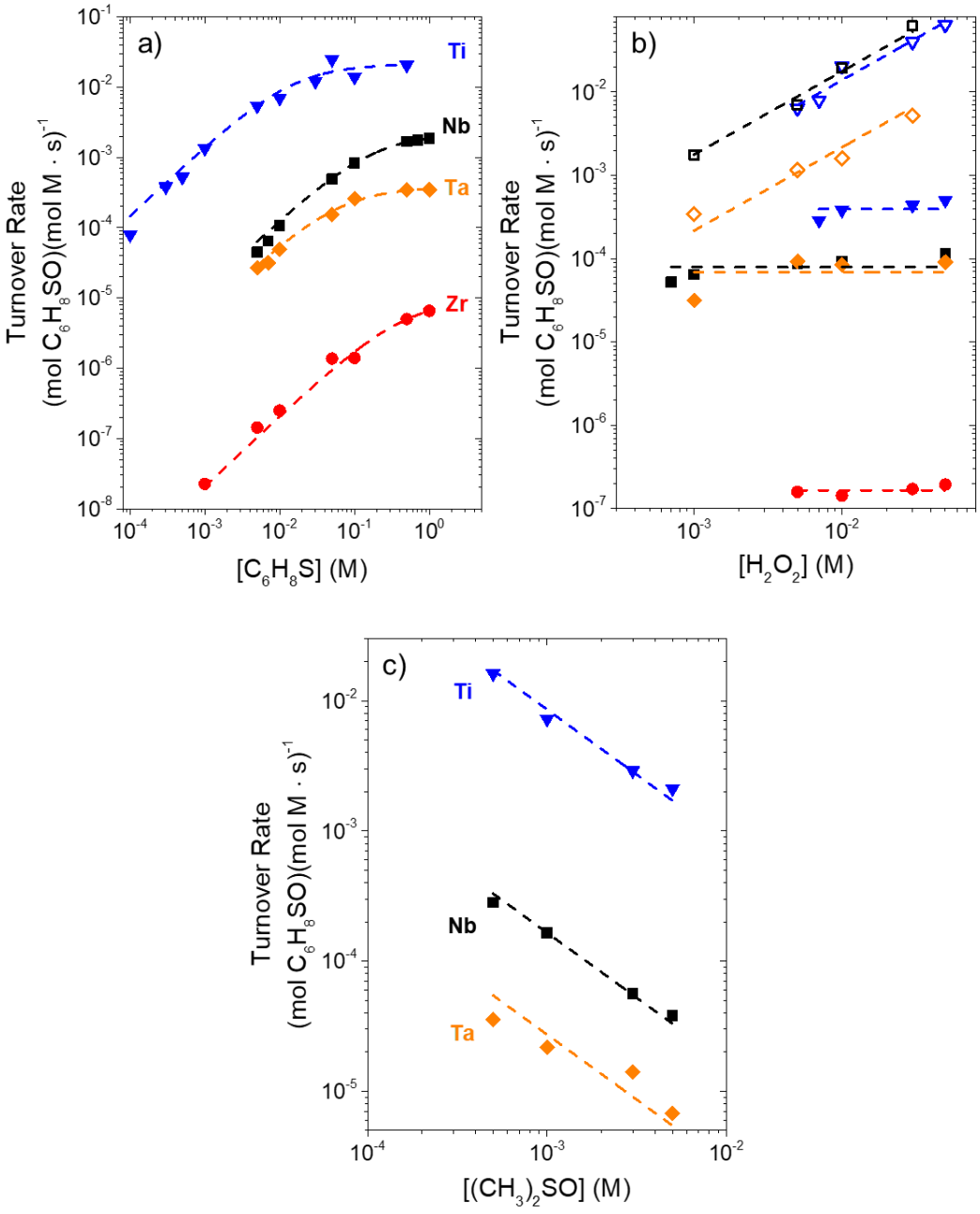

Figure 4.4. Turnover rates for the formation of C_6H_8SO as a function of (a) $[C_6H_8S]$ for Ti-BEA (▼, 0.01 M H_2O_2), Nb-BEA (■, 1 mM H_2O_2), Ta-BEA (◆, 1 mM H_2O_2), and Zr-BEA (●, 0.01 M H_2O_2); (b) $[H_2O_2]$ for Ti-BEA (▼, 0.7 mM C_6H_8S; ▽ 0.5 M C_6H_8S), Nb-BEA (■, 7 mM C_6H_8S; □, 1 M C_6H_8S), Ta-BEA (◆, 7 mM C_6H_8S; ◇, 1 M C_6H_8S), and Zr-BEA (●, 5 mM C_6H_8S); and (c) $[(CH_3)_2SO]$ for Ti-BEA (▼, 0.01 M H_2O_2, 5 M C_6H_8S), Nb-BEA (■, 1 mM H_2O_2, 1 M C_6H_8S), and Ta-BEA (◆, 1 mM H_2O_2, 1 M C_6H_8S) at 313 K. Dashed lines represent least squares regression fits to the relevant equations in the main text (i.e., equations 4.4, 4.6, and 4.8).

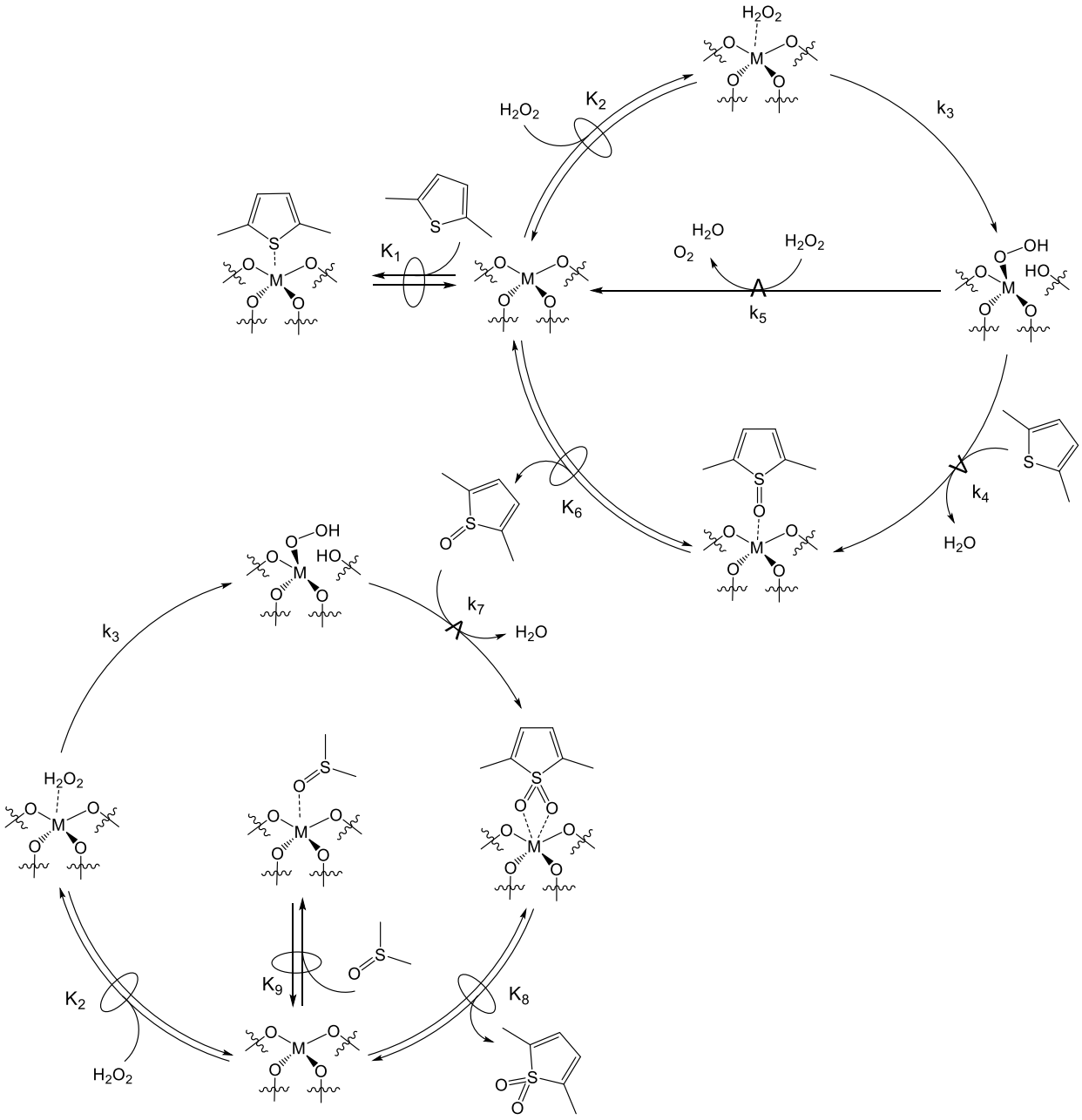

Scheme 4.1. Proposed Mechanism for the Oxidation of C_6H_8S and C_6H_8SO with H_2O_2 over M-BEA. For brevity, only group 4 M-BEA (e.g., Ti- or Zr-BEA) closed sites are shown. The symbol ⇄ represents a quasi-equilibrated step, while → represents a kinetically relevant step. Note, the depiction of M-(O_2) and adsorbed C_6H_8S, C_6H_8SO, $C_6H_8SO_2$, $(CH_3)_2SO$, and H_2O_2 are meant to represent different types of surface species, rather than suggest a specific coordination to the active catalytic site.

Rates of C_6H_8S oxidation (r_{Ox}) are equal to that for the kinetically relevant reaction of C_6H_8S with M-(O_2) intermediates, which takes the form:

$$r_{Ox} = k_4[M-(O_2)][C_6H_8S] \tag{4.1}$$

where k_x is the rate constant for step x in Scheme 4.1, and [M-(O_2)] is the number of active M-(O_2) intermediates. Application of the pseudo steady-state hypothesis (Section C4.1) to [M-(O_2)] transforms equation 4.1 to:

$$r_{Ox} = \frac{k_3 k_4 K_2 [C_6H_8S][H_2O_2][*]}{k_4[C_6H_8S]+k_5[H_2O_2]+k_7[C_6H_8SO]} \tag{4.2}$$

where K_x is the equilibrium constant for step x in Scheme 4.1 and [*] is the number of unoccupied active sites that can bind to or react with specific species in solutions. An expression for [*] is given from the sum of all plausible surface intermediates

$$[L] = [*] + [M-(O_2)] + [C_6H_8S*] + [H_2O_2*] + [C_6H_8SO*] + [C_6H_8SO_2*] + [(CH_3)_2SO*] \tag{4.3}$$

where [L] is the total number of catalytically active metal atoms in the BEA framework, and [C_6H_8S*], [H_2O_2*], [C_6H_8SO*], [$C_6H_8SO_2$*], and [$(CH_3)_2SO$*] are the number of adsorbed molecules of C_6H_8S, H_2O_2, C_6H_8SO, $C_6H_8SO_2$, and $(CH_3)_2SO$, respectively. Finally, equations 4.2 and 4.3 can be combined to yield a full rate expression for C_6H_8S oxidation

$$\frac{r_{Ox}}{[L]} = \frac{\frac{k_3 k_4 K_2 [C_6H_8S][H_2O_2]}{k_4[C_6H_8S]+k_5[H_2O_2]+k_7[C_6H_8SO]}}{\gamma} \tag{4.4}$$

where γ describes the sum of terms that represent all potential surface species

$$\gamma = [1] + \frac{k_3 K_2 [H_2O_2]}{k_4[C_6H_8S]+k_5[H_2O_2]+k_7[C_6H_8SO]} + K_1[C_6H_8S] + K_2[H_2O_2] + K_6[C_6H_8SO] + K_8[C_6H_8SO_2] + K_9[(CH_3)_2SO] \tag{4.5}$$

such that the seven terms in γ correspond to the number of sites occupied by CH_3CN (i.e., the solvent), M-(O_2) intermediates, and adsorbed C_6H_8S, H_2O_2, C_6H_8SO, $C_6H_8SO_2$, and $(CH_3)_2SO$,

respectively. At sufficiently low [C_6H_8S], and in the absence of $(CH_3)_2SO$, M-(O_2) intermediates become the MASI, which simplifies equation 4.4 to yield

$$\frac{r_{Ox}}{[L]} = k_4[C_6H_8S] \tag{4.6}$$

which is quantitatively consistent with rates of C_6H_8S oxidation that depend linearly on [C_6H_8S] (Figure 4.4a) and not on [H_2O_2] (Figure 4.4b). Similarly, at higher ratios of [C_6H_8S]:[H_2O_2] the oxidation products (e.g., C_6H_8SO) become the MASI, which appears as turnover rates that possess no dependence on [C_6H_8S] and increase proportionally to [H_2O_2]. When values of [C_6H_8S]:[H_2O_2] are large, the values of k_2[C_6H_8S] (C_6H_8S sulfoxidation) are much larger than for the terms k_4[H_2O_2] (H_2O_2 decomposition) and k_7[C_6H_8SO] (C_6H_8SO oxidation), because k_2 and k_4 are similar in magnitude and much larger than k_7 because C_6H_8SO resists oxidation.[209] This simplifies equation 4.4 to yield

$$\frac{r_{Ox}}{[L]} = \frac{k_3K_2[H_2O_2]}{K_6[C_6H_8SO]} \tag{4.7}$$

Equation 4.7 matches the ways in which r_{Ox} change with [H_2O_2] and [C_6H_8S] (Figures 4.4a and 4.4b). Changes in r_{Ox} as a function of [$(CH_3)_2SO$] were measured to emulate the effect of sulfoxide adsorption on rates, and the presence of $(CH_3)_2SO$* is accounted for by the form of the site balance in equation 4.5. Equation 4.4 simplifies when $(CH_3)_2SO$* becomes the MASI (i.e., at high [C_6H_8S]) leading to:

$$\frac{r_{Ox}}{[L]} = \frac{k_3K_2[H_2O_2]}{K_9[(CH_3)_2SO]} \tag{4.8}$$

which resembles the observed dependence on [$(CH_3)_2SO$] on Ti-, Nb-, and Ta-BEA (Figure 4.4c). Rates of C_6H_8S oxidation on Zr-BEA were immeasurable ($<10^{-8}$ (mol C_6H_8SO)(mol M · s)$^{-1}$) in the presence of $(CH_3)_2SO$. The implied presence of high coverages of M-(O_2) intermediates and $(CH_3)_2SO$ on active sites under the ranges of reaction conditions discussed with Figure 4.4 were probed directly by UV-vis spectra of M-BEA materials acquired in situ [58, 121, 164].

4.3.4 Effects of Reactant Concentrations and Solvents on Coverages of Active Species

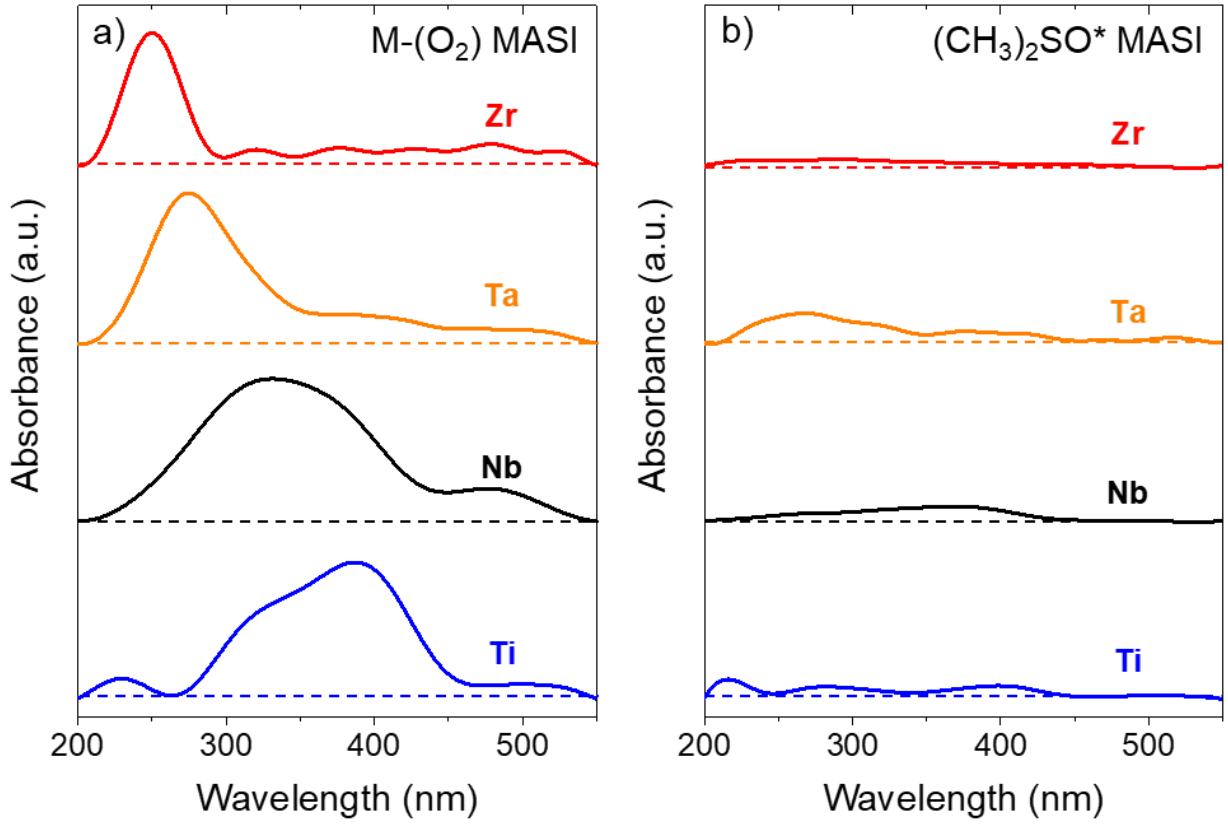

Figure 4.5. Steady-state UV-vis spectra (solid lines) obtained in situ at conditions that generate (a) M-(O_2) saturated surfaces on Ti-BEA (blue; 0.7 mM C_6H_8S, 0.01 M H_2O_2), Nb-BEA (black; 7 mM C_6H_8S, 0.01 M H_2O_2), Ta-BEA (orange; 7 mM C_6H_8S, 0.01 M H_2O_2), and Zr-BEA (red; 5 mM C_6H_8S, 0.01 M H_2O_2); and at conditions that form (b) $(CH_3)_2SO$ saturated surfaces on Ti-BEA (blue; 5 mM $(CH_3)_2SO$, 0.01 M H_2O_2), Nb-BEA (black; 5 mM $(CH_3)_2SO$, 0.01 M H_2O_2), Ta-BEA (orange; 5 mM $(CH_3)_2SO$, 0.01 M H_2O_2), and Zr-BEA (red; 5mM $(CH_3)_2SO$, 0.01 M H_2O_2). C_6H_8S was omitted from reaction solutions containing $(CH_3)_2SO$, because these solutions absorbed 300-500 nm light, which obscured features for M-(O_2) intermediates. Dashed lines represent baselines for each spectrum.

UV-vis spectra collected in situ are needed to qualitatively determine the coverages of M-(O_2) and $(CH_3)_2SO$ surface species and to confirm the assumptions used to derive the rate expression for sulfoxidation (vide infra). Figure 4.5 shows in situ UV-vis spectra of M-BEA catalysts during steady-state ODS at two relevant limits of reaction conditions: high ratios of [H_2O_2] to [C_6H_8S] that are expected to produce M-(O_2) saturated surfaces (Figure 4.5a) and low ratios that should form sulfoxide covered surfaces (Figure 4.5b), as suggested by the interpretation

of measured rates in Figure 4.4 (Section 4.3.3). The UV-vis spectrum obtained in situ under conditions likely to produce a M-(O_2) saturated surface (Figure 5a, 0.01 M H_2O_2, 0.7 mM C_6H_8S, 313 K, Ti-BEA) shows a complex absorbance feature between 300 – 420 nm, which is consistent with those of Ti-OOH and Ti-(η^2-O_2) species on Ti atoms grafted to mesoporous silicas[11, 58, 164, 210] and within the framework of MFI[121, 164, 211] and BEA[11, 54, 199] zeolites. Alternatively, these UV-vis absorbance features are absent in the presence of $(CH_3)_2SO$ and H_2O_2 (Figure 4.5b, 5 mM $(CH_3)_2SO$, 0.01 M H_2O_2, 313 K), which suggests that sulfoxides bind strongly to the Lewis acidic metal centers and prevent the activation of H_2O_2 to form M-(O_2). Notably, identical observations were made on all M-BEA, which corroborates the interpretation of measured rate dependencies on [H_2O_2] and [$(CH_3)_2SO$] (Figure 4.4) that M-(O_2) and $(CH_3)_2SO$* become the MASI in the limits of low and high [C_6H_8S]:[H_2O_2], respectively (vide infra).

Oxidation turnover rates that decrease upon adding $(CH_3)_2SO$ and the displacement of reactive M-(O_2) intermediates by the sulfoxide imply that the identity and chemical nature of the solvent for ODS will influence rates of H_2O_2 activation and oxidation of thiophenes. Figure 4.6 shows the turnover rates for C_6H_8S oxidation and the UV-vis absorbance intensities for Ti-(O_2) within six different solvent mixtures relevant for sulfoxidation catalysis[212-214] (note, all UV-vis spectra were obtained from a single Ti-BEA pellet to facilitate equitable comparisons). Among these solvents, sulfoxidation turnover rates are greatest in 10% v/v C_4H_8O in $C_{10}H_{22}$ ($9\cdot10^{-3}$ (mol C_6H_8SO)(mol Ti $\cdot$ s)$^{-1}$) and CH_3CN ($7\cdot10^{-3}$ (mol C_6H_8SO)(mol Ti $\cdot$ s)$^{-1}$), in part, because both these solvents allow for the formation of M-(O_2) saturated active sites as demonstrated by the intensity of the UV-Vis feature for M-(O_2) species (Figure 6; 0.01 M H_2O_2, 313K). These observations, together with the rate dependencies shown in Figure 4.4, demonstrate that these solvent molecules do not effectively compete for Lewis acidic metal centers during catalysis. Turnover rates for C_6H_8S oxidation are significantly lower in oxygenated solvents (e.g., acetone ($(CH_3)_2CO$), *p*-dioxane ($C_4H_8O_2$), and ethanol (C_2H_5OH)), and become nearly immeasurable in $(CH_3)_2SO$. In addition, small amounts of dimethylsulfone ($(CH_3)_2SO_2$) formed when the solvent was $(CH_3)_2SO$, which correspond to a turnover rate of $5\cdot10^{-6}$ (mol $(CH_3)_2SO_2$)(mol Ti $\cdot$ s)$^{-1}$. The UV-vis spectra of M-(O_2) surface intermediates obtained for this series of solvents show a concomitant decrease in the peak areas for M-(O_2) absorbance features with the decrease in the turnover rates for sulfoxidation, which further suggests that these Lewis basic solvents competitively adsorb and displace reactive intermediates from the Lewis acidic Ti sites. Specifically, the strong Lewis basicity of O-atom

lone pairs within the oxygenated solvents rivals that of H_2O_2, and together with the greater concentrations of the solvent molecules, leads to the saturation of Lewis acidic Ti metal centers by solvent molecules. The decrease in Ti-(O_2) coverage (taken to be proportional to the UV-vis absorbance feature area) does not change quantitatively with the differences in reaction rates in Figure 6, which is apparent when comparing measurements with CH_3CN and C_2H_5OH. This disparity suggests, unsurprisingly, that solvents play a role beyond simple site competition and may change activation barriers for sulfoxidations either by changing the stability of transition states for oxidation of the sulfide moiety or by influencing the enthalpic cost to generate unoccupied active sites that subsequently bind and activate H_2O_2 within the catalytic cycle.[215] These energetic penalties result in an increase in the apparent activation barriers, which contribute to the large discrepancies in turnover rates that cannot be explained simply by competitive adsorption changing the surface coverage of M-(O_2) intermediates.

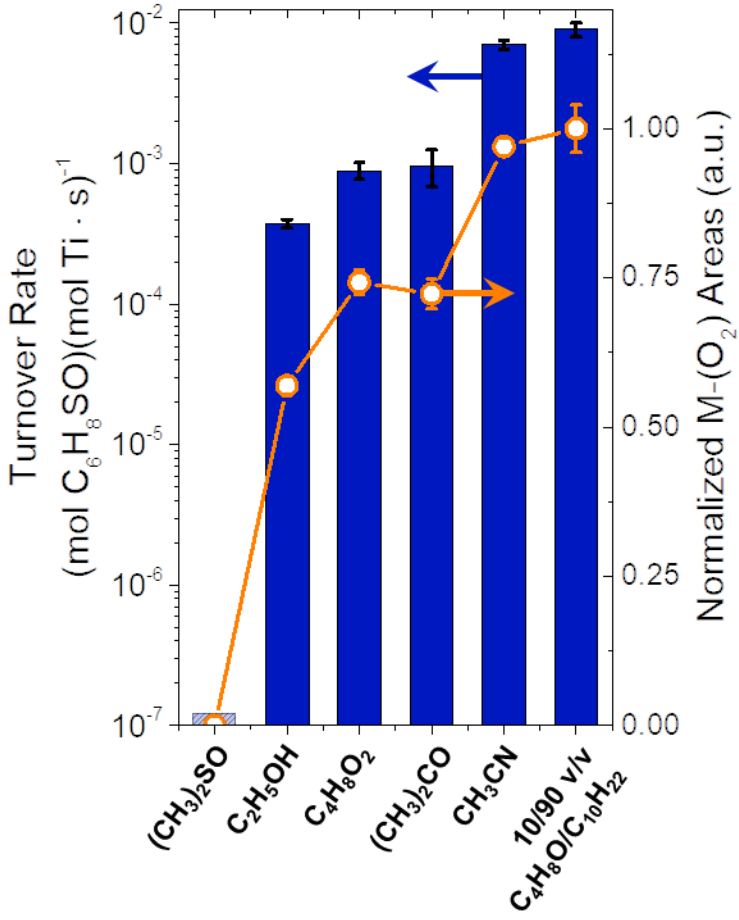

Figure 4.6. Turnover rates (bars; 0.01 M C_6H_8S, 0.01 M H_2O_2, 313 K)) and UV-vis absorbance feature areas (○, for Ti-OOH and Ti-(η^2-O_2) intermediates, obtained in situ; 0.01 M H_2O_2, 313 K) for the oxidation of C_6H_8S as a function of solvent over Ti-BEA. The transparent bar for $(CH_3)_2SO$ represents that no measurable rate of C_6H_8S could be detected. For clarity, 10/90 v/v $C_4H_8O/C_{10}H_{22}$ represents 10 %, by volume, of tetrahydrofuran in decane.

Quantitative comparisons of the nucleophilicity of small molecules were proposed by Mayr and co-workers based upon changes in first order rate constants for Friedel-Crafts aromatic substitutions that accompany differences in the electrophilicity of a complementary substrate (e.g., substitution of a phenyl-ring substitution).[216-218] Mayr showed that the first-order rate constants for the solvolysis of benzylhydrinium salts (by varying phenyl-ring substitution to vary the electrophilicity) depend strongly on the structure and mole fraction (for binary mixtures) of the solvent, which are used to calculate the solvent nucleophilicity parameter (N_1).[218] Establishing the functional dependence of sulfoxidation turnover rates on N_1 using a select subset of solvents

provides one method to show rates for C_6H_8S oxidation depend on the Lewis basicity of solvent molecules and, potentially, to predict rates in untested solvent mixtures.

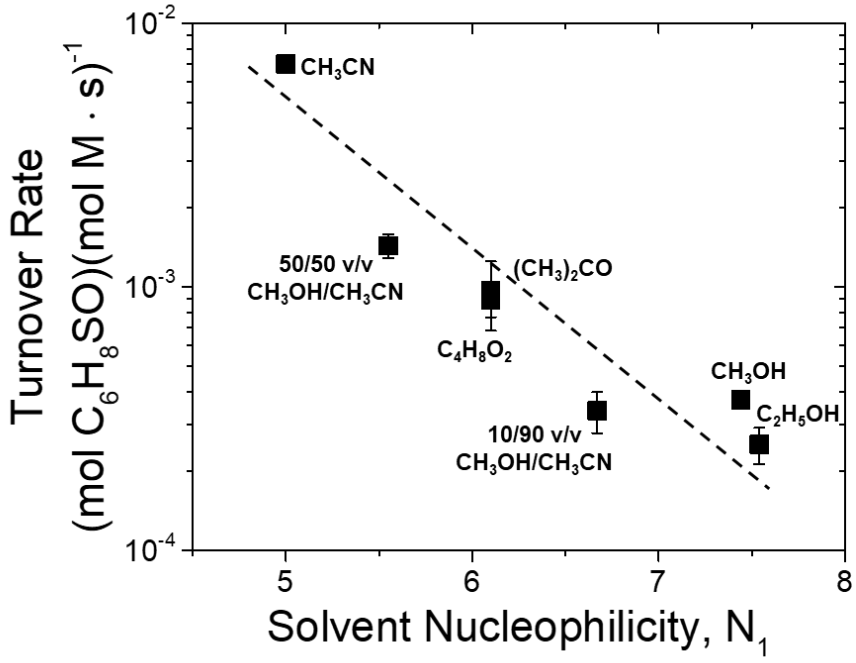

Figure 4.7. Turnover rates for the oxidation of C_6H_8S as a function of N_1 over Ti-BEA (0.01 M C_6H_8S, 0.01 M H_2O_2, 313 K). For clarity, 50/50 v/v CH_3OH/CH_3CN represents an equi-volume mixture of CH_3OH and CH_3CN. The dashed line is intended to guide the eye.

Figure 4.7 shows turnover rates for the formation of C_6H_8SO on Ti-BEA as a function of N_1 for solvents and solvent mixtures relevant to ODS processes (0.01 M C_6H_8S, 0.01 M H_2O_2, 313 K). Turnover rates decrease exponentially with increasing values of N_1, which supports the hypothesis that these Lewis basic solvents competitively adsorb to the catalyst active sites and reduce rates of thiophene oxidation. This dependence also describes binary solvent mixtures (e.g., 50/50 and 10/90 v/v mixtures of CH_3OH and CH_3CN). Importantly, these comparisons seem useful to connect reports for H_2O_2-mediated oxidation catalysis on similar Lewis acid active sites (e.g., sulfoxidation, epoxidations, alcohol dehydrogenations). For example, alkene epoxidations are commonly performed within CH_3CN in academic studies,[51, 58, 88, 199] whereas, industrial processes often utilize other solvents (e.g., methanol for the epoxidation of propylene).[5] The correlation shown in Figure 4.7 suggests that other liquid-phase oxidation reactions in an untested solvent or

solvent mixture *may* be predicted semi-quantitatively using known values of N_1 and the volumetric ratio of the solvent components.

4.3.5 Influence of Active Site Electron Affinity on Oxidation Rates and Selectivities

Transition state theory (TST) provides a foundation to quantify the differences in stability (e.g., free energy or enthalpy) between a reference state and a transition state for C_6H_8S oxidation or H_2O_2 decomposition.[215] Meaningful comparisons can be made between activation barriers for M-BEA catalysts to probe how the metal identity and electronic properties of the active site influence catalysis, provided that these measurements involve comparable references states (e.g., an M-(O_2) MASI). The application of TST assumes that the state immediately preceding the transition state and the transition state are in equilibrium, which is expressed as

$$M-(O_2)+C_6H_8S \overset{K_{Ox}^{\ddagger}}{\rightleftharpoons} M-(O_2)-C_6H_8S^{\ddagger} \tag{4.9}$$

where M-(O_2)-$C_6H_8S^{\ddagger}$ and $K^{\ddagger}_{Ox}$ represent the transition states and transition state equilibrium constants for C_6H_8S oxidation, respectively. The rates for C_6H_8S oxidation can then be expressed in terms of the numbers of transition states, resulting in

$$\frac{r_{Ox}}{[L]} = \frac{k_b T}{h}[M-(O_2)-C_6H_8S^{\ddagger}] \tag{4.10}$$

where T is the absolute temperature in Kelvin, and k_b and h are Boltzmann's and Planck's constants, respectively. Measurement of the reaction rates under a M-(O_2) MASI allows equation 4.10 to be combined with equation 4.6 to be re-expressed as

$$\frac{r_{Ox}}{[L]} = \frac{k_b T}{h} K_{Ox}^{\ddagger}[C_6H_8S] \tag{4.11}$$

which allows for $K^{\ddagger}_{Ox}$ to be determined by measurement of turnover rates for each reaction pathway at a given temperature. A comparable derivation is performed for H_2O_2 decomposition in

Appendix C (section C4.2). Activation enthalpies ($\Delta H^{\ddagger}$) for both C_6H_8S oxidation and H_2O_2 decomposition are determined by regression of measured $K^{\ddagger}$ ($K^{\ddagger}_{Ox}$ and $K^{\ddagger}_{Dec}$ (i.e., for H_2O_2 decomposition)) for these pathways as functions of inverse temperature (Figure 7) using the Eyring equation [215].

Table 4.2. Activation Enthalpies for C_6H_8S Oxidation ($\Delta H^{\ddagger}_{Ox}$) and H_2O_2 Decomposition ($\Delta H^{\ddagger}_{Dec}$) over M-BEA Catalysts Measured on M-(O_2) Saturated Surfaces[a]

Sample	$\Delta H^{\ddagger}_{Ox}$ (kJ mol^{-1})	$\Delta H^{\ddagger}_{Dec}$ (kJ mol^{-1})
Ti-BEA	36 ± 3	31 ± 10
Nb-BEA	50 ± 5	45 ± 5
Ta-BEA	57 ± 6	56 ± 5
Zr-BEA	62 ± 4	65 ± 8

Table 4.2 shows the activation enthalpies for C_6H_8S oxidation ($\Delta H^{\ddagger}_{Ox}$) and H_2O_2 decomposition ($\Delta H^{\ddagger}_{Dec}$) measured at reaction conditions that produce M-(O_2) as the MASI on all M-BEA.[219] Table 4.2 shows that the differences in $\Delta H^{\ddagger}_{Ox}$ are consistent with the differences between sulfoxidation turnover rates across the M-BEA catalysts (Figures 4.3 and 4.4). For example, the $\Delta H^{\ddagger}_{Ox}$ over Ti-BEA is 26 kJ mol^{-1} lower than Zr-BEA, which is consistent with the $3.5 \cdot 10^4$-fold greater turnover rate on Ti-BEA compared to Zr-BEA (Figure 4.4).

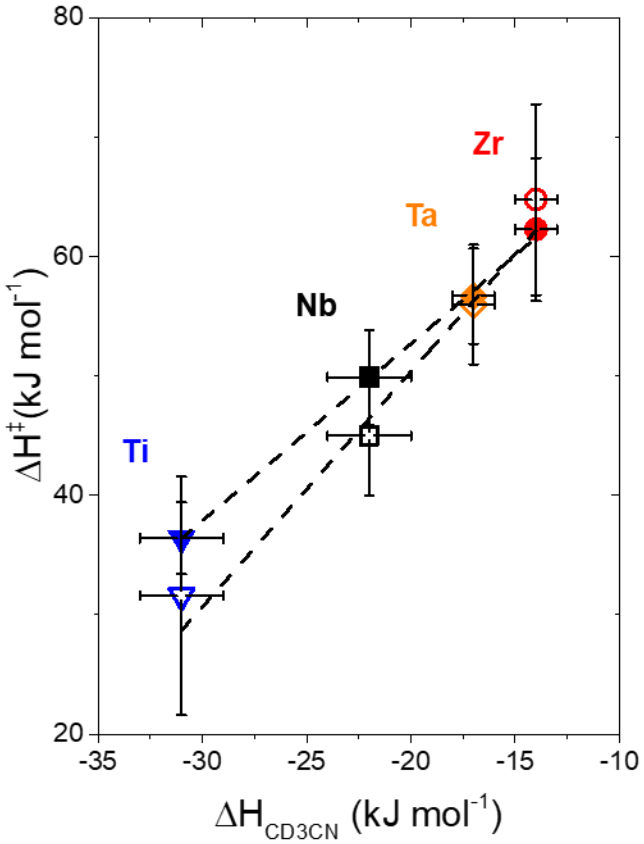

Figure 4.8. Activation enthalpies for C_6H_8S oxidation (closed symbols) and H_2O_2 decomposition (open symbols) measured on M-(O_2) saturated active sites as a function of ΔH_{CD_3CN} coordinated to Lewis acid sites in Ti- (▼, ▽), Nb- (■, □), Ta- (◆, ◇), and Zr-BEA (●, ○). Dashed lines represent linear fits to the two sets of data.

Figure 4.8 shows that values of $\Delta H^{\ddagger}_{Ox}$ and $\Delta H^{\ddagger}_{Dec}$ depend linearly on the enthalpy of adsorption for CD_3CN (ΔH_{CD_3CN}) among the M-BEA catalysts.[220] The values of ΔH_{CD_3CN} (Table 4.1) coordinated to Lewis acid sites provide quantitative measures of the electron affinity of the transition metal ion that constitutes the active site as it exists within the M-BEA framework. The linear correlation in Figure 4.8 strongly suggests that the metal atoms that have greater electron affinities (i.e., "stronger" Lewis acids) present lower barriers for oxidation of thiophenes and therefore give greater turnover rates. These trends resemble those for alkene epoxidation, where M-BEA catalysts with larger ΔH_{CD_3CN} possess higher turnover rates and H_2O_2 selectivities for alkene epoxidation.[11, 199] Interestingly, $\Delta H^{\ddagger}_{Ox}$ and $\Delta H^{\ddagger}_{Dec}$ depend less strongly on ΔH_{CD_3CN} (slope

of ~1.5 and 1.9, respectively) than the activation enthalpies for cyclohexene[199] and styrene[11] epoxidation, which both possess a slope of ~3 when active sites are saturated with M-(O_2) intermediates. These comparisons suggest that the transition states for C_6H_8S oxidation involve less electron withdrawal from the M-(O_2) intermediate than those for alkene epoxidations. Collectively, these differences in the functional dependence of $\Delta H^{\ddagger}$ values on the electron affinity of the active sites appear consistent with the Lewis acid-base interactions contained within plausible transition state complexes, in which the electron-rich functions of the reactant (i.e., lone pairs on the S-atom of thiophene or on the O-atoms of H_2O_2, or the C=C in alkenes) interact with the electron-deficient M-(O_2) intermediate. Chemical intuition suggests that the lone pairs on S- and O-atoms possess similarities and have greater electron densities than the C=C in alkenes. These M-BEA do not possess significant differences in the productive use of H_2O_2 (Figure 4.4), which is explained by the similar values and dependencies of $\Delta H^{\ddagger}_{Ox}$ and $\Delta H^{\ddagger}_{Dec}$ on ΔH_{CD3CN} (Figure 4.8). A possible explanation for this is that the M-(O_2) intermediates upon C_6H_8S oxidation or H_2O_2 decomposition must react with the lone pair of a S or O atom, respectively, which likely exchange charge and form bonds with M-(O_2) intermediates in similar ways.

4.4 Conclusions

Group 4 (Ti and Zr) and 5 (Nb and Ta) atoms substituted into the *BEA zeolite framework (M-BEA) irreversibly activate H_2O_2 to form pools of metal- hydroperoxide (M-OOH) and peroxide (M-(η^2-O_2)) intermediates that are critical for oxidative desulfurization (ODS) processes. These M-OOH and M-(η^2-O_2) surface species oxidize C_6H_8S (a representative thiophene) to form C_6H_8SO, which is then oxidized at much lower rates to form C_6HSO_2 by oxidative dearomatization. Interpretation of measured reaction kinetics, in conjunction with in situ UV-vis spectroscopy, show that C_6H_8S oxidation occurs through sets of elementary steps which have equivalent kinetic relevance on all M-BEA. Moreover, these steps and the derived oxidation rate expressions closely resemble those for cyclohexene and styrene epoxidations with H_2O_2 on these materials. Rates of sulfoxidation vary by several orders of magnitude across the series of M-BEA catalysts, however, the selectivities for H_2O_2 towards thiophene oxidation are relatively constant. Activation enthalpies for C_6H_8S oxidation and H_2O_2 decomposition are similar on each catalyst when M-(O_2) species dominate surfaces, which shows that both reaction pathways are equally sensitive to changes in the electron affinity (i.e., Lewis acidity) of the active sites that are quantified

by differences in the enthalpy for adsorption of acetonitrile to these same sites. These comparisons indicate that the lone pairs on both the C_6H_8S and H_2O_2 interact in a similar fashion with the reactive intermediates such that the most "Lewis acidic" catalyst (i.e., Ti-BEA) results in the highest rates without sacrificing H_2O_2 selectivity.

The use of coordinating solvents has a great effect on sulfoxidation rates due to competitive adsorption to the active sites. Thiophene consumption rates decrease exponentially with the Mayr solvent nucleophilicity (N_1), which indicates that sulfoxidation rates in unknown solvents or solvent mixtures may be predicted by a quantifiable property of the reaction media. Interpretation of UV-vis spectra collected in situ during experiments that utilize solvents with varying values of N_1 shows that these changes are due, in part, to competitive adsorption of solvent molecules to active sites and the concomitant decrease in turnover rates. Collectively, this work reveals that turnover rates for sulfoxidation are maximized when highly electrophilic active sites (i.e., stronger Lewis acids) are combined with non-coordinating (i.e., weaker Lewis bases) solvents, which may guide the design of next-generation catalytic systems for sulfide oxidation.

CHAPTER FIVE

Consequences of Confinement for Alkene Epoxidation with Hydrogen Peroxide on Highly Dispersed Group 4 and 5 Metal Oxide Catalysts[IV]

Abstract

Ti, Nb, and Ta atoms substituted into the framework of zeolite *BEA (M-BEA) or grafted onto mesoporous silica (M-SiO_2) irreversibly activate hydrogen peroxide (H_2O_2) to form pools of metal- hydroperoxide (M-OOH) and peroxide (M-(η^2-O_2)) species for alkene epoxidation. The product distributions from reactions with *Z*-stilbene, in combination with time-resolved UV-vis spectra of the reaction between H_2O_2-activated materials and cyclohexene, show that M-OOH surface intermediates epoxidize alkenes on Ti-based catalysts, while M-(η^2-O_2) moieties epoxidize substrates on the Nb- and Ta-containing materials. Kinetic measurements of styrene (C_8H_8) epoxidation reveal that these materials first adsorb and then irreversibly activate H_2O_2 to form pools of interconverting M-OOH and M-(η^2-O_2) intermediates, which then react with styrene or H_2O_2 to form either styrene oxide or H_2O_2 decomposition products, respectively. Activation enthalpies ($\Delta H^{\ddagger}$) for C_8H_8 epoxidation and H_2O_2 decomposition decrease linearly with increasing heats of adsorption for pyridine or deuterated acetonitrile coordinated to Lewis acid sites, which suggests that materials with greater electron affinities (i.e., stronger Lewis acids) are more active for C_8H_8 epoxidation. Values of $\Delta H^{\ddagger}$ for C_8H_8 epoxidation and H_2O_2 decomposition also decrease linearly with the ligand-to-metal charge transfer (LMCT) band energies for the reactive intermediates, which is a more relevant measure of the requirements for the active sites in these catalytic cycles. Epoxidation rates depend more strongly on the LMCT band energy than H_2O_2 decomposition rates, which shows that more electrophilic M-OOH and M-(η^2-O_2) species (i.e., those formed at stronger Lewis acid sites) give both greater rates and greater selectivities for epoxidations. Thermochemical analysis of $\Delta H^{\ddagger}$ for C_8H_8 epoxidation and adsorption enthalpies for C_8H_8 within the pores of *BEA and SiO_2 reveal that the 0.7 nm pores within M-BEA preferentially stabilize transition states for C_8H_8 epoxidation with respect to the 5.4 nm pores of M-SiO_2, while

[IV]This chapter has been adapted from the following publication:
Bregante, D.T.; Thornburg, N.E.; Notestein, J.M.; Flaherty, D.W.; "Consequences of Confinement for Alkene Epoxidation with Hydrogen Peroxide on Highly Dispersed Group IV and V Metal Oxide Catalysts"
ACS Catalysis, **2018**, *8*, 2995 – 3010.

H_2O_2 decomposition is unaffected by the differences between these pore diameters due to the small Stokes diameter of H_2O_2. Thus, the differences in reactivity and selectivity between M-BEA and M-SiO_2 materials is solely attributed to confinement of the transition state and not differences in the identity of the reactive intermediates, mechanism for alkene epoxidation, or intrinsic activation barriers. Consequently, the rates and selectivities for alkene epoxidation reflect at least two orthogonal catalyst design criteria – the electronegativities of the transition metal atoms that determine the electronic structure of the active complex and the mean diameters of the surrounding pores that can selectively stabilize transition states for specific reaction pathways.

5.1 Introduction

Highly-dispersed metal oxides are ubiquitous in the selective oxidation of various alkanes, alkenes, aromatics, alcohols and aldehydes to produce both commodity and fine chemicals.[221-223] The production of epoxides from alkenes is important, because epoxides are precursors for the manufacture of plastics, fragrances, and pharmaceuticals.[72-74] In recent years, a number of studies have investigated the use of highly-dispersed group 4 and 5 metal oxides (e.g., grafted onto mesoporous silica[51, 147] or incorporated into a zeolite framework[54, 199]) to activate hydrogen peroxide (H_2O_2) for epoxidation reactions.[82] The interest in H_2O_2 is motivated, in part, by the lower environmental impact for the use of this oxidant in comparison to Cl_2 (e.g., used in the chlorohydrin process)[138] and organic oxidizers (e.g., *t*-butyl hydroperoxide and ethylbenzene hydroperoxide).[77] Epoxidations that utilize H_2O_2 form only H_2O as a byproduct, and hence, do not require the regeneration or sale of organic co-products nor the remediation of environmentally impactful waste streams.

Large amounts of titanium silicalite (TS-1) are used in the hydrogen peroxide-propylene oxide process to catalyze the activation of H_2O_2 and the epoxidation of propylene.[144-145] However, many other monomeric metal centers and small oligomers of metal oxides (e.g., Al,[47-48] Ti,[49-52] Zr,[51, 53] Nb,[54-56] and Ta[57-59]) activate H_2O_2 and catalyze alkene epoxidations as well. Recent reports from our group show that the rates and selectivities for cyclohexene epoxidation increase with increasing heat of adsorption for Lewis acid bound deuterated acetonitrile, which suggests that materials that possess greater electron affinities (i.e., stronger Lewis acids) are more productive catalysts for this chemistry.[54, 152, 199] Despite the plethora of literature on the epoxidation of alkenes with H_2O_2,[55, 224-226] the changes in rates and selectivities that result from differences in the

electronic structure due to changing pore environment (e.g., type or morphology of support) and changes in the solvating environment (i.e., catalyst pore diameter) have not been fully described in the open literature, to the best of our knowledge.

Here, we seek to establish and explain the relationships that exist between the rates and selectivities for alkene epoxidation and the electronic structure of the reactive intermediates and morphological properties (e.g., metal atom coordination and mean pore diameters) of two series of catalysts that contain monomeric Ti-, Nb-, or Ta-atoms on siliceous supports. The two categories of materials consist of transition metal atoms (Ti, Nb, or Ta) incorporated into the framework of zeolite *BEA (M-BEA)[199] or those same atoms grafted onto mesoporous silica (M-SiO_2).[51] UV-vis spectra obtained in situ suggest that all materials irreversibly activate H_2O_2 to form pools of M-OOH and M-(η^2-O_2) intermediates. Transient in situ UV-vis spectra obtained during reaction of these species with cyclohexene, in conjunction with the isomeric distribution of the products from *Z*-stilbene epoxidation, show that Ti-BEA and Ti-SiO_2 catalysts react through M-OOH, while Nb and Ta materials epoxidize cyclohexene through M-(η^2-O_2). Changes in the rates of styrene (C_8H_8) epoxidation and H_2O_2 decomposition as functions of reactant concentrations show that the active M-OOH and M-(η^2-O_2) intermediates form following adsorption and irreversible activation of H_2O_2, after which these species react with C_8H_8 or H_2O_2 to form the epoxidation or decomposition products, respectively. Epoxidation and H_2O_2 decomposition rates and selectivities depend exponentially on the extent of electron exchange between the reactive intermediate and the metal atom, as assessed by the ligand-to-metal charge transfer (LMCT) energy measured via UV-vis. Activation enthalpies ($\Delta H^{\ddagger}$) for C_8H_8 epoxidation are systematically lower on M-BEA materials than M-SiO_2 by ~20 kJ mol^{-1}, while $\Delta H^{\ddagger}$ for H_2O_2 decomposition do not depend on the type of silica support used. Thermochemical analysis of the values of $\Delta H^{\ddagger}$ for C_8H_8 epoxidation and the adsorption enthalpies for C_8H_8 adsorption into the purely siliceous materials show that transition states for C_8H_8 epoxidation are preferentially stabilized within the microporous *BEA framework relative to those in mesoporous SiO_2, while transition states for H_2O_2 decomposition are not affected because the Stokes diameter of H_2O_2 (~0.24 nm) is too small to be significantly stabilized by dispersive interactions with the pore walls of these materials. Consequently, the design of materials that maximize the extent of solvation of the desired alkene reactant in the microporous voids will result in a catalyst with increased rates and selectivities for this chemistry.

5.2 Materials and Methods

5.2.1 Catalyst Synthesis

All M-BEA and M-SiO_2 catalysts used in this study have been synthesized and characterized by the authors within previous reports.[51, 54, 147, 199] The most relevant results are summarized here, with additional characterization data and interpretation provided in Appendix D, section D1.

M-BEA catalysts were prepared by the liquid-phase post-synthetic modification of commercially-available NH_4^+-BEA (Zeolyst, CP814E).[49, 54, 96, 101, 103, 199] In short, NH_4^+-BEA (Si:Al ~ 12.5) was dealuminated by reflux in concentrated HNO_3 (Macron Chemicals, 68 – 70 wt. %, 20 cm^3 g^{-1}) for 18 h. The solids were recovered by vacuum filtration and washed thoroughly with H_2O (17.8 MΩ·cm, 50 cm^3 g^{-1}) and heated at 5 K min^{-1} to 823 K in flowing air (Airgas, Ultra-zero grade, 100 cm^3 min^{-1}) and held for 6 h to produce Si-BEA (Si:Al > 1200, determined by ICP-OES). The incorporation of Ti, Nb, or Ta atoms into the dealuminated framework involved stirring a suspension of Si-BEA in a solution of $TiCl_4$ (Sigma Aldrich, 99.9%; note: $TiCl_4$ will violently react with the moisture in air to form TiO_2 and HCl and should be handled carefully), $NbCl_5$ (Sigma-Aldrich, 99.9%), or $TaCl_5$ (Sigma-Aldrich, 99%) in dichloromethane (Fisher Chemicals, Certified ACS stabilized) for $TiCl_4$ or isopropanol (Fisher Chemicals, Certified ACS plus) for $NbCl_5$ and $TaCl_5$ at 333 K for 3 h. Volatile components were then removed by rotary evaporation. Recovered solids were heated at 5 K min^{-1} to 823 K in flowing air (Airgas, Ultra-zero grade, 100 cm^3 min^{-1}) and held for 6 h to produce the corresponding M-BEA catalyst. The metal loading within the catalysts were varied by changing the concentration of the MCl_x solution used during the liquid-phase treatments.

All M-SiO_2 materials were synthesized using standard glove box and Schlenk techniques.[227-230] $TiCl_4(THF)_2$ (Strem Chemicals, >97% metals basis), $NbCl_5$ (Strem Chemicals, >99%), and $TaCl_5$ (Strem Chemicals, >99%) metal precursors were stored and weighed in an Ar glovebox. 1,3-Dimethoxy-*tert*-butylcalix[4]arene ("dmCalix") was prepared from *p-tert*-butylcalix[4]arene ("Calix," Sigma-Aldrich, >95%) according to previously published procedures.[231] Briefly, Ti-, Nb-, and Ta-calixarene complexes were synthesized by refluxing the metal chloride precursors with stoichiometric amounts of dmCalix (Ti) or Calix (Nb, Ta) in dry, degassed toluene under an N_2 atmosphere for 14 h. Then, partially dehydroxylated SiO_2 (Selecto Scientific, 32-62 μm particle size, 570 m^2 g^{-1}, 5.4 nm average pore diameter, treated at 573 K under

dynamic vacuum (<5 Pa) for 10 h) was added to the flask, and the suspension was refluxed for an additional 24 h. Solids were vacuum-filtered and washed with fresh toluene, then Soxhlet-extracted with toluene, and dried under dynamic vacuum (<40 mTorr) to yield bright-orange (Calix-Ti-SiO_2 and Calix-Nb-SiO_2) or light-brown (Calix-Ta-SiO_2) solids. Calix-M-SiO_2 solids were then heated at 5 K min^{-1} to 823 K in flowing air (Airgas, Ultra-zero grade, 100 cm^3 min^{-1}) and held for 6 h to remove the calixarene ligands and produce highly dispersed M-SiO_2 materials (bleached white in appearance).

5.2.2 Catalyst Characterization

The metal contents (Table 5.1) of the M-BEA and M-SiO_2 materials was quantified using inductively coupled plasma-optical emission spectroscopy (ICP-OES), which was calibrated against known dilution standards. M-BEA materials were synthesized to produce ~0.6 – 1 M atom (unit cell)$^{-1}$. Consequently, statistical arguments suggest that the majority of transition metal atoms are well separated and that each unit cell of the M-BEA materials contains ~4-5 silanol nests on average (after post-synthetic modification), which results in highly hydrophilic pores and external surfaces.

Table 5.1. Band Edge Energies,[a] Metal Loadings,[b] Fraction of Active Metal,[c] and Enthalpies of Adsorption[d] for Pyridine (ΔH_{Py}) and CD_3CN (ΔH_{CD_3CN}) Coordinated to Lewis Acid Sites on M-BEA and M-SiO_2 Catalysts.

Sample	Band edge (eV)	Metal loading (mmol g^{-1})	Percent Active Metal (%)	ΔH_{Py} (kJ mol^{-1})	ΔH_{CD_3CN} (kJ mol^{-1})
Ti-BEA	4.0	0.22	96 ± 5	-45 ± 3	-31 ± 2
Nb-BEA	4.2	0.16	99 ± 8	-25 ± 3	-22 ± 2
Ta-BEA	4.8	0.16	99 ± 4	-20 ± 3	-17 ± 1
Ti-SiO_2	3.8	0.18	77 ± 10	-34 ± 4	-[e]
Nb-SiO_2	4.0	0.18	60 ± 7	-16 ± 2	-[e]
Ta-SiO_2	4.5	0.19	60 ± 5	-11 ± 2	-[e]

[a]Measured using DRUV-vis; [b]Measured by ICP-OES; [c]Determined by in situ methylphosphonic acid (for M-BEA) and phenylphosphonic acid (for M-SiO_2) titrations; [d]Determined from adsorption isobars using FTIR; [e]Not measured because CD_3CN readily cokes on M-SiO_2 at temperatures >373 K.

The crystallinity of each *BEA and M-BEA material was confirmed by powder X-ray diffraction using a diffractometer (Siemens/Bruker, D5000) with Cu Kα radiation (0.15418 nm) under ambient conditions. Figure D1 shows the X-ray diffractograms of all M-BEA. The similarities between the diffractograms for all M-BEA suggests that the *BEA framework is intact after post-synthetic modification.

Band edge energies (E_g) for each M-BEA and M-SiO_2 material were determined from extrapolation of the linear portion of the corresponding Tauc plot calculated from diffuse reflectance UV-vis spectra (DRUV-vis) (Figure D2). Total reflectance spectra were measured at ambient conditions with a UV-vis-NIR spectrophotometer (Agilent CARY 5 for M-BEA; Shimadzu UV-3600 for M-SiO_2) with magnesium oxide (MgO, Sigma Aldrich, 99.995%, for M-BEA) or polytetrafluoroethylene powder (for M-SiO_2) as a solid diluent and background. The relatively large band gaps (Table 5.1), and lack of significant shoulders on the absorbance features suggests that the transition metal atoms in *BEA and on SiO_2 are highly disperse and contain little oligomeric or bulk oxide phases. The Ta-SiO_2 material is the sole exception and possesses a small shoulder on the UV-vis absorbance spectra (Figure D2), which suggests that small TaO_x oligomers form upon oxidative heat treatments.[51] In this work, all reported rates were normalized by the fraction of *active* metal in the M-BEA and M-SiO_2 catalysts using in situ methylphosphonic acid (for M-BEA) or phenylphosphonic acid (for M-SiO_2) site titrations (see below).[147, 232] Thus, the presence of TaO_x oligomers does not significantly affect reported rates.

The presence of Lewis acid sites in M-BEA and M-SiO_2 was characterized by the infrared (IR) spectra of adsorbed pyridine (Sigma Aldrich, >99%) using a custom-built transmission cell[200] coupled to a Fourier transform-infrared (FTIR) spectrometer (Bruker, Tensor 37) with a liquid-N_2-cooled HgCdTe detector. Catalysts were pressed into self-supporting disks (~60 mg) and placed within the transmission cell, which was assembled using CaF_2 windows and connected to a gas manifold with lines heated to 423 K. All materials were first heated to 423 K at 10 K min^{-1} and held for 2 h under flowing He (50 cm^3 min^{-1}; Airgas, Ultra-zero grade), with the intent to desorb water and residual organics. Pyridine (0.1 kPa; Sigma-Aldrich, 99%) was introduced via a syringe pump (KD Scientific, Legato 100) and vaporized in the heated gas-transfer lines into a stream of flowing He (50 cm^3 min^{-1}). Steady-state IR spectra (128 scans, 1 cm^{-1} resolution; Figure 5.1) of pyridine adsorbed to the M-BEA and M-SiO_2 samples were obtained while flowing the pyridine/He stream over the samples.

Figure 5.1 shows steady-state IR spectra of pyridine adsorbed to M-BEA and M-SiO_2 materials (0.1 kPa pyridine, 50 cm^3 min^{-1} He, ~393 K). All materials possess absorbance features between 1575 – 1625 cm^{-1} and at ~1490 cm^{-1}, which are associated with pyridine coordinated to either Lewis or Brønsted acid sites (Figure 5.1; red region).[9, 233-234] Yet, absorbance features at ~1540 cm^{-1} arise only from pyridinium ions bound to Brønsted acid sites (Figure 5.1; green region).[9, 233-234] These pyridinium ions likely bind to metal-hydroxyl species as observed for similar Ta-BEA materials,[9] however, M-BEA materials possess trace aluminum (Si:Al > 1200 as detected by ICP-OES) and the Brønsted acid sites may be attributed to trace aluminum that remains in the framework. Absorbance features at ~1450 cm^{-1} correspond only to pyridine bound to Lewis acid sites (Figure 5.1; blue region).[9, 233-234] The enthalpies of pyridine adsorption (ΔH_{Py}) to Lewis acid sites were determined by van't Hoff analysis of the IR feature at ~1450 cm^{-1} (Figure D3) to obtain one potential measure of the electron affinity (i.e., a measure of "Lewis acid strength") for each catalyst. Table 5.1 contains the experimentally determined values for ΔH_{Py} on all M-BEA and M-SiO_2 materials. Table 5.1 also contains values for the enthalpy of adsorption for deuterated acetonitrile (ΔH_{CD_3CN}) coordinated to Lewis acid sites obtained using similar methodology by our group.[199]

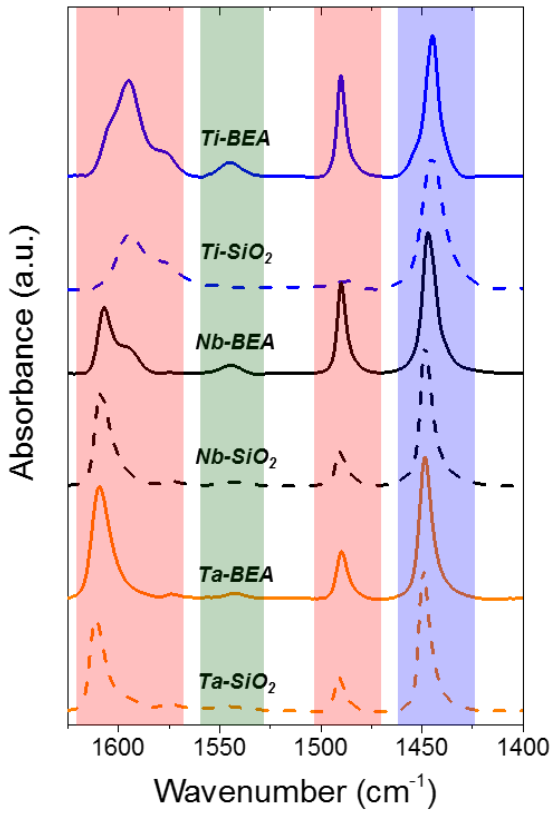

Figure 5.1. Infrared spectra of pyridine bound to Lewis and Brønsted acid sites on M-BEA (solid) and M-SiO_2 (dashed) materials containing Ti- (blue), Ta- (orange), or Nb-atoms (black). All spectra are normalized to the feature at ~1450 cm^{-1} and were acquired in flowing He (0.1 kPa pyridine, 50 cm^3 min^{-1}, ~393 K). Colored regions along the horizontal axis denote the expected location of absorbance features for pyridine coordinated to only Brønsted acid sites (green), only Lewis acid sites (blue), and both Lewis and Brønsted acid sites (red).

X-ray photoelectron spectroscopy (XPS) was used to determine the oxidation state of transition metal atoms on bare and H_2O_2-activated Ti-, Nb-, and Ta-BEA and -SiO_2 materials. The XPS measurements were performed on a spectrometer (Kratos, AXIS Ultra) equipped with a monochromatic Al-Kα (1486.6 eV) X-ray source. M-BEA and M-SiO_2 materials were activated with H_2O_2 by creating a slurry of catalyst (~60 mg) with a mixture of 2.5 cm^3 H_2O_2 (4.9 M; 30 wt. % in H_2O; Fisher Scientific) in acetonitrile (CH_3CN; Macron Chemicals, >99.8%) and stirring at 333 K for 1 h. Volatile components were then removed in vacuo via a rotary evaporator (IKA, RV 10) and dried under dynamic vacuum for 12 h (~0.02 kPa). This treatment produced pale yellow solids from Ti and Nb materials and a cream colored solid for Ta catalysts. High-resolution XP

spectra were collected with a 40 eV pass energy, and the photoelectron binding energies were calibrated using the C1s peak for aliphatic species at 284.8 eV. The Shirley background was subtracted and peaks were fit using Gaussian curves.

Styrene (C_8H_8) adsorption enthalpies were measured by van't Hoff analysis of the change in C_8H_8 uptake into Si-BEA and SiO_2 as a function of temperature within the linear regime of the adsorption isotherm. A solution of C_8H_8 (Sigma-Aldrich, 99%) in CH_3CN was heated to a desired temperature while stirring in a 100 cm^{-3} round-bottom flask. An initial (solids-free) aliquot was taken and analyzed via gas chromatography (GC; HP 5890, Series A) to determine the initial concentration of C_8H_8. An appropriate amount of Si-BEA or SiO_2 was then added to the stirring solution of C_8H_8 and allowed to equilibrate at a given temperature. An aliquot of solution was then passed through a syringe filter (polypropylene, 0.22 μm) to remove the solids and was analyzed via GC. The difference in GC peak area between the aliquot after Si-BEA or SiO_2 introduction and the initial sample was assumed to be proportional to the amount of styrene adsorbed to the purely siliceous solids. Multiple concentrations of C_8H_8 were tested to determine a concentration that is well within the linear regime for the C_8H_8 adsorption isotherm (5×10^{-6} – 10^{-3} M [C_8H_8]). The uptake of C_8H_8 was then measured as a function of temperature to determine the enthalpies for adsorption of styrene from the CH_3CN solution to the siliceous support (ΔH_{ads}; Figure D4), and were found to be -35 ± 6 and -18 ± 3 for Si-BEA and SiO_2, respectively.

5.2.3 Measurement of Rates for Epoxide Formation and H_2O_2 Decomposition

Rates for C_8H_8 epoxidation and H_2O_2 decomposition were measured using batch reactors (100 cm^3, three-neck round-bottom flasks) equipped with reflux condensers to minimize evaporative losses. C_8H_8 (Sigma-Aldrich, 99%) and H_2O_2 (Fischer Chemicals, 30 wt. % in H_2O) were added to a solution of CH_3CN and benzene (internal standard for GC analysis; Sigma-Aldrich, thiophene-free, >99%) and heated to the desired temperature (303 – 348 K) while stirring at 600 rpm. H_2O_2 (30% w/v) was distilled via rotary evaporation to produce ~90% w/v H_2O_2 and was combined with an appropriate amount of H_2O to quantify the effects of H_2O on styrene epoxidation rates. The reactions were initiated by addition of the M-BEA or M-SiO_2 catalysts and small aliquots (~300 μL) of the reaction solution were extracted as a function of time through a 0.22 μm syringe filter (to remove suspended catalyst and stop the reactions from proceeding). The concentrations of the organic components within these aliquots were quantified via a GC equipped

with a flame-ionization detector. All species were identified and calibration factors were quantified using standards of known concentration. The concentration of H_2O_2 in each aliquot was measured by colorimetric titration using an aqueous solution of $CuSO_4$ (8.3 mM, Fisher Chemicals, >98.6%), neocuproine (12 mM, Sigma-Aldrich, >98%), and ethanol (25% v/v, Decon Laboratories Inc., 100%). The concentration of H_2O_2 was calculated by comparison of the absorbance at 454 nm to calibrated standards, measured using a visible-light spectrophotometer (Spectronic, 20 Genesys). Test reactions using purely siliceous Si-BEA and SiO_2 materials (0.01 M C_8H_8, 1 mM H_2O_2, 313 K) reveal that no reaction (i.e., epoxidation or H_2O_2 decomposition) occurs in the absence of the metal atoms.

The number of catalytically *active* metal atoms in M-BEA samples were determined using in situ site titrations with methylphosphonic acid (MPA; Sigma-Aldrich, 99%) during the epoxidation of cyclohexene (C_6H_{10}; Sigma-Aldrich, 99%).[147, 232] Briefly, M-BEA was combined with a solution of MPA and C_6H_{10} with the intent for MPA to irreversibly bind to the active sites and inhibit epoxidation catalysis. An appropriate amount of H_2O_2 was then spiked into the reactor to initiate the reaction. Reactions were run with varying ratios of MPA-to-metal (MPA:M) where the MPA:M ratios that correspond to extrapolated turnover rates of zero are taken to be the fraction of active metal in M-BEA (Table 5.1; see Section D1.2). Cyclohexene epoxidation on all M-BEA produced only cyclohexene oxide, as no other oxidation products (e.g., cyclohexeneone, 1-cyclohexen-3-ol, cyclohexanediol) were observed under differential conversion. Turnover rates were calculated by calculating the change in turnover number (the total amount of oxygenate product formed or amount of H_2O_2 consumed normalized by the total number of *active* M atoms used in a given reaction) as a function of time at differential conversion. In all reported data, the carbon balance closed within 98% and the standard uncertainty for measured reaction rates was < 7%. Rates for the conversion of C_8H_8 and H_2O_2 were measured as functions of [H_2O_2] and [C_8H_8], and all reported results were obtained at differential conversion (i.e., < 1% conversion of the limiting reagent for epoxide formation rates and < 5% conversion of H_2O_2 for H_2O_2 consumption rates). Reported rates were measured in the absence of intra-pellet mass transfer artifacts, as shown by satisfaction of the Madon-Boudart criterion[111] for Ti-BEA (i.e., the catalyst with the smallest pore diameter and largest rates; Section D1.3) by performing reactions under identical conditions with Ti-BEA samples containing different metal loadings (Section D1.3). Over the loadings tested,

epoxidation rates do not depend on the metal content, which shows that concentration gradients do not exist within the reactor or catalyst particles.

Styrene oxidation results in the formation of styrene oxide (C_8H_8O), phenylacetaldehyde, and benzaldehyde (C_7H_6O). Extrapolation of the selectivity for each of these products to the limit of zero C_8H_8 conversion shows that phenylacetaldehyde forms by isomerization of C_8H_8O over Lewis acid sites[235] and that both C_8H_8O and C_7H_6O form via primary reaction pathways (i.e., both give non-zero selectivities at nearly zero conversion). There are reports that benzaldehyde forms within the injection port of the gas chromatograph via oxidative decarboxylation of 1-phenyl-1,2-ethanediol.[236] Control experiments where a solution of 1-phenyl-1,2-ethanediol ("diol"; Sigma-Aldrich, 97%) in CH_3CN (~0.01 M) was injected into the GC injection port show that <1% of the diol is converted to benzaldehyde under the GC method used. Additionally, C_7H_6O was not produced on any M-BEA materials and was produced with varying initial selectivities (30 – 50%) on all M-SiO_2 catalysts, which suggests that benzaldehyde forms catalytically and not within the GC. Here, the combined concentrations of C_8H_8O and phenylacetaldehyde are used to calculate initial rates for epoxidation reactions, which are used to develop the relationships between catalyst structure and function for alkene epoxidation.

5.2.4 Detection of Reactive Intermediates via In Situ UV-Vis and Raman Spectroscopy

In situ UV-vis spectroscopy was used to identify the intermediates formed upon H_2O_2 activation and confirm which among those intermediates are active for alkene epoxidation on M-BEA and M-SiO_2 materials.[199] Samples were pressed into 7 mm diameter pellets (~5 mg) and loaded into a custom built temperature-controlled UV-vis liquid flow cell. UV-vis spectra (100 scans, 600 ms integration time) were collected using a 45-degree diffuse reflection probe (Avantes, solarization-resistant fibers) coupled to a fiber-optic spectrometer (Avantes, AvaFast 2048) equipped with a compact deuterium-halogen light source (Avantes, AvaLight-DHc). Reactant and solvent solutions were introduced using a high-performance liquid chromatography pump (HPLC; Waters, 515). Background UV-vis spectra were obtained for each material by exposing the sample to a flowing CH_3CN solution (0.4 M H_2O, 1 cm^3 min^{-1}) at 313 K for 1 h. Samples were then activated with H_2O_2 by changing to a flowing solution of H_2O_2 in CH_3CN (0.1 M H_2O_2, 0.4 M H_2O, 1 cm^3 min^{-1}) at 313 K and continuing until the UV-vis spectra became constant (i.e., implying a steady-state coverage of surface intermediates). Samples were then flushed with pure CH_3CN (1

cm^3 min^{-1}) at 313 K for 10 min to remove residual H_2O_2 that had not been activated. Experiments to assign UV-vis features to specific surface intermediates (e.g., M-OOH or M-(η^2-O_2)) were performed by collecting UV-vis spectra at steady state while contacting M-BEA pellets with a solution of NH_4OH (Macron Chemicals, 28-30%; 0.01 M NH_4OH, 0.1 M H_2O_2, 0.4M H_2O in CH_3CN, 313K) and HCl (Ricca, 10 M; 0.01 M HCl, 0.1 M H_2O_2, 0.4M H_2O in CH_3CN, 313K) to shift the equilibrium between M-OOH and M-(η^2-O_2) intermediates (Section 5.3.1).

The reactivities of the surface intermediates observed in the UV-vis spectra were determined by continuously acquiring UV-vis spectra as a function of time while flowing a solution of cyclohexene (C_6H_{10}; Sigma Aldrich, 99%) in CH_3CN (0.1 M C_6H_{10}, 0.4 M H_2O, 1 cm^3 min^{-1}) over H_2O_2-activated M-BEA and M-SiO_2 catalysts. Cyclohexene was used for these experiments to avoid complexities related to the secondary reactions that occur during styrene epoxidation. Specifically, the epoxidation of C_8H_8 resulted in the parallel reaction pathway that produced benzaldehyde on M-SiO_2 (see above), which prohibits detection of the reactive intermediate implicated in alkene epoxidation on M-SiO_2 materials. Rate constants for the consumption of these surface species via epoxidation and isomerization reaction were calculated by mathematically modeling the rates of peak attenuation (Section D2). Notably, independent experiments showed that the UV-vis absorbance features for H_2O_2-activated materials do not change or attenuate (within a period of 2 h) under a flowing stream of either CH_3CN (0.4 M H_2O, 1 cm^3 min^{-1}) or pure H_2O (1 cm^3 min^{-1}) at 313 K. Processes for peak smoothing, background subtraction, and peak fitting are described in Appendix D (Section D2).

In situ Raman spectra were collected on a Raman microscopy (Renishaw, inVia) equipped with a 442 nm laser (Kimmon, IK3). Samples were pressed into 7 mm diameter pellets and were loaded into a custom Raman flow cell with a quartz window for spectral acquisition. Spectra were obtained using a long 50X objective with line-scan mode (~25 μm^2) and a laser power of 90 mW with 0.1 s acquisition times (300 co-averaged spectra). Reaction solutions were introduced via a HPLC pump and steady-state conditions were reached (i.e., where the spectra were unchanging with time) before acquiring spectra. Titanium oxysulfate (50 uL; Sigma, in 27-31% H_2SO_4) was combined with 1 uL of H_2O_2 (30% in H_2O) and was used to produce Ti(η^2-O_2)SO_4 for use as a reference compound.[237]

5.3 Results and Discussion

5.3.1 Intermediates Formed upon Activation of H_2O_2

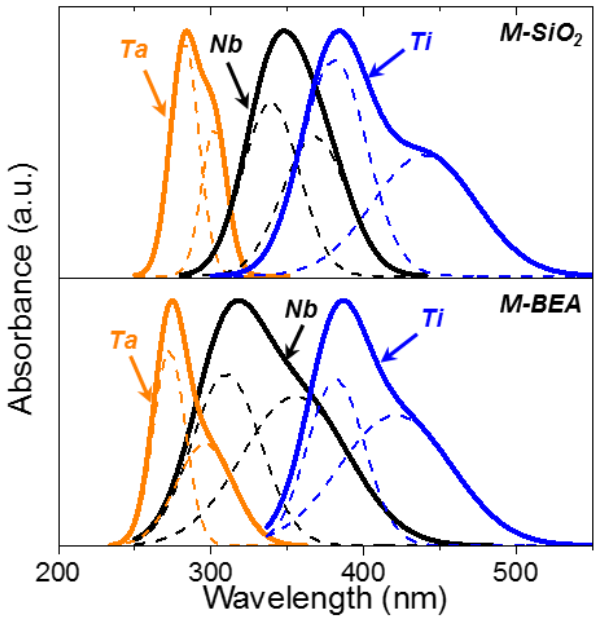

Figure 5.2. UV-vis spectra of H_2O_2-activated M-SiO_2 (top) and M-BEA (bottom) materials. Spectra were acquired in situ in flowing H_2O_2 in CH_3CN (0.1 M H_2O_2, 0.4 M H_2O, 1 cm^3 min^{-1}) at 313 K. Different colors indicate: Ta (orange), Nb (black), and Ti (blue), and dashed lines represent deconvoluted Gaussian peaks for M-(η^2-O_2) and M-OOH species.

Figure 5.2 shows the UV-vis spectra of H_2O_2-activated M-BEA and M-SiO_2 materials acquired in situ (0.1 M H_2O_2, 0.4 M H_2O, in CH_3CN, 1 cm^3 min^{-1}). In all cases, UV-vis spectra possess two overlapping absorbance features, whose intensities are assumed to be proportional to the surface coverage of each UV-vis-active species. Previous reports from our lab mistakenly assigned the higher wavelength feature to hydroperoxide/peroxide (M-OOH/(η^2-O_2)) intermediates and the lower wavelength feature to the superoxide (M-$(O_2)^{-\bullet}$) moiety.[54, 199] These assignments were based on published peak assignments that used a combination of in situ EPR and UV-vis spectroscopy to identify similar overlapping features on TS-1 to Ti-OOH and Ti-$(O_2)^{-\bullet}$,[50, 122, 238] and studies of amorphous Nb_2O_5 and Ta_2O_5 bulk oxides that assigned similar overlapping features on Nb and Ta contacted with H_2O_2 to the Nb-OOH (380 nm) and Nb-$(O_2)^{-\bullet}$ (320 nm) features.[124] Moreover, X-ray photoelectron spectra of H_2O_2-activated M-BEA (Section D1.3) show that Nb- and Ta-atoms reduce from M^{5+} to M^{4+},[54] however, it appears that the X-ray radiation caused photoreduction of the reactive complexes.[239] These data and literature precedents

can lead to the incorrect conclusion that the UV-vis spectra contain features corresponding to M-$(O_2)^{-\bullet}$.

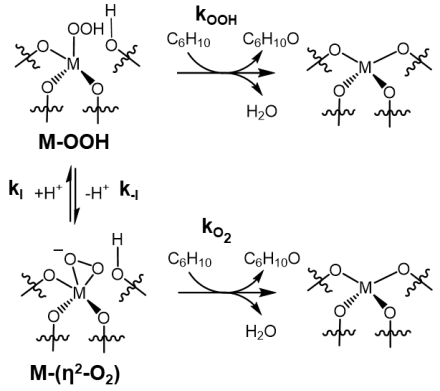

Scheme 5.1. Consumption and interconversion of M-OOH and M-(η^2-O_2) species upon reaction with C_6H_{10} on group 4 metals.

M-OOH intermediates are commonly invoked as the reactive intermediates on Ti-based heterogeneous catalysts for alkene epoxidation,[117, 121, 123, 164, 211, 240-241] while both M-OOH and M-(η^2-O_2) have been observed spectroscopically on a various Ti, Nb, and Ta catalysts.[242-244] Yet much less is known about the identity of the reactive species involved in alkene epoxidation on Nb- and Ta-based heterogeneous catalysts, particularly in comparison to Ti-based catalysts (especially TS-1).

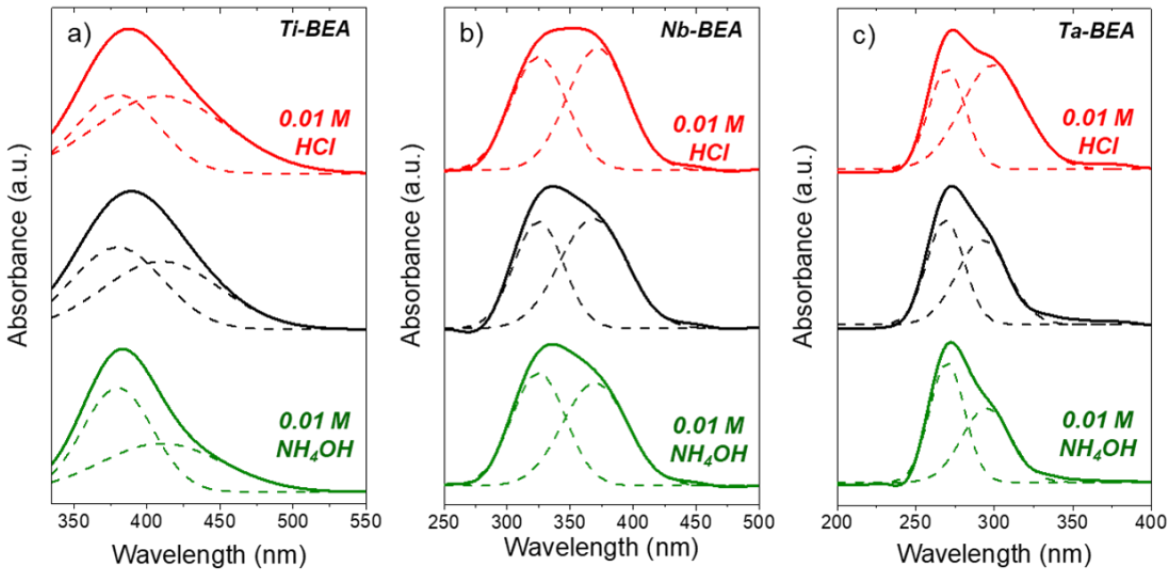

Figure 5.3. UV-vis spectra of H_2O_2-activated (a) Ti-BEA, (b), Nb-BEA, and (c) Ta-BEA. Spectra were acquired in situ in flowing H_2O_2 in CH_3CN (0.1 M H_2O_2, 0.4 M H_2O, 1 cm^3 min^{-1}; black), with HCl (0.01 M HCl, 0.1 M H_2O_2, 0.4 M H_2O, 1 cm^3 min^{-1}; red) or NH_4OH (0.01 M NH_4OH, 0.1 M H_2O_2, 0.4 M H_2O, 1 cm^3 min^{-1}; green) at 313 K. Dashed lines represent Gaussian peak fits for M-(η^2-O_2) and M-OOH species.

Figure 5.3 shows steady-state UV-vis spectra (0.1 M H_2O_2, 0.4 M H_2O in CH_3CN, 313 K) taken under basic (0.01 M NH_4OH), neutral, and acidic (0.01 M HCl) conditions for all M-BEA catalysts. For all Ti-, Nb- and Ta-BEA catalysts, the ratio of the intensities of the absorbance feature at higher wavelengths to that of lower wavelength increases with the concentration of protons, which is determined by the water and NH_4OH or HCl present in the solvent. This suggests that the chemical species that is responsible for the UV-vis feature at higher wavelengths possesses an acidic proton and can be reversibly deprotonated to form a chemical species responsible for the lower wavelength feature. Scheme 5.1 shows that M-OOH forms M-(η^2-O_2) via reversible deprotonation, and the equilibrium between the two depends on the concentration of protons in the solvent.[164, 211] Figure D10a shows Raman spectra collected in situ on Ti-BEA taken under identical neutral (0.1 M H_2O_2, 0.4 M H_2O, in CH_3Cl, 313 K), basic (0.01 M NH_4OH), and acidic (0.01 M HCl) solutions as those used in Figure 5.3. The Raman features at 491 and 750 cm^{-1} correspond to vibrations of the zeolite framework (e.g., O-atom vibration perpendicular to M-O-M moieties).[245] The Raman feature at 621 cm^{-1} is well-known to correspond to ν(Ti-O_2) of Ti-(η^2-O_2).[117, 211] The peak area of this 621 cm^{-1} feature increases upon adding NH_4OH and decreases upon adding HCl,

which qualitatively corroborates the phenomena observed in Figure 5.3. Figure D10b shows the peak area of the 380 nm UV-vis feature correlates to the peak area of the 621 cm^{-1} Raman feature of Ti-(η^2-O_2), which shows that these two features correspond to the same species. In addition, both UV-vis and Raman show the changes in the peak areas are fully reversible (Figure D11), which demonstrates that these changes reflect the interconversion of these reactive intermediates and not their consumption by reaction with NH_4OH or HCl. These in situ UV-vis and Raman spectra of H_2O_2 activated catalysts together with reports of Tilley and coworkers[54] and Ivanchikova *et al.*[210] show that the higher wavelength species must be a M-OOH intermediate and the lower wavelength species should be a M-(η^2-O_2) on each M-BEA and M-SiO_2 catalyst.

Notably, the flow of deionized H_2O or CH_3CN (1 cm^3 min^{-1}, 313 K) over H_2O_2-activated samples does not attenuate the UV-vis absorbance features during a period of 2 h on any of the M-BEA or M-SiO_2 samples, which suggests that H_2O_2 is activated irreversibly to form the M-(η^2-O_2) and M-OOH intermediates on these materials. Additionally, the similarities between the absorbance features (i.e., Figure 5.2) suggest that changing the type of silica support (i.e., M-BEA versus M-SiO_2) does not greatly affect the electronic properties or identity of the M-OOH and M-(η^2-O_2) species formed upon H_2O_2 activation.

In summary, these in situ UV-vis and Raman spectra strongly suggest that M-OOH (higher wavelength) and M-(η^2-O_2) (lower wavelength) species form irreversibly upon activation of H_2O_2 in CH_3CN, and that these species are plausible surface intermediates for alkene epoxidation.

5.3.2 Identification of Intermediates Responsible for Alkene Epoxidation

The identification of the exact active intermediate for alkene epoxidation among these M-BEA and M-SiO_2 materials is necessary in order to relate electronic structure of the reactive intermediates to epoxidation rates and selectivities. Figure 5.4 shows that the normalized intensities of the UV-vis absorbance features for M-OOH and M-(η^2-O_2) intermediates attenuate exponentially with time upon contact with a flowing solution containing cyclohexene (C_6H_{10}; 0.1 M, 0.4 M H_2O, in CH_3CN, 313 K). Differences in the rate of attenuation for individual UV-vis absorbance features indicate that specific intermediates are more reactive than others on each catalyst. For example, on Ti-BEA and Ti-SiO_2, the UV-vis features corresponding to Ti-OOH attenuate at a greater rate than those for Ti-(η^2-O_2), whereas the opposite trend is observed on Nb- and Ta-based catalysts.

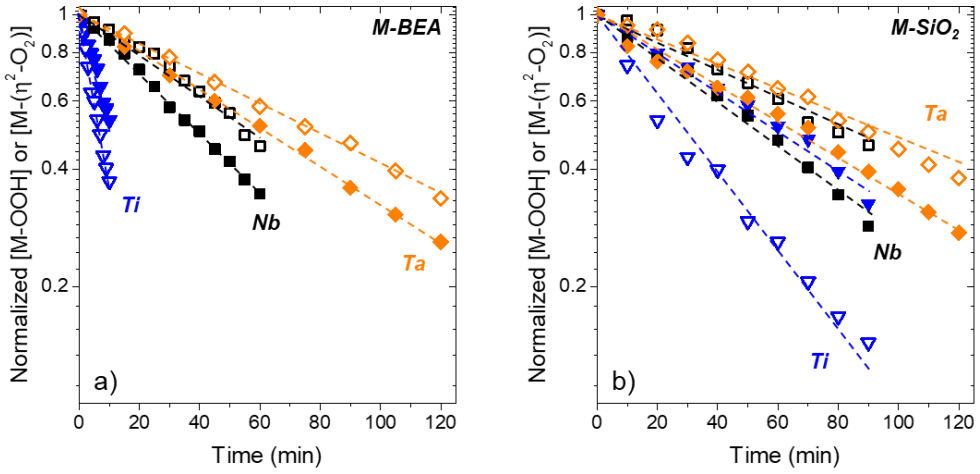

Figure 5.4. Change in the normalized surface coverages of M-OOH (open symbols) and M-(η^2-O_2) (closed symbols) as a function of time over (a) M-BEA and (b) M-SiO_2 materials. UV-vis spectra were obtained in situ upon contacting H_2O_2-activated materials with a solution of C_6H_{10} (0.1 M, 0.4 M H_2O, in CH_3CN, 1 cm^3 min^{-1}) at 313 K. Dashed lines represent fits to differential equations associated with Scheme 5.1 (Section D2). Symbols and colors represent Ti- (▼), Nb- (■) and Ta- (♦) materials. Note that the vertical axes are log scale.

Table 5.2. Ratio of the rate constants for the consumption of M-OOH to that of M-(η^2-O_2) by reaction with C_6H_{10} and *Z:E* (*cis:trans*) product ratios from the epoxidation of *Z*-stilbene (0.003 M *Z*-stilbene, 0.005 M H_2O_2, in CH_3CN, 313 K).

Sample	k_{OOH}:k_{O_2}	*Z:E* ratio
Ti-BEA	1.7	9.2 ± 0.3
Nb-BEA	0.6	1.0 ± 0.1
Ta-BEA	0.6	1.0 ± 0.1
Ti-SiO_2	11.1	10.1 ± 0.4
Nb-SiO_2	0.4	0.9 ± 0.1
Ta-SiO_2	0.5	0.9 ± 0.1

Scheme 5.1 shows that H_2O_2 activates on M-BEA and M-SiO_2 materials to form a pool of M-OOH and M-(η^2-O_2) intermediates which then either interconvert or react with alkenes to yield epoxides and to regenerate the active site. The interconversion of these two species (k_I and k_{-I}) must be accounted for in order to accurately estimate the values of the rate constants for the consumption of M-OOH (k_{OOH}) and M-(η^2-O_2) (k_{O_2}) species by reaction with cyclohexene. The relationship between k_I and k_{-I} are constrained by the equilibrium coefficient (K_I, i.e., ratio of k_I to

k_{-I}) that represents the ratio of M-OOH to M-(η^2-O_2) species under reaction conditions (Section D2.3 outlines the procedure for estimating K_I on the different M-BEA).

Table 5.2 shows the ratio of the rate constants for the reaction between M-OOH with C_6H_{10} to M-(η^2-O_2) with C_6H_{10} on all materials that are calculated by mathematically modeling the rate expressions derived from the mechanism in Scheme 5.1 (section D2) and numerically determining the rate constants from the consumption of the species detected via in situ UV-vis (Figure 5.4). The differences between the rate constants for epoxidation by M-OOH and M-(η^2-O_2) intermediates reveal distinct periodic trends in reactivity.[199] Comparison of the ratio of calculated rate constants for M-OOH to M-(η^2-O_2) consumption on Ti materials show that the rate constant for Ti-OOH to epoxidize cyclohexene is greater than that for epoxidation by M-(η^2-O_2) (i.e., $k_{OOH} > k_{O_2}$), while the opposite is true for reactions on Nb- and Ta- catalysts (i.e., $k_{O_2} > k_{OOH}$). The difference between values of k_{OOH} and k_{O_2} on M-BEA and M-SiO_2 materials suggests that the active intermediate on Ti catalysts is Ti-OOH species, while Nb- and Ta- materials react through Nb-(η^2-O_2) and Ta-(η^2-O_2) complexes, respectively. The implication of these specific reactive intermediates on these materials was tested also by a complementary and independent method, described next.

Analysis of the isomeric distribution of epoxide products formed by the reaction of *Z*-stilbene with H_2O_2 on M-BEA and M-SiO_2 catalysts (0.003 M *Z*-stilbene, 0.005 M H_2O_2, in CH_3CN, 313 K) can provide direct evidence for the identity of the reactive surface species (i.e., the "radical clock" technique).[29] Epoxidations of alkenes that involve M-OOH species proceed through a concerted O-atom transfer step that retains the stereochemistry of the alkene reactant (i.e., through a "butterfly" transition state or Prilezhaev-type mechanism).[65, 246-247] Alternatively, epoxidations that occur via M-(η^2-O_2) intermediates must react through a multi-step mechanism that involves the stepwise formation of the two C-O bonds that allows for rotation about the C-C bond to form the *E*-isomer. Examples of such mechanisms include those postulated for the stepwise formation of oxirane rings on homogeneous Mo complexes (later disproven)[248] and a bi-radical mechanism for homogeneous vanadium complexes.[130, 249] Either mechanism could reproduce the mixture of isomers observed to form on the group 5 M-BEA and M-SiO_2 catalysts. Table 5.2 shows that Ti catalysts preferentially form *Z*-stilbene oxide, while Nb and Ta materials give nearly equimolar distributions of *Z*- and *E*-stilbene oxide products. Consequently, these selectivities indicate that epoxidations occur primarily through Ti-OOH on Ti-BEA and Ti-SiO_2

and via Nb-(η^2-O_2) and Ta-(η^2-O_2) on the Nb- and Ta- catalysts, which are consistent with the interpretation of the in situ UV-vis measurements (Figure 5.4). Previous studies have shown that the microporous nature of the *BEA framework does not inhibit the diffusion of *Z*-stilbene or influence the preference for *Z*- or *E*- isomer formation,[199] which suggests also that the larger-pore SiO_2 supports do not influence the distribution among these epoxide products.

In summary, the independent estimates for the values of rate constants for specific elementary steps (Scheme 5.1) derived from the in situ UV-vis experiments (Figure 5.4) and the observed isomeric product distributions from reactions of *Z*-stilbene with H_2O_2 (Table 5.2) both indicate that all Ti-based materials in this study epoxidize alkenes through the Ti-OOH intermediate, while Nb- and Ta-based catalysts react through M-(η^2-O_2) species. Notably, the

difference in coordination environment (i.e., metal atoms incorporated into the *BEA framework compared to those grafted onto mesoporous SiO_2) does not significantly affect the electronic structure (Figure 5.2) of the intermediates formed upon H_2O_2 activation.

5.3.3 Mechanistic Interpretations of Styrene Epoxidation

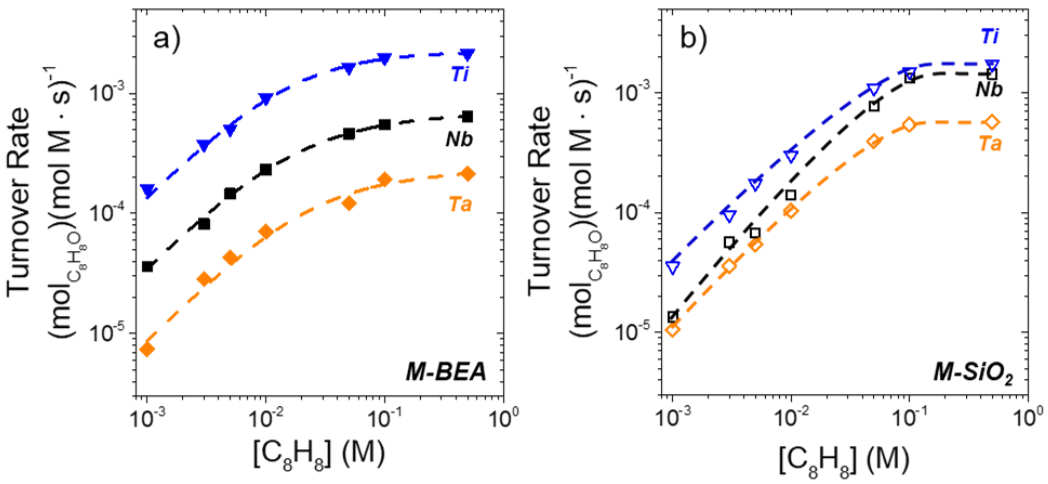

Figure 5.5. Turnover rates for the formation of styrene oxide via primary reaction pathways as a function of [C_8H_8] for (a) M-BEA (closed symbols), including Ti-BEA (blue ▼, 0.01 M H_2O_2), Nb-BEA (black ■, 1 mM H_2O_2), and Ta-BEA (orange ♦, 1 mM H_2O_2) and (b) M-SiO_2 (open symbols), including Ti-SiO_2 (blue ▼, 0.01 M H_2O_2), Nb-SiO_2 (black ■, 0.01 M H_2O_2), and Ta-SiO_2 (orange ♦, 0.01 M H_2O_2) in CH_3CN at 313 K. Dashed lines are intended to guide the eye.

Figure 5.5 shows turnover rates for the formation of styrene oxide (C_8H_8O) via primary reaction pathways as a function of [C_8H_8] (0.001 – 0.5 M) over M-BEA (Figure 5.5a) and M-SiO_2 (Figure 5.5b) catalysts at constant [H_2O_2] and temperature (313 K). For all materials, rates of C_8H_8O formation increase linearly with [C_8H_8] and are independent of [H_2O_2] (Figure D12a) and [H_2O] (Figure D12c) at the lower values of [C_8H_8] (<0.01 M C_8H_8), which suggests that surfaces are saturated with a H_2O_2-derived species. As the concentration of [C_8H_8] increases (>0.05 M C_8H_8), the rate of C_8H_8O formation eventually becomes independent of [C_8H_8] and proportional to [H_2O_2] (Figure D12b). These concomitant changes in the dependence of the reaction rate on [C_8H_8] and [H_2O_2] suggest that the identity of the most abundant reactive intermediate (MARI) changes from a H_2O_2-derived species to one originating from C_8H_8. Scheme 5.2 depicts a series of elementary steps that account for the measured effects of [C_8H_8] (Figure 5.5) and [H_2O_2] (Figure D9) on the rates of C_8H_8 epoxidation. The catalytic cycle involves the quasi-equilibrated adsorption of C_8H_8 (step 1) and H_2O_2 (step 2), followed by the irreversible activation of H_2O_2 (step 3) to form a pool of M-OOH and M-(η^2-O_2) intermediates, which are collectively denoted as "M-(O_2)" for the subsequent development of rate expressions. The active M-(O_2) intermediates either react with C_8H_8 to form the epoxide (C_8H_8O, step 4) or with H_2O_2 (step 6) to decompose nonproductively. The C_8H_8O product subsequently desorbs in a quasi-equilibrated manner (step 5). C_8H_8O formation rates represent the kinetically relevant reaction of M-(O_2) with C_8H_8

$$r_E = k_4[C_8H_8][M-(O_2)] \tag{5.1}$$

where r_E is the rate of C_8H_8O formation, [M-(O_2)] is the number of the reactive M-OOH complexes (for Ti) or M-(η^2-O_2) species (for Nb and Ta), and k_x is the rate constant for step *x* in Scheme 2. The application of the pseudo-steady state hypothesis on the M-(O_2) intermediates, in conjunction with a site balance to account for all possible surface intermediates allows equation 1 to be restated as

$$\frac{r_E}{[L]} = \frac{\frac{k_3 k_4 K_2 [C_8H_8][H_2O_2]}{k_4[C_8H_8]+k_6[H_2O_2]}}{1+K_1[C_8H_8]+K_2[H_2O_2]+\frac{k_3 K_2[H_2O_2]}{k_4[C_8H_8]+k_6[H_2O_2]}+\frac{[C_8H_8O]}{K_5}} \tag{5.2}$$

where [L] is the total number of metal atoms (proportional to the mass of a given catalyst) present during the reaction, K_y is the equilibrium constant for step *y*, and the five terms in the denominator of equation 5.2 correspond (in series) to catalytic sites occupied by CH_3CN (i.e., the reaction solvent), C_8H_8, H_2O_2, M-(O_2), or C_8H_8O (or phenylacetaldehyde), respectively. The complete derivation of the rate expression (equation 2) is shown in Appendix D (section D3.1).

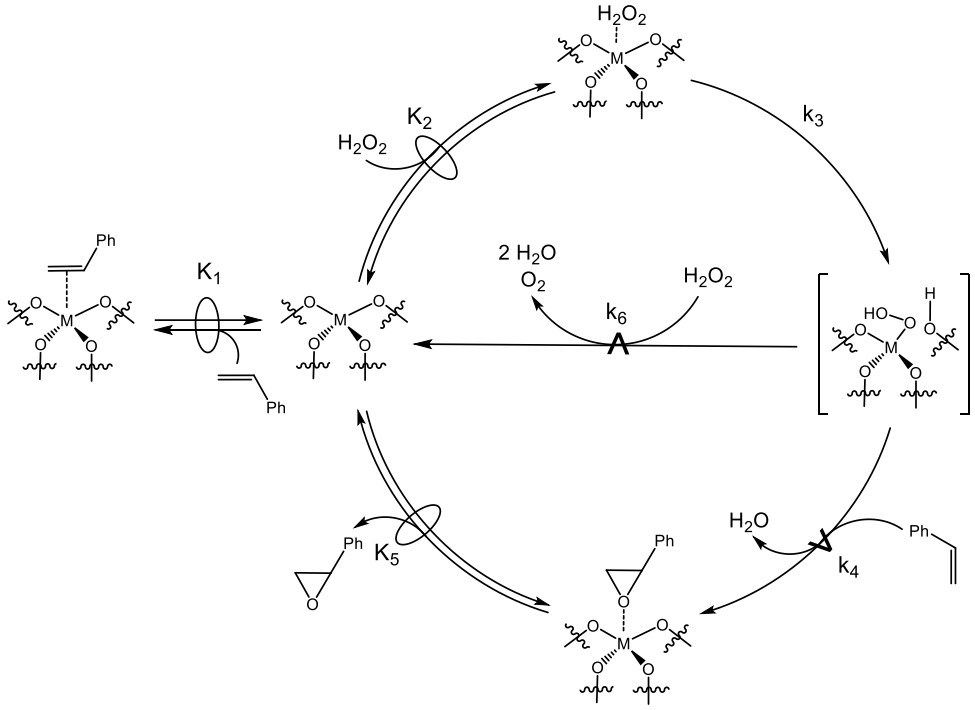

Scheme 5.2. Proposed Elementary Steps for C_8H_8 Epoxidation and H_2O_2 Decomposition over M-BEA and M-SiO_2 Catalysts. For brevity, only group 4 catalysts (i.e., Ti) are shown. The symbol ⇄ represents a quasi-equilibrated step, while → represents a kinetically relevant step. Note, the depiction of M-OOH and adsorbed- C_8H_8, H_2O_2, and C_8H_8O are meant to represent different types of surface species, rather than suggest a specific type of coordination to the active catalytic site. Scheme S1 shows an analogous proposed set of elementary steps for group 5 (i.e., Nb and Ta) catalysts. The M-OOH intermediates drawn are intended to represent the pool of M-OOH and M-(η^2-O_2) species that are present as shown by UV-vis (Figure 5.2).

Equation 5.2 reproduces the observed effects of [C_8H_{10}] (Figure 5.5) and [H_2O_2] (Figure D12) on epoxidation turnover rates. At low ratios of [C_8H_8] to [H_2O_2] (e.g., <5 on M-SiO_2 materials), M-(O_2) species are the MARI and equation 5.2 simplifies to the form

$$\frac{r_E}{[L]} = k_4[C_8H_8] \tag{5.3}$$

which is quantitatively consistent with turnover rates for styrene epoxidation that increase linearly with [C_8H_8] (Figure 5.5) and do not depend on [H_2O_2] (Figure D12a). Similarly, at higher [C_8H_8] (e.g., >0.1 M) the reaction products (e.g., C_8H_8O or phenylacetaldehyde) become the MARI as indicated by epoxidation rates that are independent of [C_8H_8] (Figure 5.5) and proportional to [H_2O_2] (Figure D12b). In this limit, the rate of epoxidation is much greater than the rate of H_2O_2 decomposition (i.e., $k_4[C_8H_8] >> k_6[H_2O_2]$; Table D4), which simplifies equation 5.2 to yield

$$\frac{r_E}{[L]} = \frac{k_3 K_2 K_5 [H_2 O_2]}{[C_8 H_8 O]} \tag{5.4}$$

Equation 5.4 matches the ways in which r_E changes with variations in [C_8H_8] and [H_2O_2] at high [C_8H_8]. Notably, the dependence of styrene epoxidation rates on [C_8H_8] and [H_2O_2] resemble the changes in epoxidation turnover rates during cyclohexene epoxidation on M-BEA materials previously reported to occur through a perfectly analogous set of elementary steps.[54, 199]

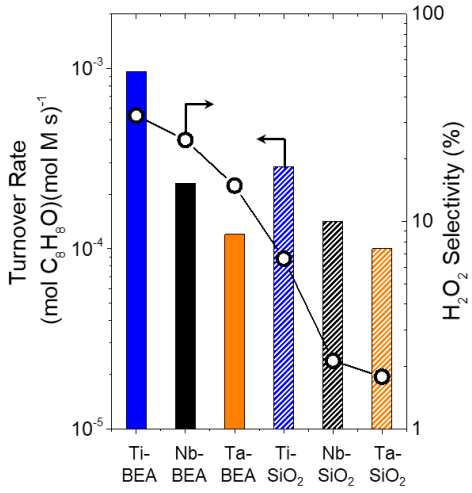

Figure 5.6. Turnover rates for the epoxidation of C_8H_8 (M-BEA - solid bars; M-SiO_2 - striped bars; 0.01 M C_8H_8, 5 mM H_2O_2, 313 K) and H_2O_2 selectivities (calculated as the ratio of the rate of C_8H_8 epoxidation to total H_2O_2 consumption; black ○).

Equitable comparisons of turnover rates and selectivities require that the reaction conditions result in comparable MARIs (e.g., M-(O_2) across all M-BEA and M-SiO_2 materials. Figure 5.6 shows that rates and selectivities for C_8H_8 epoxidation differ significantly among the M-BEA and M-SiO_2 catalysts at standard conditions that result in M-(O_2) MARI for all materials

(0.01 M C_8H_8, 5 mM H_2O_2, 313 K). For example, epoxidation turnover rates on Ti-BEA are ~10 times greater than those for Ta-BEA. In addition, H_2O_2 selectivities vary by a factor of 30 among these catalysts. Overall, epoxidation rates and selectivities are systematically greater for M-BEA materials than for the M-SiO_2 counterparts (e.g., rates and selectivities for Ti-BEA are greater than those on Ti-SiO_2 by factors of 7 and 5, respectively).

The underlying reasons for these large differences in rates and selectivities between Ti-, Nb-, and Ta-atoms coordinated to the *BEA framework and those grafted to mesoporous SiO_2 must be related to physical differences between the two forms of silica supports. Specifically, these differences do not arise from changes in the identity of the reactive intermediates (Section 5.3.2), which are constant for a given metal atom nor from the reaction mechanisms, which are indistinguishable among the catalysts described here. Therefore, the differences among the performance of the catalysts must be caused by consequential differences in the apparent activation barriers for C_8H_8 epoxidation and H_2O_2 decomposition, respectively, that are associated with the crystallographic or morphological differences between the crystalline *BEA framework and the amorphous mesoporous silica support.

5.3.4 Influence of Metal Identity on Activation Barriers

Transition state theory (TST) provides a theoretical foundation to quantify the stabilities of the transition states for C_8H_8 epoxidation (Equation 5.5) and for H_2O_2 decomposition (Equation 5.6) relative to a known reference state in the catalytic cycle (e.g., the state in which the MARI occupies the active site; Section D3.2).[136] In order to make equitable comparisons between M-BEA and M-SiO_2 catalysts, activation barriers must be measured from comparable MARI. Application of TST assumes that the elementary step immediately preceding the transition state (e.g., M-(O_2) and fluid-phase C_8H_8 or H_2O_2) and the transition state are in equilibrium,[136] which is represented by

$$M-(O_2)+C_8H_8 \rightleftharpoons M-(O_2)-C_8H_8^{\ddagger} \tag{5.5}$$

$$M-(O_2)+H_2O_2 \rightleftharpoons M-(O_2)-H_2O_2^{\ddagger} \tag{5.6}$$

where M-(O_2)-$C_8H_8^{\ddagger}$ and M-(O_2)-$H_2O_2^{\ddagger}$ represent the epoxidation and H_2O_2 decomposition transition states, respectively. Consequently, the apparent free energies of activation ($\Delta G^{\ddagger}$) represent the difference in the relative free energy between the transition state and reference states, as shown by

$$\Delta G^{\ddagger} = G^{\ddagger} - G_{M-(O_2)} - G_x \tag{5.7}$$

where $G^{\ddagger}$ is the free energy of the relevant transition state (i.e., for C_8H_8 epoxidation or H_2O_2 decomposition), $G_{M-(O_2)}$ is the free energy of the M-(O_2) reactive intermediates, and G_X is the free energy of fluid-phase C_8H_8 or H_2O_2. Equation 5.7 emphasizes the need to have a consistent MARI on all catalysts, in order to probe how differences in the identity of the transition metal atoms or type of silica support (i.e., M-BEA versus M-SiO_2) used influence activation barriers for epoxidation and H_2O_2 decomposition. Values of the activation enthalpies ($\Delta H^{\ddagger}$) and entropies ($\Delta S^{\ddagger}$) for reactions shown in equations 5.5 and 5.6 are obtained by analysis of transition state equilibrium constants measured as functions of inverse temperature (Figure D13; Section D3.2) using the Eyring equation.[136]

Table 5.3. Activation Enthalpies and Entropies for C_8H_8 Epoxidation ($\Delta H^{\ddagger}_E$ and $\Delta S^{\ddagger}_E$) and H_2O_2 Decomposition ($\Delta H^{\ddagger}_D$ and $\Delta S^{\ddagger}_D$) over M-BEA and M-SiO_2 Catalysts Measured on M-(O_2) Saturated Active Sites.[a]

Sample	$\Delta H^{\ddagger}_E$ (kJ mol^{-1})	$\Delta S^{\ddagger}_E$ (J mol^{-1} K^{-1})	$\Delta H^{\ddagger}_D$ (kJ mol^{-1})	$\Delta S^{\ddagger}_D$ (J mol^{-1} K^{-1})
Ti-BEA	9 ± 3	-200 ± 55	31 ± 10	-104 ± 40
Nb-BEA	39 ± 5	-150 ± 34	45 ± 5	-91 ± 30
Ta-BEA	50 ± 6	-130 ± 45	56 ± 5	-61 ± 25
Ti-SiO_2	30 ± 4	-90 ± 25	34 ± 5	-110 ± 25
Nb-SiO_2	57 ± 5	-75 ± 20	42 ± 4	-99 ± 18
Ta-SiO_2	71 ± 5	-68 ± 15	60 ± 5	-75 ± 20

[a]Reported values are calculated from transition state equilibrium constants for styrene epoxidation and H_2O_2 decomposition determined as functions of inverse temperature (Figure D13, Section D3.2).

Table 5.3 shows activation enthalpies and entropies for both C_8H_8 epoxidation ($\Delta H^{\ddagger}_E$ and $\Delta S^{\ddagger}_E$) and H_2O_2 decomposition ($\Delta H^{\ddagger}_D$ and $\Delta S^{\ddagger}_D$) obtained at reaction conditions that result in a M-(O_2) MARI on each M-BEA and M-SiO_2 sample and in the absence of mass-transfer and diffusive limitations (Section S1.3). Table 5.3 shows that $\Delta H^{\ddagger}$ values increase in the order of Ti < Nb < Ta for a given type of catalyst (i.e., M-BEA or M-SiO_2), which is consistent with the differences in turnover rates in Figure 5.5 and in agreement with previous findings for cyclohexene epoxidation on M-BEA (M = Ti, Nb, Ta, Zr, and Hf) catalysts.[199] Values of $\Delta H^{\ddagger}_E$ for M-BEA materials are, on average, ~20 kJ mol^{-1} lower than the values for the corresponding M-SiO_2 catalysts (e.g., 9 ± 3 kJ mol^{-1} versus 30 ± 4 kJ mol^{-1} for Ti-BEA and Ti-SiO_2, respectively).

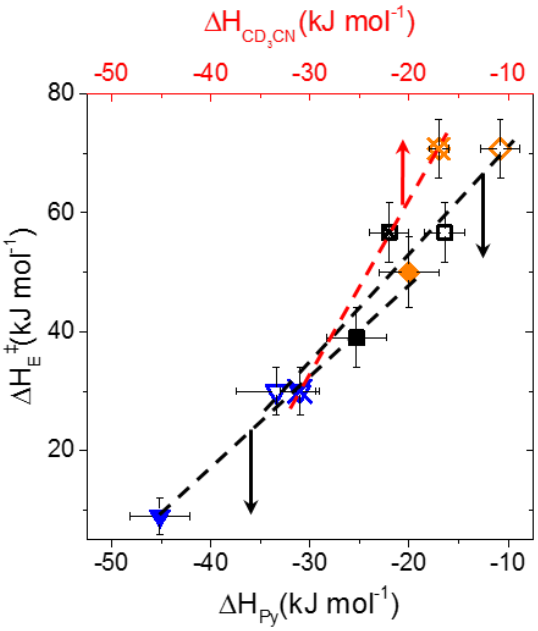

Figure 5.7. Comparisons between activation enthalpies for C_8H_8 epoxidation ($\Delta H^{\ddagger}_E$) and the enthalpies of adsorption for pyridine (ΔH_{Py}; solid and open symbols) or deuterated acetonitrile (ΔH_{CD_3CN}; symbols with cross (X) through them) bound to Lewis acid sites over M-BEA (solid and crossed symbols) or M-SiO_2 (open symbols) measured on a M-(O_2) saturated surface. Color symbols represent: Ti (▼), Nb (■), and Ta (♦). Dashed lines are intended to guide the eye.

Values of $\Delta H^{\ddagger}_D$, however, do not depend on the identity of the support for a given metal atom (e.g., 45 ± 5 kJ mol^{-1} versus 42 ± 4 kJ mol^{-1} for Nb-BEA and Nb-SiO_2, respectively). Additionally, $\Delta S^{\ddagger}_E$ values do not change significantly within a given type of material (e.g., across M-SiO_2), within the uncertainty of measurements. $\Delta S^{\ddagger}_E$ values reflect the loss of translational

entropy that arises from coordination of C_8H_8 to the active M-(O_2) species, which is not expected to depend on the identity of the metal. Notably, values of $\Delta S^{\ddagger}_E$ for M- BEA are ~50 J mol^{-1} K^{-1} more negative than M-SiO_2 (i.e., a greater entropic loss on M-BEA) which likely arises from the smaller pores of the *BEA framework (0.7 nm for *BEA versus 5.4 nm for SiO_2) confining the epoxidation transition state to a greater extent than SiO_2. Interestingly, $\Delta S^{\ddagger}_D$ values do not change when the identity of the metal or the type of silica support (i.e., M-BEA and M-SiO_2) are changed, which suggests that neither the difference in transition metal identity nor change in pore diameter significantly influences the transition state for H_2O_2 decomposition.

Figure 5.7 shows that values of $\Delta H^{\ddagger}_E$ for C_8H_8 epoxidation correlate linearly with the enthalpies of adsorption for CD_3CN or pyridine (Table 5.1, section 5.2.2) coordinated to Lewis acid sites, which each provide a functional probe of the strength of Lewis acid sites among M-BEA and M-SiO_2 catalysts. These values (i.e., ΔH_{Py} and ΔH_{CD_3CN}) are *not* measurements of Lewis acid strength and *cannot* be used to compare properties of Lewis acid sites on M-BEA to those on M-SiO_2, because the values of ΔH_{Py} and ΔH_{CD_3CN} also depend on dispersive interactions (i.e., van der Waals forces) between the adsorbates and the surfaces of the microporous *BEA or the mesoporous SiO_2. These results (i.e., linear correlations in Figure 5.7) resemble the linear relationships reported between the activation enthalpies cyclohexene epoxidation and ΔH_{CD_3CN} previously reported for M-BEA catalysts (M = Ti, Zr, Hf, Nb, and Ta),[199] for which the stabilization of cyclohexene epoxidation transition states by dispersive interactions was similar among all M-BEA.

The underlying causes of these observed trends (Figure 5.7) and the correlations shown for cyclohexene epoxidation[199] are nuanced and do not reflect a simple linear dependence on "Lewis acid strength", which cannot be readily measured. $\Delta H^{\ddagger}_E$ values correlate to the adsorption enthalpies for pyridine and CD_3CN coordinated to Lewis acid sites for these materials, but these correlations may be fortuitous. Rather, values of $\Delta H^{\ddagger}_E$ (and thus, epoxidation rates) depend on the electrophilicity of the reactive intermediates (M-(O_2)), which in turn are influenced by the tendency of the metal center to withdraw electron density from the –OOH or $–O_2^-$ moieties. Figure 5.7 suggests that pyridine and CD_3CN donate electrons to these Lewis acidic sites in ways that happen to be similar to the distribution of charge at the transition state for epoxidation, and as a result, a linear correlation exists.

UV-vis spectra of H_2O_2-activated catalysts provide direct and quantitative measures of the electronic structure of the reactive M-OOH and M-(η^2-O_2) complexes in the form of ligand-to-metal charge transfer band energies (LMCT hν). These LMCT hν values reflect the tendency of the metal atoms to accept electrons from these moieties (i.e., another functional measure of the Lewis acid strength).[199] Figure 5.8a shows that values of $\Delta H^{\ddagger}_D$ depend linearly on LMCT hν for all materials, which strongly suggests that materials that possess more electrophilic M-OOH and M-(η^2-O_2) intermediates give greater rates for H_2O_2 decomposition. Similarly, Figure 5.8b demonstrates that values of $\Delta H^{\ddagger}_E$ for C_8H_8 and C_6H_{10} epoxidation over M-BEA and M-SiO_2 also depend linearly on the value of the LMCT hν, and moreover, the slopes for these dependencies are nearly equal on both M-BEA and M-SiO_2 catalysts. These comparisons suggest that more electrophilic M-OOH and M-(η^2-O_2) species are also more reactive for alkene epoxidation. However, $\Delta H^{\ddagger}_E$ depends more strongly on LMCT hν in all cases (slope ~ 28 kJ mol^{-1} eV^{-1}; Figure 5.8b) than does $\Delta H^{\ddagger}_D$ (slope ~ 15 kJ mol^{-1} eV^{-1}; Figure 5.8a), which indicates that the selectivities for epoxidation also increase with the electrophilicity of the reactive M-OOH and M-(η^2-O_2) intermediates. The greater dependence of $\Delta H^{\ddagger}_E$ on LMCT hν than $\Delta H^{\ddagger}_D$ may be attributed to the inherent instability of the peroxide (i.e., O-O) bond in H_2O_2, as the decomposition of H_2O_2 by reaction with M-OOH intermediates in Ti-SBA-15 has been proposed to occur through a homolytic pathway (i.e., that involves the cleaving of the HO-OH bond).[164] Finally, the correlation of $\Delta H^{\ddagger}_E$ for C_8H_8 epoxidation to the values of LMCT hν (Figure 5.8b) show that $\Delta H^{\ddagger}_E$ are consistently ~20 kJ mol^{-1} greater for M-SiO_2 catalysts in comparison to M-BEA materials with similar LMCT hν.

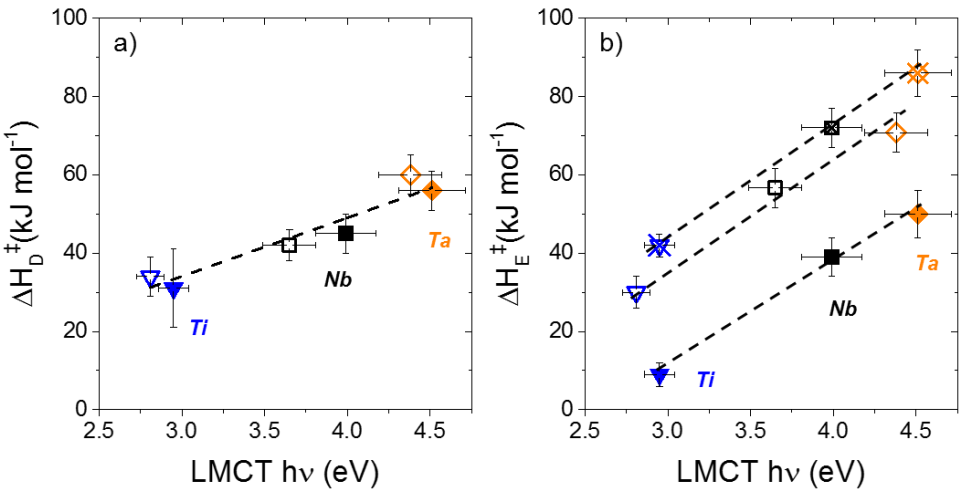

Figure 5.8. Activation enthalpies for (a) H_2O_2 decomposition ($\Delta H^{\ddagger}_{D;}$ solid and open symbols for M-BEA and M-SiO_2, respectively) and (b) epoxidation of C_8H_8 ($\Delta H^{\ddagger}_{E}$; solid and open symbols for M-BEA and M-SiO_2, respectively) or C_6H_{10} (open symbols with a cross (X) for M-BEA) epoxidation measured on M-(O_2) saturated surfaces as a function of ligand-to-metal charge transfer energy (LMCT hν) of the reactive intermediate identified via in situ UV-vis (Section 5.3.1) and *Z*-stilbene epoxidation product distributions. Color symbols represent: Ti (▼), Nb (■), and Ta (♦). Dashed lines are intended to guide the eye.

The clear correlations between $\Delta H^{\ddagger}$ and LMCT hν values shown in Figure 5.8 are more relevant and meaningful than the correlations to ΔH_{Py} and ΔH_{CD_3CN} (Figure 5.7), because values of LMCT hν report on the electronic structure of an intermediate directly involved in the kinetically relevant steps that dictate turnover rates and selectivities for epoxidations (Scheme 5.2, steps 4 and 6). Interpretation of the trends shown in Figure 5.8b reveal several important phenomena. First, the increasing rates and selectivities with decreasing LMCT hν (i.e., more electrophilic M-OOH and M-(η^2-O_2) intermediates that are associated with lower-energy electronic transitions) suggests that these intermediates are electrophilic in nature, which results from the stronger electron-withdrawing nature of the Lewis acidic metal center. Second, the unchanging dependence of LMCT hν on $\Delta H^{\ddagger}_{E}$ for both C_8H_8 and C_6H_{10} epoxidation suggests that there may be little, if any, benefit (i.e., changes in selectivities differing from the trend observed in Figure 5.8) to changing the identity of the metal for different alkene substrates. Third, the constant vertical offset in $\Delta H^{\ddagger}_{E}$ for C_8H_8 epoxidation of M-BEA and M-SiO_2, and lack thereof for $\Delta H^{\ddagger}_{D}$, suggests that the pore size of the *BEA framework relative to SiO_2 primarily influences the rates of epoxidation, but not

H_2O_2 decomposition. Each of these observations and suggested descriptions is discussed in detail in the following sections.

The electrophilic nature of the M-OOH and M-(η^2-O_2) species and the unchanging trend in epoxidation rates for C_8H_8 and C_6H_{10} epoxidation on M-BEA can be probed further by measuring the changes in reactions rates that result from systematically changing the electronic structure of the C=C bond in styrene by incorporating different substituents at the *para*-position. Figure 5.9 shows that the ratio of the turnover rates for the epoxidation of *para*-substituted styrenes (x-C_8H_7, where x = -NO_2, -Br, -H, -Me, or -OMe) to C_8H_8 (R_X/R_H) decreases exponentially with increasing values of the *para* Hammett substituent constant (σ_{para}) on all M-BEA and M-SiO_2 catalysts at a standard set of conditions (3 mM x-C_8H_7, 0.01 M H_2O_2, in CH_3CN, 313K). These data strongly suggest that epoxidation rates increase with the electron-donating ability of the *para* substituent among these reactants. Values of R_X/R_H depend similarly on σ_{para} for all M-BEA and M-SiO_2, and are fit using the Hammett equation

$$log\left(\frac{k_x}{k_H}\right) = \sigma_{para} \cdot \rho \tag{5.8}$$

where k_X and k_H are the rate constants for x-C_8H_7 epoxidation and ρ is the reaction constant (calculated ρ values for all M-BEA and M-SiO_2 are in Table D4).

The turnover rates for x-C_8H_7 epoxidation (R_X) were used in place of k_X, because all reactions were run at equivalent conditions. The average value of ρ (calculated by averaging all ρ for each M-BEA and M-SiO_2 material; Table D5) is -0.9 ± 0.1, whose negative sign agrees with the loss of negative charge (i.e., reduction of M-OOH or M-(η^2-O_2) during epoxidation) that occurs during the 2-electron oxidation of x-C_8H_7 and shows that electrophilic intermediates possess lower activation barriers (i.e., higher rates) for the epoxidation of increasingly electron-rich C=C.[75] Further, the invariance of ρ (i.e., the similarity among values of ρ; Table D5) between all M-BEA and M-SiO_2 suggests that the rates of alkene epoxidation change similarly on all materials when the identity (and electronic properties) of the alkene is changed. This suggests that the chemoselectivity for alkene epoxidation (specifically for molecules with multiple C=C) is largely independent of the type of metal atom used in these M-BEA or M-SiO_2 materials.

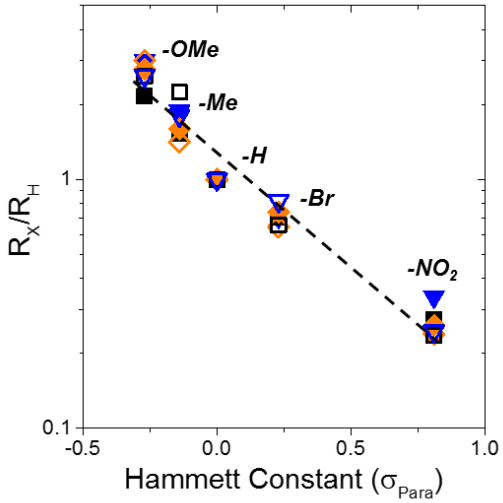

Figure 5.9. Ratio of the turnover rates for the epoxidation of *para*-substituted styrene (x-C_8H7; x = -NO_2, -Br, -H, -Me, or -OMe) to styrene (3 mM x-C_8H_8, 0.01 M H_2O_2, in CH_3CN, 313 K) as a function of the Hammett constant (i.e., a Hammett plot) on M-BEA (solid symbols) and M-SiO_2 (open symbols) . Color symbols represent: Ti (▼), Nb (■), and Ta (♦). The dashed line represents a fit of equation 5.8 to all data, which yields a reaction constant (ρ; Table D5 for all individual ρ values) of -0.9 ± 0.1.[75]

5.3.5 Influence of the Average Pore Diameter of the Catalysis on Activation Barriers

Scheme 5.3 shows changes in enthalpies that correspond to a set of hypothetical elementary steps for the epoxidation of styrene on M-BEA and M-SiO_2 catalysts that correspond to the proposed catalytic cycle (Scheme 5.2) and the prevalence of M-OOH and M-(η^2-O_2) species on the active sites at the conditions (i.e., the reference state) used to measure apparent $\Delta H^{\ddagger}_{E}$ values (i.e., $\Delta H^{\ddagger}_{App}$).[13, 136] Briefly, styrene adsorbs from the fluid phase into the micro- or mesoporous environment near the active M-OOH or M-(η^2-O_2) complex, which corresponds to the enthalpy for adsorption into the porous environment (i.e., ΔH_{Ads}). Subsequently, adsorbed styrene and M-OOH or M-(η^2-O_2) combine to form the transition state for epoxidation and undergo an enthalpy change equal to the intrinsic activation enthalpy for the epoxidation reaction ($\Delta H^{\ddagger}_{Int}$).

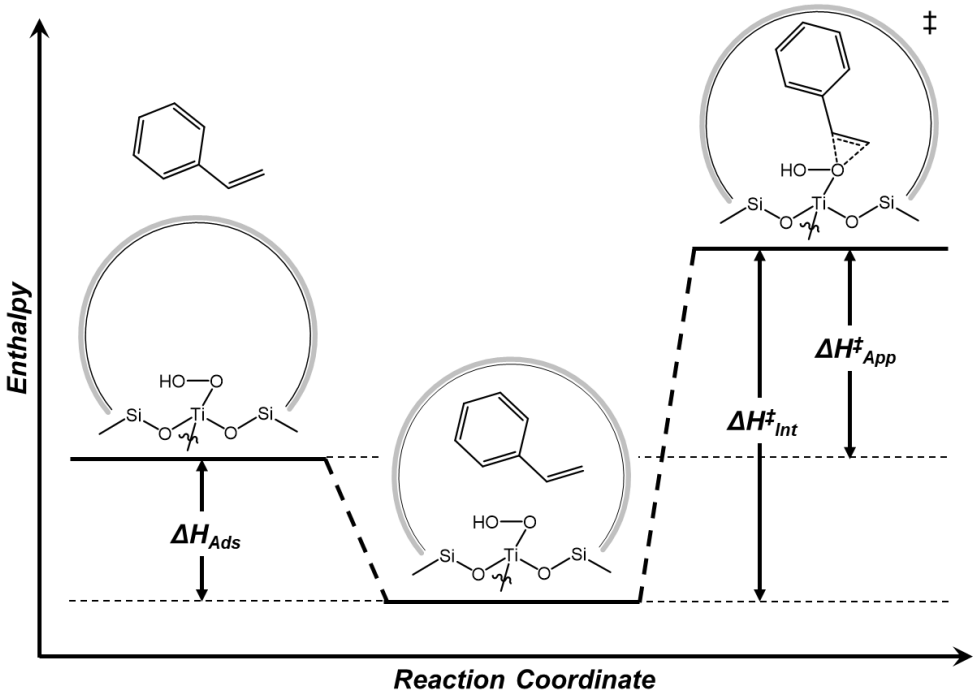

Scheme 5.3. Changes in Enthalpies Due to the Intermediate Steps that Form the Transition State for C_8H_8 Epoxidation from a M-(O_2) Saturated Surface and Fluid-Phase C_8H_8.[a] Ti-OOH is shown to illustrate the relationship between $\Delta H^{\ddagger}_{App}$, ΔH_{Ads}, and $\Delta H^{\ddagger}_{Int}$. This thermochemical sequence for the epoxidation of C_8H_8 with a Ti-OOH reference state (i.e., Ti-OOH MASI) uses a transition state theory formalism that involves the quasi-equilibrated adsorption of C_8H_8 into the pores of *BEA or SiO_2, and the kinetically relevant reaction of C_8H_8 with Ti-OOH.

Scheme 5.3 shows that $\Delta H^{\ddagger}_{App}$ can be related to the other two enthalpy differences as follows

$$\Delta H^{\ddagger}_{App} = \Delta H^{\ddagger}_{Int} - |\Delta H_{Ads}| \tag{5.9}$$

In this sequence (Scheme 5.3), both the ΔH_{Ads} into the porous voids and, by extension, $\Delta H^{\ddagger}_{App}$ depend on morphological properties of the catalyst (e.g., pore size) and the kinetic diameter of the alkene. Values for ΔH_{Ads} are measured directly by applying van't Hoff analysis to measurements of C_8H_8 uptake obtained at identical liquid-phase concentrations (0.03 mM for Si-BEA and 0.007 mM for SiO_2). These ΔH_{Ads} (35 ± 6 kJ mol^{-1} and 18 ± 3 kJ mol^{-1} for Si-BEA and SiO_2, respectively) are measured in liquid CH_3CN (the reaction solvent) to account for the

displacement of CH_3CN from the vicinity of the active site. The values of $\Delta H^{\ddagger}_{Int}$ for each catalyst are calculated using equation 10 and measured values for ΔH_{Ads} and $\Delta H^{\ddagger}_{App}$.

Figure 5.10 shows that $\Delta H^{\ddagger}_{Int}$ for C_8H_8 epoxidation for all M-BEA and M-SiO_2 materials correlate linearly with the LMCT hν. Moreover, all $\Delta H^{\ddagger}_{Int}$ fall near a single line, which suggests that subtle differences between the coordination of these transition metal centers to crystalline *BEA or amorphous SiO_2 do not change the relationship between $\Delta H^{\ddagger}_{Int}$ and the electronic structure (i.e., LMCT hν) of the reactive M-OOH or M-(η^2-O_2) intermediates (Section 5.3.1). These similarities seem to be a reasonable result of the nearly equivalent values for LMCT hν for specific M-(O_2) complexes on *BEA and SiO_2 supports (i.e., LMCT hν for Ti-BEA is not statistically different from that for Ti-SiO_2), suggested by the corresponding UV-vis spectra (Section 5.3.1, Figure 5.2). Consequently, these data (Figure 5.10) suggest that the electronic structure and the intrinsic reactivity of these M-OOH and M-(η^2-O_2) complexes do not depend on the choice of siliceous support.

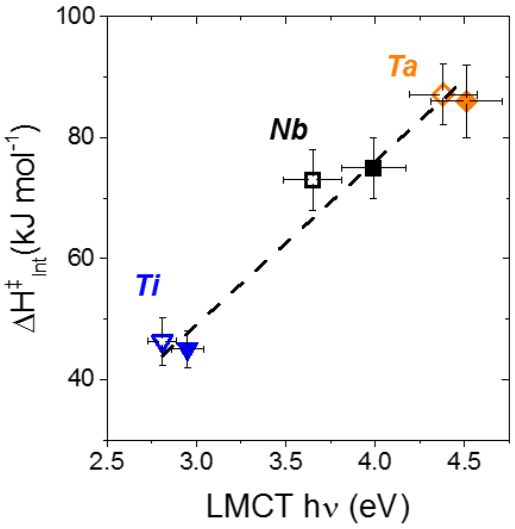

Figure 5.10. Intrinsic activation enthalpies ($\Delta H^{\ddagger}_{Int}$) for the epoxidation of C_8H_8 over M-BEA (closed symbols) and M-SiO_2 (open symbols) measured on a M-(O_2) saturated surface (Figure 8b) as a function of ligand-to-metal charge transfer energies (LMCT hν). Color symbols represent: Ti (▼), Nb (■), and Ta (♦). Dashed line represents a linear regression to all data.

The combination of nearly equal values for $\Delta H^{\ddagger}_{Int}$ on a given transition metal in *BEA or SiO_2, the similar LMCT hν for these same complexes, and the relationships depicted in Scheme 5.3 indicate that the differences in turnover rates, selectivities, and $\Delta H^{\ddagger}_{App}$ are consequences of

differences in the values of ΔH_{Ads} for styrene within the pores of *BEA (-35 ± 6 kJ mol^{-1} in 0.7 nm siliceous pores)[95] and SiO_2 (-18 ± 3 kJ mol^{-1} in 5.4 nm siliceous pores). Thus, stronger, dispersive interactions within the smaller pores of *BEA preferentially stabilize the transition state for styrene epoxidation relative to that in SiO_2 (and also H_2O_2 decomposition transition states in both materials) and leads to $\Delta H^{\ddagger}_{E}$ values that are systematically ~20 kJ mol^{-1} lower in M-BEA than on M-SiO_2 catalysts (Figure 5.8b). Notably, values of $\Delta H^{\ddagger}_{D}$ (Figure 5.8a) do not depend on the pore size of the catalyst, which suggests that the same dispersive interactions that preferentially stabilize the transition state for C_8H_8 epoxidation do not affect H_2O_2 decomposition. H_2O_2 has a Stokes diameter (~0.24 nm)[250] that is significantly smaller than the diameter of the pores within *BEA (~0.7 nm) or SiO_2 (5.4 nm), which suggests that H_2O_2 cannot be stabilized as significantly as styrene by interactions with the pore walls at the transition state for decomposition. Previous studies investigating the oxidation of alkanes and alkenes on TS-1 and Ti-silicate (TiO_2-SiO_2) have shown that TS-1 possesses significantly higher rates and selectivities for 1-hexene epoxidation and cyclohexanone ammoxidation using aqueous H_2O_2.[29, 119, 251] These reports attributed the large differences in reactivity (i.e., a 30-fold increase in rates and 10-fold increase in selectivities for 1-hexene epoxidation) to a smaller number of Ti active sites that are available for reaction in TiO_2-SiO_2 than TS-1.[29] However, it seems likely that the differences may have arisen from greater heats of adsorption of 1-hexene (and likely cyclohexanone) in the MFI framework relative to mesoporous TiO_2-SiO_2 which results in a concomitant decrease in the apparent activation enthalpies for epoxidation[29] (and ammoxidation).[119, 251] Consequently, these data and interpretations reveal two orthogonal design criteria for alkene epoxidation catalysts. First, the design of materials with greater electron affinities (i.e., stronger Lewis acids) will result in more electrophilic M-(O_2) intermediates that possess both increased rates and selectivities for alkene epoxidation. Second, the pore environment (i.e., pore diameter, and likely the hydrophobic/hydrophilic character)[8, 252-254] surrounding the active sites can be selected to maximize dispersive interactions with the desired alkene and increase the transition state stabilization for epoxidation to confer both greater rates and selectivities. Ongoing studies in our group seek to understand the effects of silanol density (and how this relates to hydrophilicity) on the rates and selectivities of alkene epoxidation within similar materials.

5.4 Conclusions

In situ UV-vis spectroscopy reveal that Ti, Nb, and Ta metal atoms incorporated into the *BEA zeolite framework or atomically grafted onto mesoporous SiO_2 irreversibly activate H_2O_2 to form pools of hydroperoxide and peroxide. The isomeric product distributions from reactions with *Z*-stilbene, in conjunction with time-resolved UV-vis spectra of the reaction of H_2O_2-activated materials with cyclohexene, reveal that Ti-materials primarily react through the Ti-OOH intermediate, while Nb- and Ta- catalysts react through the M-(η^2-O_2) species. This suggests that changing the type of silica support from the *BEA framework to mesoporous SiO_2 does not significantly influence the identity or electronic properties of the reactive intermediates for epoxidation by these group IV and V catalysts. Moreover, the dependence of styrene oxide formation rates on reactant (i.e., C_8H_8 and H_2O_2) concentrations show that all M-BEA and M-SiO_2 react through a nearly identical mechanism. All catalysts first adsorb H_2O_2, followed by irreversible activation to form a pool of M-OOH and M-(η^2-O_2) intermediates, which then react with styrene or H_2O_2 to form the corresponding epoxide or decomposition products, respectively. Correlation of activation enthalpies for C_8H_8 epoxidation and H_2O_2 decomposition, on all M-BEA and M-SiO_2 catalysts, to the ligand-to-metal charge transfer band energies of the reactive intermediates show more electrophilic M-OOH or M-(η^2-O_2) species are both *more reactive and selective* for alkene epoxidation. Hammett analysis for the epoxidation of *para*-substituted styrene shows that all M-BEA and M-SiO_2 possess similar chemoselectivities for the epoxidation of alkenes with varying electronic properties. The rates and selectivities of C_8H_8 epoxidation are systematically higher on M-BEA than M-SiO_2 materials, which arise from increased dispersive interactions of the transition state for epoxidation with the walls of *BEA relative to that of SiO_2. This work reveals two discrete design criteria for epoxidation catalysts – the electron affinity of the catalytic site that affects the electrophilicity of the active complex, where more electrophilic intermediates are more active and selective for epoxidation, and the size of the surrounding pore, which can selectively stabilize transition states for epoxidation relative to H_2O_2 decomposition.

CHAPTER SIX

Heteroatom Substituted Zeolite FAU with Ultra Low Al Content for Alkene Epoxidation Catalysis[V]

Abstract

Heteroatom framework-substituted zeolites are important materials that enable shape- and size-selective catalysis. The efficacy of these materials for desired catalytic reactions depends critically on dispersive interactions between the microporous void of the zeolite and the reactant molecules stabilized within it. Here, we develop a post-synthetic method to synthesize base and transition metal-substituted (Ti, Nb, Ta, and Sn) FAU with ultralow Al contents (Si:Al > 900), which is confirmed using X-ray diffraction, elemental analysis, and N_2 volumetric adsorption and ^{29}Si MAS-NMR, DRUV-vis, and IR spectroscopic characterization. Ti-FAU selectively stabilized styrene (C_8H_8) within its pores during epoxidation with H_2O_2. Turnover rates for C_8H_8 epoxidation within Ti-FAU are 2- and 7-fold greater than in analogous Ti-BEA and Ti-SiO_2, respectively; yet, turnover rates of H_2O_2 decomposition are similar for all three materials. Consequently, Ti-FAU gives greater rates and selectivities for this reaction than common Ti-bearing silicates. The mechanism for epoxidation remains constant for all Ti-silicates examined (i.e., Ti-FAU, Ti-BEA, and Ti-SiO_2). Therefore, the improved performance of Ti-FAU reflects differences in activation free energies for epoxidation that show an enthalpic preference in Ti-FAU relative to Ti-SiO_2 and an entropic gain relative to Ti-BEA. These results demonstrate the synthesis of M-FAU with ultralow Al contents are useful for catalytic reactions involving bulky reactants that cannot occur in smaller pore zeotype materials (Ti-MFI), that exhibit deactivation due to changes in Ti-atom coordination (e.g., Ti-SiO2), and that are prone to losses catalyzed by residual Brønsted acid sites (e.g., epoxidations, oxidations, and isomerization reactions).

[V]This chapter has been adapted from the following publication:
Bregante, D.T.; Tan, J.Z.; Sutrisno, A.; Flaherty, D.W.; "Heteroatom Substituted Zeolite FAU with Ultralow Al Contents for Liquid-Phase Oxidation Catalysis"
Catalysis Science & Technology, **2020**, *10*, 635 – 647.

6.1 Introduction

Decades of research[1-2, 7, 14, 28-29, 66, 255] devoted to zeolite and zeotype catalysts have focused on understanding how the unique pore structure of these materials enables size- and shape-selective catalysis. The rates and selectivities toward specific, desired catalytic transformations depends critically on the dispersive interactions between the micropores of the zeolite catalyst and the reactants contained within these spaces.[7, 13, 187] These interactions provide a basis to modify rates and selectivities by stabilizing surface intermediates and transition states along reaction coordinates.

Zeolite catalysts that contain framework-substituted Lewis acidic heteroatoms (e.g., Ti, Sn, Nb, Ta) catalyse stereoselective mono- and di-saccharide isomerization,[8, 33] aldol condensation,[9, 63, 91] alcohol dehydration,[256-257] Baeyer-Villiger oxidation,[35, 152, 258] and alkene epoxidation reactions.[11, 21, 54, 82, 152, 199, 259] For example, the discovery that Sn-substituted zeolite *BEA (Sn-BEA) activates ketones for Baeyer-Villiger oxidation[259] with hydrogen peroxide (H_2O_2) catalysed a renaissance of work with Sn-BEA for use in other reactions (e.g., glucose isomerization,[8, 260] ethanol dehydration[256-257]). Titanium-substituted silicalite-1 (TS-1) was developed in the 1980's and has found industrial application as a catalyst for propylene epoxidation with H_2O_2,[82] which inspired the development of subsequent design principles for epoxidation reactions.[11, 21, 28-29, 69, 88, 187, 199, 261] The presence of Brønsted acid sites (e.g., those formed at framework Al or B atoms)) catalyse secondary reactions that are detrimental to the desired chemistry, even when Al atoms remain in trace quantities (Si:Al = 10 - 150).[262-265] In the context of alkene epoxidation, the desired epoxides formed by primary reaction pathways readily undergo undesirable ring opening hydrolysis over Brønsted acids,[75] which decreases yields. Therefore, researchers invested significant effort into developing synthetic methods that avoid forming these deleterious sites through direct hydrothermal synthesis[8, 69, 260] or through the post-synthetic removal of adventitious Al atoms.[96, 162, 266]

The zeolite faujasite (FAU) is an important structure used in 95% of the catalyst market (by mass),[267] due to its widespread use in fluid catalytic cracking units. The synthesis of Al-free metal-substituted FAU (M-FAU) materials have not been reported, despite the widespread use of this framework in the oil and gas industries. Current methods for the synthesis of M-FAU either rely on the post-synthetic modification of Al-FAU[258, 268-270] or direct hydrothermal synthesis in the presence of $AlNaO_2$.[271] For example, Trejda et al. synthesized Nb- and Ta-substituted FAU

hydrothermally in the presence of sodium aluminate (needed to crystalize the structure) yet, this approach produced in M-Al-FAU materials with a Si:Al ratio equal to 2.3.[271] Methods for the post-synthetic modification of Al-FAU rely on steaming at high temperatures[268] or acid treatments[258, 269] to partially remove Al from framework positions and create vacant silanol nest ($(SiOH)_4$) defects that can be substituted with the desired metal atoms. In all previous reports, a significant amount of Al (Si:Al ratios = 19 – 150) remains,[258, 268-270, 272] which is detrimental for a number of relevant reactions. Consequently, the advent of synthetic methods to produce Al-free M-FAU would be impactful for numerous industrially practiced catalytic reactions including alkene epoxidation and biomass upgrading.

Here, we show that sequential treatments of Al-FAU in concentrated HNO_3 removes nearly all of the Al within these materials and increase Si:Al ratios from 15 to values greater than 900. The incorporation of base and early-transition metals into the FAU framework preserves the crystallinity of these materials and is confirmed using a combination of techniques including X-ray diffraction, N_2 volumetric adsorption, diffuse-reflectance UV-vis spectroscopy, ^{29}Si nuclear magnetic resonance spectroscopy, and infrared spectroscopy. Infrared spectra of pyridine adsorbed within M-FAU synthesize by these methods show the presence of Lewis acid sites and undetectable numbers of Brønsted acid sites (within the sensitivity of the method).

Comparisons of the rates and selectivities for styrene (C_8H_8) epoxidation with H_2O_2 over Ti-FAU to that in other Ti-silicates demonstrates advantages of locating Ti active sites within the supercages of the FAU structure. Turnover rates for styrene epoxidation over Ti-FAU are 2- and 7-fold greater than those in Al-free Ti-BEA (0.65 nm pore diameter) and Ti-SiO_2 (5.4 nm pore diameter), respectively. Rates of H_2O_2 decomposition (2.7 ± 0.9 (mmol H_2O_2)(mol Ti $\cdot$ s)$^{-1}$) remain constant for all structures, and therefore, do not depend on the characteristic dimensions of these Ti-silicate catalysts. Consequently, Ti-FAU gives greater selectivities and greater turnover rates for styrene epoxidation than Ti-BEA and Ti-SiO_2. Mechanistic interpretation of epoxidation rates measured as a function of reactant concentrations show that all Ti-silicates irreversibly activate H_2O_2 to form Ti-OOH intermediates that react with C_8H_8 in a kinetically relevant step to form styrene oxide. Measured activation enthalpies for C_8H_8 epoxidation decrease monotonically with pore size among these materials (e.g., Ti-SiO_2 (37 ± 4 kJ mol^{-1}) > Ti-FAU (22 ± 2 kJ mol^{-1}) > Ti-BEA (9 ± 2 kJ mol^{-1})), which shows that the micropores of BEA enthalpically stabilize C_8H_8 epoxidation transition states relative to the Ti-OOH reactive intermediate. Apparent activation

entropies, however, become increasingly negative with decreasing pore size (-155 to -234 J mol^{-1} K^{-1}) suggesting that the dispersive interactions between C_8H_8 epoxidation transition states and the pore walls of BEA results in the significant loss of translational and vibrational entropy. Consequently, the greater rates and selectivities for C_8H_8 epoxidation within Ti-FAU arise from the balance of enthalpy-entropy compensation effects that depend on the pore structure of the silicate. The 1.3 nm voids of FAU give enthalpic benefits for C_8H_8 epoxidation, relative to Ti-SiO_2, yet does not incur the same entropic losses suffered within Ti-BEA. Collectively, these methods and data provide a pathway to synthesize Al-free M-FAU materials, from synthetic or natural Al-FAU, that can be used for adsorption, separations, or catalysis, and which can allow for the access of other Ti-zeolite structures through inter-zeolitic transformations.

6.2 Materials and Methods

6.2.1 FAU Dealumination and Heteroatom Incorporation

Heteroatom-substituted FAU (M-FAU) were prepared through the post-synthetic modification of H^+-form Al-FAU (Zeolyst, CBV 720; Si:Al ~ 15). Al-FAU was treated in HNO_3 (Macron Chemicals, 68 – 70 wt. %, 20 cm^3 $g_{Al\text{-}FAU}^{-1}$) at reflux for 18 hours with the intent to remove framework Al by forming soluble $Al(NO_3)_3$. The solids were recovered by vacuum filtration, washed with additional HNO_3 (5 cm^3 $g_{Al\text{-}FAU}^{-1}$), and deionized H_2O (17.8 MΩ · cm; 25 cm^3 $g_{Al\text{-}FAU}^{-1}$). *Note that concentrated HNO_3 can easily cause chemical burns and should be handled carefully*. These washed solids were then dried at 823 K (5 K min^{-1}) for 6 h in flowing air (Airgas, Ultra-zero grade; 100 cm^3 min^{-1}) to produce a partially-dealuminated FAU with a Si:Al of ~200 (estimated by energy dispersive X-ray fluorescence, see below). The partial dealumination may result from the redeposition of Al into the FAU framework during filtration at room temperature. To further remove Al atoms, these dried solids were then subjected to a second dealumination sequence identical to that described above to produce Si-FAU with a Si:Al greater than 900.

Ti and Sn atoms were incorporated into the FAU framework through the liquid-phase grafting of $TiCl_4$ (Sigma-Aldrich, 99.9%) or $SnCl_4{\cdot}5H_2O$ (Sigma-Aldrich, 98%) in dichloromethane (DCM, Fisher Chemicals, Certified ACS Stabilized, 25 cm^3 $g_{Si\text{-}FAU}^{-1}$). Nb- and Ta-substituted FAU were prepared by refluxing $Nb(OEt)_5$ (Sigma Aldrich, 99.95%) or $Ta(OEt)_5$ (Sigma-Aldrich, 99.98%) in isopropanol (Fisher Chemical, Optima, 25 cm^3 $g_{Si\text{-}FAU}^{-1}$). In all cases,

the suspensions containing Si-FAU and MCl_4 or $M(OEt)_5$ were kept under an argon atmosphere using standard Schlenk technique for at least 6 h. Prior to introduction of the solvent and the MCl_x or $M(OEt)_5$ precursor, the Si-FAU was dehydrated at 473 K under vacuum (<5 Pa) for 3 h to desorb any residual H_2O that may hydrolyze the metal precursors. Dehydration of Si-FAU is particularly important when using the $TiCl_4$ precursor, which readily hydrolyzes to form oligomeric and bulk TiO_x aggregates. The solvent and other volatile components were removed via rotary evaporation and the recovered solids were heated in flowing air (100 cm^3 min^{-1}) to 823 K at 5 K min^{-1} and held for 6 h to yield bright white-colored solids in all cases.

Titanium substituted BEA (Ti-BEA) and Ti-grafted SiO_2 (Ti-SiO_2) materials were used within a previous study,[11] which presents the detailed chemical and physical characterization of these materials. The titanium silicalite-1 (TS-1) material was synthesized according to the recommended procedure from the International Zeolite Association's Synthesis Commission to contain 0.3 wt. % Ti.[273] The relevant characterization data is presented within Appendix E.

Briefly, Ti-BEA was prepared by the post-synthetic modification of commercial Al-BEA (Zeolyst, CP814E). Al-BEA was contacted with HNO_3 at reflux for 18 h with the intent of forming soluble $Al(NO_3)_3$. The solids were recovered by vacuum filtration and washed thoroughly with H_2O prior to dehydration at 823 K (6 h; 5 K min^{-1}) in flowing air (100 cm^3 min^{-1}), which produced Si-BEA (Si:Al > 1200). Ti atoms were incorporated into Si-BEA through the liquid-phase incorporation of $TiCl_4$ in DCM at reflux. Volatile components were removed via rotary evaporation and recovered solids were treated at 823 K (5 K min^{-1}) for 6 h in flowing air (100 cm^3 min^{-1}) to produce Ti-BEA.

Ti-SiO_2 was synthesized through the grafting of titanium 1,3-dimethoxy-*tert*-butylcalix[4]arene (Ti-dmCalix) onto SiO_2 (Selecto Scientific, 32 – 62 μm particle size, 5.4 nm pore diameter) through reflux in toluene in an Ar atmosphere.[11] Prior to grafting, SiO_2 was dehydroxylated at 573 K under vacuum (<5 Pa) for 10 h to produce isolated SiOH and minimize any Ti-O-Ti oligomer formation. Ti-dmCalix-grafted SiO_2 was recovered by vacuum filtration and treated at 823 K (5 K min^{-1}) for 6 h in air (100 cm^3 min^{-1}) to produce Ti-SiO_2.

TS-1 was synthesized hydrothermally in hydroxide media. In short, 150 mg of titanium (IV) butoxide (TBOT; Sigma-Aldrich, 97%) was dissolved in 27.7 g of tetraethylorthosilicate (TEOS; Sigma-Aldrich, 98%) in a polypropylene container to form a homogeneous solution and was subsequently cooled to 273 K. Separately, a mixture of 28.7 g of tetrapropylammonium

hydroxide (TPAOH; Sachem, 40% in H_2O) and 50.5 g of H_2O was cooled to 273 K and was slowly added (over ~1 min) to the solution of TBOT and TEOS, which yielded a biphasic mixture. This solution was then warmed to 298 K and stirred for 12 h to produce a homogeneous solution, which indicates complete hydrolysis of the TBOT and TEOS. The cover was then removed to evaporate the ethanol and butanol formed through hydrolysis and produce a solution with the approximate composition of 1 Si : 0.0033 Ti : 0.43 TPAOH : 28.3 H_2O. This solution was then loaded into a Teflon-lined stainless-steel autoclave (Parr instruments, 125 cm^3) that contained 5% (relative to SiO_2 in the gel) TS-1 from a previous synthesis. This autoclave was heated to 443 K while rotating (30 rpm) in a convection oven for 3 days. The resulting solids were recovered by centrifugation, washed with H_2O, and dried for 16 h at 373 K. The dried solids were then heated in flowing air (100 cm^3 min^{-1}) at 823 K (1 K min^{-1}) for 10 h to produce TS-1.

6.2.2 Catalyst Characterization

The metal contents of all M-FAU were determined using energy dispersive X-ray fluorescence. Finely-ground M-FAU samples were loaded into a polypropylene sample holder (2.45 cm aperture) which was sealed with ultralene film. These samples were loaded into a spectrometer (Shimadzu, EDX-7000) whose sample chamber was purged with He (Airgas, Ultra-zero grade) prior to measurement. Spectra were obtained between 0 and 30 keV (500 scans), and the relative intensities of the element-specific fluorescence features and their associated calibration factors were used to determine the percent, by mass, of each element within the sample.

The crystallinity and contraction/expansion of the FAU framework was measured through X-ray diffraction. Samples were loaded onto a polypropylene holder and X-ray diffractograms were collected on a diffractometer (Siemens/Bruker, D5000) with Cu Kα radiation (0.15418 nm) under ambient conditions.

The surface area and pore-size distributions of M-FAU were determined by N_2 adsorption. Gas-phase N_2 adsorption isotherms (77 K) were collected on a volumetric adsorption instrument (Micromeritics, 3Flex). Samples (50 – 100 mg) were pelletized and sieved to retain particles between 250 and 500 μm in diameter. These samples were degassed by heated under vacuum (<0.7 Pa, 673 K) for 6 h prior to adsorption measurements. Pore size distributions were determined from N_2 adsorption isotherms using a cylindrical pore model with non-local density functional theory (NLDFT) in the 3Flex software.

The presence of highly-disperse M atoms (and absence of bulk or oligomeric MO_x domains) was inferred by the band edge energies, which were measured using diffuse reflectance UV-vis spectroscopy. Total reflectance spectra were measured under ambient conditions using a diffuse-reflectance accessory (Harrick, Cricket) with a UV-Vis-NIR spectrophotometer (Agilent, CARY 5). Prior to measurement, samples were intimately mixed with magnesium oxide (MgO; Sigma-Aldrich, 99.995%) in a 1:10 ratio by mass.

Infrared (IR) spectra of adsorbed pyridine (Sigma-Aldrich, 99.8%) were used to confirm the presence of Lewis acid sites within M-FAU and to detect Bronsted acid sites associated with remaining framework Al atoms. IR spectra (128 scans, 4 cm^{-1}) were obtained at equilibrium pyridine coverages using a custom-built temperature-controlled transmission cell coupled to a Fourier-transform IR spectrometer (Bruker, Tensor 37) with a liquid N_2-cooled HgCdTe detector. Thin catalyst pellets (~45 mg) were loaded into the transmission cell, which was configured with CaF_2 windows and connected to a gas manifold equipped with a liquid-injection port. All materials were first heated to 573 K (10 K min^{-1}) and held for >2 h in flowing He (50 cm^3 min^{-1}) to desorb any volatile compounds. Pyridine was introduced using a syringe pump (KD Scientific, Legato 100) and vaporized in the gas-transfer lines into a stream of He (50 cm^3 min^{-1}) to contact the M-FAU pellets.

The fraction of Si atoms that exist as $Si(OSi)_3OH$ (ϕ_{NMR}) within M-FAU samples were determined using ^{29}Si magic angle spinning-nuclear magnetic resonance (MAS-NMR) spectroscopy. MAS-NMR spectra (4,000 scans) were collected on a spectrometer (Varian, Unity Inova 300 MHz; 7.05 T), operating at 59.6 MHz Larmor frequency, equipped with a 4 mm MAS probe (Varian-Chemagnetics, double-resonance HX, APEX) under ambient conditions. M-FAU samples (~70 mg) were loaded into 4.0 mm outer diameter zirconia rotors that were spun at 10 kHz. Powdered octakis(trimethylsiloxy)silsesquioxane (Q_8M_8) was used for ^{29}Si chemical shift referencing (Q_8M_8 has a chemical shift of 11.45 ppm relative to tetramethylsilane (TMS) at 0 ppm). Pulse width calibration was performed on Si-FAU, which yielded a 90° pulse width of 1.5 μs. The recycling delay (d_1) for SI-FAU was varied between 5 and 15 s to determine how ϕ_{NMR} changed with d_1; a d_1 of 10 s was used for all M-FAU as ϕ_{NMR} was identical for a d_1 of 10 and 15 s.

6.2.3 Measurement of Epoxidation Rates

For all kinetic measurements, a Ti-FAU sample with 0.3 wt.% Ti atoms was used to avoid artifacts from internal mass-transfer restrictions. Rates of styrene (C_8H_8; Sigma-Aldrich, 99%) and 2,4-dimethylstyrene ($C_{10}H_{12}$; Sigma-Aldrich, 97%) epoxidation were measured in batch reactors (100 cm^3, three-neck round bottom flasks) equipped with reflux condensers to minimize evaporative losses. Solutions of C_8H_8 or $C_{10}H_{12}$ and H_2O_2 (Fisher; 30 wt.% in H_2O) with Benzene (internal standard; Sigma-Aldrich, >99% thiophene-free) in acetonitrile (Fisher Chemicals, HPLC grade) was heated to the desired temperature (308 – 348 K) while stirring at 700 rpm. Epoxidation was initiated by the introduction of Ti-FAU and small aliquots were extracted as a function of time through a 0.22 μm syringe filter. The concentrations of all organic components within these aliquots were determined using a gas chromatograph (HP, 5890 Series A) equipped with a flame-ionization detector. The concentration of H_2O_2 in each aliquot was determined by colorimetric titration using aqueous $CuSO_4$ (8.3 mM, Sigma-Aldrich, >98%) indicator with neocuproine (12 mM, Sigma-Aldrich, >98%) and ethanol (25% v/v, Decon Laboratories, 100%). Notably, styrene oxidation results in the formation of styrene oxide (C_8H_8O) and phenylacetaldehyde. Extrapolation of the selectivity towards each of these species to the limit of zero conversion shows that phenylacetaldehyde forms by C_8H_8O isomerization. Here, the combined concentrations of C_8H_8O and phenylacetaldehyde were used to calculate the turnover rates for epoxidation reactions.

6.3 Results and Discussion

6.3.1 Crystallinity of FAU is Maintained During Post-Synthetic Modification

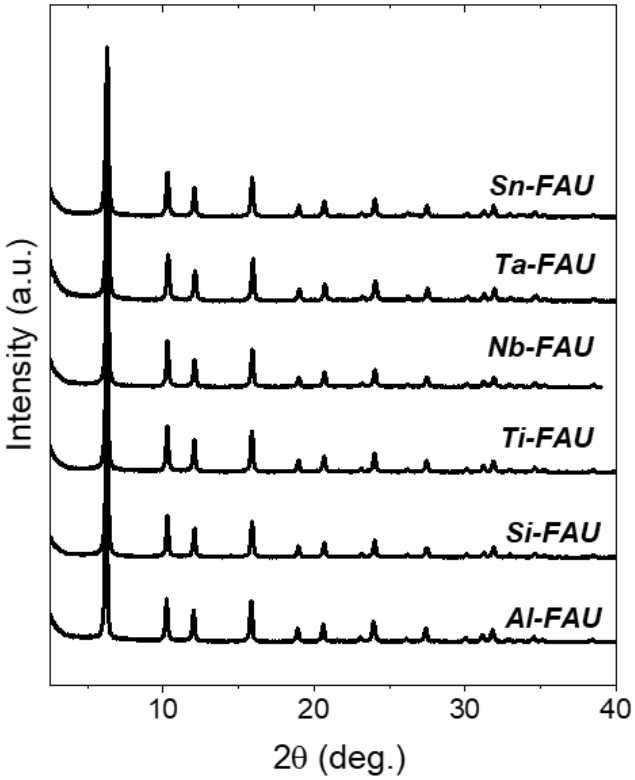

Figure 6.1. X-ray diffractograms for Al-, Si-, Ti-, Nb-, Ta-, and Sn-FAU. Diffractograms are vertically offset for clarity.

Table 6.1. Si:Al and Si:M Ratios, Metal Loadings, Relative Crystallinities, Optical Band Gaps, BET Surface Areas, Fraction of Si Atoms Existing as SiOH (ϕ_{NMR}), and Relative Densities of Hydrogen-Bonded SiOH (ϕ_{IR}) within M-FAU.

Sample	Si:Al[a]	Si:M[a]	Metal Loading (wt. %)[a]	Crystallinity (%)[b]	Band Gap (eV)[c]	BET Surface Area ($m^2\ g^{-1}$)[d]	ϕ_{NMR}[e]	ϕ_{IR}[f]
Al-FAU	14.8	14.8	2.85	100	--	800	--[g]	--[h]
Si-FAU	>900	--	--	96	--	760	0.091	3.4 ± 0.2
Ti-FAU	>900	39.1	1.97	106	4.4	740	0.051	2.1 ± 0.1
Nb-FAU	>900	37.9	3.85	105	4.8	--	0.049	2.5 ± 0.2
Ta-FAU	>900	47.3	5.90	108	4.8	--	0.055	2.7 ± 0.2
Sn-FAU	>900	42.3	4.42	99	4.2	--	0.053	1.9 ± 0.1

[a]Measured by EDXRF. [b]Determined by DRUV-vis spectroscopy by extrapolating the linear portion of the leading edge of the corresponding Tauc plot (Figure 6.3). [c]Estimated by taking the ratio of the intensity for the 10.3° to the 6.3° diffraction features and assuming perfect 100% crystallinity for Al-FAU. [d]Calculated using N_2 adsorption isotherms (Figure 6.2a). [e]Quantified using ^{29}Si MAS-NMR (Figure 4). [f]Determined from FTIR spectra of dehydrated M-FAU (Figure 6.5a) [g]NMR features for Si atoms residing as $Si(OAl)(OSi)_3$ and $Si(OSi)_3OH$ overlap and precludes determination. [h]ν(O-H) of H^+ bound to Si-O-Al moieties overlap with ν(O-H) of hydrogen-bonded SiOH, which prevents quantification.

Titanium, niobium, tantalum, and tin framework-substituted FAU (M-FAU) were synthesized through the post-synthetic modification of H^+-form Al-FAU. Figure 6.1 shows X-ray diffractograms for M-FAU all possess features indicative of the FAU framework. The relative crystallinity for each M-FAU was estimated by taking the ratio of the 10.3° and 6.3° and assuming 100% crystallinity within Al-FAU. There is no apparent loss in crystallinity upon post-synthetic modification (Table 6.1), which suggests that dealumination and subsequent metal substitution does not alter the FAU framework. The d_{111} spacing[258] shifts from 6.23° to 6.28° (Figure E3) upon dealumination, which is consistent with the contraction of the FAU framework resulting from appreciable densities of silanol nests ($(SiOH)_4$). The incorporation of heteroatoms shifts the d_{111} spacing to 6.24° (in the case of Ti), which indicates that the M atoms are integrated into the $(SiOH)_4$ nests formed by dealumination to produce framework heteroatoms sites with the capacity for catalysis.

6.3.2 Post-Synthetic Modification Does Not Form Mesopores

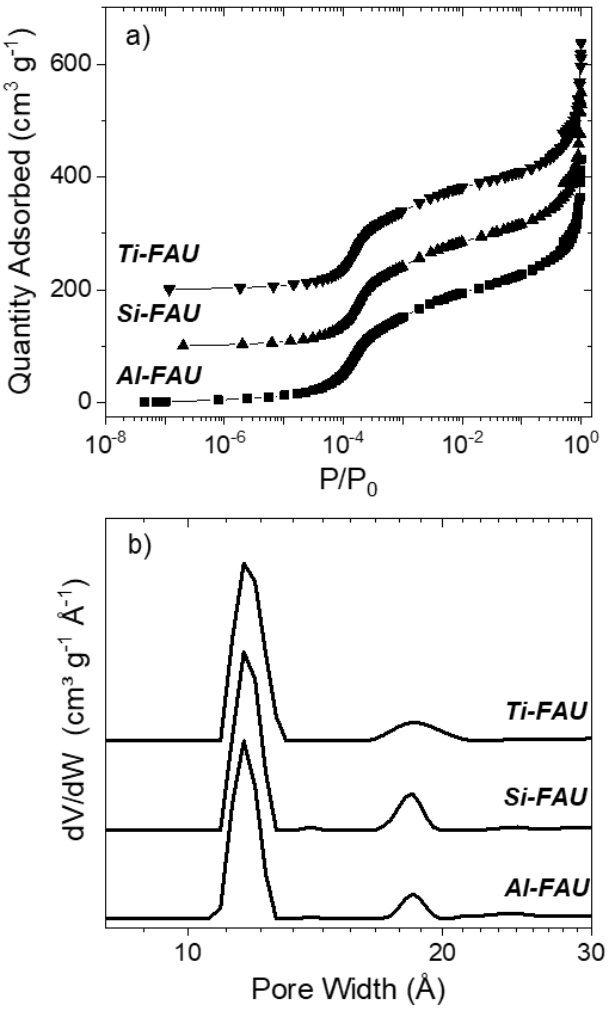

Figure 6.2. (a) Nitrogen adsorption isotherms (77 K; offset by 100 cm^3 g^{-1} for clarity) and (b) pore-size distributions for Al-FAU, Si-FAU, and Ti-FAU. The pore-size distributions were calculated using a cylindrical pore model with NLDFT. Pore-size distributions are normalized to the 1.15 nm feature and offset for clarity.

Nitrogen adsorption isotherms (77 K; Figure 6.2a) were measured on Al-, Si-, and Ti-FAU to probe changes in the physical properties (i.e., Brunauer-Emmett-Teller (BET) surface area, pore-size distribution) of the FAU framework upon dealumination and subsequent Ti-atom incorporation. The adsorption profile for N_2 is characteristic of weak adsorbate-adsorbent interactions (Type III) and approaches micropore filling below a relative pressure (P/P_0) of 10^{-4}.[274] As P/P_0 is increased, N_2 adsorption resembles a typical Type I isotherm that is characteristic of adsorption within a microporous solid. Figure 6.2a contains a log-scale for the abscissa that gives

the illusion that N_2 adsorption resembles a Type IV isotherm; however, the linear-scaling of P/P_0 (Figure E4) reveals the Type 1 nature of N_2 adsorption. The surface area of M-FAU was estimated using BET theory[274] and yielded equivalent values for the three samples tested (740 – 800 $m^2\ g^{-1}$, Table 6.1), which further suggests that post-synthetic modification of Al-FAU does not modify the long-range order of the framework or create sufficiently large defects that change the internal surface area. Figure 6.2b shows the pore-size distributions calculated for Al-, Si-, and Ti-FAU all possess a significant feature with a characteristic pore width of ~1.3 nm, which corresponds to the supercage within the FAU framework.[95] The small feature around 1.8 nm may result from defects that partially connect two adjacent cages. Importantly, the similarities between the pore-size distributions, the BET surface areas, and the characteristics of N_2 adsorption all suggest that post-synthetic modification does not significantly alter the FAU framework. Nitrogen possesses a significant quadrupolar moment that may lead to specific interactions with adsorption sites, which typically prompts the use of argon as an adsorptive.[274] The similarities between the adsorption isotherms here, however, further suggests the FAU framework is unchanged upon post-synthetic treatment.

6.3.3 Metal Sites Within FAU Framework are Highly Disperse

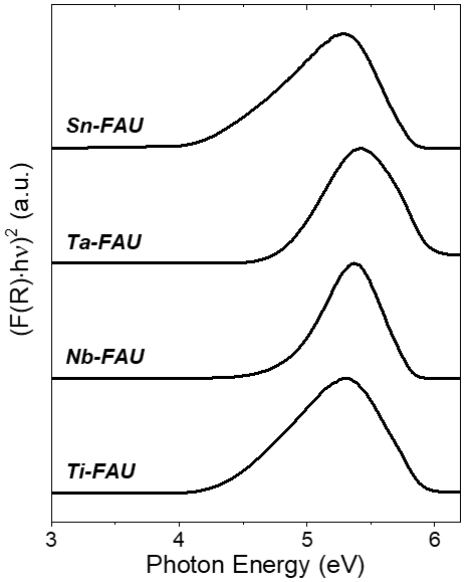

Figure 6.3. Tauc plots for Ti-, Nb-, Ta-, and Sn-FAU. Note that F(R) corresponds to the Kubelka-Munk pseudo-absorbance. All spectra were normalized to the most-intense feature and are offset for clarity. Optical band gaps were calculated from regressing the linear portion of the leading edge to a value of zero.

Optical band gaps reports on the speciation (and dispersion) of semi-conducting and insulating solids.[51, 199, 275] Figure 6.3 shows Tauc plots for M-FAU all possess a single prominent absorbance feature between 5.1 and 5.3 eV, which corresponds to the ligand-to-metal charge transfer between the O atoms within the framework of FAU and the M atom within the sample (e.g., charge transfer between the 2p orbitals of oxygen to the 3d orbitals of Ti^{4+}). Table 6.1 shows that the band gaps for these Ti-, Nb-, Ta-, and Sn-FAU are all significantly larger those of the bulk MO_x analogues (bulk anatase TiO_2, Nb_2O_5, Ta_2O_5, and SnO_2 have band gaps of 3.2,[276] 3.4,[100] 3.9,[277] and 3.6 eV,[278] respectively). Moreover, the band gaps for these M-FAU samples are comparable to those for hydrothermally-synthesized M-BEA[21, 168, 256] and M-MFI[168, 279-281] zeolites, which suggests these metal atoms are incorporated into the FAU framework. The large band gaps for the M-FAU within this study, relative to bulk MO_x, suggest that metal atoms are well isolated within the zeolite framework and that these samples contain negligible amounts of M-O-M linkages.

6.3.4 Grafting of Metal Ions Leads to Reduction in the Number of SiOH

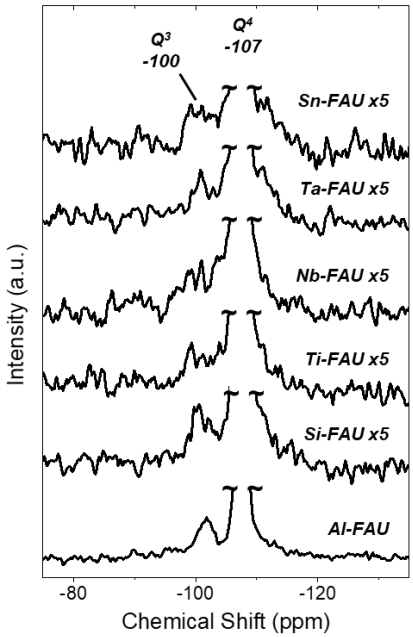

Figure 6.4. ^{29}Si direct polarization MAS-NMR spectra of Al-, Si-, Ti-, Nb-, Ta-, and Sn-FAU. Spectra are normalized to the Q^4 feature and scaled to the indicated value (e.g., x5 magnification for Si-FAU). The intense Q^4 feature has been truncated and spectra are vertically offset for clarity. Figure E5 shows ^{29}Si MAS-NMR spectra that includes the Q^4 feature.

The fraction of Si atoms that exist as SiOH within each M-FAU can provide indirect evidence for the formation and elimination of $(SiOH)_4$ upon dealumination and subsequent metal-ion incorporation. Figure 6.4 shows ^{29}Si MAS-NMR spectra that contain distinct NMR features at chemical shifts of -107 and -100 ppm on all M-FAU. The feature at -107 ppm corresponds to Si atoms within the FAU framework coordinated to four siloxane functions (i.e., $Si(OSi)_4$, denoted as Q^4 sites) or to three siloxanes and a substituted metal atom (i.e., $Si(OSi)_3OM$; M = Ti, Nb, Ta, Sn).[69, 282] Figure E5b shows the full width-half max of the Q^4 feature increases from 0.9 ppm for Si-FAU to 1.1 – 1.2 ppm for M-FAU, which indicates this feature contains contributions from both $Si(OSi)_4$ and $Si(OSi)_3OM$ moieties. The broad feature at -100 ppm for Al-FAU corresponds to Si atoms that possess an adjacent Al atom (i.e., $Si(OAl)(OSi)_3$).[283] For all other M-FAU, the small feature at -100 ppm corresponds to Si atoms that possess a single pendant hydroxyl (i.e., $Si(OSi)_3OH$, denoted as Q^3 sites).[284-285] The fraction of Si atoms that reside as $Si(OSi)_3OH$ (ϕ_{NMR}) is described by the fraction of Q_3 sites to the sum of Q^3 and Q^4 sites

$$\varphi_{NMR} = \frac{A_{Q^3}}{A_{Q^3} + A_{Q^4}} \tag{6.1}$$

where A_{Q^3} and A_{Q^4} are the areas of the deconvoluted ^{29}Si MAS-NMR features for Q^3 and Q^4 sites, respectively (Section E3.1) shows representative peak fits to determine the Q^3 and Q^4 areas). Table 6.1 shows that ϕ_{NMR} decreases from 0.09 to 0.05 upon framework substitution into Si-FAU samples, which follows expectations based upon the liberation of HCl or EtOH upon metal grafting onto $(SiOH)_4$ and formation of Si-O-M linkages. A statistical distribution of $(SiOH)_4$ within the framework before and after the substitution of M atoms (assuming a final Si:M ratio of ~40; Table 6.1) suggests a ~35% reduction in the total number of $(SiOH)_4$, which qualitatively agrees with the measured changes in ϕ_{NMR} between Si-FAU and M-FAU (~44% reduction). Values of ϕ_{NMR}, however, do not directly represent the density of $(SiOH)_4$ (i.e., SiOH formed upon dealumination), because these values encompass all Si atoms that exist as SiOH including those at point defects and on the external surface of FAU particles.

6.3.5 Metal Ions Within M-FAU Occupy $(SiOH)_4$ and Are Lewis Acidic

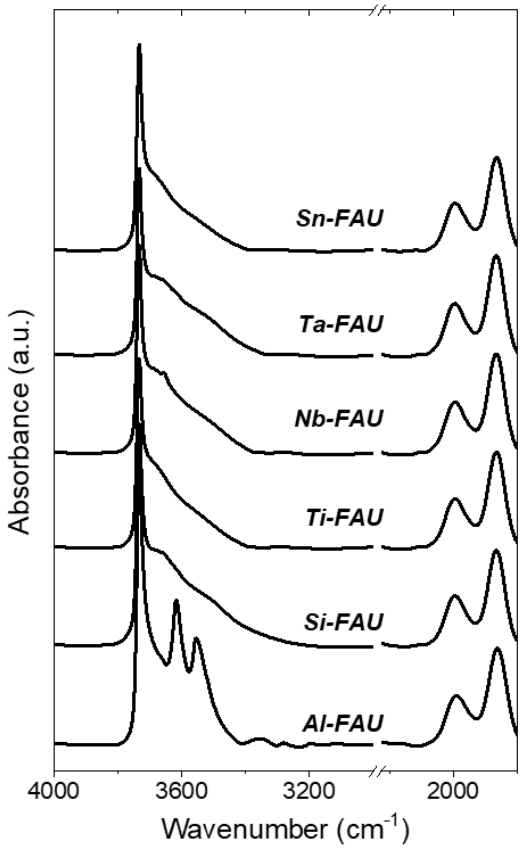

Figure 6.5. Infrared spectra of dehydrated Al-, Si-, Ti-, Nb-, Ta-, and Sn-FAU in flowing He (50 cm^3 min^{-1}, 573 K). Spectra have been normalized to ν(Si-O-Si) at 1865 cm^{-1} and are vertically offset for clarity.

Isolated SiOH and hydrogen-bonded $(SiOH)_4$ moieties in M-FAU materials possess distinct ν(O-H) that can be used to yield semiquantitative estimates for the relative density of $(SiOH)_4$ groups. Figure 6.5 shows IR spectra of dehydrated M-FAU samples (573 K in He) all possess distinct features at 1990 and 1865 cm^{-1}, which correspond to ν(Si-O-Si) overtones[35, 286] that reflect contributions from the FUA framework. The complex broad features between 3750 – 3400 cm^{-1} correspond to ν(O-H) modes of distinct types of SiOH. The sharp feature at 3740 cm^{-1} within all M-FAU corresponds to ν(O-H) of isolated SiOH that do not interact with nearby hydrogen bond-acceptor moieties. Within Al-FAU, the sharp features at 3640 and 3550 cm^{-1} are characteristic of Brønsted acid sites within the supercage and sodalite cages of FAU, respectively.[287-288] The broad ν(O-H) feature extending between 3750 – 3400 cm^{-1} in M-FAU (M

= Si, Ti, Nb, Ta, and Sn) samples corresponds to $(SiOH)_x$ (e.g., $(SiOH)_4$) that contain adjacent hydrogen-bonded -OH groups.[21, 49]

Relative densities of isolated SiOH and $(SiOH)_4$ among M-FAU samples are estimated by normalizing each infrared spectra to the total number of framework bonds, which is assumed to be constant among these samples and is represented by the intensity of the ν(Si-O-Si) (1865 cm^{-1}) within this study. Peak fitting (Section E3.2) of the ν(O-H) region allows for the deconvolution of isolated SiOH (3740 cm^{-1}) and $(SiOH)_4$ groups (3300 – 3740 cm^{-1}); where the ratio of the cumulative area of ν(O-H) for $(SiOH)_4$ ($A_{(SiOH)_4}$) normalized to that of ν(Si-O-Si) ($A_{Si-O-Si}$) yields a quantitative estimate for the relative density of $(SiOH)_4$ (ϕ_{IR}) among M-FAU materials.

$$\varphi_{IR} = \frac{A_{(SiOH)_4}}{A_{Si-O-Si}} \tag{6.2}$$

Table 6.1 shows values of ϕ_{IR} decrease from 3.4 ± 0.2 for Si-FAU to ~2 ± 0.1 for M-FAU. The decrease in ϕ_{IR} (~40%) for Ti- and Sn-FAU is quantitatively consistent with the expected loss of $(SiOH)_4$ (~35%) upon metal-atom incorporation. Nb- and Ta-FAU are pentacoordinate and possess a pendant -OH, which obviates how changes in ν(O-H) solely result in the loss of $(SiOH)_4$; however, the general trend in decreasing ϕ_{IR} for these materials suggests the incorporation of Nb and Ta atoms into $(SiOH)_4$. Collectively, the data and interpretation from X-ray diffraction, diffuse reflectance, UV-vis, N_2 volumetric adsorption, ^{29}Si MAS-NMR, and IR spectroscopy experiments suggest that the post-synthetic modification procedure presented here first generates a nearly siliceous FAU material with a number of $(SiOH)_4$ nests equal to the original number of Al atoms, and second, substitutes the desired M atoms (M = Ti, Nb, Ta, Sn) into the zeolite framework.

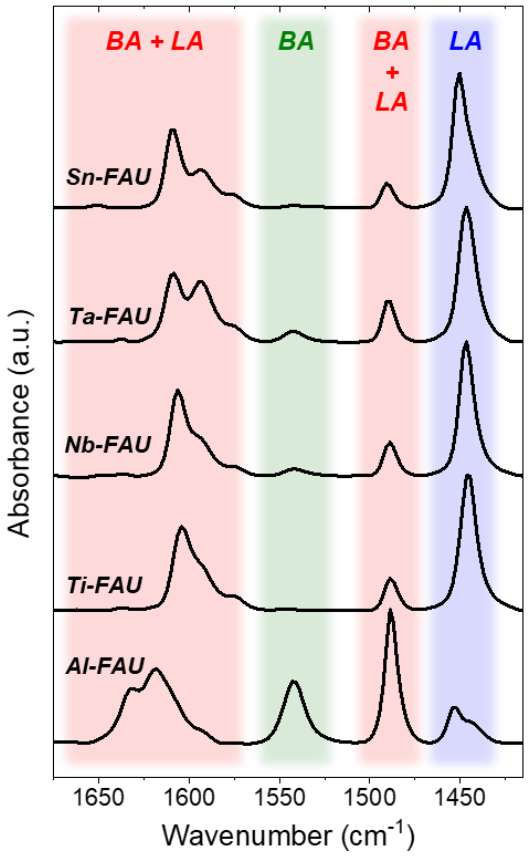

Figure 6.6. Infrared spectra of Al-FAU, Ti-FAU, Nb-FAU, Ta-FAU, and Sn-FAU in contact with gaseous pyridine (0.25 kPa, 101 kPa He, 473 K). All spectra were normalized to the most-intense feature between 1700 – 1400 cm^{-1} and are offset for clarity. Colored regions correspond to expected regions for vibrational modes of pyridine coordinated to Lewis acid sites (LA; blue), Brønsted acid sites (BA; green), and both Brønsted and Lewis acid sites (BA + LA; red).

Heteroatom-substituted zeolites often act as solid Lewis acid catalysts, where the efficacy of these materials depends strongly on the electron affinity (described colloquially as the "Lewis acid strength") of the active site.[11, 63, 152, 168, 199] Pyridine molecules bound to Brønsted acid sites form pyridinium ions that possess vibrational modes distinct from pyridine molecules bound to Lewis acid sites, and these differences provides a means to discriminate between different types of acid sites within solid materials. Figure 6.6 shows IR spectra of M-FAU materials in contact with dilute streams of vapor-phase pyridine (0.25 kPa, 101 kPa He, 473 K). All M-FAU possess significant absorbance features between 1650 – 1575 cm^{-1} and at 1500 cm^{-1}, which correspond to vibrational modes of pyridine molecules adsorbed to either Brønsted or Lewis acid sites.[233-234] The absorbance features around 1450 cm^{-1} are assigned to the vibrational modes of pyridine adsorbed solely to Lewis acid sites, while the absorbance feature at 1540 cm^{-1} is attributed to the vibrational

modes of the pyridinium ion. Al-FAU clearly possesses the greatest density of Brønsted acid sites among these materials. Within Ti-, and Sn-FAU the feature at 1540 cm^{-1} is nearly indistinguishable from baseline, which suggests these materials do not possess spectroscopically observable densities of Brønsted acid sites. Figure 6.6 shows that Nb- and Ta-FAU possess significant amounts of adsorbed pyridinium, because Nb and Ta atoms within zeolites are five coordinate and possess a pendant -OH,[89, 103] which may act as a Brønsted acid. Notably, the presence of Brønsted acid sites within Nb- and Ta-FAU cannot be due to residual Al atoms, as the vibrational features that discriminate these features are not present on Ti- or Sn-FAU, which were synthesized using the same batch of Si-FAU. For all M-substituted FAU, there is a significant increase in intensity for absorbance features that correspond to pyridine bound to Lewis acid sites, which is consistent with reports for these metal atoms substituted into other silicate frameworks.[11, 162, 258, 289] These Lewis acidic active sites constitute an important class of catalysts for a variety of reactions (see above), and the stabilization of intermediates critical to epoxidation catalysis within the FAU framework is demonstrated on Ti-FAU in the following section.

6.3.6 Reaction Pathways for Alkene Epoxidation with Hydrogen Peroxide

Zeolites and mesoporous silicates bind reactants by charge transfer at active sites but also permit the selective stabilization of surface intermediates through combinations of van der Waals and specific interactions among the extended zeolite surface, the solvent molecules and the reactive species. The extent of stabilization depends on both the size and shape of the confining pore and the reactive species contained within these spaces. Figure 6.7 shows turnover rates for styrene (C_8H_8) epoxidation with hydrogen peroxide (H_2O_2) are significantly greater on Ti-FAU (1.3 nm supercage) than for Ti-BEA (0.65 nm pore) and Ti-SiO_2 (5.4 nm pore) at all reaction conditions examined. Specifically, epoxidation rates over Ti-FAU are greater than Ti-BEA and Ti-SiO_2 by factors of 2 and 7, respectively. H_2O_2 selectivities represent the percent of H_2O_2 molecules that are consumed by epoxidation reaction pathways and decrease in the same fashion as epoxidation turnover rates between Ti-FAU (47%), Ti-BEA (30%), and Ti-SiO_2 (6%). Rates of H_2O_2 decomposition (2.7 ± 0.9 (mmol H_2O_2)(mol Ti $\cdot$ s)$^{-1}$) are nearly identical on Ti-FAU, Ti-BEA, and Ti-SiO_2 because the transition states for H_2O_2 decomposition are too small to experience interactions with the pore walls of the silicate hosts that differ among these materials. The importance of ultralow Al contents is exemplified in reactions that include Al-FAU to simulate a

Si:Al of 150. The presence of Al-FAU results in no measurable C_8H_8O formation; yet, rather forms 1-phenyl-1,2-ethanediol (from C_8H_8O ring opening) and 1-phenylethanol (from C_8H_8 hydration over H^+ sites). Therefore, the differences in C_8H_8 epoxidation catalysis and the corresponding H_2O_2 selectivity must relate to how the stability of C_8H_8-derived intermediates depend on the characteristics of the Ti-silicate catalyst.

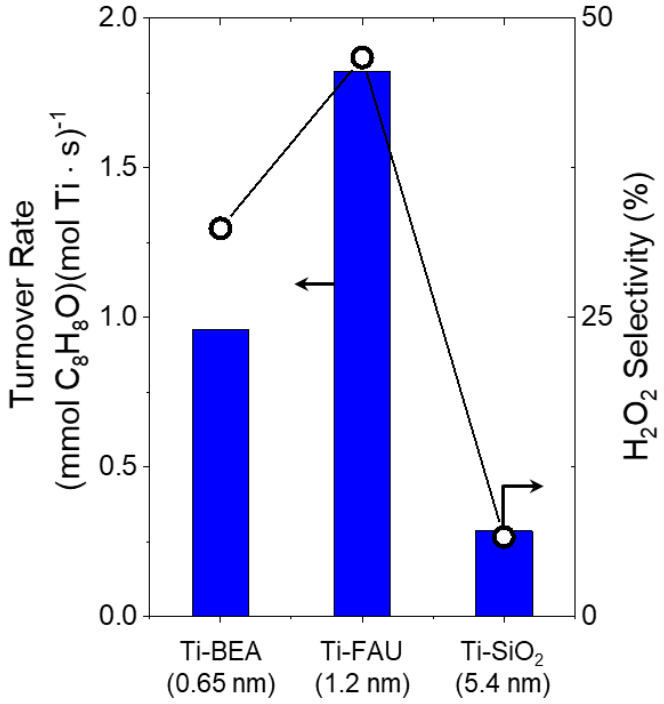

Figure 6.7. Turnover rates for C_8H_8 epoxidation (blue bars) and H_2O_2 selectivities towards epoxidation products (○) over Ti-BEA, Ti-FAU, and Ti-SiO_2 with the characteristic pore dimension indicated. All reactions were run at standard conditions that lead to rates that are proportional to C_8H_8 concentrations (0.01 M C_8H_8, 0.01 M H_2O_2 in CH_3CN, 313 K).

Turnover rates for (C_8H_8) epoxidation with hydrogen peroxide (H_2O_2) were measured as a function of C_8H_8 and H_2O_2 concentration to provide insight as to the mechanism for alkene epoxidation and reconcile the differences in rates and selectivities for C_8. Notably, the Ti-FAU sample used within these kinetic measurements was synthesized to contain 0.3 %, by weight, Ti atoms to avoid artifacts that may arise from internal concentration gradients (i.e., to satisfy the Madon-Boudart criterion).[111] Figure 6.8 shows that Ti-FAU, Ti-BEA, and Ti-FAU all possess nearly indistinguishable dependencies on the concentrations of C_8H_8 (Figure 6.8a) and H_2O_2 (Figure 6.8b) despite significant differences between the topologies of these silicate frameworks.

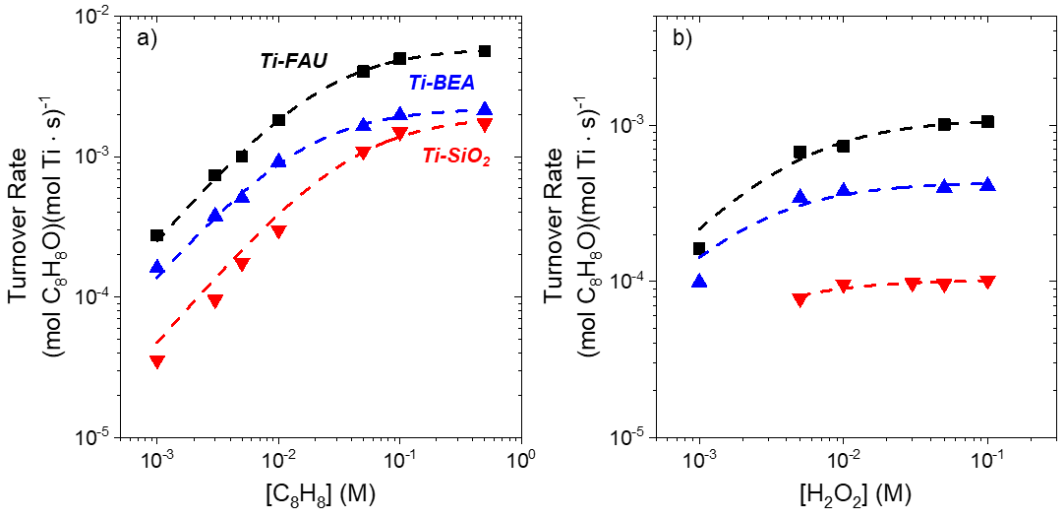

Figure 6.8. Turnover rates for C_8H_8 epoxidation as a function of (a) $[C_8H_8]$ (0.01 M H_2O_2) and (b) $[H_2O_2]$ ($3 \cdot 10^{-3}$ M C_8H_8) on Ti-FAU (■), Ti-BEA (▲), and Ti-SiO_2 (▼) in CH_3CN at 313 K. Dashed lines represent fits to equation 6.4. Data for Ti-BEA and Ti-SiO_2 are adapted from ref [11]. Errors in C_8H_8O formation rates are <10% and error bars are omitted for clarity.

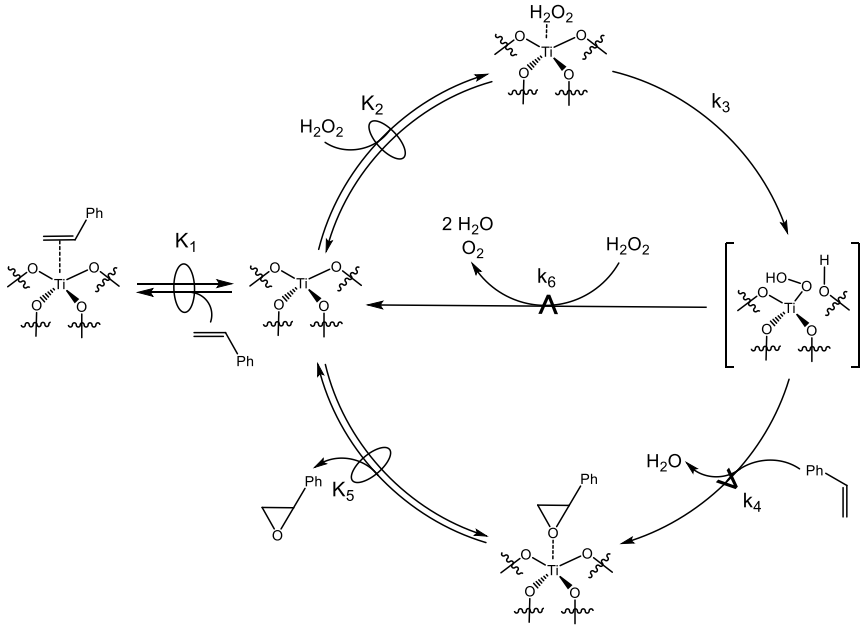

Scheme 6.1. Proposed series of elementary steps for the epoxidation of C_8H_8 over Ti-based catalysts. The symbol ⇄ represents a quasi-equilibrated step, while →A represents a kinetically relevant step.

All Ti-based catalysts exhibit two kinetic regimes that differ in how epoxidation rates depend on the concentrations of reactants. At low $[C_8H_8]$:$[H_2O_2]$ (<1), turnover rates increase

linearly with [C_8H_8] and do not vary with [H_2O_2] (when [H_2O_2] is >$5\cdot10^{-3}$ M), which suggests that active sites are saturated with reactive species derived from H_2O_2 (e.g., Ti-OOH). At low values of [H_2O_2] (<$5\cdot10^{-3}$ M), turnover rates over Ti-BEA and Ti-FAU show a first-order dependence on both [C_8H_8] and [H_2O_2], which suggests that active sites are saturated with solvent molecules, rather than an intermediate derived from the reactants. At high [C_8H_8]:[H_2O_2] (>10), turnover rates are independent of [C_8H_8], indicating that the identity of the most abundant reactive intermediate (MARI) under these conditions is derived from C_8H_8 (e.g., styrene oxide; C_8H_8O). The dependence of C_8H_8O formation on reactant concentrations are identical with prior findings within our group for the epoxidation of cyclohexene,[54, 199] styrene,[11] 1-octene,[21] and sulfoxidation of 2,5-dimethylthiophene[275] over groups 4 and 5-substituted zeolite BEA.

Scheme 6.1 shows a series of elementary steps that account for the measured effects of [C_8H_8] and [H_2O_2] on the rates of C_8H_8O formation. This proposed catalytic cycle involves the quasi-equilibrated adsorption of C_8H_8 (step 1) and H_2O_2 (step 2) followed by the irreversible activation of H_2O_2 (step 3) to form Ti-OOH surface intermediates.[11, 199] These Ti-OOH intermediates then react with C_8H_8 (step 4) or H_2O_2 (step 6) through rate-determining processes to form Ti-bound C_8H_8O or H_2O_2-decomposition products, respectively. Finally, C_8H_8O molecules desorption is quasi-equilibrated and reforms the Ti active site.[11] Rates of C_8H_8O formation (r_E) are given by

$$r_E = k_4[C_8H_8][Ti-OOH] \tag{6.3}$$

where k_i is the rate constant for step *I* in Scheme 1 and [Ti-OOH] is the number of Ti-OOH surface intermediates. Application of the pseudo steady-state hypothesis to Ti-OOH surface intermediates, combined with a site balance over all possible configurations for surface intermediates bound to Ti active sites, yields

$$\frac{r_E}{[L]} = \frac{\frac{k_3k_4K_2[C_8H_8][H_2O_2]}{k_4[C_8H_8]+k_6[H_2O_2]}}{1+K_1[C_8H_8]+K_2[H_2O_2]+\frac{k_3K_2[H_2O_2]}{k_4[C_8H_8]+k_6[H_2O_2]}+\frac{[C_8H_8O]}{K_5}} \tag{6.4}$$

where K_i is the equilibrium constant for step *I*, [L] is the total number of Ti atoms loaded into the reactor, and the five terms within the denominator correspond to Ti active sites that are occupied

by solvent molecules, adsorbed C_8H_8, adsorbed H_2O_2, Ti-OOH intermediates, and adsorbed C_8H_8O, respectively.

Reaction conditions where turnover rates depend linearly on $[C_8H_8]$ and are independent of $[H_2O_2]$ result in active sites that are saturated with Ti-OOH intermediates and reduces equation 6.4 to yield

$$\frac{r_E}{[L]} = k_4[C_8H_8] \tag{6.5}$$

which matches the experimental observations within Figure 6.8 at low $[C_8H_8]$:$[H_2O_2]$. Equation 6.4 reproduces the measured dependence on $[C_8H_8]$ at high $[C_8H_8]$:$[H_2O_2]$ when two conditions are met. First, the formation of appreciable concentrations of C_8H_8O results in the competitive adsorption of epoxide products, which has been observed for the binding of epoxide products to Lewis acidic Ti atoms within Ti-BEA[11, 21, 199] and TS-1.[290] Second, at high $[C_8H_8]$, values of $k_4[C_8H_8]$ become much greater than $k_6[H_2O_2]$ which reduces equation 6.4 to

$$\frac{r_E}{[L]} = \frac{k_3K_2K_5[H_2O_2]}{[C_8H_8O]} \tag{6.6}$$

Equation 6.6 is consistent with the independence of epoxidation turnover rates on $[C_8H_8]$ at high $[C_8H_8]$:$[H_2O_2]$ within Figure 6.8a. Despite the indistinguishable mechanisms between Ti-FAU, Ti-BEA, and Ti-SiO_2, there are significant differences in the magnitude of the rates of epoxidation (e.g., a factor of ~10 difference between Ti-FAU and Ti-SiO_2). To understand the origin of these differences, equitable comparisons of turnover rates and apparent activation enthalpies and entropies must be made at conditions that result in comparable coverages of surface intermediates.

6.3.7 Thermochemical Analysis Shows Transition State Stabilization

Transition state theory postulates that the rate of reaction depends on the stability of an activated complex (i.e., a transition state) relative to the stability of the stable intermediate

immediately preceding it along a reaction trajectory (Scheme 6.2).[215] In the context of alkene epoxidation, Ti-OOH-$C_8H_8^{\ddagger}$ represents the transition state for C_8H_8 epoxidation which forms transiently upon reaction between Ti-OOH reactive intermediates with proximate C_8H_8.

Scheme 6.2. Proposed equilibrium for the formation of Ti-OOH-$C_8H_8^{\ddagger}$ from Ti-OOH and C_8H_8.

$$Ti-OOH + C_8H_8 \overset{K_E^{\ddagger}}{\rightleftharpoons} Ti-OOH-C_8H_8^{\ddagger}$$

Within the tenets of transition state theory, turnover rates for C_8H_8 epoxidation, under conditions that result in Ti-OOH MARI, are given by

$$\frac{r_E}{[L]} = \frac{k_B T}{h} K_E{}^{\ddagger}[C_8H_8] \tag{6.7}$$

where k_B is the Boltzmann constant, h is Planck's constant, T is the absolute temperature, and $K_E{}^{\ddagger}$ is the transition state equilibrium constant for epoxidation. $K_E{}^{\ddagger}$ depends on the thermodynamic stability of the transition state relative to the reference state and takes the form

$$K_E{}^{\ddagger} = e^{\frac{-(\Delta H_{App}^{\ddagger} - T\Delta S_{App}^{\ddagger})}{RT}} \tag{6.8}$$

where $\Delta H_{App}^{\ddagger}$ and $\Delta S_{App}^{\ddagger}$ are the apparent activation enthalpy and entropy for epoxidation, respectively.

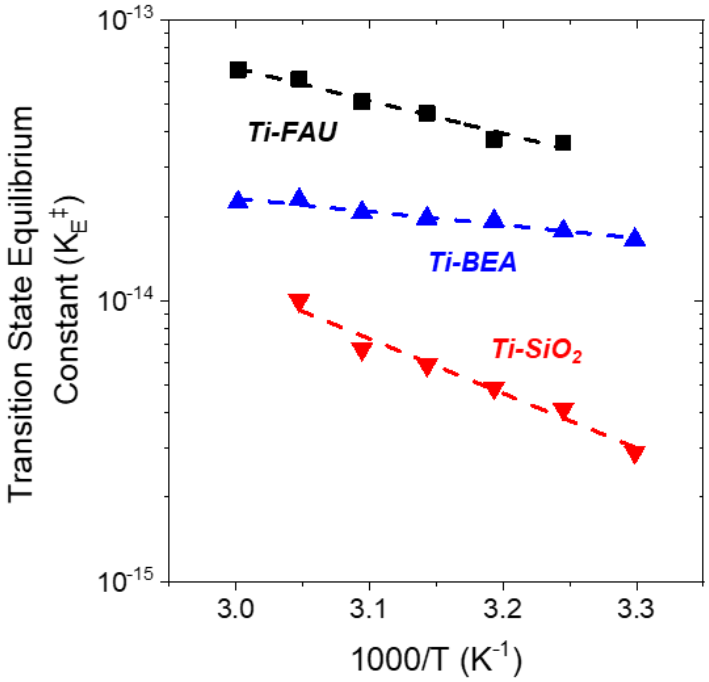

Figure 6.9. Transition state equilibrium constants for the formation of Ti-OOH-$C_8H_8^{\ddagger}$ as a function of inverse temperature over Ti-FAU (■), Ti-BEA (▲), and Ti-SiO_2 (▼) under conditions that result in Ti-OOH MARI ($3 \cdot 10^{-3}$ M C_8H_8, 0.01 M H_2O_2 in CH_3CN). Dashed lines represent fits to equation 6.8 (i.e., the Eyring equation), whose slopes and intercepts are proportional to $\Delta H_{App}^{\ddagger}$ and $\Delta S_{App}^{\ddagger}$, respectively.

Table 6.2. Apparent activation enthalpies and entropies for C_8H_8 epoxidation over Ti-FAU, Ti-BEA, and Ti-FAU under reaction conditions that result in a Ti-OOH saturated surface.

Catalyst	$\Delta H_{App}^{\ddagger}$ (kJ mol^{-1})	$\Delta S_{App}^{\ddagger}$ (J mol^{-1} K^{-1})
Ti-FAU	22 ± 2	-185 ± 15
Ti-BEA	9 ± 2	-234 ± 20
Ti-SiO_2	37 ± 4	-155 ± 15

Figure 6.9 shows $K_E^{\ddagger}$ as a function of inverse temperature for Ti-FAU, Ti-BEA, and Ti-SiO_2 used to determine the $\Delta H_{App}^{\ddagger}$ and $\Delta S_{App}^{\ddagger}$. Table 6.2 shows $\Delta H_{App}^{\ddagger}$ and $\Delta S_{App}^{\ddagger}$ both C_8H_8 epoxidation obtained under reaction conditions that result in Ti-OOH saturated surfaces and in the absence of mass-transfer restrictions. Values of $\Delta H_{App}^{\ddagger}$ increase in the order of Ti-BEA < Ti-FAU < Ti-SiO_2, which suggests that the smaller pores of the *BEA framework (~0.65 nm) enthalpically stabilize the transition state for C_8H_8 epoxidation relative to FAU (1.3 nm) and SiO_2 (5.4 nm). This

stabilization results from the solvation of Ti-OOH-$C_8H_8^{\ddagger}$ from the pore walls of the silicate support. The great extent of confinement of C_8H_8 epoxidation transition states within the voids of the Ti-catalyst, however, results in a disproportionate entropy of activation, where epoxidation within Ti-BEA incurs the greatest entropic loss, followed by Ti-FAU and Ti-SiO_2. This entropy of activation primarily reflects the loss of translational motion from fluid-phase C_8H_8 upon adsorption and formation of Ti-OOH-$C_8H_8^{\ddagger}$. For example, within Ti-SiO_2, the mesopore surrounding the Ti active site allows for the greatest flexibility of the C_8H_8 transition state, which results in the smallest loss of entropy among these three catalysts. Epoxidation within Ti-FAU results in intermediate values of $\Delta H_{App}^{\ddagger}$ and $\Delta S_{App}^{\ddagger}$, which results in favorable enthalpic stabilization due to the surrounding supercage relative to Ti-SiO_2; yet, provides enough flexibility for Ti-OOH-$C_8H_8^{\ddagger}$ as compared to Ti-BEA. Ti-SiO_2 possesses a greater dependence on temperature than Ti-FAU, which suggests that at a high enough temperature the rates should be greater on Ti-SiO_2. The isokinetic point (i.e., the temperature at which the rates of C_8H_8 epoxidation are equal) between Ti-FAU and Ti-FAU, however, lies outside the solvent temperature window (CH_3CN has a boiling point of 82 ^oC at atmospheric pressure), such that Ti-FAU will always possess a greater rate than Ti-SiO_2 within these types of reactors. Additional evidence for the selective stabilization of bulky aromatic transition states (i.e., for 2,4-dimethylstyrene) within Ti-FAU relative to other Ti-silicates is provided within Section E4. In the context of this study, C_8H_8 can be thought of as a proverbial "Goldilocks," while Ti-FAU is the optimal "bear's bed."

6.4 Conclusions

Multiple treatments of Al-FAU (Si:Al = 15) in HNO_3 removes nearly all of the Al atoms to produce siliceous FAU (Si:Al >900). These treatments are necessary to remove the adventitious Al atoms, that may act as deleterious sites during zeolite catalysis (e.g., within sugar isomerization, alcohol upgrading, alkene epoxidation). The liquid-phase grafting of metal chlorides and alkoxides leads to the isomorphic substitution of metal (M = Ti, Nb, Ta, Sn) atoms into the framework of FAU. Ti-FAU catalysts efficiently activate H_2O_2 to form Ti-OOH intermediates that are active for alkene epoxidation. In the case of styrene epoxidation, Ti-FAU possesses rates of epoxidation that are greater than Ti-BEA and Ti-SiO_2 by factors of 2 and 7, respectively. Rates of H_2O_2 decomposition, however, are invariant with the characteristic pore diameter of the Ti-silicate

catalyst. Differences in catalysis are not due to differences in the mechanism for epoxidation; yet, reflect differences in the stability of the transition states for C_8H_8 epoxidation. Specifically, C_8H_8 epoxidation transition states are enthalpically stabilized within Ti-FAU relative to Ti-SiO_2 and also possess greater entropic freedom than within Ti-BEA, which results in the lowest free energies within the bounds of solvent stability. The work presented here serves as an exemplary example for how zeolite framework topology can be chosen to selectively stabilize desired surface intermediates. The synthetic protocols established here will enable the design of new materials in the quest for the rational development of catalysts.

CHAPTER SEVEN

Cooperative Effects Between Hydrophilic Pores and Solvents: Catalytic Consequences of Hydrogen Bonding on Alkene Epoxidation in Zeolites[VI]

Abstract

Hydrophobic voids within titanium silicates have long been considered necessary to achieve high rates and selectivities for alkene epoxidations with H_2O_2. The catalytic consequences of silanol groups and the hydrogen-bonded networks of water (H_2O) that they stabilize, however, have not been demonstrated in ways that lead to a clear understanding of their importance. Here, we compare turnover rates for 1-octene epoxidation and H_2O_2 decomposition over a series of Ti-substituted zeolite *BEA (Ti-BEA) that contain densities of silanol nests ($(SiOH)_4$) varying from 0 to ~5 $(unit\ cell)^{-1}$. The most hydrophilic Ti-BEA give epoxidation turnover rates that are 100-fold larger than those in defect-free Ti-BEA, while rates of H_2O_2 decomposition are invariant with the density of $(SiOH)_4$, which contradicts conventional wisdom. Spectroscopic, thermodynamic, and kinetic evidence indicate that these catalytic differences are not due to changes in the electronic affinity of the active site, the electronic structure of Ti-OOH intermediates, or the mechanism for epoxidation. Comparisons of apparent activation enthalpies and entropies reveal that the differences in epoxidation rates and selectivities primarily reflect favorable entropy gains produced when epoxidation transition states disrupt hydrogen bonded H_2O clusters anchored to $(SiOH)_4$ near active sites. Transition states for H_2O_2 decomposition are smaller and hydrogen bond with H_2O similarly to Ti-OOH reactive species, such that the decomposition pathway appears insensitive to the presence of $(SiOH)_4$. Collectively, these findings clarify how molecular interactions between reactive species, hydrogen-bonded solvent networks, and polar surfaces can influence rates and selectivities for epoxidation (and other reactions) in zeolite catalysts.

[VI]This chapter has been adapted from the following publication:
Bregante, D.T.; Johnson, AM.; Patel, A.Y.; Ayla, E.Z.; Cordon, M.J.; Bukowski, B.C.; Greeley, J.; Gounder,. R.; Flaherty, D.W.; "Impact of Specific Interactions Among Reactive Surface Intermediates and Confined Water on Epoxidation Catalysis and Adsorption in Lewis Acid Zeolites"
Journal of the American Chemical Society, **2019**, *141*, 2995 – 3010.

7.1 Introduction

Microporous catalytic materials (e.g., zeolites and zeotype structures) are of great industrial[5-6] and academic interest[7-10] because these catalysts provide the means to discriminate between reactants via shape selectivity and size exclusion[291] and to accelerate reactions and increase selectivities by stabilizing specific transition states.[11-13] Dispersive interactions with pore walls are largely responsible for the solvation of transition states (and other reactive intermediates) when the surrounding voids are vacant, such as found using gaseous reactants at high temperatures.[7, 16] The number, variety, and complexity of interactions increase significantly when zeolite pores contain higher densities of reactive species or solvent molecules during catalysis in the liquid phase.[22] Specific interactions (e.g., hydrogen bonding, dipole interactions) between transition states, solvent molecules, and surface functions within pores are individually much weaker than the covalent and ionic bonds formed between reactive intermediates and active sites, however, the collective effects of weak specific forces can create extended (>1 nm) structures that surround catalytic active sites and reactive species.[25, 252] These extended structures reorganize to accommodate intermediates and transition states as reactions proceed, and correspondingly, contribute to the free energy change associated with each elementary step along the reaction coordinate *via* changes in excess free energies (G^{ε}).

Solvent reorganization influences reactions within liquids promoted by homogeneous, enzymatic, or heterogeneous catalysts;[241, 292-293] however, quantitative descriptions of these effects remain elusive, particularly at the solid-liquid interface.[18, 294] Many catalytic reactions (e.g., alkene epoxidation,[28-32] glucose isomerization,[22, 33-34] Baeyer-Villiger oxidation[35]) at surfaces respond sensitively to the presence of water (H_2O), proximate hydroxyl groups, and hydrogen bonding even when these species exist at trace levels. The effects of H_2O and the associated hydrogen-bonded networks it forms are particularly significant within the sub-nanometer pores of zeolite catalysts, which either preclude the formation of H_2O clusters when surfaces are non-polar and hydrophobic or nucleate these same clusters when pore walls contain polar, hydrogen-bonding functions. Within the context of zeolite and zeotype catalysts, the densities of isolated silanol groups (SiOH) and of silanol nests ($(SiOH)_4$) within the material are known to have drastic effects on the adsorption properties and intrapore condensation of small molecules (e.g., H_2O,[36-39] CH_3OH,[33, 39] C_2H_5OH[24, 37]). Once stabilized within the pores, these species influence the stability of co-adsorbates, reactive intermediates, and transition states through specific intermolecular

interactions, such as hydrogen bonds. Unfortunately, the catalytic contributions of silanol groups and the networks of H_2O (or other solvents) they stabilize are not clear due to concomitant changes in other properties of the catalysts and reaction systems in previous investigations.

The role of hydrogen bonding within Ti-based zeolite catalysts on alkene epoxidation has been a topic of debate for decades.[14, 29-30, 32, 64, 69-71, 295] Seminal studies on epoxidation within titanium silicalite-1 (TS-1) reported that the hydrophobic nature of pristine TS-1 gives greater yields of epoxide products with respect to hydrophilic titanium silicates (e.g., Ti-BEA, TiO_2-SiO_2), which was interpreted to be a consequence of increasing the concentration of the alkene substrate near active Ti active sites.[29-30, 69] These foundational findings inspired a plethora of work on liquid-phase oxidations that sought to relate changes in the catalyst hydrophilicity to observed yields of oxidation products.[69-71] The reported differences in reactivity between TS-1 and other titanium silicates, however, likely reflects the convolution of transition state confinement via dispersive interactions between pore walls and surface intermediates in addition to contributions related to the density and proximity of SiOH moieties. These results may also reflect different extents of intraparticle mass transfer constraints because of variations in particle diameters and the strong dependence of effective diffusion coefficients on pore diameters.[111, 215]

Recent studies that investigate the role of SiOH density in TS-1 specifically report epoxide yields that increase with expected densities of silanol groups, which directly contradict conclusions described above.[32, 71, 295] For example, rates for epoxidation of 1-hexene are greater in TS-1 samples (relative to conventionally synthesized TS-1) with increased numbers of SiOH groups regardless of the method used to introduce these defects: crystallization in the presence of dimethyldimethoxysilane to produce geminal di-silanols,[32] seeding with Al-doped TS-1 seeds to create a hierarchically-structured material,[71] or introduction of ethylenediamine to nucleate the formation of TiOH and SiOH defects.[295] In each of these studies, the authors conclude that the synthesis techniques changed either the electronic structure of the active sites[295] or the local concentrations of reactants;[32, 71] however, these studies did not conclusively relate systematic differences in the catalyst structure to fundamental parameters for epoxidation catalysis. Recently, Grosso-Giordano *et al.* reported that initial turnover rates for cyclohexene epoxidation by *tert*-butyl hydroperoxide were a factor of 5 greater at Ti active sites (contained within a surface-grafted calix[4]arene) complexes grafted onto UCB-4 in comparison to the same Ti-calix[4]arene complex bound to MCM-41, which was attributed to consequential interactions between a

proximate SiOH group and the Ti active sites on UCB-4 that facilitates either the activation of hydroperoxides or oxygen transfer to the alkene substrate via outer-sphere interactions mediated by the solvent.[296] Contradicting reports regarding hydrophobic effects in TS-1 and related Ti-silicates, together with varied explanations for the origins of the differences in rates and yields, demonstrate the complexities of these systems and the difficulties in developing molecular interpretations of experimental results. Consequently, the catalysis community has not reached a consensus on the effects of SiOH groups and the associated hydrogen-bonded networks of solvent molecules on epoxidation catalysis, not to mention, the fundamental origin of these effects and how they influence the stability of reactants and transition states.

Here, we incorporate Ti atoms into the *BEA framework through post-synthetic modification of dealuminated *BEA and by hydrothermal synthesis to create a series of Ti-BEA catalysts with a wide range of silanol nest ($(SiOH)_4$) densities ($0 – 5$ $(SiOH)_4$ $(unit\ cell)^{-1}$) but with constant pore diameters and active Ti site densities. We use this series of Ti-BEA to investigate the catalytic consequences of differences in only the density of $(SiOH)_4$ on turnover rates for 1-octene (C_8H_{16}) epoxidation and H_2O_2 decomposition, an undesirable parallel reaction pathway. Turnover rates of C_8H_{16} epoxidation are 100-times greater on Ti-BEA that contain ~5 $(SiOH)_4$ $(unit\ cell)^{-1}$ than on defect-free materials. H_2O_2 decomposition rates, however, do not change with the density of $(SiOH)_4$. These large differences in epoxidation rates and H_2O_2 selectivities do not reflect differences in the electron affinities of the active sites, the identity of the active intermediates, or changes in the mechanism for epoxidation, all of which remain constant among the Ti-BEA catalysts within this study. Rather, the differences in epoxidation rates and the productive use of H_2O_2 among the Ti-BEA catalysts result from the short-range interactions between transition states for epoxidation (and H_2O_2 decomposition) with H_2O clusters that nucleate and bind to $(SiOH)_4$ in close proximity to the Ti active sites. These H_2O clusters stabilized by $(SiOH)_4$ exist in semi-ordered, hydrogen-bonded configurations within the pores of Ti-BEA. The formation of transition states for epoxidation requires that solvent molecules restructure to accommodate the activated complex. These changes disrupt stable hydrogen bonds and increase the entropy of the H_2O clusters in ways that overwhelm the associated enthalpy penalty. In contrast, transition states for H_2O_2 decomposition readily hydrogen bond and stabilize H_2O clusters, in ways reminiscent of the Ti-OOH species that saturate active sites, and, thus, show no discernible dependence on $(SiOH)_4$ density. Collectively, the findings presented here show that

the excess free energies of the transition states for epoxidation is influenced by the density and proximity of $(SiOH)_4$ moieties and provides a quantitative relationship that describes the interaction of extended hydrogen-bonding structures with the transition states for epoxidation.

7.2 Materials and Methods

7.2.1 Catalyst Synthesis

Ti-BEA-X, where X refers to the initial Si:Al ratio of the parent Al-BEA (X = 12.5 – 250), catalysts were prepared by post-synthetic modification of commercial Al-BEA samples (see Table 1 for manufacturer and initial Si:Al ratio).[49, 54, 96, 101, 103, 199] Al-BEA was treated in refluxing HNO_3 (Macron Chemicals, 68-70 wt. %, 20 $cm^3\ g^{-1}$; *Caution: HNO_3 is extremely caustic and will readily cause a chemical burn and should be handled carefully*) with the intent to remove framework Al atoms by forming soluble $Al(NO_3)_3$. The solids were then recovered by vacuum filtration and washed with H_2O (17.8 MΩ · cm, 50 $cm^3\ g^{-1}$) followed by heating at 5 K min^{-1} in flowing air (100 $cm^3\ min^{-1}$) and holding at 823 K for 6 h to remove residual volatile and organic species and to produce Si-BEA-X. Materials produced in this manner possessed Si:Al ratios greater than 1400, as determined by energy dispersive X-ray fluorescence spectroscopy. Ti atoms were incorporated by combining a stirred suspension of Si-BEA-X in CH_2Cl_2 (Fisher Chemicals, Certified ACS Stabilized) with an appropriate amount of $TiCl_4$ (Sigma Aldrich, 99.9%; *Caution: $TiCl_4$ will violently react with moisture in the air to form HCl and should be handled carefully*) at reflux. All volatile components were then removed by rotary evaporation. The recovered solids were light-brown, and these materials were treated by heating in flowing air (100 $cm^3\ min^{-1}$) at 5 K min^{-1} and holding at 823 K for 6 h, which produced bright white solid powders.

Ti-BEA-F was synthesized in fluoride media using a previously published procedure.[22, 69] Briefly, 4.89 g of tetraethylammonium fluoride (TEAF, Alfa Aesar, 97 wt. %) was combined with 7.25 g of deionized H_2O (18.2 MΩ · cm) in a perfluoroalkoxy alkane (PFA) container (Savillex Corporation) with 10 g of tetraethylorthosilicate (TEOS, Sigma Aldrich, >98 wt. %) to form a gel. This gel was stirred for 1 h prior to the addition of 0.682 g of titanium(IV) isopropoxide (TIPO, Sigma Aldrich, 99.999%), after which, the PFA container was sealed and the contents stirred for 16 h at ambient temperature. The cover was then removed and the excess ethanol, isopropanol, and water was allowed to evaporate at ambient temperature to yield a gel with a final molar composition of 1 SiO_2:0.008 TIPO: 0.55 TEAF: 7.15 H_2O. This gel was then loaded into a Teflon-

lined stainless-steel autoclave (Parr instruments, 45 cm^3) and heated to 413 K while rotating (60 rpm) in a convection oven (Yamato, DKN-402C) for 25 days. The resultant solids were recovered, washed with H_2O and acetone (Sigma Aldrich, >99.5 wt. %) 6 times each (20 cm^3 g^{-1}) and dried for 16 h at 373 K. The dried solids were then heated in flowing air (1.67 cm^3 s^{-1} (g solids)$^{-1}$) at 853 K (1 K min^{-1}) for 10 h to produce a bleached-white solid.

7.2.2 Catalyst Characterization

The metal contents of Ti-BEA-X were determined using energy dispersive X-ray fluorescence. In short, ~30 mg of Ti-BEA was finely ground and loaded into a polypropylene sample holder (1 cm diameter) that was sealed with ultralene film. These were then loaded into a spectrometer (Shimadzu, EDX-7000), whose sample chamber compartment was purged with He (Airgas, Ultra-zero grade). Measurements were taken between 0 – 30 keV (100 scans), and the relative intensities of the fluorescence features for each element was used to calculate the mass of each element within the sample.

X-ray diffractograms of all Ti-BEA were obtained using a diffractometer (Siemens/Bruker, D5000) with Cu Kα radiation (0.15418 nm) under ambient conditions. Figure F1 shows the X-ray diffractograms of all Ti-BEA. The similarities between all diffractograms suggests that all Ti-BEA possess the *BEA zeolite framework.

Band edge energies (E_g, Table 6.1) for each Ti-BEA were determined from extrapolation of the linear portion of the corresponding Tauc plot calculated from diffuse reflectance UV-vis spectra (DRUV-vis) (Figure F2). Total reflectance spectra were measured at ambient conditions with a UV-vis-NIR spectrophotometer (Agilent CARY 5) with magnesium oxide (MgO, Sigma Aldrich, 99.995%) as a solid diluent and background.

Solid-state magic angle spinning-nuclear magnetic resonance (MAS-NMR) spectroscopy was performed on a spectrometer (Varian, Unity Inova 300 MHz) equipped with a 4 mm MAS probe (Varian-Chemagnetics, double resonance APEX HX) under ambient conditions. Prior to measurement, Ti-BEA was dehydrated in flowing He (100 cm^3 min^{-1}) at 573 K for 3 h. Ti-BEA was then loaded (~35 mg) into a zirconia rotor, that was spun at 10 kHz within the spectrometer. Powdered octakis(dimethylsilyloxy)silsesquioxane (Q_8M_8) was used for pulse calibration and ^{29}Si chemical shift referencing (Q_8M_8 has a chemical shift of 11.45 ppm). ^{29}Si direct polarization MAS-NMR was performed with a 10 s recycle delay with the averaging of 8,000 scans.

Infrared (IR) spectra of adsorbed CD_3CN (Cambridge Labs, 99.8% D atom) were obtained using a custom-built transmission cell[200] coupled to a Fourier transform-infrared (FTIR) spectrometer (Bruker, Tensor 37) with a liquid-N_2-cooled HgCdTe detector. Catalysts were pressed into self-supporting disks (~60 mg) and placed within the transmission cell, which was assembled using CaF_2 windows and connected to a gas manifold. All materials were first heated to 573 K at 10 K min^{-1} and held for at least 3 h in flowing He (50 cm^3 min^{-1}; Airgas, Ultra-zero grade) with the intent to desorb water and volatile organics. CD_3CN was introduced via a syringe pump (KD Scientific, Legato 100) and vaporized in the gas-transfer lines into a stream of flowing He (50 cm^3 min^{-1}). Steady-state IR spectra (128 scans, 1 cm^{-1} resolution) of CD_3CN adsorbed to the M-BEA were obtained while flowing the CD_3CN/He stream over the samples.

Vapor-phase H_2O adsorption isotherms were collected on a volumetric adsorption instrument (Micromeritics, 3Flex). Ti-BEA samples (50 - 70 mg) were pelletized and sieved to retain particles between 250 – 500 μm in diameter. These were degassed by heating under vacuum ($<7 \cdot 10^{-4}$ kPa, 673 K) for 6 h prior to adsorption measurements. H_2O (17.8 MΩ · cm) was purified via one freeze-pump-thaw cycle prior to measurement.

The uptake of 1-octene (C_8H_{16}) was measured by combining Ti-BEA (~10 mg) in a solution of C_8H_{16} (10^{-4} M C_8H_{16}, 0.039 M H_2O, 10 cm^3) with CH_3CN at 313 K. An initial (solids-free) aliquot was taken and analyzed via gas chromatography (GC; HP 5890, Series A) to determine the initial concentration of C_8H_{16}. Ti-BEA was then added to the stirring solution of C_8H_{16} and allowed to equilibrate at a given temperature. An aliquot of solution was then filtered (polypropylene, 0.22 μm) to remove the solids and was analyzed via GC. The adsorbed quantity was determined from the difference in GC peak area between the aliquot after introduction of Ti-BEA and the initial sample.

7.2.3 Measurement of Rates for Epoxide Formation and H_2O_2 Decomposition

Rates for C_8H_{16} epoxidation and H_2O_2 decomposition were measured using batch reactors (100 cm^3, three-neck round-bottom flasks) equipped with reflux condensers to minimize evaporative losses. C_8H_{16} (Sigma-Aldrich, 98%), 5-hexen-1-ol ($C_6H_{12}O$; Sigma-Aldrich, 98%), *Z*-stilbene (Alfa-Aesar, 97%, 75:1 *Z:E* ratio) and H_2O_2 (Fischer Chemicals, 30 wt. % in H_2O) or *tert*-butyl hydroperoxide (*t*-BuOOH; Sigma Aldrich, 5.5 M in decane) were added to a solution of CH_3CN and benzene (internal standard for GC analysis; Sigma-Aldrich, thiophene-free, >99%)

and was heated to the desired temperature (303 – 348 K) while stirring at 700 rpm. The reactions were initiated by addition of Ti-BEA and small aliquots (~500 μL) of the reaction solution were extracted as a function of time through a syringe filter (0.22 μm, polypropylene). The concentrations of the organic components within these aliquots were quantified via a GC equipped with a flame-ionization detector. All species were identified, and calibration factors were quantified using standards of known concentration. The concentration of H_2O_2 in each aliquot was measured by colorimetric titration using an aqueous solution of $CuSO_4$ (8.3 mM, Fisher Chemicals, >98.6%), neocuproine (12 mM, Sigma-Aldrich, >98%), and ethanol (25% v/v, Decon Laboratories Inc., 100%). The concentration of H_2O_2 was calculated by comparison of the absorbance at 454 nm to calibrated standards, measured on a spectrophotometer (Spectronic, 20 Genesys). In all reported data, the carbon balance closed within 95% and the standard uncertainty for measured reaction rates was < 10%. Rates for the conversion of C_8H_{16} and H_2O_2 were measured as functions of [H_2O_2] and [C_8H_{16}], and all reported results were obtained at differential conversion (i.e., <5% conversion of the limiting reagent). The identity of the products of 5-hexen-1-ol oxidation were confirmed using mass spectrometry. In short, liquid samples were injected into a gas chromatograph (Agilent, 6890N) and the resolved chromatographic features were subsequently analyzed in a mass spectrometer (Agilent, 5975B) using electron ionization techniques to determine the relevant mass-to-charge ratios.

The percent of active Ti atoms in each Ti-BEA was determined by in situ site titrations with methylphosphonic acid (MPA; Sigma-Alrich, 99%) during the epoxidation of C_8H_{16} (0.01 M C_8H_{16}, 0.01 M H_2O_2, 313 K). In short, a suspension containing Ti-BEA (~30 mg), C_8H_{16}, benzene (as an internal standard), and MPA in CH_3CN was stirred for at least one hour at 313 K with the intent to irreversibly bind MPA to active sites and inhibit epoxidation catalysis. Then, H_2O_2 was added to the reactor to initiate catalysis. Epoxidation rates were measured for systems with ratios of MPA:Ti ranging from zero to unity, and the number of active sites were determined by linear extrapolation of these data to determine the MPA:Ti ratio that gives a rate equal to zero (Figure F3).

7.2.4 Detection of Reactive Intermediates via In Situ UV-Vis Spectroscopy

UV-vis spectra were collected using a 45-degree diffuse reflection probe (Avantes, solarization-resistant fibers) coupled to a fiber-optic spectrometer (Avantes, AvaFast 2048) with a

compact deuterium-halogen light source (Avantes, AvaLight-DHc). Samples were pressed into 7 mm diameter pellets (~5 mg) and loaded into liquid flow cell (~100 μL) with temperature control. Reactant and solvent solutions were introduced using a high-performance liquid chromatography pump (Waters, 515). Background UV-vis spectra (average of 100 scans) were obtained for each material by exposing the sample to a flowing CH_3CN solution (0.039 M H_2O, 1 cm^3 min^{-1}) at 313 K for 1 h. Spectra were obtained while flowing solutions of H_2O_2 in CH_3CN (0.1 M H_2O_2, 0.4 M H_2O, 1 cm^3 min^{-1}) at 313 K and continuing until the UV-vis spectra became constant, implying that the system reached steady-state. Displayed UV-vis spectra represent the difference between the experimental spectra and background spectra.

7.2.5 Computation Methods to Probe Interactions between CD_3CN and Adsorption Sites in Ti-BEA

Periodic, self-consistent density functional theory (DFT) using the Vienna Ab-initio Simulation Package (VASP) was used to model the enthalpy and entropy of adsorption in zeolite BEA.[297-300] The computational details and unit cell specifications were similar to those used previously to model ethanol dehydration in Sn-BEA.[301] In short, the Bayesian error estimation functional (BEEF-vdw) was used with projector augmented wave (PAW) pseudopotentials.[302-304] A plane wave cutoff of 520 eV was used with a single gamma point and spin polarization. A force criterion of 20 meV/Å was used for geometric convergence. Optimized BEA unit cell lattice constants were within 1.9% of that reported by the international zeolite database (IZA).[305]

Ab-initio molecular dynamics (AIMD) simulations were performed with VASP at 350 K in an NVT ensemble using a Nosé-Hoover thermostat and a timestep of 1 fs. CD_3CN was modelled within these AIMD simulations. Each MD simulation was equilibrated for at least 5 ps, followed by a 25 ps production run. Enthalpy changes ($\Delta H_{CD_3CN,x}$) were defined as an ensemble average of the AIMD energies (E) for gas-phase CD_3CN ($E_{CD_3CN(g)}$), the empty adsorption site (E_x), and CD_3CN interacting with adsorption site *x* ($E_{CD_3CN,x}$; e.g., Ti atoms)

$$\Delta H_{CD_3CN,x} = \langle E_{CD_3CN,x} \rangle - E_{CD_3CN(g)} - \langle E_x \rangle \quad (7.1)$$

where brackets denote an arithmetic averaging of accessible energies from the ensemble sampled by the thermostat.

The entropy of adsorbates was calculated using a 2-phase thermodynamic model, which decomposes molecular trajectories into their translational, rotational, and vibrational degrees of freedom, expressed as the vibrational density of states (VDOS). Each VDOS was decomposed into their gaseous and solid components according to the original algorithm[306-308] and integrated to obtain entropies accounting for plasticity of the BEA framework, as previously applied in the BEA framework for ethanol dehydration. The TRAVIS molecular trajectory code was used to analyze the calculated trajectories.[309] Estimates of the entropy loss upon physisorption involved calculating the principal root-mean-square fluctuations of CD_3CN from the AIMD trajectories.[310] Thus, the entropy loss upon physisorption is predominantly caused by reduction in the translational degrees of freedom. The entropies of adsorption of CD_3CN on Ti and $(SiOH)_4$ defects were calculated as the differential changes in translational, rotational, and vibrational degrees of freedom, relative to those calculated for the physisorbed state. This approach was necessary, due to the difficulty in a direct AIMD method that describes absolute adsorption onto these sites from the gas phase. This, in part, may be due to the long timescales required to fully sample the relative translational and rotational modes available to gas-phase species. Thus, on Ti and $(SiOH)_4$ defects, the entropy change is modified by the non-rigid modes calculated by AIMD as compared to the non-rigid modes for physisorption, including the root-mean-square fluctuations.

The T8 crystallographic T-site of BEA was used to represent substitutional doping by Ti and $(SiOH)_4$. The T8 site was chosen based upon previous reports of adsorbate stability at this site.[301] The Si atom occupying the T8 site was removed, and either the resulting vacancy was replaced with a Ti atom, or the four framework oxygen atoms were bound by hydrogen atoms to simulate a $(SiOH)_4$ site. Isolated SiOH defects were not considered computationally, as their formation at crystal grain boundaries and meso-scale defects precludes such sites from being constructed within a periodic unit cell. The simulated Si:Ti ratio within these calculations was 63:1, which corresponds to one Ti atom per unit cell.

7.3 Results and Discussion

7.3.1 Quantifying the Density of Distinct Silanol Species with ^{29}Si MAS-NMR and FTIR Spectroscopy

Table 7.1. Initial Si:Al ratios, Metal Loadings, Band Gaps, and Fraction of Active Metal Atoms in Ti-BEA

Sample Name	Zeolite Vendor	Initial Si:Al Ratio[a]	Ti Loading (wt. %)[b]	Band Gap (eV)[c]	Catalytically Active Ti Atoms (%)[d]
Ti-BEA-12.5	Zeolyst	12.5	0.20	4.2	102 ± 7
Ti-BEA-14	Tosoh	14	0.30	4.3	94 ± 6
Ti-BEA-20	Tosoh	20	0.34	4.3	97 ± 10
Ti-BEA-75	ACS Material	75	0.28	4.2	94 ± 7
Ti-BEA-150	Zeolyst	150	0.33	4.2	89 ± 7
Ti-BEA-250	Tosoh	250	0.42	4.2	93 ± 7
Ti-BEA-F	--	∞	0.15	4.3	92 ± 6

[a]Taken from technical data sheet supplied from manufacturer. [b]Measured by EDXRF. [c]Measured using DRUV-vis by extrapolating the linear portion of the leading edge in the corresponding Tauc plot. [d]Determined by in situ site titrations with methylphosphonic acid, where the rate measured as a function of MPA:Ti was extrapolated to a value of zero.

Ti-BEA-X (X = initial Si:Al ratio or F for hydrothermally synthesized) were synthesized through the post-synthetic modification of commercially available Al-BEA (initial Si:Al ~ 12.5 – 250) and through hydrothermal synthesis in fluoride media to prepare a suite of Ti-BEA with varying densities of $(SiOH)_4$ groups (Table 7.1). All Ti-BEA possess a single prominent UV-vis absorbance edge at ~300 nm that corresponds to the charge transfer from the 2p orbitals of oxygen to the 3d orbitals of Ti^{4+}.[51, 205] This results in a band gap for Ti-BEA equal to 4.2-4.3 eV (Table 7.1; Figure F2). This suggests that the Ti-BEA used within this study contain highly disperse Ti atoms and few TiO_x oligomers or larger aggregates. The number of catalytically active sites were determined by in situ site titrations with methylphosphonic acid (MPA; Section 7.2.3). Titrations with MPA show that turnover rates decrease linearly as a function of the molecular ratio of MPA:Ti for all Ti-BEA (Figure F3) and that rates become immeasurable when the MPA:Ti ratio approaches unity. These data suggest nearly all Ti atoms form active sites, and the linearity of these titrations indicate that rates of epoxidations at all active sites are approximately equal within a given Ti-BEA catalyst. The combined results of titrations with MPA and the interpretations of band gaps

measured via UV-vis support the conclusion that Ti atoms are highly disperse within the Ti-BEA samples.

Table 7.2. Fraction of Si Atoms Existing as SiOH (Φ_{NMR}), Relative Densities of Hydrogen-Bonded SiOH (Φ_{IR}), Adsorption Enthalpies for CD_3CN Bound to Ti Atoms ($\Delta H_{CD_3CN,Ti}$), Ligand-to-Metal Charge Transfer Energies of Ti-(η^2-O_2) and Ti-OOH, *E:Z* ratios for the Epoxidation of *Z*-Stilbene over Ti-BEA

Sample Name	Φ_{NMR}[a]	Φ_{IR}[b]	$\Delta H_{CD_3CN,Ti}$ (kJ mol^{-1})[c]	Ti-OOH LMCT Energy (eV)[d]	Ti-(η^2-O_2) LMCT Energy (eV)[d]	*Z:E* Ratio *Z*-Stilbene[e]
Ti-BEA-12.5	0.062	2.30	-32 ± 1	3.1	3.6	14 ± 2
Ti-BEA-14	0.055	2.52	-29 ± 2	3.1	3.5	10 ± 3
Ti-BEA-20	0.052	1.90	-30 ± 1	3.0	3.6	9 ± 2
Ti-BEA-75	0.056	2.21	-31 ± 2	3.1	3.7	11 ± 4
Ti-BEA-150	0.047	1.64	-30 ± 2	2.9	3.6	6 ± 2
Ti-BEA-250	0.041	1.26	-28 ± 1	3.0	3.6	5 ± 1
Ti-BEA-F	~0	0.08	-32 ± 1	3.1	3.8	7 ± 2

[a]Determined from ^{29}Si NMR spectra of dehydrated Ti-BEA. [b]Determined from FTIR spectra of dehydrated Ti-BEA. [c]Corresponds to CD_3CN bound to Ti atoms, determined from adsorption isobars using FTIR. [d]Determined from in situ UV-vis (0.01 M H_2O_2 in CH_3CN, 313 K). [e]Calculated from product selectivities of *Z*-stilbene epoxidation (1 mM *Z*-stilbene, 0.01 M H_2O_2 in CH_3CN, 313 K).

The fraction of Si atoms coordinated to -OH groups (i.e., SiOH) within each Ti-BEA material was estimated using ^{29}Si solid-state magic-angle spinning nuclear magnetic resonance (MAS-NMR) spectroscopy. Figure 7.1 shows ^{29}Si MAS-NMR spectra contain distinct NMR features at chemical shifts of -102, -112, -113, and -116 ppm on dehydrated Ti-BEA-14, Ti-BEA-75, Ti-BEA-250, and Ti-BEA-F (^{29}Si NMR spectra for all Ti-BEA are shown in Figure F4). The feature at -102 ppm corresponds to Si atoms that possess a single pendant hydroxyl moiety (i.e., $Si(OSi)_3(OH)$, denoted as Q^3 sites),[284-285] and peaks at -112, -113, and -116 ppm originate from Si atoms within the framework of *BEA coordinated to 4 siloxane functions (i.e., $Si(OSi)_4$, denoted as Q^4 sites). The splitting among these Q^4 sites reflects contributions from the 9 crystallographically-distinct tetrahedral sites of *BEA, which are clearly resolved in materials with the greatest degree of crystallinity (e.g., Ti-BEA-F). The ratio of the peak areas for the Q^3 sites to

the sum of those for the Q^3 and Q^4 sites (Φ_{NMR}) provides a quantitative measure of the fraction of Si atoms that reside as SiOH functions

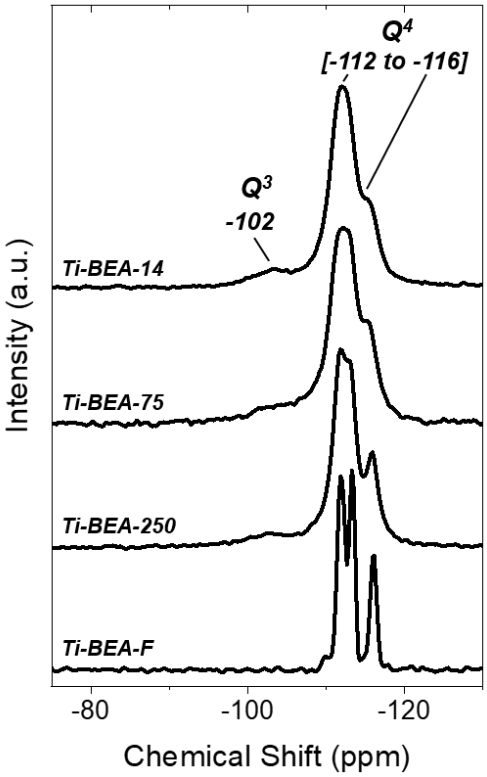

Figure 7.1. ^{29}Si direct polarization MAS-NMR of Ti-BEA-14, Ti-BEA-75, Ti-BEA-250, and Ti-BEA-F. Spectra are normalized to the Q^4 feature and are vertically offset for clarity.

$$\Phi_{NMR} = \frac{A_{Q^3}}{A_{Q^3}+A_{Q^4}} \tag{7.2}$$

where A_{Q^3} and A_{Q^4} represent the areas of the deconvoluted ^{29}Si NMR features for Q^3 and Q^4 sites, respectively (Section F1 shows ^{29}Si NMR spectra for all Ti-BEA and representative peak fits used to calculate values of Φ_{NMR}; Figure F5). Table 7.2 shows that Φ_{NMR} decreases systematically as the initial ratio of Si:Al increases for post-synthetically modified Ti-BEA catalysts and is nearly zero for Ti-BEA-F. Notably, Φ_{NMR} does not represent the density of $(SiOH)_4$ groups (i.e., $[(SiOH)_4]$), because isolated silanol groups (e.g., on the external surface of Ti-BEA particles) also contribute to the Q^3 feature. Consequently, clear relationships between the number of $(SiOH)_4$ and

fundamental quantities that determine turnover rates and selectivities for epoxidations in these catalysts require a more specific measure of the [$(SiOH)_4$] for each material.

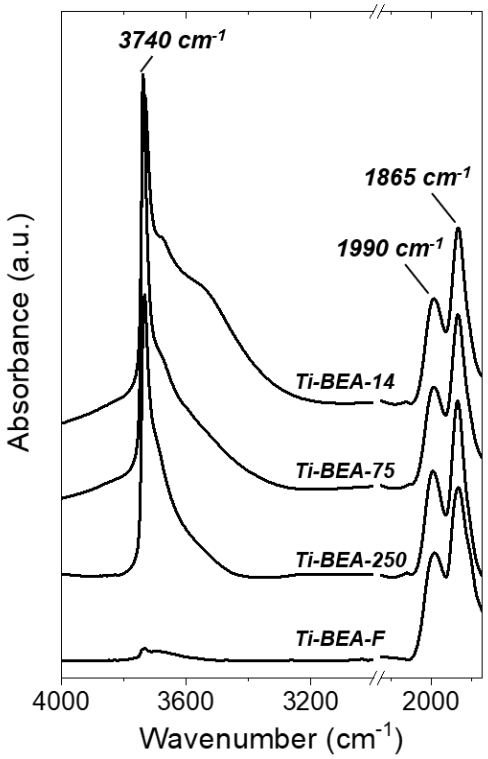

Figure 7.2. Infrared spectra of dehydrated Ti-BEA-14, Ti-BEA-75, Ti-BEA-250, and Ti-BEA-F (50 cm^3 min^{-1} He, 573 K). All spectra are normalized to the ν(Si-O-Si) overtone at 1865 cm^{-1}, assumed to have a constant extinction coefficient for all Ti-BEA. Spectra are vertically offset for clarity.

Infrared spectra of *BEA catalysts contain distinct ν(O-H) modes between 3300 – 3750 cm^{-1} that can be deconvoluted into semi-quantitative estimates for the number of isolated and hydrogen-bonded (e.g., $(SiOH)_4$) silanol groups.[35, 49, 286] Figure 7.2 shows infrared spectra of Ti-BEA-14, Ti-BEA-75, Ti-BEA-250, and Ti-BEA-F after treatments that desorb adventitious H_2O (IR spectra for all Ti-BEA are shown in Figure F6). These spectra show distinct features at 1990 and 1865 cm^{-1} that reflect ν(Si-O-Si) overtones (i.e., contributions from the *BEA framework) and between 3300 – 3750 cm^{-1}, which correspond to ν(O-H) modes of distinct SiOH species.[35, 286, 311] The sharp peak at 3740 cm^{-1} corresponds to the ν(O-H) of isolated SiOH groups that do not hydrogen bond or interact with other species (i.e., crystal defects within the zeolite or SiOH on the surface of the zeolite particle). The broad feature extending from 3300 – 3750 cm^{-1} reflects

$(SiOH)_x$ groups (e.g., $(SiOH)_4$) that contain proximate, hydrogen-bonded –OH functions.[49, 312] The most hydrophilic Ti-BEA contain multiple $(SiOH)_4$ per unit cell, which suggests that a significant fraction of these $(SiOH)_4$ will be paired with another and may lead to greater extent of hydrogen-bonding (i.e., resulting in the bi-modal character of ν(O-H) within hydrophilic Ti-BEA).

Differences in the density of isolated SiOH and $(SiOH)_4$ groups on each material across the series of Ti-BEA are determined by normalizing spectra by the intensity of the ν(Si-O-Si) modes (i.e., assuming a constant density of framework Si-O-Si bonds) and deconvoluting the peaks for SiOH (3740 cm^{-1}) and $(SiOH)_4$ groups (3300-3700 cm^{-1}), as shown in Appendix F (Figure F7). The ratios of the integrated areas (Φ_{IR}) for ν(O-H) of $(SiOH)_4$ ($A_{(SiOH)_4}$) to those for ν(Si-O-Si) ($A_{(Si-O-Si)}$) provide measures of the relative density of $(SiOH)_4$ for each Ti-BEA

$$\Phi_{IR} = \frac{A_{(SiOH)_4}}{A_{(Si-O-Si)}} \tag{7.3}$$

Table 7.2 shows that values for Φ_{IR} decrease as the initial ratio of Si:Al increases in the parent BEA zeolites, which is consistent with the trends observed for the total number of Si atoms coordinated to -OH groups (shown by Φ_{NMR}). Φ_{IR}, as defined here, provides semi-quantitative measure for changes in the number of $(SiOH)_4$ groups that result from differences in synthesis protocols for a given zeolite framework, however, comparisons between frameworks require values for extinction coefficients since these likely vary for ν(Si-O-Si) modes across structures.

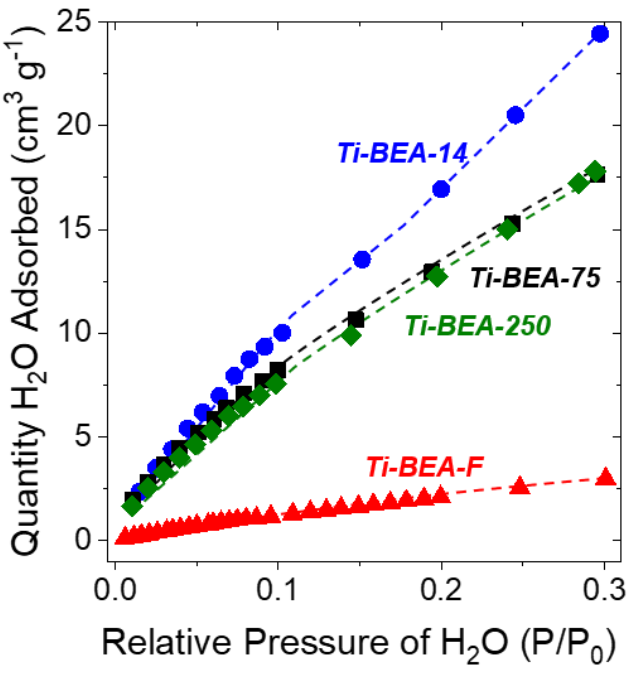

Figure 7.3. H_2O adsorption isotherms for Ti-BEA-14 (●), Ti-BEA-75 (■), Ti-BEA-250 (♦), and Ti-BEA-F (▲) at 293 K. Dashed curves are intended to guide the eye.

Figure 7.3 shows isotherms for adsorption of H_2O as functions of relative H_2O pressures (P/P_0) onto Ti-BEA-14, Ti-BEA-75, Ti-BEA-250, and Ti-BEA-F, and notably the uptake of H_2O onto Ti-BEA-F is much smaller than for Ti-BEA synthesized by post-synthetic modification at P/P_0 values below 0.3 (adsorption isotherms for all Ti-BEA are shown in Figure F8). At low values of P/P_0 (i.e., <0.05), H_2O adsorbs to SiOH and $(SiOH)_4$, which appears as nearly identical uptakes among Ti-BEA synthesized by post-synthetic modification. Ti-BEA-F, however, adsorbs significantly less H_2O at all P/P_0 as this material does not contain sufficient densities of SiOH or $(SiOH)_4$ to nucleate the formation of stable H_2O clusters. Notably, H_2O cluster formation upon adsorption occurs via stabilizing hydrogen-bonding interactions with SiOH and $(SiOH)_4$, as observed experimentally and computationally for zeolites with the MFI framework.[36-38] H_2O molecules bind exothermically to monomeric, dimeric, or oligomeric H_2O clusters with adsorption enthalpies of approximately –33 kJ mol^{-1},[313] which indicates that small H_2O clusters form spontaneously within Ti-BEA following the stable coordination of a few molecules to silanol defects. This suggests, that H_2O adsorption cannot capture nuanced differences in the density of SiOH groups, whose quantification requires spectroscopic interrogation (see above).

7.3.2 Identifying Chemically Distinct Binding Sites within Ti-BEA by Adsorption of CD_3CN

Infrared spectra of CD_3CN adsorbed onto Ti-BEA were used to determine the adsorption enthalpies and entropies of distinguishable adsorption sites, including Ti atoms, SiOH or $(SiOH)_4$ groups, and siloxane regions of the pore walls (denoted as Si-O-Si)[33, 159] and to compare electron affinities of Ti active sites in Ti-BEA. Figures 7.4a and 7.4b shows infrared spectra obtained during adsorption isotherms of CD_3CN onto Ti-BEA-12.5 and Ti-BEA-F, respectively. The absorbance features at 2263, 2274, and 2302 cm^{-1} correspond to the $\nu(C\equiv N)$ of CD_3CN molecules physisorbed to Si-O-Si, adsorbed to SiOH and $(SiOH)_4$ functions, and bound to Lewis acidic framework Ti atoms, respectively.[54, 107, 159] Features at 2215 and 2115 cm^{-1}, correspond to $\nu_{as}(CD_3)$ and $\nu_s(CD_3)$, respectively.[54] The areas of the $\nu(C\equiv N)$ absorbance bands for CD_3CN ($A_{\nu(C\equiv N),x}$) bound to SiOH moieties, Ti atoms, and Si-O-Si are assumed to be proportional to their fractional coverage ($\theta_{CD_3CN,x}$).

$$\theta_{CD_3CN,x} = \frac{A_{\nu(C\equiv N),x}}{A_{\nu(C\equiv N),sat}} \tag{7.4}$$

where $A_{\nu(C\equiv N),sat}$ is the area of the $\nu(C\equiv N)$ feature for CD_3CN bound to a given adsorption site x (i.e., SiOH, Ti, or Si-O-Si) at saturation coverage.

The increases in $\theta_{CD_3CN,x}$ with the partial pressure of CD_3CN (P_{CD_3CN}) at each of the three chemically distinct locations (insets of Figure 7.4a and 7.4b) are each consistent with the functional form of a Langmuirian adsorption isotherm[215] represented by

$$\theta_{CD_3CN,x} = \frac{K_x P_{CD_3CN}}{1+K_x P_{CD_3CN}} \tag{7.5}$$

where K_x is the equilibrium coefficient for CD_3CN adsorption onto adsorption site x. A representative peak fitting procedure to determine these areas is given in Section F2.1. The close agreement between the Langmuirian model and the measured coverages suggests that all adsorption locations within each category of sites are chemically similar and that adsorbed CD_3CN molecules do not interact significantly with one another at these conditions. Consequently,

enthalpies ($\Delta H_{CD_3CN,x}$) and entropies ($\Delta S_{CD_3CN,x}$) for the adsorption of CD_3CN to a given site *x* are determined from values of K_x, following van't Hoff's approach

$$K_x = e^{\left(\frac{-\Delta H_{CD_3CN,x}}{RT}\right)} e^{\left(\frac{\Delta S_{CD_3CN,x}}{R}\right)} \tag{7.6}$$

Table 7.3 shows values of $\Delta H_{CD_3CN,x}$ and $\Delta S_{CD_3CN,x}$ for CD_3CN bound to Ti atoms, SiOH, and Si-O-Si on Ti-BEA-12.5 and Ti-BEA-F, measured experimentally (0.46 kPa CD_3CN, 373 – 423 K, Fig. F10) and calculated from ab initio molecular dynamics (AIMD) simulations. Experimental values of $\Delta H_{CD_3CN,Ti}$ and $\Delta S_{CD_3CN,Ti}$ do not differ between Ti-BEA-12.5 and Ti-BEA-F within the measured uncertainty, which suggests that the density or proximity of SiOH and $(SiOH)_4$ groups does not influence the coordination and stability of CD_3CN bound to framework Ti-atoms. The value of $\Delta S_{CD_3CN,Ti}$ calculated by AIMD agrees closely with the experimental values of $\Delta S_{CD_3CN,Ti}$ (-85 versus -83 to -99 J mol^{-1} K^{-1}); however, values of $\Delta H_{CD_3CN,Ti}$ estimated from AIMD are lower (-20 versus -32 kJ mol^{-1}) than those measured experimentally.

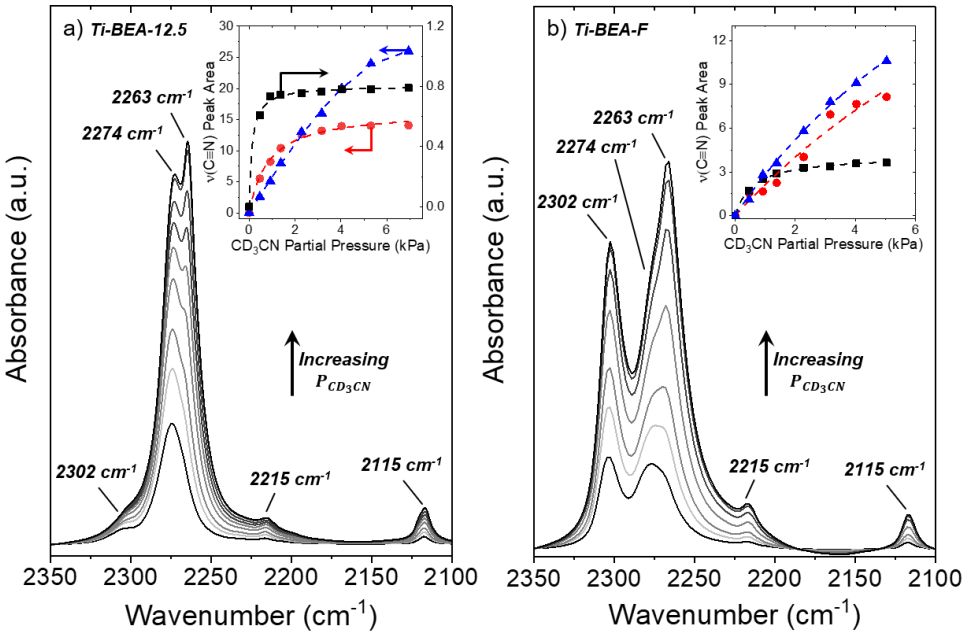

Figure 7.4. Infrared spectra of equilibrium coverages of adsorbed CD_3CN on (a) Ti-BEA-12.5 (0.46 – 6.95 kPa CD_3CN, 346 K), and (b) Ti-BEA-F (0.46 – 5.03 kPa CD_3CN, 387 K). The inset shows peak areas of the ν(C≡N) IR absorbance features for CD_3CN bound to SiOH and $(SiOH)_4$ groups (●), Ti atoms (■), and Si-O-Si (▲). Dashed lines represent least-squares regression fits of equation 7.5.

Table 7.3. Adsorption Enthalpies and Entropies for CD_3CN bound to Lewis Acidic Ti Atoms, $(SiOH)_x$ Moieties, and to Si-O-Si on Ti-BEA-12.5 and Ti-BEA-F

Sample	$\Delta H_{CD_3CN,Ti}$ (kJ mol^{-1})	$\Delta H_{CD_3CN,(SiO}$ (kJ mol^{-1})[a]	$\Delta H_{CD_3CN,Si-}$ (kJ mol^{-1})	$\Delta S_{CD_3CN,Ti}$ (J mol^{-1} K^{-1})	$\Delta S_{CD_3CN,(SiOH)_x}$ (J mol^{-1} K^{-1})[a]	$\Delta S_{CD_3CN,Si-O-Si}$ (J mol^{-1} K^{-1})
Ti-BEA-12.5	-32 ± 1	-55 ± 4	--[b]	-83 ± 5	-150 ± 10	--[b]
Ti-BEA-F	-32 ± 1	-19 ± 1	-12 ± 1	-99 ± 10	-87 ± 6	-75 ± 8
DFT Model[c]	-20	-41[d] / -33[e]	-22	-85	-117[d] / -134[e]	-67

[a]The subscript *x* is equal to either 1 (for Ti-BEA-F) or 4 (for Ti-BEA-12.5 and within the DFT model) to denote isolated SiOH or $(SiOH)_4$, respectively. [b]CD_3CN physisorbed to Ti-BEA-12.5 was not spectroscopically observable at the pressure (0.46 kPa) and temperatures (373 – 423 K) used for van't Hoff analysis. [c]Estimated by ab-initio molecular dynamics at 350 K with one Ti or $(SiOH)_4$ per unit cell. [d]Corresponds to the adsorption of CD_3CN onto $(SiOH)_4$. [e]Corresponds to adsorption of three CD_3CN per $(SiOH)_4$ nest.

Molecules of CD_3CN physisorb to Si-O-Si pore walls more weakly than to Ti atoms ($\Delta H_{CD_3CN,Si-O-Si}$= -12 kJ mol^{-1}; versus $\Delta H_{CD_3CN,Ti}$ = -32 kJ mol^{-1}), as expected because the adsorption of CD_3CN to Ti atoms involves specific Lewis acid-base interactions. As a result, entropy losses upon binding to siloxane regions are also smaller than those for Ti atoms ($\Delta S_{CD_3CN,Si-O-Si}$= -75; $\Delta S_{CD_3CN,Ti}$ = -83 to -99 J mol^{-1} K^{-1}). The measured entropy lost upon adsorption to Si-O-Si is similar to estimates from AIMD simulations (-75 versus -67 J mol^{-1} K^{-1}). Yet, calculated values of $\Delta H_{CD_3CN,Si-O-Si}$ are significantly larger than those measured (-22 versus -12 kJ mol^{-1}) and are identical to calculated values of $\Delta H_{CD_3CN,Ti}$. These systematic discrepancies between measured and calculated adsorption enthalpies likely reflect errors in the functional used to assess weak Lewis acid-base interactions. Notably, however, these calculations do seem to describe accurately the entropy for adsorption of CD_3CN to Si-O-Si and Ti sites.

Ti-BEA-F contains primarily isolated SiOH that form through stochastic processes which introduce crystallographic defects during hydrothermal synthesis. Molecules of CD_3CN adsorb more weakly onto SiOH within Ti-BEA-F than $(SiOH)_4$ within Ti-BEA-12.5 ($\Delta H_{CD_3CN,SiOH}$ = -19 kJ mol^{-1}; $\Delta H_{CD_3CN,(SiOH)_4}$= -31 kJ mol^{-1}). Moreover, CD_3CN bound to $(SiOH)_4$ within Ti-BEA-12.5 possess lower entropies than CD_3CN adsorbed to SiOH within Ti-BEA-F ($\Delta S_{CD_3CN,(SiOH)_4}$ = = -150 J mol^{-1} K^{-1}; $\Delta S_{CD_3CN,SiOH}$ = -87 J mol^{-1} K^{-1}). Notably, values of $\Delta S_{CD_3CN,SiOH}$ are similar to

$\Delta S_{CD_3CN,Ti}$ because CD_3CN, when bound to isolated SiOH, are oriented into the pore of *BEA and likely possess similar vibrational entropic modes (e.g., frustrated translation, hindered rotation). As mentioned above, we did not investigate AIMD simulations for the interaction of CD_3CN with isolated SiOH, because exact structure of these isolated defects within *BEA are not known.

AIMD simulations for a single CD_3CN adsorbed to $(SiOH)_4$ show similar enthalpic stabilities to those measured ($\Delta H_{CD_3CN,(SiOH)_4}$ = -41 versus -55 kJ mol^{-1}), yet underestimate the entropy lost upon adsorption ($\Delta S_{CD_3CN,(SiOH)_4}$ = -117 versus -150 J mol^{-1} K^{1-}). It is possible, however, that silanol nests may stabilize the adsorption of multiple adsorbates, as the adsorption geometries of molecules onto $(SiOH)_4$ have not previously been elucidated. Indeed, the adsorption of three CD_3CN to $(SiOH)_4$ results in AIMD-derived $\Delta H_{CD_3CN,(SiOH)_4}$ values that are similar to those predicted for a single CD_3CN molecule, suggesting that there is minimal enthalpic change (per molecule) for the adsorption of one or multiple CD_3CN to $(SiOH)_4$. Further, the adsorption of three CD_3CN molecules onto $(SiOH)_4$ does, in fact, show average entropies lost upon adsorption that are similar to those measured (-134 versus 150 J mol^{-1} K^{-1}).

The representative geometries for CD_3CN bound to $(SiOH)_4$ (Figure F12d) shows that a molecule of CD_3CN is projected perpendicularly to the 12-membered pore of *BEA in a vacancy produced from $(SiOH)_4$. The peak position of $\nu_s(-CD_3)$ is blue shifted with increasing $\theta_{CD_3CN,(SiOH)_4}$ (Figure F11), which reflects the interaction between the $-CD_3$ moiety and an electron-rich moiety (e.g., the -OH in $(SiOH)_4$).[314] This shift in $\nu_s(-CD_3)$ supports the results from AIMD, which suggest that CD_3CN may adsorb into $(SiOH)_4$ perpendicular to the main pore of *BEA in the space afforded from $(SiOH)_4$. The adsorption of CD_3CN perpendicular to the 12-membered ring of *BEA results primarily in a significant loss of rotational entropy. This interpretation (i.e., the loss in rotation entropy) is supported also by estimates for entropies of adsorption, calculated using the model of Campbell *et al* (equation F1, Section F2.2).[315]

The differences in $\Delta S_{CD_3CN,(SiOH)_4}$ and $\Delta S_{CD_3CN,Ti}$ primarily reflect the differences in the frustrated translational and hindered rotational entropy of CD_3CN adsorbed to $(SiOH)_4$ or Ti atoms, respectively. Decomposition of the translational and rotational contributions to the adsorbate entropy within the AIMD simulations (Table F1) show that the difference between $\Delta S_{CD_3CN,(SiOH)_4}$ and $\Delta S_{CD_3CN,Ti}$ is consistent with the difference in rotational entropy of CD_3CN bound to Ti atoms versus $(SiOH)_4$. The entropy of CD_3CN bound to Ti atoms and $(SiOH)_4$ was

estimated also using the Sackur-Tetrode equation and the corresponding partition functions that describe frustrated translation and hindered rotation in Section F2.3 (Table 7.1). Estimates for the entropy of hindered rotations of CD_3CN bound to Ti provide a value of 40 J mol^{-1} K, when the maximum degree of rotation is assumed to be 40 degrees. This estimate compares favorably to the measured difference in adsorption entropies determined experimentally (65 ± 10 kJ mol^{-1}) and predicted from AIMD simulations (49 kJ mol^{-1} K^{-1}) for CD_3CN bound to $(SiOH)_4$ in comparison to Ti sites, which further suggests that the adsorption of CD_3CN onto $(SiOH)_4$ results in the strong interaction of CD_3CN with the side channel afforded by $(SiOH)_4$.

Values of $\Delta H_{CD_3CN,Ti}$ reflect the formation of a Lewis acid-base adduct and may seem small in comparison to $\Delta H_{CD_3CN,SiOH}$; however, the strength of these interactions are consistent with measured heats of reaction for complexes of CH_3CN and homogeneous Lewis acids.[316-318] For example, $SbCl_5$ is used for comparisons of Lewis acidity,[75] and the heat of formation of the CH_3CN–$SbCl_5$ is -59 kJ mol^{-1} (in dichloroethane).[316] Moreover, $SbCl_5$ is a stronger Lewis acid than Ti alkoxides (e.g., $Ti(OiPr)_4$), which may possess electron affinities similar to framework Ti atoms in Ti-BEA. As such, the measured values of $\Delta H_{CD_3CN,Ti}$ on Ti-BEA-12.5 and Ti-BEA-F seem reasonable, and differences between these zeolitic materials arise predominantly in the density and types of SiOH or $(SiOH)_4$ sites.

In summary, the principal differences between the Ti-BEA do not reflect differences between the electronic properties (i.e., electron affinity) of the active sites among these materials, therefore, any catalytic differences that may arise must relate to differences in the properties of the active intermediates (Section 7.3.3), mechanism for epoxidation (Section 7.3.4) or density of $(SiOH)_4$ (Section 7.3.5).

7.3.3 Identity and Electronic Properties of Reactive Species Formed Upon H_2O_2 Activation

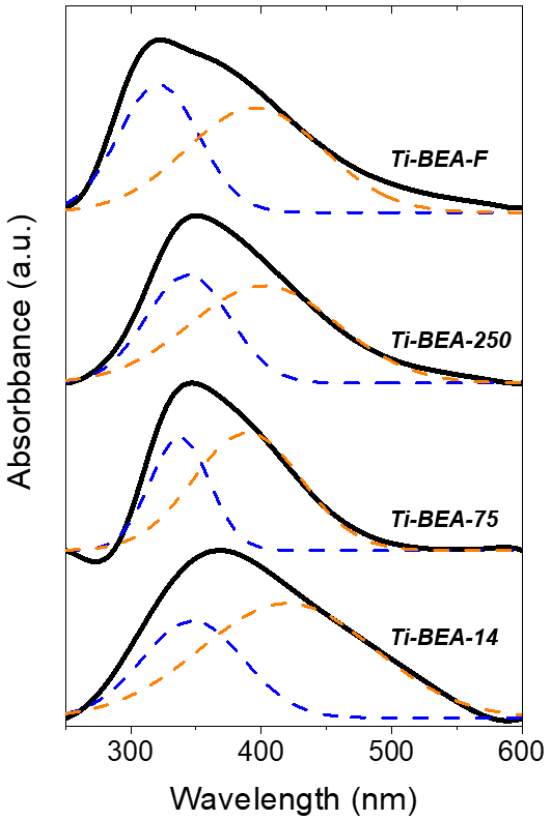

Figure 7.5. UV-vis spectra of Ti-(η^2-O_2) (blue) and Ti-OOH (orange) saturated surfaces of Ti-BEA-14, Ti-BEA-75, Ti-BEA-250, and Ti-BEA-F obtained in situ (0.01 M H_2O_2 in CH_3CN, 313 K). Dashed curves represent gaussian fits to UV-vis absorbance features. The background for each spectrum was obtained in flowing CH_3CN at 313 K. Spectra are normalized by their maximum absorbance and vertically offset for clarity.

Comparisons of steady-state UV-vis spectra of Ti-BEA in contact with solutions of H_2O_2 were used to determine if differences in the [$(SiOH)_4$] lead to changes in the identity or electronic properties of the reactive surface species formed following H_2O_2 activation. Atomically disperse Ti atoms, on surfaces of amorphous silicas[11, 58, 164, 210] and within zeolites (e.g., TS-1[64, 117, 121, 164] and Ti-BEA[11, 30, 66, 199, 275]) activate H_2O_2 to form pools of titanium-hydroperoxo (Ti-OOH) and peroxo (Ti-(η^2-O_2)) intermediates. The ligand-to-metal charge transfer (LMCT) energies of such species reflect the tendency of these intermediates to exchange electron density with the active site, and therefore, provide one quantitative measure of the electronic structure of these reactive surface species. Figure 7.5 shows steady-state UV-vis spectra of Ti-BEA-14, Ti-BEA-75, Ti-BEA-250, and Ti-BEA-F (0.01 M H_2O_2, 0.04 M H_2O, in CH_3CN, 313 K), and the corresponding UV-

vis spectra for all Ti-BEA are shown in Figure F13. All UV-vis spectra reveal complex absorbance features between 280 and 550 nm, consistent with reports for Ti-OOH and Ti-(η^2-O_2) species on Ti atoms grafted to mesoporous silicas[11, 58, 164, 210] and within the framework of MFI[121, 164, 211] or BEA zeolites.[11, 54, 199] Spectral deconvolution of these UV-vis features reveals two distinct bands at ~310 nm and ~410 nm, which correspond to Ti-(η^2-O_2) and Ti-OOH, respectively.[11, 164, 210] Table 7.2 and Figure F13b show that LMCT energies for neither Ti-(η^2-O_2) nor Ti-OOH depend on [$(SiOH)_4$], which strongly suggests that the proximity and density of $(SiOH)_4$ has a negligible impact on the electronic properties of the active intermediates for alkene epoxidation on Ti-BEA.

The identity of the reactive intermediate was probed by examining the stereospecificity for the epoxidation of *Z*-stilbene over all Ti-BEA (1 mM *Z*-stilbene, 0.01 M H_2O_2 in CH_3CN, 313 K). Hydroperoxide species (i.e., M-OOH) epoxidize C=C through a "butterfly" transition state that results in a concerted O atom transfer and retains the stereochemistry of the alkene.[65, 246-247] Alternatively, peroxo complexes (i.e., Ti-(η^2-O_2)) may react through a step-wise mechanism that allows for C-C bond rotation and different stereochemistry for the product.[248-249] Table 7.2 shows that epoxidation of *Z*-stilbene over Ti-BEA-X produces predominantly *Z*-stilbene oxide in all cases, which suggests that Ti-OOH is the active species for epoxidation and does not vary significantly with [$(SiOH)_4$]. These observations agree with the general consensus that Ti-OOH species are responsible for epoxidation reactions on TS-1,[64, 123, 246, 319] Ti-SiO_2,[51, 85, 164, 240] and Ti-BEA materials.[11, 66, 199]

These analyses show that variations in [$(SiOH)_4$] do not cause detectable changes in the identity or LMCT energies of the Ti-OOH species that participate in epoxidations of alkenes. Such conclusions are also consistent with the quantitative similarities in $\Delta H_{CD_3CN,Ti}$ (see above), which show that the electronic exchange between adsorbates and framework Ti atoms do not vary over the range of [$(SiOH)_4$] studied here. Collectively, these results suggest that any catalytic consequences related to changes in the value of [$(SiOH)_4$] are not likely caused by simple differences in charge transfer among only reactive species and framework Ti atoms.

7.3.4 Reaction Pathways for Epoxidation and H_2O_2 Decomposition over Ti-BEA Catalysts

Turnover rates for epoxidation[11, 54, 199] and sulfoxidation[275] reactions depend on the concentrations of the organic substrate, the oxidant (H_2O_2), and the reaction products (e.g., epoxides and sulfoxides), because these concentrations determine the coverage of reactive surface

species at Ti atoms and the availability of co-reactants. Figure 7.6 shows that all Ti-BEA give turnover rates for 1-octene epoxidation that exhibit nearly indistinguishable dependencies on the concentrations of 1-octene (C_8H_{16}) (Figure 7.6a), H_2O_2 (Figure 7.6b), or H_2O (Figure 7.6c) despite significant differences in the [$(SiOH)_4$] and in the turnover rates. Notably, Ti-BEA-14 (the material with the greatest density of silanol nests) gives epoxidation turnover rates that are two-orders of magnitude greater than those for Ti-BEA-F (the sample with the fewest silanol groups), which indicates that the presence of $(SiOH)_4$ results in a significant increase in epoxidation rates at these conditions. Specifically, turnover rates for 1-octene in Ti-BEA materials increase monotonically with the density of $(SiOH)_4$ groups across the seven Ti-BEA structures (Figure 7.7a), for reasons described below. For clarity, turnover rates as a function of reactant and co-product concentrations for materials with intermediate densities of $(SiOH)_4$ groups (i.e., Ti-BEA-12.5, -20, and -150) are shown only in Figures F14a – F14c.

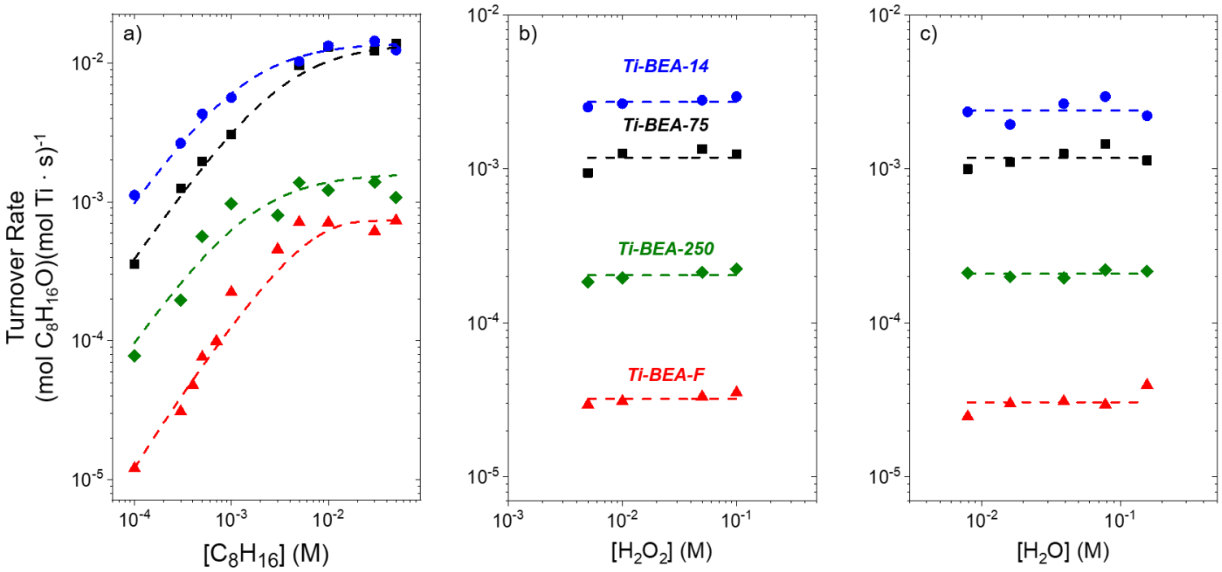

Figure 7.6. Turnover rates for the formation of $C_8H_{16}O$ as a function of (a) [C_8H_{16}] (0.01 M H_2O_2, 0.039 M H_2O), (b) [H_2O_2] ($3 \cdot 10^{-4}$ M C_8H_{16}), and (c) [H_2O] ($3 \cdot 10^{-4}$ M C_8H_{16}, 0.01 M H_2O_2) on Ti-BEA-14 (●), Ti-BEA-75 (■), Ti-BEA-250 (♦), and Ti-BEA-F (▲) in CH_3CN at 313 K. Dashed lines represent fits to equation 7.8 (Figure 7.6a) and 7.9 (Figures 7.6b and 7.6c).

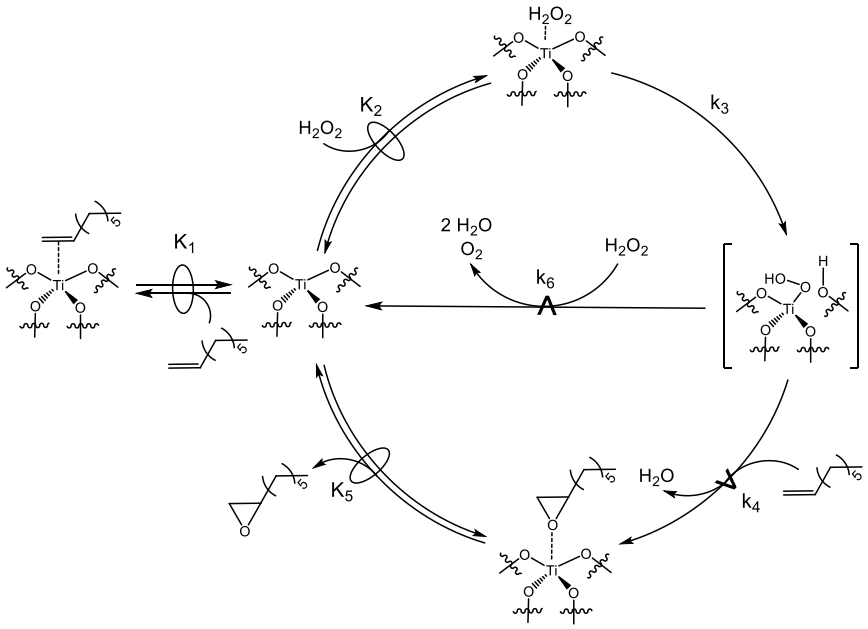

Scheme 7.1. Proposed Elementary Steps for C_8H_{16} Epoxidation and H_2O_2 Decomposition over Ti-BEA. The symbol ⇄ represents a quasi-equilibrated step, while → represents a kinetically relevant step. The Ti-OOH intermediate drawn are intended to represent the pool of Ti-OOH and Ti-(η^2-O_2) species that are present as shown by UV-vis (Figure 7.5).

All Ti-BEA exhibit two regimes that differ in how turnover rates depend on the concentrations of reactants. At low $[C_8H_{16}]$:$[H_2O_2]$ (<< 0.5), rates increase linearly with $[C_8H_{16}]$ and remain constant for different $[H_2O_2]$, which suggests that reactive intermediates derived from H_2O_2 (i.e., Ti-OOH) cover a majority of active sites. At greater values of $[C_8H_{16}]$:$[H_2O_2]$ (>> 0.5), turnover rates do not depend on $[C_8H_{16}]$, which indicates that C_8H_{16}-derived intermediates saturate active sites. Notably, rates remain constant with changes in $[H_2O]$ (4 mM – 160 mM), presumably because the quantities of H_2O in the pores of each BEA structure remain nearly constant within this range of $[H_2O]$. The dependence of $C_8H_{16}O$ formation on reactant and co-product (i.e., H_2O) concentrations agree closely with prior findings for group 4 and 5 metal atoms substituted into zeolite *BEA for the epoxidation of cyclohexene,[54, 199] styrene,[11] and the sulfoxidation of 2,5-dimethylthiophene.[275]

Scheme 7.1 depicts a series of elementary steps that describe the measured effects of $[C_8H_{16}]$, $[H_2O_2]$, and $[H_2O]$ on the rates of $C_8H_{16}O$ formation. This catalytic cycle involves the quasi-equilibrated adsorption of C_8H_{16} (step 1) and H_2O_2 (step 2), and the irreversible activation of adsorbed H_2O_2 (step 3) to form a pool of intermediates. Within this pool of species, Ti-OOH (Section 7.3.3) reacts with proximate C_8H_{16} (step 4) or H_2O_2 (step 6) molecules within kinetically

relevant processes to form $C_8H_{16}O$ or decomposition products (e.g., O_2 and H_2O), respectively. Molecules of $C_8H_{16}O$ desorb in a quasi-equilibrated manner (step 5) after their formation.[11, 54, 199] Following Scheme 7.1, rates for $C_8H_{10}O$ formation (r_E) take the form

$$r_E = k_4[C_8H_{16}][Ti-OOH] \tag{7.7}$$

where [Ti-OOH] is the number of Ti-OOH intermediates, and k_i is the rate constant for step *i* in Scheme 7.1. The application of the pseudo-steady state hypothesis to the number of Ti-OOH and a site balance over all possible states of the Ti active site allows equation 7.7 to be restated as

$$\frac{r_E}{[L]} = \frac{\frac{k_3 k_4 K_2 [C_8H_{16}][H_2O_2]}{k_4[C_8H_{16}]+k_6[H_2O_2]}}{1+K_1[C_8H_{16}]+K_2[H_2O_2]+\frac{k_3K_2[H_2O_2]}{k_4[C_8H_{16}]+k_6[H_2O_2]}+\frac{[C_8H_{16}O]}{K_5}} \tag{7.8}$$

where [L] is the total number of active sites and K_i is the equilibrium constant for step *i*. The five terms in the denominator correspond to active metal atoms occupied by CH_3CN (i.e., the solvent), C_8H_{16}, H_2O_2, Ti-OOH, or $C_8H_{16}O$, respectively. The derivation of the analogous rate expression for H_2O_2 decomposition is shown in Section F4.2.

Reaction conditions that give turnover rates that are proportional to $[C_8H_{16}]$ and invariant with changes in $[H_2O_2]$ result in surfaces saturated with pools containing reactive Ti-OOH intermediates,[11, 54, 199, 275] which reduces equation 7.8 to the form

$$\frac{r_E}{[L]} = k_4[C_8H_{16}] \tag{7.9}$$

The form of equation 7.9 reproduces the observed dependencies of turnover rates on $[C_8H_{16}]$, $[H_2O_2]$, and $[H_2O]$ from Figures 7.6a – 7.6c, at those conditions where $[H_2O_2]$ is greater than $[C_8H_{16}]$. When values of $[C_8H_{16}]$ significantly exceed those for $[H_2O_2]$, the full rate expression (equation 7.8) only reproduces the observed dependence on $[C_8H_{16}]$ in two limiting conditions. In one instance, equation 7.8 matches these data when adsorbed $C_8H_{16}O$ is the most abundant reactive intermediate (MARI) and the rate of epoxidation is far greater than H_2O_2 decomposition (i.e., $k_4[C_8H_{16}] > k_6[H_2O_2]$), which agrees with results from the epoxidation of cyclohexene[199] and

styrene[11] and the sulfoxidation of 2,5-dimethylthiophene[275] on Ti-BEA. Then, equation 7.8 reduces to yield

$$\frac{r_E}{[L]} = \frac{k_3 K_2 K_5 [H_2O_2]}{[C_8H_{16}O]} \tag{7.10}$$

which describes epoxidation rates that do not depend on $[C_8H_{16}]$ (Figure 7.6a). This series of assumptions holds for hydrophilic Ti-BEA-X (X = 12.5, 14, 20, and 75), where rates of epoxidation are greater than rates of H_2O_2 decomposition at high $[C_8H_{16}]$:$[H_2O_2]$. Yet, these conditions are not met for hydrophobic Ti-BEA-X (X = 150, 250, and F) samples, because rates for H_2O_2 decomposition are similar or greater than those for epoxidation. In these conditions, the general rate expression recreates measured concentration dependencies when Ti active sites become saturated with C_8H_{16}, which simplifies equation 7.8 to

$$\frac{r_E}{[L]} = \frac{k_3 k_4 K_2 [H_2O_2]}{k_6 K_1} \tag{7.11}$$

Equation 7.11 is consistent with the measured dependence of epoxidation rates on $[C_8H_{16}]$ (Figure 7.6a). Equitable comparisons of turnover rates and apparent activation barriers across this series of Ti-BEA catalysts can only be made at reaction conditions that result in equivalent surface coverages of surface species (i.e., all Ti-BEA saturated with Ti-OOH) and equal concentrations of liquid-phase reagents. The next section describes a series of such measurements and the associated interpretations that reveal the molecular interactions responsible for a 100-fold increase in epoxidation turnover rates and selectivities introduced by increasing the density of $(SiOH)_4$ groups.

7.3.5 Effects of Hydrogen-Bonding Interactions with Silanol Groups on Turnover Rates and Excess Free Energies of Activation

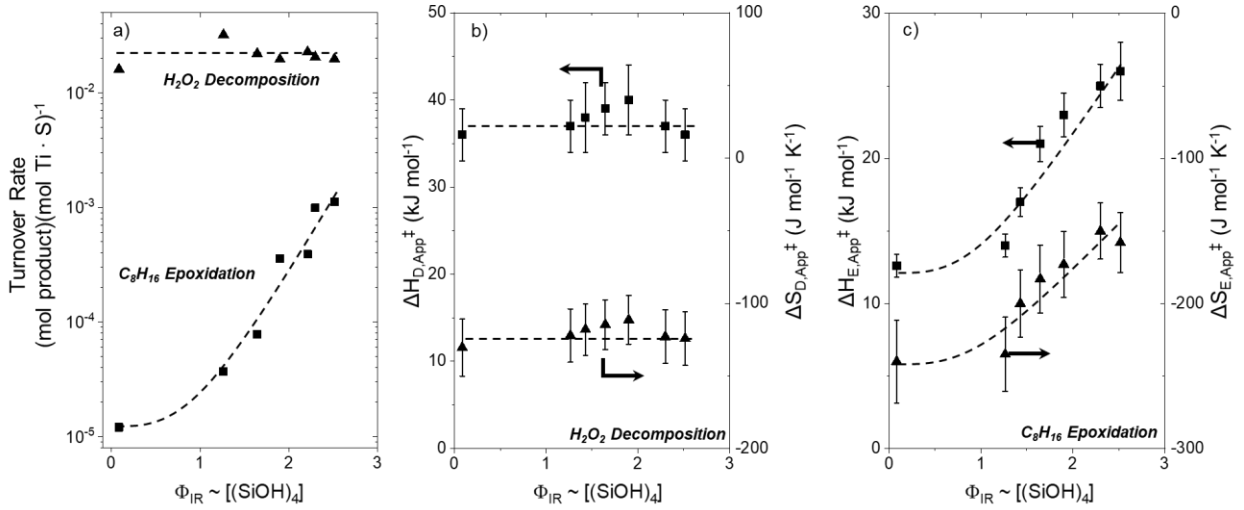

Figure 7.7. (a) Turnover rates for C_8H_{16} epoxidation (■) and H_2O_2 decomposition (▲) (0.1 mM C_8H_{16}, 0.01 M H_2O_2, 0.039 M H_2O, 313 K). Apparent activation enthalpies (■) and entropies (▲) for (b) H_2O_2 decomposition and (c) C_8H_{16} epoxidation (0.1 mM C_8H_{16}, 0.01 M H_2O_2, 0.039 M H_2O) as functions of Φ_{IR} (i.e., a measure of [(SiOH)$_4$]; section 7.3.1). Dashed curves are intended to guide the eye. Polanyi plots used to determine $\Delta H_{App}^{\ddagger}$ and $\Delta S_{App}^{\ddagger}$ are shown in Figure F15.

Turnover rates for C_8H_{16} epoxidation increase by a factor of 100 between the most hydrophobic and hydrophilic Ti-BEA. H_2O_2 decomposition rates, however, remain constant with differences in [(SiOH)$_4$] for this series of Ti-BEA (Figure 7.7a; 0.1 mM C_8H_{16}, 10 mM H_2O_2, 39 mM H_2O, 313 K). These differences lead to significantly greater epoxidation turnover rates and H_2O_2 selectivities on Ti-BEA with greater [(SiOH)$_4$], where selectivity is defined here as the ratio of the rate of epoxide formation to that of H_2O_2 consumption. These large changes in epoxidation turnover rates do not reflect differences in intra-porous H_2O_2 or C_8H_{16} concentrations,[29, 32, 71] because turnover rates do not depend on [H_2O_2] under these conditions and the measured uptake of C_8H_{16} is identical among all Ti-BEA (0.1 mM C_8H_{16}, 0.039 M H_2O, 313 K; Figure F16). Moreover, the significant differences in epoxidation turnover rates and selectivities do not arise from differences in the electronic properties of the active site (Section 7.3.2) or active intermediates (Section 7.3.3), nor are they due to differences in the mechanism for epoxidation (Section 7.3.4), as all of these factors are indistinguishable among the Ti-BEA catalysts within this study.

Figure 7.7b shows that apparent activation enthalpies and entropies for H_2O_2 decomposition ($\Delta H_{D,App}^{\ddagger}$ and $\Delta S_{D,App}^{\ddagger}$) do not vary with [$(SiOH)_4$] when measured at identical coverages of reactive species (i.e., Ti-OOH MARI), which suggests that the transition state for H_2O_2 decomposition is not sensitive to the proximity and density of $(SiOH)_4$. In contrast, Figure 7.7c indicates that apparent activation enthalpies and entropies for C_8H_{16} epoxidation ($\Delta H_{E,App}^{\ddagger}$ and $\Delta S_{E,App}^{\ddagger}$) vary between the most hydrophobic and hydrophilic Ti-BEA by 12 kJ mol^{-1} and 93 J mol^{-1} K^{-1}, respectively. These differences in the values for $\Delta H_{E,App}^{\ddagger}$ and $\Delta S_{E,App}^{\ddagger}$ account for the 100-fold increase in turnover rates across these materials. Notably, comparisons of these $\Delta H_{App}^{\ddagger}$ and $\Delta S_{App}^{\ddagger}$ values between the two reaction pathways strongly suggest that differences in the stability of transition states for epoxidation (and not the stability of the Ti-OOH surface species) are primarily responsible for the catalytic differences among Ti-BEA caused by the presence of $(SiOH)_4$ groups.

Transition state theory postulates that reaction rates reflect the stability of an activated complex (i.e., a transition state) relative to a known reference state (i.e., Ti-OOH and fluid-phase C_8H_{16} or H_2O_2) within the catalytic cycle (Scheme 7.2). Here, Ti-OOH-$C_8H_{16}^{\ddagger}$ and Ti-OOH-$H_2O_2^{\ddagger}$ are the transition states for C_8H_{16} epoxidation and H_2O_2 decomposition, respectively, and $K_x^{\ddagger}$ are the corresponding transition state equilibrium constants for epoxidation ($K_E^{\ddagger}$) or H_2O_2 decomposition ($K_D^{\ddagger}$).

Scheme 7.2. Proposed Sequence of Steps for the Formation of the Transition State for Epoxidation (2.1) or Decomposition of H_2O_2 (step 2.2)

$$Ti-(OOH)+C_8H_{16} \overset{K_E^{\ddagger}}{\rightleftharpoons} Ti-(OOH)-C_8H_{16}^{\ddagger} \quad (2.1)$$

$$Ti-(OOH)+H_2O_2 \overset{K_D^{\ddagger}}{\rightleftharpoons} Ti-(OOH)-H_2O_2^{\ddagger} \quad (2.2)$$

These catalytic reactions occur at solid-liquid interfaces that introduce specific molecular interactions (e.g., hydrogen bonds) that introduce thermodynamic non-idealities and require rates be described as functions of reactant activities and activity coefficients.[320] Within this conceptual framework, and with Ti-OOH as the MARI, rates of epoxidation (r_E) and H_2O_2 decomposition (r_D) equal

$$r_E = \frac{k_B T}{h} e^{\left(\frac{-\Delta {G_E}^{0,\ddagger}}{RT}\right)} \frac{a_{Ti-OOH}}{\gamma_{\ddagger,\mathrm{E}}} a_{C_8H_{16}} \tag{7.12a}$$

$$r_D = \frac{k_B T}{h} e^{\left(\frac{-\Delta {G_D}^{0,\ddagger}}{RT}\right)} \frac{a_{Ti-OOH}}{\gamma_{\ddagger,\mathrm{D}}} a_{H_2O_2} \tag{7.12b}$$

Within each equation, $\Delta G^{0,\ddagger}$ is the Gibbs free energy of activation at the standard state, a_j is the thermodynamic activity of species *j*, and $\gamma_\ddagger$ is the activity coefficient for the relevant transition state complex. For the comparisons made here, the standard state is defined as one that contains negligible hydrogen bond donors present at the solid-liquid interface, which is best represented by the pore environment of hydrophobic Ti-BEA-F. The activity coefficients of Ti-OOH, C_8H_{16}, and H_2O_2 will depend on hydrogen-bonding interactions, which can be described as a function of the excess Gibbs free energy (${G_j}^{\varepsilon}$) contribution

$$\gamma_j = e^{\left(\frac{{G_j}^{\varepsilon}}{RT}\right)} \tag{7.13}$$

by combining free energy terms, Equation 7.12 is then restated as

$$\frac{r_E}{[L]} = \frac{k_B T}{h} e^{\left(\frac{-\Delta {G_{E,App}}^{\ddagger}}{RT}\right)} [C_8H_{16}] \tag{7.14a}$$

$$\frac{r_D}{[L]} = \frac{k_B T}{h} e^{\left(\frac{-\Delta {G_{D,App}}^{\ddagger}}{RT}\right)} [H_2O_2] \tag{7.14b}$$

which also recognizes that the number of Ti-OOH intermediates ([Ti-OOH]) equals that of the active sites ([L]) at the conditions used to measure ${\Delta H_{App}}^{\ddagger}$ and ${\Delta S_{App}}^{\ddagger}$ values. Apparent free energies of activation (${\Delta G_{App}}^{\ddagger}$) are given by

$${\Delta G_{E,App}}^{\ddagger} = ({G_E}^{0,\ddagger} + {G_E}^{\varepsilon,\ddagger}) - ({G_{Ti-OOH}}^{0} + {G_{Ti-OOH}}^{\varepsilon}) - ({G_{C_8H_{16}}}^{0} + {G_{C_8H_{16}}}^{\varepsilon}) \tag{7.15a}$$

$$\Delta G_{D,App}{}^{\ddagger} = (G_D{}^{0,\ddagger} + G_D{}^{\varepsilon,\ddagger}) - (G_{Ti-OOH}{}^{0} + G_{Ti-OOH}{}^{\varepsilon}) - (G_{H_2O_2}{}^{0} + G_{H_2O_2}{}^{\varepsilon}) \quad (7.15a)$$

where $G^{\ddagger}$, G_{Ti-OOH}, and G_j are the free energies of the transition state, Ti-OOH, and fluid-phase coreactants, respectively. The excess free energy terms of the fluid phase co-reactants (i.e., $G_{C_8H_{16}}{}^{\varepsilon}$ and $G_{H_2O_2}{}^{\varepsilon}$) do not vary with [(SiOH)$_4$], because these species are not contained within the pores of Ti-BEA. Consequently, differences in the apparent activation free energies ($\Delta\Delta G^{\ddagger}$) between a given Ti-BEA and Ti-BEA-F reflects changes only in the excess properties of the relevant transition states and Ti-OOH

$$\Delta\Delta G_E{}^{\ddagger} = G_E{}^{\varepsilon,\ddagger} - G_{Ti-OOH}{}^{\varepsilon} \quad (7.16a)$$

$$\Delta\Delta G_D{}^{\ddagger} = G_D{}^{\varepsilon,\ddagger} - G_{Ti-OOH}{}^{\varepsilon} \quad (7.16b)$$

Activation parameters for H_2O_2 decomposition do not vary with [(SiOH)$_4$] ($\Delta H_{D,App}{}^{\ddagger}$ = 37 ± 8 kJ mol^{-1}; $\Delta S_{D,App}{}^{\ddagger}$ = -120 ± 45 J mol^{-1} K^{-1}), which indicates that $G_D{}^{\varepsilon,\ddagger}$ and $G_{Ti-OOH}{}^{\varepsilon}$ are either serendipitously equal or that the free energies of these complexes do not depend on the [(SiOH)$_4$] within these materials (i.e., $G_D{}^{\varepsilon,\ddagger}$ and $G_{Ti-OOH}{}^{\varepsilon}$ equal zero). The invariance in these values may be explained in two ways. First, Ti-OOH and the transition states for H_2O_2 decomposition may nucleate small clusters of H_2O, as both species are capable of donating and accepting hydrogen bonds. The formation of H_2O clusters at Ti-OOH and H_2O_2 decomposition transition states diminishes the effects of nearby H_2O clusters that form at proximate (SiOH)$_4$.[321-322] Second, the effective diameter of Ti-OOH and the transition state for H_2O_2 decomposition may be too small to interact the pore walls of BEA[11] and, thus, may be insensitive to nearby (SiOH)$_4$ and H_2O clusters stabilized at these sites. In the context of either explanation, the strong dependence of turnover rates for C_8H_{16} epoxidation on the number of proximate (SiOH)$_4$ groups must arise from differences in the excess free energies of transition states for epoxidation (i.e., $G_E{}^{\varepsilon,\ddagger}$).

Values of $G_E{}^{\varepsilon,\ddagger}$, and by extension $H_E{}^{\varepsilon,\ddagger}$ and $S_E{}^{\varepsilon,\ddagger}$, that recognize differences in the density of (SiOH)$_4$ groups seem likely to do so *via* interactions of the aliphatic tail of this transition state

with the local environment. Values of $\Delta H_{E,App}^{\ddagger}$ are lowest in Ti-BEA-F because the aliphatic tail of the transition state interacts weakly with siloxane pore walls through dispersive forces. The pores of Ti-BEA-F should contain acetonitrile and negligible concentrations of water molecules, primarily in loosely bound, disordered states. Consequently, the values of $\Delta S_{E,App}^{\ddagger}$, which are most negative for Ti-BEA-F among all Ti-BEA, predominantly reflect the loss of entropy related to coordination of 1-octene to Ti-OOH and changes in structure of solvating acetonitrile. However, hydrogen-bonded clusters of water molecules near active sites within hydrophilic Ti-BEA materials (e.g., Ti-BEA-14) interact unfavorably with the alkyl chain of epoxidation transition states, which appear as greater values of $\Delta H_{E,App}^{\ddagger}$ (from 12 kJ mol^{-1} for Ti-BEA-F to 25 kJ mol^{-1} for Ti-BEA-14) as a result of increasing the $H_E^{\varepsilon,\ddagger}$. The disruption of these hydrogen-bonded water clusters manifests as large positive $S_E^{\varepsilon,\ddagger}$ values that reflect the reorganization of these confined water clusters to accommodate epoxidation transition states. Ultimately, differences among activation free energies for epoxidation ($\Delta\Delta G_{E,App}^{\ddagger}$) are dominated by entropic contributions at these conditions, which agrees with the expectations that such changes are exacerbated within confining environments that can lead to significant reorganization of molecules.[323-325]

Values of $H_E^{\varepsilon,\ddagger}$and $S_E^{\varepsilon,\ddagger}$ that increase with [(SiOH)$_4$] in Ti-BEA (Figures 7.7b and 7.7c) are semi-quantitatively consistent with the expected enthalpic costs and entropic benefits of disrupting hydrogen-bonded water clusters, in this case, by the formation of the transition states. The rupture of a single hydrogen bond among water molecules at the interface between bulk liquid water and a non-polar solute increases the enthalpy of the system by ~10 kJ mol^{-1} and simultaneously increases the entropy by 25 J mol^{-1} K.[326-327] Water confined within nanometer-scale voids (e.g., in a zeolite) possesses significantly lower entropies than bulk H_2O as a result of structuring and highly correlated molecular motion within pores less than 1 nm in diameter.[324-325] Thus, the interaction of transition states for epoxidation with H_2O clusters in these confined spaces results in an entropic gain much larger than anticipated from comparisons to bulk liquid water. The changes in $G_E^{\varepsilon,\ddagger}$ do not, however, correspond entirely to restructuring of confined H_2O clusters, because the value of $G_E^{\varepsilon,\ddagger}$ reflects the net change in free energy that results from interactions among silanol nests, the H_2O clusters stabilized at these nests, the surrounding CH_3CN solvent molecules, and the epoxidation transition states. Deconvolution of these effects require detailed kinetic and calorimetric measurements obtained over a range of conditions, which are in

progress. Despite the difficulties in deconvoluting the contributions of each set of molecular interactions, these changes in $G_E^{\varepsilon,\ddagger}$ can be attributed to water-mediated hydrogen bond donation and acceptance among the species present about the active site. In the following section, we demonstrate that the hydrogen bonds between silanol nests, H_2O clusters, and transition states within the pores of Ti-BEA catalysts increase alkene epoxidation rates regardless of the identity of the oxidant by comparing rates obtained under hydrous and anhydrous conditions.

7.3.6 Differences in Epoxidation Rates with Ti-BEA Caused by Hydrogen Bonding Among Reactants, Surfaces, and Solvents

Figure 7.8 shows that turnover rates for C_8H_{16} epoxidation with aqueous H_2O_2 (0.1 mM C_8H_{16}, 39 mM H_2O, 10 mM H_2O_2) increase by a factor of 100 as the density of silanol groups increases approximately from ~0 to 5 (unit cell)$^{-1}$ between the most hydrophobic and hydrophilic Ti-BEA. In contrast, epoxidation turnover rates using *tert*-butyl hydroperoxide (*t*-BuOOH) under anhydrous conditions (0.1 mM C_8H_{16}, 10 mM *t*-BuOOH, 313K) give turnover rates that differ by less than a factor of two. Under anhydrous reaction conditions, $(SiOH)_4$ groups cannot readily influence the stability of transition states for epoxidation due to the lack of water clusters to facilitate these interactions. Yet, the turnover rates for C_8H_{16} epoxidation with *t*-BuOOH increase by a factor of 20 when the density of $(SiOH)_4$ is increased from ~0 to 5 (unit cell)$^{-1}$ in the presence of small amounts of H_2O (39 mM H_2O). Presumably, these small concentrations of H_2O introduce similar differences in $G_E^{\varepsilon,\ddagger}$ across the series of Ti-BEA as observed in epoxidations with aqueous H_2O_2 (Section 7.3.5). Turnover rates for epoxidation within Ti-BEA-F are largely unaffected by the addition of H_2O to the solvent, which is consistent with the expectation that extended H_2O clusters cannot form within pores of Ti-BEA-F at these conditions.[36-37] These observations and interpretations further support that conclusion the presence of structured H_2O clusters within pores leads to large changes in $G_E^{\varepsilon,\ddagger}$ within the most hydrophilic Ti-BEA that reflect the complex network of hydrogen bonds formed between the transition states for epoxidation, nearby H_2O clusters, and $(SiOH)_4$ groups.

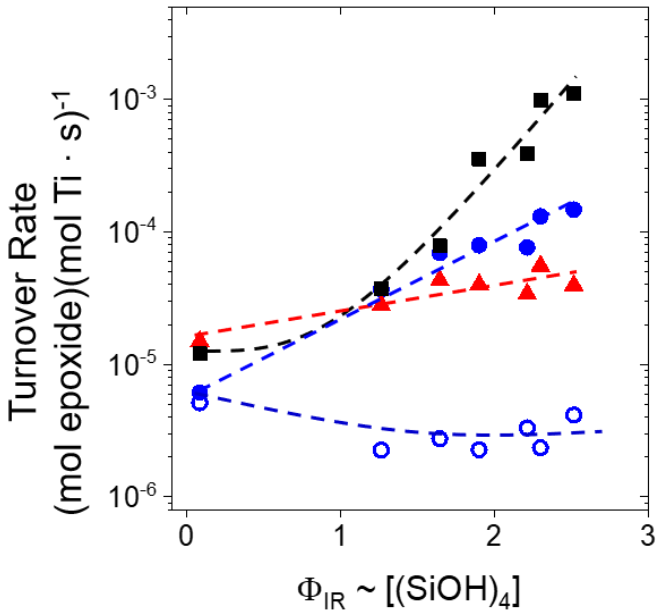

Figure 7.8. Turnover rates for C_8H_{16} epoxidation (■; 0.1 mM C_8H_{16}, 0.01 M H_2O_2, 0.039 M H_2O, 313 K), C_8H_{16} epoxidation with *t*-BuOOH (0.1 mM C_8H_{16}, 0.01 M *t*-BuOOH, 313 K) under anhydrous conditions (○) and with 0.039 M H_2O (●), and $C_6H_{11}OH$ epoxidation (▲; 0.1 mM $C_6H_{11}OH$, 0.01 M H_2O_2, 0.039 M H_2O, 313 K) over Ti-BEA as function of Φ_{IR} (i.e., a measure of $[(SiOH)_4]$. Dashed curves are intended to guide the eye.

The chemical functionality of the reactant should also influence the dependence of $G_E^{\varepsilon,\ddagger}$ on $[(SiOH)_4]$, particularly if the transition state for epoxidation can donate or accept hydrogen bonds. Figure 7.8 shows that turnover rates for 5-hexene-1-ol ($C_6H_{11}OH$) epoxidation increase with silanol density by only a factor of 5 across this series of catalysts, which is much less than the 100-fold difference for epoxidation of C_8H_{16} across the same materials. The transition state for $C_6H_{11}OH$ epoxidation includes a terminal -OH which is less likely to perturb the structure of proximate H_2O clusters than C_8H_{16}. The comparison between the change in epoxidation rates for these two substrates (i.e., $C_6H_{11}OH$ and C_8H_{16}) are consistent with rates that increase due to disruptive interactions between the epoxidation transition states and H_2O clusters and the associated entropy gains.

7.3.7 Implications of Relative Hydrophilicity within Zeolite Catalysis

Collectively, these data show that the changes in the density of $(SiOH)_4$ can greatly influence the rates of a given reaction in the presence of H_2O. The analysis presented here, that describes how the excess free energies of the transition state for a given reaction may change with

[$(SiOH)_4$], is extended to other catalytic chemistries within zeolites to yield new interpretations for the effects of hydrophobicity in liquid-phase catalysis.

Rates of Baeyer-Villiger (BV) oxidations are greater for Sn-BEA catalysts synthesized by post-synthetic modification relative to defect-free materials (i.e., synthesized in fluoride media), such that oxidation rates of cyclohexanone with aqueous H_2O_2 (0.33 M cyclohexanone, 0.5 M H_2O_2, 1.8 M H_2O, 353 K)[35] and for 2-adamantanone with anhydrous *t*-BuOOH (2 M ketone, 4 M *t*-BuOOH, 363 K),[328] differ by factors of 6 and 3, respectively, between post-synthetically modified Sn-BEA and defect-free Sn-BEA. The original authors proposed that silanol groups increase BV oxidation rates by facilitating the coordination of cyclohexanone to the Sn active sites.[35] Differences in the rates of 2-adamantanone oxidation, on the other hand, were attributed to diffusion limitations within pores of defect-free Sn-BEA that reduced the availability of reactants at Sn active sites.[328] The observations in these publications are consistent with the manner by which rates should change as a result of $G^{\varepsilon,\ddagger}$ for BV oxidation (i.e., the Criegee adduct)[259] that decrease due to disruption of the confined H_2O or ROH clusters stabilized at nearby $(SiOH)_4$.

Meerwin-Ponndorf-Verley (MPV) reduction rates are greater in defect-free Zr-BEA (synthesized in fluoride media) relative to those synthesized by post-synthetic incorporation of Zr atoms. Specifically, MPV rates were 1.5-times higher in the hydrophobic Zr-BEA (522 versus 350 h^{-1}, 1 M 4-*tert*-butylcyclohexanone in 2-propanol, 355 K).[329] The authors do not discuss the origins of these differences within their manuscript.[329] These MPV reactions were conducted under ostensibly anhydrous conditions, such that ROH clusters, rather than H_2O, are likely formed through hydrogen-bonding interactions with $(SiOH)_4$. Based upon our analysis, values of $G^{\varepsilon,\ddagger}$ for MPV reduction (i.e., the intermolecular hydride transfer between 2-propanol and ketone bound to the same Zr site)[330] may increase with $(SiOH)_4$, because the bulky *tert*-butyl moieties of the ketone interact with the defect-free pore walls and are enthalpically stabilized (i.e., lower $H^{\varepsilon,\ddagger}$). Clusters of 2-propanol clusters that form at nearby $(SiOH)_4$ are not stabilized by hydrogen bonds to the same extent as H_2O, and consequently, these clusters do not provide large entropy gains when they accommodate transition states. Collectively, the $G^{\varepsilon,\ddagger}$ for MPV reduction are dictated by the changes in the excess enthalpies that arise from interactions of the hydrophobic ketone with the pore walls of Zr-BEA.

The interpretation of the influence of hydrogen-bonding interactions among SiOH, H_2O, and alkene epoxidation transition states seems consistent also with reported comparisons among

cyclohexene and 1-hexene.[32, 295] epoxidation rates on Ti-containing zeolite catalysts. For example, the rates of cyclohexene epoxidation with aqueous H_2O_2 are 50% greater on Ti-MWW catalysts synthesized by post synthetic modification than on defect-free [Ti,B]-MWW (27 h^{-1} versus 18 h^{-1}; 5 M cyclohexene, 1 M H_2O_2, 3.9 M H_2O, 333 K).[266] Here, the authors proposed differences in epoxidation rates result from decreases in the zeolite framework electronegativity that arise from Lewis acidic B atoms. Similarly, epoxidation rates of 1-hexene are 65 - 125% greater on hydrophilic TS-1 as compared to conventional hydrophobic TS-1 (1 M 1-hexene, 1 M H_2O_2, 3.9 M H_2O, 333 K).[32, 295] The authors in one study proposed that the increased rates reflected a greater concentration of H_2O_2 near active sites caused by favorable interactions with SiOH groups. Alternatively, in the other study, the large differences in epoxidation rates were attributed to differences in the electronic properties of the Ti active sites.[295] It seems more likely, however, that the presence of H_2O stabilized at SiOH within the Ti-zeolite catalysts in these studies results in large increases in the excess entropy of the epoxidation transition states (i.e., $S^{\varepsilon,\ddagger}$) due to disruption of these confined H_2O clusters within the hydrophilic zeolite pores.

These studies represent only a portion of an extensive body of literature that seeks to explain differences in rates and selectivities among materials with varying hydrophilicity, which often can be thought of as differences in densities of various silanol features. Collectively, the analysis and interpretation of results (within this work and those cited above) show that the excess free energies of the transition states for a given reaction pathway depend strongly on the presence, density, and proximity of extended hydrogen-bonded networks within zeolite catalysts. These complex interactions encompass the formation and restructuring of these intra-porous solvent networks, which depend intimately on the chemical functionality of the reactants.

7.4 Conclusions

Epoxidation of alkenes by H_2O_2 and H_2O_2 decomposition reactions occur at framework Ti atoms within Ti-BEA catalysts, and turnover rates for epoxidation depend strongly on the presence, density and proximity of the epoxidation transition states to $(SiOH)_4$ moieties. Turnover rates for 1-octene epoxidation increase monotonically with the density of $(SiOH)_4$ in Ti-BEA, where materials containing ~5 $(SiOH)_4$ $(unit\ cell)^{-1}$ possess rates that are 100-fold greater than Ti-BEA that are nearly defect free. Rates of H_2O_2 decomposition, however, are insensitive to $[(SiOH)_4]$ across the Ti-BEA tested here. These differences in epoxidation catalysis do not reflect

variations in the electron affinity of the Ti active sites among the series of Ti-BEA, because neither measured adsorption enthalpies for CD_3CN to Ti atoms nor ligand-to-metal charge transfer energies for Ti-OOH and Ti-(η^2-O_2) species differ with the density of $(SiOH)_4$. Mechanistic interpretations of epoxidation rates measured as a function of reactant concentrations, in combination with in situ UV-vis measurements and radical-clock reactions with cis-stilbene, show that the mechanism for epoxidation and the identity and electronic properties of reactive Ti-OOH intermediates do not vary with $(SiOH)_4$ density.

Apparent free energies of activation for 1-octene epoxidation decrease with increasing densities of $(SiOH)_4$ within reactant solutions that contain small concentrations of water (39 mM), which indicates that water molecules and their hydrogen-bonding interactions help stabilize epoxidation transition states. Specifically, apparent activation enthalpies and entropies for 1-octene epoxidation are 13 kJ mol^{-1} lower and 93 J mol^{-1} K^{-1} more negative on defect-free Ti-BEA than Ti-BEA containing ~5 $(SiOH)_4$ $(unit\ cell)^{-1}$, respectively. Yet, these same quantities for the decomposition of H_2O_2 remain constant, within the uncertainty of the measurements, for all Ti-BEA. These comparisons show that smaller apparent entropy losses for forming epoxidation transition states in Ti-BEA with the most $(SiOH)_4$ are responsible for the significantly greater epoxidation turnover rates and selectivities in these materials.

The differences in apparent activation enthalpies and entropies with the density of $(SiOH)_4$ arise from excess enthalpies and entropies of the transition states for epoxidation that reflect enthalpically unfavorable interactions between the aliphatic chain of the transition states and water clusters present near $(SiOH)_4$. Within hydrophilic Ti-BEA, clusters of water confined near $(SiOH)_4$ reorganize in response to the formation of transition states for epoxidation, which leads to the rupture of hydrogen bonds and increases in the entropy of these water clusters. However, the apparent activation enthalpies and entropies for H_2O_2 decomposition are not affected by the presence of water because the transition state for H_2O_2 decomposition interacts with these hydrogen-bonded networks in ways similar to Ti-OOH reactive species. These interpretations are consistent with the fact that turnover rates for 1-octene epoxidation vary by less than a factor of two across the same series of Ti-BEA catalysts when reactions proceed in the absence of water (i.e., using *tert*-butyl hydroperoxide under anhydrous conditions). Epoxidation turnover rates recover their sensitivity to $(SiOH)_4$ groups and exhibit a 20-fold increase with increases in $[(SiOH)_4]$ when small amounts of H_2O were added to the otherwise anhydrous solutions. These

data support the conclusion that changes in excess free energies reflect dynamic changes in the structure of water clusters near active sites that result from changes in coverage and molecular structure of the species bound to framework Ti as the reaction proceeds.

Overall, the data and interpretations presented here suggest that the excess free energies of the transition states for liquid-phase reactions within zeolites will be influenced by the density and proximity of $(SiOH)_4$ moieties in the presence of hydrogen-bonding solvents or reactants. Small confined clusters of hydrogen-bond donating or accepting molecules (e.g., H_2O or ROH) nucleate at $(SiOH)_4$ and must reorganize to accommodate the adsorption of reactants and the formation of transition states. This solvent reorganization will result in a change in the transition states excess free energy that is a complex function of the chemical and physical properties of the reactant (e.g., hydrogen-bonding character, and polarity) and of the catalyst (e.g., $(SiOH)_4$ density, pore diameter). The deconvolution of these individual types of interactions and the associated effects on liquid-phase catalysis remains challenging and requires a combination of kinetic, spectroscopic, calorimetric and computational methods - such work represents an important area of research that must be developed to increase understanding of catalysis at solid-liquid interfaces.

CHAPTER EIGHT

Impact of Specific Interactions Among Reactive Surface Intermediates and Confined Water on Epoxidation Catalysis and Adsorption in Lewis Acid Zeolites[VII]

Abstract

Molecular interactions at solid-liquid interfaces greatly influence the stability of surface intermediates central to adsorption and catalysis. These complex interactions include the reorganization of solvent molecules near active sites to accommodate the formation of reactive surface intermediates. The consequences of these interactions and how they depend on the chemical functionality of the extended surface within pores have not been demonstrated in ways that permit the rational use of excess thermodynamic properties in the design of catalytic sites. Here, we show that adsorption enthalpies and entropies for 1,2-epoxyoctane ($C_8H_{16}O$) increase by 19 kJ mol^{-1} and 75 J mol^{-1} K^{-1}, respectively, when the density of silanol nests decrease from ~5 to 0 $(unit\ cell)^{-1}$ within Ti-substituted zeolite BEA (Ti-BEA) in the presence of trace H_2O. In contrast, these properties are indistinguishable across all Ti-BEA samples under anhydrous conditions, which suggests that H_2O proximate to Ti adsorption sites interacts with bound $C_8H_{16}O$. In situ infrared spectra of hydrophilic Ti-BEA show that coordination of $C_8H_{16}O$ to framework Ti-sites reduces the extent of hydrogen bonding with and among H_2O molecules, which is reflected by changes in the frequencies of O-H stretching modes and molecular librations. Adsorption of $C_8H_{16}O$ into hydrophobic Ti-BEA, however, does not cause detectable changes in the vibrational spectra of nearby H_2O. The combination of these results, along with values of activation enthalpies and entropies for epoxidation reactions in the same materials, show that the disruption of hydrogen-bonded H_2O near Ti-atoms introduce excess free energies of adsorption that can be manipulated by controlling the number of solid- and liquid-phase hydrogen bond donors and acceptors at interfaces. These findings reveal the complex role of surface moieties on epoxidation reactions in Ti-silicates, show how silanol groups may impact other liquid-phase reactions within zeolites, and provide a basis to understand the manner by which surface chemistry impacts structure of the surrounding solvent.

[VII]This chapter has been adapted from the following publication:
Bregante, D.T.; Flaherty, D.W.; "Impact of Specific Interactions Among Reactive Surface Intermediates and Confined Water on Epoxidation Catalysis and Adsorption in Lewis Acid Zeolites"
ACS Catalysis, **2019**, 9, 10951 - 10962.

8.1 Introduction

Zeolite and zeotype materials are attractive scaffolds for catalytic and separation processes, due to their ability to discriminate among molecules by size exclusion and shape selectivity.[3-4] When zeolite pores are largely vacant, van der Waals interactions with surfaces contribute to the stability of adsorbates and reactive intermediates that bind to active sites. The level of complexity increases further when pores contain liquid-like densities of molecules that can assemble into structures governed by specific interactions among these molecules and with surfaces. Adsorption and reaction at active sites surrounded by solvation shells requires that these structures change to accommodate the surface species that form, which introduces excess free energy differences to adsorption, reaction, and activation processes.[18, 21, 292-293, 331]

Hydrogen-bonding interactions between entrained solvent molecules (e.g., R-OH; R = H, alkyl), adsorbates, and surfaces within microporous materials affect uptake, intrapore diffusion, and surface reactions and have been implicated in studies that focus on the adsorption of alcohols and water in microporous solids,[36-37, 332-337] the enhancement of water transport via highly-structured hydrogen-bonded networks within carbon nanotubes,[338-342] the formation and stabilization of hydronium ions within zeolites,[20, 23] and liquid-phase oxidations within micro- and meso-porous silicates.[11, 21-22, 30, 32, 35, 199, 252, 296, 343-344] For example, silicalite-1 synthesized in OH^- media (MFI-OH) adsorbs significantly more water below and near the saturation pressure (P/P_0 ~ 0.95) than silicalite-1 crystallized in F^- media, because the greater density of internal silanol (SiOH) defects in MFI-OH assist in stabilizing hydrogen-bonded H_2O clusters.[24-25, 27, 37] For decades hydrophobic Ti-silicates have been reported to be more productive catalysts for epoxidations, in comparison to analogous hydrophilic structures, which was ascribed to enrichment of alkene reactants near active sites or to increased rates of alkene diffusion in different studies.[14, 29-30, 32, 64, 69-71, 295] Recent results from our group[21] and others[32, 71, 295] show, however, that the presence of internal SiOH groups increases rates and selectivities for alkene epoxidations when water is present in the solvent. These observations seem inconsistent with previous hypotheses for the mechanisms by which SiOH affect epoxidation reactions and require alternative explanations, and specifically, ones that address the stabilities of relevant transition state structures.

The stability of transition states for epoxidations, but also numerous other liquid-phase reactions, depend on chemical interactions between these structures and the surrounding solvent molecules, and these interactions impact catalytic rates and selectivities as a result.[18, 293, 345]

Dumesic and coworkers used a combination of rate measurements and ab initio molecular dynamics to evince linear free energy relationships that quantitatively describe changes in the extent of solvation (i.e., solvation shells of H_2O and co-solvents) between the initial and transition states for acid-catalyzed dehydration reactions of sugars and alcohols, which can lead to a nearly 400-fold increase in rates.[346-348] These results demonstrate the manner by which specific interactions with H_2O confer stability to activated complexes and facilitate homogeneous reactions, but we are not aware of demonstrations for similar phenomena at solid-liquid interfaces. As such, the community lacks molecular descriptions and quantitative relationships that describe the interaction among confined solvent molecules (e.g., H_2O), reactive species at active sites, and the extended surface of solid catalysts that can demonstrate how these interactions impact adsorption and catalysis.[18, 21-22, 35, 296, 343, 349]

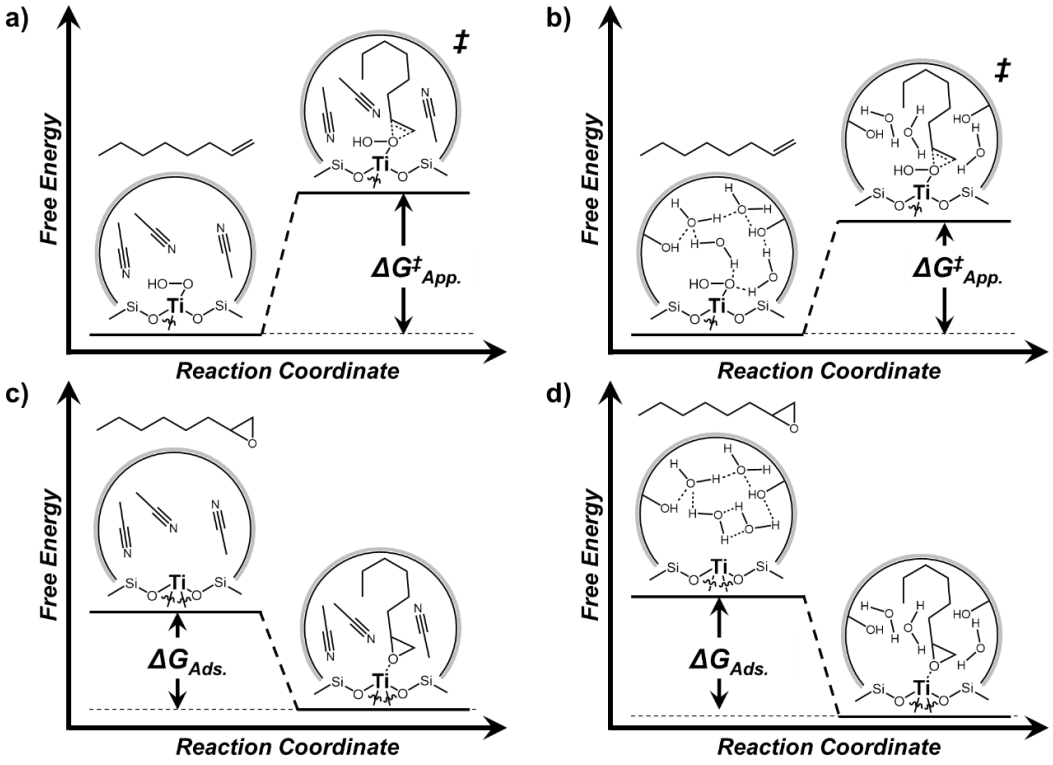

Scheme 8.1. Changes in Free Energy Due to (a and b) Formation of the C_8H_{16} Epoxidation Transition State and (c and d) Adsorption of $C_8H_{16}O$ over (a and c) hydrophobic and (b and d) hydrophilic Ti-BEA to show exaggerated changes in solvent structure. These thermochemical sequences for C_8H_{16} epoxidation and $C_8H_{16}O$ adsorption have Ti-OOH and solvent-covered Ti active sites with fluid-phase C_8H_{16} and $C_8H_{16}O$ as the reference states, respectively. Dashed lines in the reference states provide a visual representation of the hydrogen-bonding network of H_2O within hydrophilic Ti-BEA.

Rates and selectivities for 1-octene (C_8H_{16}) epoxidation are 100-fold greater in Ti-BEA materials that contain ~5 silanol nests ($(SiOH)_4$) (unit cell)$^{-1}$ in comparison to hydrophobic, defect-free Ti-BEA.[21] These findings contradict earlier reports for alkene epoxidation in Ti-silicates (*vide infra*) that emphasized the need to eliminate SiOH defects to concentrate alkene reactants near active sites or to alleviate diffusional constraints. These differences in rates and selectivities were attributed to excess enthalpies ($H^{\ddagger,e}$) and entropies ($S^{\ddagger,e}$) of C_8H_{16} epoxidation transition states (Scheme 8.1a) caused by interactions of the aliphatic octyl chain with proximate H_2O structures stabilized at nearby $(SiOH)_4$ groups. The putative cause of these excess quantities is the need for solvent structures to reorganize to accommodate the formation of reactive surface intermediates as the reaction progresses throughout the catalytic cycle. The differences in catalytic behavior between defective and defect-free Ti-BEA materials suggests that interactions between solvent molecules, reactive intermediates, and the catalyst surface have consequences for catalysis. These proposals result largely from the analysis and interpretation of kinetic measurements, and therefore, direct observations for changes in the structure of the solvent and quantitative measures of the impact on elementary steps relevant for catalysis are needed to gain deeper understanding of the role of these solvent-mediated processes for reactions within microporous materials.

Here, we report calorimetric and spectroscopic evidence that differences in the thermodynamics of 1,2-epoxyoctane ($C_8H_{16}O$) adsorption in Ti-BEA reflect changes in the solvent structure about active sites and that these changes can be controlled by intentionally incorporating SiOH defects near Ti atoms. Results from isothermal titration calorimetry (ITC) show that adsorption enthalpies and entropies, of $C_8H_{16}O$ (ΔH_{Ads}, ΔS_{Ads}) to framework Ti atoms are 19 kJ mol^{-1} and 75 J mol^{-1} K^{-1} more positive on nearly defect-free Ti-BEA than those containing ~5 $(SiOH)_4$ (unit cell)$^{-1}$ in the presence of H_2O. Under anhydrous conditions, however, values of ΔH_{Ads} and ΔS_{Ads} do not depend on the density of $(SiOH)_4$. Silanol nests stabilize semi-ordered clusters of H_2O that must reorganize to accommodate the adsorption of $C_8H_{16}O$. These differences in adsorption thermodynamics result from the short-range interactions between adsorbed $C_8H_{16}O$ and clusters of H_2O that are proximate to Ti active sites. Additionally, the interaction between the aliphatic tail of bound $C_8H_{16}O$ and nearby H_2O molecules increase the entropy of the surrounding solvent structures to a greater extent than observed for the disruption of hydrogen bonds within bulk H_2O. Comparisons of in situ infrared spectra show that the extent of hydrogen bonding among intraporous H_2O molecules decreases significantly in the presence of $C_8H_{16}O$ bound to Ti atoms

in hydrophilic Ti-BEA; yet, there is no observable difference in the vibrational features associated with hydrogen-bonded H_2O within hydrophobic materials. These differences further suggest that $C_8H_{16}O$ disrupts stable clusters of H_2O present at proximate $(SiOH)_4$. Within defect-free Ti-BEA, however, intraporous H_2O molecules are not localized near Ti active sites and do respond to the formation of stable Ti-bound adducts. The interactions between the octyl chain of adsorbed $C_8H_{16}O$ and proximate solvent structures form a linear free energy relationship with the associated reorganization of H_2O that occurs during the epoxidation of 1-octene. Collectively, the data and interpretations presented here show that intentional changes in the chemical functionality of micropores can be used to control the interactions between proximate solvent structures and surface intermediates that are critical to both catalysis and adsorption processes.

8.2 Materials and Methods

8.2.1 Ti-BEA Synthesis

Ti-BEA-X, where X refers to the initial Si:Al ratio of the parent Al-BEA (X = 12.5 – 250), catalysts were prepared by post-synthetic modification of commercial Al-BEA samples. Al-BEA was treated in refluxing HNO_3 (Macron Chemicals, 68-70 wt. %, 20 cm^3 g^{-1}; *Caution: HNO_3 is extremely caustic and will readily cause a chemical burn and should be handled carefully*) with the intent to remove framework Al atoms by forming soluble $Al(NO_3)_3$. The solids were then recovered by vacuum filtration and washed with H_2O (17.8 MΩ · cm, 50 cm^3 g^{-1}) followed by heating at 5 K min^{-1} in flowing air (100 cm^3 min^{-1}) and holding at 823 K for 6 h to remove residual volatile and organic species and to produce Si-BEA-X. Materials produced in this manner possessed Si:Al ratios greater than 1400, as determined by energy dispersive X-ray fluorescence spectroscopy. Ti atoms were incorporated by combining a stirred suspension of Si-BEA-X in CH_2Cl_2 (Fisher Chemicals, Certified ACS Stabilized) with an appropriate amount of $TiCl_4$ (Sigma Aldrich, 99.9%; *Caution: $TiCl_4$ will violently react with moisture in the air to form HCl and should be handled carefully*) at reflux. All volatile components were then removed by rotary evaporation. The recovered solids were light-brown, and these materials were treated by heating in flowing air (100 cm^3 min^{-1}) at 5 K min^{-1} and holding at 823 K for 6 h, which produced bright white solid powders.

Ti-BEA-F was synthesized hydrothermally in fluoride media by adapting a previously published procedure.[22, 69] Briefly, tetraethylammonium fluoride (TEAF, Alfa Aesar, 97 wt. %) was

dissolved in deionized H_2O (18.2 MΩ · cm) in a polypropylene container and combined with titanium(IV) isopropoxide (TIPO, Sigma Aldrich, 99.999%) to produce a clear homogeneous solution. Tetraethylorthosilicate (TEOS, Sigma Aldrich, >98 wt. %) was then added dropwise over a period of one minute to this solution, which formed a bi-phasic mixture initially. The mixture was then stirred for 16 h to produce an opaque homogeneous solution. The cover was then removed to evaporate the ethanol and isopropanol that form through the hydrolysis of the TEOS and TIPO, respectively. To ensure that the alcohols were completely removed, an additional 15 wt. % of the calculated mass of the alcohols produced was evaporated from the solution. Subsequently, deionized H_2O was added to yield a gel with a final molar composition of 1 SiO_2:0.0033 TIPO: 0.56 TEAF: 7 H_2O. *Note: this synthesis procedure leads to MFI formation when the ethanol and isopropanol are not entirely evaporated.* This gel was then loaded into a Teflon-lined stainless-steel autoclave (Parr instruments, 45 cm^3) that contained 5% (relative to SiO_2 within the gel) dealuminated BEA (Zeolyst, Si:Al = 12.5, see above) as seeds to promote the formation of the BEA zeolite. This autoclave was then heated to 413 K while rotating (60 rpm) in a convection oven for 25 days. The resultant solids were recovered, washed with H_2O and dried for 16 h at 373 K. The dried solids were then heated in flowing air (100 $cm^3\ min^{-1}$) at 823 K (1 K min^{-1}) for 10 h to produce a bleached-white solid.

8.2.2 Ti-BEA Characterization

The Ti-BEA-X materials (created by post-synthetic modification) were used within a previous study,[21] and the detailed chemical and physical characterization of these materials has been described there.

The metal contents of Ti-BEA-X were quantified using energy dispersive X-ray fluorescence. Briefly, ~30 mg of Ti-BEA was loaded into a polypropylene sample holder (1 cm diameter) that was sealed with ultralene film. These samples were loaded into a spectrometer (Shimadzu, EDX-7000), whose sample chamber was purged with He (Airgas, Ultra-zero grade) prior to measurement. Measurements were taken between 0 – 30 keV (100 scans averaged), and the relative intensities of the fluorescence features of each element were used to calculate the percent, by mass, of each element within the sample. The density of $(SiOH)_4$ per unit cell ($[(SiOH)_4]$; Table 8.1) were estimated by taking the initial density of Al per unit cell and subtracting the difference due to the incorporation of Ti atoms.

Table 8.1. Ti metal loadings, band edge energies, estimated number of $(SiOH)_4$ per unit cell, and relative densities of hydrogen-bonded SiOH (ϕ_{IR}) for all Ti-BEA-X

Sample	Ti Content[a] (wt. %)	Band Edge Energy[b] (eV)	$[(SiOH)_4]^c$ (unit cell)$^{-1}$	ϕ_{IR}[d]
Ti-BEA-12.5	0.20	4.2	4.8	2.30
Ti-BEA-20	0.34	4.3	2.9	1.90
Ti-BEA-75	0.28	4.2	0.6	1.60
Ti-BEA-150	0.33	4.2	0.2	1.64
Ti-BEA-250	0.42	4.2	0.1	1.26
Ti-BEA-F	0.15	4.3	0	0.08

[a]Measured by EDRXF. [b]Determined from leading edge of Tauc plot from DRUV-vis. [c]Estimated based upon Al removed and Ti replaced within the parent Al-BEA-X. [d]Determined from FTIR spectra of dehydrated Ti-BEA-X.

X-ray diffractograms were collected using a diffractometer (Siemens/Bruker, D5000) with a Cu Kα radiation source (0.15418 nm) under ambient conditions. The similarities between the diffraction patterns for all Ti-BEA-X (Figure G1) suggests that all samples within this study possess the *BEA framework.

Band edge energies (E_g, Table 8.1) were measured by diffuse reflectance UV-vis spectroscopy. In short, samples were intimately ground with magnesium oxide (MgO; Sigma-Aldrich, 99.995%) in a 1:10 (Ti-BEA to MgO) by mass ratio. These samples were loaded into a Harrick diffuse-reflectance accessory and spectra were obtained using a spectrophotometer (Agilent, CARY5) with MgO used as the background. All Ti-BEA possess a single UV-vis absorbance feature around 4.5 eV (Figure G2) and band edges that are significantly greater than bulk TiO_2 (~3.2 eV),[51] which suggests that all Ti-BEA within this study contain highly-disperse Ti atoms and larger TiO_x aggregates.

Infrared (IR) spectra of dehydrated Ti-BEA-X were obtained using a custom-built transmission cell[200] coupled to a Fourier transform-infrared (FTIR) spectrometer (Bruker, Tensor 37) with a liquid-N_2-cooled HgCdTe detector. Catalysts were pressed into self-supporting disks (~60 mg) and placed within the transmission cell, which was assembled using CaF_2 windows and connected to a gas manifold. All materials were first heated to 573 K at 10 K min^{-1} and held for at least 3 h in flowing He (50 cm^3 min^{-1}; Airgas, Ultra-zero grade) with the intent to desorb water and volatile organics. Spectra (128 scans, 1 cm^{-1}) were obtained at 573 K in flowing He with an empty cell used as the background. Infrared spectra of dehydrated Ti-BEA (Figure G3; Section

G1) show distinct ν(O-H) and ν(Si-O-Si) overtone vibrational modes between 3300 – 3750 cm^{-1} and 1800 – 2000 cm^{-1}, respectively. The ratios of the integrated areas (Φ_{IR}) for ν(O-H) of $(SiOH)_4$ ($A_{(SiOH)_4}$) to those for ν(Si-O-Si) ($A_{(Si-O-Si)}$) provide measures of the relative density of $(SiOH)_4$ for each Ti-BEA

$$\Phi_{IR} = \frac{A_{(SiOH)_4}}{A_{(Si-O-Si)}} \tag{8.1}$$

Table 8.1 shows that values of ϕ_{IR} decrease monotonically with the increasing Si:Al ratio of the parent zeolite, which provides a quantitative measure of the density of $(SiOH)_4$ within Ti-BEA samples.

8.2.3 Isothermal Titration Calorimetry

The heat released upon $C_8H_{16}O$ or H_2O_2 titration onto Ti-BEA-X were measured using a calorimeter (TA Instruments, NanoITC) equipped with gold reference and sample cells (V = 176 μL). Titrations were carried out using a 50 μL ITC syringe at 313 K with a stirring rate of 250 rpm. For all measurements, the CH_3CN (Fisher Chemicals, HPLC grade) used was first dried over activated 3 Å molecular sieves for 3 days. The water content of the CH_3CN is estimated to be <0.1 μM,[350] based upon the use of molecular sieves. Briefly, ~30 mg of Ti-BEA-X was suspended in 500 μL of CH_3CN (*neat* or with 39 mM H_2O; 18.2 MΩ · cm) via sonication for 20 minutes and subsequently loaded into the sample cell of the calorimeter, while the reference cell was filled with *neat* CH_3CN for all measurements. The concentration of H_2O (39 mM) was chosen to facilitate comparisons between the free energies of $C_8H_{16}O$ adsorption and the free energies for C_8H_{16} epoxidation (Section 8.3.3).[21] Solutions of 1,2-epoxyoctane (Sigma Aldrich, 98%) or H_2O_2 (Fisher Chemicals, 30 wt. % in H_2O) in CH_3CN (*neat* or with 39 mM H_2O) were loaded into the titration syringe and the system was allowed to reach thermal equilibrium for up to 2 h prior to the start of the experiment. Injections of 1 μL were made at regular intervals (5-60 minutes) in each experiment, which allowed the system to return to the baseline heating rate prior to a subsequent injection. Data analysis was performed within NanoAnalyze (TA instruments).

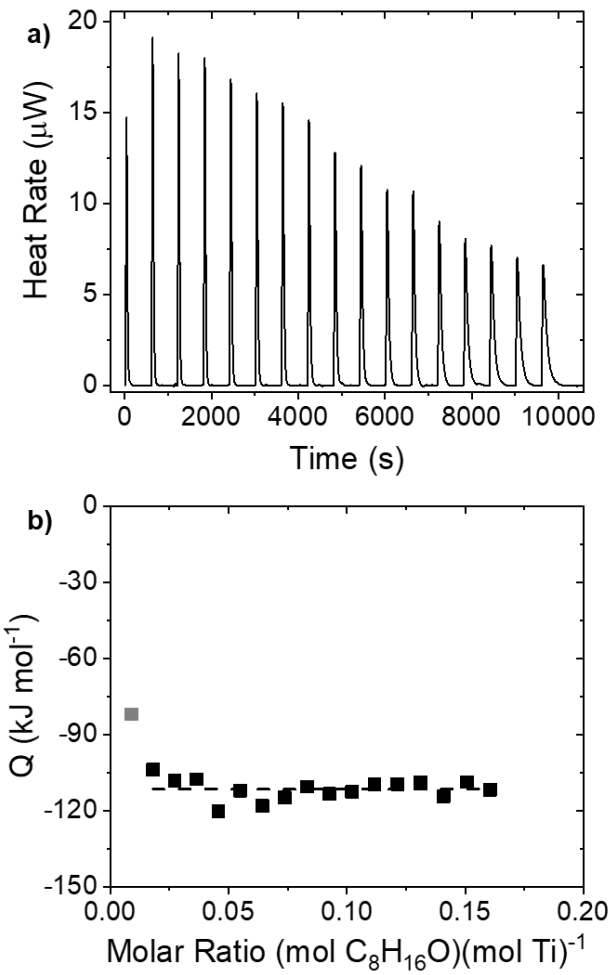

Figure 8.1. Representative (a) real-time ITC thermogram for the titration of Ti-BEA-75 with $C_8H_{16}O$ (5 mM $C_8H_{16}O$, anhydrous CH_3CN), and (b) corresponding heat released (Q) as a function of $C_8H_{16}O$-to-Ti molar ratio. The transparent point was omitted from the calculation of the adsorption enthalpy (denoted by dashed line), due to common errors associated with early injections.

Figures 8.1a and 8.1b show an exemplary real-time ITC thermogram and the corresponding integrated heat (Q) released, respectively, for the adsorption of $C_8H_{16}O$ onto Ti-BEA-75 in anhydrous CH_3CN. Adsorption enthalpies (ΔH_{Ads}) were determined by averaging the integrated heats for $C_8H_{16}O$ (or H_2O_2) titration onto Ti-BEA-X at low coverages (<0.2 (mol titrant)(mol Ti)$^{-1}$), and reported uncertainties in ΔH_{Ads} were calculated from a single standard deviation among these points. Values of the adsorption entropies (ΔS_{Ads}) were calculated by fitting a single-site binding model (Section G2.1) to full-coverage integrated heat data (Section 8.3.1) while constraining values of ΔH_{Ads} to equal those determined from low-coverage adsorption isotherms. Liquid-phase adsorption within confined environments is complex and reflects charge transfer

between the adsorbate and the adsorption site, dispersive interactions with the pore walls, and the solvent reorganization required upon adsorption. The model used to determine values of ΔS_{Ads} (Section G2.1) assumes that all active sites are equivalent, and by extension that all adsorption events involve the same degree of charge transfer, dispersive interactions, and solvent reorganization. These assumptions are necessary to determine values of ΔS_{Ads}, yet the Ti-BEA materials contain Ti active sites with a distribution of proximities from silanol nests and resulting hydrogen bonding interactions. Consequently, differences in ΔS_{Ads} (and ΔH_{Ads}) values across this series of Ti-BEA-X reflect how systematic changes in the physical properties of these materials affect these ensemble-averaged values. These full-coverage adsorption isotherms were obtained by combining the integrated heat data from low-coverage (<0.2 (mol $C_8H_{16}O$)(mol Ti)$^{-1}$) experiments with those from high-coverage (0.2 – 2 (mol $C_8H_{16}O$)(mol Ti)$^{-1}$). All ITC integrated heat data were corrected for the heats of mixing at infinite dilution (see Section G2.2 for details).

8.2.4 In Situ Attenuated Total Reflection Infrared Spectroscopy and Modulation Excitation

Attenuated total reflectance infrared (ATR-IR) spectroscopy was used to characterize the vibrational structure of H_2O located within the pores of Ti-BEA samples with different densities of $(SiOH)_4$. A given Ti-BEA (~30 mg) was first dispersed into CH_3CN (~1 cm^3) via sonication and was drip coated onto a ZnSe cylindrical internal reflection element (IRE; International Crystal Labs). The catalyst-coated IRE was loaded into an ATR flow cell (Axiom, TNL-120), which was mounted onto a Fourier-transform infrared spectrometer (Bruker, Vertex 70). Two high-pressure piston pumps (SSI, Series 1) were used to introduce H_2O and CH_3CN solutions and were controlled using LabView. The cell was heated by a resistive heating cartridge placed within the wall of the cell, which was controlled by an electronic temperature controller (Watlow, EZ-Zone). IR spectra (128 scans, 4 cm^{-1} resolution) were obtained continuously during the modulation of H_2O. Background spectra were obtained in *neat* CH_3CN (1 cm^3 min^{-1}, 313 K).

Modulation excitation spectroscopy (MES) uses a periodic stimulation and continuous acquisition of spectra throughout time to obtain time-resolved structural information with high signal-to-noise ratios. Time domain responses are converted to the phase domain, and the spectral changes that occur at the frequency of the applied stimulation are extracted using a phase sensitive detection (PSD) method described by the following equation:

$$A_k(\varphi_k^{PSD}) = \frac{2}{T}\int_0^T A(t)\sin(k\omega t + \varphi_k^{PSD})dt \quad (8.2)$$

where *A(t)* and $A_k(\varphi_k^{PSD})$ are time- and phase- domain response of the active species respectively, *T* is the length of a period, ω is the demodulation index, *k* is the demodulation index (with value of one), and φ_k^{PSD} is the user-defined phase demodulation angle. The application of the MES-PSD technique to FTIR spectra of intermediates on catalytic surfaces greatly increases the signal to noise ratio, suppresses the spectral contributions of static (i.e., spectator) species, and reveals high quality spectra containing contributions only of species that change during modulation.[114]

The concentration of H_2O (0 – 5.5 M) within CH_3CN was modulated sinusoidally by controlling the flow rate of liquid through the two piston pumps such that the set points of the pumps were changed in a step-wise manner every 0.5 s to approximate a sine wave with the desired period. The period length was determined by H_2O cutoff experiments (i.e., switch to anhydrous CH_3CN from 5.5 M H_2O), where the time needed to achieve a ~95% attenuation of H_2O vibrational features was used as the period length for modulations. The total flow rate was kept at 1 cm^3 min^{-1} by setting the two piston pumps perfectly out of phase with one another. Spectra (4 cm^{-1} resolution, 128 scans; Figure G5) were acquired continuously over 3 hours, averaged to a single period, and subsequently converted to the phase domain using equation 1 (Figure G6). The concentration of 5.5 M H_2O was chosen for ATR-IR experiments, because the lower concentrations of 39 mM used in ITC experiments (Section 8.3.1) and in C_8H_{16} epoxidation reactions (Section 8.3.3) resulted in IR spectra that had very low signal-to-noise ratios (less than 2 – 3). Turnover rates for C_8H_{16} epoxidation in Ti-BEA do not depend on the concentration of H_2O at these conditions,[21] and therefore, the thermodynamics of $C_8H_{16}O$ adsorption and kinetics of C_8H_{16} epoxidation (Section 8.3.3) are unlikely to differ at the concentrations of H_2O used for ATR-IR measurements. These proposals are supported by the similarities between measured values of ΔH_{Ads} for $C_8H_{16}O$ onto Ti-BEA-12.5 within 39 mM H_2O in CH_3CN (-95 ± 2 kJ mol^{-1}) and in 5.5 M H_2O in CH_3CN (-91 ± 4 kJ mol^{-1}).

Phase resolved spectra were then subjected to multivariate curve resolution-alternating least squares (MCR-ALS) to extract the spectral contributions of independent species.[351] Singular value decomposition show that the combination of two independent species fully describes the phase resolved spectra in all cases. Two sine wave functions were used as initial guesses for time

dependent concentrations of species, and the spectra were constrained to solve for positive features. The MATLAB program iteratively solved for spectra and surface coverages until the convergence criteria were met and the sum of residuals was less than 10^{-6}. The resulting spectra were normalized to the most intense ν(O-H) feature using OriginPro9 software. In all cases, greater than 95% of the variance of the phase-resolved spectra was described by a single component, which implies this component represents the H_2O that enters the pores of Ti-BEA during the modulation experiments.

8.3 Results and Discussion

8.3.1 Effects of Proximate Solvent Structure on Adsorbate Stability

Isothermal titration calorimetry was used to understand how the presence, proximity, and density of $(SiOH)_4$ affects the stability of the $C_8H_{16}O$ bound to Ti active sites. Figures 8.2a and 8.2b show the integrated heats (Q) released upon titration of Ti-BEA with $C_8H_{16}O$ within aqueous CH_3CN (39 mM H_2O) and anhydrous CH_3CN, respectively. In all cases, values of Q remain constant at low coverages (<0.2 (mol $C_8H_{16}O$)(mol Ti)$^{-1}$), which suggests that these values represent the isosteric adsorption enthalpies (ΔH_{Ads}) at differential coverage. Table 8.2 shows that values of ΔH_{Ads} are 19 kJ mol^{-1} larger on the most hydrophobic Ti-BEA (Ti-BEA-F) than on the most hydrophilic material (Ti-BEA-12.5) when a small amount of H_2O is present ($\Delta H_{Ads,Aq}$; Table 8.2; Figure 8.2a). In contrast, values of ΔH_{Ads} for all T-BEA are indistinguishable within anhydrous CH_3CN ($\Delta H_{Ads,Anh}$; Table 8.2; Figure 8.2b). These comparisons suggest that silanol nests ($(SiOH)_4$) present within Ti-BEA do not influence the stability of surface-bound intermediates in the absence of H_2O molecules. The presence of H_2O, however, is required to mediate the interaction between $(SiOH)_4$ and Ti-bound species, which is observed experimentally by measurable changes in $\Delta H_{Ads,Aq}$.

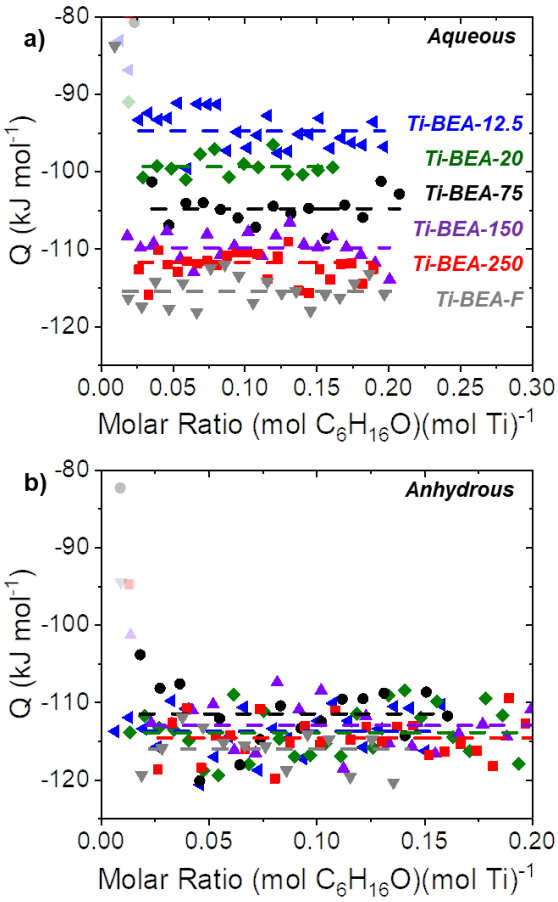

Figure 8.2. Heats released upon $C_8H_{16}O$ titration onto Ti-BEA as a function of $C_8H_{16}O$:Ti molar ratio in (a) aqueous CH_3CN (39 mM H_2O) and (b) anhydrous CH_3CN. Dashed lines represent the averaged values of ΔH_{Ads}. The transparent points were omitted from calculations of ΔH_{Ads}, due to common errors associated with early ITC injections. The colored symbols correspond to: Ti-BEA-12.5 (◀), Ti-BEA-20 (♦), Ti-BEA-75 (●), Ti-BEA-150 (▲), Ti-BEA-250 (■), and Ti-BEA-F (▼).

Figures 8.3a and 8.3b show representative full-coverage isotherms for the titration of Ti active sites with $C_8H_{16}O$ over Ti-BEA-12.5 and Ti-BEA-F, respectively. At low coverages (<0.2 (mol $C_8H_{16}O$)(mol Ti)$^{-1}$), the heats released upon incremental titration of Ti atoms are nearly constant (*vide infra*). As additional $C_8H_{16}O$ is introduced, the heat released per injection decreases with an inflection point centered around a molar ratio of $C_8H_{16}O$ to Ti equal to one, which indicates that each Ti atom binds an average of one $C_8H_{16}O$ molecule in the limit of full saturation.[352] In the presence of H_2O, values of ΔS_{Ads} are 75 J mol^{-1} K^{-1} more positive in Ti-BEA-12.5 than Ti-BEA-F ($\Delta S_{Ads,Aq}$; Table 8.1). Under anhydrous conditions, however, values of ΔS_{Ads} do not depend on the density of $(SiOH)_4$ within Ti-BEA ($\Delta S_{Ads,Anh}$; Table 8.1). The dependence of ΔS_{Ads} on the density of $(SiOH)_4$ supports the interpretation developed based upon changes in ΔH_{Ads} (see above)

in the presence of H_2O: H_2O molecules must restructure to accommodate the formation of surface species. Quantifying the interactions between H_2O that is stabilized at $(SiOH)_4$ and Ti-bound surface species and understanding what these changes represent molecularly requires a rigorous thermodynamic framework that deconstructs how the stability of the bound complex and the reactant states are affected by the presence and proximity of $(SiOH)_4$.

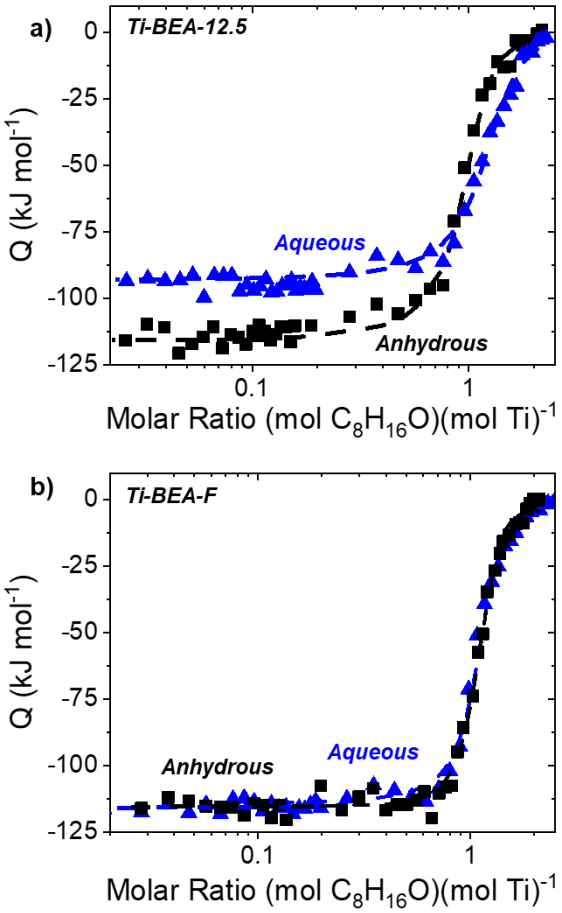

Figure 8.3. Heats released upon $C_8H_{16}O$ titration onto (a) Ti-BEA-12.5 and (b) Ti-BEA-F as a function of $C_8H_{16}O$:Ti molar ratio in aqueous CH_3CN (39 mM H_2O; ▲) and anhydrous CH_3CN (■). Dashed lines represent fits of a single-site independent binding model (Section G2). Values of *Q* above and below ~0.2 (mol $C_8H_{16}O$)(mol Ti)$^{-1}$ were collected from independent experiments and combined to estimate values of ΔH_{Ads} and ΔS_{Ads}.

As depicted in Scheme 8.1, the measured free energies of adsorption (ΔG_{Ads}) represent the difference in thermodynamic stability of the initial and final states of the adsorption process

$$\Delta G_{Ads} = G_{C_8H_{16}O-Ti} - G_{C_8H_{16}O} - G_{Ti} \tag{8.3}$$

where G_j represents the free energy of species j (e.g., adsorbed $C_8H_{16}O$). Analogous equalities describe the quantities that determine ΔH_{Ads} and ΔS_{Ads}. The free energies of each of these species depend on specific interactions at solid-liquid interfaces, which can be described as excess free energy contributions (${G_j}^{\varepsilon}$).

$$\Delta G_{Ads}|_{Ti-BEA-X} = \left({G_{C_8H_{16}O-Ti}}^{o} + {G_{C_8H_{16}O-Ti}}^{\varepsilon}\right) - \left({G_{C_8H_{16}O}}^{o} + {G_{C_8H_{16}O}}^{\varepsilon}\right) - \left({G_{Ti}}^{o} + {G_{Ti}}^{\varepsilon}\right) \quad (8.4)$$

Table 8.2. Enthalpies[a] and entropies[b] of adsorption of $C_8H_{16}O$ onto Ti-BEA-X within aqueous CH_3CN (39 mM H_2O; $\Delta H_{Ads,Aq}$, $\Delta S_{Ads,Aq}$) and anhydrous CH_3CN ($\Delta H_{Ads,Anh}$, $\Delta S_{Ads,Anh}$), excess enthalpies and entropies of adsorption of $C_8H_{16}O$ into Ti-BEA-X (${H_{C_8H_{16}O-Ti}}^{\varepsilon}$ abd ${S_{C_8H_{16}O-Ti}}^{\varepsilon}$), and enthalpies of H_2O_2 adsorption-and-activation ($\Delta H_{Ads,H_2O_2}$).[a,c]

Sample	$\Delta H_{Ads,Aq}$ (kJ mol^{-1})	$\Delta S_{Ads,Aq}$ (J mol^{-1} K^{-1})	$H_{C_8H_{16}O-Ti}$ (kJ mol^{-1})	${S_{C_8H_{16}O-Ti}}^{\varepsilon}$ (J mol^{-1} K^{-1})	$\Delta H_{Ads,Anh}$ (kJ mol^{-1})	$\Delta S_{Ads,Anh}$ (J mol^{-1} K^{-1})	$\Delta H_{Ads,H_2O_2}$ (kJ mol^{-1})
Ti-BEA-12.5	-95 ± 2	-240 ± 10	19 ± 4	75 ± 14	-114 ± 3	-296 ± 11	-36 ± 6
Ti-BEA-20	-99 ± 3	-250 ± 12	15 ± 5	65 ± 15	-118 ± 3	-300 ± 20	-42 ± 8
Ti-BEA-75	-106 ± 2	-279 ± 8	8 ± 4	36 ± 12	-114 ± 4	-301 ± 15	-39 ± 8
Ti-BEA-150	-110 ± 4	-300 ± 12	4 ± 5	15 ± 15	-113 ± 2	-299 ± 15	-40 ± 4
Ti-BEA-250	-112 ± 4	-312 ± 11	2 ± 5	3 ± 14	-116 ± 4	-292 ±11	-33 ± 6
Ti-BEA-F	-114 ± 4	-315 ± 10	0 ± 4	0 ± 10	-115 ± 3	-300 ± 15	-33 ± 4

[a]Values of ΔH_{Ads} were determined by averaging the integrated heats obtained from low-coverage (<0.2 (mol $C_8H_{16}O$)(mol Ti)$^{-1}$) ITC experiments. [b]Values of ΔS_{Ads} were determined by fitting the single-site independent binding model (Section G2.1) to the combined low- and high-coverage integrated heat data, while constraining the value of ΔH_{Ads} to that determined from low-coverage experiments. [c]H_2O_2 titrations give heats that reflect both adsorption of H_2O_2 and its activation to form Ti-OOH species.[11, 21, 54, 199, 275]

where $\Delta G_{Ads}|_{Ti-BEA-X}$ is the free energy of $C_8H_{16}O$ adsorption onto Ti-BEA-X and ${G_j}^{o}$ is the standard-state Gibbs free energy of species *j*, which is selected to be those for the system with the least-significant hydrogen bonding (i.e., ${G_j}^{o}$ reflects the stability of species within Ti-BEA-F).

$$\Delta G_{Ads}|_{Ti-BEA-F} = {G_{C_8H_{16}O-Ti}}^{o} - {G_{C_8H_{16}O}}^{o} - {G_{Ti}}^{o} \quad (8.5)$$

The value of ${G_{C_8H_{16}O}}^{\varepsilon}$ is negligible, because the activity of the fluid-phase $C_8H_{16}O$ is not affected by the density of $(SiOH)_4$ within the pores of Ti-BEA. Consequently, differences in the adsorption free energies of $C_8H_{16}O$ measured among a given Ti-BEA-X and Ti-BEA-F ($\Delta\Delta G_{Ads}$)

reflect only differences in the excess free energies of adsorbed $C_8H_{16}O$ and the solvent-saturated Ti sites prior to $C_8H_{16}O$ adsorption

$$\Delta\Delta G_{Ads} = \Delta G_{Ads}|_{Ti-BEA-X} - \Delta G_{Ads}|_{Ti-BEA-F} = \ {G_{C_8H_{16}O-Ti}}^{\varepsilon} - {G_{Ti}}^{\varepsilon} \quad (8.6)$$

Deconvoluting the individual contributions of ${G_{C_8H_{16}O-Ti}}^{\varepsilon}$ and ${G_{Ti}}^{\varepsilon}$ and to show how these depend on [$(SiOH)_4$] requires a calorimetric measurements of a separate, but fundamentally related, adsorption process.

Titrations of Ti atoms with H_2O_2 involves the adsorption and activation of H_2O_2 to form the Ti-OOH intermediates that form and react with alkenes during epoxidations.[11, 21, 54, 85, 121, 164, 199, 240, 275] Accordingly, the measured free energies of H_2O_2 adsorption-and-activation ($\Delta G_{Ads,H_2O_2}$) are given by

$$\Delta G_{Ads,H_2O_2} = ({G_{Ti-OOH}}^{o} + {G_{Ti-OOH}}^{\varepsilon}) - \left({G_{H_2O_2}}^{o} + {G_{H_2O_2}}^{\varepsilon}\right) - ({G_{Ti}}^{o} + {G_{Ti}}^{\varepsilon}) \quad (8.7)$$

where nomenclature follows that defined above. Values of $\Delta H_{Ads,H_2O_2}$ (Table 1) do not depend on [$(SiOH)_4$], which suggests that either ${H_{Ti-OOH}}^{\varepsilon}$ and ${H_{Ti}}^{\varepsilon}$ are coincidentally equal and opposite in magnitude or that neither vary with [$(SiOH)_4$], which seems more probable across the set of six materials.[353] The apparent independence of ${H_{Ti-OOH}}^{\varepsilon}$ with [$(SiOH)_4$] reflects the tendency for Ti-OOH to donate and accept hydrogen bonds and spontaneously stabilize H_2O,[321-322] which obviates the differences introduced by the presence of H_2O held at nearby $(SiOH)_4$. Prior to titration with $C_8H_{16}O$, titanium atoms in all Ti-BEA are coordinated to solvent molecules (i.e., CH_3CN), which suggests that the initial state of the Ti active sites are not affected by proximate H_2O in materials with varying [$(SiOH)_4$]. Consequently, the measured values of $\Delta H_{Ads,H_2O_2}$ suggest that $\Delta\Delta G_{Ads}$ among Ti-BEA materials reflect only the manner in which values of ${G_{C_8H_{16}O-Ti}}^{\varepsilon}$ depend on [$(SiOH)_4$] and the H_2O clusters that nearby defects stabilize. Monte Carlo simulations for H_2O adsorption into silicalite-1 with varying densities of $(SiOH)_4$ (0.125 – 4 (unit cell)$^{-1}$) show that the low-coverage heats of adsorption for H_2O onto $(SiOH)_4$ are independent of $(SiOH)_4$ density.[354] Therefore, measured changes in ${G_{C_8H_{16}O-Ti}}^{\varepsilon}$ do not reflect differences in the stability of H_2O within different Ti-BEA-X; rather, values of ${G_{C_8H_{16}O-Ti}}^{\varepsilon}$ reflect the interactions between $C_8H_{16}O$

and H_2O stabilized at $(SiOH)_4$, where the magnitude of these values depends critically on the likelihood that a $(SiOH)_4$ is near the Ti active sites. The apparent independent behavior between Ti atoms and nearby $(SiOH)_4$ within hydrophilic Ti-BEA under anhydrous conditions may be attributed to the non-polar chemical functionality of adsorbed $C_8H_{16}O$ or manifests from the molecular length of $C_8H_{16}O$. Adsorbates that are sufficiently long or possess hydrogen bond-donating or -accepting functional groups may interact with nearby $(SiOH)_4$, even within anhydrous conditions, such that the thermodynamic stability of these adsorbates may possess a measurable dependence on $[(SiOH)_4]$. In short, the differences in the thermodynamics of adsorption directly report on the outer-sphere interactions between adsorbed species and the extended surface of the zeolite that are mediated by the solvent structures confined within these voids.

8.3.2 Spectroscopic Evidence for the Disruption of Hydrogen Bonds

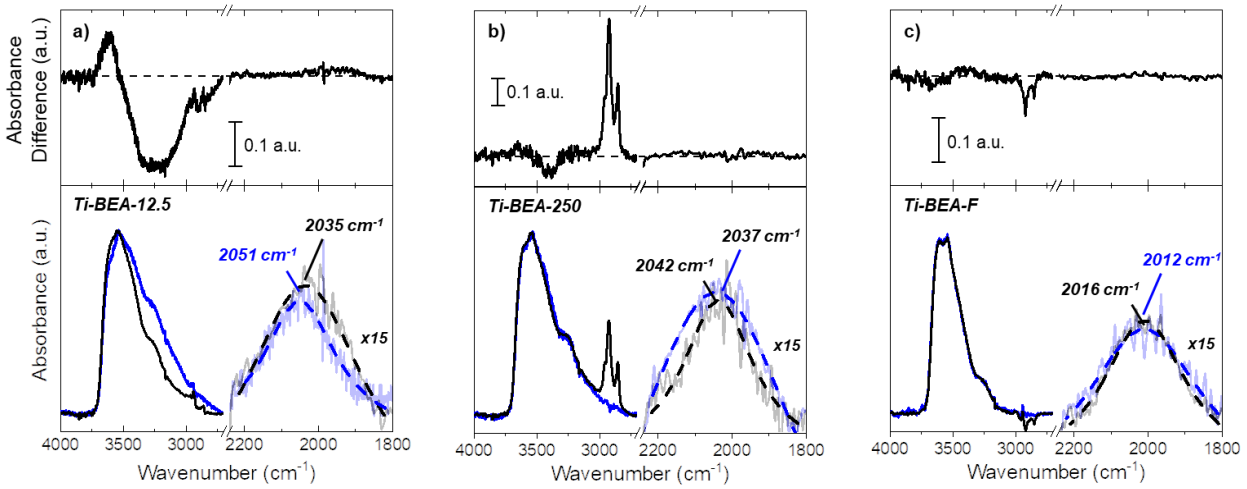

Figure 8.4. Infrared spectra obtained through multivariate analysis of modulation excitation experiments (Section 2.4) of H_2O in CH_3CN (0 – 5.5 M H_2O; blue) and in a solution of $C_8H_{16}O$ in CH_3CN (0.1 M $C_8H_{16}O$, 0 – 5.5 M H_2O; black) over: a) Ti-BEA-12.5, b) Ti-BEA-250, and c) Ti-BEA-F. All spectra are normalized to the most-intense ν(O-H) feature (~3540 cm^{-1}) and have a resolution of 5 cm^{-1}. The region between 1800 – 2250 cm^{-1} have been scaled by a factor of 15. The dashed curves represent Lorentzian fits, which were used to quantify the peak center of the combination band. The top spectra for each panel is the difference spectra that represents that changes in the vibrational features for H_2O that result from the presence of $C_8H_{16}O$.

In situ attenuated total reflectance-infrared spectroscopy (ATR-IR) in conjunction with modulation excitation provides direct evidence for the interactions between confined H_2O and hydrophobic surface species (i.e., adsorbed $C_8H_{16}O$). Figure 8.4 shows the extracted spectra of intermediates in Ti-BEA-12.5 (Figure 8.4a), Ti-BEA-250 (Figure 8.4b), and Ti-BEA-F (Figure

8.4c), during modulation of H_2O in the presence and absence of $C_8H_{16}O$; these features reflect the spectral contributions that change because H_2O molecules enter the pores of each Ti-BEA. The corresponding difference spectra are shown in the top panels within Figure 8.4 to more-clearly depict those features that change in response to adsorbed $C_8H_{16}O$ and to facilitate comparisons among different Ti-BEA samples. The absorbance features at ~2050 cm^{-1} and between 3000-3750 cm^{-1} correspond to the combination (bending+libration) mode of H_2O molecules and the stretching of hydroxyl groups (ν(O-H)), respectively.[355] Features near 2950 cm^{-1} correspond to ν(C-H) of the methyl and methylene units of $C_8H_{16}O$.[356] Within Ti-BEA-250 there is a prominent ν(C-H) in the presence of $C_8H_{16}O$, which likely arises from small differences in the concentration of $C_8H_{16}O$ in the two solutions during modulation of H_2O. Notably, this cannot be attributed to the expulsion of $C_8H_{16}O$ from Ti-BEA due to the introduction of H_2O, as this would result in a negative absorbance feature.

Coordination of the epoxide to framework Ti atoms results in distinct changes in the structure of the aqueous solvent, and the extent of these differences depend on the density of silanol groups in Ti-BEA and their proximity to Ti sites. In Ti-BEA-12.5, the presence of $C_8H_{16}O$ leads to a significant loss in intensity of ν(O-H) around 3250 cm^{-1} and a simultaneous increase in intensity near 3700 cm^{-1}, which are consistent with expectations for spectral differences caused by a decrease in the average number of hydrogen bonds among H_2O molecules near active sites. Moreover, the combination band (~2050 cm^{-1}) shifts to lower wavenumbers, which reflects lower barriers for librations of individual H_2O molecules within their environments, another indication of diminished hydrogen bonding.[355] In contrast, spectra obtained from hydrophobic Ti-BEA-250 (Figure 8.4b) and Ti-BEA-F (Figure 8.4c) do not show any differences in features corresponding to ν(O-H) or to combination modes for H_2O associated with the presence of adsorbed $C_8H_{16}O$. These similarities suggest that the small amounts of H_2O located within the pores do not interact with epoxide bound to Ti atoms, presumably because H_2O molecules are not stabilized as clusters near the Ti sites by interactions with $(SiOH)_4$ groups. This interpretation is further supported by the reduced intensity of the ν(O-H) band at lower wavenumbers (~3250 cm^{-1}) of both Ti-BEA-250 and Ti-BEA-F, in comparison to Ti-BEA-12.5, which indicates that the H_2O within these hydrophobic materials possess fewer hydrogen bonds than those within Ti-BEA-12.5. Notably, the spectrum of H_2O within Ti-BEA-250 shows slightly greater absorbance near 3250 cm^{-1} that that of Ti-BEA-F and suggests a greater extent of hydrogen bonding likely caused by residual

silanol nests or defects introduced by the post-synthetic modification procedure. Despite the presences of these surface functions, the vibrational modes H_2O are not affected by the presence of $C_8H_{16}O$, which demonstrates that H_2O molecules within Ti-BEA-250 are too far from active sites to be influenced by adsorption of $C_8H_{16}O$ to Ti atoms. Spectra from the clean ZnSe internal reflection element (Figure G7) exhibit no change in ν(O-H) or shift in the combination band of H_2O in the presence of $C_8H_{16}O$, which further demonstrates the differences within spectra from Ti-BEA samples arise from the interactions among H_2O and $C_8H_{16}O$ at the framework Ti atoms within the zeolites and not from the bulk solution.

8.3.3 Linear Free Energy Relationships Describe Solvent Reorganization at the Solid-Liquid Interface

Calorimetric and spectroscopic results strongly suggest that molecular interactions between the hydrophobic chain of adsorbed $C_8H_{16}O$ and nearby clusters of H_2O molecules stabilized by $(SiOH)_4$ structures cause $H_{C_8H_{16}O-Ti}{}^{\varepsilon}$ and $S_{C_8H_{16}O-Ti}{}^{\varepsilon}$ values (Table 8.2) to depend strongly on the density of $(SiOH)_4$ in Ti-BEA (Table 8.1). These differences indicate that $C_8H_{16}O$ bound to Ti atoms within hydrophobic Ti-BEA materials (Ti-BEA-F, Ti-BEA-250) interact primarily with intraporous CH_3CN, because the nearly-pristine siloxane pores contain negligible amounts of H_2O near Ti atoms. In contrast, the more hydrophilic Ti-BEA materials (e.g., Ti-BEA-12.5) contain multiple $(SiOH)_4$ groups per unit cell which anchor clusters of H_2O near Ti active sites. These H_2O clusters (and nearby CH_3CN molecules) restructure to accommodate adsorbed $C_8H_{16}O$, which incurs an enthalpic penalty from the disruption of hydrogen bonds (i.e., $\Delta H_{Ads,Aq}$ increases with $[(SiOH)_4]$ due to differences in $H_{C_8H_{16}O-Ti}{}^{\varepsilon}$; Table 8.1). These solvent-adsorbate interactions result also in large positive values of $S_{C_8H_{16}O-Ti}{}^{\varepsilon}$ generated by the reorganization of confined H_2O clusters.

The changes in $H_{C_8H_{16}O-Ti}{}^{\varepsilon}$ and $S_{C_8H_{16}O-Ti}{}^{\varepsilon}$ that increase with $[(SiOH)_4]$ (Table 8.1) are qualitatively consistent with the expected enthalpy and entropy changes associated with disrupting hydrogen bonds within bulk H_2O. The breaking of a single hydrogen bond within liquid water by interaction with a non-polar solute increases the enthalpy of the system by ~8 kJ mol^{-1} and results in a concomitant increase in entropy of ~20 J mol^{-1} K^{-1}.[326-327] Figure 8.5 shows the relationships between excess enthalpies and the commensurate excess entropies that describe the restructuring of H_2O clusters to accommodate C_8H_{16} epoxidation transition states ($H^{\ddagger,\varepsilon}$ and $S^{\ddagger,\varepsilon}$) and adsorbed

$C_8H_{16}O$ ($H_{C_8H_{16}O-Ti}{}^{\varepsilon}$ and $S_{C_8H_{16}O-Ti}{}^{\varepsilon}$) together with the corresponding enthalpy-entropy compensation effects for hydrogen bonding in bulk water. Water confined within nanopores (e.g., within Ti-BEA) possess significantly lower entropies than bulk H_2O,[323-325] which suggests that disruption of confined H_2O structures should result in a larger entropy gain and smaller enthalpy cost relative to that observed in bulk H_2O. The greater entropic compensation for the disruption of H_2O confined within Ti-BEA results from the reduced dimensionality of the H_2O molecules. These micropores (~0.65 Å diameter) cannot accommodate the tetrahedral coordination and three-dimensions of hydrogen-bonding that H_2O molecules possess in bulk solutions. Therefore, the entropy gained upon disrupting these hydrogen-bonding interactions is greater within Ti-BEA, because fewer hydrogen bonds must be broken to destabilize (or "free") each H_2O molecule.

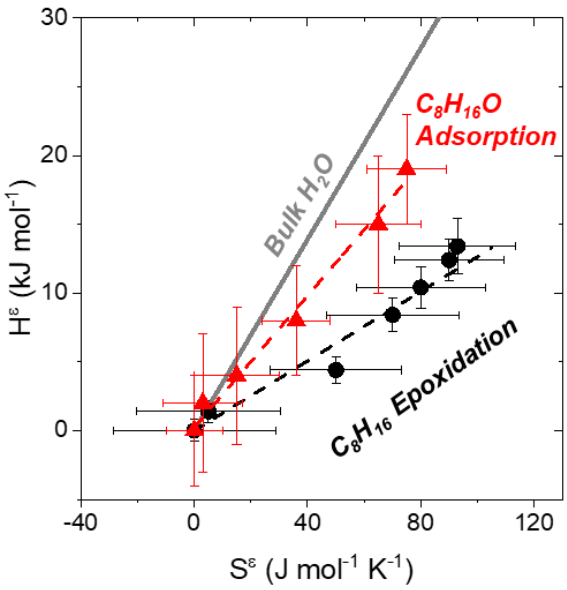

Figure 8.5. Excess enthalpies as a function of excess entropies for C_8H_{16} epoxidation transition states (●; i.e., $H^{\ddagger,\varepsilon}$ and $S^{\ddagger,\varepsilon}$) and $C_8H_{16}O$-Ti (▲; i.e., $H_{C_8H_{16}O-Ti}{}^{\varepsilon}$ and $S_{C_8H_{16}O-Ti}{}^{\varepsilon}$). The dashed lines represent linear fits to the data and the bold gray line represents the enthalpy-entropy compensation effect that describes changes in hydrogen bonding within bulk H_2O (e.g., by solvating a non-polar solute).[326]

Figures 8.6a and 8.6b show that the excess enthalpies and entropies for $C_8H_{16}O$ epoxidation transition states ($H^{\ddagger,\varepsilon}$ and $S^{\ddagger,\varepsilon}$; 0.1 mM C_8H_{16}, 0.01 M H_2O_2, 0.039 M H_2O, in CH_3CN, 313 K)[21] increase linearly as a function of the respective excess enthalpies and entropies for $C_8H_{16}O$ adsorption ($H_{C_8H_{16}O-Ti}{}^{\varepsilon}$ and $S_{C_8H_{16}O-Ti}{}^{\varepsilon}$). These values exhibit a strong linear free energy

relationship (LFER) that suggests that the outer-sphere interactions that affect the stability of C_8H_{16} epoxidation transition states are chemically similar to those that affect $C_8H_{16}O$ adsorption.[75, 357] Linear free energy relationships for elementary steps in catalysis commonly follow the form[357]

$$\Delta G^{\ddagger} = \alpha \cdot \Delta G_{Ads} + \beta \tag{8.8}$$

where $\Delta G^{\ddagger}$ describes the activation free energy for an elementary step (e.g., reaction of Ti-OOH with an alkene), ΔG_{Ads} is the free energy change corresponding to the step, α is the similarity (or transmission) coefficient, and β is a constant representing an intrinsic activation barrier for the elementary step. The LFERs shown in Figure 8.6 describe the endothermic changes in solvent structure (see comparisons within Table 8.2) that are associated with the perturbation of H_2O proximate to Ti active sites upon formation of the C_8H_{16} epoxidation transition states or upon $C_8H_{16}O$ adsorption. These comparisons between thermodynamic and kinetic parameters (i.e., with similarity coefficients that approach unity) show that the differences in hydrogen bonding within nearby H_2O clusters affect the stability of adsorbed $C_8H_{16}O$ in ways that strongly resemble their influence on the stability of 1-octene epoxidation transition states, because the values of the excess contributions of these specific interactions are proportional (e.g.,, $H_{C_8H_{16}O-Ti}{}^{\varepsilon} \sim H^{\ddagger,\varepsilon}$) and similar in Ti-BEA.

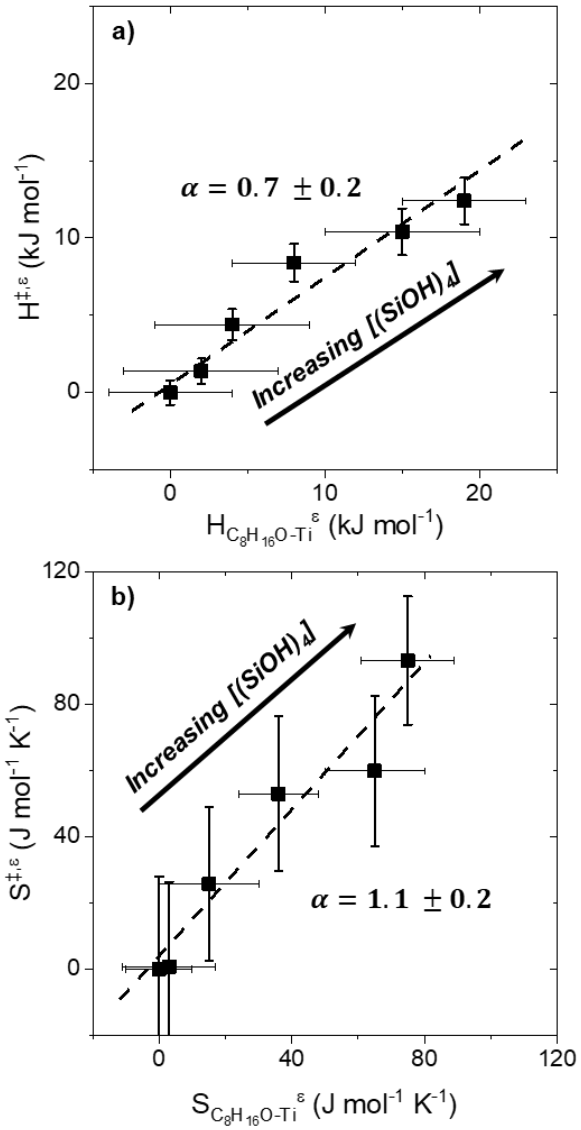

Figure 8.6. (a) Excess enthalpies and (b) excess entropies for C_8H_{16} epoxidation (($H^{\ddagger,\varepsilon}$ and $S^{\ddagger,\varepsilon}$) as a function of $C_8H_{16}O$ adsorption ($H_{C_8H_{16}O-Ti}{}^{\varepsilon}$ and $S_{C_8H_{16}O-Ti}{}^{\varepsilon}$,) over Ti-BEA-X, respectively. The bold gray line represents parity and the dashed lines are linear fits to the data, where the slope of these fits are indicated by the values of α.

In short, the analysis and interpretation of results show that the excess free energies of surface intermediates critical to catalysis and adsorption depend intimately on the presence, density, and proximity of hydrogen-bonded solvent structures, which underscores the complexity of solid-liquid interfaces. These findings suggest that interactions between confined solvent structures and reactive species at proximate active sites can be used to change the thermodynamics of adsorption and the kinetics of catalytic reactions. Ongoing work seeks to elucidate how the

chemical and physical properties of the pore walls (e.g., zeolite topology) impact the structuring of solvent molecules and the ensuing interactions with surface intermediates.

8.4 Conclusions

The thermodynamic stability of surface intermediates critical to catalysis and adsorption depend intimately on the presence, proximity, and density of $(SiOH)_4$ near active sites. Within aqueous solutions of acetonitrile, silanol nests in pores of Ti-BEA nucleate hydrogen-bonded clusters of H_2O that must restructure to accommodate surface intermediates bound to nearby active sites. The reorganization of the solvent results in adsorption enthalpies and entropies for $C_8H_{16}O$ that are 19 and 75 kJ mol^{-1} more-positive in Ti-BEA that contain ~5 $(SiOH)_4$ $(unit\ cell)^{-1}$ than those for defect-free materials. These differences, however, become negligible under anhydrous conditions that fill micropores only with CH_3CN solvent molecules that restructure to similar extents for BEA samples with all $(SiOH)_4$ densities examined: enthalpies and entropies for $C_8H_{16}O$ adsorption are similar across all Ti-BEA samples in the absence of H_2O. The adsorption of $C_8H_{16}O$ disrupts hydrogen-bonding interactions among H_2O molecules in hydrophilic Ti-BEA as demonstrated by a significant loss in the absorbance of ν(O-H) around 3250 cm^{-1} and a red shift in the libration+bending combination band for H_2O molecules. The vibrational spectra of H_2O in the presence or absence of $C_8H_{16}O$ are, however, indistinguishable in defect-free Ti-BEA, which suggests that H_2O molecules that reside within these hydrophobic pores do not interact with species that form at Ti active sites. The excess free energies of adsorption that describe the restructuring of confined H_2O molecules form a linear free energy relationship with the associated excess properties for 1-octene epoxidation transition states, because these excess quantities predominantly reflect the changes in interactions among nearby solvent structures induced by the presence of the octyl chain of these reactive surface intermediates.

Collectively, the data and interpretations presented here demonstrate that complex outer-sphere interactions at solid-liquid interfaces follow linear free energy relationships. Specifically, small confined clusters of hydrogen-bonding solvent molecules (e.g., H_2O or ROH) nucleate at polar functions within extended pores and must reorganize to accommodate the formation of surface intermediates critical to catalysis or adsorption. The reorganization energy typically manifests within excess free energies that depend sensitively on the combination of the chemical and physical properties of the reactant, solvent, and catalyst. These conclusions suggest that

chemical modifications of extended solid surfaces can be used to regulate adsorption and catalysis by sets of interactions that are orthogonal to those that control charge transfer at active sites.

CHAPTER NINE

Roles of Oxidant Structure and Pore Size on Mediating Interactions Within Alkene Epoxidation Transition States in Titanium Silicates[VIII]

Abstract

Ti atoms incorporated into the framework of zeolite *BEA (Ti-BEA) or grafted onto SBA-15 (Ti-SBA-15) catalyze the epoxidation of alkenes using hydrogen peroxide (H_2O_2), *t*-butyl hydrogen peroxide (TBHP), or cumene hydroperoxide (CHP). Micro- and mesopores surrounding active sites induce dispersive, non-specific interactions among the surface species (e.g., Ti-bound oxidant and alkene) which lead to significant changes in the thermodynamic stability of reactive intermediates. The ways in which these interactions depend on the size and polarity of the surrounding void have not been demonstrated that allows for the rational design of catalytic materials. Here, we demonstrate that the strength of inner-sphere interactions among the alkyl groups of TBHP or CHP with a 1-alkene depend on the size of the void surrounding active sites through comparisons of 1-alkene epoxidation kinetics with H_2O_2, TBHP, and CHP over Ti-BEA and Ti-SBA-15. Rates of 1-octene epoxidation are 1700- and 40-fold greater with H_2O_2 than CHP within Ti-BEA and Ti-SBA-15, respectively. Epoxidations with H_2O_2 yield the greatest rates, as Ti-OOH intermediates are more electrophilic than Ti-OO*t*Bu and Ti-OOcumyl species which is associated with the electron-donating alkyl functional groups. The differences between H_2O_2 and CHP within Ti-BEA-12.5 *relative to* Ti-SBA-15, however, are not due to changes in the electronic structure of the reactive Ti-OOR intermediates within the different pore environments. Rather, the decreased sensitivity of epoxidation rates on oxidant identity within Ti-SBA-15 reflects inner-sphere interactions among Ti-OOR intermediates with 1-alkenes at the epoxidation transition states. Within Ti-BEA, apparent activation enthalpies ($\Delta H^{\ddagger}$) for 1-octene epoxidation with TBHP and CHP are 8 and 12 kJ mol^{-1} greater than values of $\Delta H^{\ddagger}$ for reactions with H_2O_2, respectively. Values of $\Delta H^{\ddagger}$ for 1-octene epoxidation in Ti-SBA-15, however, are identical among TBHP and H_2O_2 and are 7 kJ mol^{-1} lower when CHP is used as the oxidant. Analysis of a hypothetical Born-Haber thermochemical cycle shows that differences in $\Delta H^{\ddagger}$ (30 ± 5 kJ mol^{-1}) for reactions with

[VIII]This chapter has been adapted from the following publication:
Bregante, D.T.; Tan, J.Z.; Schultz, R.L.; Potts, D.S.; Ayla, E.Z.; Torres, C.; Flaherty, D.W.; "Roles of Oxidant Structure and Pore Size on Mediating Interactions Within Alkene Epoxidation Transition States in Titanium Silicates"
To be submitted.

H_2O_2 in Ti-BEA and Ti-SBA-15 are solely attributed to differences in the adsorption enthalpies of 1-octene in *BEA relative to SBA-15 (34 ± 6 kJ mol^{-1}). Consequently, the mesopores of Ti-SBA-15 allow Ti-OOR intermediates to interact with 1-octene at epoxidation transition states in ways that lower the free energy of the aggregate complex relative to microporous Ti-BEA. The findings presented here clarify how molecular interactions among multiple reactive species are mediated by the presence of a confining pore wall and can influence the thermodynamic stability of surface intermediates critical to adsorption or catalysis.

9.1 Introduction

Specific molecular interactions among surface intermediates during catalysis contribute directly to changes in the free energy of critical reactive species,[18, 22, 256] and therefore, impact rates and selectivities. Interactions between ligands bound to an active site with molecules within the outer-coordination sphere (e.g., solvents, pore walls, are colloquially referred to as "outer-sphere" interactions, while "inner-sphere" interactions are between functions bound directly to active metal atoms.[147, 296] Organometallic chemists commonly consider both inner- and outer-sphere interactions to design complex ligands that facilitate reactions at molecular complexes;[358-359] yet, the heterogeneous catalysis community less frequently invokes these principles to design solid surfaces for desired chemical transformations. This is due, in part, to the increased complexity of these interactions associated with the presence of a surface, pore walls, and confined solvent structures (that possess chemical and physical properties that differ significantly from bulk solutions) that surround reactive intermediates.[14, 18, 252]

The presence, shape, and size of a pore wall surrounding catalytically-active metal atoms can influence the orientation of surface species bound to active sites[7, 15] and, in turn, control the ways in which reactive species interact. Zeolites (e.g., MFI, BEA, FAU) and mesoporous silicas (e.g., SBA-15,[85, 226] MCM-41[360-361]) provide a convenient platform to understand how these molecular interactions depend on the extent of confinement and pore functionality (e.g., hydrophilicity), because they can be synthesized with well-defined pore geometries to study these effects. Alkene epoxidation over Lewis acid-incorporated (e.g., Ti-,[28-29, 51, 66, 164, 232] Nb-,[51, 147, 190] Ta-[51, 58, 88]) silicates with peroxide-containing oxidants occurs through transition states that involve reactive metal-peroxide, hydroperoxide, alkyl peroxide, and oxo intermediates and bound alkenes. As such, alkene epoxidation with different types of (alkyl)hydroperoxide oxidants provides an

ideal platform to study how the physicochemical properties of the Lewis acidic zeotype influences interactions among the surface intermediates that evolve during catalysis.

The role of reactant and oxidant chemical identity on epoxidation within Ti-based zeotypes has been a topic of research for decades.[30, 64-66, 82, 296] Despite commercialization of processes that use either hydrogen peroxide (H_2O_2; Hydrogen peroxide-propylene oxide process[82]), *t*-butyl hydrogen peroxide (TBHP; e.g., the Halcon or ARCO processes[362-364]), or ethylbenzene hydroperoxide (e.g., Shell styrene monomer-propylene oxide process[363]) as oxidants for the production of propylene oxide, there are few studies that systematically study the effects of oxidant identity and intramolecular interactions that result from the functionality of the oxidant and alkene. Tatsumi and coworkers showed that the epoxidation of cyclic alkenes (C_6, C_7, and C_{12}) is nearly 5-fold slower with TBHP than H_2O_2 over Ti-BEA.[365] Within this work, the authors attributed the large decrease in rates to the steric bulk of the Ti-OO*t*Bu intermediates which may inhibit formation of the epoxidation transition state. Similarly, rates of cyclohexene epoxidation with H_2O_2 are 20% greater than with TBHP over Ti-substituted MCM-41 materials;[366] however, the reasons for the observed change in rates were not discussed. Within hierarchical mesoporous TS-1, 1-octene epoxidation rates are 6-fold higher with TBHP than H_2O_2,[367] which was associated with increased rates of mass transfer through the mesopores of this material. The (few) reports on differences in reactivity among TBHP and H_2O_2 oxidants within Ti-silicates, however, may also reflect the convolution of confinement within the meso- or microporous environments with varying extents of intraparticle mass-transfer restrictions that can greatly affect measured rates. As such, the community lacks a consensus for how the shape and size of the surrounding pore influences the stability and interactions of reactive species during epoxidation catalysis.

Here, we investigate the role of pore size and hydrophilicity on inner-sphere interactions among reactive oxidants and alkenes, by systematically studying how 1-alkene epoxidation rates depend on the identity of the oxidant (i.e., hydrogen peroxide (H_2O_2), *t*-butyl hydrogen peroxide (TBHP), and cumene hydroperoxide (CHP)), the size of the confining void, and the length of the 1-alkene reactant. Rates of 1-octene (C_8H_{16}) epoxidation are 1700- and 40-fold greater with H_2O_2 than CHP within Ti-BEA and Ti-SBA-15, respectively. These catalytic consequences of oxidant identity do not reflect differences in the mechanism for epoxidation, which are nominally the same among all oxidants and Ti-silicates tested within this study. Rather, epoxidations with H_2O_2 yield the greatest rates because Ti-OOH intermediates are more electrophilic than Ti-OO*t*Bu and Ti-

OOcumyl species which is attributed to the electron-donating alkyl functional groups increasing the electron density on the O-O function. The differences in turnover rate ratios between reactions with H_2O_2 and CHP within Ti-BEA-12.5 *relative to Ti-SBA-15*, however, are not due to changes in the electronic structure of the reactive Ti-OOR intermediates within the different pore environments. Instead, the decreased sensitivity of epoxidation rates on oxidant identity within Ti-SBA-15 relative to Ti-BEA-12.5 reflects stabilizing inner-sphere interactions among Ti-OOR intermediates with the alkene at epoxidation transition states. In particular, bulky Ti-OO*t*Bu and Ti-OOcumyl intermediates and loosely bound C_8H_{16} at epoxidation transition states can form specific conformations within mesoporous Ti-SBA-15 that lower the free energy of the cumulative complex with respect to the analogous transition state within Ti-BEA-12.5. Collectively, the findings presented here rationalizes how a confining void can control inner-sphere interactions among reactive species during liquid-phase catalysis.

9.2 Materials and Methods

9.2.1 Catalyst Synthesis

Ti-BEA-12.5, where "12.5" refers to the initial Si:Al ratio of the parent Al-BEA (Zeolyst, CP814E; Si:Al ~ 12.5), was prepared by post-synthetic modification of Al-BEA. Al-BEA was refluxed in HNO_3 (Macron Chemicals, 68-70 wt. %; 20 $cm^3\ g_{Al\text{-}BEA}^{-1}$; *Caution: HNO_3 is a strong oxidant, will readily cause a chemical burn and should be handled carefully*) with the intent to remove framework Al atoms by forming soluble $Al(NO_3)_3$. The solids were then recovered by vacuum filtration and washed with H_2O (17.8 MΩ · cm, 50 $cm^3\ g^{-1}$) followed by heating at 5 K min^{-1} in flowing air (100 $cm^3\ min^{-1}$) and holding at 823 K for 6 h to remove residual volatile and organic species and to produce Si-BEA-X. Materials produced in this manner possessed Si:Al ratios greater than 1400, as determined by energy dispersive X-ray fluorescence spectroscopy. Ti atoms were incorporated by combining a stirred suspension of Si-BEA-X with an appropriate amount of $TiCl_4$ in CH_2Cl_2 (Fisher Chemicals, Certified ACS Stabilized) at reflux. *Caution: $TiCl_4$ will violently react with moisture in the air to form HCl and should be handled carefully*. All volatile components were then removed by rotary evaporation. The recovered solids were light-brown, and these materials were heated in flowing air (100 $cm^3\ min^{-1}$) at 5 K min^{-1} and holding at 823 K for 6 h, which produced bright white solid powders.

Ti-BEA-F was synthesized hydrothermally in fluoride media by adapting a previously published procedure.[22, 69] Tetraethylammonium fluoride (TEAF, Alfa Aesar, 97 wt. %) was dissolved in deionized H_2O (18.2 MΩ · cm) in a polypropylene container and combined with titanium(IV) isopropoxide (TIPO, Sigma Aldrich, 99.999%) to produce a clear homogeneous solution. Tetraethylorthosilicate (TEOS, Sigma Aldrich, >98 wt. %) was then added slowly over a period of one minute to this solution under static conditions, which formed a bi-phasic mixture initially. The mixture was then stirred for 16 h to produce an opaque homogeneous solution. The lid to the polypropylene container was then removed to evaporate the ethanol and isopropanol that form through the hydrolysis of the TEOS and TIPO, respectively. To ensure that the alcohols evaporated completely, the solution was left open while stirring until the mass of the solution decreased by 115% the value of the estimated mass of the alcohols. Subsequently, deionized H_2O was added to yield a gel with a final molar composition of 1 SiO_2: 0.0033 TIPO: 0.56 TEAF: 7 H_2O. *Note: this synthesis procedure produces MFI when crystallized if the ethanol and isopropanol are not entirely evaporated.* This gel was then loaded into a Teflon-lined stainless-steel autoclave (Parr instruments, 45 cm^3) that contained 5 wt. % (relative to SiO_2 within the gel) dealuminated BEA (Zeolyst, Si:Al = 12.5, see above) as seeds to promote the formation of the BEA zeolite. This autoclave was then sealed and heated to 413 K while rotating (60 rpm) in a convection oven (Yamato, DKN602C) for 25 days. The resultant solids were recovered, washed with H_2O and dried for 16 h at 373 K. The dried solids were then heated in flowing air (100 cm^3 min^{-1}) at 823 K (1 K min^{-1}) for 10 h to produce a bleached-white solid.

Ti-SBA-15 was synthesized by the liquid-phase grafting of titanocene dichloride ($TiCp_2Cl_2$; Sigma-Aldrich, 97%) onto a mesoporous silica (SBA-15; ACS Material, 7-10 nm pores).[85, 226] SBA-15 was treated in flowing air (100 cm^3 min^{-1}) at 823 K (5 K min^{-1}) to dehydrate and partially dehydroxylate the surface. The dried SBA-15 was stored within a vacuum desiccator until further use. The dried SBA-15 was then stirred in a solution of $TiCp_2Cl_2$ in CH_2Cl_2 under an argon atmosphere at 298 K using standard Schlenk technique which yielded a bright-red slurry. A desired amount of triethylamine ($N(Et)_3$; Sigma-Aldrich, 99.5%) was then added (in a 2.5:1 ratio, relative to $TiCp_2Cl_2$) to the slurry, with the intention of deprotonating surface SiOH which leads to $TiCp_2Cl_2$ grafting. This suspension was stirred for 6 h at 298 K; over this time period, the suspension slowly turned bright yellow in color. The solids were then recovered via filtration and were washed with CH_2Cl_2 (20 cm^3 g^{-1}). The recovered solids were pale yellow in appearance and

were treated in flowing at (100 cm^3 min^{-1}) at 823 K (5 K min^{-1}) for 6 h to remove the cyclopentadienyl ligands and produce a bleached white solid.

9.2.2 Catalyst Characterization

The Ti-BEA-12.5 and Ti-BEA-F materials were used within a previous study,[21] and the results of chemical and physical characterization have been described there.

Metal contents were quantified using energy dispersive X-ray fluorescence (EDXRF). Briefly, ~30 mg of the catalyst was loaded into a polypropylene sample holder (1 cm diameter) that was sealed with ultralene film. Samples were loaded into a spectrometer (Shimadzu, EDX-7000), whose sample chamber was purged with then He (Airgas, Ultra-zero grade). Measurements were taken between 0 – 30 keV (100 co-averaged scans), and the relative intensities of the element-specific fluorescence features were used to calculate the percent, by mass, of each element within the sample.

Table 9.1. Ti metal loadings and band edge energies for Ti-BEA and Ti-SBA-15 materials

Sample	Ti Content[a] (wt. %)	Band Edge Energy[b] (eV)
Ti-BEA-12.5	0.20	4.2
Ti-BEA-F	0.15	4.3
Ti-SBA-15	0.30	4.0

[a]Measured by EDRXF. [b]Determined from leading edge of Tauc plot from DRUV

X-ray diffractograms were collected using a diffractometer (Siemens/Bruker, D5000) with a Cu Kα radiation source (0.15418 nm) under ambient conditions. The X-ray diffractograms (Figure H1) for Ti-BEA-12.5 and Ti-BEA-F match the known diffraction patterns of *BEA, which suggests both samples contain similar pore structures and sizes (i.e., that of *BEA).

Band edge energies (Table 9.1) were measured by diffuse reflectance UV-vis spectroscopy (DRUV-vis). In short, samples were intimately ground with magnesium oxide (MgO; Sigma-Aldrich, 99.995%) in a 1:10 (Ti-silicate to MgO) by mass ratio. These samples were loaded into a Harrick diffuse-reflectance accessory and spectra were obtained using a spectrophotometer

(Agilent, CARY5) with MgO used as the background. All materials possess a single UV-vis absorbance feature around 4.5 eV (Figure H2) and band edges (Table 9.1) that are significantly greater than bulk TiO_2 (~3.2 eV),[51] which suggests that all Ti-silicates within this study contain highly-disperse Ti atoms and do not possess larger TiO_x aggregates.

1-Octene (C_8H_{16}) adsorption enthalpies were measured by van't Hoff analysis of the change in C_8H_{16} uptake into Si-BEA-12.5 and SBA-15 as a function of temperature within the linear regime of the adsorption isotherm. A solution of C_8H_{16} in CH_3CN (20 cm^3) was heated to the desired temperature (308 – 333 K) within a 25 cm^3 reaction vessel and was shaken at 250 rpm. An initial (silicate-free) aliquot was taken and analyzed via gas chromatography (GC; HP, 5890, Series A) to determine the initial peak areas of C_8H_{16} at a given concentration. A desired amount of BEA-12.5 or SBA-15 (~60 mg) was then added to the reactor and was equilibrated at a given temperature for 1 h. An aliquot was then filtered through a syringe filter (0.22 um; polypropylene) to remove the solids and was subsequently analyzed via GC. The difference in peak area between the initial aliquot and the one after silicate introduction is assumed to be proportional to the amount of C_8H_{16} absorbed within the solids. This process was repeated for a series of C_8H_{16} concentrations (1 μM – 1 mM) to determine the region where C_8H_{16} is proportional to the concentration of C_8H_{16} in the equilibrated solution (Section S1.3). The uptake of C_8H_{16} was then measured as a function of temperature to determine the enthalpies of adsorption for C_8H_{16} into BEA-12.5 and SBA-15, which are calculated as -85 ± 6 and -51 ± 5 kJ mol^{-1}, respectively.

9.2.3 Measurement of Epoxidation Rates

1-Hexene (C_6H_{12}; Sigma-Aldrich, >99%), 1-heptene (C_7H_{14}; TCI Chemicals, >98%), 1-octene (C_8H_{16}; Sigma-Aldrich, 98%), 1-nonene (C_9H_{18}, TCI Chemicals, >95%), 1-decene ($C_{10}H_{20}$, TCI Chemicals, >95%), styrene (Sigma-Aldrich, ReagentPlus, >99%), 4-bromostyrene (TCI Chemicals, >95%), H_2O_2 (Fischer Chemicals, 30 wt. % in H_2O), *tert*-butyl hydroperoxide (TBHP; Sigma Aldrich, 5.5 M in decane), cumene hydroperoxide (CHP; TCI Chemicals, 80% with aromatic hydrocarbons), decane (TCI Chemicals, >99%), Acetonitrile (CH_3CN; Fisher Chemicals, HPLC Grade), and H_2O (18.2 MΩ cm) were used as received.

Rates of alkene epoxidation and oxidant decomposition were measured using batch reactors (100 cm^3, three-neck round-bottom flasks) equipped with reflux condensers to minimize evaporative losses. An alkene and a peroxide oxidant (i.e., H_2O_2, TBHP, or CHP) were added to a

solution of CH_3CN and decane (used as an internal standard for GC analysis) and heated to the desired temperature (303 – 348 K) while stirring at 700 rpm. The reactions were initiated by addition of a catalyst and small aliquots (~500 μL) of the reaction solution were extracted through a syringe filter (0.22 μm, polypropylene) as a function of time. The concentrations of the organic components within these aliquots were quantified via a GC (HP, 5890) equipped with a flame-ionization detector. All species were identified, and calibration factors were quantified using standards of known concentration. The concentration of H_2O_2 in each aliquot was measured by colorimetric titration using an aqueous solution of $CuSO_4$ (8.3 mM, Fisher Chemicals, >98.6%), neocuproine (12 mM, Sigma-Aldrich, >98%), and ethanol (25% v/v, Decon Laboratories Inc., 100%). The concentration of H_2O_2 was calculated by comparison of the absorbance at 454 nm to calibrated standards, measured on a spectrophotometer (Spectronic, 20 Genesys). In all reported data, the standard uncertainty for measured reaction rates was <10%. Rates for the conversion of alkene and oxidant were measured as functions of reactant concentrations and all reported results were obtained at differential conversion (i.e., <1% conversion of the limiting reagent).

9.2.4 In Situ UV-Vis Spectroscopy

UV-vis spectra were collected using a 45-degree diffuse reflection probe (Avantes, solarization-resistant fibers) coupled to a fiber-optic spectrometer (Avantes, AvaFast 2048) with a compact deuterium-halogen light source (Avantes, AvaLight-DHc). Samples were pressed into 7 mm diameter pellets (~5 mg) and loaded into liquid flow cell with temperature control. Solutions were introduced using a high-performance liquid chromatography pump (Teledyne SSI, M1). Background UV-vis spectra (average of 100 scans) were obtained for each material by exposing the sample to a flowing CH_3CN solution (0.039 M H_2O, 1 cm^3 min^{-1}) at 313 K for 0.5 h. Spectra were obtained while flowing solutions of H_2O_2 or CHP in CH_3CN at 313 K and continuing until the UV-vis spectra became constant, implying that the system reached steady-state. Notably, the presented UV-vis spectra represent the difference between the experimental spectra and background spectra (i.e., contacting the solution of CH_3CN).

9.3 Results and Discussion

9.3.1 Activation of Oxidants at Ti Active Sites

Hydrogen peroxide and cumene hydroperoxide (CHP) react over Ti atoms incorporated into the zeolite framework to form activated Ti-OOR (R = H or cumyl) intermediates. Figure 9.1 shows UV-vis spectra of H_2O_2- and CHP-activated Ti-BEA-12.5 possess a broad, asymmetric feature whose peak areas are assumed to be proportional to the surface coverage of each UV-vis active intermediate. The broad feature between 300 – 450 nm for H_2O_2-activated Ti-BEA-12.5 (Fig. 9.1, bottom) and Ti-SBA-15 (Fig. H4, bottom) represents overlapping ligand-to-metal charge transfer (LMCT) bands that are assigned to the Ti-(η^2-O_2) and Ti-OOH intermediates,[11, 21, 117, 121, 144, 164, 240] which will be collectively referred to as Ti-OOH for the purposes of this study. Titanium cumyl-peroxide (Ti-OOcumyl) species show a LMCT absorbance between 300 – 450 nm (Figs. 9.1 and H4, top). This complex UV-vis feature is not due to any absorbance from the fluid-phase CHP or 2-phenyl-2-propanol that may be present within the solution, as these species have absorbance features around 260 nm.[368] Notably, we were unable to obtain UV-vis features for TBHP-activated samples, because the active titanium *t*-butyl-peroxide (Ti-OO*t*Bu) intermediates do not possess a LMCT band that is within the measurable range of our instrument (i.e., absorbs light below 200 nm). Consequently, the results and interpretations for CHP activation (see below) are extended to TBHP, as we expect similar trends in reactivity among alkyl hydroperoxide oxidants in terms of their mode of activation over Ti active sites.

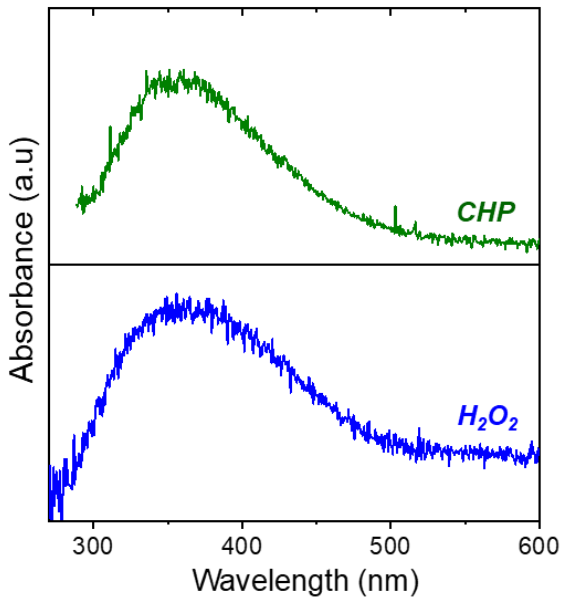

Figure 9.1. UV-vis difference spectra of H_2O_2- (bottom, 0.01 M H_2O_2, 0.039 M H_2O) and CHP-activated (top, 0.3 M CHP, 0.039 M H_2O) Ti-BEA-12.5 in CH_3CN at 313 K. In both cases, the background spectra is of Ti-BEA-12.5 in CH_3CN (0.039 M H_2O) at 313 K.

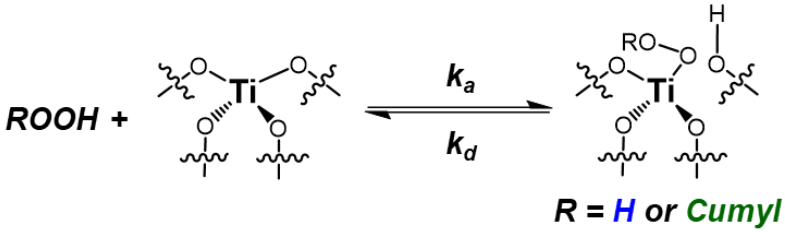

Scheme 9.1. Adsorption and activation of H_2O_2 or CHP to form Ti-OOH or Ti-OOcumyl intermediates, respectively. k_a and k_d represent the apparent first-order rate constants for the adsorption and activation or desorption, respectively, of H_2O_2 or CHP.

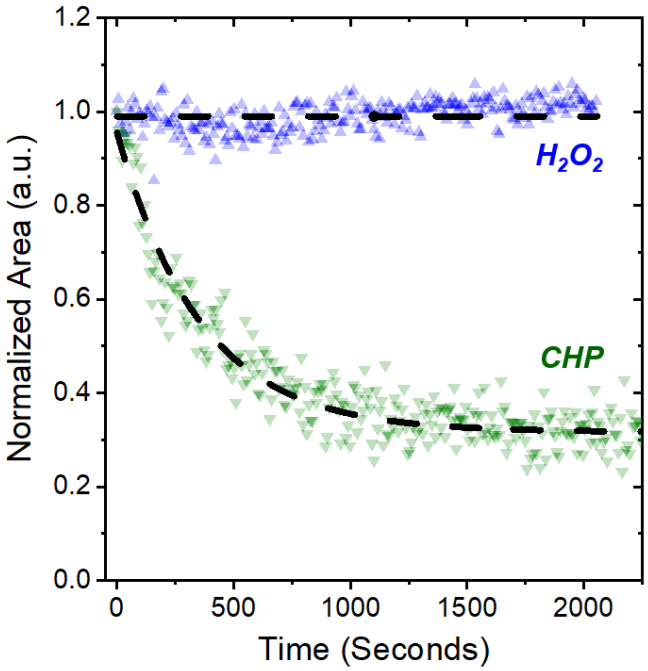

Figure 9.2. Areas for the LMCT bands of Ti-OOH (▲) and Ti-OOcumyl (▼) as a function of time as CH_3CN (0.039 M H_2O, 313 K) flowed over H_2O_2- or CHP-activated Ti-BEA-12.5, respectively. The dashed black curve for H_2O_2 is meant to guide the eye, while the curve for CHP represents an exponential decay fit. All areas were normalized to the initial area (i.e., at time = 0) before introduction of the oxidant-free CH_3CN solution.

The epoxidation catalysis community lacks a consensus regarding the series of elementary steps leading to ROOH activation over Ti-silicates. For example, there are many studies that claim ROOH activation is reversible and quasi- equilibrated,[51, 232, 240, 369] while other groups have suggested that Ti-OOH formation is irreversible.[11, 21, 199] On-going efforts within our group (including what is presented here), suggest that the mechanism for ROOH activation over early transition metals supported in zeolites or on mesoporous oxides depends on the combination of ROOH and solvent identity. Understanding the mechanism for ROOH activation is crucial to deconvolute specific interactions that influence the stability of reaction intermediates.

Figure 9.2 shows normalized peak areas for the LMCT bands of Ti-OOH and Ti-OOcumyl species as a function of time when a solution of CH_3CN was flowed over the samples with the intention to desorb Ti-OOR intermediates (i.e., to test for the reversibility of ROOH activation). The number of Ti-OOH species do not change as a function of time when H_2O_2-activated Ti-BEA-12.5 is contacted with CH_3CN, which suggests that these intermediates form irreversibly within CH_3CN (i.e., values of k_d for H_2O_2 are immeasurably small). Ti-OOcumyl species, however,

desorb with pseudo first-order kinetics (Figs. 9.2 and H5), which suggests that these species form reversibly over Ti active sites. Notably, the non-zero area after CHP desorption is not due to residual Ti-OOcumyl species, as it does not decrease further when a solution of 1-octene is introduced with the intention of reacting away any residual Ti-OOcumyl intermediates. The constant area after the initial desorption, rather, is likely due to a change in baseline as the experiment progresses. The rate constant for the desorption of CHP from Ti-OOcumyl intermediates from Ti-BEA-12.5 and Ti-SBA-15 (Section H2) is $2.8 \cdot 10^{-3}$ and $3.3 \cdot 10^{-2}$ s^{-1}, respectively, whose values will have implications in the formulation of the rate expression for alkene epoxidation in Section 9.3.2. Collectively, these data and interpretations show that within CH_3CN, alkyl hydroperoxide activation is reversible, while H_2O_2 activates irreversibly to form Ti-OOH intermediates.

9.3.2 Series of Elementary Steps that Describe Alkene Epoxidation

Rates of alkene epoxidation[11, 21, 54, 67, 199] (and thiophene oxidation[275]) depend on the concentrations of alkene and oxidant reactants in ways that describe the series of elementary steps that lead to epoxide formation, respectively. Figure 9.3 shows turnover rates for 1-octene (C_8H_{16}) epoxidation exhibit nearly-identical dependencies on the concentrations (denoted by brackets, [ ]) of C_8H_{18} (Fig. 9.3a and 9.3b) and oxidants (Fig. 9.3c) within both Ti-BEA-12.5 and Ti-SBA-15 when H_2O_2, TBHP, or CHP is used. It should be noted that all reactions contained equal concentrations of H_2O to minimize the effects of confined H_2O clusters near active sites that are intrinsic to reactions using H_2O_2.[21, 370] Difference in rates resulting from the identity of the oxidant used or pore diameter are not due to internal mass transfer restrictions, as these reactions were conducted under conditions where there are no apparent internal concentration gradients (i.e., the Madon-Boudart criterion is satisfied).[111] Rather, these differences relate to changes in the electronic properties of the reactive Ti-OOR (R = H, *t*Bu, or cumyl) intermediates (see below).

All combinations of oxidant and Ti-silicates possess two kinetic regimes that differ in how turnover rates depend on the concentration of reactants. At low [C_8H_{16}], rates increase in proportion to [C_8H_{16}] and are independent of [ROOH], suggesting that active Ti atoms are saturated with reactive intermediates derived from the respective oxidant (e.g., Ti-OOR). At higher concentrations of [C_8H_{16}], turnover rates are invariant with [C_8H_{16}], which indicates that C_8H_{16}-derived species are the most abundant reactive intermediate (MARI).

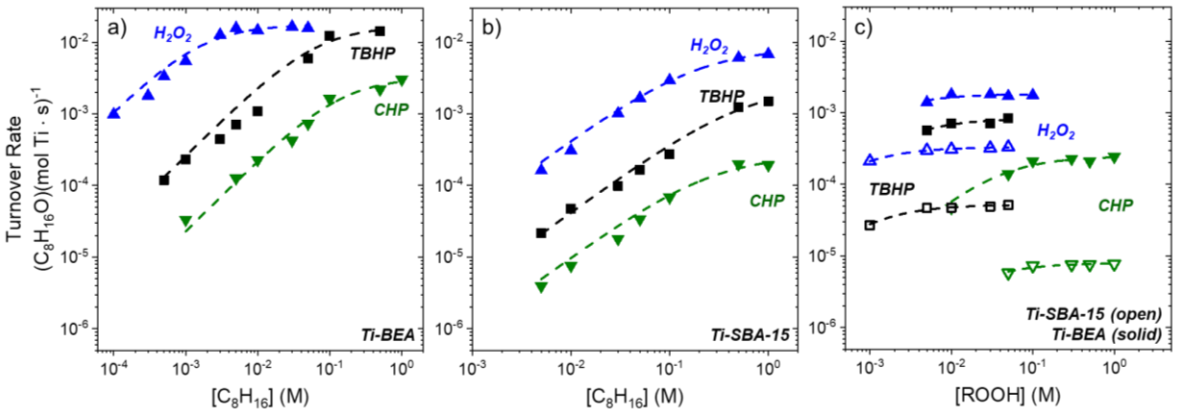

Figure 9.3. Turnover rates for the formation of $C_8H_{16}O$ as a function of $[C_8H_{16}]$ and $[H_2O_2]$ (▲), [TBHP] (■), or [CHP] (▼; collectively denoted as [Oxidant]) over (a) Ti-BEA, (b) Ti-SBA-15, and (c) both Ti-BEA-12.5 (closed) and Ti-SBA-15 (open symbols) in CH_3CN (0.039 M H_2O) at 313 K. Within panels (a) and (b), the concentrations of H_2O_2, TBHP, and CHP used were 0.01 M, 0.01 M, and 0.3 M, respectively. Within panel (c), the concentration of C_8H_{16} was 0.01 M for all Ti-SBA-15 reactions and were 0.3 mM, 5 mM, and 0.01 M for H_2O_2, TBHP, and CHP with Ti-BEA-12.5, respectively. Dashed lines represent fits to equations 9.2a or 9.2b (for H_2O_2 or TBHP/CHP, respectively).

Scheme 9.2. Proposed catalytic cycle for C_8H_{16} epoxidation with hydrogen peroxide, *t*-Butyl hydrogen peroxide, or cumene hydroperoxide over Ti-silicates.[a]

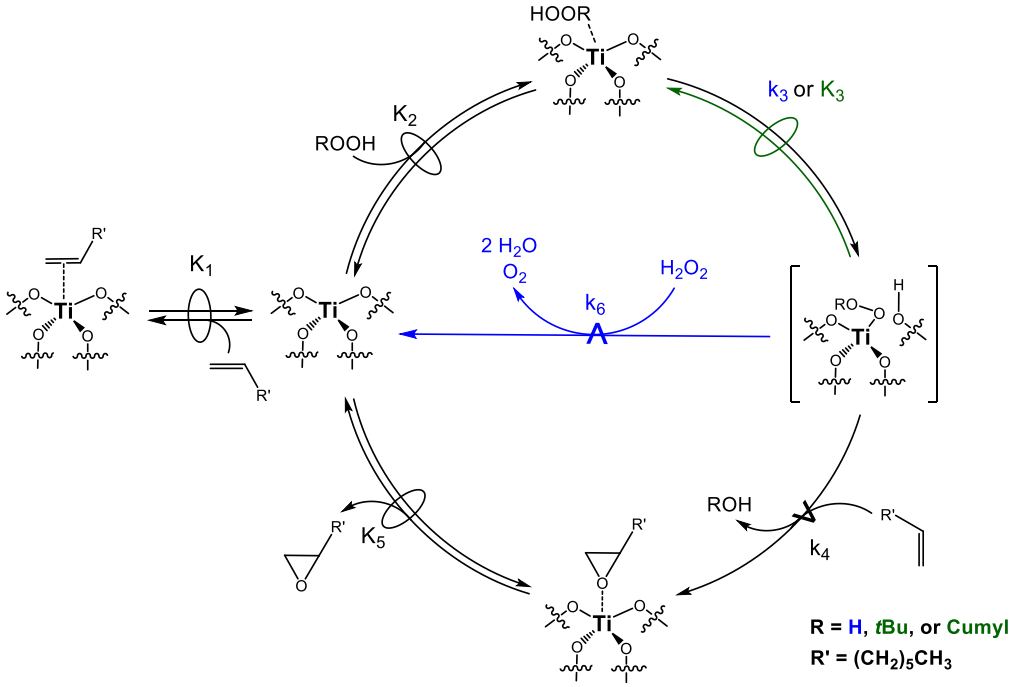

[a]The symbol ⇌ represents a quasi-equilibrated step, while ⟶ represents a kinetically relevant step. The blue arrow (and corresponding rate constant) is unique to when H_2O_2 is used as an oxidant, while the green arrow and quasi-equilibrium in step 3 oval applies only to TBHP and CHP oxidants within this study.

Scheme 9.2 shows a series of hypothetical elementary steps that describe the ways in which turnover rates of $C_8H_{16}O$ formation depend on $[C_8H_{16}]$ and [ROOH] on both Ti-BEA-12.5 and Ti-SBA-15. This catalytic cycle involves the quasi-equilibrated adsorption of C_8H_{16} (step 1) and ROOH (step 2; R = H, *t*Bu, or cumyl), and the irreversible activation of adsorbed H_2O_2 *or* the quasi-equilibrated activation of CHP or TBHP (step 3; Section 9.3.1) to form a pool of Ti-OOR intermediates. The adsorption-and-activation of CHP and TBHP are assumed to be quasi-equilibrated, as the rates of desorption from *in situ* UV-vis experiments (see above) are much greater than the turnover rates for epoxidation, which suggests that this step is, for all intents and purposes, quasi-equilibrated with respect to kinetically relevant epoxidation (step 4). Notably, rates of TBHP and CHP decomposition were immeasurably small ($< 10^{-7}$ (mol oxidant)(mol Ti · s)$^{-1}$), while rates of H_2O_2 decomposition were similar among Ti-BEA-12.5 and Ti-SBA-15 materials (~2.7 (mmol H_2O_2)(mol Ti · s)$^{-1}$, 0.01 M H_2O_2, 313 K) which suggests that there is a parallel reaction pathway for Ti-OOH intermediates to decompose by reaction with an additional H_2O_2 molecule (step 6).[67] Finally, $C_8H_{16}O$ molecules desorb in a quasi-equilibrated manner (step 5) to yield the final product. Rates of $C_8H_{16}O$ formation (r_E) are given by

$$r_E = k_4[C_8H_{16}][Ti-OOR] \tag{9.1}$$

where [Ti-OOR] is the number of reactive Ti-OOR intermediates and k_i is the rate constant for step *i* in scheme 9.1. The use of the pseudo-steady state hypothesis on Ti-OOH intermediates, the assumption of quasi-equilibrated Ti-OOR (R = *t*Bu, cumyl) formation, and a site balance over all possible species formed at Ti active sites allows for the formation of two distinct rate expressions for H_2O_2:

$$\frac{r_E}{[L]} = \frac{\frac{k_3 k_4 K_2 [C_8H_{16}][H_2O_2]}{k_4[C_8H_{16}]+k_6[H_2O_2]}}{1+K_1[C_8H_{16}]+K_2[H_2O_2]+\frac{k_3K_2[H_2O_2]}{k_4[C_8H_{16}]+k_6[H_2O_2]}+\frac{[C_8H_{16}O]}{K_5}} \tag{9.2a}$$

and for TBHP and CHP:

$$\frac{r_E}{[L]} = \frac{k_4K_2K_3[C_8H_{16}][ROOH]}{1+K_1[C_8H_{16}]+K_2[ROOH]+K_2K_3[ROOH]+\frac{[C_8H_{16}O]}{K_5}} \tag{9.2b}$$

where, [L] is the total number of Ti active sites and K_j is the equilibrium constant for step j. The five terms in the denominator of both equations represent Ti atoms that are saturated with molecules of CH_3CN or H_2O (i.e., the solvent), C_8H_{16}, ROOH, Ti-OOR, or $C_8H_{16}O$, respectively.

At low [C_8H_{16}], Ti-OOR intermediates are most abundant on Ti active sites, which reduces equation 9.2 to

$$\frac{r_E}{[L]} = k_4[C_8H_{16}] \tag{9.3}$$

Equation 9.3 reproduces the experimental observations for how $C_8H_{16}O$ formation rates depend on [C_8H_{16}] and [ROOH] in Figure 9.3. When the concentration of C_8H_{16} is increased to the point that turnover rates are independent of [C_8H_{16}], the MARI changes to one derived from C_8H_{16}. For H_2O_2, we have previously shown that the MARI becomes $C_8H_{18}O$ which coincides with a rate of epoxidation that is far greater than the rate of H_2O_2 decomposition (i.e., $k_4[C_8H_{16}] >> k_6[H_2O_2]$, Section H3), which reduces equation 9.2 to

$$\frac{r_E}{[L]} = \frac{k_3K_2K_5[H_2O_2]}{[C_8H_{16}O]} \tag{9.4}$$

Alternatively, for TBHP and CHP, Ti active sites under sufficiently high [C_8H_{16}] become saturated with C_8H_{16}, which simplifies equation 9.2

$$\frac{r_E}{[L]} = \frac{k_4K_2K_3[ROOH]}{K_1} \tag{9.5}$$

Both equations 9.4 and 9.5 show epoxidation turnover rates that are independent of [C_8H_{16}], which is consistent with observations in Figure 9.3.

The series of elementary steps for C_8H_{16} epoxidation with H_2O_2, TBHP, and CHP possess many commonalities over Ti-BEA-12.5 and Ti-SBA-15 catalysts. Despite the similarities in mechanism, the measured rates of C_8H_{16} epoxidation vary greatly among both ROOH and Ti-silicate identity. For example, within Ti-BEA-12.5, under conditions with similar MARI (i.e., Ti-OOR; 1 mM C_8H_{16} in Fig. 9.3a), rates of epoxidation with H_2O_2 are greater than reactions with TBHP or CHP by factors of 30 and 1700, respectively. These catalytic differences among

epoxidations with ROOH are significantly smaller within Ti-SBA-15, where C_8H_{16} epoxidation rates using H_2O_2 are greater than TBHP and CHP by 7 and 40-fold (0.01 M C_8H_{16}, Fig. 9.3b), respectively. The electronic properties of reactive Ti-OOR intermediates greatly affect rates of alkene epoxidation; consequently, the strong dependence of epoxidation rates on both ROOH identity and pore size *may* relate to changes in the charge transfer among reactive species and Ti active sites.

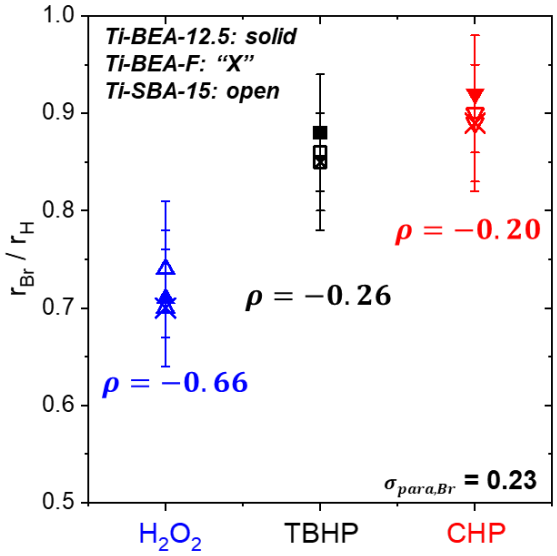

Figure 9.4. Ratio of epoxidation turnover rates for *p*-bromostyrene relative to styrene (r_{Br}/r_H) as a function of oxidant identity for Ti-BEA-12.5 (solid symbols), Ti-SBA-15 (open symbols), and Ti-BEA-F (symbols with an "X"). All reactions contained 0.01 M alkene, 0.039 M H_2O, and either 0.01 M H_2O_2, 0.01 M TBHP, or 0.3 M CHP in CH_3CN at 313 K. The reaction constants (ρ) shown are averaged values for all three Ti-silicates using the Hammett equation (equation 9.6).

The electrophilic nature of Ti-OOR species within Ti-BEA-12.5, Ti-SBA-15, and Ti-BEA-F (i.e., a hydrophobic Ti-BEA) is inferred by changes in reaction rates that result from systematically changing the electronic structure of the C=C bond within *para*-substituted styrenes (i.e., styrene and *p*-bromostyrene). Bromine atoms at the para position are electron withdrawing (as shown by a Hammett substituent constant, σ_{para}, of 0.23),[75] which is expected to lead to decreased epoxidation reactivity. Figure 9.4 shows that the ratio of epoxidation turnover rates for *p*-bromostyrene relative to styrene (r_{Br}/r_H) is smaller when H_2O_2 is used as the oxidant relative to TBHP and CHP. The ways in which r_{Br}/r_H vary with σ_{para} is fit using the Hammett equation

$$log\left(\frac{k_x}{k_H}\right) = \sigma_{para} \cdot \rho \tag{9.6}$$

where k_x and k_H are the rate constants for (substituted) styrene epoxidation and ρ is the reaction constant. The turnover rates in Figure 9.4 were used in place of rate constants, as these reactions were run under conditions where turnover rates depend identically on alkene concentrations and are independent of oxidant concentration. In all cases, values of ρ are negative, which is expected for alkene epoxidation reactions where there is the loss of negative charge during the reduction of Ti-OOR intermediates to form the epoxide product.[75] Values of ρ are greatest for reactions with H_2O_2 and are smaller when TBHP or CHP is used as the oxidant, which suggests that Ti-OO*t*Bu and Ti-OOcumyl intermediates are less electrophilic than Ti-OOH species as less electron density is transferred during reaction (as indicated by smaller ρ values). These data show that Ti-OO*t*Bu and Ti-OOcumyl intermediates are less electrophilic than Ti-OOH, which results from the electron-donating nature of alkyl substituents,[75] that increase the electron density (or nucleophilicity) of the peroxidic function. Bromine functional groups are halogen-bond acceptors[371] that may form X—H bonds with H_2O that is localized near Ti active sites. As such, comparisons among Ti-BEA-12.5 and Ti-BEA-F are included to account for changes in epoxidation that result from differences in the proximity of H_2O to active sites, as Ti-BEA-F does not possess significant densities of H_2O near Ti atoms.[21] Within the different Ti-silicates, however, there is no apparent change in values of ρ *for a given oxidant* suggesting that the electronic properties of the reactive Ti-OOR species do not depend measurably on the size (or hydrophilicity) of the pore environment. The differences in epoxidation catalysis between the three ROOH within a given pore environment (e.g., Ti-BEA-12.5; Fig. 9.3a) reflects contributions from the electrophilic nature of the Ti-OOR intermediates. The dependence of C_8H_{16} epoxidation rates on ROOH identity within the *different pore environments* (i.e., within Ti-BEA-12.5 compared to Ti-SBA-15), however, suggests that there are additional interactions among reactive species that affect the thermodynamic stability of kinetically-relevant intermediates because the electronic properties of Ti-OOR intermediates appear to be pore-size agnostic.

Consequently, a molecular and quantitative understanding for the interactions among Ti-OOR intermediates with alkene reactants at the transition states for epoxidation require the development of a reaction mechanism (Scheme 9.2) and corresponding rate expression for C_8H_{16} to make equitable comparisons among Ti-silicates and ROOH oxidants. As such, reaction

conditions that result in similar reference (e.g., Ti-OOR MARI) and transition states will allow us to measure activation enthalpies and entropies (Section 9.3.3) that contain meaningful information regarding how the physical and chemical structure of the reacting species affects epoxidation catalysis.

9.3.3 Thermochemical Interpretation for Changes in Catalysis Resulting from Oxidant Identity and Pore Size

Alkene epoxidation with H_2O_2, TBHP, or CHP occurs through reactive Ti-OOR intermediates that influence the stability of the epoxidation transition states through inner-sphere interactions between the "-R" group and the alkene reactant. These interactions depend intimately on the size of the surrounding void (i.e., pore size), which dictates the available number of microstates available for the surface species to exist in. Deciphering how these interactions depend on oxidant identity and are influenced by the surrounding pore walls requires an understanding for how the apparent activation free energies (and, by extension enthalpies and entropies) systematic vary among these catalysts and oxidants.

Transition state theory posits that reaction rates are proportional to the abundance of an activated complex (i.e., a transition state) that is in equilibrium with the state immediately preceding it within a catalytic cycle (Scheme 9.3).[34, 136, 372]

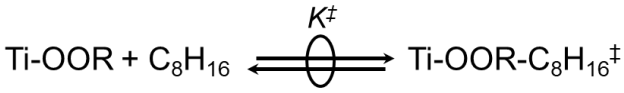

Scheme 9.3. Proposed Equilibrium for the Formation of C_8H_{16} Epoxidation Transition States.

Here, Ti-OOR-$C_8H_{16}^{\ddagger}$ represents the transition state for C_8H_{16} epoxidation and $K^{\ddagger}$ is the transition state equilibrium constant. Under reaction conditions that result in a Ti-OOR MARI (Section 9.3.2; equation 9.3), the corresponding rate expression for epoxidation can be expressed as

$$\frac{r_E}{[L]} = \frac{k_b T}{h} e^{\left(\frac{-\Delta G^{\ddagger}_{App}}{RT}\right)} [C_8H_{16}] \tag{9.7}$$

where k_b and h are the Boltzmann and Planck constants, respectively, R is the ideal gas constant, T is the absolute temperature, and $\Delta G_{App}^{\ddagger}$ is the apparent free energy of activation.

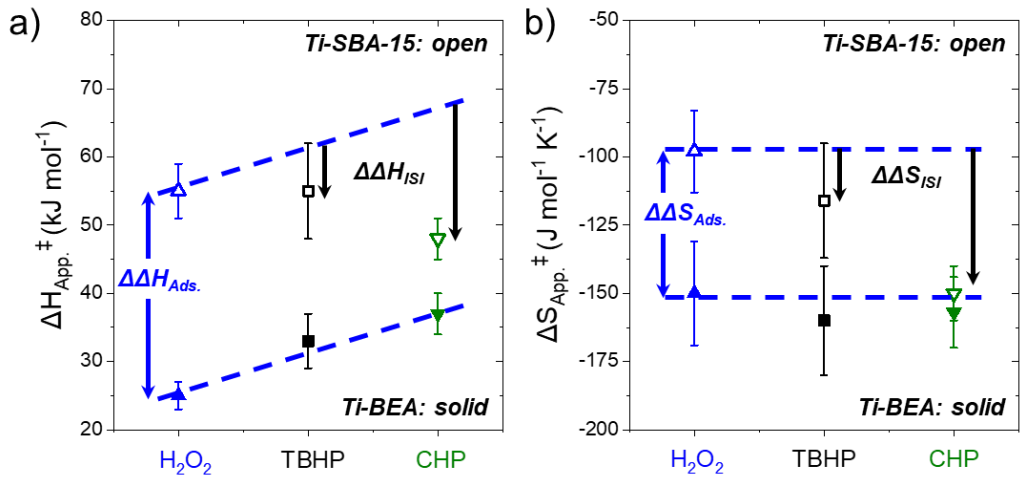

Figure 9.5. Values of (a) apparent activation enthalpies ($\Delta H_{App}^{\ddagger}$) and (b) entropies ($\Delta S_{App}^{\ddagger}$) for C_8H_{16} epoxidation with H_2O_2, TBHP, and CHP over Ti-BEA-12.5 (solid symbols) and Ti-SBA-15 (open symbols) on Ti-OOR saturated active sites. For reactions with H_2O_2, differences in $\Delta H_{App}^{\ddagger}$ and $\Delta S_{App}^{\ddagger}$ between Ti-BEA-12.5 and Ti-SBA-15 represent differences in the adsorption enthalpies or entropies for C_8H_{16} into the *BEA framework, relative to SBA-15 (denoted as $\Delta\Delta H_{Ads}$ or $\Delta\Delta S_{Ads}$). The dashed line for Ti-BEA-12.5 is intended to guide the eye, while the vertical offset is equal to values of $\Delta\Delta H_{Ads}$ or $\Delta\Delta S_{Ads}$, such that deviations from this curve for TBHP and CHP oxidants are indicative of differences in the inner-sphere interactions among -*t*Bu or -cumyl groups with C_8H_{16} at the transition states (denoted as $\Delta\Delta H_{ISI}$ or $\Delta\Delta S_{ISI}$).

Figure 9.5 shows how apparent activation enthalpies ($\Delta H_{App}^{\ddagger}$) and entropies ($\Delta S_{App}^{\ddagger}$) depend on oxidant identity within both Ti-BEA-12.5 and Ti-SBA-15. Within Ti-BEA-12.5, $\Delta H_{App}^{\ddagger}$ are lowest with H_2O_2 and are greater by 7 and 12 kJ mol^{-1} when TBHP or CHP are used as the oxidant, respectively. Values of $\Delta S_{App}^{\ddagger}$, however, do not depend on oxidant identity within Ti-BEA-12.5 because the dominant losses in entropy result from the adsorption of C_8H_{16} from the fluid phase to form the epoxidation transition states. It should be noted that the differences in stability of Ti-OOR intermediates due to dispersive interactions between the "-R" groups and the pore walls of *BEA or SBA-15 do not affect the measured values of $\Delta H_{App}^{\ddagger}$ and $\Delta S_{App}^{\ddagger}$ because they are presumed to affect the transition states and Ti-OOR intermediates to similar extents. Within Ti-SBA-15, values of $\Delta H_{App}^{\ddagger}$ are identical for epoxidations with H_2O_2 and TBHP; yet, are 7 kJ mol^{-1} lower when CHP is used as the oxidant. Apparent activation entropies, however, are 15 and 43 J mol^{-1} K^{-1} more

negative in reactions with TBHP or CHP in comparison to H_2O_2, respectively. This compensation effect for how the apparent activation enthalpies and entropies change with oxidant identity in Ti-SBA-15 relative to Ti-BEA-12.5 are consistent with the differences in epoxidation turnover rates (Fig. 9.3).

The Born-Haber approach deconstructs the individual thermodynamic parameters that result in changes in $\Delta G_{App.}^{\ddagger}$ from interactions among the reactive Ti-OOR species, C_8H_{16} bound at transition states, and the surrounding porous environment. Scheme 9.4 shows a thermochemical cycle that relates $\Delta G_{App}^{\ddagger}$ to the hypothetical series of steps that connect the reference state (i.e., Ti-OOR and fluid-phase C_8H_{16}) to the kinetically relevant transition state. In this framework, C_8H_{16} first adsorbs into the voids of the Ti-silicate and interacts with the surrounding pore walls through dispersive interactions, which is described by a free energy of adsorption ($\Delta G_{Ads.}$). Alkenes that are loosely bound to Ti active sites interact with the Ti-OOR intermediates through inner-sphere, non-specific interactions (ΔG_{ISI}) prior to the transfer of electron density between the C=C and Ti-OOR intermediates to form the oxirane ring at the transition state ($\Delta G_{Int.}^{\ddagger}$). Values of $\Delta G_{App}^{\ddagger}$ are given by

$$\Delta G_{App}^{\ddagger} = \Delta G_{Int.}^{\ddagger} + \Delta G_{Ads} + \Delta G_{ISI} \tag{9.8}$$

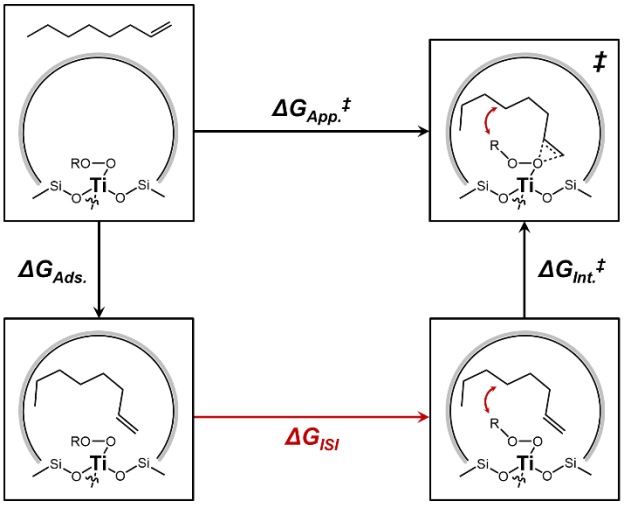

Scheme 9.4. Thermochemical cycle for the formation of C_8H_{16} epoxidation transition states. Apparent free energies of activation ($\Delta G_{App.}^{\ddagger}$) depend on the intrinsic activation free energy ($\Delta G_{Int.}^{\ddagger}$), the free energy of C_8H_{16} adsorption ($\Delta G_{Ads.}$), and changes in free energy resulting from inner-sphere interactions among Ti-OOR intermediates and adsorbed C_8H_{16} (ΔG_{ISI}).

The adsorption of C_8H_{16} into the pores of *BEA and SBA-15 depends strongly on the topological properties (i.e., pore size) of the silicate, which greatly affects the thermodynamic stability of intraporous reactive complexes.[11, 67] The adsorption enthalpies (ΔH_{Ads}) for C_8H_{16} into siliceous BEA-12.5 and SBA-15 were determined through van't Hoff analysis of C_8H_{16} uptake into these materials within the Henry's law regime (Section H1.3). The measured values of ΔH_{Ads} within BEA-12.5 and SBA-15 are -85 ± 6 and -51 ± 5 kJ mol^{-1}, respectively, which reflect enthalpy differences associated with van der Waal interactions between the SiO_2 pore walls with the aliphatic alkene as well as the displacement of CH_3CN solvent. The difference in ΔH_{Ads} between BEA-12.5 and SBA-15 ($\Delta\Delta H_{Ads}$; 34 kJ mol^{-1}) reflects the difference in stabilization between C_8H_{16} within the *BEA framework relative to SBA-15 and is similar to the difference in values of $\Delta H_{App}^{\ddagger}$ with H_2O_2 in these materials. These data suggest that for H_2O_2, the intrinsic activation enthalpy ($\Delta H_{Int.}^{\ddagger}$) does not depend on the morphology of the silicate support because the differences in $\Delta H_{App}^{\ddagger}$ among Ti-BEA-12.5 and Ti-SBA-15 are equal to $\Delta\Delta H_{Ads}$. Moreover, the similarity in electronic properties of Ti-OOR intermediates (Section 9.3.2; Fig. 9.4) suggest that values of $\Delta H_{Int.}^{\ddagger}$ among all ROOH tested here do not depend on the size of the confining void (i.e., $\Delta H_{Int.}^{\ddagger}$ within Ti-SBA-15 and Ti-BEA-12.5 are equal).

Consequently, a molecular understanding for how each of the constituent free energies depends on the identity of the reactive Ti-OOR intermediate and size of the porous environment within Ti-SBA-15, relative to Ti-BEA-12.5 is given by

$$\Delta\Delta G_{App}^{\ddagger} \equiv \Delta G_{App,Ti-SBA-15}^{\ddagger} - \Delta G_{App,Ti-BEA-12.5}^{\ddagger} = \Delta\Delta G_{Ads} + \Delta\Delta G_{ISI} \quad (9.9)$$

where $\Delta\Delta G_{ISI}$ is the difference in free energy due to inner-sphere interactions among Ti-OOR and C_8H_{16} within Ti-SBA-15 relative to Ti-BEA-12.5.

The vertical offset in the dashed lines in Figure 9.5 are equal to the measured value of $\Delta\Delta H_{Ads}$ (and the presumed value of $\Delta\Delta S_{Ads}$), which represent the difference in expected values of $\Delta H_{App}^{\ddagger}$ and $\Delta S_{App}^{\ddagger}$ if there were no specific interactions among Ti-OOR intermediates with the alkyl tail of the transition states. Values of $\Delta H_{App}^{\ddagger}$ and $\Delta S_{App}^{\ddagger}$ for reactions with TBHP and CHP show a clear deviation from expected values of $\Delta H_{App}^{\ddagger}$ and $\Delta S_{App}^{\ddagger}$, which suggests the presence of dispersive interactions among -*t*Bu or -cumyl functional groups with C_8H_{16}. The mesopores of

SBA-15 allow for the bulky, alkyl Ti-OOR intermediates to sample a larger volume around the Ti active sites, while microporous Ti-BEA-12.5 likely forces the Ti-OO*t*Bu and Ti-OOcumyl species into a specific conformation. As such, C_8H_{16} epoxidation transition states within Ti-SBA-15 have the physical space to find specific molecular orientations that lead to large decrease in enthalpy ($\Delta\Delta H_{ISI}$ is -8 and -19 kJ mol^{-1} for TBHP and CHP, respectively). These van der Waal-type interactions among the aliphatic tail of C_8H_{16} with the alkyl peroxide, however, also lead to significant losses in entropy ($\Delta\Delta S_{ISI}$ is -15 and -43 kJ mol^{-1} for TBHP and CHP, respectively). During low-temperature catalysis, the inner-sphere interactions between -*t*Bu and -cumyl groups with C_8H_{16} decrease the free energy of the aggregate transition state (by -4 and -6 kJ mol^{-1}, respectively, at 303 K), which explains why the rates of epoxidation within Ti-SBA-15 are less sensitive to ROOH identity than Ti-BEA-12.5 (Fig. 9.3). Collectively, these data show how the chemical functionality of the "-R" group and the size of the surrounding void influences the stability of intermediates critical to catalysis.

9.3.4 Lateral Intra-Complex Interactions Between *N*-Alkenes and Ti-OOR Intermediates

Dispersive, enthalpically-stabilizing interactions among the alkyl groups within Ti-OOR intermediates and the reactant alkenes depend on the size of the reactants which can reveal how these interactions may be understood, quantified, and used to stabilize specific chemical structures. Figure 9.6 shows how epoxidation turnover rates depend on the chain length of the 1-alkene (C_6 – C_{10}) with H_2O_2, TBHP, and CHP in the different Ti-silicate materials. All rates were normalized to the turnover rate using C_6H_{12} to facilitate comparisons among oxidants and materials. It should be noted that the electronic properties of the C=C within 1-alkenes are presumed to be similar as the additional methylene units are too far from the alkene functional groups to induce a change in electronic structure. As such, the change in epoxidation rates resulting from differences in chain length are predominately associated with inner-sphere interactions between the aliphatic tails with the surrounding environment (e.g., pore walls, solvent structures, reactive Ti-OOR intermediates).

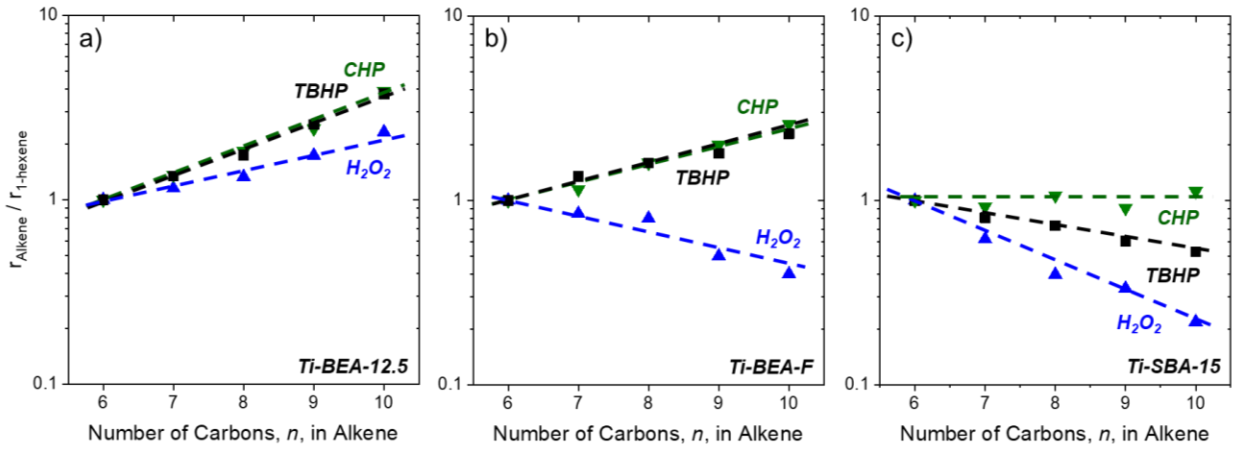

Figure 9.6. Epoxidation turnover rates for C_nH_{2n} (n = 6 – 10; for 1-alkenes) relative to C_6H_{12} as a function of carbon number, n, over (a) Ti-BEA-12.5, (b) Ti-BEA-F, and (c) Ti-SBA-15 with 0.01 M H_2O_2 (▲), 0.01 M TBHP (■), or 0.3 M CHP (▼) in CH_3CN (with 0.039 M H_2O) at 313 K. Within panels (a) and (b), reactions with H_2O_2, TBHP, and CHP contained 0.5 mM, 0.01 M, or 0.01 M alkene, respectively. In panel (c), all reactions contained 0.01 M alkene.

Within Ti-BEA-12.5, rates of epoxidation with H_2O_2 increase exponentially with the number of methylene (-CH_2-) units. This dependence on chain length relates to entropic stabilization resulting from the perturbation of H_2O clusters that are localized near active sites, whose quantification is on-going work in our lab.[21, 370] In the case of TBHP and CHP, the dependence of epoxidation rates on chain length are indistinguishable, which suggests that the aliphatic tail of the 1-alkenes are within similar chemical environments (Fig. 9.6a). Reactions with Ti-BEA-F were used to further explore the reaction volume that the methylene tail of the alkenes sample during epoxidation catalysis within the *BEA framework. Epoxidation rates with TBHP and CHP show an indistinguishable dependence on carbon number within Ti-BEA-F (Fig. 9.6b) and possess nearly identical trends to those within Ti-BEA-12.5. The pores within Ti-BEA-F predominately contain CH_3CN and negligible amounts of H_2O, such that increases in the chain length of the alkene leads to large entropic losses that result in a decrease in measured rates. Within the confines of the *BEA framework, Ti-OO*t*Bu and Ti-OOcumyl intermediates appear similar to alkene reactants at the transition state, regardless of pore hydrophilicity. This suggests that the micropores of *BEA mediate the structure of the transition state such that the alkene reactant is interacting with a geminal-dimethyl functional group. The aryl ring within the cumyl functional group is likely pointed away from the alkene, as the opposite would likely result in large increases in free energy due to steric repulsion. The presence of these bulky alkyl substituents (i.e., *t*Bu and

cumyl groups) also likely create a hydrophobic environment around the Ti active sites, which obviates the differences in catalysis that would be associated with confined H_2O structures.[21]

The mesopores of SBA-15 do not confine reactants to the same extent as *BEA and allow for greater degrees of freedom regarding how reactive species orient. Epoxidation rates with H_2O_2 in Ti-SBA-15 decrease significantly with -CH_2-, by a factor of 5 between $C_{10}H_{20}$ and C_6H_{12} (Fig. 9.6c). This decrease in epoxidation rates is due to the large losses in entropy associated with forming the transition state for $C_{10}H_{20}$ epoxidation relative to C_6H_{12}. When TBHP is used as the oxidant, rates of epoxidation still decrease with carbon number; yet, are less sensitive than reactions with H_2O_2. Moreover, reactions with CHP over Ti-SBA-15 show no dependence on alkene chain length, which suggests that the alkyl groups within Ti-OOR intermediates form distinct structures that interact with the alkenes at the transition states leading to significant enthalpic stabilization that compensates the entropic losses. As a result, epoxidation turnover rates using TBHP or CHP show less (or no) sensitivity to the number of -CH_2- when compared to reactions with H_2O_2, because values of $\Delta\Delta G_{ISI}$ becomes increasingly negative with carbon number for TBHP and CHP. It should not be lost, however, that despite the stabilizing interactions between -*t*Bu or -cumyl groups of Ti-OOR and the aliphatic tails of the 1-alkene, reaction rates using H_2O_2 are significantly greater in all cases (Fig. 9.3), which is associated with the electrophilicity of Ti-OOH intermediates.

Collectively, the data and interpretations presented here show how microporous environments mediate interactions among surface intermediates and suggests that changes in the surface chemistry and pore size can be used to control the stability of desired species.

9.4 Conclusions

Alkene epoxidation with H_2O_2, TBHP, and CHP occurs at Ti active sites within micro- and mesoporous Ti-silicates (Ti-BEA and Ti-SBA-15) and turnover rates depend strongly on the identity of the oxidant and the shape and size of the surrounding void. Turnover rates of 1-octene epoxidation with H_2O_2 in Ti-BEA-12.5 are 30- and 1700-fold higher than reactions with TBHP or CHP, respectively. C_8H_{16} epoxidation with H_2O_2 in Ti-SBA-15, in comparison, yields a modest increase of a factor of 6 or 40 over TBHP or CHP, respectively. The consequences of oxidant identity and pore size is not due to differences in the series of elementary steps that lead to epoxidation, which are very similar among every combination tested here. Rather, Ti-OOH

intermediates that form upon H_2O_2 activation are significantly more electrophilic than the analogous Ti-OO*t*Bu or Ti-OOcumyl intermediates due to electron donation from the alkyl functions, which explains the greater reactivity in epoxidations using H_2O_2. The electronic properties of Ti-OOR intermediates do not vary with pore size, which suggests that the differences in rate ratios among reactions involving TBHP or CHP *relative to* H_2O_2 between Ti-BEA-12.5 and Ti-SBA-15 result from inner-sphere interactions that are mediated by the surrounding void.

Inner-sphere interactions between surface functions (e.g., Ti-OOR and alkenes) bound *to the same active site* are mediated by the shape and size of the surrounding voids. Transition state theory formalisms analyzed through a Born-Haber thermochemical cycle show that the mesopores of Ti-SBA-15 allow for stabilizing interactions among reactive Ti-OOR intermediates with alkene reactants bound at the transition states. Within the micropores of *BEA, reactive Ti-OO*t*Bu and Ti-OOcumyl intermediates interact with 1-alkenes at the transition states for epoxidation in similar ways, because of steric limitations that inhibit the formation of specific conformations (i.e., the aliphatic tail of the 1-alkene interactions with the geminal dimethyl of *t*Bu or cumyl functional groups). These stabilizing interactions at the transition states for epoxidation are on the order of several kJ mol^{-1}, which can have large implications during low-temperature liquid catalysis.

Collectively, the data and interpretations presented here suggest that micropore-mediated interactions among reactive species can be tuned by engineering the shape and size of the surrounding pore environments which will influence the stability of critical reactive intermediates. The deconvolution of the specific interactions (e.g., between reactive species, solvents, pore walls) and the associated effects on catalysis at solid-liquid (and solid-gas) interfaces remains challenging and is on-going work within our group.

CHAPTER TEN
Conclusions and Future Outlook

10.1 Conclusions

The work within this dissertation have focused on developing quantitative structure-activity relationships (QSAR) that describe how inner- and outer-sphere interactions at solid-liquid interfaces in zeolites can be manipulated through changes in the identity of the active metal atom, size of the confining void, functionality of the nearby pores, choice of solvent, and reactive oxidant used. Collectively, the results presented show these *orthogonal* changes to the catalytic system can lead to differences in rates in excess of 10^6-fold. The QSARs developed here expand the field's understanding of what catalyst properties affect the rates and selectivities of liquid-phase oxidant catalysis, rationalize decades of observations within the literature, and will ultimately aid the rational design of new technologies and catalysts for desired liquid-phase catalytic transformations.

In Chapter 2, we proposed a series of elementary steps (i.e., a mechanism) to describe kinetic observations for alkene epoxidation with H_2O_2. First, H_2O_2 adsorbs to Lewis acidic active sites and is irreversibly activated to form a pool of metal hydroperoxide (M-OOH) and peroxide (M-(η^2-O_2)) intermediates. Fluid-phase alkene then enter the pores of the zeotype catalyst and react with the M-OOH and M-(η^2-O_2) intermediates through an Eley-Rideal type mechanism to form an epoxide, which then desorbs. Notably, the proposed mechanism is pervasive throughout this dissertation as it appears to explain observations on all group 4 and 5 metal-substituted zeolites and grafted silicates tested. Measurements of apparent activation enthalpies ($\Delta H_{App.}^{\ddagger}$) and entropies ($\Delta S_{App.}^{\ddagger}$) show that cyclohexene epoxidation is entropically favored over H_2O_2 decomposition, which shows that higher temperatures should be utilized in epoxidation reactions to maximize the selective use of H_2O_2.

Chapter 3 detailed how alkene epoxidation depends on the elemental identity of the active site. Specifically, groups 4 and 5 metal-substituted BEA activate H_2O_2 to form M-OOH and M-(η^2-O_2) intermediates. A combination of time-resolved *in situ* UV-vis spectroscopy and the isomeric distributions of reactions of cis-stilbene reveal that group 4 metals (i.e., Ti, Zr, and Hf) react primarily through M-OOH intermediates, while group 5 elements catalyze epoxidation through M-(η^2-O_2) moieties. Turnover rates for cyclohexene epoxidation and H_2O_2 increase

exponentially with the ligand-to-metal charge transfer energy of the reactive M-OOH and M-(η^2-O_2) intermediates. Specifically, epoxidation rates and selectivities vary over five- and two-orders of magnitude, respectively, between the weakest and strongest Lewis acids (i.e., Hf- and Ti-BEA). Chapter 4 extends these findings to the sulfoxidation of 2,5-dimethylthiophene. Similar to alkene epoxidation, rates of sulfoxidation increase by several orders of magnitude with the functional Lewis acid strength of the active metal center. Here, we also show that the turnover rates for sulfoxidation depend exponentially on the Mayr nucleophilicity of the solvent, which suggests that the coordination of solvent molecules to Lewis acidic Ti centers can greatly affect the measured reactivity of the catalyst.

In Chapters 5 and 6, we discussed the role of confinement within *hydrophilic* microporous and mesoporous materials on alkene epoxidation. All hydrophilic materials were chosen within these studies to minimize the effects of localized, intraporous H_2O on epoxidation kinetics to the best of our abilities. Within Ti-, Nb-, and Ta-substituted zeolites (BEA and FAU) and grafted mesoporous silica, there is no functional change in the mechanism for alkene epoxidation or identity of reactive intermediates responsible for reaction. Rather, measured kinetic differences among porous supports reflect differences in the $\Delta H_{App.}^{\ddagger}$ and $\Delta S_{App.}^{\ddagger}$ that systematically depend on the size of the voids surrounding active sites. Thermochemical analysis of measured $\Delta H_{App.}^{\ddagger}$ and $\Delta S_{App.}^{\ddagger}$ show that styrene is preferentially, enthalpically stabilized within the pores of *BEA (0.65 nm), relative to FAU (1.3 nm) and mesoporous SiO_2 (~5.4 nm). This enthalpic stabilization comes with an entropic cost, whose compensation presents an energetic optimum within Ti-FAU. Specifically, the FAU framework is a Goldilocks case among *BEA and SiO_2, where there is the "right" combination of enthalpic stabilization from dispersive interactions among pore walls and stabilized epoxidation transition states, while providing enough steric freedom to mimize entropic losses. Collectively, these results show that traditional confinement effects can stabilize surface intermediates (e.g., transition states) critical to catalysis; yet, there are considerable finite-size effects that must be considered during liquid-phase catalysis and that enthalpic stabilization does not necessarily equate to more-productive materials.

The structure of H_2O within zeolite materials and how it impacts the stability of surface intermediates was explored within Chapters 7 and 8. In these studies, the role of H_2O and pore hydrophilicity was studied within Ti-BEA materials, which was crucial so that differences in confinement *between different silicate supports* would not convolute results. Turnover rates for 1-

octene epoxidation with H_2O_2 are 100-fold greater on Ti-BEA that contain ~5 $(SiOH)_4$ *per unit cell* in comparison to defect-free, hydrophobic analogues. Rates of H_2O_2 decomposition, however, show no functional dependence on the hydrophilicity of the pores, which show that the most hydrophilic Ti-BEA are simultaneously the more reactive and selective catalysts for epoxidation reactions. These catalytic differences are no caused by changes in the mechanism for epoxidation, electronic affinity of the active site, identity of the reactive intermediate, or intraporous mass transfer restrictions. Rather, the disruption of confined H_2O structures proximate to Ti active sites upon formation of epoxidation transition states leads to large increases in excess entropy, which decreases the free energy of the epoxidation transition states. Comparisons of measured $\Delta H_{App.}^{\ddagger}$ and $\Delta S_{App.}^{\ddagger}$ to the heats of adsorption for 1,2-epoxyoctane into these materials in the presence of H_2O reveal linear free energy relationships that describe the ways in which the octyl tail of the epoxide disrupts confined H_2O structures. Collectively, these findings clarify how molecular interactions between reactive species, hydrogen-bonded solvent networks, and polar surfaces and influence the thermodynamic stability of surface intermediates.

Chapter 9 laid the foundation for understanding how lateral, inner-sphere interactions among reactive titanium alkyl/hydroperoxide intermediates and loosely bound alkenes at epoxidation transition states influence the stability of the aggregate complex. Rates of 1-octene epoxidation are 1700- and 40-fold greater with H_2O_2 than CHP within Ti-BEA and Ti-SBA-15, respectively. Epoxidations with H_2O_2 yield the greatest rates, as Ti-OOH intermediates are more electrophilic than Ti-OO*t*Bu and Ti-OOcumyl species which is associated with the electron-donating alkyl functional groups. Differences in epoxidation catalysis via H_2O_2 in Ti-BEA and Ti-SBA-15 relate only to differences in the adsorption enthalpy for the corresponding alkene into the two porous frameworks because the H atom does not interact with the alkene to any measurable extent within these materials. Reactive *t*-butyl and cumyl hydroperoxide intermediates formed at Ti active sites within Ti-BEA interaction with *n*-alkene epoxidation transition states to similar extents, because the micropores of *BEA require that the *t*Bu and cumyl functional groups orient themselves with the geminal dimethyl moiety pointed towards the aliphatic carbon tail. Within mesoporous Ti-SBA-15, however, the larger reaction volume surrounding active sites gives the cumyl functional groups the flexibility to interact with the methylene tails to a greater extent than -*t*Bu or -H functions. These interactions manifest as differences in the free energies, which we denote as inner-sphere interactions among these reactive ligands bound to the same active site. The

findings presented clarify how these interactions depend on the shape and size of the surrounding void and ultimately influence the stability of the surface complex, which may have large ramifications on catalysis and separations processes.

This dissertation presents *experimental* synthetic, kinetic, spectroscopic, and thermodynamic methods to determine how changes to the catalytic system are manifested in specific free energies that influence the stability of complexes critical to catalysis. Specifically, these methods are laid out in the context of liquid-phase oxidation catalysis; yet, are generalizable and may be extended to other catalytic systems (e.g., MOFs, AlPOs, SAPOs), reactions (e.g., aldol condensation, hydrogenolysis), and phases (e.g., in gas-phase catalysis).

10.2 Future Outlook

The following sections are meant to outline several future researcher directions for developing quantitative structure-activity relationships in the context of epoxidation catalysis. Specifically, I try to detail my thought processes when motivating and describing these future projects and intend to for these sections to serve as "food for thought."

10.2.1 Structure of Water within Zeolites

The presence, proximity, and structure of H_2O clusters near Ti active sites influence the stability of intermediates critical to catalysis and greatly impact measured rates and selectivities. Within Ti-BEA, our results (Chapters 7 and 8) show that H_2O loses three-dimensional order, with respect to bulk H_2O, and forms discrete water structures that are highly sensitive to the presence of hydrophobic surface intermediates (e.g., epoxidation transition states). The methodology presented in these chapters is amenable to studying more broadly how the shape and size of a zeolitic pore affects the structure of H_2O, considering there have been numerous studies[14, 29-30, 32, 64, 69-71, 295] that implicate hydrophilicity on affecting alkene epoxidation catalysis. Deconvoluting the structure of H_2O and its effects on surface intermediates relies on synthesizing a series of Ti-substituted zeolites with the same framework structure, yet varying densities of internal silanol groups to systematically vary the amount of H_2O localized near active sites.

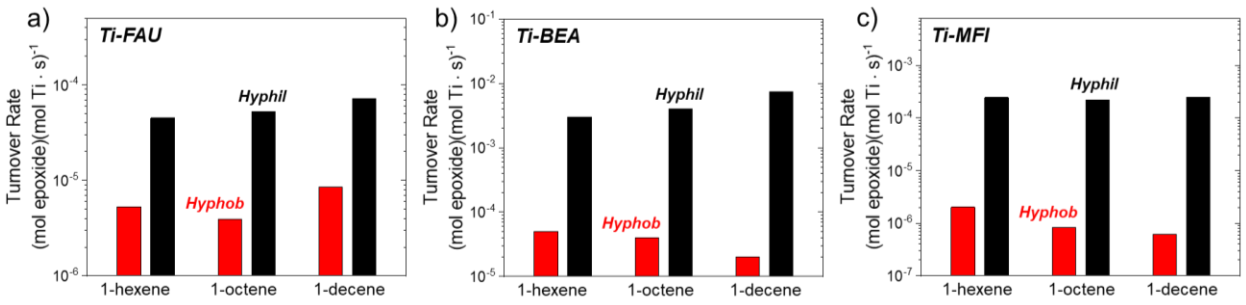

Figure 10.1 Turnover rates for 1-hexene, 1-octene, and 1-decene epoxidation (0.5 mM alkene, 10 mM H_2O_2, 39 mM H_2O, in CH_3CN, 313 K) over hydrophilic and hydrophobic (a) Ti-FAU, (b) Ti-BEA, and (c) Ti-MFI materials.

Figure 10.1 shows how turnover rates for *n*-alkene epoxidation vary with increasing chain length of the alkene over hydrophobic and hydrophilic variants of Ti-FAU, Ti-BEA, and Ti-MFI. Within Ti-FAU, rates of 1-hexene, 1-octene, and 1-decene are 10-fold greater on hydrophilic materials than their hydrophobic analogues and this difference does not appear to depend strongly on the chain length of the alkene. Rates of 1-hexene epoxidation are 60-fold greater in hydrophilic Ti-BEA than hydrophobic Ti-BEA, and the difference in catalytic performance between these two materials increases with alkene chain length to a factor of 150 for 1-decene. These differences are exacerbated within Ti-MFI materials, where the difference in turnover rates among hydrophilic and hydrophobic materials increases from a factor of 100 to 400 between 1-hexene and 1-decene. Similar to Chapter 7, these data show that the rates of *n*-alkene epoxidation are greater in hydrophilic Ti-zeolites than their hydrophobic analogues. Further, that the magnitude of these differences and the dependence on chain length appear to be intimately coupled with the shape and size of the surrounding pore. Further exploration of how H_2O structures within these environments and how restructuring upon formation of epoxidation transition states should rely on the methods to deconvolute excess enthalpic and entropic contributions that arise from differences in SiOH density among these materials. These results should be paired with *in situ* vibrational spectroscopy to deconvolute the different vibrational modes of H_2O and relate the aggregate spectra to broad changes in the number of hydrogen bonds among H_2O molecules. Finally, the data should be compared to molecular dynamics simulations for H_2O within these structures to build a molecular picture of how solvent structure dynamics influence the stability of surface intermediates.

10.2.2 Synthetic Methods to Tune Hydrophilicity

The catalytic prowess of a material may strongly correlate with the density of polar functions contained within it. In our work, we have seen that epoxidation rates and selectivities vary by orders of magnitude among nominally similar Lewis acid zeolite structures with varying densities of SiOH functions. To fully vet this area of investigation, new synthetic methods that allow control over the density of SiOH "defects" within zeolites are needed. Zeolites are typically synthesized hydrothermally in either hydroxide (OH^-) or fluoride (F^-) media,[22] which can tune the nominal hydrophilicity of the crystalline product. In general, solvated OH^- possess greater hydration radii than solvated F^-, which promotes disorder during crystallization and results in the presence of point defects within the final zeolite crystals.[373] Synthesis in F^- media is usually achieved using a structure directing agent (SDA) that is either in fluoride form (e.g., tetrapropylammonium fluoride, TPAF) or by the addition of hydrofluoric acid (HF) to a hydroxide-form SDA (e.g., tetrapropylammonium hydroxide; TPAOH). The recombination of HF with TPAOH forms a stoichiometric amount of TPAF and H_2O. Therefore, we hypothesize that the hydrophilicity of the end material can be controlled through systematically changing the HF:SDA ratio in the synthesis gel, prior to crystallization.

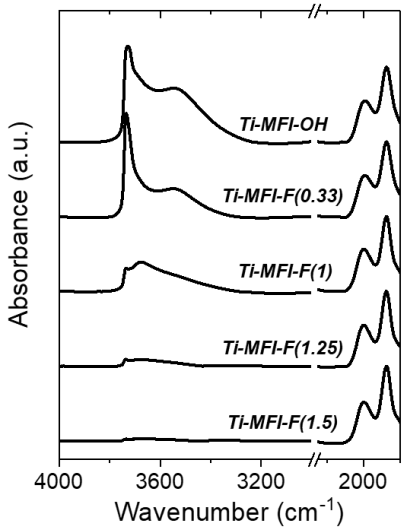

Figure 10.2. Infrared difference spectra of Ti-MFI-OH and Ti-MFI-F(*x*) under He flow (50 cm^3 min^{-1}) at 573 K. All spectra have been normalized to v(Si-O-Si) overtones at 1860 cm^{-1} and are vertically offset for clarity.

We have adapted the synthesis procedure for Ti-MFI-OH from the International Zeolite Association,[67] where we add specific amounts of HF to the synthesis gel. We adapt the naming nomenclature Ti-MFI-F(*x*), where *x* represents the HF:SDA ratio in the original synthesis gel. Figure 10.2 shows infrared spectra under dehydrating conditions for Ti-MFI synthesized using this methodology. Most hydrothermal syntheses that use HF only do so in a 1:1 ratio with the hydroxide SDA. Figure 10.2 shows that the average SiOH density (indicated by the area of v(O-H) between 3200 – 3800 cm^{-1}) decreases systematically with the amount of HF included in the synthesis gel. Moreover, there is still significant v(O-H) bands in Ti-MFI-F(1), which suggests that even materials synthesized with a stoichiometric amount of HF (or presumably using the fluoride-containing SDA) result in crystals containing a significant amount of SiOH defects. The vibrational features of SiOH are nearly immeasurable when a 50% excess of HF is added, likely because the equilibrium is biased for all SDA molecules to exist in the fluoride form via le Châtlier's principle. This work is currently on-going but exemplifies the utility in varying the amount of HF in a synthesis to control the hydrophilicity of the end material. For example, this methodology can likely be extended to the synthesis of other Lewis and Brønsted acid zeotypes (e.g., Ti-BEA, Ti-MWW, Ti-MOR, …).

10.2.3 Influence of Solvent Identity on Epoxidation

The hydrogen peroxide-propylene oxide (HPPO) process is one of the few industrially practiced methods to synthesize an epoxide from H_2O_2. This process relies on a Ti-MFI (also known as TS-1) catalysis that reacts with high pressure propylene and H_2O_2 in a methanol solvent. Several groups have investigated the role of solvent identity on liquid-phase oxidation catalysis with Ti-Zeolite catalysts;[30, 65, 213, 374] however, most studies rely on phenomenological observations and do not relate differences in measured catalysis to thermodynamic or spectroscopic measurements to infer how the solvents influence the stability of reactive species. The kinetic, spectroscopic and thermodynamic analyses used within this dissertation are amenable to understanding how solvents structure within microporous environments and, in turn influence the stability of reactive species. The fundamental understanding for solvent-dependent stabilization of surface intermediates is critical so that future systems may be rationally designed with these principles considered.

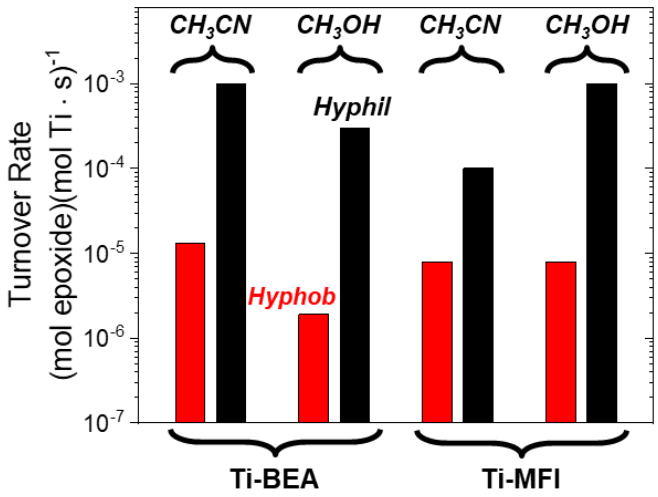

Figure 10.3. Turnover rates for 1-octene epoxidation with H_2O_2 (0.5 mM 1-octene, 10 mM H_2O_2, 39 mM H_2O, 313 K) over hydrophilic and hydrophobic Ti-BEA or Ti-MFI.

Figure 10.3 shows how 1-octene epoxidation turnover rates vary in methanol (CH_3CN) and acetonitrile (CH_3CN) solvents over hydrophilic and hydrophobic Ti-BEA and Ti-MFI. Within Ti-BEA, rates of epoxidation are greater on hydrophilic materials by a factor of ~100; yet, are lower by a factor of ~5 in CH_3OH when compared to CH_3CN. Alternatively, epoxidation appears to be insensitive to solvent within hydrophobic Ti-MFI, while reactions in CH_3OH are an order-of-magnitude faster than those within CH_3CN in hydrophilic Ti-MFI. These data clearly show how epoxidation rates depend strongly on the choice of solvent, polarity of the pores, and the size of the confining void. An initial reading of the literature suggests that Ti-MFI activates H_2O_2 within CH_3OH to form reactive "five-membered ring" Ti-OOH intermediates that are stabilized by an ancillary CH_3OH,[356] which may explain the differences between catalysis within the MFI and BEA frameworks. Our preliminary data, however, suggests that this may not be the sole reason for these differences, as hydrophilic Ti-MFI appears to be highly sensitive to the choice of solvent while hydrophobic Ti-MFI are catalytically agnostic. This suggests that the presence and proximity of SiOH to Ti active sites may stabilize or nucleate *ordered* CH_3OH that influences the stability of reactive intermediates. Deconvoluting how the proximity and topology of CH_3OH structures within Ti-zeolites affects epoxidation catalysis from changes in the electronic structure of reactive intermediates will require an in-depth kinetic, spectroscopic, thermodynamic, and computational

study to understand how finite-size effects on solvent molecules influences catalysis within these microporous materials.

10.2.4 Solvent-Water Mixtures to Stabilize Intermediates

Solvents influence catalysis by altering the thermodynamic stability of intermediates and reactive complexes, changing barriers for kinetically relevant processes, or facilitating mass transfer.[18, 348] Recent publications have combined rate measurements with *ab initio* molecular dynamics for alcohol dehydration by a homogeneous acid catalyst.[346, 348] Specifically, these studies showed that aqueous organic solvents (e.g., *gamma*-valerolactone (GVL), dimethylsulfoxide (DMSO)) form hydrophilic domains surrounded by organic residues around transition states for dehydration. These core-shell solvent structures increase the average lifetime of the hydrogen bonding interactions among H_2O molecules with the hydrophilic transition states that leads to reaction rates that are greater within purely aqueous solvent. These mixed-solvent structures form around highly polar species, which suggests that these same structures may form during epoxidation catalysis. For example, reactive Ti-OOH intermediates may nucleate similar H_2O-organic solvent structures that can be used to tune rates of epoxidation.

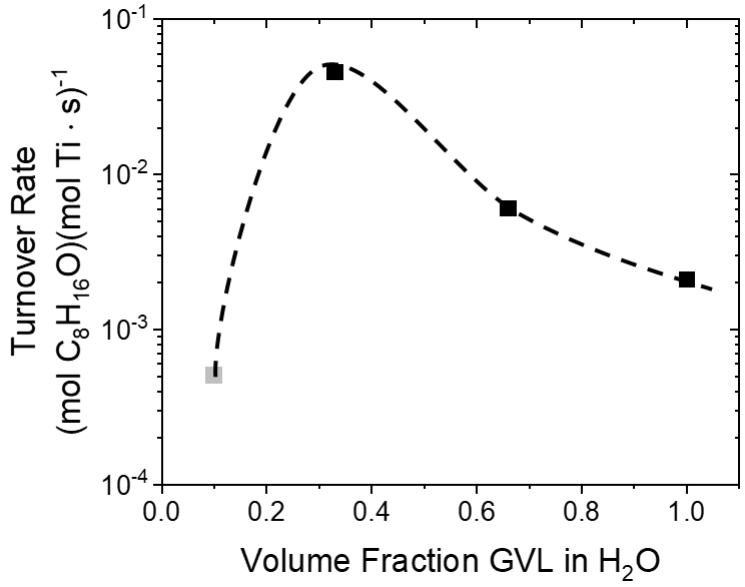

Figure 10.4. Turnover rates for 1-octene epoxidation over Ti-BEA as a function of *gamma*-valerolactone (GVL) volume fraction in H_2O (10 mM 1-octene, 10 mM H_2O_2, 313 K). The transparent point for a 0.1 GVL volume fraction signifies that no measurable rate was obtained. The dashed curve is intended to guide the line.

Figure 10.4 shows how turnover rates for 1-octene epoxidation varies as a function of GVL volume fraction, in H_2O, over hydrophilic Ti-BEA. Rates of epoxidation are immeasurable at low GVL volume fractions (10%), increase to a maximum at 33%, and subsequently decrease as the fraction of GVL is increased further. Importantly, the rate of 1-octene epoxidation with 33% GVL in H_2O is a factor of 5 greater than in CH_3CN (Chapter 7). These data collectively suggest that specific aqueous organic structures may form around active intermediates and transition states that lead to large changes in the rates and selectivities for epoxidation. Future studies should start by screening epoxidation reactions among organic-H_2O mixtures (e.g., *gamma*-valerolactone, *delta*-valerolactone, *gamma*-butyrolactone, acetonitrile, methanol, ethanol, dimethylformamide, tetrahydrofuran between volume fractions of 0.1 – 1 to quickly assess whether there is a strong influence of organic-H_2O structure on measured catalysis. For these initial experiments, I recommend looking for differences that are greater than a factor of 5. Notably, the use of ketone solvents is not recommended as Ti-zeolites are known to catalyze the Baeyer-Villiger reaction, which may obviate results. Further, DMSO and other sulfoxides are discouraged as solvents because they can undergo oxidation to form the corresponding sulfone (Chapter 4). Once the solvent choice has been narrowed down, turnover rates should be measured as a function of reactant concentrations to confirm that the solvent is not participating as a co-catalyst; rather, is affecting the thermodynamic stability of specific surface intermediates. Comparisons of activation enthalpies among different solvent mixtures, *at a common reference state*, should be used to guide one's intuition regarding how the stability of surface intermediates are changing. *In situ* attenuated total reflectance-infrared spectroscopy (ATR-IR; Chapter 8) should be used to compare changes in the structure of H_2O through qualitative analysis of v(O-H) in the different samples. Finally, isothermal titration calorimetry (Chapter 8) can be used to look at the enthalpic stability of reactive Ti-OOH intermediates and bound epoxide products within the different solvent mixtures to map out the enthalpy landscape for a given catalytic reaction.

10.2.5 Functional Group Additivity on Inner-Sphere Interactions

In the context of transition state theory, turnover rates for epoxidation depend exponentially on an apparent free energy of activation $\Delta G_{App}^{\ddagger}$, which is given by

$$\Delta G_{App}^{\ddagger} = \Delta G_{Int.}^{\ddagger} + \Delta G_{Excess} \quad (10.1)$$

where $\Delta G_{Int.}^{\ddagger}$ is the intrinsic free energy of activation and ΔG_{Excess} is the excess free energies that encompasses any non-idealities that result from inner- or outer-sphere interactions with the transition states for epoxidation. This dissertation has laid the groundwork for how ΔG_{Excess} can be further deconvoluted

$$\Delta G_{Excess} = \Delta G_{Ads} + \Delta G_{ISI} + \Delta G_{Solv.} + \cdots \quad (10.2)$$

which contains contributions from adsorption (ΔG_{Ads}), inner-sphere interactions among reactive species (ΔG_{ISI}), and solvent restructuring ($\Delta G_{Solv.}$). The ellipses in included to signify that there may be other contributions to ΔG_{Excess} that have not been explored within these studies. Chapter 9 discussed the ramifications of inner-sphere interactions among multiple surface intermediates that are bound to a single active site (i.e., ΔG_{ISI}). To the best of our knowledge, there are few, if any, studies in the open literature that quantify these interactions. As such, the literature would benefit greatly from an in-depth study that quantifies ΔG_{ISI} for a broad range of reactants to understand how these interactions depend on the chemical and physical properties of the surface intermediate and the size of the surrounding pore.

The work outlined within this dissertation focused primarily on developing the experimental and analysis tools to understand and quantify interactions among Ti-OO*t*Bu or Ti-OOcumyl intermediates with 1-octene at epoxidation transition states. Values of ΔG_{ISI} cannot be determined directly; rather, their dependence on reactant structure and pore size depends on the assignment of a relevant reference state. As such, we assigned hydrophilic Ti-BEA as the reference state to understand how these alkyl peroxide intermediates interact with loosely bound alkenes when they are nominally unconfined (i.e., within mesoporous Ti-SBA-15). Future studies that flesh out these interactions should start with similar catalysts (i.e., Ti-BEA and Ti-SBA-15) and systematically vary the alkene used for epoxidation (e.g., 1-hexene, 1-heptene, 1-octene, 1-nonene, 1-decene, cyclopentene, cyclohexene, cycloheptene, styrene, allyl alcohol, allyl nitrile). Studies should begin by measuring the concentration dependence of epoxidation turnover rates on each alkene to find reaction conditions that result in a common reference state (e.g., fluid-phase alkene and Ti-OOalkyl intermediates). In short, the development of a model for how these inner-sphere

interactions depend on the chemical functionality of the alkene will require measurement of activation enthalpies and adsorption enthalpies for each of these alkenes over Ti-BEA and Ti-SBA-15 catalysts. The ways in which $\Delta\Delta G_{ISI}$ (for Ti-SBA-15 relative to Ti-BEA) depend on the identity of the alkene should then be correlated with some steric or chemical parameter of the alkene (e.g., methylene units, H-bonding donor-acceptor number, kinetic diameter) to evince a quantitative relationship that describes these interactions.

10.2.6 Condensed-Phase Solvation in Gas-Phase Epoxidation Catalysis

Catalytic reactions that proceed at solid-liquid interfaces possess all of the complexities of gas-phase catalysis, but also involve solvating interactions that can further stabilize intermediates.[18, 346] These interactions are often beneficial in terms of increasing the rates of reaction and can be used to fine-tune selectivity. Gas-phase catalysis, depending on the physical properties of the reactants and products, offers to ability to easily separate products from reactants and may require fewer down-stream separations units. There is a large opportunity to study the effects of solvation within microporous materials on epoxidation catalysis as there are few, if any, studies that systematically study the effects of solvation in gas- and liquid-phases on this reaction. This will require the use of a gas-phase packed-bed reactor with in-line reactant vaporization. A systematic study for gas-phase epoxidation kinetics can be made analogously to liquid-phase epoxidation over various Ti-silicate materials (e.g., Ti-MFI, Ti-BEA, Ti-FAU, Ti-SBA-15). Turnover rates should be measured as a function of reactant pressure and temperature to determine reaction conditions where surface coverages of reactive species are comparable to those measured in liquid-phase reactions. At sufficiently low pressures and high temperatures, the micropores will be predominantly empty and the primary mode of solvation will be through dispersive interactions among reactive species and the pore walls. The micropores within zeolites enable capillary condensation of species at pressures well below the vapor pressure,[274] which may allow reactants or spectator molecules (e.g., common solvents) to condense within the micropores.

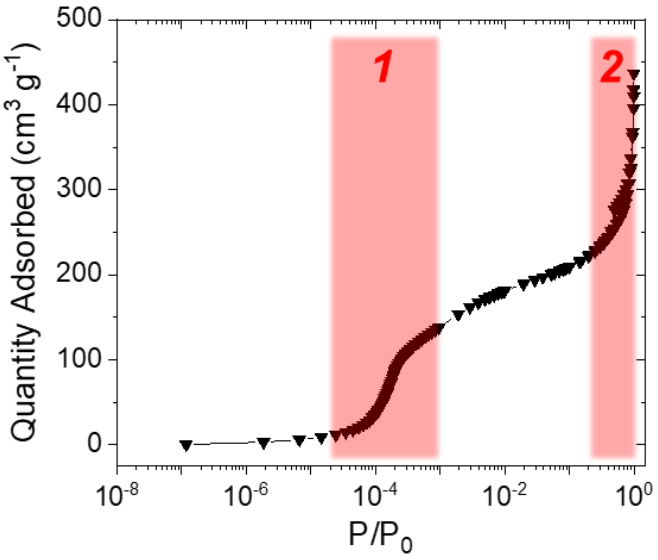

Figure 10.5. Nitrogen adsorption isotherm (77 K) over Ti-FAU.

Figure 10.5 shows a nitrogen adsorption isotherm (77 K) for Ti-FAU as an illustrative case for how volumetric adsorption experiments can inform kinetics. Within the adsorption isotherm, the region labelled "1" corresponds to the relative pressure (P/P_0) that corresponds to capillary condensation within micropores, while the region denoted "2" indicates mesopore filling. Adsorption isotherms of H_2O, alkenes, epoxide products, and "solvent" molecules (e.g., CH_3CN, CH_3OH) should be measured *at reaction temperature* to determine relative pressures that correspond to micropore filling. For example, transition states for epoxidation within Ti-BEA may be stabilized through the presence of condensed-phase CH_3CN, which will be observed by differences in apparent activation barriers during gas- versus liquid-phase catalysis. Acetonitrile may be vaporized in-line in the gas-phase reactor at pressures that correspond to micropore filling (via the corresponding adsorption isotherm for CH_3CN). The effects of micropore condensation during gas-phase catalysis may enable *nominal* gas-phase catalysis with the stabilization afforded by the liquid phase. Notably, pore condensation may be observed by vibrational spectroscopy (e.g., infrared) by a sharp increase in the vibrational features of adsorbed CH_3CN with partial pressure. A way to begin these studies may be to measure steady-state turnover rates at a constant alkene and H_2O_2 partial pressure, while increasing the pressure of CH_3CN to see how epoxidation rates depend on the presence of this "spectating" molecule. Once a system for gas-phase epoxidation catalysis is operational, there is a significant opportunity to study how the different facets of the catalyst affect measured rates (e.g., silanol density, metal identity, pore size).

10.2.7 Periodic Trends in Gas-Phase Epoxidation Catalysis

The stability of epoxidation transition states depends strongly on the identity of the active metal atom. Chapters 3 and 4 discussed how changing the identity of the active site from Ti to Hf within the *BEA framework decreases rates and selectivities for epoxidation by factors of 100,000 and 100-fold, respectively. These differences were observed within liquid-phase catalysis; yet, there may be significant differences when the micropores are empty as is in gas-phase catalysis. The speciation of the resting active site (e.g., open versus closed sites)[159, 163] may influence how reactive species form and react. For example, a pendant -OH on either group 4 open sites (e.g., $Zr(OSi)_3OH$) or group 5 active sites (e.g., $Nb(OSi)_4OH$) can nucleate small hydrogen-bonded solvent structures that may stabilize reactive intermediates to varying extents. It should be noted that, in my opinion, there is no convincing evidence for the presence of titanium open sites in zeolites. As such, one of the predominant differences may be the presence of the hydroxyl moiety on group 5 catalysts.

The formation of surface intermediates may be highly sensitive to the presence of this extra ligand, which may induce specific interactions that were obviated within the liquid phase. To explore these interactions, a systematic study for gas-phase epoxidation over groups 4 and 5 catalysts should be conducted. Initial experiments should focus on Ti- and Nb-zeolites as prototypical groups 4 and 5 metals, respectively. Kinetic measurements should be made as a function of reaction conditions to infer specific conditions that correspond to specific most abundant reactive intermediates (MARI; See Section 10.2.7), such that measurements of activation enthalpies are comparable among materials. In situ or operando vibrational spectroscopy should be coupled with kinetic measurements to relate perturbations in the v(O-H) from the active sites upon formation of various surface intermediates during catalysis. Transient kinetic analysis of "cut-on" or "cut-off" experiments may reveal how the surface coverages of M-OOH and M-(η^2-O_2) are affected by nearby -OH functions during their formation or consumption. Specifically, researchers should look for "heartbeat" features (akin to a cardiogram) in the vibrational spectra, which will indicate the weakening or strengthening of a specific vibrational feature due to intra-molecular interactions among surface intermediates. Finally, determining how these differences correlate with the steric bulk of the alkene (e.g., 1-hexene, cyclohexene, 2,4-dimethylbutene) may evince how the presence of this hydroxyl function affects this chemistry and contributes to measured catalysis in excess of solely electronic arguments related to the identity of the active site.

10.2.8 Supported Rhenium Ions for Oxidation Catalysis

Methyltrioxorhenium (MTO) is a homogeneous catalyst that catalyzes alkene epoxidation with H_2O_2. Goldsmith *et al.* showed that H_2O acts as a co-catalyst for epoxidation with MTO, where apparent rate constants for cyclohexene epoxidation increase by a factor of 2 when the concentration of H_2O is increased from 0 to 5 M.[31] Rhenium oxides supported in zeolites (through incipient wetness impregnation of ammonium perrhenate)[375] can form monomeric silyloxy-trioxorhenium structures (Figure 10.6) that are chemically similar to MTO. There is a dearth of literature on supported trioxorhenium species, as most studies focus on rhenium oxide nanoparticles supported within zeolites for hydrogenation and dehydrogenation catalysis. As such, there is a tremendous opportunity to study Re incorporated into zeolites and silicates for oxidation catalysis. Initial studies should attempt to post-synthetically modify zeolite *BEA with a Rhenium chloride (e.g., $ReCl_3$) using liquid-phase incorporation techniques. Raman spectroscopy should then be used to characterize ν(Re=O), which has a strong absorbance around 950 cm^{-1}.[375] Unpublished results from our group shows that Mo atoms incorporated into *BEA readily leach into solution, which is likely due to the oxidative cleavage of the SiO-Mo bonds. Comparisons of Re and Mo bis-pyrazine-dithiolene complexes show that Re analogues require significantly more-negative redox potentials (~ -2.0 V for Re^{IV}/Re^{V} versus -0.4 V Mo^{IV}/Mo^{V}, referenced to Fc/Fc^{+}),[376] which suggests that Re may be stable under epoxidation conditions. Initial experiments with Re-silicates should check for leaching via hot-filtration experiments to confirm this hypothesis. If Re does leach from these materials, I recommend the use of a gas-phase epoxidation system (see above) as an attempt to study these materials.

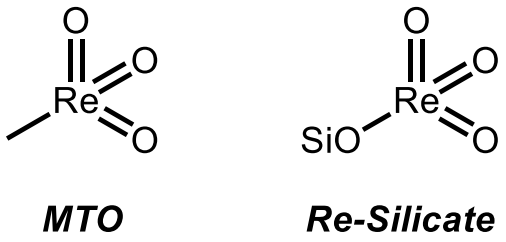

Figure 10.6. Methyltrioxorhenium (MTO) and rhenium grafted onto a SiOH function (Re-Silicate; e.g., within a zeolite or on a silicate).

Epoxidation catalysis by MTO is highly sensitive to the presence of H_2O (see above), which suggests that Re-silicate catalysts may also exhibit strong dependencies on the density of

polar functions (e.g., SiOH groups). As such, there are a plethora of studies that can relate to how Re-silicate catalysts respond to differences in silanol density (Chapters 7 and 8). Silanols and silanol nests proximate to Re active sites may form specific solvent structures that ligate Re atoms in ways similar to MTO that may affect the stability of reactive species and improve rates of epoxidation. These H_2O-Re structures may also be studied using in situ vibrational spectroscopy and isothermal titration calorimetry to confirm their existence and relate their thermochemical properties to differences in catalysis.

10.2.9 Extension of Methodology to Other Catalytic Systems

This dissertation focused predominantly on liquid-phase epoxidation catalysis within early transition metals incorporated into porous silicates. The methodology developed, as such, was primarily in the context of zeolite and silicate catalysis; however, these kinetic, spectroscopic, and thermodynamic analyses are easily extended to other systems. There are numerous other types of porous materials that are often investigated for catalysis, including metal organic frameworks (MOFs), aluminum phosphates (AlPOs), and silicon aluminum phosphates (SAPOs), among others. These materials are encompassed within the term "zeotype," which describes any family of materials that are based or inspired by the structure of zeolites. For example, there are several studies that detail the synthesis of Ti- and Nb-incorporated ALPOs[377-378] that are isostructural to the MFI framework, that may be good candidates for alkene epoxidation catalysis. Anh *et al.* have recently shown that Nb and Ti atoms grafted onto Zr nodes of the NU-1000 MOF are active for alkene epoxidation.[379] MOFs are a potentially attractive framework to study these effects, as there is an incredible amount of flexibility in terms of tuning the pore size, functionality, and active site identity within these materials.

REFERENCES

1. Corma, A.; Fornes, V.; Pergher, S. B.; Maesen, T. L. M.; Buglass, J. G., Delaminated zeolite precursors as selective acidic catalysts. *Nature* **1998,** *396*, 353-356.

2. Li, C.; Paris, C.; Martínez-Triguero, J.; Boronat, M.; Moliner, M.; Corma, A., Synthesis of reaction-adapted zeolites as methanol-to-olefins catalysts with mimics of reaction intermediates as organic structure-directing agents. *Nature Catal.* **2018,** *1*, 547-554.

3. Rangnekar, N.; Mittal, N.; Elyassi, B.; Caro, J.; Tsapatsis, M., Zeolite membranes - a review and comparison with MOFs. *Chem. Soc. Rev.* **2015,** *44*, 7128-7154.

4. Lai, Z.; Bonilla, G.; Diaz, I.; Nery, J. G.; Sujaoti, K.; Amat, M. A.; Kokkoli, E.; Terasaki, O.; Thompson, R. W.; Tsapatsis, M.; Vlachos, D. G., Microstructural Optimization of a Zeolite Membrane for Organic Vapor Separation. *Science* **2003,** *300*, 456-460.

5. Bassler, P.; Göbbel, H.; Weidenbach, M., The new HPPO Process for Propylene Oxide: From Joint Development to Worldscale Production. *Chem. End. Trans.* **2010,** *21*, 571-577.

6. Russo, V.; Tesser, R.; Santacesaria, E.; Di Serio, M., Chemical and Technical Aspects of Propene Oxide Production via Hydrogen Peroxide (HPPO Process). *Ind. Eng. Chem. Res.* **2013,** *52*, 1168-1178.

7. Noh, G.; Shi, Z.; Zones, S. I.; Iglesia, E., Isomerization and β-scission reactions of alkanes on bifunctional metal-acid catalysts: Consequences of confinement and diffusional constraints on reactivity and selectivity. *J. Catal.* **2018,** *368*, 389-410.

8. Gounder, R.; Davis, M. E., Monosaccharide and disaccharide isomerization over Lewis acid sites in hydrophobic and hydrophilic molecular sieves. *J. Catal.* **2013,** *308*, 176-188.

9. Müller, P.; Burt, S. P.; Love, A. M.; McDermott, W. P.; Wolf, P.; Hermans, I., Mechanistic Study on the Lewis Acid Catalyzed Synthesis of 1,3-Butadiene over Ta-BEA Using Modulated Operando DRIFTS-MS. *ACS Catal.* **2016,** *6*, 6823-6832.

10. Corma, A.; Llabre´s i Xamena, F. X.; Prestipino, C.; Renz, M.; Valencia, S., Water Resistant, Catalytically Active Nb and Ta Isolated Lewis Acid Sites, Homogeneously Distributed by Direct Synthesis in a Beta Zeolite. *J. Phys. Chem. C* **2009,** *113*, 11306-11315.

11. Bregante, D. T.; Thornburg, N. E.; Notestein, J. M.; Flaherty, D. W., Consequences of Confinement for Alkene Epoxidation with Hydrogen Peroxide on Highly Dispersed Group 4 and 5 Metal Oxide Catalysts. *ACS Catal.* **2018,** *8*, 2995-3010.

12. Boronat, M.; Concepción, P.; Corma, A.; Navarro, M. T.; Renz, M.; Valencia, S., Reactivity in the confined spaces of zeolites: the interplay between spectroscopy and theory to develop structure–activity relationships for catalysis. *Phys. Chem. Chem. Phys.* **2009,** *11*, 2876-2884.

13. Gounder, R.; Iglesia, E., The catalytic diversity of zeolites: confinement and solvation effects within voids of molecular dimensions. *Chem. Commun.* **2013,** *49*, 3491-3509.

14. Gounder, R.; Davis, M. E., Beyond shape selective catalysis with zeolites: Hydrophobic void spaces in zeolites enable catalysis in liquid water. *AlChE J.* **2013,** *59*, 3349-3358.

15. Sarazen, M. L.; Iglesia, E., Stability of bound species during alkene reactions on solid acids. *Proc. Natl. Acad. Sci.* **2017,** *114*, E3900-E3908.

16. Kosinov, N.; Liu, C.; Hensen, E. J. M.; Pidko, E. A., Engineering of Transition Metal Catalysts Confined in Zeolites. *Chem. Mater.* **2018,** *30*, 3177-3198.

17. Van Speybroeck, V.; Hemelsoet, K.; Joos, L.; Waroquier, M.; Bell, R. G.; Catlow, C. R. A., Advances in theory and their application within the field of zeolite chemistry. *Chem. Soc. Rev.* **2015,** *44*, 7044-7111.

18. Sievers, C.; Noda, Y.; Qi, L.; Albuquerque, E. M.; Rioux, R. M.; Scott, S. L., Phenomena Affecting Catalytic Reactions at Solid–Liquid Interfaces. *ACS Catal.* **2016,** *6*, 8286-8307.

19. Koval, C. A.; Lercher, J. A.; Scott, S. L. *Basic Research Needs for Catalysis Science to Transform Energy Technologies*; Department of Energy, Basic Energy Sciences: 2018.

20. Eckstein, S.; Hintermeier, P. H.; Zhao, R.; Barath, E.; Shi, H.; Liu, Y.; Lercher, J. A., Influence of Hydronium Ions in Zeolites on Sorption. *Angew. Chem. Int. Ed.* **2019,** *58*, 3450-3455.

21. Bregante, D. T.; Johnson, A. M.; Patel, A. Y.; Ayla, E. Z.; Cordon, M. J.; Bukowski, B. C.; Greeley, J.; Gounder, R.; Flaherty, D. W., Cooperative Effects between Hydrophilic Pores and Solvents: Catalytic Consequences of Hydrogen Bonding on Alkene Epoxidation in Zeolites. *J. Am. Chem. Soc.* **2019,** *141*, 7302-7319.

22. Cordon, M. J.; Harris, J. W.; Vega-Vila, J. C.; Bates, J. S.; Gupta, M.; Witzke, M. E.; Wegener, E. C.; Miller, J. T.; Flaherty, D. W.; Hibbitts, D. D.; Gounder, R., The Dominant Role of Entropy in Stabilizing Sugar Isomerization Transition States within Hydrophobic Zeolite Pores. *J. Am. Chem. Soc.* **2018,** *140*, 14244-14266.

23. Wang, M.; Jaegers, N. R.; Lee, M.-S.; Wan, C.; Hu, J. Z.; Shi, H.; Mei, D.; Burton, S. D.; Camaioni, D. M.; Gutierrez, O. Y.; Glezakou, V.-A.; Rousseau, R.; Wang, Y.; Lercher, J. A., Genesis and Stability of Hydronium Ions in Zeolite Channels. *J. Am. Chem. Soc.* **2019,** *141*, 3444-3455.

24. Bai, P.; Tsapatsis, M.; Siepmann, J. I., Multicomponent adsorption of alcohols onto silicalite-1 from aqueous solution: isotherms, structural analysis, and assessment of ideal adsorbed solution theory. *Langmuir* **2012,** *28*, 15566-76.

25. Farzaneh, A.; DeJaco, R. F.; Ohlin, L.; Holmgren, A.; Siepmann, J. I.; Grahn, M., Comparative Study of the Effect of Defects on Selective Adsorption of Butanol from Butanol/Water Binary Vapor Mixtures in Silicalite-1 Films. *Langmuir* **2017,** *33*, 8420-8427.

26. Saleheen, M.; Heyden, A., Liquid-Phase Modeling in Heterogeneous Catalysis. *ACS Catal.* **2018,** *8*, 2188-2194.

27. Wang, C.-H.; Bai, P.; Siepmann, J. I.; Clark, A. E., Deconstructing Hydrogen-Bond Networks in Confined Nanoporous Materials: Implications for Alcohol–Water Separation. *J. Phys. Chem. C* **2014,** *118*, 19723-19732.

28. Dartt, C. B.; Davis, M. E., Characterization and catalytic activity of titanium containing SSZ-33 and aluminum-free zeolite beta. *Appl. Catal. A* **1996,** *143*, 53-73.

29. Khouw, C. B.; Dartt, C. B.; Labinder, J. A.; Davis, M. E., Studies on the Catalytic Oxidation of Alkanes and Alkenes by Titanium Silicates. *J. Catal.* **1994,** *149*, 195-205.

30. Corma, A.; Esteve, P.; Martínez, A., Solvent Effects during the Oxidation of Olefins and Alcohols with Hydrogen Peroxide on Ti-Beta Catalyst: The Influence of the Hydrophilicity-Hydrophobicity of the Zeolite. *J. Catal.* **1996,** *161*, 11-19.

31. Goldsmith, B. R.; Hwang, T.; Seritan, S.; Peters, B.; Scott, S. L., Rate-Enhancing Roles of Water Molecules in Methyltrioxorhenium-Catalyzed Olefin Epoxidation by Hydrogen Peroxide. *J. Am. Chem. Soc.* **2015,** *137*, 9604-16.

32. Wang, L.; Sun, J.; Meng, X.; Zhang, W.; Zhang, J.; Pan, S.; Shen, Z.; Xiao, F. S., A significant enhancement of catalytic activities in oxidation with H_2O_2 over the TS-1 zeolite by adjusting the catalyst wettability. *Chem. Commun.* **2014,** *50*, 2012-2014.

33. Vega-Vila, J. C.; Harris, J. W.; Gounder, R., Controlled insertion of tin atoms into zeolite framework vacancies and consequences for glucose isomerization catalysis. *J. Catal.* **2016,** *344*, 108-120.

34. Bhan, A.; Gounder, R.; Macht, J.; Iglesia, E., Entropy considerations in monomolecular cracking of alkanes on acidic zeolites. *J. Catal.* **2008,** *253*, 221-224.

35. Conrad, S.; Wolf, P.; Müller, P.; Orsted, H.; Hermans, I., Influence of Hydrophilicity on the Snβ-Catalyzed Baeyer-Villiger Oxidation of Cyclohexanone with Aqueous Hydrogen Peroxide. *ChemCatChem* **2017,** *9*, 175-182.

36. Trzpit, M.; Soulard, M.; Patarin, J.; Desbiens, N.; Cailliez, F.; Boutin, A.; Demachy, I.; Fuchs, A. H., The Effect of Local Defects on Water adsorption in Silicalite-1 Zeolite: A Joint Experimental and Molecular Simulation Study. *Langmuir* **2007,** *23*, 10131-10139.

37. Zhang, K.; Lively, R. P.; Noel, J. D.; Dose, M. E.; McCool, B. A.; Chance, R. R.; Koros, W. J., Adsorption of water and ethanol in MFI-type zeolites. *Langmuir* **2012,** *28*, 8664-73.

38. Özgür Yazaydın, A.; Thompson, R. W., Molecular simulation of water adsorption in silicalite: Effect of silanol groups and different cations. *Microporous Mesoporous Mater.* **2009,** *123*, 169-176.

39. Nguyen, V. T.; Nguyen, P. T. M.; Dang, L. X.; Mei, D.; Wick, C. D.; Do, D. D., A comparative study of the adsorption of water and methanol in zeolite BEA: a molecular simulation study. *Molecular Simulation* **2014,** *40*, 1113-1124.

40. World Propylene Oxide Supply to Exceed 9.2 Mln Tonnes in 2017, According to New Report by Merchant Research & Consulting. <http://www.prweb.com/releases/2014/02/prweb11552989.htm> (accessed September 18th, 2016).

41. Kahlich, D.; U., W.; Lindner, J., Propylene Oxide. In *Ullmann's Encyclopedia of Industrial Chemistry*, Wiley: 2005.

42. Propylene Oxide. <https://www.ihs.com/products/chemical-technology-propylene-oxide.html> (accessed September 18th, 2016).

43. Anastas, P. T.; Zimmerman, J. B., *Innovations in Green Chemistry and Green Engineering*. Springer Science & Business Media: 2012.

44. Doble, M.; K., R.; Kumar, A., *Green Chemistry and Engineering*. Academic Press: 2010.

45. Taramasso, M.; Perego, G.; Notari, B. Preparation of porous crystalline synthetic material comprised of silicon and titanium oxides. 1983.

46. Clerici, M. G., Titanium Silicalite-1. *Metal Oxide Catalysis*. Wiley-VCH: 2009.

47. van Vliet, M. C. A.; Mandelli, D.; Arends, I. W. C. E.; Schuchardt, U.; Sheldon, R. A., Alumina: a cheap, active and selective catalyst for epoxidations with (aqueous) hydrogen peroxide. *Green Chem.* **2001,** *3*, 243-246.

48. Mandelli, D.; van Vliet, M. C. A.; Sheldon, R. A.; Schuchardt, U., Alumina-catalyzed alkene epoxidation with hydrogen peroxide. *Appl. Catal. A* **2001,** *219*, 209-213.

49. Wolf, P.; Hammond, C.; Conrad, S.; Hermans, I., Post-synthetic preparation of Sn-, Ti- and Zr-beta: a facile route to water tolerant, highly active Lewis acidic zeolites. *Dalton Trans* **2014,** *43*, 4514-9.

50. Srinivas, D.; Manikandan, P.; Laha, S. C.; Kumar, R.; Ratnasamy, P., Reactive oxo-titanium species in titanosilicate molecular sieves: EPR investigations and structure–activity correlations. *J. Catal.* **2003,** *217*, 160-171.

51. Thornburg, N. E.; Thompson, A. B.; Notestein, J. M., Periodic Trends in Highly Dispersed Groups IV and V Supported Metal Oxide Catalysts for Alkene Epoxidation with H_2O_2. *ACS Catal.* **2015,** *5* (9), 5077-5088.

52. Notestein, J. M.; Andrini, L. R.; Kalchenko, V. I.; Requejo, F. G.; Katz, A.; Iglesia, E., Structural Assessment and Catalytic Consequences of the Oxygen Coordination Environment in Grafted Ti-Calixarenes. *J. Am. Chem. Soc.* **2007,** *129*, 1122-1131.

53. Prasetyoko, D.; Ramli, Z.; Endud, S.; Nur, H., Enhancement of Catalytic Activity of Titanosilicalite-1 - Sulfated Zirconia Combination Towards Epoxidation of 1-Octene with Aqueous Hydrogen Peroxide *React. Kinet. Catal. Lett.* **2005,** *86*, 83-89.

54. Bregante, D. T.; Priyadarshini, P.; Flaherty, D. W., Kinetic and spectroscopic evidence for reaction pathways and intermediates for olefin epoxidation on Nb in * BEA. *J. Catal.* **2017,** *348*, 75-89.

55. Ivanchikova, I. D.; Maksimchuk, N. V.; Skobelev, I. Y.; Kaichev, V. V.; Kholdeeva, O. A., Mesoporous niobium-silicates prepared by evaporation-induced self-assembly as catalysts for selective oxidations with aqueous H_2O_2. *J. Catal.* **2015,** *332*, 138-148.

56. Aronne, A.; Turco, M.; Bagnasco, G.; Ramis, G.; Santacesaria, E.; Di Serio, M.; Marenna, E.; Bevilacqua, M.; Cammarano, C.; Fanelli, E., Gel derived niobium–silicon mixed oxides: Characterization and catalytic activity for cyclooctene epoxidation. *Appl. Catal. A* **2008,** *347*, 179-185.

57. Ruddy, D. A.; Tilley, T. D., Highly selective olefin epoxidation with aqueous H_2O_2 over surface-modified TaSBA15 prepared via the TMP method. *Chem. Commun.* **2007,** , 3350.

58. Ruddy, D. A.; Tilley, T. D., Kinetics and Mechanism of Olefin Epoxidation with Aqueous

H_2O_2 and a Highly Selective Surface-Modified TaSBA15 Heterogeneous Catalyst. *J. Am. Chem. Soc.* **2008,** *130*, 11088-11096.

59. Morlanés, N.; Notestein, J. M., Kinetic study of cyclooctene epoxidation with aqueous hydrogen peroxide over silica-supported calixarene–Ta(V). *Appl. Catal. A* **2010,** *387*, 45-54.

60. Kulkarni, B. S.; Krishnamurty, S.; Pal, S., Probing Lewis acidity and reactivity of Sn- and Ti-beta zeolite using industrially important moieties: A periodic density functional study. *J. Mol. Catal. A: Chem.* **2010,** *329*, 36-43.

61. Li, Y.-P.; Head-Gordon, M.; Bell, A. T., Analysis of the Reaction Mechanism and Catalytic Activity of Metal-Substituted Beta Zeolite for the Isomerization of Glucose to Fructose. *ACS Catal.* **2014,** *4*, 1537-1545.

62. Yang, G.; Zhou, L.; Han, X., Lewis and Brönsted acidic sites in M^{4+}-doped zeolites (M=Ti, Zr, Ge, Sn, Pb) as well as interactions with probe molecules: A DFT study. *J. Mol. Catal. A: Chem.* **2012,** *363-364*, 371-379.

63. Luo, H. Y.; Lewis, J. D.; Roman-Leshkov, Y., Lewis Acid Zeolites for Biomass Conversion: Perspectives and Challenges on Reactivity, Synthesis, and Stability. *Annu Rev Chem Biomol Eng* **2016,** *7*, 663-92.

64. Clerici, M. G., The activity of titanium silicalite-1 (TS-1): Some considerations on its origin. *Kinet. Catal.* **2015,** *56*, 450-455.

65. Clerici, M. G.; Ingallina, P., Epoxidation of Lower Olefins with Hydrogen Peroxide and Titanium Silicalite. *J. Catal.* **1993,** *140*, 71-83.

66. Corma, A.; Camblor, M. A.; Esteve, P.; Martínez, A.; Perez-Pariente, J., Activity of Ti-Beta Catalyst for the Selective Oxidation of Alkenes and Alkanes. *J. Catal.* **1994,** *145*, 151-158.

67. Bregante, D. T.; Tan, J. Z.; Sutrisno, A.; Flaherty, D. W., Heteroatom substituted zeolite FAU with ultralow Al contents for liquid-phase oxidation catalysis. *Catal. Sci. Tech.* **2020,** *10*, 635-647.

68. Célestin Bakala, P.; Briot, E.; Salles, L.; Brégeault, J.-M., Comparison of liquid-phase olefin epoxidation over MoOx inserted within mesoporous silica (MCM-41, SBA-15) and grafted onto silica. *Appl. Catal. A* **2006,** *300* (2), 91-99.

69. Blasco, T.; Camblor, M. A.; Corma, A.; Esteve, P.; Guil, J. M.; Martinez, A.; Perdigon-Melon, J. A.; Valencia, S., Direct synthesis and characterization of hydrophobic aluminum-free Ti-beta zeolite. *J. Phys. Chem. B* **1998,** *102*, 75-88.

70. Park, S.; Cho, K. M.; Youn, M. H.; Seo, J. G.; Jung, J. C.; Baeck, S.-H.; Kim, T. J.; Chung, Y.-M.; Oh, S.-H.; Song, I. K., Direct epoxidation of propylene with hydrogen peroxide over TS-1 catalysts: Effect of hydrophobicity of the catalysts. *Catal. Commun.* **2008,** *9*, 2485-2488.

71. Ge, T.; Hua, Z.; Lv, J.; Zhou, J.; Guo, H.; Zhou, J.; Shi, J., Hydrophilicity/hydrophobicity modulated synthesis of nano-crystalline and hierarchically structured TS-1 zeolites. *CrystEngComm* **2017,** *19*, 1370-1376.

72. Choi, W. J.; Choi, C. Y., Production of Chiral Epoxides: Epoxide Hydrolase-catalyzed Enantioselective Hydrolysis. *Biotech. Bioproc. Eng.* **2005,** *10*, 167-179.

73. Lehmhus, D.; Busse, M.; Herrmann, A.; Kayvantash, K., *Structural Materials and Processes in Transportation*. Wiley-VCH: Germany, 2013.

74. Subramanian, M., *Polymer Testing: New Instrumental Methods*. Momentum Press: New York, NY, 2012.

75. Anslyn, E. V.; Dougherty, D. A., *Modern Physical Organic Chemistry*. University Science: 2005.

76. Krähling, L.; Krey, J.; Jakobson, G.; Grolig, J.; Miksche, L., Allyl Compounds. **2000**.

77. Sienel, G.; Rieth, R.; Rowbottom, K. T., Epoxides. **2000**.

78. Grigoropoulou, G.; Clark, J. H.; Elings, J. A., Recent developments on the epoxidation of alkenes using hydrogen peroxide as an oxidant. *Green Chem.* **2003,** *5*, 1-7.

79. U.S. Environmental Protection Agency *Catalogue of Hazardous and Solid Waste Publications*. 1992.

80. Dilla, W.; Dillenburg, H.; Krebber, H. G.; Ploenissen, E. Process for treating waste water containing organic and inorganic compounds. 1995.

81. USP Technologies How Much does H_2O_2 Cost? ? <http://www.h2o2.com/faqs/FaqDetail.aspx?fId=25> (accessed April 22, 2016).

82. Wilson, N. M.; Bregante, D. T.; Priyadarshini, P.; Flaherty, D. W., Production and Use of H_2O_2 for Atom-Efficient Functionalization of Hydrocarbons and Small Molecules. *Catalysis* **2017,** *29*, 122-212.

83. De Ruiter, C.; Wold, J. H.; Brinkman, U. A.; Frei, R. W., Design and Evaluation of a Sandwich Phase Separator for On-line Liquid/Liquid Extraction *Anal. Chim. Acta* **1987,** *192*, 267-275.

84. Backstrom, K.; Danielsson, L. G.; Nord, L., Design and Evaluation of a New Phase Separator for Liquid-Liquid Extraction in Flow Systems *Anal. Chim. Acta* **1985,** *169*, 43-49.

85. Brutchey, R. L.; Ruddy, D. A.; Andersen, L. K.; Tilley, T. D., Influence of Surface Modification of Ti-SBA15 Catalysts on the Epoxidation Mechanism for Cyclohexene with Aqueous Hydrogen Peroxide. *Langmuir* **2005,** *21*, 9576-9583.

86. Schmidt, I.; Krogh, A.; Wienberg, K.; Carlsson, A.; Brorson, M.; Jacobsen, C. J. H., Catalytic epoxidation of alkenes with hydrogen peroxide over first mesoporous titanium-containing zeolite. *Chem. Commun.* **2000,** 2157-2158.

87. Fan, W.; Wu, P.; Namba, S.; Tatsumi, T., Synthesis and catalytic properties of a new titanosilicate molecular sieve with the structure analogous to MWW-type lamellar precursor. *J. Catal.* **2006,** *243*, 183-191.

88. Morlanés, N.; Notestein, J. M., Grafted Ta–calixarenes: Tunable, selective catalysts for direct olefin epoxidation with aqueous hydrogen peroxide. *J. Catal.* **2010,** *275*, 191-201.

89. Tielens, F.; Shishido, T.; Dzwigaj, S., What Do the Niobium Framework Sites Look Like in Redox Zeolites? A Combined Theoretical and Experimental Investigation. *J. Phys. Chem. C* **2010,** *114*, 3140-3147.

90. Hammond, C.; Conrad, S.; Hermans, I., Simple and scalable preparation of highly active Lewis acidic Sn-beta. *Angew. Chem. Int. Ed. Engl.* **2012,** *51*, 11736-9.

91. Wang, Y.; Lewis, J. D.; Román-Leshkov, Y., Synthesis of Itaconic Acid Ester Analogues via Self-Aldol Condensation of Ethyl Pyruvate Catalyzed by Hafnium BEA Zeolites. *ACS Catal.* **2016**, 2739-2744.

92. Gunther, W. R.; Michaelis, V. K.; Caporini, M. A.; Griffin, R. G.; Roman-Leshkov, Y., Dynamic nuclear polarization NMR enables the analysis of Sn-Beta zeolite prepared with natural abundance ^{119}Sn precursors. *J. Am. Chem. Soc.* **2014,** *136*, 6219-22.

93. Clerici, M. G.; Bellussi, G.; Romano, U., Synthesis of Propylene Oxide from Propylene and Hydrogen Peroxide Catalyzed by Titanium Silicalite. *J. Catal.* **1991,** *129*, 159-167.

94. Nijhuis, T. A.; Makkee, M.; Moulijn, J. A.; Weckhuysen, B. M., The Production of Propene oxide: Catalytic Processes and Recent Developments. *Ind. Eng. Chem. Res.* **2006,** *45*, 3447-3459.

95. First, E. L.; Gounaris, C. E.; Wei, J.; Floudas, C. A., Computational characterization of zeolite porous networks: an automated approach. *Phys. Chem. Chem. Phys.* **2011,** *13*, 17339-17358.

96. Tang, B.; Dai, W.; Sun, X.; Guan, N.; Li, L.; Hunger, M., A procedure for the preparation of Ti-Beta zeolites for catalytic epoxidation with hydrogen peroxide. *Green Chemistry* **2014,** *16*, 2281-2291.

97. Dzwigaj, S.; Peltre, M. J.; Massiani, P.; Davidson, A.; Che, M.; Sen, T.; Sivasanker, S., Incorporation of vanadium species in a dealuminated b zeolite. *Chem. Commun.* **1998**, 87-88.

98. Gao, H.; Lu, G.; Suo, J.; Li, S., Epoxidation of allyl chloride with hydrogen peroxide catalyzed by titanium silicalite 1. *Appl. Catal. A* **1996,** *138*, 27-38.

99. Escobedo Morales, A.; Sanchez Mora, E.; Pal, U., Use of diffuse reflectance spectroscopy for optical characterization of un-supported nanostructures. *Revista Mexicana De Fisica* **2007,** *53*, 18-22.

100. Zhao, Y.; Zhou, X.; Ye, L.; Tsang, S. C. E., Nanostructured Nb2O5 catalysts. *Nano Reviews* **2012,** *3*, 1-11.

101. Dzwigaj, S.; Millot, Y.; Méthivier, C.; Che, M., Incorporation of Nb(V) into BEA zeolite investigated by XRD, NMR, IR, DR UV–vis, and XPS. *Microporous Mesoporous Mater.* **2010,** *130*, 162-166.

102. Sushkevich, V. L.; Ivanova, I. I.; Tolborg, S.; Taarning, E., Meerwein–Ponndorf–Verley–Oppenauer reaction of crotonaldehyde with ethanol over Zr-containing catalysts. *J. Catal.* **2014,** *316*, 121-129.

103. Dzwigaj, S.; Millot, Y.; Che, M., Ta(V)-Single Site BEA Zeolite by Two-Step Postsynthesis Method: Preparation and Characterization. *Catal. Lett.* **2010,** *135*, 169-174.

104. International Zeolite Association: Verified Syntheses of Zeolitic Materials: Characterization by IR Spectroscopy. <http://www.iza-online.org/synthesis/VS_2ndEd/IR_Spectroscopy.htm> (accessed October 11, 2017).

105. Burcham, L. J.; Datka, J.; Wachs, I. E., In Situ Vibrational Spectroscopy Studies of Supported Niobium Oxide Catalysts. *J. Phys. Chem. B* **1999,** *103*, 6015-6024.

106. Roy, S.; Bakhmutsky, K.; Mahmoud, E.; Lobo, R. F.; Gorte, R. J., Probing Lewis Acid Sites in Sn-Beta Zeolite. *ACS Catal.* **2013,** *3*, 573-580.

107. Sushkevich, V. L.; Vimont, A.; Travert, A.; Ivanova, I. I., Spectroscopic Evidence for Open and Closed Lewis Acid Sites in ZrBEA Zeolites. *J. Phys. Chem. C* **2015,** *119*, 17633-17639.

108. Wang, J.; Kispersky, V. F.; Nicholas Delgass, W.; Ribeiro, F. H., Determination of the Au active site and surface active species via operando transmission FTIR and isotopic transient experiments on 2.3wt.% Au/TiO2 for the WGS reaction. *J. Catal.* **2012,** *289*, 171-178.

109. Baga, A. N.; Johnson, A.; Nazhat, N. B.; Saadalla-Nazhat, R. A., A Simple Spectrophotometric Determination of Hydrogen Peroxide at Low Concentrations in Aqueous Solution *Anal. Chim. Acta* **1988,** *204*, 349-353.

110. Wilson, N. M.; Flaherty, D. W., Mechanism for the Direct Synthesis of H_2O_2 on Pd Clusters: Heterolytic Reaction Pathways at the Liquid-Solid Interface. *J. Am. Chem. Soc.* **2016,** *138*, 574-586.

111. Madon, R. J.; Boudart, M., Experimental Criterion for the Absence of Artifacts in the Measurement of Rates of Heterogeneous Catalytic Reactions. *Ind. Eng. Chem. Fundam.* **1982,** *21*, 438-447.

112. Coudurier, G.; Naccache, C.; Vedrine, J. C., Uses of I.R. Spectroscopy in identifying ZSM Zeolite Structure *Chem. Commun.* **1982,** 1413-1415.

113. Miessner, H.; Kosslick, H.; Lohse, U.; Parlitz, B.; Tuan, V., Characterization of Highly Dealuminated Faujasite-Type Zeolites: Ultrastable Zeolite Y and ZSM-20. *J. Phys. Chem.* **1993,** *97*, 9741-9748.

114. Urakawa, A.; Bürgi, T.; Baiker, A., Sensitivity enhancement and dynamic behavior analysis by modulation excitation spectroscopy: Principle and application in heterogeneous catalysis. *Chem. Eng. Sci.* **2008,** *63*, 4902-4909.

115. Giguere, P. A.; Harvey, K. B., On the Infrared Absorption of Water and Heavy Water in Condensed States *Can. J. Chem.* **1956,** *34*, 798.

116. Lin, W.; Frei, H., Photochemical and FT-IR Probing of the Active Site of Hydrogen Peroxide in Ti Silicalite Sieve. *J. Am. Chem. Soc.* **2002,** *124*, 9292-9298.

117. Bordiga, S.; Damin, A.; Bonino, F.; Ricchiardi, G.; Lamberti, C.; Zecchina, A., The Structure of the Peroxo Species in the TS-1 Catalyst as Investigated by Resonant Raman Spectroscopy. *Angew. Chem. Int. Ed. Engl.* **2002,** *41*, 4734-4737.

118. Chen, C.; Yuan, H.; Wang, H.; Yao, Y.; Ma, W.; Chen, J.; Hou, Z., Highly Efficient Epoxidation of Allylic Alcohols with Hydrogen Peroxide Catalyzed by Peroxoniobate-Based Ionic Liquids. *ACS Catal.* **2016,** *6*, 3354-3364.

119. Notari, B., Microporous Crystalline Titanium Silicates. *Adv. Catal.* **1996,** *41*, 253-334.

120. Bravo-Sua´rez, J. J.; Bando, K. K.; Lu, J.; Haruta, M.; Fujitani, T.; Oyama, S. T., Transient Technique for Identification of True Reaction Intermediates: Hydroperoxide Species in Propylene Epoxidation on Gold/Titanosilicate Catalysts by X-ray Absorption Fine Structure Spectroscopy. *J. Phys. Chem. C* **2008,** *112*, 1115-1123.

121. Bonino, F.; Damin, A.; Ricchiardi, G.; Ricci, M.; Spanó, G.; D'Aloisio, R.; Zecchina, A.; Lamberti, C.; Prestipino, C.; Bordiga, S., Ti-Peroxo Species in the TS-1/H_2O_2/H_2O System. *J. Phys. Chem. B* **2004,** *108*, 3573-3583.

122. Shetti, V. N.; Manikandan, P.; Srinivas, D.; Ratnasamy, P., Reactive oxygen species in epoxidation reactions over titanosilicate molecular sieves. *J. Catal.* **2003,** *216*, 461-467.

123. Wang, L.; Xiong, G.; Su, J.; Li, P.; Guo, H., In Situ UV Raman Spectroscopic Study on the Reaction Intermediates for Propylene Epoxidation on TS-1. *J. Phys. Chem. C* **2012,** *116*, 9122-9131.

124. Ziolek, M.; Sobczak, I.; Decyk, P.; Sobańska, K.; Pietrzyk, P.; Sojka, Z., Search for reactive intermediates in catalytic oxidation with hydrogen peroxide over amorphous niobium(V) and tantalum(V) oxides. *Appl. Catal. B* **2015,** *164*, 288-296.

125. Guzman, J.; Carrettin, S.; Corma, A., Spectroscopic Evidence for the Supploy of Reactive Oxygen during CO Oxidation. *J. Am. Chem. Soc.* **2005,** *127*, 3286.

126. Long, R. Q.; Wan, H. L., In situ confocal microprobe Raman spectroscopy study of

CeO2 catalyst for the oxidative coupling of methane. *J. Chem. Soc., Faraday Trans.* **1997,** *93*, 355.

127. Nakayama, M.; Xue, M.; An, W.; Liu, P.; White, M. G., Influence of Cluster-support Interactions on Reactivity of Size-selected Nb_xO_y Clusters. *J. Phys. Chem. C* **2015,** *119*, 14756-14768.

128. Marco, J. F.; Gancedo, J. R.; Berry, F. J., The oxidation states of titanium and niobium in compounds of composition $Sn_xNbTiP_3O_{12}$ ($O < x < 0.5$): an XPS study. *Polyhedron* **1997,** *16*, 2957-2961.

129. S.E. Stein, IR and Mass Spectra, in: W.G. Mallard, P.J. Linstrom (Eds.), NIST Chemistry WebBook, NIST Standard Reference Database Number 69; National Institute of Standards and Technology: Gaithersburg, MD, (February) 2000, Acetonitrile, Cyclohexene, and Cyclohexane (http://webbook.nist.gov).

130. Raj, N. K. K.; Ramaswamy, A. V.; Manikandan, P., Oxidation of norbornene over vanadium-substituted phosphomolybdic acid catalysts and spectroscopic investigations. *J. Mol. Catal. A: Chem.* **2005,** *227*, 37-45.

131. Sams, C. K.; Jørgensen, K. A., Mechanistic Aspects of Vanadium-Catalysed Oxygen Transfer Reactions. *Acta Chem. Scand.* **1995,** *49*, 839-847.

132. Ottenbacher, R. V.; Samsonenko, D. G.; Talsi, E. P.; Bryliakov, K. P., Enantioselective Epoxidations of Olefins with Various Oxidants on Bioinspired Mn Complexes: Evidence for Different Mechanisms and Chiral Additive Amplification. *ACS Catal.* **2016,** *6*, 979-988.

133. Zeolyst: Zeolite Beta. <http://www.zeolyst.com/our-products/standardzeolite-powders/zeolite-beta.aspx> (accessed June 1, 2016).

134. Murzin, D., *Engineering Catalysis*. de Gruyter: Gottingen, Germany, 2013.

135. Arnaut, L.; Formosinho, S.; Burrows, H., *Chemical Kinetics: From Molecular Structure to Chemical Reactivity*. Elsevier: Netherlands, 2007.

136. Flaherty, D. W.; Iglesia, E., Transition-state enthalpy and entropy effects on reactivity and selectivity in hydrogenolysis of n-alkanes. *J. Am. Chem. Soc.* **2013,** *135*, 18586-18599.

137. Czako, B.; Kurti, L., *Strategic Applications of Named Reactions in Organic Synthesis*. Academic Press: 2005.

138. Rebsdat, S.; Mayer, D., Ethylene Oxide. **2001**.

139. *Process Analyzers in Ethylene Oxide Production Plant*; Siemens: 2003; p 9.

140. Linic, S.; Barteau, M. A., Control of Ethylene Epoxidation Selectivity by Surface Oxametallacycles. *J. Am. Chem. Soc.* **2003,** *125*, 4034-4035.

141. Wen, C.; Yin, A.; Dai, W.-L., Recent advances in silver-based heterogeneous catalysts for green chemistry processes. *Appl. Catal. B* **2014,** *160-161*, 730-741.

142. Obama, B., The irreversible momentum of clean energy. *Science* **2017,** *355*, 126-130.

143. Campos-Martin, J. M.; Blanco-Brieva, G.; Fierro, J. L., Hydrogen peroxide synthesis: an outlook beyond the anthraquinone process. *Angew. Chem. Int. Ed. Engl.* **2006,** *45*, 6962-6984.

144. Gleeson, D.; Sankar, G.; Richard A. Catlow, C.; Meurig Thomas, J.; Spanó, G.; Bordiga, S.; Zecchina, A.; Lamberti, C., The architecture of catalytically active centers in titanosilicate (TS-1) and related selective-oxidation catalysts. *Phys. Chem. Chem. Phys.* **2000,** *2* (20), 4812-4817.

145. Carati, A.; Flego, C.; Previde Massara, E.; Millini, R.; Carluccio, L.; Parker, W. O.; Bellussi, G., Stability of Ti in MFI and Beta structures: a comparative study. *Microporous Mesoporous Mater.* **1999,** *30*, 137-144.

146. Park, S.; Cho, K. M.; Youn, M. H.; Seo, J. G.; Baeck, S.-H.; Kim, T. J.; Chung, Y.-M.; Oh, S.-H.; Song, I. K., Epoxidation of Propylene with Hydrogen Peroxide Over TS-1 Catalyst Synthesized in the Presence of Polystyrene. *Catal. Lett.* **2008,** *122*, 349-353.

147. Thornburg, N. E.; Nauert, S. L.; Thompson, A. B.; Notestein, J. M., Synthesis−Structure–Function Relationships of Silica-Supported Niobium(V) Catalysts for Alkene Epoxidation with H_2O_2. *ACS Catal.* **2016,** *6*, 6124-6134.

148. Cordeiro, P. J.; Guillo, P.; Spanjers, C. S.; Chang, J. W.; Lipschutz, M. I.; Fasulo, M. E.; Rioux, R. M.; Tilley, T. D., Titanium–Germoxy Precursor Route to Germanium-Modified Epoxidation Catalysts with Enhanced Activity. *ACS Catal.* **2013,** *3*, 2269-2279.

149. Cordeiro, P. J.; Tilley, T. D., Enhancement of epoxidation efficiencies for Ta-SBA15 catalysts. The influence of modification with -EMe3 (E = Si, Ge, Sn) groups. *Langmuir* **2011,** *27*, 6295-6304.

150. Guo, Y.; Solovyov, A.; Grosso-Giordano, N. A.; Hwang, S.-J.; Katz, A., Stabilizing Single Sites on Solid Supports: Robust Grafted Ti(IV)-Calixarene Olefin Epoxidation Catalysts via Surface Polymerization and Cross-Linking. *ACS Catal.* **2016**, 7760-7768.

151. Ouyang, X.; Hwang, S.-J.; Xie, D.; Rea, T.; Zones, S. I.; Katz, A., Heteroatom-Substituted Delaminated Zeolites as Solid Lewis Acid Catalysts. *ACS Catal.* **2015,** *5*, 3108-3119.

152. Boronat, M.; Corma, A.; Renz, M.; Viruela, P. M., Predicting the activity of single isolated Lewis acid sites in solid catalysts. *Chem. Eur. J.* **2006,** *12*, 7067-7077.

153. Sastre, G.; Corma, A., Relationship between structure and Lewis acidity of Ti-Beta and TS-1 zeolites: A quamtum-chemical study. *Chem. Phys. Lett.* **1999,** *302*, 447-453.

154. Jenzer, G.; Mallat, T.; Maciejewski, M.; Eigenmann, F.; Baiker, A., Continuous epoxidation of propylene with oxygen and hydrogen on a Pd-Pt/TS-1 catalyst. *Appl. Catal. A* **2001,** *208*, 125-133.

155. Bonino, F.; Damin, A.; Bordiga, S.; Carlo, L.; Zecchina, A., Interaction of CD_3CN and Pyridine with Ti(IV) Centers of TS-1 Catalysts: A Spectroscopic and Computational Study. *Langmuir* **2003,** *19*, 2155-2161.

156. Boronat, M.; Concepción, P.; Corma, A.; Renz, M.; Valencia, S., Determination of the catalytically active oxidation Lewis acid sites in Sn-beta zeolites, and their optimisation by the combination of theoretical and experimental studies. *J. Catal.* **2005,** *234*, 111-118.

157. Boronat, M.; Concepción, P.; Corma, A.; Navarro, M. T.; Renz, M.; Valencia, S., Reactivity in the confined spaces of zeolites: the interplay between spectroscopy and theory to develop structure-activity relationships for catalysis. *Phys. Chem. Chem. Phys.* **2009,** *1*, 2876-2884.

158. Lane, B. S.; Burgess, K., Metal-Catalyzed Epoxidation of Alkenes with Hydrogen Peroxide. *Chem. Rev.* **2003,** *103*, 2457-2473.

159. Harris, J. W.; Cordon, M. J.; Di Iorio, J. R.; Vega-Vila, J. C.; Ribeiro, F. H.; Gounder, R., Titration and quantification of open and closed Lewis acid sites in Sn-Beta zeolites that catalyze glucose isomerization. *J. Catal.* **2016,** *335*, 141-154.

160. Mahmoud, E.; Yu, J.; Gorte, R. J.; Lobo, R. F., Diels–Alder and Dehydration Reactions of Biomass-Derived Furan and Acrylic Acid for the Synthesis of Benzoic Acid. *ACS Catal.* **2015,** *5*, 6946-6955.

161. Daniell, W.; Topsøe, N. Y.; Knözinger, H., An FTIR Study of the Surface Acidity of USY Zeolites: Comparison of CO, CD_3CN, and C_5H_5N Probe Molecules. *Langmuir* **2001,** *17*, 6233-6239.

162. Tang, B.; Dai, W.; Wu, G.; Guan, N.; Li, L.; Hunger, M., Improved Postsynthesis Strategy to Sn-Beta Zeolites as Lewis Acid Catalysts for the Ring-Opening Hydration of Epoxides. *ACS Catal.* **2014,** *4*, 2801-2810.

163. Sushkevich, V. L.; Palagin, D.; Ivanova, I. I., With Open Arms: Open Sites of ZrBEA Zeolite Facilitate Selective Synthesis of Butadiene from Ethanol. *ACS Catal.* **2015,** *5*, 4833-4836.

164. Yoon, C. W.; Hirsekorn, K. F.; Neidig, M. L.; Yang, X.; Tilley, T. D., Mechanism of the Decomposition of Aqueous Hydrogen Peroxide over Heterogeneous TiSBA15 and TS-1 Selective Oxidation Catalysts: Insights from Spectroscopic and Density Functional Theory Studies. *ACS Catal.* **2011,** *1*, 1665-1678.

165. Ziolek, M.; Sobczak, I.; Decyk, P.; Wolski, L., The ability of Nb_2O_5 and Ta_2O_5 to generate active oxygen in contact with hydrogen peroxide. *Catal. Commun.* **2013,** *37*, 85-91.

166. Pauling, L., The Nature of the Chemical Bond. IV. The Energy of Single Bonds and the Relative Electronegativity of Atoms. *J. Am. Chem. Soc.* **1932,** *54*, 3571-3782.

167. Rohrer, G. S., *Structure and Bonding in Crystalline Materials*. Cambridge University Press: 2001; p 552.

168. Gunther, W. R.; Michaelis, V. K.; Griffin, R. G.; Román-Leshkov, Y., Interrogating the Lewis Acidity of Metal Sites in Beta Zeolites with 15N Pyridine Adsorption Coupled with MAS NMR Spectroscopy. *J. Phys. Chem. C* **2016,** *120*, 28533-28544.

169. Corilo, Y. E.; Rowland, S. M.; Rodgers, R. P., Calculation of the Total Sulfur Content in Crude Oils by Positive-Ion Atmospheric Pressure Photoionization Fourier Transform Ion Cyclotron Resonance Mass Spectrometry. *Energy & Fuels* **2016,** *30*, 3962-3966.

170. Policy, T. US: Fuels: Diesel and Gasoline. <http://www.transportpolicy.net/standard/us-fuels-diesel-and-gasoline/> (Accessed February 14th, 2017)

171. Blanco-Brieva, G.; Campos-Martin, J. M.; Al-Zahrani, S. M.; Fierro, J. L. G., Effectiveness of metal–organic frameworks for removal of refractory organo-sulfur compound present in liquid fuels. *Fuel* **2011,** *90*, 190-197.

172. Lyles, C. N.; Aktas, D. F.; Duncan, K. E.; Callaghan, A. V.; Stevenson, B. S.; Suflita, J. M., Impact of organosulfur content on diesel fuel stability and implications for carbon steel corrosion. *Environ. Sci. Technol.* **2013,** *47*, 6052-6062.

173. Oudar, J., Sulfur Adsorption and Poisoning of Metallic Catalysts. *Catal. Rev.* **2006,** *22*, 171-195.

174. Prins, R.; De Beer, V. H. J.; Somorjai, G. A., Structure and Function of the Catalyst and the Promoter in Co—Mo Hydrodesulfurization Catalysts. *Catal. Rev.* **1989,** *31*, 1-41.

175. Wang, H.; Iglesia, E., Thiophene hydrodesulfurization catalysis on supported Ru clusters: Mechanism and site requirements for hydrogenation and desulfurization pathways. *J. Catal.* **2010,** *273* (2), 245-256.

176. Wang, H.; Iglesia, E., Mechanism and Site Requirements of Thiophene Hydrodesulfurization Catalyzed by Supported Pt Clusters. *ChemCatChem* **2011,** *3*, 1166-1175.

177. Oyama, S.; Lee, Y., The active site of nickel phosphide catalysts for the hydrodesulfurization of 4,6-DMDBT. *J. Catal.* **2008,** *258*, 393-400.

178. Rodriguez, E.; Harvey, W. S.; Ásbjörnsson, E. J. In *Review of H_2S Abatement Methods in Geothermal Plants*, Thirty-Eighth Workshop on Geothermal Reservoir Engineering, Stanford University, Stanford, California, Stanford University, Stanford, California, 2014.

179. Song, T.; Zhang, Z.; Chen, J.; Ring, Z.; Yang, H.; Zheng, Y., Effect of Aromatics on Deep Hydrodesulfurization of Dibenzothiophene and 4.6-Dimethyldibenzothiophene over $NiMo/Al_2O_3$ Catalyst. *Energy & Fuels* **2006,** *20*, 2344-2349.

180. Gates, B. C.; Topsøe, H., Reactivities in deep catalytic hydrodesulfurization: challenges, opportunities, and the importance of 4-methyldibenzothiophene and 4,6-dimethyldibenzothiophene. *Polyhedron* **1997,** *16*, 3213-3217.

181. Guo, H.; Sun, Y.; Prins, R., Hydrodesulfurization of 4,6-dimethyldibenzothiophene over Pt supported on γ-Al_2O_3, SBA-15, and HZSM-5. *Catal. Today* **2008,** *130*, 249-253.

182. Rozanska, X.; van Santa, R. A.; Hutschka, F.; Hafner, J., A periodic density functional theory study of thiophenic derivative cracking catalyzed by mordenite. *J. Catal.* **2003,** *215*, 20-29.

183. Wagner, G. W.; Bartram, P. W.; Procell, L. R.; Sorrick, D. C.; Henderson, V. D.; Turetsky, A. L.; Rastogi, V. K.; Yang, Y.-C., Decon Green^{TM}: Development and Chemical Biological Agent Efficacy Testing. U.S. Army Research, Development and Engineering Command: Aberdeen Proving Ground, MD, 2004.

184. Kong, L.; Li, G.; Wang, X.; Qu, B., Oxidative Desulfurization of Organic Sulfur in Gasoline over Ag/TS-1. *Energy & Fuels* **2006,** *20*, 896-902.

185. Kong, L.; Li, G.; Wang, X., Mild oxidation of thiophene over TS-1/H_2O_2 *Catal. Today* **2004,** *93-95*, 341-345.

186. Du, Q.; Guo, Y.; Duan, H.; Li, H.; Chen, Y.; Liu, H., Synthesis of hierarchical TS-1 zeolite via a novel three-step crystallization method and its excellent catalytic performance in oxidative desulfurization. *Fuel* **2017,** *188*, 232-238.

187. Corma, A.; Iglesias, M.; Sánchez, F., Large pore Ti-zeolites and mesoporous Ti-silicalites as catalysts for selective oxidation of organic sulfides. *Catal. Lett.* **1996,** *39*, 153-156.

188. Bazyari, A.; Khodadadi, A. A.; Haghighat Mamaghani, A.; Beheshtian, J.; Thompson, L. T.; Mortazavi, Y., Microporous titania–silica nanocomposite catalyst-adsorbent for ultra-deep oxidative desulfurization. *Applied Catalysis B: Environmental* **2016,** *180*, 65-77.

189. Cojocariu, A. M.; Mutin, P. H.; Dumitriu, E.; Fajula, F.; Vioux, A.; Hulea, V., Non-hydrolytic synthesis of mesoporous silica-titania catalysts for the mild oxidation of sulfur compounds with hydrogen peroxide. *Chem Commun* **2008,** 5357-5359.

190. Thornburg, N. E.; Notestein, J. M., Rate and Selectivity Control in Thioether and Alkene Oxidation with H2O2 over Phosphonate-Modified Niobium(V)-Silica Catalysts. *ChemCatChem* **2017,** *9*, 3714-3724.

191. Hulea, V.; Fajula, F.; Bousquet, J., Mild Oxidation with H_2O_2 over Ti-Containing Molecular Sieves-A very Efficient Method for Removing Aromatic Sulfur Compounds from Fuels. *J. Catal.* **2001,** *198*, 179-186.

192. Maity, U.; Basu, J. K.; Sengupta, S., A neural network prediction of conversion of benzothiophene oxidation catalyzed by nano-Ti-beta catalyst. *Fuel* **2013,** *113*, 180-186.

193. Moreau, P.; Hulea, V.; Gomez, S.; Brunel, D.; Di Renzo, F., Oxidation of sulfoxides to sulfones by hydrogen peroxide over Ti-containing zeolites. *Appl. Catal. A* **1997,** *155*, 253-263.

194. Nemeth, L.; Bare, S. R.; Rathbun, W.; Gatter, M.; Low, J., Oxidative desulfurization of sulfur compounds: Oxidation of thiophene and derivatives with hydrogen peroxide using Ti-Beta catalyst. *Stud. Surf. Sci. Catal.* **2008,** *174*, 1017-1020.

195. Chica, A.; Corma, A.; Domine, M., Catalytic oxidative desulfurization (ODS) of diesel fuel on a continuous fixed-bed reactor. *J. Catal.* **2006,** *242*, 299-308.

196. Fraile, J. M.; Gil, C.; Mayoral, J. A.; Muel, B.; Roldán, L.; Vispe, E.; Calderón, S.; Puente, F., Heterogeneous titanium catalysts for oxidation of dibenzothiophene in hydrocarbon solutions with hydrogen peroxide: On the road to oxidative desulfurization. *Appl. Catal. B* **2016,** *180*, 680-686.

197. Jin, W.; Tian, Y.; Wang, G.; Zeng, D.; Xu, Q.; Cui, J., Ultra-deep oxidative desulfurization of fuel with H_2O_2 catalyzed by molybdenum oxide supported on alumina modified by Ca^{2+}. *RSC Adv.* **2017,** *7* (76), 48208-48213.

198. Ye, G.; Qi, H.; Li, X.; Leng, K.; Sun, Y.; Xu, W., Enhancement of Oxidative Desulfurization Performance over UiO-66(Zr) by Titanium Ion Exchange. *Chem. Phys. Chem.* **2017,** *18*, 1903-1908.

199. Bregante, D. T.; Flaherty, D. W., Periodic Trends in Olefin Epoxidation over Group IV and V Framework Substituted Zeolite Catalysts: A Kinetic and Spectroscopic Study. *J. Am. Chem. Soc.* **2017,** *139*, 6888-6898.

200. Wang, J.; Kispersky, V. F.; Delgass, N. W.; Ribeiro, F. H., Determination of the Au active site and surface active species via operando transmission FTIR and isotopic transient experiments on 2.3wt.% Au/TiO2 for the WGS reaction. *J. Catal.* **2012,** *289*, 171-178.

201. Hajjar, R.; Millot, Y.; Man, P. P.; Che, M.; Dzwigaj, S., Two Kinds of Framework Al Sites Studied in BEA Zeolite by X-ray Diffraction, Fourier Transform Infrared Spectroscopy, NMR Techniques, and V Probe. *J. Phys. Chem. C* **2008,** *112*, 20167-20175.

202. Oumi, Y.; Matsuba, K.; Kubo, M.; Inui, T.; Miyamoto, A., Selective T-site substitution as a cause of the anisotropy of lattice expansion in titanoscilicate-1 investigated by molecular dynamics and computer graphics. *Microporous Mater.* **1995,** *4*, 53-57.

203. Cullity, B. D.; Stock, S. R., *Elements of X-ray Diffraction*. Pearson: United Kingdom, 2001.

204. Samples of M-BEA with high loadings were necessary to visualize the shift in 2θ, because the low loading used for as not enough silanol nests were substituted within the M-BEA with lower metal loadings (Table 1).

205. Klaas, J.; Schulz-Ekloff, G.; Jaeger, N. I., UV-Visible Diffuse Reflectance Spectroscopy of Zeolite-Hosted Mononuclear Titanium Oxide Species. *J. Phys. Chem. B* **1997,** *101*, 1305-1311.

206. Al-Maksoud, W.; Daniele, S.; Sorokin, A. B., Practical oxidation of sulfides to sulfones by H2O2 catalysed by titanium catalyst. *Green Chem.* **2008,** *10*, 447.

207. Holmes, J. L.; Aubry, C., Group additivity values for estimating the enthalpy of formation of organic compounds: an update and reappraisal. 2. C, H, N, O, S, and halogens. *J. Phys. Chem. A* **2012,** *116*, 7196-7209.

208. Dimethylsulfoxide was used a surrogate for 2,5-dimethylthiophene oxide, as sufficiently pure samples of 2,5-dimethylthiophene oxide were not obtainable.

209. At differential conversion, $[C_6H_8SO]$ is very small, which results in a very small value of $k_7[C_6H_8SO]$.

210. Ivanchikova, I. D.; Skobelev, I. Y.; Maksimchuk, N. V.; Paukshtis, E. A.; Shashkov, M. V.; Kholdeeva, O. A., Toward understanding the unusual reactivity of mesoporous niobium silicates in epoxidation of C C bonds with hydrogen peroxide. *J. Catal.* **2017,** *356*, 85-99.

211. Bordiga, S.; Groppo, E.; Agostini, G.; van Bokhoven, J. A.; Lamberti, C., Reactivity of surface species in heterogeneous catalysts probed by in situ X-ray absorption techniques. *Chem. Rev.* **2013,** *113*, 1736-1850.

212. Hulea, V.; Moreau, P.; Renzo, F. D., Thioether oxidation by hydrogen peroxide using titanium-containing zeolites as catalysts. *J. Mol. Catal. A: Chem.* **1996,** *111*, 325-332.

213. Hulea, V.; Moreau, P., The solvent effect in the sulfoxidation of thioethers by hydrogen peroxide using Ti-containing zeolites as catalysts. *J. Mol. Catal. A: Chem.* **1996,** *113*, 499-505.

214. B., S.; Katsuki, T., Ti(salen)-catalyzed enantioselective sulfoxidation using hydrogen peroxide as a terminal oxidant. *Tetrahedron Lett.* **2001,** *42*, 3873-3876.

215. Chorkendorff, I.; Niemantsverdriet, J. W. H., *Concepts of Modern Catalysis and Kinetics*. 2nd ed.; Wiley-VCH Verlag Gmbh & Co.: Weinheim, 2007.

216. Mayr, H.; Ofial, A. R., Do general nucleophilicity scales exist? *J. Phys. Org. Chem.* **2008,** *21*, 584-595.

217. Mayr, H.; Patz, M., Scales of Nucleophilicity and Electrophilicity: A System for Ordering Polar Organic and Organometallic Reactions. *Angew. Chem. Int. Ed.* **1994,** *33*, 938-957.

218. Minegishi, S.; Kobayashi, S.; Mayr, H., Solvent Nucleophilicity. *J. Am. Chem. Soc.* **2004,** *126*, 5174-5181.

219. Under reaction conditions that result in surfaces saturated with M-(OOH) and M-(η^2-O_2) species, measured rates do not reflect processes for the activation of H_2O_2.

220. Activation enthalpies and the turnover rates for a given M-BEA do not depend on the density of active sites for a given material, but rather depend solely on how the rates of sulfoxidation change with the varied reaction condition (e.g., temperature or solvent).

221. Guo, Z.; Liu, B.; Zhang, Q.; Deng, W.; Wang, Y.; Yang, Y., Recent advances in heterogeneous selective oxidation catalysis for sustainable chemistry. *Chem. Soc. Rev.* **2014,** *43*, 3480-3524.

222. Ali, M. E.; Rahman, M. M.; Sarkar, S. M.; Hamid, S. B. A., Heterogeneous Metal Catalysts for Oxidation Reactions. *J. Nanomater.* **2014,** *2014*, 1-23.

223. Clerici, M. G.; Kholdeeva, O. A., *Liquid Phase Oxidation via Heterogeneous Catalysis: Organic Synthesis and Industrial Applications*. John Wiley & Sons: 2013.

224. Gallo, A.; Tiozzo, C.; Psaro, R.; Carniato, F.; Guidotti, M., Niobium metallocenes deposited onto mesoporous silica via dry impregnation as catalysts for selective epoxidation of alkenes. *J. Catal.* **2013,** *298*, 77-83.

225. Tiozzo, C.; Bisio, C.; Carniato, F.; Gallo, A.; Scott, S. L.; Psaro, R.; Guidotti, M., Niobium-silica catalysts for the selective epoxidation of cyclic alkenes: the generation of the active site by grafting niobocene dichloride. *Phys. Chem. Chem. Phys.* **2013,** *15*, 13354-13362.

226. Bérubé, F. O.; Nohair, B.; Kleitz, F.; Kaliaguine, S., Controlled Postgrafting of Titanium Chelates for Improved Synthesis of Ti-SBA-15 Epoxidation Catalysts. *Chem. Mater.* **2010,** *22*, 1988-2000.

227. Giannini, L.; Solari, E.; Zanotti-Gerosa, A.; Floriani, C.; Chiesi-Villa, A.; Rizzoli, C., The Organometallic Chemistry of Zirconium on an Oxo Surface Provided by p-tert-Butylcalix[4]arene. *Angew. Chem. Int. Ed.* **1996,** *35*, 86-87.

228. Castellano, B.; Solari, E.; Floriani, C.; Re, N.; Chiesi-Villa, A.; Rizzoli, C., Tantalum-Carbon Functionalities Bonded to a Calix[4]arene-Oxo Matrix: The Chemistry of Mono-, Dialkyl, and Butadiene Derivatives of Tantalum(V). *Chem. Eur. J.* **1999,** *5*, 722-737.

229. Caselli, A.; Solari, E.; Scopelliti, S.; Floriani, C.; Re, N.; Rizzoli, C.; Chiesi-Villa, A., Dinitrogen Rearranging over a Metal-Oxo Surface and Cleaving to Nitride: From the End-On to the Side-On Bonding Mode, to the Stepwise Cleavage of the N-N bonds Assited by Nb^{III}-Calix[4]arene. *J. Am. Chem. Soc.* **2000,** *122*, 3652-3670.

230. Zanotti-Gerosa, A.; Solari, E.; Giannini, L.; Floriani, C.; Re, N.; Chiesi-Villa, A.; Rizzoli, C., Titanium-carbon functionalities on an oxo surface defined by a calix[4]arene moiety and its redox chemistry. *Inorg. Chim. Acta* **1998,** *270*, 298-311.

231. Wang, W.-G.; Zheng, Q.-Y.; Huang, Z.-T., Selective Etherification of Calix[4]arenes. *Synth. Commun.* **1999,** *29*, 3711-3718.

232. Eaton, T. R.; Boston, A. M.; Thompson, A. B.; Gray, K. A.; Notestein, J. M., Counting Active Sites on Titanium Oxide-Silica Catalysts for Hydrogen Peroxide Activation through In Situ Poisoning with Phenylphosphonic Acid. *ChemCatChem* **2014,** *6*, 3215-3222.

233. Barzetti, T.; Selli, E.; Moscotti, D.; Forni, L., Pyridine and ammonia as probes for FTIR analysis of solid acid catalysts. *Faraday Trans.* **1996,** *92*, 1401-1407.

234. Kondo, J. N.; Nishitani, R.; Yoda, E.; Yokoi, T.; Tatsumi, T.; Domen, K., A comparative IR characterization of acidic sites on HY zeolite by pyridine and CO probes with silica-alumina and gamma-alumina references. *Phys. Chem. Chem. Phys.* **2010,** *12*, 11576-11586.

235. Ignacio-de Leon, P. A. A.; Contreras, C. A.; Thornburg, N. E.; Thompson, A. B.; Notestein, J. M., Catalyst structure and substituent effects on epoxidation of styrenics with immobilized Mn(tmtacn) complexes. *Appl. Catal. A* **2016,** *511*, 78-86.

236. de Boer, J. W.; Browne, W. R.; Harutyunyan, S. R.; Bini, L.; Tiemersma-Wegman, T. D.; Alsters, P. L.; Hage, R.; Feringa, B. L., Manganese catalysed asymmetric cis-dihydroxylation with H_2O_2. *Chem. Commun.* **2008**, 3747-3749.

237. Aimone-Gastin, I.; Cable, S.; Keller, J. M.; Bigard, M. A.; Champigneulle, B.; Gaucher, P.; Gueant, J. L.; Dauça, M., Studies on Peroxisomes of Colonic Mucosa in Crohn's Disease. *Digestive Diseases and Sciences* **1994,** *39*, 2177-2185.

238. Ratnasamy, P.; Srinivas, D., Active Sites and Reactive Intermediates in Titanium Silicate Molecular Sieves. *Advances in Catalysis* **2004,** *48*, 1-169.

239. Bakac, A., *Physical Inorganic Chemistry: Principles, Methods, and Models*. John Wiley & Sons: 2010.

240. Ruddy, D. A.; Brutchey, R. L.; Tilley, T. D., The Influence of Surface Modification on the Epoxidation Selectivity and Mechanism of TiSBA15 and TaSBA15 Catalysts with Aqueous Hydrogen Peroxide. *Top. Catal.* **2008,** *48*, 99-106.

241. Oyama, S. T., Rates, Kinetics, and Mechanisms of Epoxidation. In *Mechanisms in Homogeneous and Heterogeneous Epoxidation Catalysis*, Elsevier: 2008; pp 3-99.

242. Bayot, D.; Devillers, M., Peroxo complexes of niobium(V) and tantalum(V). *Coord. Chem. Rev.* **2006,** *250*, 2610-2626.

243. Bayot, D.; Tinant, B.; Devillers, M., Water-soluble niobium peroxo complexes as precursors for the preparation of Nb-based oxide catalysts. *Catal. Today* **2003,** *78*, 439-447.

244. Sergienko, V. S., Structual Characteristics of Peroxo Complexes of Group IV and V Transition Metals. Review. *Crystallography Reports* **2004,** *49*, 907-929.

245. Knops-Gerrits, P.; De Vos, D.; Feijen, E. J. P.; Jacobs, P. A., Raman spectroscopy on zeolites. *Microporous Mater.* **1997,** *8*, 3-17.

246. Stare, J.; Henson, N. J.; Eckert, J., Mechanistic Aspects of Propene Epoxidation by Hydrogen Peroxide. Catalytic Role of Water Molecules, External Electric Field, and Zeolite Framework of TS-1. *J. Chem. Inf. Model.* **2009,** *49*, 833-846.

247. Kurti, L.; Czako, B., *Strategic Applications of Named Reactions in Organic Synthesis*. Academic Press: 2005.

248. Deubel, D. V.; Sundermeyer, J.; Frenking, G., Mechanism of the Olefin Epoxidation Catalyzed by Molybdenum Diperoxo Complexes: Quantum-Chemical Calculations Give an Answer to a Long-Standing Question. *J. Am. Chem. Soc.* **2000,** *122*, 10101-10108.

249. Kuznetsov, M. L.; Pessoa, J. C., Epoxidation of olefins catalysed by vanadium-salan complexes: a theoretical mechanistic study. *Dalton Trans* **2009,** 5460-5468.

250. Bienert, G. P.; Schjoerring, J. K.; Jahn, T. P., Membrane transport of hydrogen peroxide. *Biochim. Biophys. Acta* **2006,** *1758*, 994-1003.

251. Corma, A.; Garcia, H., Lewis Acids as Catalysts in Oxidation Reactions: From Homogeneous to Heterogeneous Systems. *Chem. Rev.* **2002,** *102*, 3837-3892.

252. Gounder, R., Hydrophobic microporous and mesoporous oxides as Brønsted and Lewis acid catalysts for biomass conversion in liquid water. *Catal. Sci. Tech.* **2014,** *4*, 2877-2886.

253. Guidotti, M.; Batonneau-Gener, I.; Gianotti, E.; Marchese, L.; Mignard, S.; Psaro, R.; Sgobba, M.; Ravasio, N., The effect of silylation on titanium-containing silica catalysts for the epoxidation of functionalised molecules. *Microporous Mesoporous Mater.* **2008,** *111*, 39-47.

254. Lin, K.; Pescarmona, P. P.; Houthoofd, K.; Liang, D.; Van Tendeloo, G.; Jacobs, P. A., Direct room-temperature synthesis of methyl-functionalized Ti-MCM-41 nanoparticles and their catalytic performance in epoxidation. *J. Catal.* **2009,** *263*, 75-82.

255. Chen, N. Y.; Dengnan, T. F.; Morris Smith, C., *Molecular Transport and Reaction in Zeolites: Design and Application of Shape Selective Catalysts*. John Wiley & Sons: 1994.

256. Bates, J. S.; Gounder, R., Influence of confining environment polarity on ethanol dehydration catalysis by Lewis acid zeolites. *J. Catal.* **2018,** *365*, 213-226.

257. Bates, J. S.; Bukowski, B. C.; Harris, J. W.; Greeley, J.; Gounder, R., Distinct Catalytic Reactivity of Sn Substituted in Framework Locations and at Defect Grain Boundaries in Sn-Zeolites. *ACS Catal.* **2019,** *9*, 6146-6168.

258. Zhu, Z.; Xu, H.; Jiang, J.; Wu, P., Postsynthesis and Effective Baeyer–Villiger Oxidation Properties of Hierarchical FAU-type Stannosilicate. *J. Phys. Chem. C* **2016,** *120*, 23613-23624.

259. Corma, A.; Nemeth, L.; Renz, M.; Valencia, S., Sn-zeolite beta as a heterogeneous chemoselective catalytic for Baeyer-Villiger oxidations. *Nature* **2001,** *412*, 423-425.

260. Moliner, M.; Roman-Leshkov, Y.; Davis, M. E., Tin-containing zeolites are highly active catalysts for the isomerization of glucose in water. *Proc. Natl. Acad. Sci.* **2010,** *107*, 6164-6168.

261. Notestein, J. M.; Solovyov, E.; Andrini, L. R.; Requejo, F. G.; Katz, A.; Iglesia, E., The Role of Outer-Sphere Surface Acidity in Alkene Epoxidation Catalyzed by Calixarene-Ti(IV) Complexes. *J. Am. Chem. Soc.* **2007,** *129*, 15585-15595.

262. Takahara, I.; Saito, M.; Inaba, M.; Murata, K., Dehydration of Ethanol into Ethylene over Solid Acid Catalysts. *Catal. Lett.* **2005,** *105*, 249-252.

263. Kondo, J. N.; Ito, K.; Yoda, E.; Wakabayashi, F.; Domen, K., An Ethoxy Intermediate in Ethanol Dehydration on Bronsted Acid Sites in Zeolite. *J. Phys. Chem. B* **2005,** *109*, 10969-10972.

264. Sultana Poly, S.; Hakim Siddiki, S. M. A.; Touchy, A. S.; Yasumura, S.; Toyao, T.; Maeno, Z.; Shimizu, K.-i., High-silica Hβ zeolites for catalytic hydration of hydrophobic epoxides and alkynes in water. *J. Catal.* **2018,** *368*, 145-154.

265. Dai, W.; Wang, C.; Tang, B.; Wu, G.; Guan, N.; Xie, Z.; Hunger, M.; Li, L., Lewis Acid Catalysis Confined in Zeolite Cages as a Strategy for Sustainable Heterogeneous Hydration of Epoxides. *ACS Catal.* **2016,** *6*, 2955-2964.

266. Wu, P.; Tatsumi, T., Preparation of B-free Ti-MWW through reversible structural conversion. *Chem. Commun.* **2002,** 1026-1027.

267. Kulprathipanja, S., *Zeolites in Industrial Separation and Catalysis*. Wiley-VCH: 2010.

268. Kunitake, Y.; Takata, T.; Yamasaki, Y.; Yamanaka, N.; Tsunoji, N.; Takamitsu, Y.; Sadakane, M.; Sano, T., Synthesis of titanated chabazite with enhanced thermal stability by hydrothermal conversion of titanated faujasite. *Microporous Mesoporous Mater.* **2015,** *215*, 58-66.

269. Takata, T.; Tsunoji, N.; Takamitsu, Y.; Sadakane, M.; Sano, T., Incorporation of various heterometal atoms in CHA zeolites by hydrothermal conversion of FAU zeolite and their performance for selective catalytic reduction of NO_x with ammonia. *Microporous Mesoporous Mater.* **2017,** *246*, 89-101.

270. Lari, G. M.; Dapsens, P. Y.; Scholz, D.; Mitchell, S.; Mondelli, C.; Pérez-Ramírez, J., Deactivation mechanisms of tin-zeolites in biomass conversions. *Green Chem.* **2016,** *18*, 1249-1260.

271. Trejda, M.; Wojtaszek, A.; Floch, A.; Wojcieszak, R.; Gaigneaux, E. M.; Ziolek, M., New Nb and Ta–FAU zeolites—Direct synthesis, characterisation and surface properties. *Catal. Today* **2010,** *158*, 170-177.

272. Kuwahara, Y.; Aoyama, J.; Miyakubo, K.; Eguchi, T.; Kamegawa, T.; Mori, K.; Yamashita, H., TiO_2 photocatalyst for degradation of organic compounds in water and air supported on highly hydrophobic FAU zeolite: Structural, sorptive, and photocatalytic studies. *J. Catal.* **2012,** *285*, 223-234.

273. Verified Syntheses of Zeolitic Materials. <http://www.iza-online.org/synthesis/default.html> (Accessed July 15th, 2019)

274. Thommes, M.; Kaneko, K.; Neimark, A. V.; Olivier, J. P.; Rodriguez-Reinoso, F.; Rouquerol, J.; Sing, K. S. W., Physisorption of gases, with special reference to the evaluation of surface area and pore size distribution (IUPAC Technical Report). *Pure Appl. Chem.* **2015,** *87*, 1051-1069.

275. Bregante, D. T.; Patel, A. Y.; Johnson, A. M.; Flaherty, D. W., Catalytic Thiophene Oxidation by Groups 4 and 5 Framework-Substituted Zeolites with Hydrogen Peroxide: Mechanistic and Spectroscopic Evidence for the Effects of Metal Lewis Acidity and Solvent Lewis Basicity. *J. Catal.* **2018,** *364*, 415-425.

276. Vitiello, R. P.; Macak, J. M.; Ghicov, A.; Tsuchiya, H.; Dick, L. F. P.; Schmuki, P., N-Doping of anodic TiO2 nanotubes using heat treatment in ammonia. *Electrochem. Commun.* **2006,** *8*, 544-548.

277. Chun, W.; Ishikawa, A.; Fujisawa, H.; Takata, T.; Kondo, J. N.; Hara, M.; Kawai, M.; Matsumoto, Y.; Domen, K., Conduction and Valence Band Positions of Ta_2O_5, TaON, and Ta_3N_5 by UPS and Electrochemical Methods. *J. Phys. Chem. B* **2003,** *107*, 1798-1803.

278. Reimann, K.; Steube, N., Experimental Determination of the Electronic Band Structure of SnO_2. *Solid State Commun.* **1998,** *105*, 649-652.

279. Li, C.; Xiong, G.; Xin, Q.; Liu, J.; Ying, P.; Feng, Z.; Li, J.; Yang, W.; Wang, Y.; Wang, G.; Liu, X.; Lin, M.; Wang, X.; Min, E., UV Resonance Raman Spectroscopic Identification of Titanium Atoms in the Framework of TS-1 Zeolite. *Angew. Chem. Int. Ed.* **1999,** *38*, 2220-2222.

280. Prakash, A. M.; Kevan, L., Synthesis of Niobium Silicate Molecular Sieves of the MFI Structure: Evidence for Framework Incorporation of the Niobium Ion. *J. Am. Chem. Soc.* **1998,** *120*, 13148-13155.

281. Ko, Y. S.; Ahn, W. S., Synthesis and characterization of tantalum silicalite molecular sieves with MFI structure. *Microporous Mesoporous Mater.* **1999,** *30*, 283-291.

282. Noc, L. L.; Moulin, C. C.; Solomykina, S.; D.T., O.; Lortie, C.; Lessard, S.; Bonneviot, L., Determination of the environment of titanium atoms in TS-1 silicalite by Ti K-edge X-ray

Absorption Spectroscopy, 29Si and 1H Nuclear Magnetic Resonance. *Stud. Surf. Sci. Catal.* **1995,** *97*, 19-25.

283. Melchor, M. T.; Vaughan, D. E. W.; Pictroski, C. F., Local Environment Fine Structure in the 29Si NMR Spectra of Faujasite Zeolites. *J. Phys. Chem.* **1995,** *99*, 6128-6144.

284. Prodinger, S.; Derewinski, M. A.; Vjunov, A.; Burton, S. D.; Arslan, I.; Lercher, J. A., Improving Stability of Zeolites in Aqueous Phase via Selective Removal of Structural Defects. *J. Am. Chem. Soc.* **2016,** *138*, 4408-4415.

285. Prodinger, S.; Shi, H.; Eckstein, S.; Hu, J. Z.; Olarte, M. V.; Camaioni, D. M.; Derewinski, M. A.; Lercher, J. A., Stability of Zeolites in Aqueous Phase Reactions. *Chem. Mater.* **2017,** *29*, 7255-7262.

286. Hadjiivanov, K.; Ivanova, E.; Kefirov, R.; Janas, J.; Plesniar, A.; Dzwigaj, S.; Che, M., Adsorption properties of Fe-containing dealuminated BEA zeolites as revealed by FTIR spectroscopy. *Microporous Mesoporous Mater.* **2010,** *131*, 1-12.

287. Szanyi, J.; Kwak, J. H.; Peden, C. H. F., The Effect of Water on the Adsorption of NO2 in Na- and Ba-Y, FAU Zeolites: A Combined FTIR and TPD Investigation. *J. Phys. Chem. B* **2004,** *108*, 3746-3753.

288. Gounder, R.; Jones, A. J.; Carr, R. T.; Iglesia, E., Solvation and acid strength effects on catalysis by faujasite zeolites. *J. Catal.* **2012,** *286*, 214-223.

289. Tang, B.; Dai, W.; Sun, X.; Wu, G.; Guan, N.; Hunger, M.; Li, L., Mesoporous Zr-Beta zeolites prepared by a post-synthetic strategy as a robust Lewis acid catalyst for the ring-opening aminolysis of epoxides. *Green Chem.* **2015,** *17* 1744-1755.

290. Harris, J. W.; Arvay, J.; Mitchell, G.; Delgass, W. N.; Ribeiro, F. H., Propylene oxide inhibits propylene epoxidation over Au/TS-1. *J. Catal.* **2018,** *365*, 105-114.

291. Csicsery, S. M., Shape-selective catalysis in zeolites. *Zeolites* **1984,** *4*, 202-213.

292. Yadav, A.; Jackson, R. M.; Holbrook, J. J.; Warshel, A., Role of Solvent Reorganization Energies in the Catalytic Activity of Enzymes. *J. Am. Chem. Soc.* **1991,** *113*, 4800-4805.

293. Reichardt, D.; Welton, T., *Solvents and Solvent Effects in Organic Chemistry*. Fourth ed.; Wiley-VCH: 2010.

294. Research Areas: Catalysis Science. <https://science.energy.gov/bes/csgb/research-areas/catalysis-science/> (accessed August 8th, 2018).

295. Wu, L.; Tang, Z.; Yu, Y.; Yao, X.; Liu, W.; Li, L.; Yan, B.; Liu, Y.; He, M., Facile synthesis of a high-performance titanosilicate catalyst with controllable defective Ti(OSi)3OH sites. *Chem. Commun.* **2018,** *54*, 6384-6387.

296. Grosso-Giordano, N. A.; Schroeder, C.; Okrut, A.; Solovyov, A.; Schottle, C.; Chasse, W.; Marinkovic, N.; Koller, H.; Zones, S. I.; Katz, A., Outer-Sphere Control of Catalysis on Surfaces: A Comparative Study of Ti(IV) Single-Sites Grafted on Amorphous versus Crystalline Silicates for Alkene Epoxidation. *J. Am. Chem. Soc.* **2018,** *140*, 4956-4960.

297. Kresse, G.; Hafner, J., Ab initiomolecular-dynamics simulation of the liquid-metal–amorphous-semiconductor transition in germanium. *Phys. Rev. B* **1994,** *49*, 14251-14269.

298. Kresse, G.; Furthmùller, J., Efficient iterative schemes for ab initio total-energy calculations using a plane-wave basis set. *Phys. Rev. B* **1996,** *54*, 111869-111184.

299. Kresse, G.; Furthmùller, J., Efficiency of ab-initio total energy calculations for metals and semiconductors using a plane-wave basis set *Comput. Mater. Sci.* **1996,** *6*, 15-50.

300. Kresse, G.; Hafner, J., Ab initiomolecular dynamics for liquid metals. *Phys. Rev. B* **1993,** *47*, 558-561.

301. Bukowski, B. C.; Bates, J. S.; Gounder, R.; Greeley, J., First principles, microkinetic, and experimental analysis of Lewis acid site speciation during ethanol dehydration on Sn-Beta zeolites. *J. Catal.* **2018,** *365*, 261-276.

302. Blöchl, P. E., Projector augmented-wave method. *Physical Review B* **1994,** *50*, 17953-17979.

303. Kresse, G.; Joubert, D., From ultrasoft pseudopotentials to the projector augmented-wave method. *Phys. Rev. B* **1999,** *59*, 1758-1775.

304. Wellendorff, J.; Lundgaard, K. T.; Møgelhøj, A.; Petzold, V.; Landis, D. D.; Nørskov, J. K.; Bligaard, T.; Jacobsen, K. W., Density functionals for surface science: Exchange-correlation model development with Bayesian error estimation. *Physical Review B* **2012,** *85*, 235149

305. Baerlocher, C.; McCusker, L. B. Database of Zeolite Structures. <http://www.iza-structure.org/databases/> (Accessed November 11th, 2018)

306. Lin, S.-T.; Maiti, P. K.; Goddard, W. A., Two-Phase Thermodynamic Model for Efficient and Accurate Absolute Entropy of Water from Molecular Dynamics Simulations. *J. Phys. Chem. B* **2010,** *114*, 8191-8198.

307. Lin, S.-T.; Blanco, M.; Goddard, W. A., The two-phase model for calculating thermodynamic properties of liquids from molecular dynamics: Validation for the phase diagram of Lennard-Jones fluids. *J. Chem. Phys.* **2003,** *119*, 11792-11805.

308. Pascal, T. A.; Lin, S. T.; Goddard, W. A., 3rd, Thermodynamics of liquids: standard molar entropies and heat capacities of common solvents from 2PT molecular dynamics. *Phys. Chem. Chem. Phys.* **2011,** *13*, 169-181.

309. Brehm, M.; Kirchner, B., TRAVIS - a free analyzer and visualizer for Monte Carlo and molecular dynamics trajectories. *J. Chem. Inf. Model.* **2011,** *51*, 2007-2023.

310. Alexopoulos, K.; Lee, M.-S.; Liu, Y.; Zhi, Y.; Liu, Y.; Reyniers, M.-F.; Marin, G. B.; Glezakou, V.-A.; Rousseau, R.; Lercher, J. A., Anharmonicity and Confinement in Zeolites: Structure, Spectroscopy, and Adsorption Free Energy of Ethanol in H-ZSM-5. *J. Phys. Chem. C* **2016,** *120*, 7172-7182.

311. Bordiga, S.; Lamberti, C.; Bonino, F.; Travert, A.; Thibault-Starzyk, F., Probing zeolites by vibrational spectroscopies. *Chem. Soc. Rev.* **2015,** *44*, 7262-7341.

312. Sayed, M. B.; Kydd, R. A.; Cooney, R. P., A Fourier-Transform Infrared Spectral Study of H-ZSM-5 Surface Sites and Reactivity Sequences in Methanol Conversion. *J. Catal.* **1984,** *88*, 137-149.

313. Shields, R. M.; Temelso, B.; Archer, K. A.; Morrell, T. E.; Shields, G. C., Accurate Predictions of Water Cluster Formation, (H_2O) n = 2 - 10. *J. Phys. Chem. A* **2010,** *114*, 11725-11737.

314. Fawcett, W. R.; Liu, G.; Kessler, T. E., Solvent-Induced Frequency Shifts in the Infrared Spectrum of Acetonitrile in Organic Solvents. *J. Phys. Chem.* **1993,** *97*, 9293-9298.

315. Campbell, C. T.; Sellers, J. R., The entropies of adsorbed molecules. *J. Am. Chem. Soc.* **2012,** *134*, 18109-18115.

316. Denmark, S. E.; Beutner, G. L., Lewis base catalysis in organic synthesis. *Angew. Chem. Int. Ed. Engl.* **2008,** *47*, 1560-1638.

317. Hogg, J. M.; Brown, L. C.; Matuszek, K.; Latos, P.; Chrobok, A.; Swadzba-Kwasny, M., Liquid coordination complexes of Lewis acidic metal chlorides: Lewis acidity and insights into speciation. *Dalton Trans.* **2017,** *46*, 11561-11574.

318. Gates, B. C.; Knoezinger, H.; Jentoft, F. C., *Advances in Catalysis*. Academic Press: 2011; Vol. 54.

319. Xiong, G.; Cao, Y.; Guo, Z.; Jia, Q.; Tian, F.; Liu, L., The roles of different titanium species in TS-1 zeolite in propylene epoxidation studied by in situ UV Raman spectroscopy. *Phys. Chem. Chem. Phys.* **2016,** *18*, 190-196.

320. Madon, R. J.; Iglesia, E., Catalytic reaction rates in thermodynamically non-ideal systems. *J. Mol. Catal. A: Chem.* **2000,** *163*, 189-204.

321. Sever, R. R.; Root, T. W., DFT Study of Solvent Coordination Effects on Titanium-Based Epoxidation Catalysts. Part Two: Reactivity of Titanium Hydroperoxo Complexes in Ethylene Epoxidation. *J. Phys. Chem. B* **2003,** *107*, 4090-4099.

322. Panyaburapa, W.; Nanok, T.; Limtrakul, J. L., Epoxidation Reaction of Unsaturated Hydrocarbons with H_2O_2 over Defect TS-1 Investigated by ONIOM Method: Formation of Active Sites and Reaction Mechanisms. *J. Phys. Chem. C* **2007,** *111*, 3433-3441.

323. Chandler, D., Interfaces and the driving force of hydrophobic assembly. *Nature* **2005,** *437*, 640-647.

324. Striolo, A., Chapter 10 Nano-confined water. *Theo. Comput. Chem.* **2007,** *18*, 245-274.

325. Munoz-Santiburcio, D.; Marx, D., Chemistry in nanoconfined water. *Chem. Sci.* **2017,** *8*, 3444-3452.

326. Silverstein, K. A. T.; Haymet, A. D. J.; Dill, K. A., The Strength of Hydrogen Bonds in Liquid Water and Around Nonpolar Solutes. *J. Am. Chem. Soc.* **2000,** *122*, 8037-8041.

327. Walrafen, G. E.; Chu, Y. C., Shear Viscosity, Heat Capacity, and Fluctuations of Liquid Water, All at Constant Molal Volume. *J. Phys. Chem.* **1991,** *95*, 8909-8921.

328. Zhu, Z.; Xu, H.; Jiang, J.; Wu, H.; Wu, P., Structural reconstruction: a milestone in the hydrothermal synthesis of highly active Sn-Beta zeolites. *Chem. Commun.* **2017,** *53*, 12516-12519.

329. Wang, J.; Okumura, K.; Jaenicke, S.; Chuah, G.-K., Post-synthesized zirconium-containing Beta zeolite in Meerwein–Ponndorf–Verley reduction: Pros and cons. *Appl. Catal. A* **2015,** *493*, 112-120.

330. Moteki, T.; Rowley, A. T.; Bregante, D. T.; Flaherty, D. W., Formation Pathways toward 2- and 4-Methylbenzaldehyde via Sequential Reactions from Acetaldehyde over Hydroxyapatite Catalyst. *ChemCatChem* **2017,** *9*, 1921-1929.

331. Gould, N. S.; Xu, B., Temperature-Programmed Desorption of Pyridine on Zeolites in the Presence of Liquid Solvents. *ACS Catal.* **2018,** *8*, 8699-8708.

332. Zhang, K.; Lively, R. P.; Dose, M. E.; Brown, A. J.; Zhang, C.; Chung, J.; Nair, S.; Koros, W. J.; Chance, R. R., Alcohol and water adsorption in zeolitic imidazolate frameworks. *Chem. Commun.* **2013,** *49*, 3245-3247.

333. Shah, D.; Kissick, K.; Ghorpade, A.; Hannah, R.; Bhattacharyya, D., Pervaporation of alcohol-water and dimethylformamide-water mixtures using hydrophilic zeolite NaA membranes: mechanisms and experimental results. *J. Membr. Sci.* **2000,** *179*, 185-205.

334. Nalaparaju, A.; Zhao, X. S.; Jiang, J. W., Molecular Understanding for the Adsorption of Water and Alcohols in Hydrophilic and Hydrophobic Zeolitic Metal-Organic Frameworks. *J. Phys. Chem. C* **2010,** *114*, 11542-11550.

335. Lively, R. P.; Dose, M. E.; Thompson, J. A.; McCool, B. A.; Chance, R. R.; Koros, W. J., Ethanol and water adsorption in methanol-derived ZIF-71. *Chem. Commun.* **2011,** *47*, 8667-8669.

336. Ortiz, A. U.; Freitas, A. P.; Boutin, A.; Fuchs, A. H.; Coudert, F. X., What makes zeolitic imidazolate frameworks hydrophobic or hydrophilic? The impact of geometry and functionalization on water adsorption. *Phys. Chem. Chem. Phys.* **2014,** *16*, 9940-9949.

337. Cailliez, F.; Stirnemann, G.; Boutin, A.; Demachy, I.; Fuchs, A. H., Does Water Condense in Hydrophobic Cavaties? A Molecular Simulation Study of Hydration in Heterogeneous Nanopores. *J. Phys. Chem. C* **2008,** *112*, 10435-10445.

338. Chakraborty, S.; Kumar, H.; Dasgupta, C.; Maiti, P. K., Confined Water: Structure, Dynamics, and Thermodynamics. *Acc. Chem. Res.* **2017,** *50*, 2139-2146.

339. Majumder, M.; Chopra, N.; Andrews, R.; Hinds, B. J., Enhanced flow in carbon nanotubes. *Nature* **2005,** *438*, 44.

340. Holt, J. K.; Park, H. G.; Wang, Y.; Stadermann, M.; Artyukhin, A. B.; Grigoropoulos, C. P.; Noy, A.; Bakajin, O., Fast Mass Transport Through Sub-2-Nanometer Carbon Nanotubes. *Science* **2006,** *312*, 1034-1037.

341. Byl, O.; Liu, J. C.; Wang, Y.; Yim, W. L.; Johnson, J. K.; Yates, J. T., Unusual Hydrogen Bonding in Water-Filled Carbon Nanotubes. *J. Am. Chem. Soc.* **2006,** *128*, 12090-12097.

342. Thomas, J. A.; McGaughey, A. J. H., Reassessing Fast Water Transport Through Carbon Nanotubes. *Nano Lett.* **2008,** *8*, 2788-2793.

343. Bukowski, B. C.; Bates, J. S.; Gounder, R.; Greeley, J., Defect-Mediated Ordering of Condensed Water Structures in Microporous Zeolites *Angew. Chem. Int. Ed.* **2019**, *58*, 16422-16426.

344. Khouw, C. B.; Dartt, C. B.; Labinder, J. A.; Davis, M. E., Studies on the Catalytic-Oxidation of Alkanes and Alkenes by Titanium Silicates. *J. Catal.* **1994,** *149*, 195-205.

345. Dyson, P. J.; Jessop, P. G., Solvent Effects in Catalysis: Rational Improvements of Catalysts *via* Manipulation of Solvent Effects. *Catal. Sci. Technol.* **2016,** *6*, 3302-3316.

346. Mellmer, M. A.; Sanppitsekree, C.; Demir, B.; Bai, P.; Ma, K.; Neurock, M.; Dumesic, J. A., Solvent-Enabled Control of Reactivity for Liquid Phase Reactions of Biomass-Derived Compounds. *Nature Catal.* **2018,** *1*, 199-207.

347. Mellmer, M. A.; Sener, C.; Gallo, J. M. R.; Luterbacher, J. S.; Alonso, D. M.; Dumesic, J. A., Solvent Effects in Acid-Catalyzed Biomass Conversion Reactions. *Angew. Chem. Int. Ed.* **2014,** *53*, 11872-11875.

348. Walker, T. W.; Chew, A. K.; Li, H.; Demir, B.; Zhang, Z. C.; Huber, G. W.; Van Lehn, R. C.; Dumesic, J. A., Universal Kinetic Solvent Effects in Acid-Catalyzed Reactions of Biomass-Derived Oxygenates *Energy & Environmental Science* **2018,** *11*, 617-628.

349. Kalmutzki, M. J.; Diercks, C. S.; Yaghi, O. M., Metal-Organic Frameworks for Water Harvesting from Air. *Adv. Mater.* **2018,** *30*, e1704304.

350. Williams, D. B.; Lawton, M., Drying of organic solvents: quantitative evaluation of the efficiency of several desiccants. *J. Org. Chem.* **2010,** *75*, 8351-8354.

351. Jaumot, J.; de Juan, A.; Tauler, R., MCR-ALS GUI 2.0: New features and applications. *Chemometrics and Intelligent Laboratory Systems* **2015,** *140*, 1-12.

352. Jharimune, S.; Sathe, A. A.; Rioux, R. M., Thermochemical Measurements of Cation Exchange in CdSe Nanocrystals Using Isothermal Titration Calorimetry. *Nano Lett.* **2018,** *18*, 6795-6803.

353. The entropies of hydrogen peroxide adsorption-and-activation were not measured because the decomposition of hydrogen peroxide occured at high molar ratios of hydrogen peroxide:Ti atoms, rather than only adsorption.

354. Ahunbay, M. G., Monte Carlo simulation of water adsorption in hydrophobic MFI zeolites with hydrophilic sites. *Langmuir* **2011,** *27*, 4986-4993.

355. Verma, P. K.; Kundu, A.; Puretz, M. S.; Dhoonmoon, C.; Chegwidden, O. S.; Londergan, C. H.; Cho, M., The Bend+Libration Combination Band Is an Intrinsic, Collective, and Strongly Solute-Dependent Reporter on the Hydrogen Bonding Network of Liquid Water. *J. Phys. Chem. B* **2018,** *122*, 2587-2599.

356. 1,2,-Epoxyoctane. <https://www.chemicalbook.com/SpectrumEN_2984-50-1_IR2.html> (accessed March 4th, 2019).

357. Williams, A., *Free Energy Relationships in Organic and Bio-Organic Chemistry*. Royal Society of Chemistry: Cambridge, UK, 2003.

358. Eisenstein, O.; Crabtree, R. H., Outer sphere hydrogenation catalysis. *New J. Chem.* **2013,** *37*, 21-27.

359. Peris, E.; Crabtree, R. H., Key factors in pincer ligand design. *Chem. Soc. Rev.* **2018,** *47*, 1959-1968.

360. Abrantes, M.; Gago, S.; Valente, Anabela A.; Pillinger, M.; Gonçalves, Isabel S.; Santos, Teresa M.; Rocha, J.; Romão, Carlos C., Incorporation of a (Cyclopentadienyl)molybdenum Oxo Complex in MCM-41 and Its Use as a Catalyst for Olefin Epoxidation. *Eur. J. Inorg. Chem.* **2004,** *2004*, 4914-4920.

361. Bigi, F.; Piscopo, C. G.; Predieri, G.; Sartori, G.; Scotti, R.; Zanoni, R.; Maggi, R., Molybdenum-MCM-41 silica as heterogeneous catalyst for olefin epoxidation. *J. Mol. Catal. A: Chem.* **2014,** *386*, 108-113.

362. LyondellBasell's $2.4bn PO/TBA project driven by technology and feedstocks. <https://www.icis.com/explore/resources/news/2017/07/26/10127843/lyondellbasell-s-2-4bn-po-tba-project-driven-by-technology-and-feedstocks/> (accessed March 2nd, 2019).

363. Weissermel, K.; Arpe, H.-J., *Industrial Organic Chemistry*. Fourth ed.; Wiley-VCH: 2003.

364. Mimoun, H., Do metal peroxides as homolytic and heterolytic oxidative reagents. Mechanism of the halcon epoxidation process. *Catal. Today* **1987,** *1*, 281-295.

365. Xia, Q. H.; Chen, X.; Tatsumi, T., Epoxidation of cyclic alkenes with hydrogen peroxide and tert-butyl hydroperoxide on Na-containing Ti-Beta zeolites. *J. Mol. Catal. A* **2001,** *176*, 179-193.

366. Fraile, J. M.; García, J. I.; Mayoral, J. A.; Vispe, E.; Brown, D. R.; Naderi, M., Is MCM-41 really advantageous over amorphous silica? The case of grafted titanium epoxidation catalysts. *Chem. Commun.* **2001,** 1510-1511.

367. Sanz, R.; Serrano, D. P.; Pizarro, P.; Moreno, I., Hierarchical TS-1 zeolite synthesized from SiO2 TiO2 xerogels imprinted with silanized protozeolitic units. *Chem. Eng. J.* **2011,** *171* (3), 1428-1438.

368. Hydroperoxide, 1-methyl-1-phenylethyl. <https://webbook.nist.gov/cgi/cbook.cgi?Source=1969FIH%2F141&Mask=400> (accessed February, 25th).

369. Kwon, S.; Schweitzer, N. M.; Park, S.; Stair, P. C.; Snurr, R. Q., A kinetic study of vapor-phase cyclohexene epoxidation by H_2O_2 over mesoporous TS-1. *J. Catal.* **2015,** *326*, 107-115.

370. Bregante, D. T.; Flaherty, D. W., Impact of Specific Interactions Among Reactive Surface Intermediates and Confined Water on Epoxidation Catalysis and Adsorption in Lewis Acid Zeolites. *ACS Catal.* **2019,** *9*, 10951-10962.

371. Cavallo, G.; Metrangolo, P.; Milani, R.; Pilati, T.; Priimagi, A.; Resnati, G.; Terraneo, G., The Halogen Bond. *Chem. Rev.* **2016,** *116*, 2478-2601.

372. Wilson, N. M.; Schröder, J.; Priyadarshini, P.; Bregante, D. T.; Kunz, S.; Flaherty, D. W., Direct synthesis of H2O2 on PdZn nanoparticles: The impact of electronic modifications and heterogeneity of active sites. *J. Catal.* **2018,** *368*, 261-274.

373. Di Iorio, J. R.; Gounder, R., Controlling the Isolation and Pairing of Aluminum in Chabazite Zeolites Using Mixtures of Organic and Inorganic Structure-Directing Agents. *Chem. Mater.* **2016,** *28*, 2236-2247.

374. Ramachandran, C.; Du, H.; Kim, Y.; Kung, M.; Snurr, R.; Broadbelt, L., Solvent effects in the epoxidation reaction of 1-hexene with titanium silicalite-1 catalyst. *J. Catal.* **2008,** *253*, 148-158.

375. Wu, Y.; Holdren, S.; Zhang, Y.; Oh, S. C.; Tran, D. T.; Emdadi, L.; Lu, Z.; Wang, M.; Woehl, T. J.; Zachariah, M.; Lei, Y.; Liu, D., Quantification of rhenium oxide dispersion on zeolite: Effect of zeolite acidity and mesoporosity. *J. Catal.* **2019,** *372*, 128-141.

376. Chrysochos, N.; Ahmadi, M.; Wahlefeld, S.; Rippers, Y.; Zebger, I.; Mroginski, M. A.; Schulzke, C., Comparison of molybdenum and rhenium oxo bis-pyrazine-dithiolene complexes - in search of an alternative metal centre for molybdenum cofactor models. *Dalton Trans.* **2019,** *48*, 2701-2714.

377. Mominou, N., Removal of Sulphides and Benzene in Fluid Catalytic Cracking Gasoline by Insitu Hydrogenation Over NbFAPSO-5. *Am. J. Appl. Chem.* **2019,** *7*, 59.

378. Gellert, M.; Dashjav, E.; Grüner, D.; Ma, Q.; Tietz, F., Compatibility study of oxide and olivine cathode materials with lithium aluminum titanium phosphate. *Ionics* **2017,** *24*, 1001-1006.

379. Ahn, S.; Nauert, S. L.; Hicks, K. E.; Ardagh, M. A.; Schweitzer, N. M.; Farha, O. K.; Notestein, J. M., Demonstrating the Critical Role of Solvation in Supported Ti and Nb Epoxidation Catalysts via Vapor-Phase Kinetics. *ACS Catal.* **2020,** *10*, 2817-2825.

380. Baurecht, D.; Fringeli, U. P., Quantitative modulated excitation Fourier transform infrared spectroscopy. *Rev. Sci. Instrum.* **2001,** *72*, 3782.

381. Diebold, U.; Madey, T. E., TiO_2 by XPS. *Surf. Sci. Spectra* **1996,** *4*, 227-231.

382. Kurtz, R. L.; Henrich, V. E., Comparison of Ti 2p Core-Level Peaks from TiO_2, Ti_2O_3, and Ti Metal, by XPS. *Surf. Sci. Spectra* **1998,** *5*, 179-181.

383. Reddy, G. R.; Balasubramanian, S.; Chennakesavulu, K., Zeolite encapsulated active metal composites and their photocatalytic studies for rhodamine-B, reactive red-198 and chloro-phenols. *RSC Adv.* **2015,** *5*, 81013-81023.

384. Haber, F.; Weiss, J., Über die Katalyse des Hydroperoxydes. *Naturwissenschaften* **1932,** *20*, 948-950.

385. Jahandar Lashaki, M.; Fayaz, M.; Niknaddaf, S.; Hashisho, Z., Effect of the adsorbate kinetic diameter on the accuracy of the Dubinin-Radushkevich equation for modeling adsorption of organic vapors on activated carbon. *J. Hazard. Mater.* **2012,** *241-242*, 154-163.

386. Perez-Pariente, J.; Sanz, J.; Fornes, V.; Corma, A., ^{29}Si and ^{27}Al MAS NMR Study of Zeolite Beta with Different Si/Al Ratios. *J. Catal.* **1990,** *124*, 217-223.

387. Pelmenschikov, A. G.; van Santen, R. A.; Jänchen, J.; Meijer, E., CD3CN as a Probe of Lewis and Bronsted Acidity of Zeolites. *J. Phys. Chem.* **1993,** *97*, 11071-11074.

388. *CRC Handbook of Chemistry and Physics*. CRC Press: 2012.

389. McQuarrie, D. A., *Statistical Mechanics*. University Science Books: Mill Valley, 2000.

390. Ayala, P. Y.; Schlegel, H. B., Identification and treatment of internal rotation in normal mode vibrational analysis. *J. Chem. Phys.* **1998,** *108*, 2314-2325.

391. Storhoff, B. N.; Lewis, H. C., Organonitrile Complexes of Transition Metals. *Coord. Chem. Rev.* **1977,** *23*, 1-29.

392. Computational Chemistry Comparison and Benchmark DataBase. https://cccbdb.nist.gov/exp2x.asp?casno=75058 (accessed June 1st, 2018).

393. Reedijk, J.; Groeneveld, W. L., Complexes with Ligands Containing Nitrile Groups. *Recueil* **1968,** *87*, 1079-1088.

394. Baker, B. M.; Murphy, K. P., Evaluation of Linked Protonation Effects in Protein Binding Reactions Using Isothermal Titration Calorimetry. *Biophys. J.* **1996,** *71*, 2049-2055.

395. Dam, T. K.; Roy, R.; Pagé, D.; Brewer, C. F., Thermodynamic Binding Parameters of Individual Epitopes of Multivalent Carbohydrates to Concanavalin A As Determined by "Reverse" Isothermal Titration Microcalorimetry. *Biochemistry* **2002,** *41*, 1359-1363.

APPENDIX A

Supplementary Information and Data for Chapter Two

A.1. Catalyst Characterization

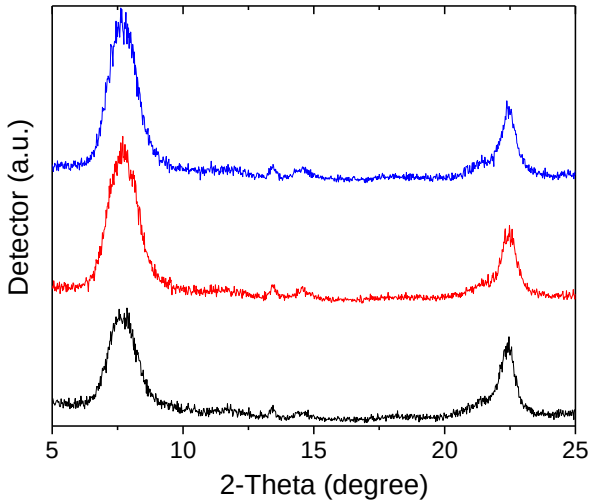

Figure A1. Powder X-ray diffractograms for commercial NH_4^+-BEA (black), Si-BEA (red), and $Nb_{1.5}$-BEA (blue).

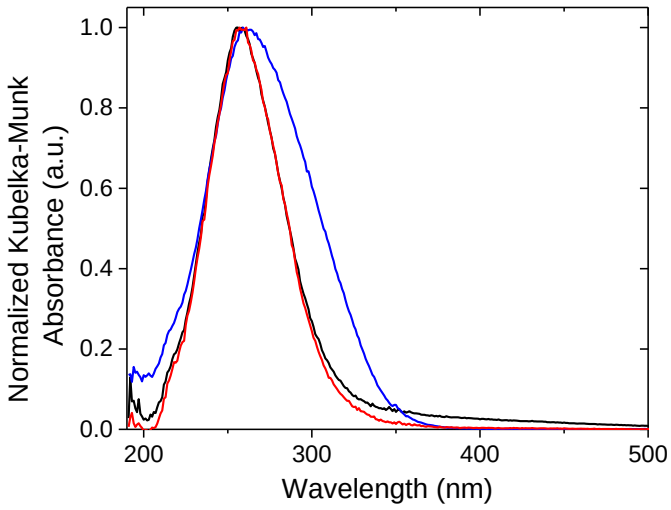

Figure A2. Diffuse reflectance UV-visible spectra for $Nb_{0.7}$-BEA (red), $Nb_{1.5}$-BEA (black), and 10 wt. % Nb-SiO_2 (blue) normalized to the maximum feature. MgO was used as a reference to collect a total reflectance background spectrum. $Nb_{0.15}$-BEA was omitted and did not have a band edge calculated because its low absorbance yielded a noisy signal.

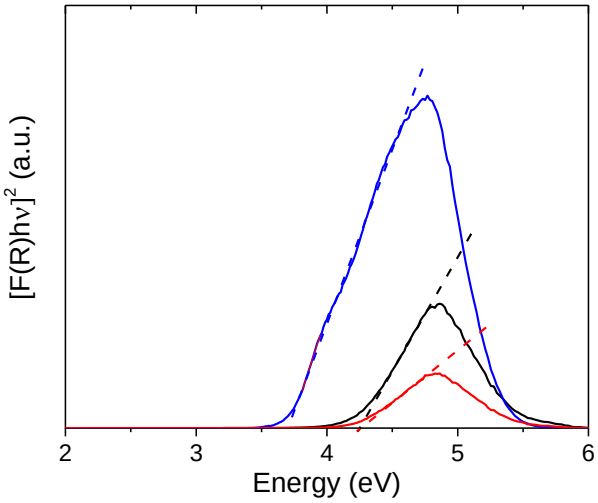

Figure A3. Tauc plots for $Nb_{0.7}$-BEA (red), $Nb_{1.5}$-BEA (black), and 10 wt % Nb-SiO_2 (blue) using the DRUV-vis data from Figure A2. Dotted lines (with respective color) represents the fit to determine the band edge for each material.

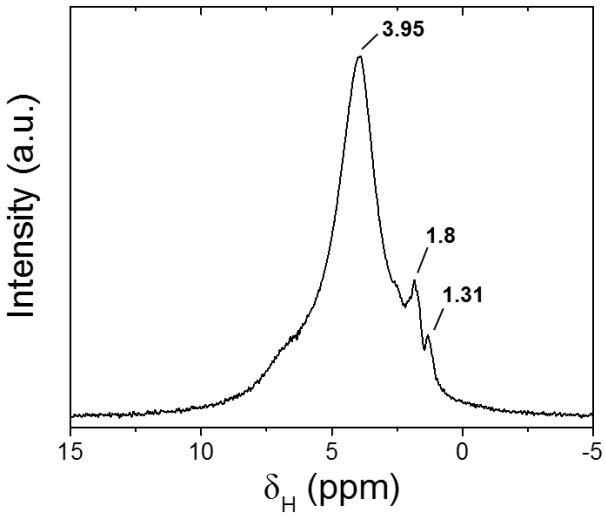

Figure A4. ^{1}H MAS NMR spectra of $Nb_{1.5}$-BEA, recorded at ambient conditions in a 4 mm diameter zirconia rotor.

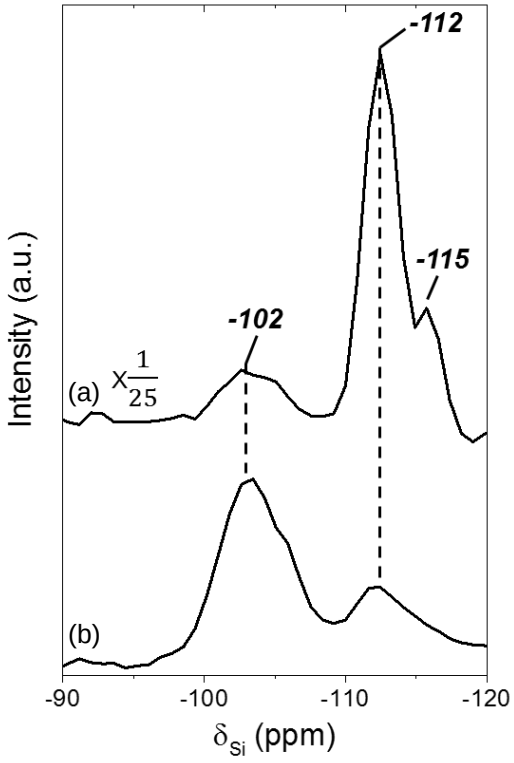

Figure A5. ^{29}Si MAS NMR spectra of $Nb_{1.5}$-BEA with (a) $^{1}H \rightarrow ^{29}Si$ cross or (b) ^{29}Si direct polarization recorded at ambient conditions in a 4 mm diameter zirconia rotor

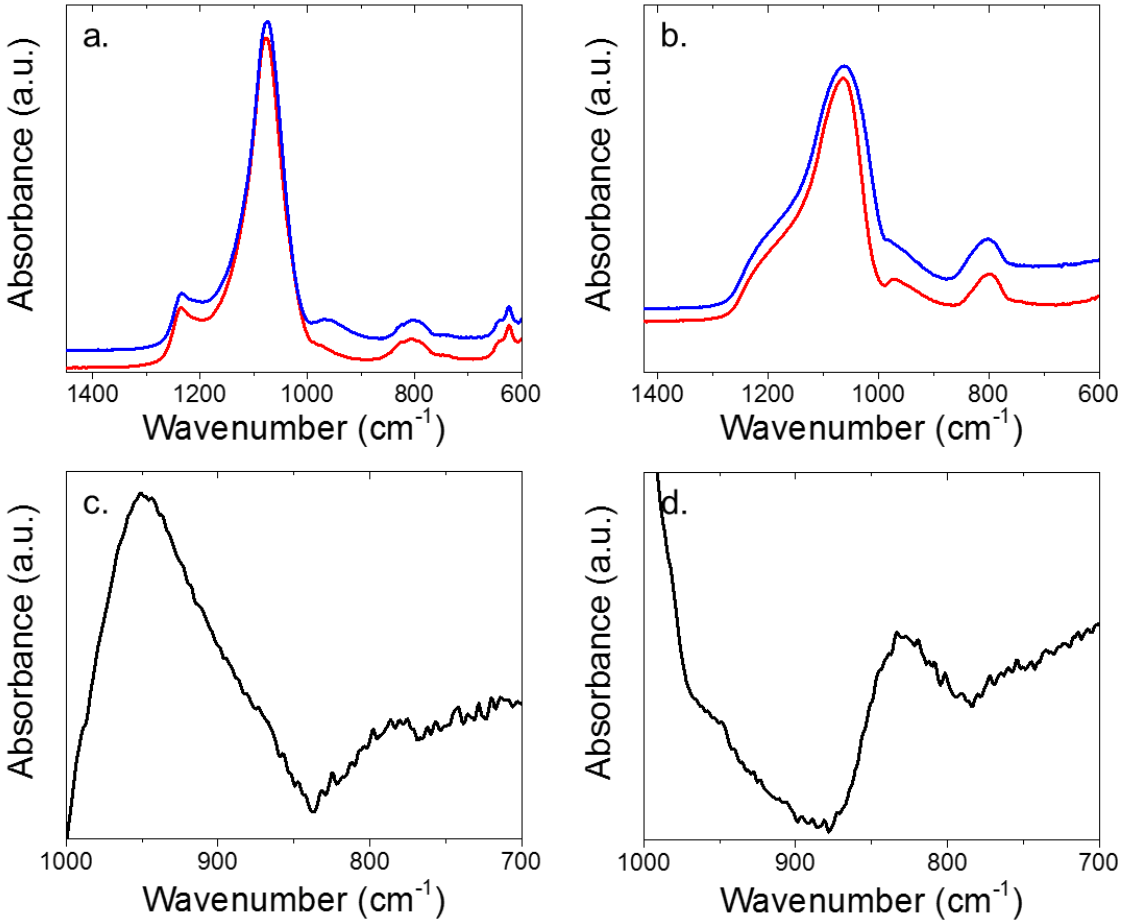

Figure A6. Normalized ATR-IR spectra of (a) Si-BEA (red) and $Nb_{1.5}$-BEA (blue), (b) SiO_2 (red) and $Nb_{10.0}$-SiO_2 (blue), (c) difference spectra of $Nb_{1.5}$-BEA with respect to Si-BEA, and (d) difference spectra of $Nb_{10.0}$-SiO_2 with respect to SiO_2.

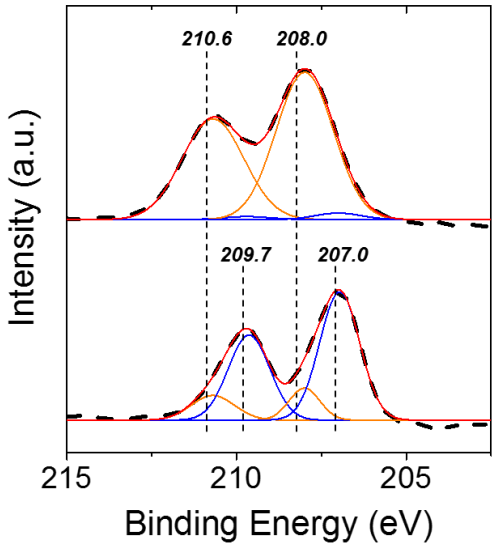

Figure A7. X-ray photoelectron spectra (black, dashed) of the Nb 3d region with peak fittings (colored, solid) for (a) untreated $Nb_{5.0}$-BEA and (b) H_2O_2-treated $Nb_{5.0}$-BEA. The peak fittings from the different oxidation states are color-coded for clarity: Nb^{4+} (blue), Nb^{5+} (orange), and cumulative peak fit (red, -). Spectra are referenced to an aliphatic C 1s feature at 284.8 eV.

Figure A7a (top curve) contains two large features (orange curves) at 210.6 and 208 eV, which are attributed to the Nb 3d 3/2 and 5/2 electrons for Nb^{5+}, while the corresponding Nb^{4+} features (blue curves) are negligible in magnitude. While in contrast, Fig. A7b (bottom curve), contains two doublet features that correspond to both Nb^{5+} and Nb^{4+} features, which would be expected for the Nb-OOH/Nb-$(O_2)^{2-}$ (i.e., hydroperoxide and peroxide) and Nb-$(O_2)^{-}$ (i.e., superoxide) species, respectively.

A.2. Control Experiments to Test Importance of Mass-Transfer Restrictions

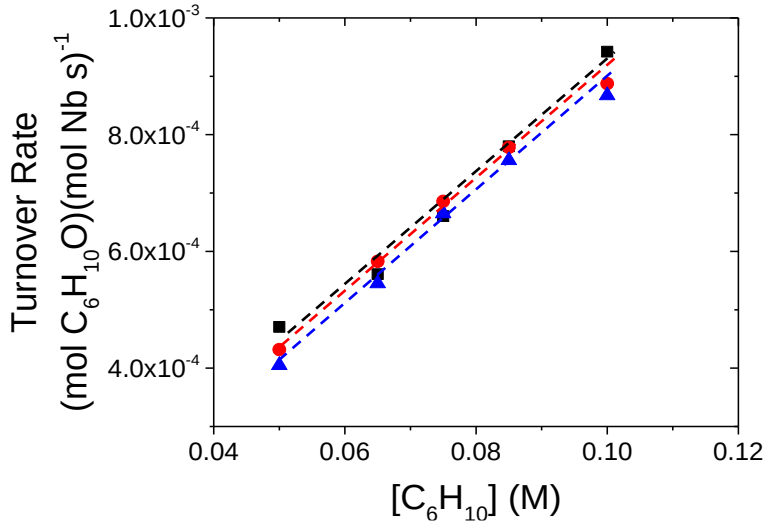

Figure A8. $C_6H_{10}O$ turnover rates as a function of $[C_6H_{10}]$ in 1mM H_2O_2 with $Nb_{1.5}$-BEA (■), $Nb_{0.7}$-BEA (●) and $Nb_{0.15}$-BEA (▲) (30 mg catalyst, 30 cm^3 CH_3CN, 313 K). Lines are intended to guide the eye.

Figure A8 Shows cyclohexene oxide formation measured as a function of cyclohexene concentration for multiple metal loads of Nb in Nb-BEA. The slope is independent of metal loading at all metal loadings tested (0.15, 0.7, 1.5 wt%), indicating that the Madon-Boudart criterion[111] is satisfied for Nb-BEA catalysts used to determine the kinetics of the reaction. Within Figure A8, the maximum difference in turnover rate values ($7.5 \cdot 10^{-5}$ (mol $C_6H_{10}O$)(mol Nb · s)$^{-1}$) is within the maximum observed error for these reactions (<7% error). Moreover, the differences between the turnover rates on these catalysts are not systematic across the range of cyclohexene concentrations, which indicates that these differences result from random error. Thus, we do not interpret any minute changes in turnover rates as an indicator about a change in the catalyst structure.

A.3. In Situ UV-vis Spectroscopy

A.3.1. Data Acquisition and Processing

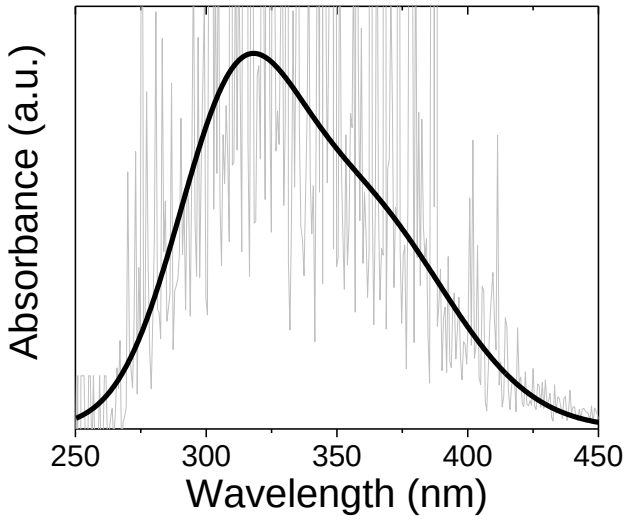

Figure A9. UV-vis absorbance spectrum (raw data, gray) of H_2O_2-treated $Nb_{0.3}$-BEA at 313 K in flowing CH_3CN (0.4 M H_2O) and smoothed data (bold, black) using a finite fourier transform with 40 points of smoothing between 250 and 500 nm. Data smoothing performed in OriginPro®.

A.3.2. Kinetic Parameter Optimization

Scheme A1. Proposed mechanism for the formation of Nb-OOH and Nb-$(O_2)^-$ with interconversion between the two proposed intermediates followed by epoxidation of C_2H_4.

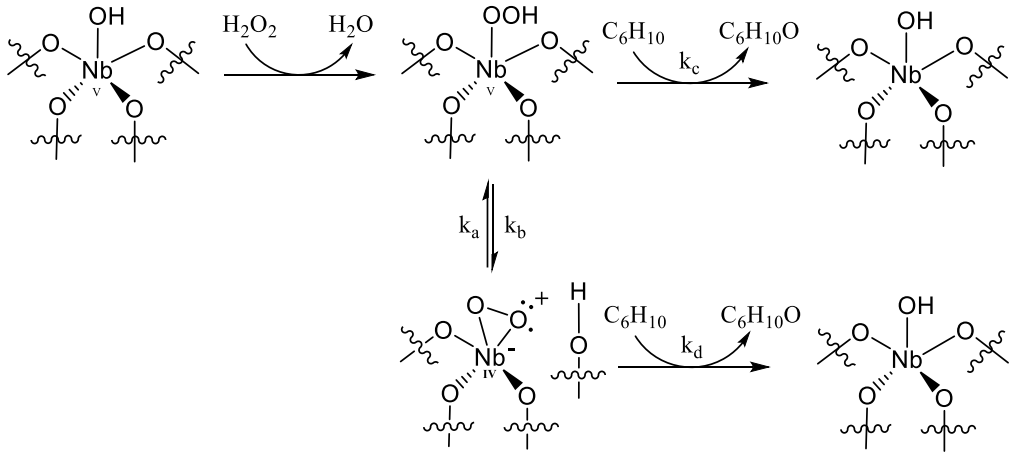

[a]Formation of Nb-OOH and Nb-$(O_2)^-$ occurs during the activation of H_2O_2 over $Nb_{1.5}$-BEA with subsequent drying steps to remove formed and adsorbed H_2O (Section 2.4).

The ODE45 function in MATLAB™ was used to simultaneously solve equations 2.2 and 2.3 with an initial guess for the kinetic parameters (i.e., k_a, k_b, k_c, and k_d, Scheme A1). The sum of the square of the differences between the solution of the two coupled differential equation and the experimental data was used to calculate a residual value. The "fmincon" function was used with a lower bound of 0 for all parameters to optimize the k_a, k_b, k_c, and k_d values to minimize the residual between the simulated differential equations and our experimental data. The initial guess used was 0.01, 0.01, 0.001, and 0.001 for k_a, k_b, k_c, and k_d, respectively. Changes of each of the values by an order of magnitude (increasing and decreasing) led to the same optimized results, which suggests that the fit values for rate constants are not in a local minimum in solution space. As such, the unconstrained solution is presumed to be correct (Table 2.3), as there is no evidence for Nb-OOH being inactive for consumption by reaction with C_6H_{10}; while the high ratio of k_d to k_c (i.e., $\sim 2 \cdot 10^4$) strongly suggests that Nb-$(O_2)^-$ is the active intermediate for alkene epoxidation.

A.4. In Situ FTIR Spectroscopy

A.4.1. MES-PSD Data Analysis

The raw time resolved FTIR spectra are collected and processed through various mathematical steps before analysis. The time-domain raw spectra are first averaged onto a single period using:

$$A_{average}(t) = \frac{T}{T_{total}} \sum_{i=0}^{\frac{T_{total}}{T}} A(t + iT) \tag{A1}$$

where $A(t + iT)$ is the absorbance at each time point, $A_{average}(t)$ is the absorbance after averaging into a single period, T is the time period of stimulation, and T_{total} is the total time for which the experiment was run. Hence, $\frac{T_{total}}{T}$ represents the total number of periods of stimulations for which an experiment was run. The averaged spectra are then subjected to demodulation by phase sensitive detection (PSD) using:

$$\mathrm{A_k}\left(\varphi_{\mathrm{k}}^{\mathrm{PSD}}\right) = \frac{2}{\mathrm{T}}\int_0^{\mathrm{T}} \mathrm{A_{average}}(\vartheta, \mathrm{t}) \sin\left(\mathrm{k}\omega\mathrm{t} + \varphi_{\mathrm{k}}^{\mathrm{PSD}}\right)\mathrm{dt} \quad \text{(A2)}$$

Equation A2 is transformed into a Fourier series by Fourier's theorem for a periodic function:

$$A(\vartheta, t) = \sum_{i=1}^{N} A_{i,0}(\vartheta) + \sum_{i=1}^{N} \sum_{k=1}^{\infty}\left(A_{i,k}^{0^\circ}(\vartheta)\, cos\, k\omega t + A_{i,k}^{90^\circ}(\vartheta)\, sin\, k\omega t\right) \quad \text{(A3)}$$

where $A_{i,0}$ is the dc component, and $A_{i,k}^{0^\circ}$ and $A_{i,k}^{90^\circ}$ are the orthogonal components of the vector. Each of the above terms in the integral is converted into a single equation using Simpson's Rule:

$$\int_0^T y(t)dt = \frac{\Delta t}{3}(y_0 + 4y_1 + 2y_2 + 4y_3 + \cdots + 2y_{n-2} + 4y_{n-1} + y_n) = \frac{\Delta t}{3}\sum_{i=0}^{n} s_i y_i \quad \text{(A4)}$$

where $\mathrm{s_i}$, is Simpson's coefficient (where n must be an even number). A detailed mathematical derivation and implications were discussed in detail by Baurecht et. al.[380] A self-developed code in MATLAB™ was used to resample the acquired spectra and perform the phase sensitive detection analysis using equations A1 – A4.

A.4.2. Verification of Sinusoidal Reactant Modulation

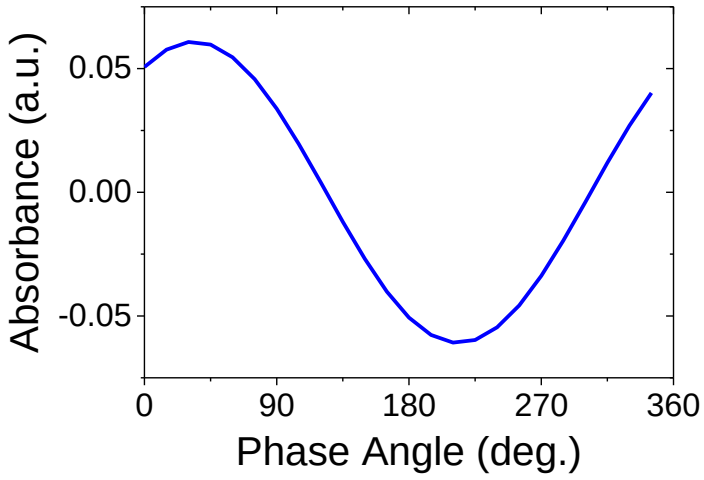

Figure A10. Infrared absorbance value at 1630 cm^{-1} (bending mode of liquid H_2O) as a function of phase angle obtained while sinusoidally modulating the flowrates of C_6H_{10} (0.1 M C_6H_{10} in CH_3CN) and H_2O_2 (0.065 M H_2O_2 in CH_3CN, i.e., H_2O-free liquid stream) solutions (0.5 cm^3 total volumetric flowrate, 333 K, Section 2.5)

A.4.3. Steady-State FTIR Spectra Showing Stability of Nb-(O_2)* Species

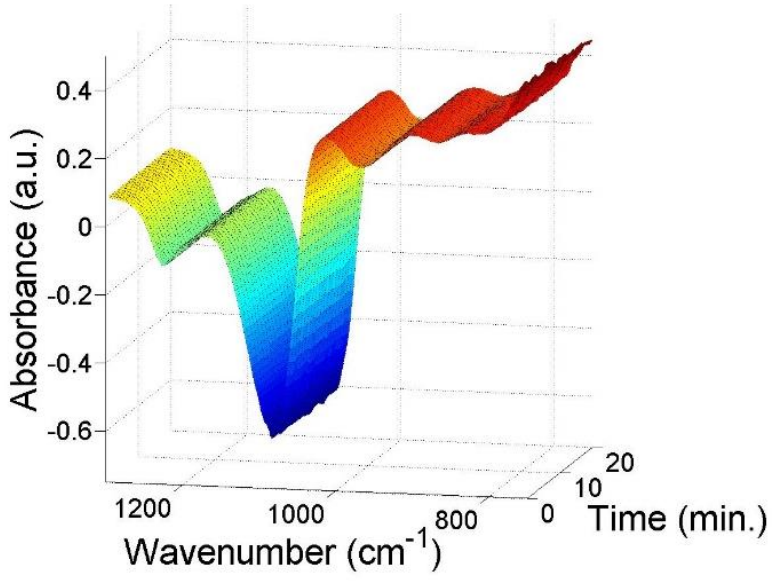

Figure A11. Time-resolved in situ IR spectra showing stability of Nb-$(O_2)^-$ and Nb-OOH after contact with flowing H_2O_2 (Fig. 2.3a), while DI H_2O flow (0.5 cm^3 min^{-1}) was initiated at 333 K.

A.4.4. Proposed Mechanism for Alkene Epoxidation with Nb-$(O_2)^-$

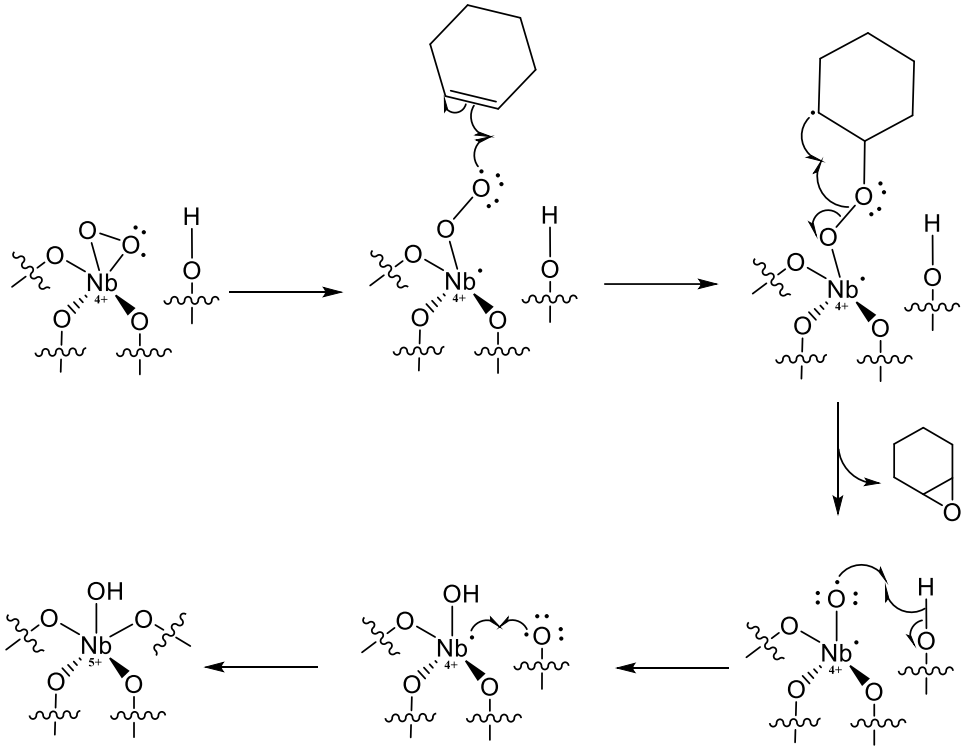

Scheme A2. Proposed bi-radical pathway for the epoxidation of cyclohexene by Nb-$(O_2)^-$, similar to those proposed for epoxidation with homogeneous vanadium complexes.[130,131]

A.5. Previously Proposed Mechanisms for Alkene Epoxidation[58-59, 98]

Previous models for alkene epoxidation on metal-oxide catalysts (i.e., TS-1[98] and Ta[58-59] grafted onto silica) are inconsistent with the experimental data obtained for C_6H_{10} epoxidation over Nb-BEA, specifically, these previous models assume quasi-equilibrated (QE) formation of a reactive intermediate (i.e., Ti- or Ta-(O_2)*) which does not encompass the observed dependence on epoxide concentration, likely because these studies did not test for oxygenate (e.g., epoxide) dependencies.

A reactive intermediate (Nb-$(O_2)^-$) reacts with C_6H_{10} in solution (Scheme 2.1, step 4) to yield the following rate expression:

$$r_E = k_4[C_6H_{10}][Nb-(O_2)^-] \quad \text{(A5)}$$

where r_E is the turnover rate of $C_6H_{10}O$ formation, $[Nb-(O_2)^-]$ is the number of Nb-$(O_2)^-$, and k_4 is the rate constant for the epoxidation of C_6H_{10} with Nb-(O_2)*. When adsorption of the alkene, H_2O_2, epoxide, and the formation of a reactive intermediate are all assumed to be QE with alkene epoxidation being kinetically relevant (KR), the following rate equation emerges:

$$r_E = \frac{(k_4 K_2 K_3 K_5 [C_6H_{10}][H_2O_2])}{[H_2O]} \quad [*] \tag{A6}$$

where k_x and K_x are the rate and equilibrium constants, respectively, for each step x and [*] is the number of available Nb-OH moieties (i.e. active sites) that bind and react with species in solution. An expression for $[*]$is given from summing the number of likely surface intermediates:

$$[L] = [*] + [C_6H_{10}\,*] + [H_2O_2\,*] + [Nb-(O_2)^-] + [C_6H_{10}O\,*] \tag{A7}$$

where $[L]$ is the total number of active sites and $[C_6H_{10}\,*]$, $[H_2O_2\,*]$, and $[C_6H_{10}O\,*]$ are adsorbed C_6H_{10}, H_2O_2, and $C_6H_{10}O$ species, respectively, and $[Nb-(O_2)^-]$ is the reactive intermediate. Equation A7 can then be re-expressed in terms of the rate and equilibrium constants as well as the reactant concentrations:

$$[L] = ([*] + K_1[C_6H_{10}][*] + K_2K_3[H_2O_2][*] + K_5[C_6H_{10}O][*]) \tag{A8}$$

The combination of equations A6 and A8 yield the complete rate expression for $C_6H_{10}O$ formation:

$$\frac{r_E}{[L]} = \frac{k_4 K_2 K_3 K_5 [C_6H_{10}][H_2O_2]}{[H_2O](1+K_1[C_6H_{10}]+K_2K_3[H_2O_2]+K_5[C_6H_{10}O])} \tag{A9}$$

Active sites become saturated with H_2O_2-derived intermediates (i.e. H_2O_2 or Nb-$(O_2)^-$ is the MASI) in the limit of low $[C_6H_{10}]$:$[H_2O_2]$, reducing the rate expression to

$$\frac{r_E}{[L]} = \frac{k_4 K_5 [C_6H_{10}]}{[H_2O]} \tag{A10}$$

Equation A10 is consistent with the $C_6H_{10}O$ formation rates that increase in proportion to $[C_6H_{10}]$ at low $[C_6H_{10}]$:$[H_2O_2]$ (Figure 3a, 0.01 – 0.1 M C_6H_{10}), and which do not depend on $[H_2O_2]$ (Figure 2.7b, 0.5 – 5 mM H_2O_2, 5 mM C_6H_{10}). The coverage of C_6H_{10} increases with $[C_6H_{10}]$ such that C_6H_{10}* becomes the MASI when $[C_6H_{10}]$ is greater than 0.5 M (when $[H_2O_2]$ is 1 mM), which causes equation A9 to take the form:

$$\frac{r_E}{[L]} = \frac{k_4 K_2 K_3 K_5 [H_2O_2]}{K_1 [H_2O]} \tag{A11}$$

This expression agrees with the $C_6H_{10}O$ formation rates seen in Fig. 5a, in that the rate of reaction is independent of $[C_6H_{10}]$. Additionally, equation A11 is in agreement with the results shown in Fig. 5b, where the turnover rate for epoxidation is proportional to $[H_2O_2]$ at high $[C_6H_{10}]$. Moreover, equations A9 – A11 are identical to rate expressions derived previously for alkene epoxidations on similar metal-oxide catalysts.[58-59, 98] However, the rate expressions obtained do not account for turnover rates for $C_6H_{10}O$ formation being inversely proportional to $C_6H_{10}O$ concentration. If $C_6H_{10}O$ is assumed to become the MASI at high $[C_6H_{10}]$, then equation A9 reduces to:

$$\frac{r_E}{[L]} = \frac{k_4 K_2 K_3 [C_6H_{10}][H_2O_2]}{K_5 [H_2O][C_6H_{10}O]} \tag{A12}$$

which possesses first-order dependence on $[C_6H_{10}]$.

A.6. Rate Expression for H_2O_2 Decomposition by Nb-BEA

When Nb-$(O_2)^-$ undergoes a biomolecular reaction with H_2O_2 (Scheme 2.3, Step 6) the following rate expression is given as:

$$r_D = k_4[H_2O_2][Nb-(O_2)^-] \tag{A13}$$

where r_D is the rate of H_2O_2 decomposition, $[Nb-(O_2)^-]$ is the concentration of Nb-$(O_2)^-$, and k_6 is the rate constant for the decomposition of H_2O_2 with Nb-$(O_2)^-$. When we apply the observation (Section 2.3.3) that Nb-$(O_2)^-$ formation is irreversible, and all adsorption/desorption steps are QE we equation A13 becomes:

$$r_D = \frac{(k_6K_2K_3K_5[H_2O_2]^2)\ \ [*]}{(k_4K_5[C_6H_{10}]+k_6[H_2O_2])} \tag{A14}$$

where k_x and K_x are the rate and equilibrium constants, respectively, for each step x and [*] is the number of available Nb-OH moieties (i.e. active sites) that bind and react with species in solution. An expression for $[*]$is given from summing the number of likely surface intermediates:

$$[L] = ([*] + [C_6H_{10}\,*] + [H_2O_2\,*] + [Nb-(O_2)\,*] + [C_6H_{10}O\,*]) \tag{A15}$$

where $[L]$ is the total number of active sites and $[C_6H_{10}\,*]$, $[H_2O_2\,*]$, and $[C_6H_{10}O\,*]$ are adsorbed C_6H_{10}, H_2O_2, and $C_6H_{10}O$ species, respectively, and Nb-$(O_2)^-$ is the reactive intermediate. Equation A14 can then be re-expressed in terms of the rate and equilibrium constants as well as the reactant concentrations:

$$[L] = \left([*] + K_1[C_6H_{10}][*] + K_2[H_2O_2][*] + \frac{k_3K_2[H_2O_2][*]}{(k_4K_5[C_6H_{10}]+k_6[H_2O_2])} + K_5[C_6H_{10}O][*]\right) \quad \text{(A16)}$$

The combination of equations A14 and A16 yield the complete rate expression for H_2O_2 decomposition:

$$\frac{r_D}{[L]} = \frac{k_3k_6K_2[H_2O_2]^2}{(k_4K_5[C_6H_{10}]+k_6[H_2O_2])\left(1+K_1[C_6H_{10}]+K_2[H_2O_2]+\frac{k_3K_2[H_2O_2]}{(k_4K_5[C_6H_{10}]+k_6[H_2O_2])}+K_5[C_6H_{10}O]\right)} \quad \text{(A17)}$$

The form of this full rate equation simplifies in the limit when active sites become saturated with H_2O_2-derived intermediates (i.e. Nb-$(O_2)^-$ is the MASI) as is expected in the limit of low $[C_6H_{10}]$:$[H_2O_2]$:

$$\frac{r_D}{[L]} = k_6[H_2O_2] \quad \text{(A18)}$$

which shows that the apparent dependence on $[H_2O_2]$ for H_2O_2 decomposition is first order.

A.7. H_2O_2 Selectivity as a Function of C_6H_{10} Concentration

H_2O_2 selectivities expressed as α values (the ratio of the turnover numbers for $C_6H_{10}O$ formation to that of H_2O_2 consumption) were calculated across the range of cyclohexene concentrations used in study. In general, H_2O_2 is used more selectively to form $C_6H_{10}O$ at the greatest C_6H_{10} to H_2O_2 ratios.

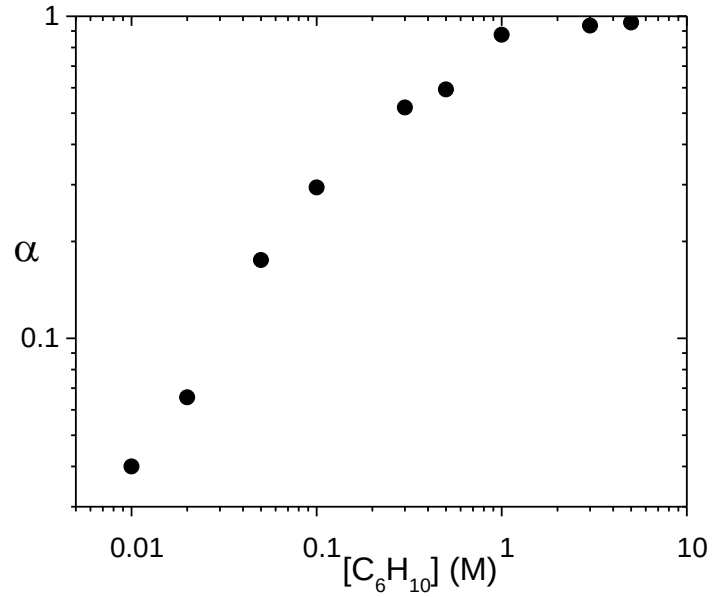

Figure A12. H_2O_2 selectivity (α, Section 2.3.4) for epoxidation as a function of $[C_6H_{10}]$ over $Nb_{1.5}$-BEA (1 mM H_2O_2, ~30 cm^3 CH_3CN, 313 K)

A.8. Temperature Dependence of $C_6H_{10}O$ Formation and H_2O_2 Decomposition

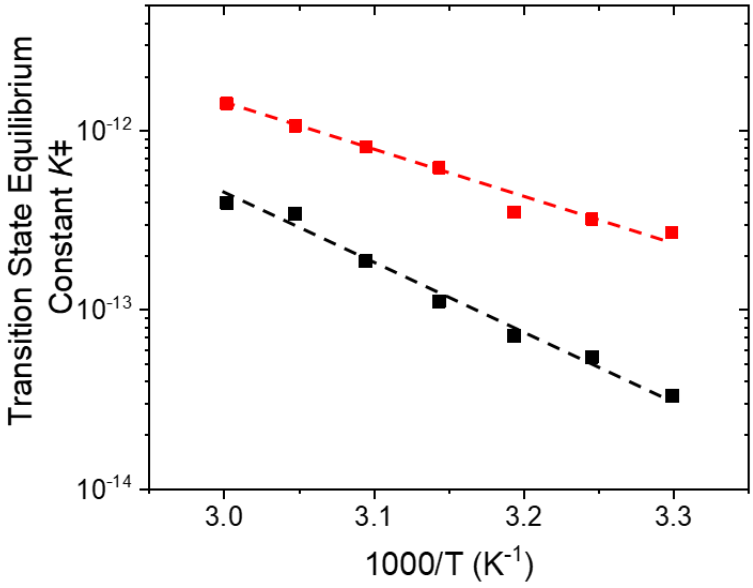

Figure A13. Transition state equilibrium constants, ($K^{\ddagger}$), for C_6H_{10} epoxidation (●) and H_2O_2 decomposition (■) as functions of inverse temperature on $Nb_{1.5}$-BEA (0.05 M C_6H_{10}, 1 mM H_2O_2) with a Nb-$(O_2)^-$ MASI. Error bars were omitted for clarity. In all reported rate data, error was <10%. Lines represent fits to the Eyring equation (equation 2.23).

APPENDIX B

Supplementary Information and Data for Chapter Three

B.1. Additional Catalyst Characterization and Verification of Measuring True Kinetics

B.1.1. Catalyst Characterization

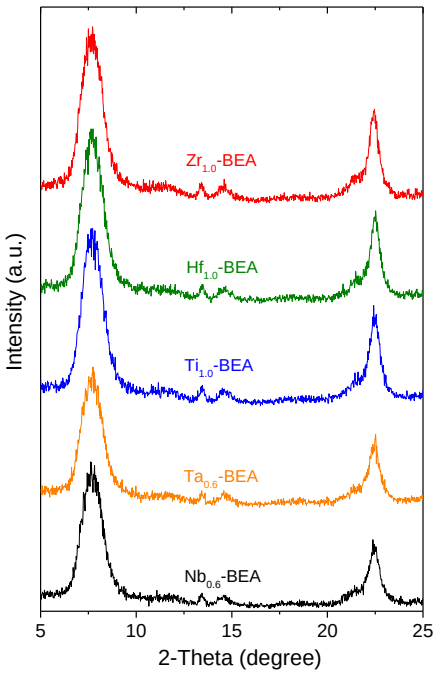

Figure B1. X-ray diffractograms for $Ti_{1.0}$- (blue), $Zr_{1.0}$- (red), $Hf_{1.0}$- (green), $Nb_{0.6}$- (black) and $Ta_{0.6}$-BEA (orange).

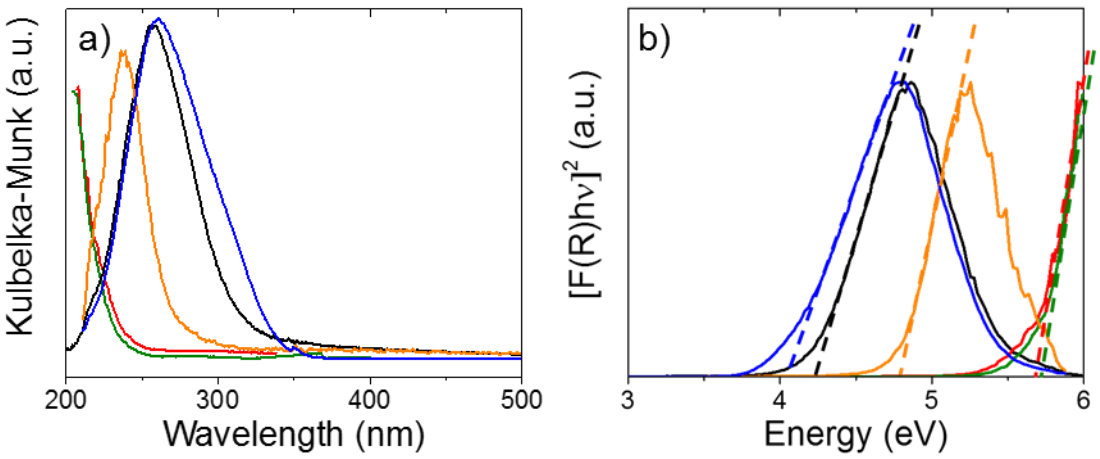

Figure B2. (a) Diffuse reflectance UV-vis spectra and (b) normalized tauc plots for $Ti_{0.6}$- (blue), $Nb_{1.0}$- (black) and $Ta_{1.0}$-BEA (orange), $Zr_{0.6}$- (red), $Hf_{0.6}$- (green). X-axis intercept of dashed lines represents the band edge for each material.

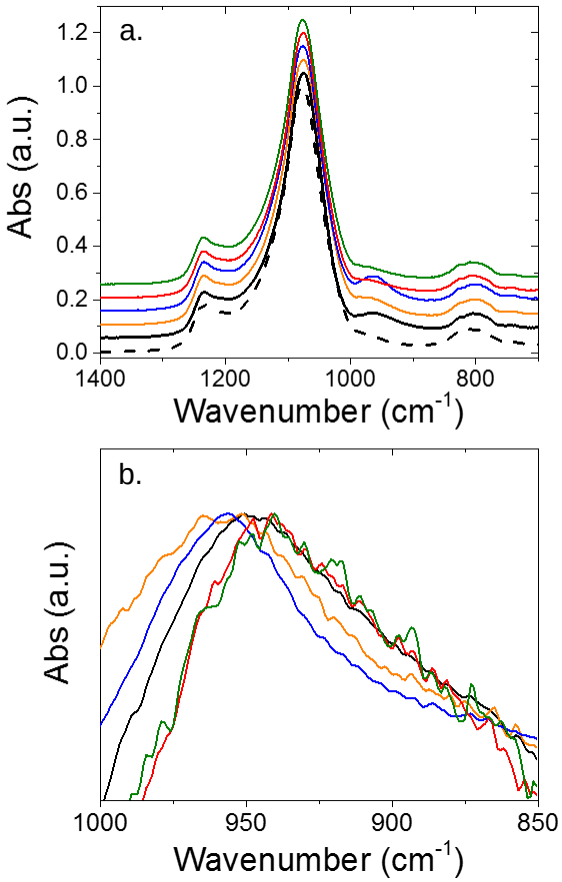

Figure B3. IR spectra for (a) $Ti_{1.0}$- (blue), $Zr_{1.0}$- (red), $Hf_{1.0}$- (green), $Nb_{0.6}$- (black) and $Ta_{0.6}$-BEA (orange), and Si-BEA (dashed) obtained at ambient conditions and (b) M-BEA with Si-BEA spectra subtracted with normalization to the ~960 cm^{-1} feature to observe ν(Si-O-M) feature.

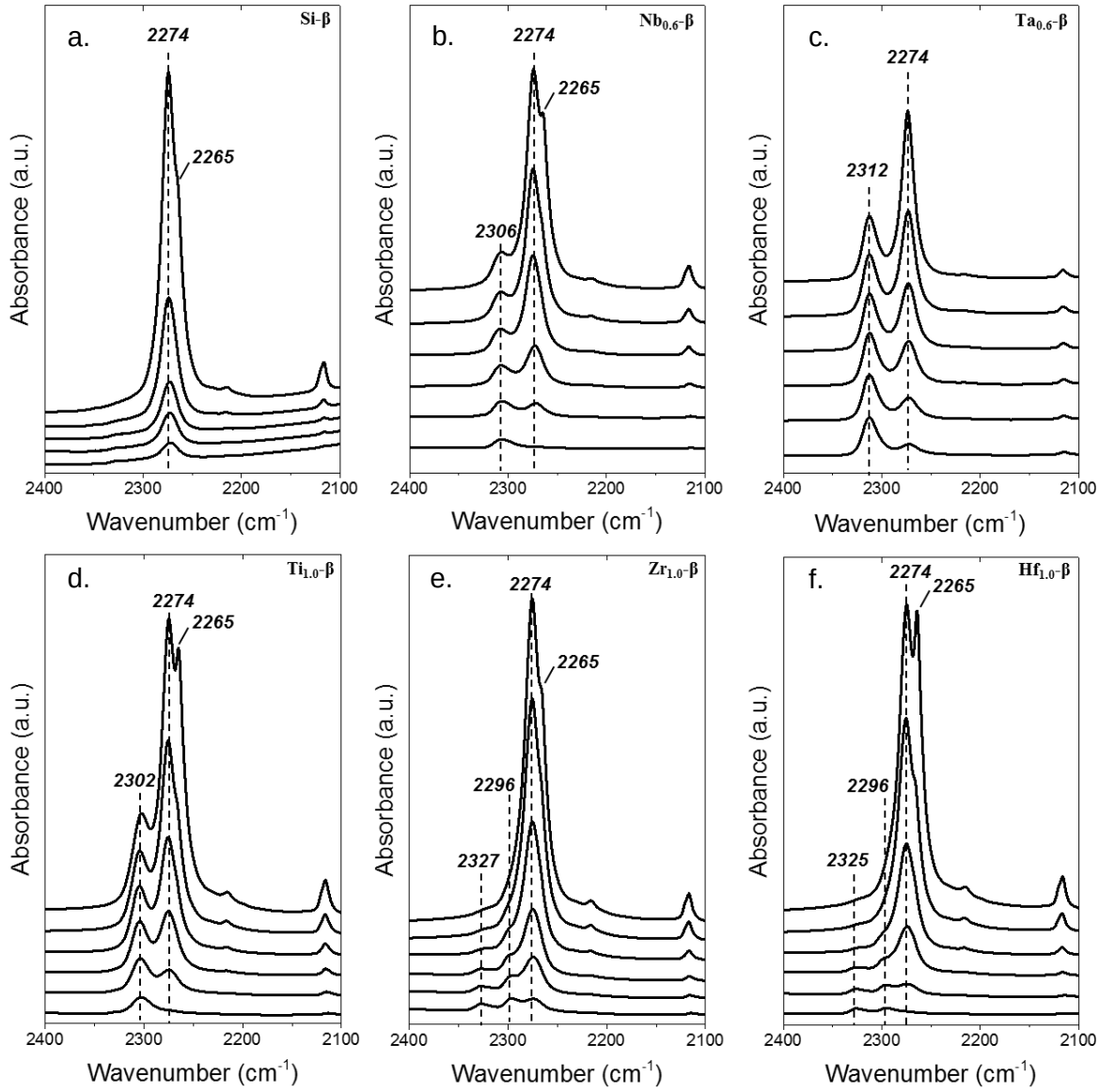

Figure B4. IR spectra of adsorbed CD_3CN (1.0 kPa, 50 cm^3 min^{-1} in He) at 298 K followed by desorption (50 cm^3 min^{-1} He) as the temperature was increased to 423 K (5 K min^{-1}) to resolve Lewis-acid bound ν(C≡N) on (a) Si-BEA, (b) $Nb_{0.6}$-BEA, (c) $Ta_{0.6}$-BEA, (d) $Ti_{1.0}$-BEA, (e) $Zr_{1.0}$-BEA, and (f) $Hf_{1.0}$-BEA.

Figure B4. shows FTIR spectra of CD_3CN adsorbed onto all M-BEA catalysts, where absorption features between 2260 – 2340 cm^{-1} correspond to the ν(C≡N) mode.[106, 156] The absorbance peak located at 2274 cm^{-1} is assigned to CD_3CN hydrogen bonded to surface SiOH groups, while the shoulder at 2265 cm^{-1} is attributed to physisorbed CD_3CN.[106, 156] After the

surfaces are saturated with CD_3CN (i.e., $\nu(C{\equiv}N)$ of SiOH-bound CD_3CN stopped increasing), the flow of CD_3CN is stopped and the temperature of the FTIR cell is increased under a constant flow of He (50 cm^3 min^{-1}).

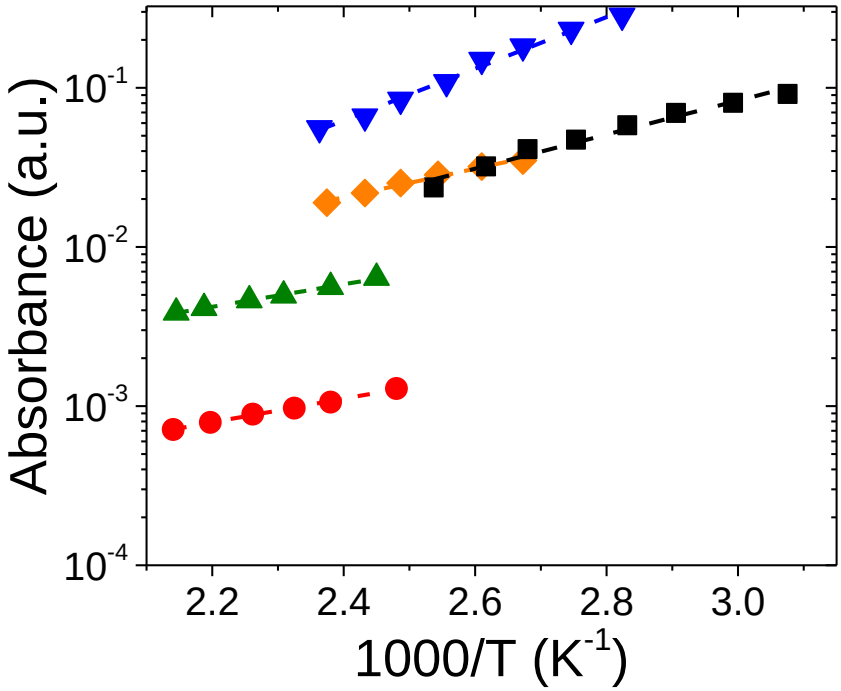

Figure B5. IR absorbances for the Lewis-acid bound ν(C≡N) depicted in Fig. B5b-f. on $Nb_{0.6}$-BEA (■, 2306 cm^{-1}, Fig. B5b), $Ta_{0.6}$-BEA (♦, 2312 cm^{-1}, Fig. B5c), $Ti_{1.0}$-BEA (▼, 2302 cm^{-1}, Fig. B5d), $Zr_{1.0}$-BEA (●, 2296 cm^{-1}, Fig. B5e), and $Hf_{1.0}$-BEA (▲, 2296 cm^{-1}, Fig. B5f) as a function of inverse temperature (1.5 kPa CD_3CN, 99 kPa He, 50 cm^3 min^{-1} He) after background subtraction. Dashed lines represent linear fits, whose slope are proportional to the value of ΔH_{CD3CN}.

B.1.2. Control Experiments to Test Importance of Mass Transfer

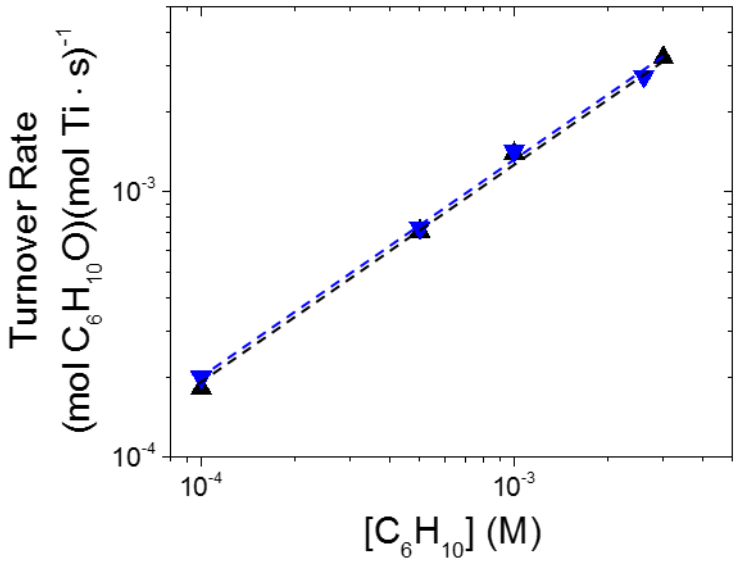

Figure B6. Turnover rates for the formation of C_6H_{10} measured as a function of $[C_6H_{10}]$ on $Ti_{1.0}$-BEA (▼, 0.01 M H_2O_2, 313 K) and $Ti_{0.1\text{-BEA}}$ (▲, 0.01 M H_2O_2, 313 K). Dashed lines are intended to guide the eye.

Figure B6 shows rates for the formation of cyclohexene oxide measured as a function of cyclohexene concentration for multiple metal loadings of Ti in Ti-BEA. The rate of $C_6H_{10}O$ formation is independent of metal loading (over 0.141 – 1.2 wt. % Ti), which indicates that the Madon-Boudart criterion is satisfied for Ti-BEA.[111] Under the conditions tested, we see that the turnover rate for $C_6H_{10}O$ formation is proportional to $[C_6H_{10}]$ and independent of $[H_2O_2]$, which corresponds to a simplified rate expression (Section 3.3.2 of main text) of:

$$\frac{r_E}{[L]} = k_3[C_6H_{10}] \tag{B1}$$

where r_E is the rate of $C_6H_{10}O$ formation, [L] is the total number of metal atoms in the reactor, k_3 is the rate constant for step 3 of scheme 3.2, and $[C_6H_{10}]$ is the concentration of C_6H_{10}. For a first-order reaction (such as in equation B1), an effective Thiele modulus for a spherical pellet[111] can be defined as:

$$\varphi = \left(\frac{k_3 R^2 [C_6H_{10}]}{D_e}\right)^{1/2} \tag{B2}$$

where ϕ is the Thiele modulus, R is the radius of the spherical pellet, [C_6H_{10}] is the bulk concentration of C_6H_{10}, and D_e is the effective diffusivity of C_6H_{10} through the pellet. The Madon-Boudart criterion is an experimental way to determine the relative value of the Thiele modulus, where the independent of turnover rates on metal loading signifies a relatively small Thiele modulus. When the Thiele modulus is small, the rates of diffusion are much greater than those for the inherent kinetics of the reaction (at reactant concentrations equal to that in the bulk fluid phase), which shows that the measured reaction rates are not corrupted by diffusion restrictions within the catalyst particles.

In Figure 3.4, epoxidation turnover rates decrease in the following order: Ti > Nb > Ta >> Zr ~ Hf under conditions that result in a M-(O_2) saturated surface. Therefore, for all M-BEA other than Ti, the value of k_3 is much smaller while all other terms are identical. Therefore, the change in k_3 gives a smaller value of the Thiele moduli for Nb-, Ta-, Zr-, and Hf-BEA than for Ti-BEA. Therefore, satisfaction of the Madon-Boudart criterion for Ti-BEA proves that the other M-BEA are also not mass-transfer limited and all measured reaction rates are reflect only chemical kinetics.

B.2. In Situ UV-Visible Spectroscopy and Identification of Active Intermediates

B.2.1. Sample Raw UV-Vis Spectrum and Method for Processing Spectra

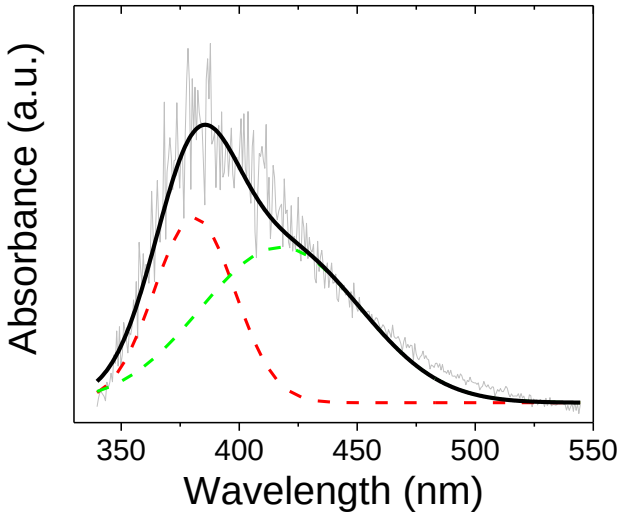

Figure B7. UV-vis absorbance spectrum (raw data, gray) of H_2O_2-treated $Ti_{1.0}$-BEA at 313 K in flowing CH_3CN (0.4 M H_2O) and smoothed data (bold black line) using a finite fourier transform. Dashed red and green curves represent Gaussian peak fittings, performed in OriginPro®.

B.2.2. In Situ UV-Vis Spectra with Peak Fits

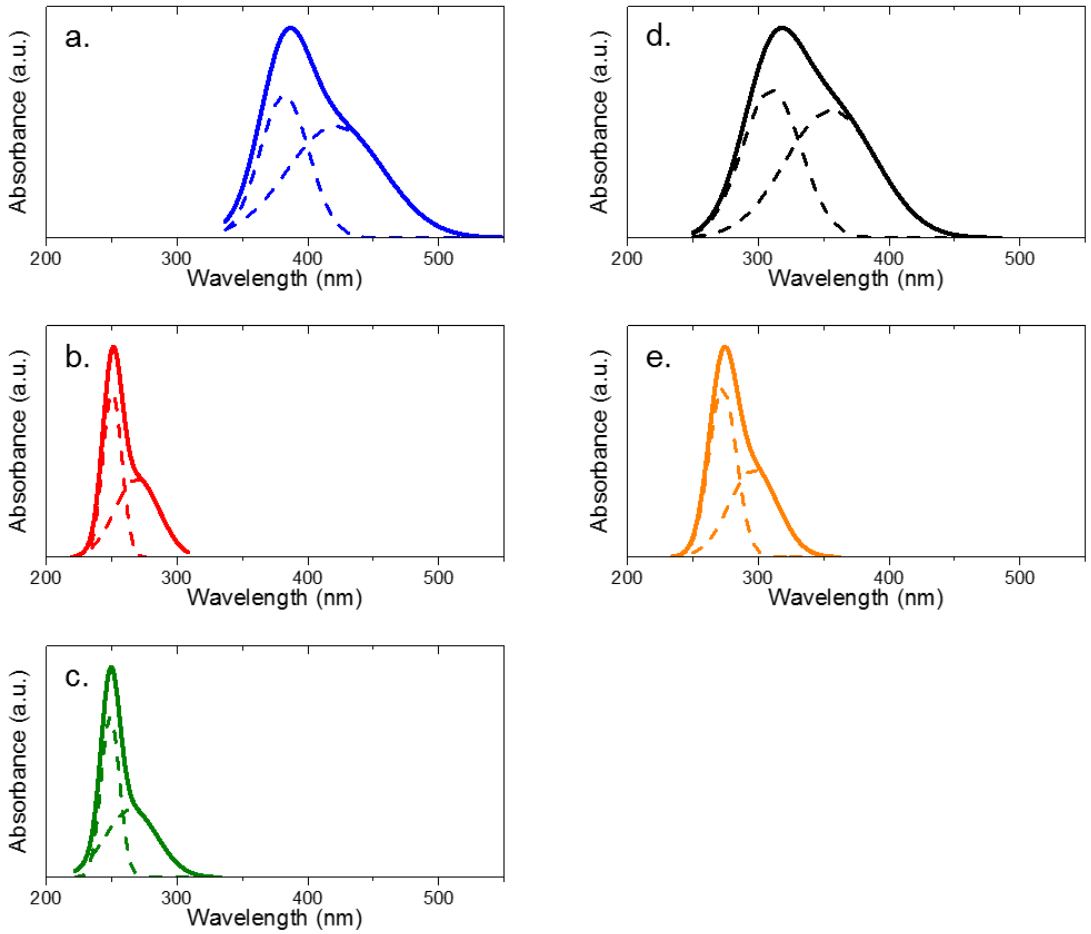

Figure B8. Normalized UV-vis absorbance spectrum of H_2O_2-activated (section 2.4) (a) $Ti_{1.0}$-BEA, (b) $Zr_{1.0}$-BEA, (c) $Hf_{1.0}$-BEA, (d) $Nb_{0.2}$-BEA, and (e) $Ta_{0.6}$-BEA in flowing CH_3CN (0.4 M H_2O, 1 cm^3 min^{-1}) at 313 K. Dashed curves represent Gaussian peak fittings (performed in OriginPro®) to show M-$(O_2)^-$ (lower wavelength) and M-OOH/M-$(O_2)^{2-}$ (higher wavelength) species.

Table B1. Ligand to metal charge transfer energies (hν) for the M-OOH/-$(O_2)^{2-}$ and M-$(O_2)^-$ intermediates as detected via *in situ* UV-vis spectra (Fig. B8).

Metal	hν (eV) for M-(OOH)/-$(O_2)^{2-}$	hν (eV) for M-$(O_2)^-$
Ti	2.95	3.25
Zr	4.61	4.94
Hf	4.66	5.04
Nb	3.48	3.99
Ta	4.56	4.21

B.2.3. Time-Resolved In Situ UV-Vis Spectroscopy and Kinetic Parameter Optimization

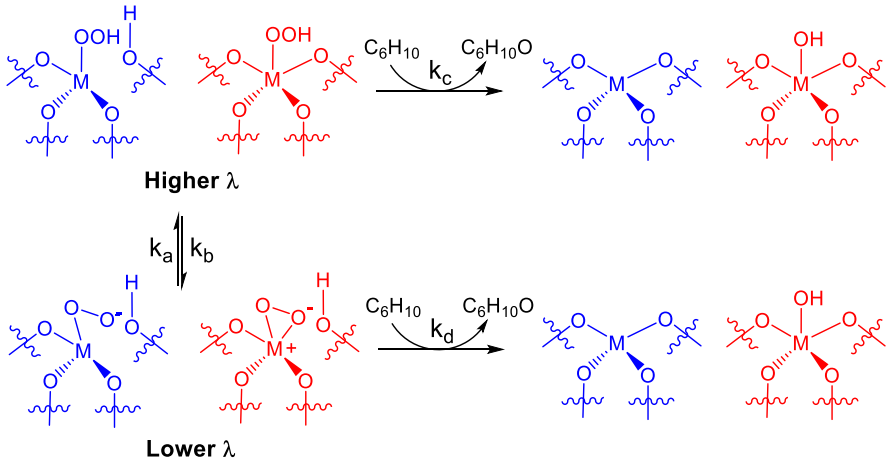

Scheme B1. Interconversion and consumption of M-OOH/M-$(O_2)^{2-}$ (M-OOH) shown) and M-$(O_2)^-$ species upon reaction with C_6H_{10}. Color coding is for clarity: group 4 (Ti, Zr, and Hf, blue) and 5 (Nb and Ta, red).

The change in surface coverage of the M-OOH/M-$(O_2)^{2-}$ and M-$(O_2)^-$ species depends on the summed rates of formation/consumption via interconversion and consumption by reaction with C_6H_{10}, which take the forms of:

$$\frac{d[M-(O_2)^-]}{dt} = k_a[M-OOH] - k_b[M-(O_2)^-] - k_d[M-(O_2)^-][C_6H_{10}] \quad \text{(B3)}$$

$$\frac{d[M-OOH]}{dt} = k_b[M-(O_2)^-] - k_a[M-OOH] - k_c[M-OOH][C_6H_{10}] \quad \text{(B4)}$$

where [M-OOH] and [M-$(O_2)^-$] represent the coverages (via UV-vis) of M-OOH/M-$(O_2)^{2-}$ and M-$(O_2)^-$, respectively, and k_x is the rate constant for step x in scheme 3.1. Pseudo first-order kinetics

are assumed for the reaction between M-(O_2) intermediates and C_6H_{10}, as throughout the experiment the ratio of [C_6H_{10}] to number of metal atoms exceeds 10^5 in all cases. MATLAB™ is used to numerically estimate the kinetic parameters, by fitting the data (Fig. 3.3) to the coupled differential equations (eqns. B3 and B4). The initial guesses used for the rate constants were 0.01, 0.01, 0.001, 0.001 for k_a, k_b, k_c, and k_d, respectively. Changes of the initial values by an order of magnitude (increasing and decreasing) did not change the optimized parameter values.

Table B2. Numerically optimized rate constants, k_i (s^{-1}), for the interconversion of M-OOH/M-$(O_2)^{2-}$ and M-$(O_2)^-$ (Scheme B1) and reaction with C_6H_{10}.

Sample	k_a	k_b	k_c	k_d
$Ti_{1.0}$-BEA	$1.5\cdot10^{-3}$	$5.0\cdot10^{-4}$	$2.9\cdot10^{-2}$	$1.7\cdot10^{-4}$
$Nb_{0.6}$-BEA	$3.8\cdot10^{-6}$	$3.3\cdot10^{-4}$	$2.2\cdot10^{-7}$	$4.5\cdot10^{-3}$
$Ta_{0.6}$-BEA	$4.3\cdot10^{-3}$	$4.3\cdot10^{-3}$	$1.0\cdot10^{-4}$	$3.3\cdot10^{-3}$
$Zr_{1.0}$-BEA	-	-	$< 10^{-6}$	$< 10^{-6}$
$Hf_{1.0}$-BEA	-	-	$< 10^{-6}$	$< 10^{-6}$

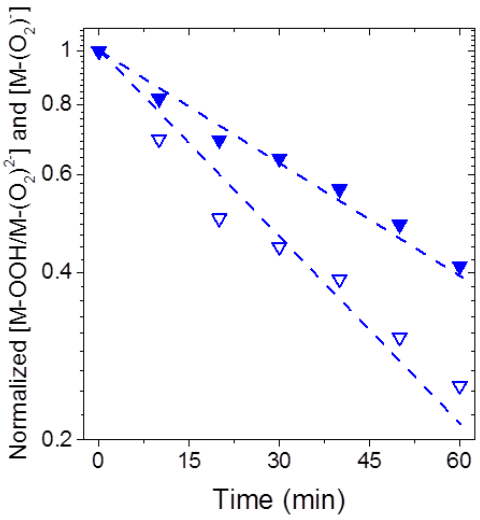

Figure B9. Change in the normalized surface coverage of M-OOH/M-$(O_2)^{2-}$ (open symbols) and M-$(O_2)^-$ (closed symbols) species as a function of time for $Ti_{1.0}$-BEA. Spectra were acquired *in situ* upon flowing *cis*-stilbene in CH_3CN (0.01 M *cis*-stilbene, 0.4 M H_2O, 0.25 cm^3 min^{-1}) over H_2O_2-activated samples (Section 3.2.4) at 313K. To avoid misinterpretation, it should be noted that the Y-axis is log scale.

B.3. Additional Kinetic Data, Derivation of Relevant Rate Expressions and Transition-State Theory

B.3.1. Derivation of Full Rate Expression for C_6H_{10} Epoxidation

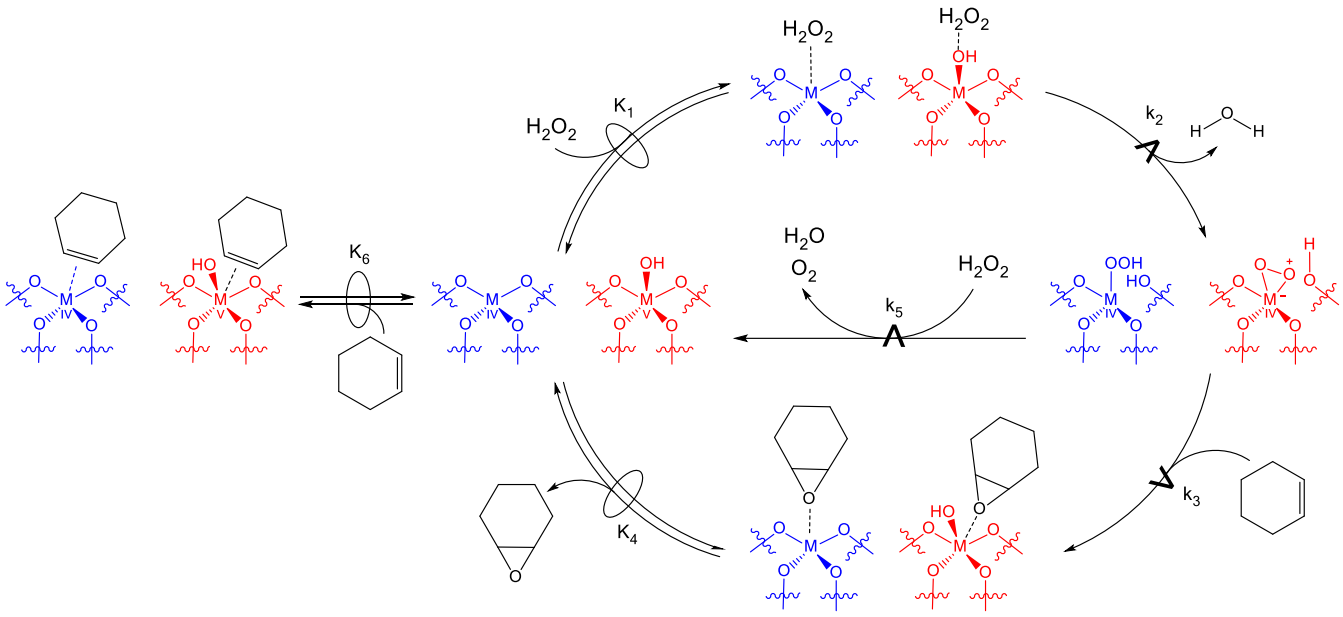

Scheme B2. Proposed mechanism for the epoxidation of C_6H_{10} with H_2O_2 over group 4 (Ti, Zr, and Hf, M-OOH shown, blue) and group 5 (Nb and Ta, red) M-BEA. The symbol ⇄ represents a quasi-equilibrated step, while → represents a kinetically relevant step. Note, the unoccupied metal atoms are meant to be representations of an empty site, rather than suggest all metal atoms exist as closed sites, as both open and closed sites likely exist in these materials (see characterization results, Section 3.2.2).

Scheme B2 shows a series of elementary steps that account for the measured effects of $[C_6H_{10}]$ and $[H_2O_2]$ (Fig. 3.4) on both rates of C_6H_{10} epoxidation. The catalytic cycle involves the quasi-equilibrated adsorption of H_2O_2 (step 1),[58, 111] followed by the irreversible activation of H_2O_2 (step 2) to form a pool of M-$(O_2)^-$ (group 5, superoxide) and M-OOH/M-$(O_2)^{2-}$ (group 5, hydroperoxide/peroxide)[82, 116-117, 121] active intermediates (referred to collectively as M-(O_2)), which then react with C_6H_{10} to form $C_6H_{10}O$ (step 3), followed by $C_6H_{10}O$ desorption (step 4) or decompose by reaction with H_2O_2 (step 5). Measured C_6H_{10} epoxidation rates represent the kinetically relevant reaction of the active form of the oxidizing surface intermediate with a C_6H_{10} molecule:

$$r_E = k_3[M - O_2][C_6H_{10}] \quad \text{(B5)}$$

where r_E is the rate of C_6H_{10} epoxidation, [M-(O_2)] is the collective coverage of M-OOH/M-$(O_2)^{2-}$ (group4) and M-$(O_2)^-$ (group 5), k_x is the rate constant for step x in Scheme B2, and [C_6H_{10}] is the concentration of C_6H_{10}. Application of the pseudo-steady state hypothesis to the M-(O_2) intermediates, results in:

$$r_E = \frac{k_2 k_3 K_1 [C_6H_{10}][H_2O_2][*]}{(k_3[C_6H_{10}]+k_5[H_2O_2])} \quad \text{(B6)}$$

Where K_x is the equilibrium constant for step x and [*] is the total number of empty (i.e., unoccupied) M atoms. An expression for [*] is given by the summation of all likely surface-bound intermediates:

$$[L] = [*] + [C_6H_{10}\,*] + [H_2O_2\,*] + [M - (O_2)] + [C_6H_{10}O\,*] \quad \text{(B7)}$$

where [L] is the total number of M atoms, [M-(O_2)] is the pool of M-OOH/M-$(O_2)^{2-}$ and M-$(O_2)^-$ intermediates, and [C_6H_{10}*], [H_2O_2*], and [C_6H_{10}O*] are surface-bound C_6H_{10}, H_2O_2, and C_6H_{10}O molecules, respectively. Equation B7 can then be restated in terms of the rate and equilibrium constants, as well as liquid-phase reactant concentrations and unoccupied M atoms by application of the PSSH to each specie to yield:

$$[L] = [*] + K_6[C_6H_{10}][*] + K_1[H_2O_2][*] + \frac{k_2 K_1 [H_2O_2][*]}{(k_3[C_6H_{10}]+k_5[H_2O_2])} + K_4[C_6H_{10}O][*] \quad \text{(B8)}$$

Substitution of equation B8 into B6 yields the full rate expression for C_6H_{10}O formation:

$$\frac{r_E}{[L]} = \frac{\frac{k_2 k_3 K_1 [C_6H_{10}][H_2O_2]}{(k_3[C_6H_{10}]+k_5[H_2O_2])}}{1+K_6[C_6H_{10}]+K_1[H_2O_2]+\frac{k_2 K_1 [H_2O_2]}{(k_3[C_6H_{10}]+k_5[H_2O_2])}+K_4[C_6H_{10}O]} \quad \text{(B9)}$$

which is consistent with equation 3.2 from the main text.

B.3.2 Derivation of Full Rate Expression for H_2O_2 Decomposition

Scheme B2 shows a series of elementary steps that account for the measured effects of $[C_6H_{10}]$ and $[H_2O_2]$ (Fig. 3.4) on both rates of H_2O_2 decomposition. The catalytic cycle involves the quasi-equilibrated adsorption of H_2O_2 (step 1),[58, 111] followed by the irreversible activation of H_2O_2 (step 2) to form a pool of M-$(O_2)^-$ (group 5, superoxide) and M-OOH/M-$(O_2)^{2-}$ (group 4, hydroperoxide/peroxide)[82, 116-117, 121] active intermediates (referred to collectively as M-(O_2)), which then or decompose by reaction with H_2O_2 (step 5). Measured C_6H_{10} epoxidation rates represent the kinetically relevant reaction of the active form of the oxidizing surface intermediate with a C_6H_{10} molecule:

$$r_D = k_5[M-O_2][H_2O_2] \quad \text{(B10)}$$

where r_D is the rate of C_6H_{10} epoxidation, [M-(O_2)] is the collective coverage of M-OOH/M-$(O_2)^{2-}$ (group 4) and M-$(O_2)^-$ (group 5), k_x is the rate constant for step x in Scheme B2, and $[H_2O_2]$ is the concentration of H_2O_2. Application of the pseudo-steady state hypothesis to the M-(O_2) intermediates, results in:

$$r_D = \frac{k_2 k_5 K_1 [H_2O_2]^2 [*]}{(k_3[C_6H_{10}]+k_5[H_2O_2])} \quad \text{(B11)}$$

Where K_x is the equilibrium constant for step x and [*] is the total number of empty (i.e., unoccupied) M atoms. An expression for [*] is given by the summation of all likely surface-bound intermediates:

$$[L] = [*] + [C_6H_{10}*] + [H_2O_2*] + [M-(O_2)] + [C_6H_{10}O*] \quad \text{(B12)}$$

where [L] is the total number of M atoms, [M-(O_2)] is the pool of M-OOH/M-$(O_2)^{2-}$ and M-$(O_2)^{-}$ intermediates, and [C_6H_{10}*], [H_2O_2*], and [$C_6H_{10}O$*] are surface-bound C_6H_{10}, H_2O_2, and $C_6H_{10}O$ molecules, respectively. Equation B12 can then be restated in terms of the rate and equilibrium constants, as well as liquid-phase reactant concentrations and unoccupied M atoms by application of the PSSH to each specie to yield:

$$[L] = [*] + K_6[C_6H_{10}][*] + K_1[H_2O_2][*] + \frac{k_2K_1[H_2O_2][*]}{(k_3[C_6H_{10}]+k_5[H_2O_2])} + K_4[C_6H_{10}O][*] \quad \text{(B13)}$$

Substitution of equation B13 into B10 yields the full rate expression for H_2O_2 decomposition:

$$\frac{r_D}{[L]} = \frac{\frac{k_2k_5K_1[H_2O_2]^2}{(k_3[C_6H_{10}]+k_5[H_2O_2])}}{1+K_6[C_6H_{10}]+K_1[H_2O_2]+\frac{k_2K_1[H_2O_2]}{(k_3[C_6H_{10}]+k_5[H_2O_2])}+K_4[C_6H_{10}O]} \quad \text{(B14)}$$

At high [H_2O_2]:[C_6H_{10}] reactant ratios, M-(O_2) species are the most abundant surface intermediates (MASI) on all M-BEA (Section 3.2.2, Fig. 3.3 in the main text), which simplifies equation B14 to yield:

$$\frac{r_D}{[L]} = k_5[H_2O_2] \quad \text{(B15)}$$

Figure B11 shows H_2O_2 decomposition rates for Ti-, Nb-, and Ta-BEA as a function of $[H_2O_2]$ at constant $[C_6H_{10}]$ under a M-(O_2) MASI. In all cases, H_2O_2 decomposition rates depend linearly on $[H_2O_2]$, which is in excellent agreement with equation B14. Collectively, these data, in comparison to the derived rate expressions, strongly suggest that H_2O_2 decomposition occurs via a bimolecular reaction pathway, where H_2O_2 reacts directly with the M-(O_2) intermediates.

Total rates of H_2O_2 consumption (r_{H2O2}) are given by the sum of equations B9 and B14 to yield:

$$\frac{r_{H2O2}}{[L]} = \frac{\frac{k_2 k_5 K_1 [H_2O_2]^2}{(k_3[C_6H_{10}]+k_5[H_2O_2])} + \frac{k_2 k_3 K_1 [C_6H_{10}][H_2O_2]}{(k_3[C_6H_{10}]+k_5[H_2O_2])}}{1+K_6[C_6H_{10}]+K_1[H_2O_2]+\frac{k_2 K_1 [H_2O_2]}{(k_3[C_6H_{10}]+k_5[H_2O_2])}+K_4[C_6H_{10}O]} \qquad \text{(B16)}$$

The selectivity for H_2O_2 use in epoxidations can then be cast as the ratio of r_{H2O2} to r_E (α, i.e., equation B16 over B9) to result in:

$$\alpha = 1 + \frac{k_5[H_2O_2]}{k_3[C_6H_{10}]} \qquad \text{(B17)}$$

where the numerator (i.e., $k_5[H_2O_2]$) and denominator (i.e., $k_3[C_6H_{10}]$) may be estimated for Ti-, Nb-, and Ta-BEA by inspection of Figs. 3.3 and B11. Table B3 shows the ratio of $k_5[H_2O_2]$:$k_3[C_6H_{10}]$ for Ti-, Nb-, and Ta-BEA under conditions that result in a $C_6H_{10}O$ MASI (i.e., the conditions in Fig. 3.3b). The relative values of $k_5[H_2O_2]$:$k_3[C_6H_{10}]$ for Ti-, Nb-, and Ta-BEA under a $C_6H_{10}O$ MASI shows that $k_3[C_6H_{10}] >> k_5[H_2O_2]$.

Table B3. Calculated ratios of $k_5[H_2O_2]:k_3[C_6H_{10}]$ using interpolated values from Figs. 3.3 and B11 for $Nb_{0.6}$-, $Ta_{0.6}$-, and $Ti_{1.0}$-BEA at conditions that result in a $C_6H_{10}O$ MASI (i.e., conditions in Fig. 3.3b).

Sample	$k_5[H_2O_2]/k_3[C_6H_{10}]$
$Nb_{0.6}$-BEA	0.05
$Ta_{0.6}$- BEA	0.0009
$Ti_{1.0}$- BEA	0.025

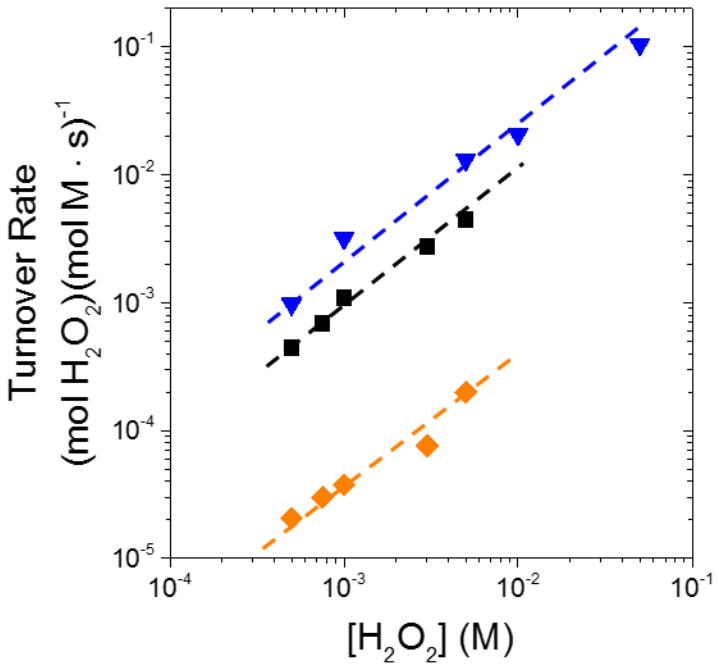

Figure B10. H_2O_2 decomposition rates as a function of $[H_2O_2]$ over $Nb_{0.6}$-BEA (■, 0.05 M C_6H_{10}, 313 K), $Ta_{0.6}$-BEA (♦, 2 mM C_6H_{10}, 313 K), and $Ti_{1.0}$-BEA (▼, 0.01 M C_6H_{10}, 313 K). Dashed lines are intended to guide the eye.

B.3.3. Transition-State Theory for Measurement of Activation Enthalpies and Entropies

Transition-state theory (TST) is used to relate the stability of the reference state (e.g., M-(O_2) intermediate) to an activated complex that leads to reaction (i.e., the transition state).[110, 136] TST, when combined with our proposed mechanism (Scheme B2), proposes that the reactant species (i.e., M-(O_2), H_2O_2, and C_6H_{10}) exist in equilibrium with the transition state to yield:

$$\frac{r_E}{[L]} = \frac{k_B T}{h} K_E^{\ddagger}[C_6H_{10}] \tag{B15}$$

$$\frac{r_E}{[L]} = \frac{k_B T}{h} K_D^{\ddagger}[H_2O_2] \tag{B16}$$

where k_B is Boltzmann's constant, h is Planck's constant, T is the temperature in kelvin, $K_E^{\ddagger}$ and $K_D^{\ddagger}$ are the Transition-state equilibrium constants for epoxidation and H_2O_2 decomposition, respectively, and [C_6H_{10}] is the concentration of C_6H_{10}. Values of $K_E^{\ddagger}$ and $K_D^{\ddagger}$ may be expressed in terms of free energy, via the Eyring equation, to result in:

$$K_x^{\ddagger} = e^{-\Delta G_x^{\ddagger}/RT} = e^{-\Delta H_x^{\ddagger}/RT} e^{\Delta S_x^{\ddagger}/R} \tag{B17}$$

Where R is the ideal gas constant and $\Delta G^{\ddagger}$, $\Delta H^{\ddagger}$, and $\Delta S^{\ddagger}$ is the apparent Gibb's free energy, enthalpy, and entropy of activation, respectively. Figure B11 shows measured values for $K_E^{\ddagger}$ and $K_D^{\ddagger}$ as a function of inverse temperature for all M-BEA.

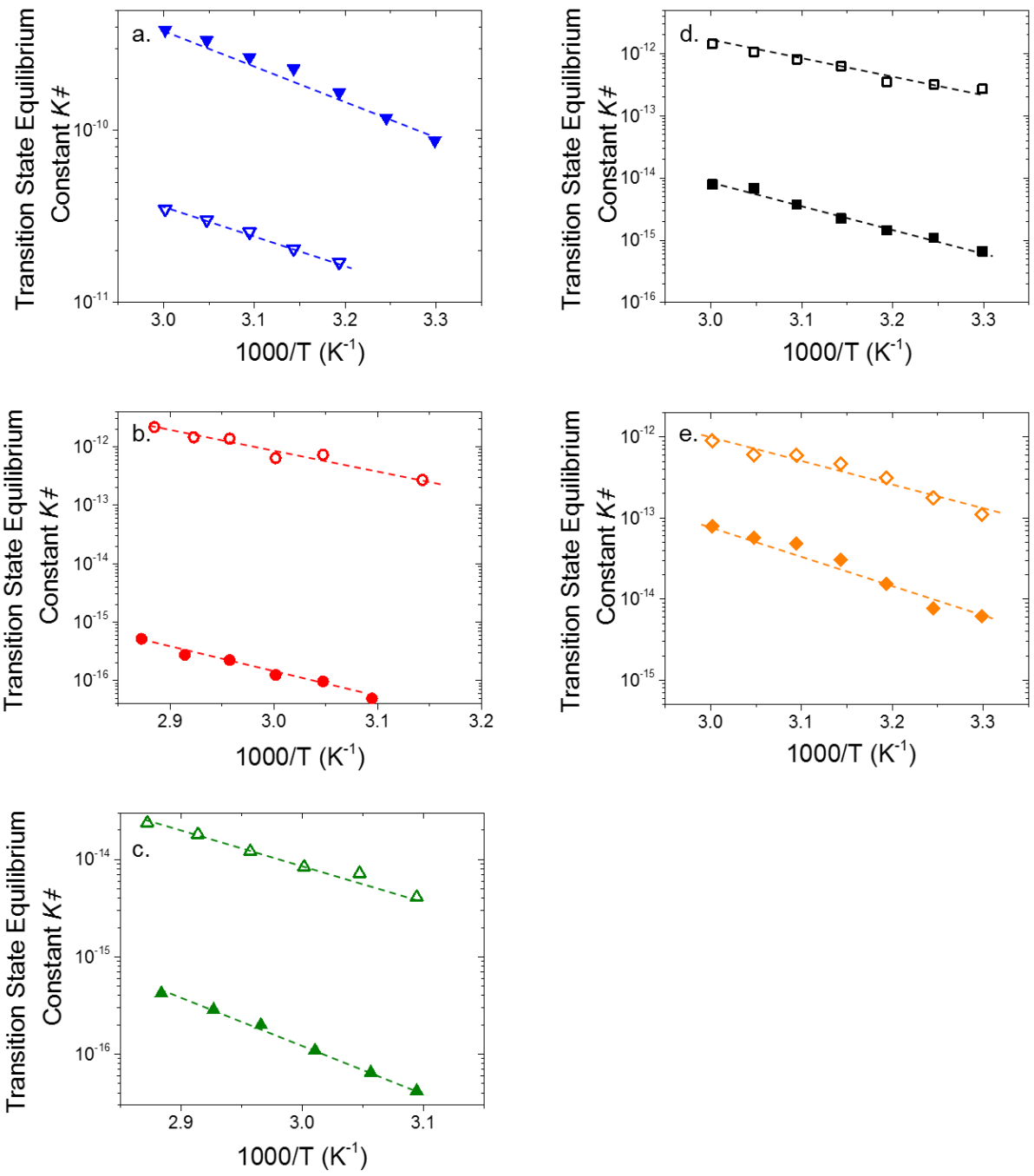

Figure B11. Transition state equilibrium constants for C_6H_{10} epoxidation ($K_E^{\ddagger}$, closed symbols) and H_2O_2 decomposition ($K_D^{\ddagger}$, open symbols) as functions of inverse temperature on (a) $Ti_{1.0}$-BEA (▼, 0.5 mM C_6H_{10}, 0.05 M H_2O_2), (b) $Zr_{1.0}$-BEA (●, 0.5 mM C_6H_{10}, 0.1 M H_2O_2), (c) $Hf_{1.0}$-BEA (▲, 0.5 mM C_6H_{10}, 0.1 M H_2O_2), (d) $Nb_{0.6}$-BEA (■, 0.05 M C_6H_{10}, 1 mM H_2O_2), and (d) $Ta_{0.6}$-BEA (♦, 0.01 M C_6H_{10}, 1 mM H_2O_2) under a M-(O_2) MASI. Error bars were omitted for clarity. In all reported data, error was < 7%. Lines represent fits to the Eyring equation (equation B17).

B.4. Effects of Metal Electronegativity (Pauling and Mulliken) on Activation Enthalpies and Measured CD_3CN Adsorption Enthalpies

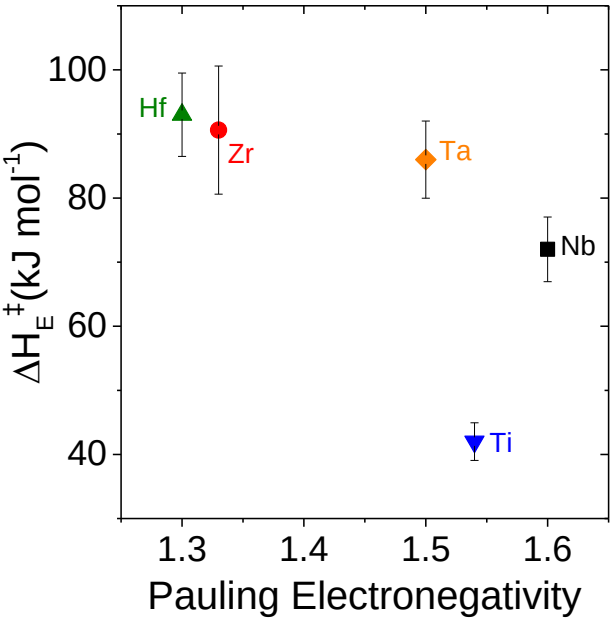

Figure B12. Activation enthalpies for C_6H_{10} epoxidation ($\Delta H_E^{\ddagger}$), measured on a M-(O_2) MASI (Fig. B11), as a function of metal-atom Pauling electronegativity on $Ti_{1.0}$-BEA (▼), $Zr_{1.0}$-BEA (●), $Hf_{1.0}$-BEA (▲), $Nb_{0.6}$-BEA (■), and $Ta_{0.6}$-BEA (♦).

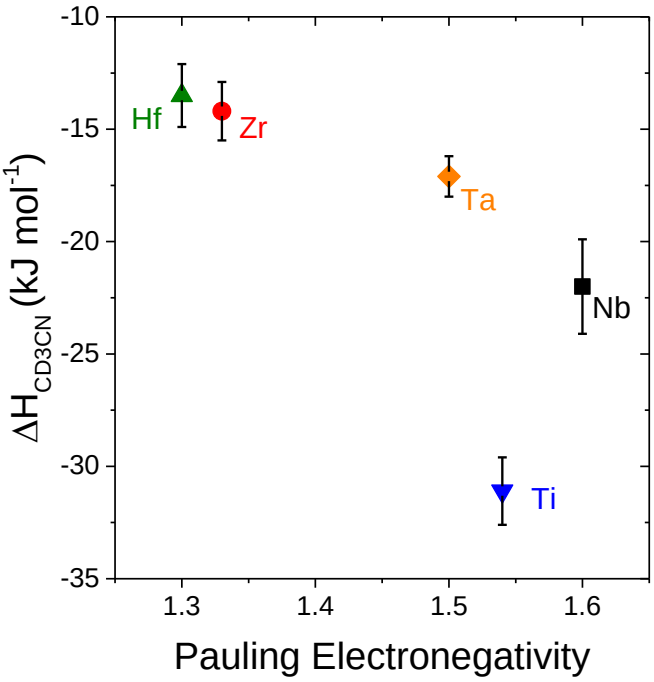

Figure B13. Measured CD_3CN adsorption enthalpies (Section 3.2.2) as a function of metal-atom Pauling electronegativity on $Ti_{1.0}$-BEA (▼), $Zr_{1.0}$-BEA (●), $Hf_{1.0}$-BEA (▲), $Nb_{0.6}$-BEA (■), and $Ta_{0.6}$-BEA (♦).

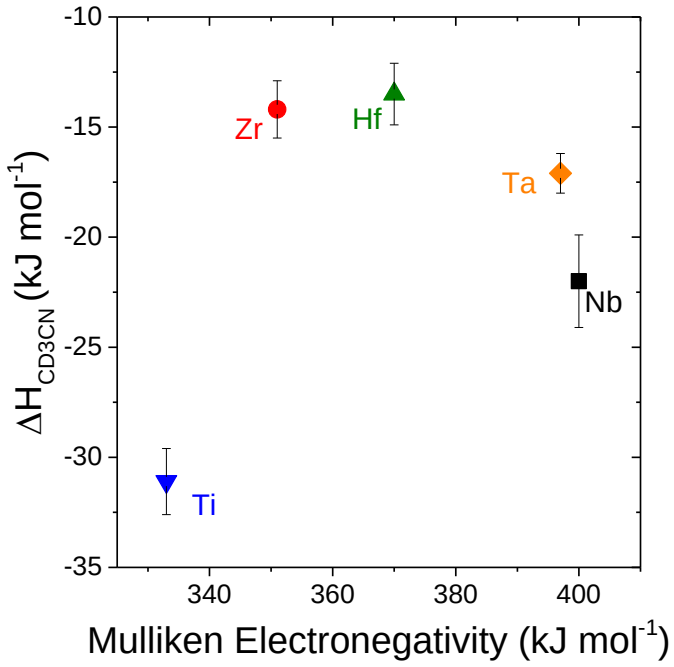

Figure B14. Measured CD_3CN adsorption enthalpies (Section 3.2.2) as a function of metal-atom Mulliken electronegativity on $Ti_{1.0}$-BEA (▼), $Zr_{1.0}$-BEA (●), $Hf_{1.0}$-BEA (▲), $Nb_{0.6}$-BEA (■), and $Ta_{0.6}$-BEA (♦). Mulliken electronegativity values are adapted from ref [14].

APPENDIX C

Supplementary Information and Data for Chapter Four

C.1. Additional Catalyst Characterization and the Absence of Mass-Transfer Restrictions

C.1.1. Catalyst Characterization

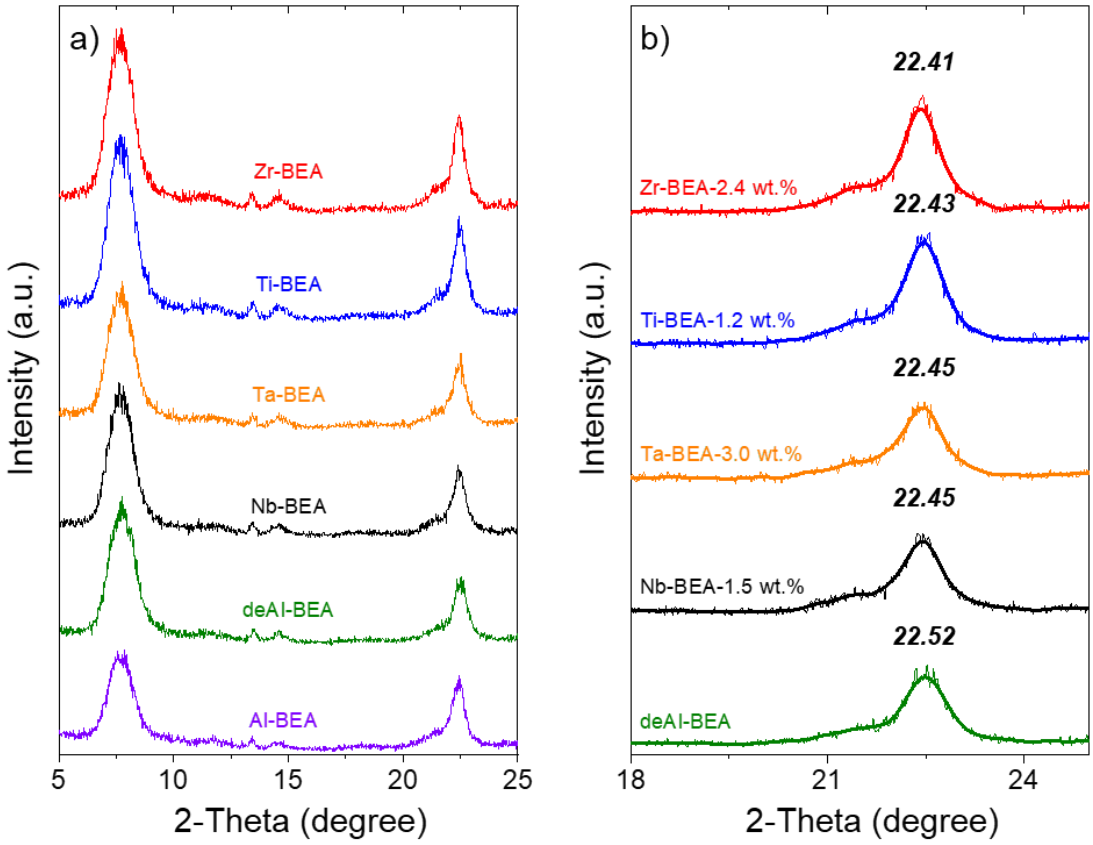

Figure C1. X-ray diffractograms for (a) Zr-BEA, Ti-BEA, Ta-BEA, Nb-BEA, dealuminated *BEA, and Al-BEA (i.e., the parent *BEA) used in the kinetic studies (Section 4.3) and (b) of Zr-BEA, Ti-BEA, Nb-BEA, Ta-BEA, with weight loadings of 2.4, 1.2, 3.0, and 1.5 wt.%, respectively, and dealuminated BEA* to visualize changes in the peak position of the ~22.5 degree X-ray diffractogram feature. Bold solid lines in panel (b) represent a finite fourier transform to smooth the data with 10 points of fitting.

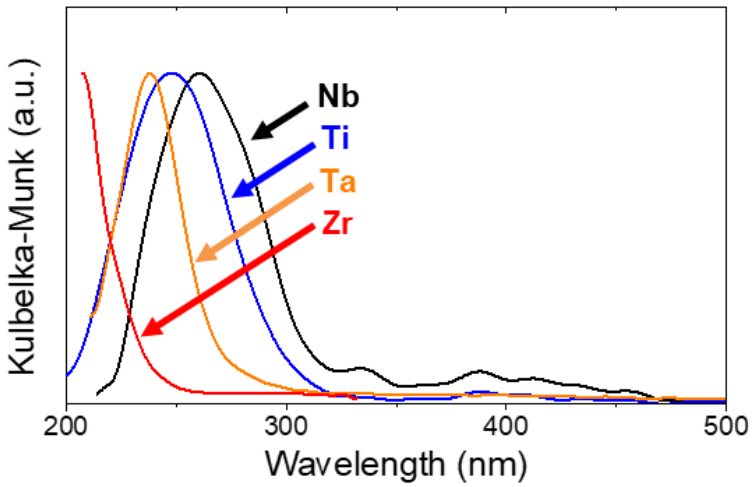

Figure C2. Normalized diffuse reflectance UV-vis spectra of Ti- (blue), Nb- (black), Ta- (orange), and Zr- (red) BEA materials diluted in a 1:10 by weight ratio with MgO. Pure MgO was used as the background. Spectral artifacts at >325 nm for Ti- and Nb-BEA arise from smoothing with a finite fourier transform with 10 points of smoothing.

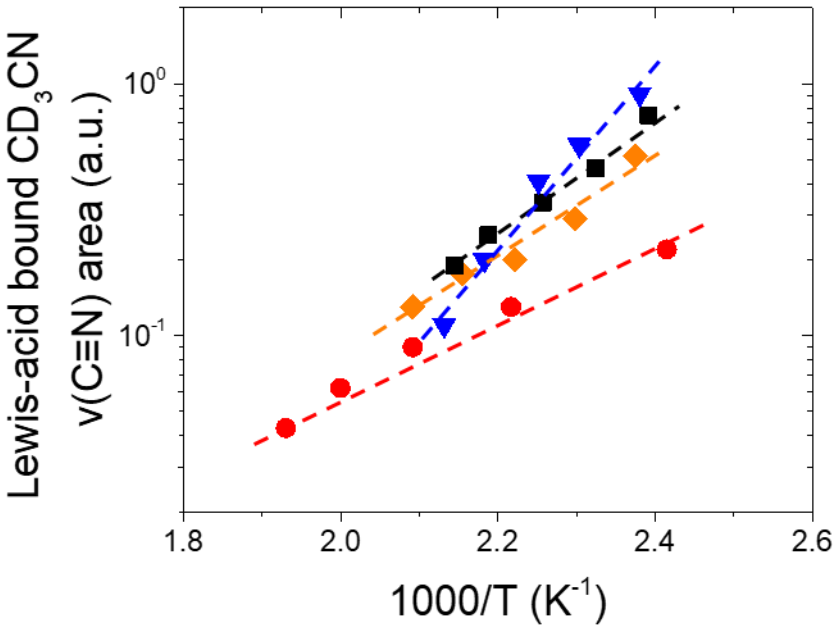

Figure C3. IR feature areas for Lewis-acid bound CD_3CN on Ti-BEA (▼, 2302 cm^{-1}), Nb-BEA (■, 2306 cm^{-1}), Ta-BEA (♦, 2312 cm^{-1}), and Zr-BEA (●, 2296 cm^{-1}) as a function of inverse temperature (1.5 kPa CD_3CN, 100 kPa He, 50 cm^3 min^{-1}) after background subtraction. Dashed lines represent linear fits, whose slopes are proportional to the value of ΔH_{CD_3CN}.

C.1.2. Experimental Verification for the Absence of Mass-Transfer Restrictions

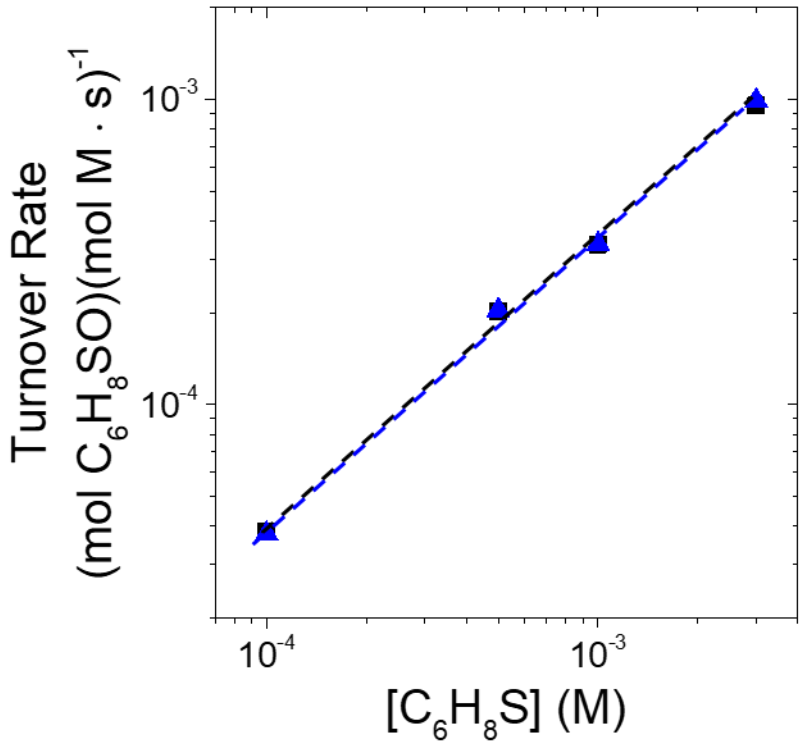

Figure C4. Turnover rates for the formation of C_6H_8SO measured as a function of [C_6H_8S] on Ti-BEA (blue solid ▲, 0.141 wt.% Ti, used in kinetics experiments in main text; 0.01 M H_2O_2, 313 K) and Ti-BEA (black ■, 0.019 wt.% Ti; 0.01 M H_2O_2, 313 K). Dashed lines are intended to guide the eye.

Figure C4 shows rates for the formation of 2,5-dimethylthiophene oxide (C_6H_8SO) measured as a function of C_6H_8S concentration for multiple metal loadings of Ti (0.141 wt.% and 0.019 wt.%) in Ti-BEA. The rate of C_8H_8O formation is invariant with metal loading, which indicates that the Madon-Boudart criterion is satisfied for Ti-BEA.[111]

In Figure 4.3, C_6H_8SO formation rates are highest for Ti-BEA (of all M-BEA) under these conditions, which suggests that satisfaction of the Madon-Boudart criterion for Ti-BEA implies that the other M-BEA (i.e., those with lower turnover rates and similar crystallite size) do not possess mass-transfer restrictions.

C.2. Sample Raw UV-Vis Spectrum and Spectral Processing

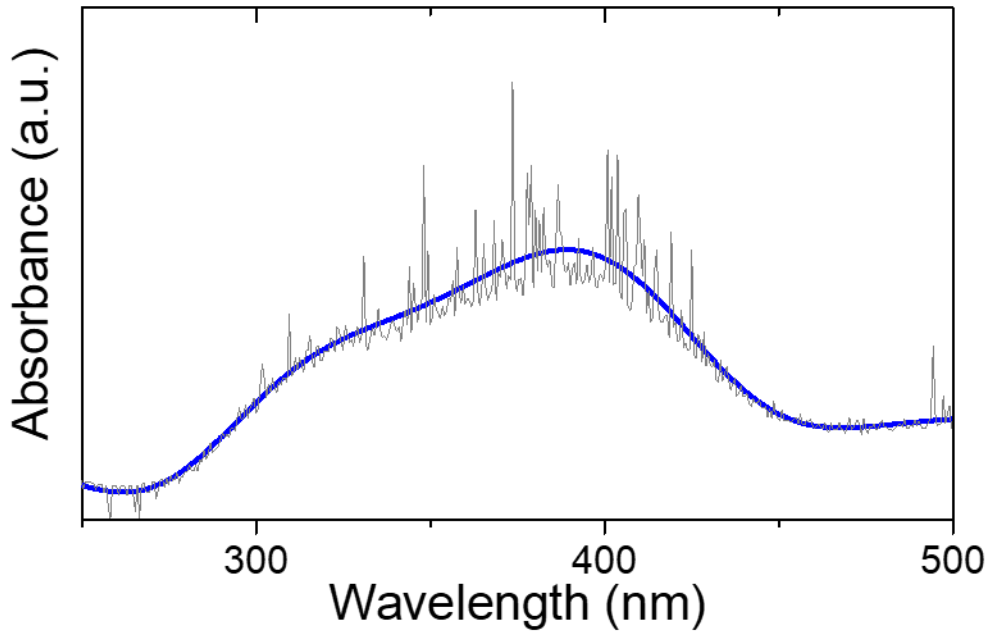

Figure C5. UV-vis absorbance spectrum (raw data, gray) of H_2O_2-treated Ti-BEA at 313 K in flowing CH_3CN (0.4 M H_2O, 0.01 M H_2O_2, 313 K) and smoothed data (bold blue line) using a finite fourier transform with 40 points of fitting performed in OriginPro®.

For all UV-vis experiments, spectra were collected at steady state (i.e., where the UV-vis features were unchanging with time) and smoothed using OriginPro® in a systematic fashion (i.e., using the same wavelength intervals and number of smoothing points).

C.3. Product Selectivities over M-BEA

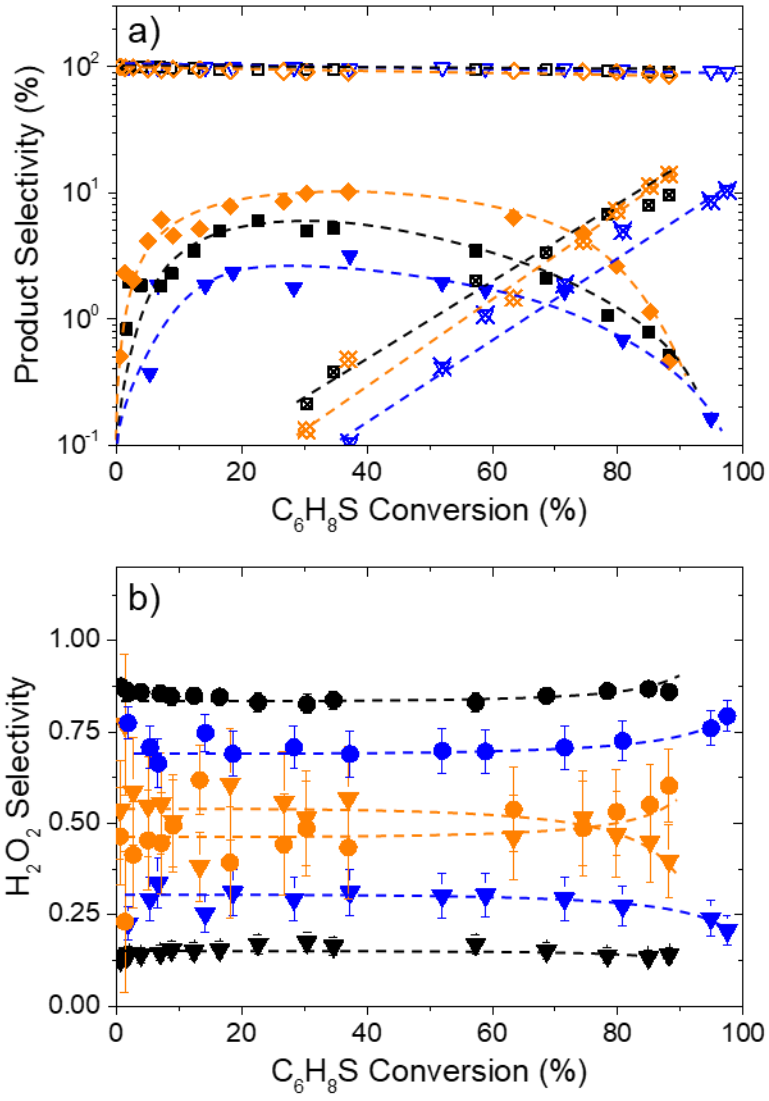

Figure C6. (a) Product selectivity towards C_6H_8SO (▽), $C_6H_8SO_2$ (▼), and $C_6H_8SO_3$ (▽ with a "X") and (b) H_2O_2 selectivity towards oxidation (▼) and H_2O_2 decomposition (●) as a function of C_6H_8S conversion (5 mM C_6H_8S, 0.05 H_2O_2, 313 K) over Ti-BEA (blue), Nb-BEA (black), and Ta-BEA (orange). Dashed curves are intended to guide the eye.

C.4. Supplemental Information for the Derivation of Rate Expression for Sulfoxidation and Transition State Theory

C.4.1. Pseudo Steady State Hypothesis Applied to M-(O_2) Intermediates

The pseudo steady state hypothesis (PSSH) assumes that the concentration (or number) of a specific reactive species is unchanging with time during a reaction. Application of the PSSH to M-(O_2) intermediates in section 4.3.3, results in the following expression:

$$\frac{d[M-(O_2)]}{dt} \approx 0 = k_3[H_2O_2\,*] - k_4[C_6H_8S][M-(O_2)] + k_5[H_2O_2][M-(O_2)] + k_7[C_6H_8SO][M-(O_2)] \quad \text{(C1)}$$

where k_x represents the rate constant for step *x*, [M-(O_2)] is the number of M-(O_2) intermediates, [H_2O_2*] is the number of H_2O_2 molecules bound to active sites, and all other species within brackets ([]) are the corresponding liquid-phase concentrations. When H_2O_2 adsorption is assumed to be quasi-equilibrated (step 2, Scheme 1), equation C1 can be rearranged to yield:

$$[M-(O_2)] = \frac{k_3K_2[H_2O_2][*]}{k_4[C_6H_8S]+k_5[H_2O_2]+k_7[C_6H_8SO]} \quad \text{(C2)}$$

where [*] is the number of unoccupied (or solvent-covered) active sites. Equation C2 is then combined with equation 4.1 to yield equation 4.2 from the main text.

C.4.2. Transition State Theory for Measurement of Activation Enthalpies and Entropies

Application of TST assumes that the state immediately preceding the transition state and the transition state are in equilibrium,[215] which takes the form of

$$M-(O_2)+H_2O_2 \overset{K^{\ddagger}_{Dec}}{\rightleftharpoons} M-(O_2)-{H_2O_2}^{\ddagger} \tag{C3}$$

where M-(O_2)-$H_2O_2^{\ddagger}$ and $K^{\ddagger}_{Dec}$ represent the transition states and transition state equilibrium constants for H_2O_2 decomposition, respectively. The rates for H_2O_2 decomposition can then be expressed in terms of the numbers of transition states, resulting in

$$\frac{r_{Dec}}{[L]} = \frac{k_b T}{h}[M-(O_2)-{H_2O_2}^{\ddagger}] \tag{C4}$$

where T is the absolute temperature in Kelvin and k_b and h are Boltzmann's and Planck's constants, respectively. Measurement of the reaction rates under a M-(O_2) MASI allows equation C4 to be re-expressed as

$$\frac{r_{Dec}}{[L]} = \frac{k_b T}{h} K^{\ddagger}_{Dec}[H_2O_2] \tag{C5}$$

which allows for $K^{\ddagger}_{Dec}$ to be determined by measurement of turnover rates for each reaction pathway at a given temperature.

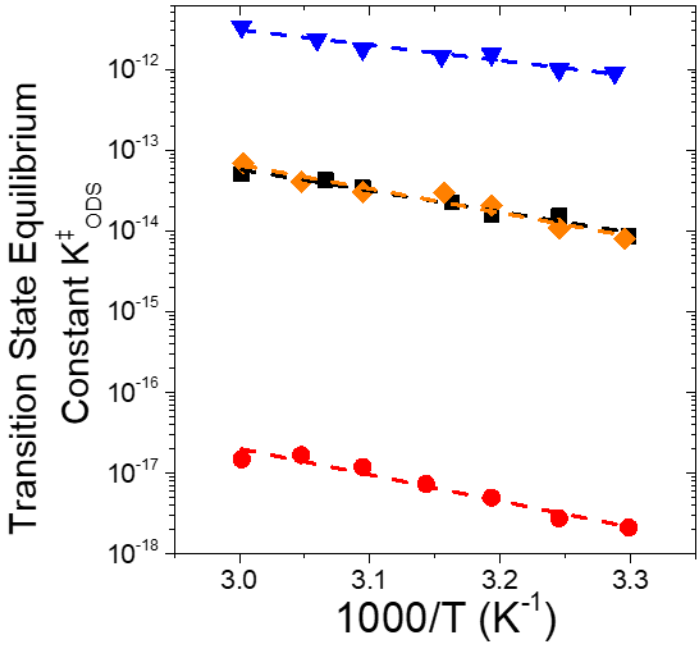

Figure C7. Transition state equilibrium constants for C_6H_8S oxidation ($K^{\ddagger}_{ODS}$) as a function of inverse temperature on Ti-BEA (▼, 3 mM C_6H_8S, 0.01 M H_2O_2), Nb-BEA (■, 3 mM C_6H_8S, 1 mM H_2O_2), Ta-BEA (♦, 3 mM C_6H_8S, 1 mM H_2O_2), and Zr-BEA (●, 10 mM C_6H_8S, 10 mM H_2O_2) in CH_3CN. Dashed lines represent fits to the Eyring equation whose slopes are proportional to $\Delta H^{\ddagger}$.

APPENDIX D

Supplementary Information and Data for Chapter Five

D.1. Additional Catalyst Characterization and Verification of Measuring True Kinetics

D.1.1. Catalyst Characterization

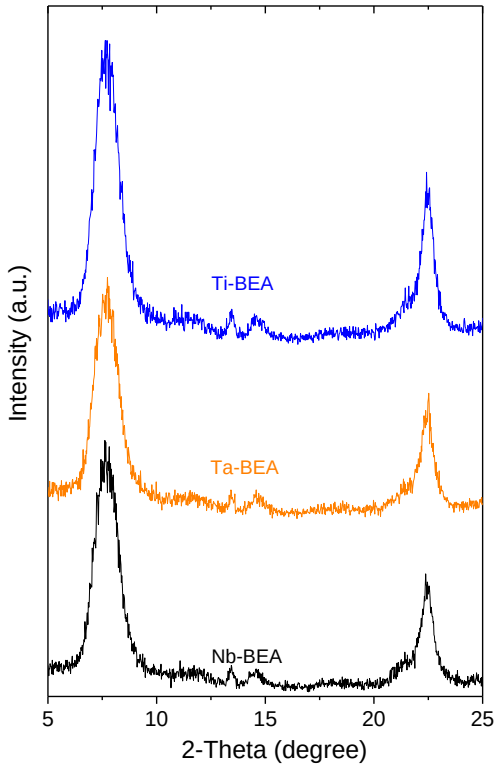

Figure D1. X-ray diffractograms for Ti- (blue), Nb- (black), and Ta-BEA (orange) taken on a Siemens/Bruker D5000 X-ray diffractometer with Cu Kα radiation (0.15418 nm) at ambient conditions.

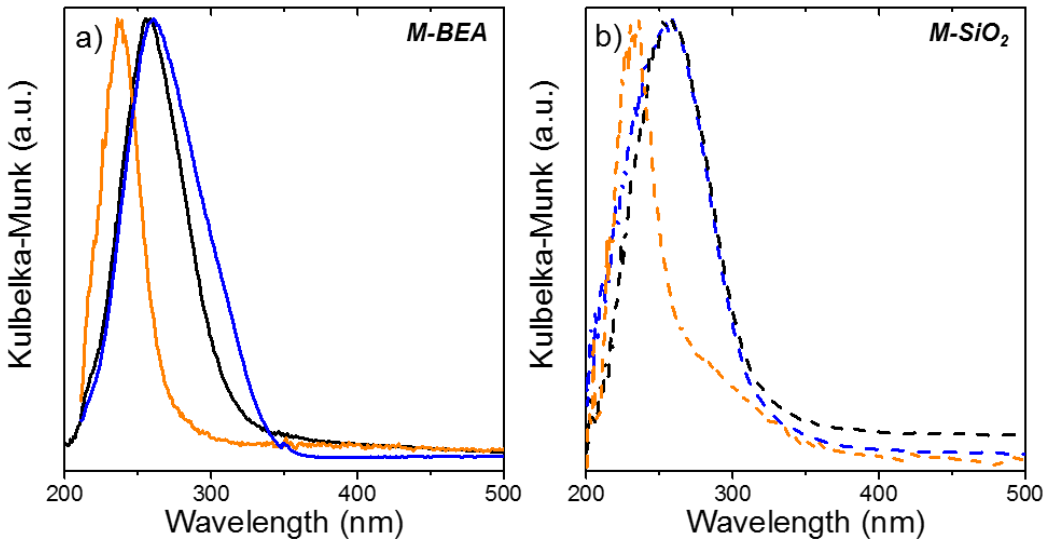

Figure D2. Diffuse reflectance UV-vis spectra for (a) M-BEA (solid lines) and (b) M-SiO_2 (dashed lines) catalysts. Colors represent: Ti (blue), Nb (black) and Ta (orange).

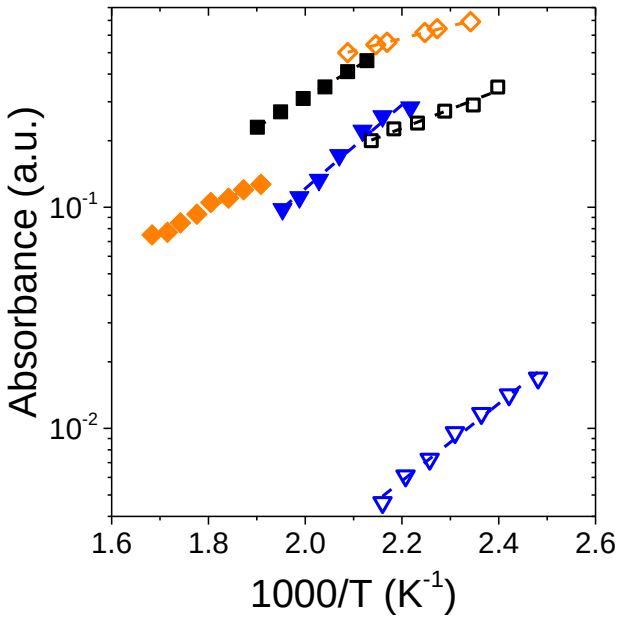

Figure D3. IR absorbance intensities for the Lewis-acid bound pyridine (~1450 cm^{-1} absorbance feature; Figure 5.1) on Ti-BEA (blue ▼, 1445 cm^{-1}), Nb-BEA (black ■, 1447 cm^{-1}), Ta-BEA (orange ♦, 1448 cm^{-1}), Ti-SiO_2 (blue open ▼, 1445 cm^{-1}), Nb-SiO_2 (black open ■, 1448 cm^{-1}), and Ta-SiO_2 (orange open ♦, 1449 cm^{-1}) as a function of inverse temperature (0.1 kPa pyridine, 101 kPa He, 50 cm^3 min^{-1}) after background subtraction. Dashed lines represent linear fits, where the slopes are proportional to the value of ΔH_{Py}.

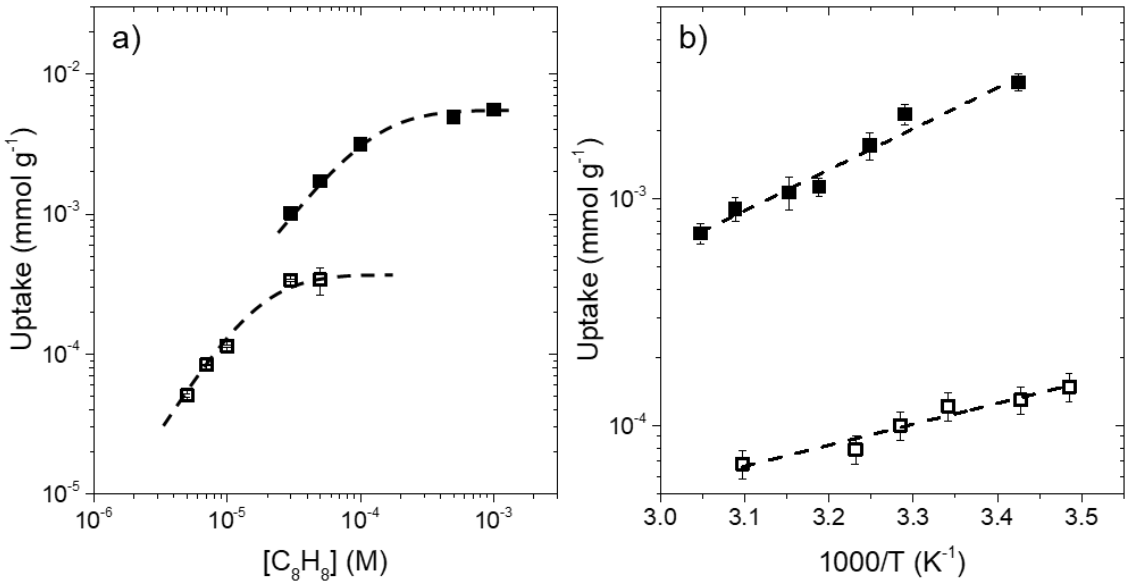

Figure D4. Styrene (C_8H_8) uptake (per gram of Si-BEA or SiO_2) into Si-BEA (solid symbols) and SiO_2 (open symbols) as a (a) function of [C_8H_8] (in CH_3CN, 313 K) and (b) inverse temperature (0.03 mM C_8H_8 for Si-BEA and 0.007 mM C_8H_8 for SiO_2 in CH_3CN). Dashed lines in Figure D4a are intended to guide the eye, while those in Figure D4b are linear fits where the slopes are proportional to ΔH_{Ads}.

Figure D4a shows two distinct regimes of C_8H_8 uptake into purely siliceous materials (i.e., Si-BEA and SiO_2), where at low [C_8H_8], uptake is proportional to the concentration of [C_8H_8] in the bulk solution and approaches a saturation value at relatively high [C_8H_8] (e.g., >0.03 mM for SiO_2). Adsorption enthalpies for C_8H_8 within a solution of CH_3CN (i.e., the solvent used for epoxidation in this study) are measured by van't Hoff analysis (Figure D4b) for the uptake of C_8H_8 into these materials. The uptake or C_8H_8 must be measured under the linear regime for C_8H_8 uptake (i.e., low [C_8H_8]) as a function of [C_8H_8] to avoid any artifacts that arise from saturation of the micropores of *BEA or mesopores of SiO_2.

D.1.2. Methylphosphonic Acid Titrations to Determine Fraction of Active Metal in M-BEA Catalysts

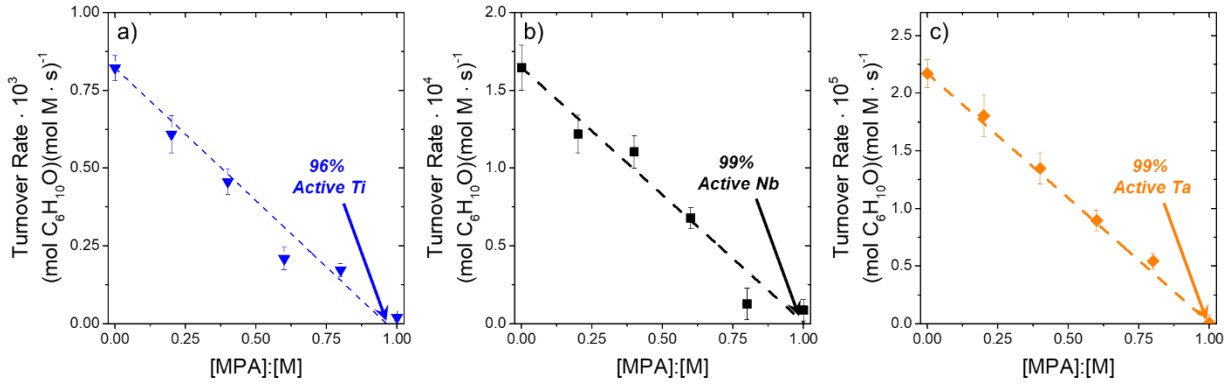

Figure D5. Turnover rates for $C_6H_{10}O$ formation as a function of methylphosphonic acid-to-metal ratio ([MPA]:[M]; 0.01 M C_6H_{10}, 0.01 M H_2O_2, 313 K) for (a) Ti-BEA, (b) Nb-BEA, and (c) Ta-BEA. Dashed lines represent linear regression fits with the y-intercept set to the turnover rate in the absence of the MPA titrant.

M-BEA was stirred with cyclohexene (0.01 M), benzene (an internal standard), CH_3CN (solvent), and an appropriate amount of methylphopshonic acid (MPA) at 313 K for 30 min with the intent of irreversibly adsorbing MPA to the active metal atoms. Epoxidations were initiated by the introduction of H_2O_2, and cyclohexene oxide ($C_6H_{10}O$) formation rates were determined using a gas chromatograph and analyzing extracted aliquots of the reaction mixture as a function of time. Figure D5 shows that turnover rates on M-BEA (M = Ti, Nb, and Ta) decrease linearly with the ratio of MPA:M, which suggests that the MPA selectively titrates the active sites for epoxidation. The extrapolation of these data to the point where turnover rates approach zero gives the fraction of metal atoms that are active for epoxidation.[232]

D.1.3. Control Experiments to Test Importance of Mass Transfer

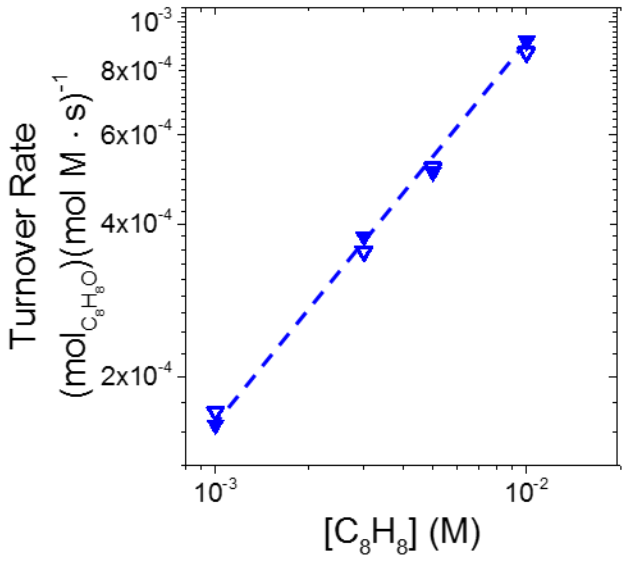

Figure D6. Turnover rates for the formation of C_6H_{10} measured as a function of $[C_6H_{10}]$ on Ti-BEA (blue solid ▼, 0.22 mmol Ti g^{-1}; 0.01 M H_2O_2, 313 K) and Ti-BEA (blue open ▼, 0.02 mmol Ti g^{-1}; 0.01 M H_2O_2, 313 K). Dashed line is intended to guide the eye.

Figure D5 shows rates for the formation of styrene oxide (C_8H_8O) via primary reaction pathways measured as a function of C_8H_8 concentration for multiple metal loadings of Ti (0.22 mmol g^{-1} and 0.02 mmol g^{-1}) in Ti-BEA. The rate of C_8H_8O formation is invariant with metal loading, which indicates that the Madon-Boudart criterion is satisfied for Ti-BEA.[111] Under the conditions tested, we see that the turnover rate for C_8H_8O formation is proportional to $[C_8H_8]$ and independent of $[H_2O_2]$, which corresponds to a simplified rate expression (Section 5.3.3 of main text) of:

$$\frac{r_E}{[L]} = k_4[C_8H_8] \qquad \text{(D1)}$$

where r_E is the rate of $C_6H_{10}O$ formation, [L] is the total number of metal atoms in the reactor, k_4 is the rate constant for step 4 of scheme 5.2, and $[C_8H_8]$ is the concentration of C_8H_8. For a first-

order reaction (such as in equation D1), an effective Thiele modulus for a spherical pellet[111] can be defined as:

$$\varphi = \left(\frac{k_4 R^2 [C_8H_8]}{D_e}\right)^{1/2} \quad \text{(D2)}$$

where ϕ is the Thiele modulous, R is the radius of the spherical pellet, $[C_8H_8]$ is the bulk concentration of C_8H_8, and D_e is the effective diffusivity of C_8H_8 through the spherical pellet. The Madon-Boudart criterion is an experimental way to determine the relative value of the Thiele modulus, where the independence of turnover rates on metal loading signifies a relatively small Thiele modulus (i.e., $\phi << 1$). When the Thiele modulous is small, the rates of diffusion are much greater than those for the inherent kinetics of the reaction (at reactant concentrations equal to that in the bulk fluid phase), which shows that the measured reaction rates are not convoluted by diffusion restrictions within the catalyst particles.

In Figure 5.5, C_8H_8 formation rates are highest for Ti-BEA (of all M-BEA and M-SiO_2) under these conditions. Therefore, all other M-BEA andM M-SiO_2 give values of k_3 that are much smaller than for Ti-BEA, which suggests that Thiele moduli on these materials are even smaller than that for Ti-BEA. Additionally, M-SiO_2 catalysts possess nominal pore diameters of 5.4 nm, which are significantly larger than those in M-BEA (~0.7 nm). This increases the effective diffusivity of C_8H_8 in M-SiO_2 materials relative to M-BEA and decreases the Thiele moduli further. Therefore, satisfaction of the Madon-Boudart criterion for Ti-BEA suggests that the other M-BEA and M-SiO_2 are also not mass-transfer limited and all measured reaction rates are reflective of only chemical kinetics.

D.1.4. X-ray Photoelectron Spectroscopy of Untreated and H_2O_2-Treated M-BEA and M-SiO_2

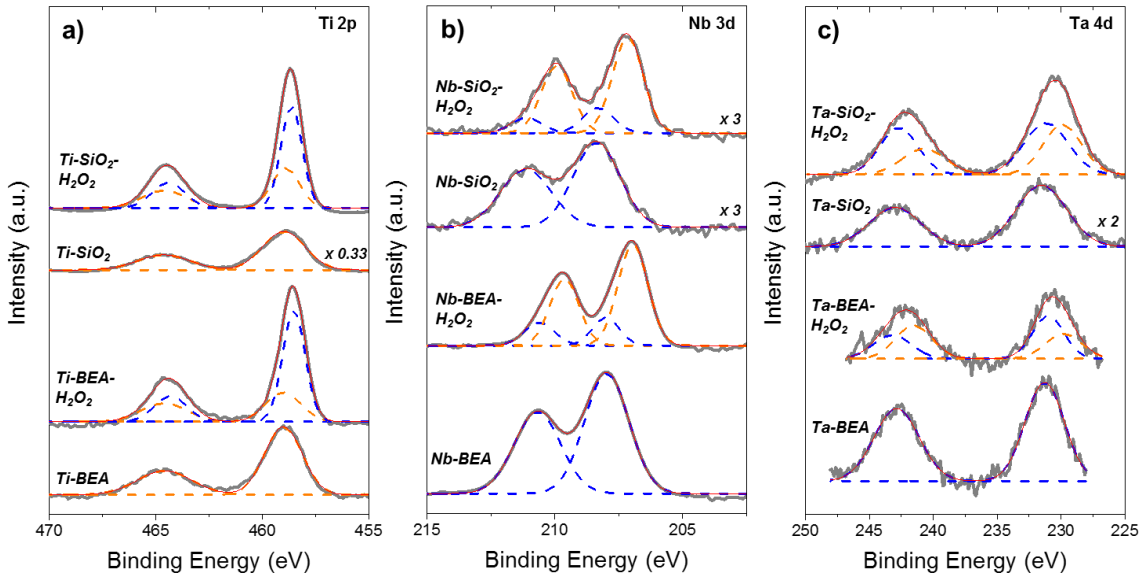

Figure D7. X-ray photoelectron spectra (gray, bold) of the (a) Ti 2*p*, (b) Nb 3*d*, and (c) Ta 4*d* regions on untreated and H_2O_2-treated (Section 2.2) Ti-, Nb-, and Ta- BEA and SiO_2. The peak fittings from the different oxidation states are color coded (blue and orange dashed curves) for clarity with the cumulative peak fit in red (solid). Table D1 contains peak center values and corresponding metal oxidation states. Spectra are references to an aliphatic C 1*s* feature at 284.8 eV.

Figure D7 shows X-ray photoelectron spectra that reveal the oxidation states of Ti, Nb, and Ta atoms in both untreated and H_2O_2-treated M-BEA and M-SiO_2. Untreated Ti-, Nb-, and Ta-materials possess doublet features that correspond to Ti^{4+} (Ti $2p_{1/2}$ and Ti $2p_{3/2}$),[381-382] Nb^{5+} (Nb $3d_{3/2}$ and Nb $3d_{5/2}$),[54, 127] and Ta^{5+} (Ta $4d_{5/2}$ and Ta $4d_{7/2}$)[383] species, respectively, both in the *BEA framework and grafted onto SiO_2. Table D1 summarizes the position of the peak centers and corresponding oxidation states. In the case of Ti-BEA and Ti-SiO_2, treatment with H_2O_2 creates two additional features with peak binding energies that are ~0.3 eV lower than those of the untreated Ti-BEA and Ti-SiO_2 materials. The red shift of ~0.3 eV indicates that a fraction of the Ti atoms are coordinated to electron rich substituents, such as for Ti-(η^2-O_2) and Ti-OOH, after treatment with H_2O_2. Notably, these shifts are not large enough, however, to suggest a full formal oxidation state change from Ti^{4+} to Ti^{3+}.[382] Nb and Ta materials show overlapping features with significant shifts (~1 eV) in electron binding energies that may indicate a fraction of the metal cations reduce from a +5 to +4 oxidation state upon reaction with H_2O_2,[127, 383] which may be due

to the Haber-Weiss decomposition of M-OOH species to produce reduced metal centers,[384] or result from X-ray induced photoreduction of Nb and Ta metal centers.[239]

Table D1. Photoelectron Binding Energies (BE) and Corresponding Oxidation States of Metal Atoms in Untreated and H_2O_2-Activated M-BEA and M-SiO_2, as Determined by X-ray Photoelectron Spectroscopy.[a]

Sample	Untreated Samples BE (eV)	Untreated Samples Oxidation States	H_2O_2-activated Samples BE (eV)	H_2O_2-activated Samples Oxidation State(s)
Ti-BEA	464.7, 459.0	+4	464.7, 459.0	+4
			464.3, 458.5	+4
Nb-BEA	210.6, 208.0	+5	210.6, 208.0	+5
			209.7, 207.0	+4
Ta-BEA	243.0, 231.3	+5	243.4, 231.0	+5
			241.1, 229.7	+4
Ti-SiO_2	464.6, 458.9	+4	464.6, 458.9	+4
			464.4, 458.6	+4
Nb-SiO_2	211.1, 208.3	+5	211.1, 208.3	+5
			209.9, 207.1	+4
Ta-SiO_2	243.0, 231.6	+5	241.8, 231.1	+5
			240.6, 229.8	+4

[a]See Figure D7 for XP spectra.

D.2. Identification of Active Intermediates via *In Situ* UV-Visible and Raman Spectroscopy

D.2.1. Sample Raw UV-Vis Spectrum and Method for Processing Spectra

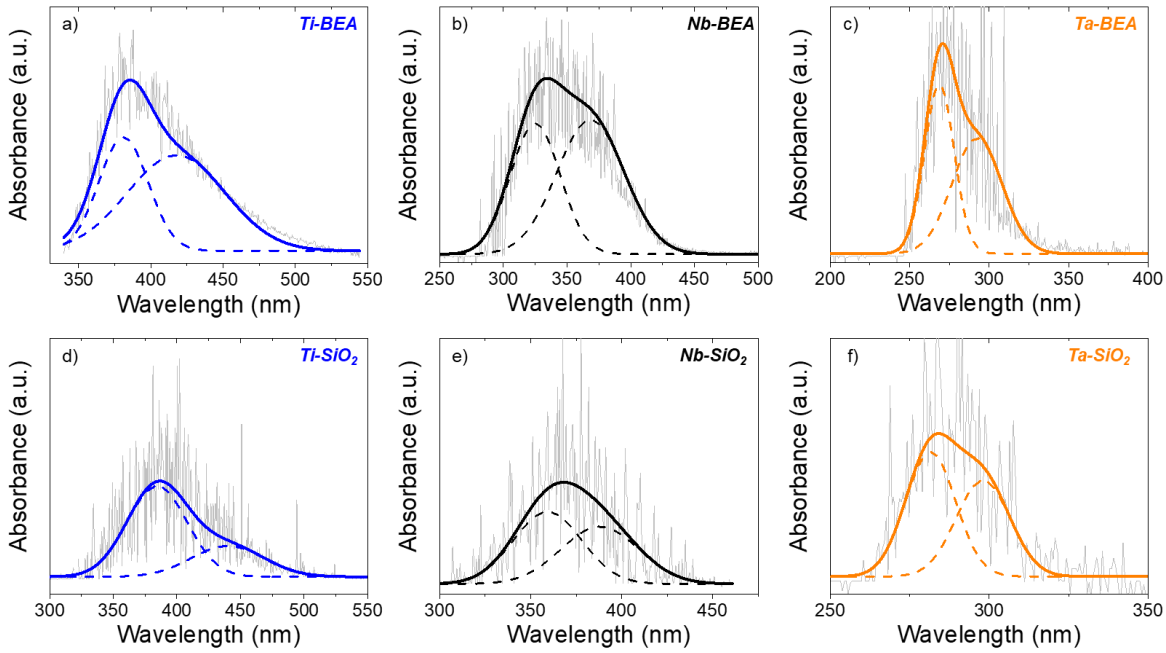

Figure D8. UV-vis absorbance spectrum (raw data, gray) of H_2O_2-treated (a) Ti-BEA, (b) Nb-BEA, (c) Ta-BEA, (d) Ti-SiO_2, (e) Nb-SiO_2, and (f) Ta-SiO_2 at 313 K in flowing CH_3CN (0.4 M H_2O) and smoothed data (bold black line) using a finite fourier transform (20 points of smoothing). Dashed curves represent peak fittings using a Gaussian function.

D.2.2. Values of Ligand to Metal Charge Transfer Energies for H_2O_2-activated M-BEA and M-SiO_2

Table D2. Ligand to Metal Charge Transfer Energies (hν) for the M-OOH and M-(η^2-O_2) Intermediates as Detected via *In Situ* UV-vis Spectra (Figure 5.2).

Material	LMCT hν (eV) for M-OOH	LMCT hν (eV) for M-(η^2-O_2)
Ti-BEA	2.95	3.25
Nb-BEA	3.48	3.99
Ta-BEA	4.21	4.54
Ti-SiO_2	2.81	3.25
Nb-SiO_2	3.36	3.65
Ta-SiO_2	4.11	4.38

D.2.3. Time-Resolved *In Situ* UV-Vis Spectroscopy and Kinetic Parameter Optimization

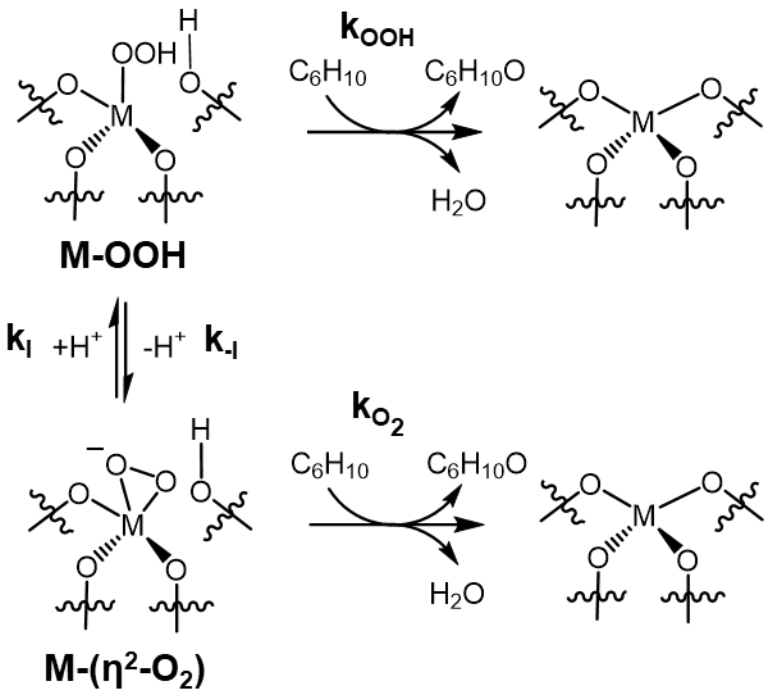

Scheme D1. Consumption and interconversion of M-OOH and M-(η^2-O_2) species upon reaction with C_6H_{10} on group 4 metals.

The change in surface coverage of the M-OOH and M-(η^2-O_2) species depends on the summed rates of formation/consumption through interconversion and consumption by reaction with C_6H_{10}, which take the forms of:

$$\frac{d[M-(\eta^2-O_2)]}{dt} = k_{-I}[M-OOH] - k_I[M-(\eta^2-O_2)] - k_{O_2}[M-(\eta^2-O_2)][C_6H_{10}] \quad \text{(D3)}$$

$$\frac{d[M-OOH]}{dt} = k_I[M-(\eta^2-O_2)] - k_{-I}[M-OOH] - k_{OOH}[M-OOH][C_6H_{10}] \quad \text{(D4)}$$

where [M-OOH] and [M-(η^2-O_2)] represent the coverages (assumed to be proportional to UV-vis absorbance feature intensities) of M-OOH and M-(η^2-O_2), respectively, and k_x is the rate constant for step x in scheme 5.1. Pseudo first-order kinetics are assumed for the reaction between M-(O_2) intermediates and C_6H_{10}, as throughout the experiment the ratio of [C_6H_{10}] to number of metal atoms exceeds 10^5 in all cases. Similarly, pseudo first-order kinetics are assumed for the

interconversion (via protonation or deprotonation) of M-OOH and M-(η^2-O_2), as this process is likely mediated by nearby H_2O molecules (where [H_2O] was kept constant at 0.4 M).

The equilibrium coefficient (K_I) for the interconversion between M-OOH and M-(η^2-O_2) must be determined to constrain the ratio of k_I to k_{-I} and is defined as

$$K_I = \frac{k_I}{k_{-I}} = \frac{[M-OOH]}{[M-(\eta^2-O_2)]} = \frac{\varepsilon_{M-OOH} A_{M-OOH}}{\varepsilon_{M-(\eta^2-O_2)} A_{M-(\eta^2-O_2)}} \quad \text{(D5)}$$

where $\varepsilon_{M-OOH}$and $\varepsilon_{M-(\eta^2-O_2)}$are the extinction coefficients (i.e., sensitivity factors) for M-OOH and M-(η^2-O_2), respectively, and A_{M-OOH} and $A_{M-(\eta^2-O_2)}$are the areas of the steady-state UV-vis features (Figure 5.2) that correspond to M-OOH and M-(η^2-O_2) species, respectively. Equation D5 shows that the ratio of $\varepsilon_{M-OOH}$to $\varepsilon_{M-(\eta^2-O_2)}$must be known to experimentally determine a value of K_I for a given catalyst.

The area of the cumulative UV-vis feature (A_{Total}) for a given M-BEA or M-SiO_2 (Figure 2) is given by

$$A_{Total} = A_{M-OOH} + A_{M-(\eta^2-O_2)} \quad \text{(D6)}$$

The total number of metal atoms ([M]) that are detected by the UV-vis spectroscopy are given by

$$[M] = \varepsilon_{M-OOH} A_{M-OOH} + \varepsilon_{M-(\eta^2-O_2)} A_{M-(\eta^2-O_2)} \quad \text{(D7)}$$

such that [M] is equal to the sum of the number of M-OOH and M-(η^2-O_2) intermediates. Equations D6 and D7 are then combined to linearize the A_{Total} as a function of $A_{M-(\eta^2-O_2)}$to yield

$$A_{Total} = \frac{[M]}{\varepsilon_{M-OOH}} + \left(1 - \frac{\varepsilon_{M-(\eta^2-O_2)}}{\varepsilon_{M-OOH}}\right) A_{M-(\eta^2-O_2)} \quad \text{(D8)}$$

The peak areas within Figure 5.3 for the cumulative UV-vis feature and the UV-vis peak that is attributed to M-(η^2-O_2) can then be used to determine the ratio of ε_{M-OOH} to $\varepsilon_{M-(\eta^2-O_2)}$. Collection of UV-vis features under varying conditions (e.g., different acid and base solutions) is necessary to estimate the ratio of ε_{M-OOH} to $\varepsilon_{M-(\eta^2-O_2)}$ because this ratio depends on shifting the

equilibrium between the M-OOH and M-(η^2-O_2) species while assuming that the total number of sites within the measurement is unchanged.

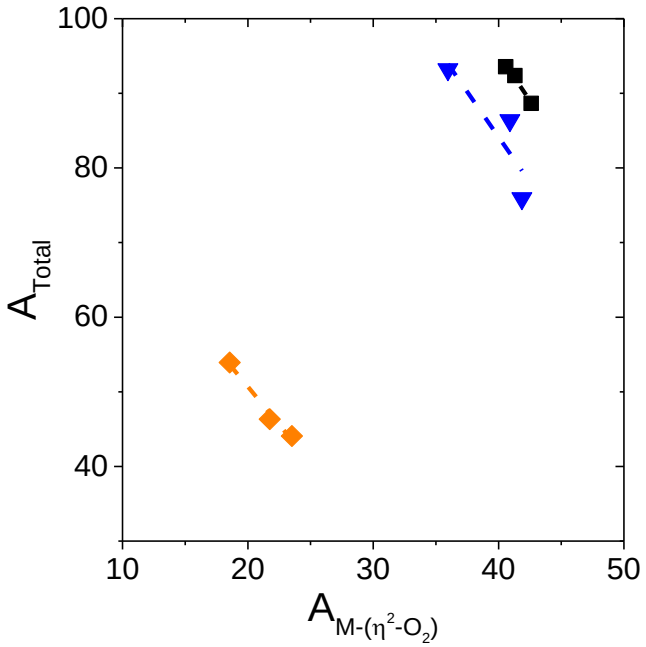

Figure D9. Total area (A_{Total}) as a function of $A_{M-(\eta^2-O_2)}$ for Ti- (▼), Nb- (■), and Ta-BEA (♦). Peak areas are from the steady-state UV-vis spectra (Figure 5.3) of these M-BEA materials when contacted with varying solutions of H_2O_2 with HCl and NH_4OH in CH_3CN (313 K). Dashed lines represent linear regression fits.

Figure D9 shows A_{Total} as a function of $A_{M-(\eta^2-O_2)}$ for all M-BEA materials, where the slope of each line is given by -2.42, -2.47, and -2.04 for Ti-, Nb-, and Ta-BEA respectively. From these slopes, equation S8 shows that the ratio of ε_{M-OOH} to $\varepsilon_{M-(\eta^2-O_2)}$ are 1.42, 1.47, and 1.04 for Ti-, Nb-, and Ta-BEA, respectively. These ratios of ε_{M-OOH} to $\varepsilon_{M-(\eta^2-O_2)}$, in conjunction with equation D5, are then used to determine values of k_I for each M-BEA and M-SiO_2 (Table D3).

MATLAB™ is used to numerically estimate the kinetic parameters, by fitting the data (Figure 5.4) to the coupled differential equations (eqns. D3 and D4). The initial guesses used for the rate constants were 0.01, 0.001, 0.001 for k_{-I}, k_{OOH}, and $k_{O_2^-}$, respectively. Values of k_I are constrained by the relationship between K_I and k_{-I} as shown in Equation D5. Changes of the initial

values by an order of magnitude (increasing and decreasing) did not change the optimized parameter values.

Table D3. Numerically Optimized Rate Constants from Figure 4 (main text), k_i (s^{-1}), and Equilibrium Constants for the Interconversion of M-OOH and M-(η^2-O_2) (Scheme 5.1) and the Ratio of Rate Constants for M-OOH to M-(η^2-O_2) Reaction with C_6H_{10}.

Sample	k_{-I} (s^{-1})	k_I (s^{-1})	$k_{OOH} : k_{O_2}$	K_I
Ti-BEA	2.2 x 10^{-4}	2.0 x 10^{-4}	1.7	0.9
Nb-BEA	1.9 x 10^{-4}	2.1 x 10^{-4}	0.6	1.1
Ta-BEA	7.9 x 10^{-5}	7.9 x 10^{-5}	0.6	1.0
Ti-SiO_2	1.3 x 10^{-4}	2.2 x 10^{-4}	11.1	1.7
Nb-SiO_2	1.5 x 10^{-4}	2.6 x 10^{-4}	0.4	1.7
Ta-SiO_2	5.0 x 10^{-4}	8.3 x 10^{-4}	0.5	1.7

D.2.4. Additional Raman Spectra of H_2O_2-Activated Ti-BEA

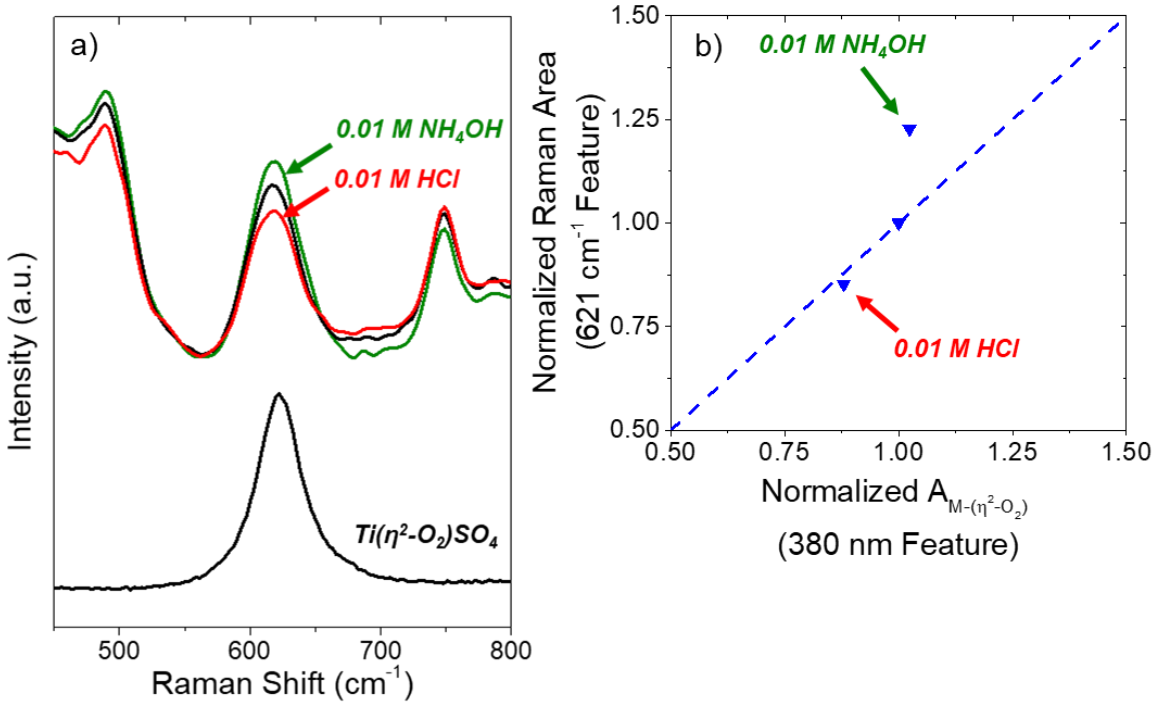

Figure D10. (a) Raman spectra of H_2O_2-activated Ti-BEA (top) and $TiOSO_4$ (to form Ti(η^2-O_2)SO_4; bottom) (λ_{ex} = 442 nm, 90 mW) and (b) correlation of the normalized 621 cm^{-1} feature peak areas to the normalized area of the UV-vis feature corresponding to Ti-(η^2-O_2) in Figure D9 when collected under identical reaction conditions. Ti-BEA Raman spectra were acquired in situ in flowing H_2O_2 in CH_3CN (0.1 M H_2O_2, 0.4 M H_2O, 1 cm^3 min^{-1}; black), with HCl (0.01 M HCl, 0.1 M H_2O_2, 0.4 M H_2O, 1 cm^3 min^{-1}; red) or NH_4OH (0.01 M NH_4OH, 0.1 M H_2O_2, 0.4 M H_2O, 1 cm^3 min^{-1}; green) at 313 K). Dashed line in Figure D10b represents parity.

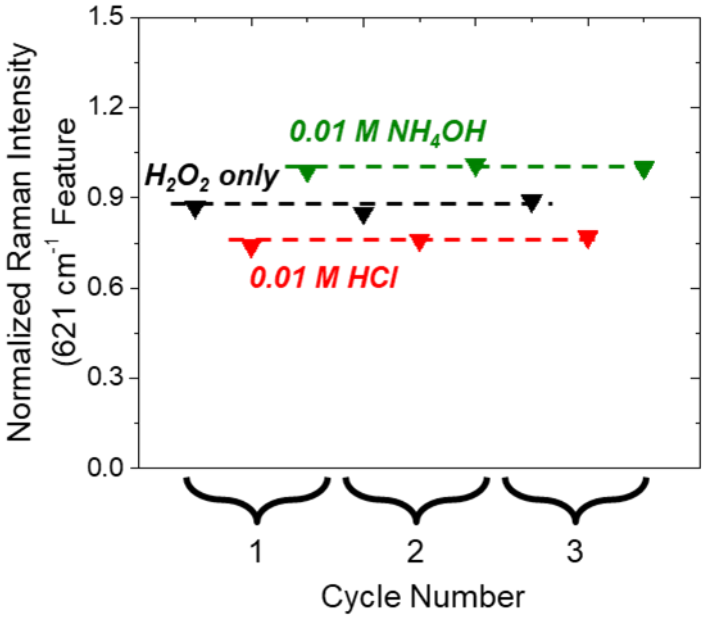

Figure D11. Steady-State peak intensities for the 621 cm^{-1} Raman feature (Figure A10) as a function of cycle number while switching from a flow of H_2O_2 in CH_3CN (0.1 M H_2O_2, 0.4 M H_2O, 1 cm^3 min^{-1}; black) to HCl (0.01 M HCl, 0.1 M H_2O_2, 0.4 M H_2O, 1 cm^3 min^{-1}; red) and finally NH_4OH (0.01 M NH_4OH, 0.1 M H_2O_2, 0.4 M H_2O, 1 cm^3 min^{-1}; green) at 313 K. Dashed lines are intended to guide the eye.

D.3. Additional Kinetic Data, Derivation of Relevant Rate Expressions and Transition State Theory

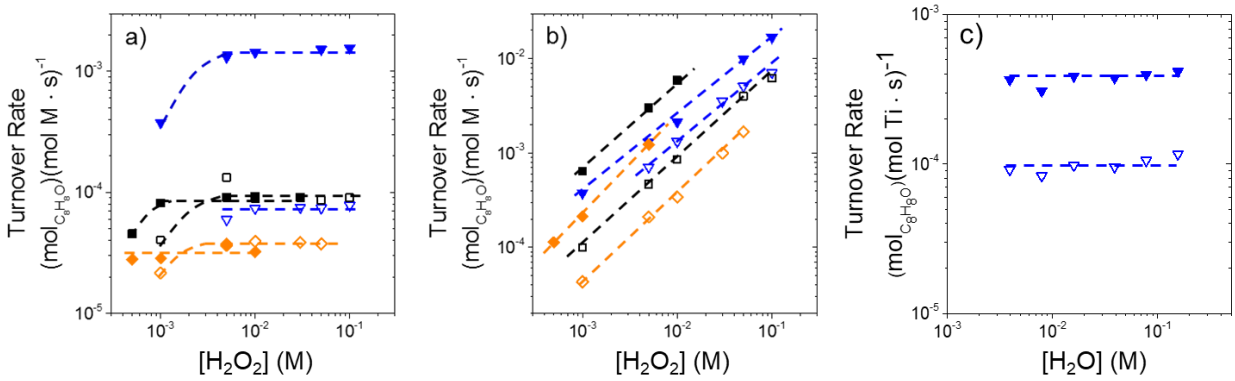

Figure D12. Turnover rates for the formation of styrene oxide via primary reaction pathways as a function of [H_2O_2] and [H_2O] for M-BEA (closed symbols) and M-SiO_2 (open symbols) at (a) 3 mM C_8H_8 (in CH_3CN, 313 K), (b) 0.5 M C_8H_8 (in CH_3CN, 313 K), and (c) 3 mM C_8H_8, 10 mM H_2O_2 (in CH_3CN, 313 K). Symbols and colors represent Ti- (▼), Nb- (■) and Ta- (♦) materials. Dashed lines are intended to guide the eye.

D.3.1. Derivation of Full Rate Expression for C_8H_8 Epoxidation

Scheme 5.2 shows a series of elementary steps that account for the measured effects of [C_8H_8] (Figure 5.5) and [H_2O_2] (Figure D10) on both rates of C_8H_8 epoxidation. The catalytic cycle involves the quasi-equilibrated adsorption of H_2O_2 (step 2),[54, 58, 111] followed by the irreversible activation of H_2O_2 (step 3) to form a pool of M-(η^2-O_2) (Nb and Ta)[54] and M-OOH (Ti)[82, 116-117, 121] active intermediates (referred to collectively as M-(O_2)), which then react with C_8H_8 to form C_8H_8O (step 4), followed by C_8H_8O desorption (step 5) or decompose by reaction with H_2O_2 (step 6). Measured C_8H_8 epoxidation rates represent the kinetically relevant reaction of the active form of the oxidizing surface intermediate with a C_8H_8 molecule:

$$r_E = k_4[M-(O_2)][C_8H_8] \tag{D9}$$

where r_E is the rate of C_6H_{10} epoxidation, [M-(O_2)] is the collective coverage of M-OOH (group 4) and M-(η^2-O_2) (group 5) species, k_x is the rate constant for step x in Scheme 5.2, and [C_8H_8] is

the concentration of C_8H_8. Application of the pseudo-steady state hypothesis to the M-(O_2) intermediates, results in:

$$r_E = \frac{k_3 k_4 K_2 [C_8H_8][H_2O_2][*]}{(k_4[C_8H_8]+k_6[H_2O_2])} \qquad \text{(D10)}$$

where K_x is the equilibrium constant for step x and [*] is the total number of sites occupied by the solvent molecule (i.e., CH_3CN). An expression for [*] is given by the summation of all likely surface-bound intermediates:

$$[L] = [*] + [C_8H_8\,*] + [H_2O_2\,*] + [M-(O_2)] + [C_8H_8O\,*] \qquad \text{(D11)}$$

where [L] is the total number of M atoms, [M-(O_2)] is the pool of M-OOH and M-(η^2-O_2) intermediates, and [C_8H_8*], [H_2O_2*], and [C_8H_8O*] are surface-bound C_8H_8, H_2O_2, and C_8H_8O molecules, respectively. Equation D11 can then be restated in terms of the rate and equilibrium constants, as well as liquid-phase reactant concentrations and unoccupied M atoms by application of the PSSH to each surface specie to yield:

$$[L] = [*] + K_1[C_8H_8][*] + K_2[H_2O_2][*] + \frac{k_3 K_2 [H_2O_2][*]}{(k_4[C_8H_8]+k_6[H_2O_2])} + K_5[C_8H_8O][*] \qquad \text{(D12)}$$

Substitution of equation D12 into D10 yields the full rate expression for $C_6H_{10}O$ formation:

$$\frac{r_E}{[L]} = \frac{\frac{k_3 k_4 K_2 [C_8H_8][H_2O_2]}{(k_4[C_8H_8]+k_6[H_2O_2])}}{1+K_1[C_8H_8]+K_2[H_2O_2]+\frac{k_3 K_2 [H_2O_2]}{(k_4[C_8H_8]+k_6[H_2O_2])}+K_5[C_8H_8O]} \qquad \text{(D13)}$$

which is consistent with equation 5.2 from the main text.

Table D4. Calculated ratios of $k_4[C_8H_8]:k_6[H_2O_2]$ using interpolated values from Figure 5.5 and H_2O_2 decomposition rates at conditions that result in a C_8H_8O MARI (i.e., 0.5 M $[C_8H_8]$ and values of $[H_2O_2]$ used in Figure 5.5).

Sample	$k_4[C_8H_8]:k_6[H_2O_2]$
Ti-BEA	6.7
Nb-BEA	5.2
Ta-BEA	6.0
Ti-SiO_2	5.0
Nb-SiO_2	12.7
Ta-SiO_2	120.2

D.3.2. Transition State Theory for Measurement of Activation Enthalpies and Entropies

Transition state theory (TST) is used to relate the stability of the reference state (e.g., the M-(O_2) intermediates) to an activated complex that leads to reaction (i.e., the transition state).[54, 110, 136] TST, when combined with our proposed mechanism (Scheme 5.2), proposes that the reactant species (i.e., M-(O_2), H_2O_2, and C_8H_8) exist in equilibrium with the transition state to yield:

$$\frac{r_E}{[L]} = \frac{k_B T}{h} K_E^{\ddagger}[C_8H_8] \tag{D14}$$

$$\frac{r_E}{[L]} = \frac{k_B T}{h} K_D^{\ddagger}[H_2O_2] \tag{D15}$$

where k_B is Boltzmann's constant, h is Planck's constant, T is the temperature in Kelvin, $K_E^{\ddagger}$ and $K_D^{\ddagger}$ are the Transition state equilibrium constants for epoxidation and H_2O_2 decomposition, respectively, and $[C_8H_8]$ is the concentration of C_8H_8. Values of $K_E^{\ddagger}$ and $K_D^{\ddagger}$ may be expressed in terms of changes in Gibbs free energy, via the Eyring equation, to result in:

$$K_x^{\ddagger} = e^{-\Delta G_x^{\ddagger}/RT} = e^{-\Delta H_x^{\ddagger}/RT} e^{\Delta S_x^{\ddagger}/R} \tag{D16}$$

where R is the ideal gas constant and $\Delta G^{\ddagger}$, $\Delta H^{\ddagger}$, and $\Delta S^{\ddagger}$ is the Gibb's free energy, enthalpy, and entropy of activation, respectively. Figure D11 shows measured values for $K_E^{\ddagger}$ and $K_D^{\ddagger}$ as a function of inverse temperature for all M-BEA and M-SiO_2.

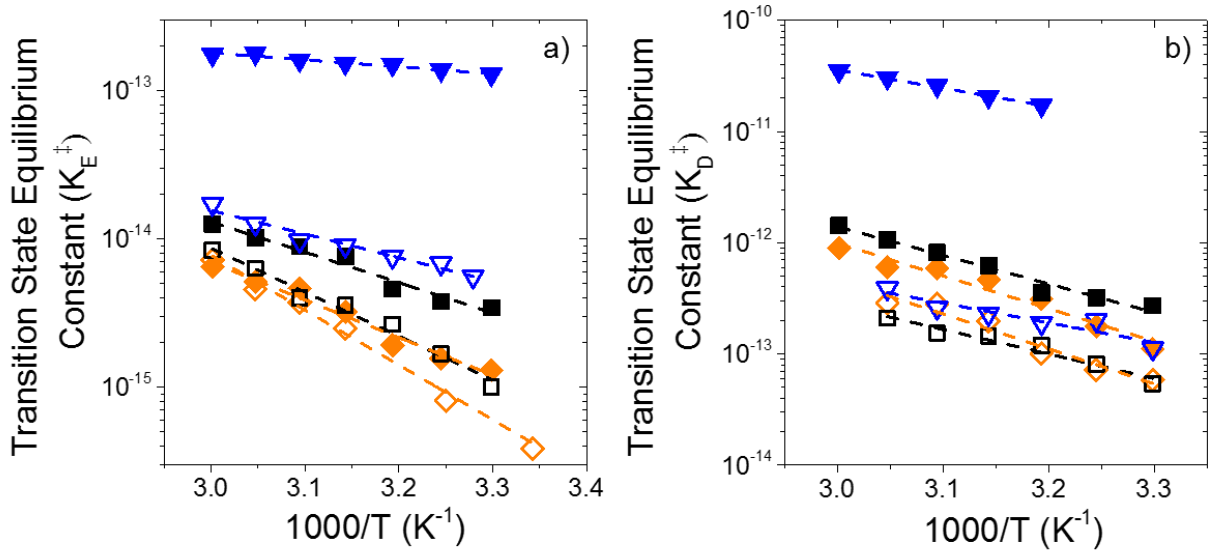

Figure D13. Transition state equilibrium constants for (a) C_8H_8 epoxidation ($K_E^{\ddagger}$) and (b) H_2O_2 decomposition ($K_D^{\ddagger}$) as functions of inverse temperature on M-BEA (closed symbols) and M-SiO_2 (open symbols). Reactions conditions: Ti-BEA (3 mM C_8H_8, 0.01 M H_2O_2), Nb-BEA (3 mM C_8H_8, 1 mM H_2O_2), Ta-BEA (3 mM, 1 mM H_2O_2), Ti-SiO_2 (3 mM C_8H_8, 0.01 M H_2O_2), Nb-SiO_2 (3 mM C_8H_8, 0.01 M H_2O_2), and Ta-SiO_2 (3 mM C_8H_8, 0.01 M H_2O_2). Symbols and colors represent Ti- (blue ▼), Nb- (black ■) and Ta- (orange ♦) materials. Error bars were omitted for clarity. In all reported data, error was <7%. Dashed lines represent fits to the Eyring equation (equation D16) whose slopes and intercepts are proportional to $\Delta H^{\ddagger}$ and $\Delta S^{\ddagger}$, respectively.

D.4. Calculated Reaction Constants for the Epoxidation of *Para*-substituted Styrene

Table D5. Reaction Constants (ρ) for the Epoxidation of x-C_8H_7 (x = -NO_2, -Br, -H, -Me, or -OMe) on M-BEA and M-SiO_2 Materials at Standard Reaction Conditions ((3 mM x-C_8H_8, 0.01 M H_2O_2, in CH_3CN, 313 K). Values of ρ Represent Least Squares Regression Fits of the Hammett Equation (Equation 5.8) to Figure 5.9.

Sample	Reaction constant (ρ)
Ti-BEA	-0.83
Nb-BEA	-0.80
Ta-BEA	-0.89
Ti-SiO_2	-0.91
Nb-SiO_2	-0.98
Ta-SiO_2	-0.93

APPENDIX E

Supplementary Information and Data for Chapter Six

E.1. Characterization of Ti-BEA, Ti-SiO_2, and TS-1

E.1.1. X-ray Diffraction of Ti-BEA and TS-1

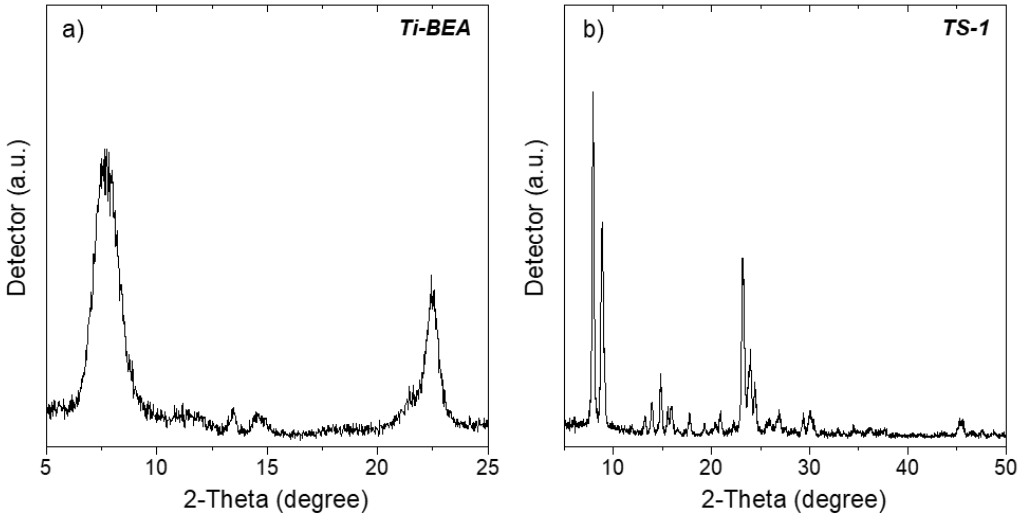

Figure E1. X-ray diffractograms of (a) Ti-BEA and (b) TS-1.

Figure E1 shows X-ray diffractograms for Ti-BEA and TS-1, which indicate that these materials contain diffraction features characteristic of the BEA and MFI zeolite frameworks, respectively.

E1.2 Diffuse Reflectance UV-vis of Ti-BEA, Ti-SiO_2, and TS-1

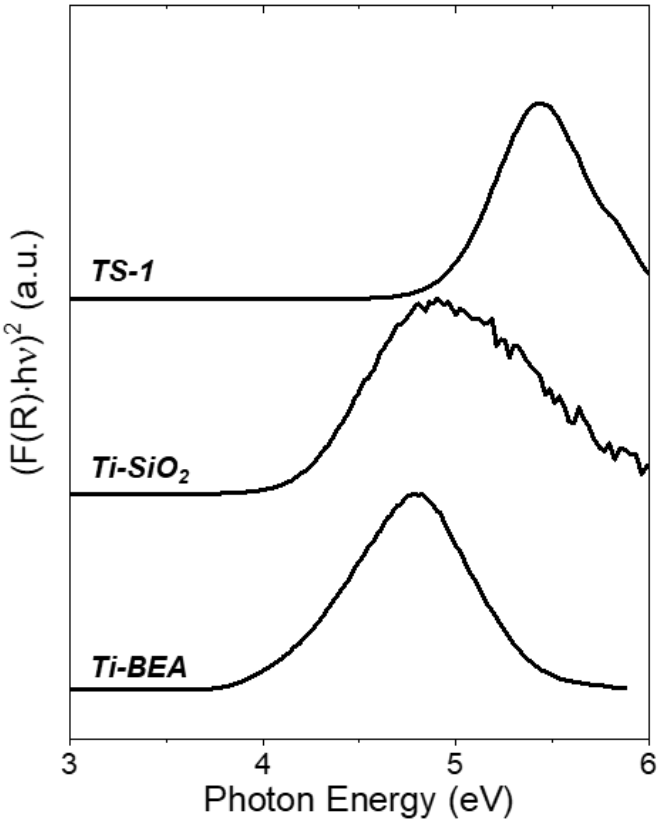

Figure E2. Tauc plots for Ti-BEA, Ti-SiO_2, and TS-1. Note that F(R) corresponds to the Kubelka-Munk pseudo-absorbance. All spectra were normalized to the most-intense feature and are vertically offset for clarity.

E.2. M-FAU Characterization

E.2.1. X-Ray Diffraction to Show Changes in Lattice Spacing

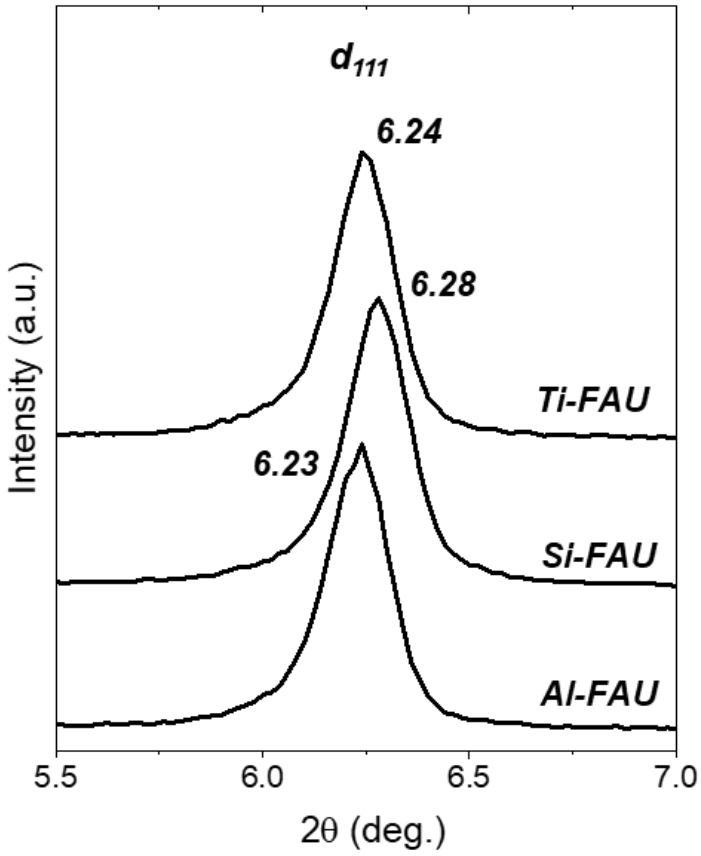

Figure E3. X-ray diffractograms for Al-, Si-, and Ti-FAU. Diffractograms are vertically offset for clarity.

E.2.2. Nitrogen Volumetric Adsorption to Show Isotherm Type

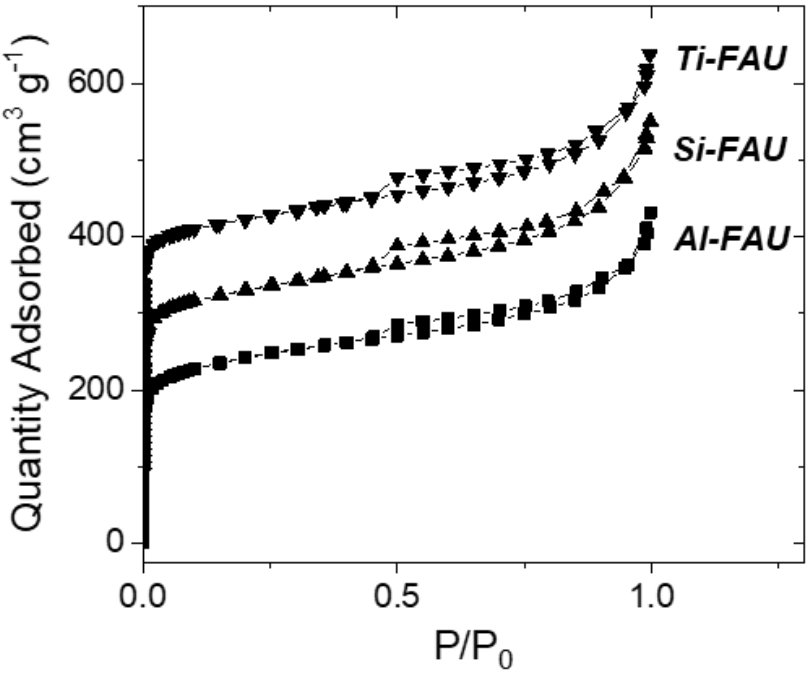

Figure E4. Nitrogen adsorption isotherms (77 K) for Al-, Si-, and Ti-FAU. Adsorption isotherms are offset for clarity.

E.2.3. ^{29}Si MAS-NMR Spectra to Visualize Q^4 Features

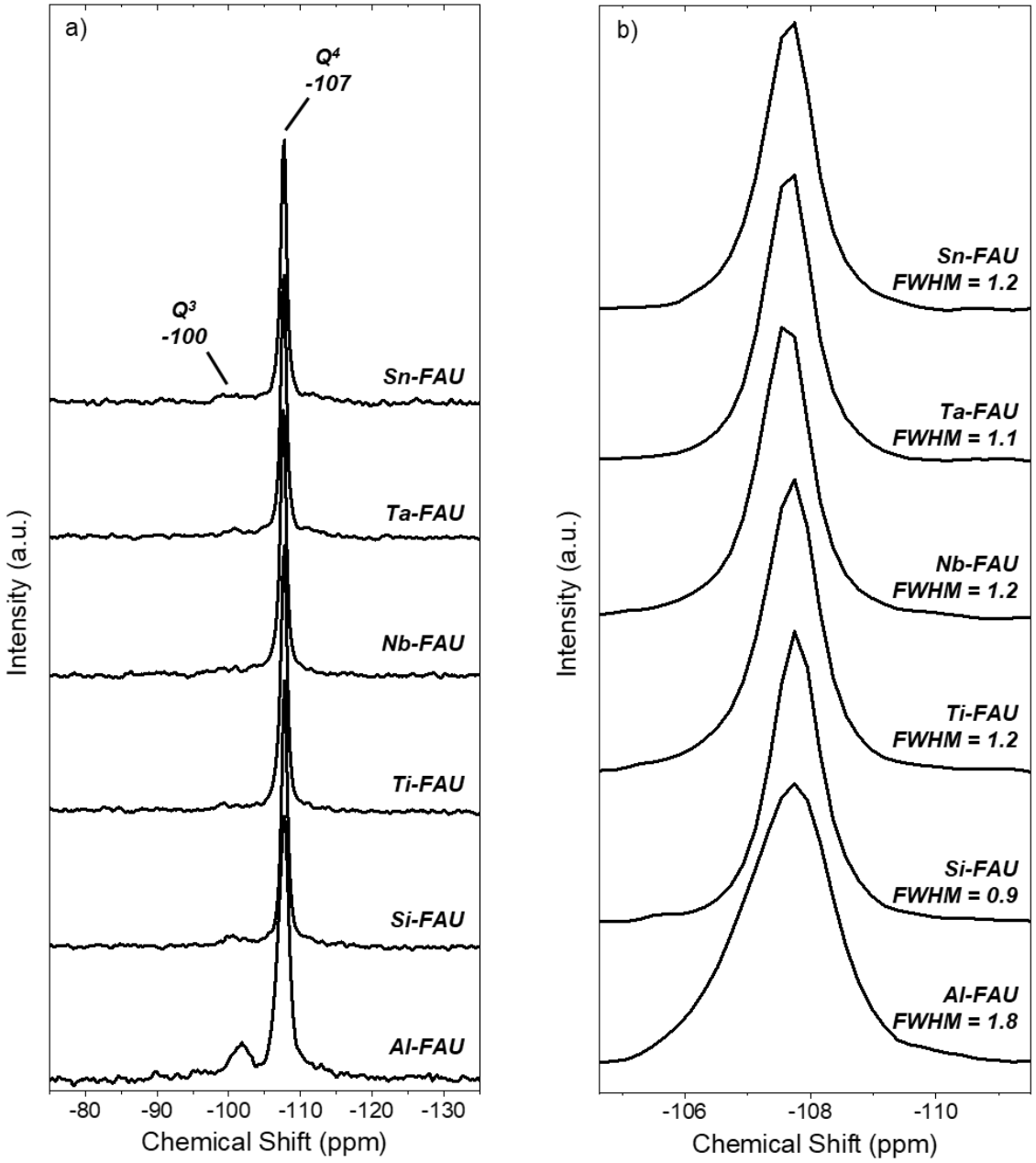

Figure E5. (a) ^{29}Si direct polarization MAS-NMR spectra of Al-, Si-, Ti-, Nb-, Ta-, and Sn-FAU. Panel (b) shows changes in the full width-half max (FWHM) of the Q^4 features within each M-FAU. All spectra are normalized to the Q^4 feature and are offset for clarity.

E.3. Peak Fitting Procedures

E.3.1. ^{29}Si MAS-NMR of Si-FAU Example Peak Fitting

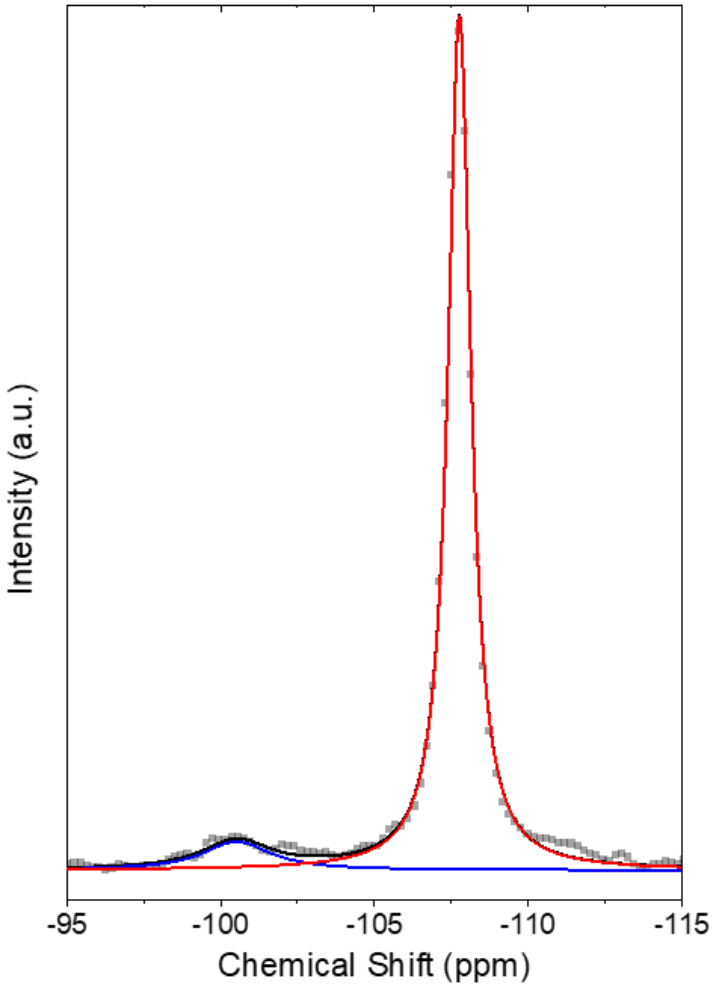

Figure E6. Example peak fitting procedure for ^{29}Si MAS-NMR spectra (gray ■) of Si-FAU. The red curve represents NMR features attributed to Q^4 sites, while the blue curve represents those belonging to Q^3 sites; the black curve is the cumulative fit. In all cases, Lorentzian curves were used for the fitting procedure. Values of ϕ_{NMR} were estimated by dividing the area under the blue curve to that of the black curve.

E.3.2. Infrared Spectroscopy of Dehydrated Si-FAU Example Peak Fitting

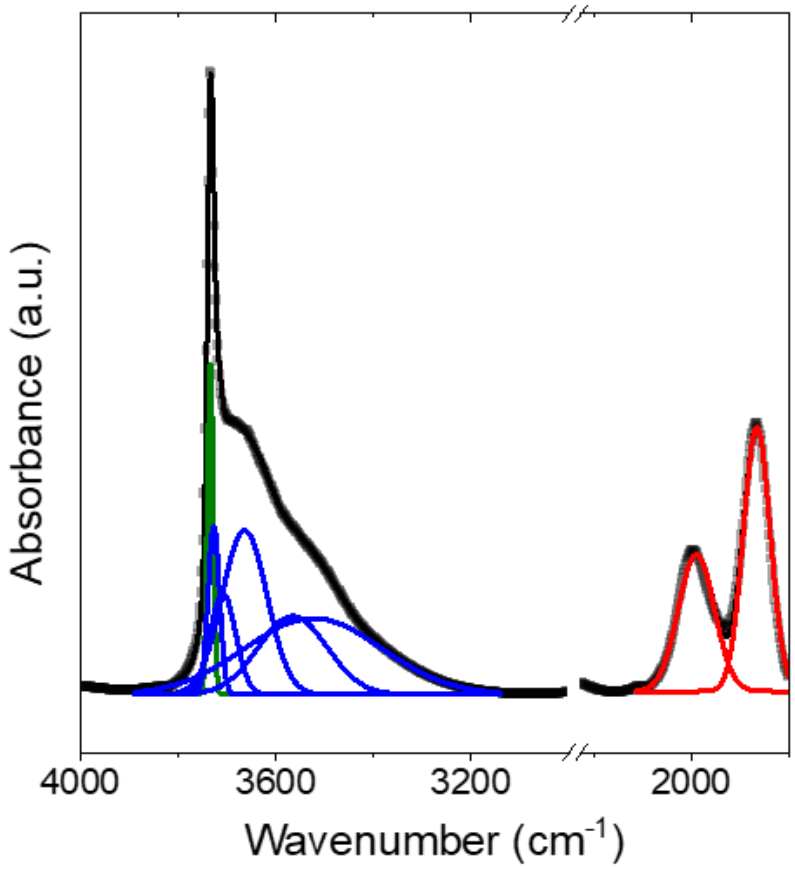

Figure E7. Infrared spectra (gray ■) of dehydrated Si-FAU (573 K, He). Gaussian curves were used to fit the data in all cases. The green curve represents ν(O-H) of isolated SiOH, the blue curves are ν(O-H) resulting from hydrogen-bonded SiOH (e.g., $(SiOH)_4$), and red curves represent ν(Si-O-Si) overtone stretches. The black curves represent cumulative fits.

Six gaussian curves were chosen to fit the infrared spectra of M-FAU in order to capture the proper curvature and yield a R^2 value >0.995. Fitting procedures using three-to-five gaussian curves yielded nearly identical values of ϕ_{IR}.

E.4. Epoxidation of 2,4-dimethylstyrene

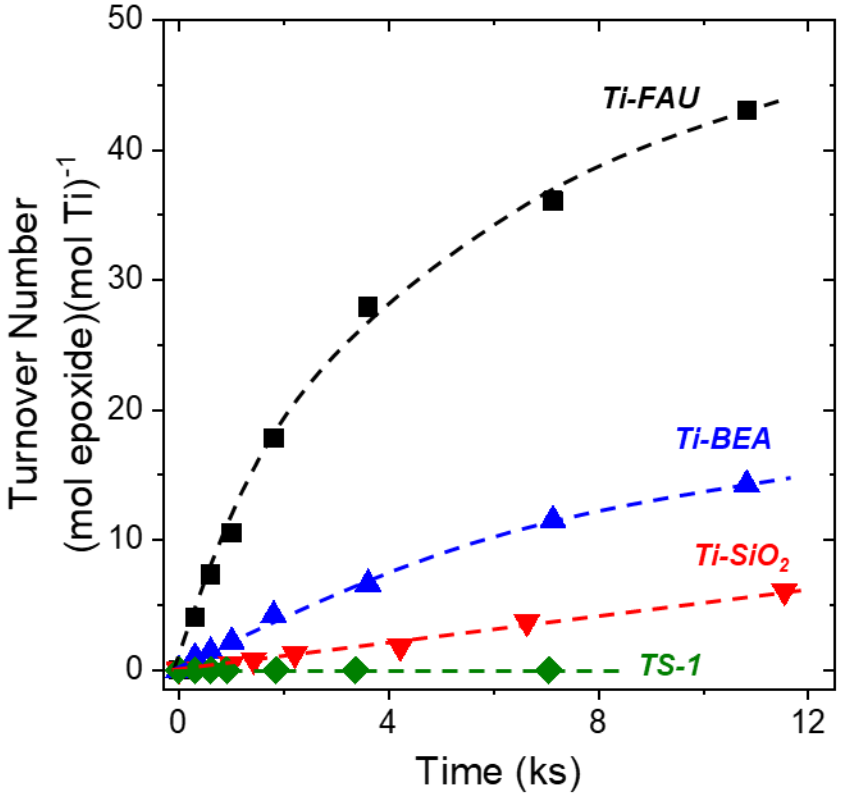

Figure E8. Turnover numbers as a function of time for the epoxidation of 2,4-dimethylstyrene (0.1 M 2,4-dimethylstyrene, 0.1 M H_2O_2, in CH_3CN, 313 K) over Ti-FAU (■), Ti-BEA (▲), Ti-SiO_2 (▼), and TS-1 (♦). Dashed curves are intended to guide the eye.

Figure E8 shows the turnover numbers for 2,4-dimethylstyrene epoxidation over Ti-FAU, Ti-BEA, Ti-SiO_2, and TS-1. Turnover numbers (and rates) for 2,4-dimethylstyrene epoxidation are greatest within Ti-FAU and decrease in the order Ti-BEA, Ti-SiO_2, and TS-1. Notably, rates of 2,4-dimethylstyrene epoxidation are immeasurable on TS-1 because TS-1 possesses pores that are 0.55 nm in diameter, which is smaller than the kinetic diameter of 2,4-dimethylstyrene (e.g., *m*-xylene has a kinetic diameter of 0.68 nm),[385] which precludes the diffusion and reaction of 2,4-dimethylstyrene within the MFI framework. The increased turnover numbers for 2,4-dimethylstyrene oxide formation within Ti-FAU relates to the increased entropic freedom of the transition state for epoxidation within Ti-FAU compared to Ti-BEA, with the increased enthalpic stabilization relative to Ti-SiO_2.

APPENDIX F

Supplementary Information and Data for Chapter Seven

F.1. Additional Catalyst Characterization

F.1.1. Catalyst Characterization

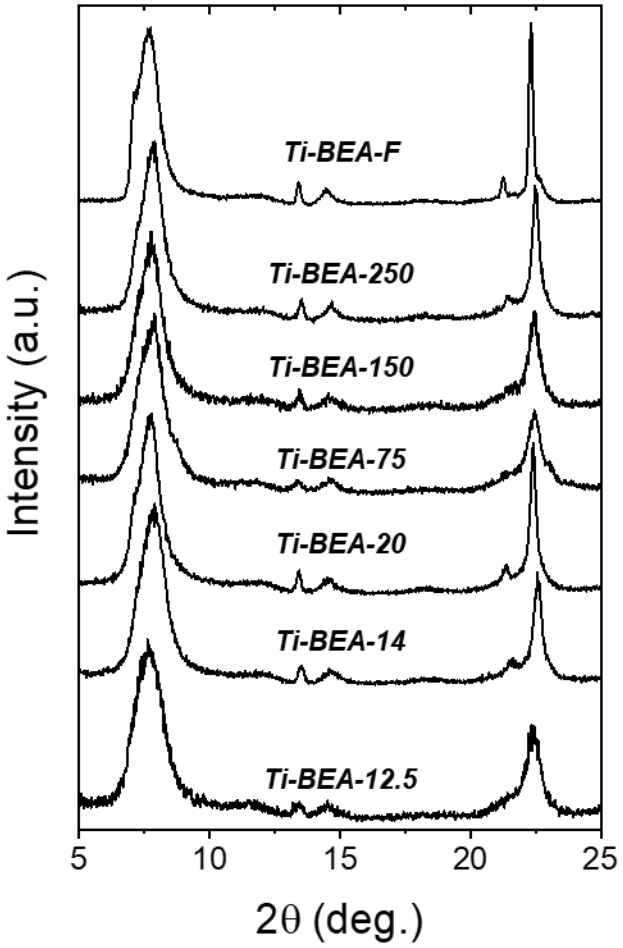

Figure F1. X-ray diffractograms for all Ti-BEA used within this study. Diffractograms are vertically offset for clarity.

Figure F1 shows X-ray diffractograms for all Ti-BEA contain distinct crystallographic features that are indicative of the *BEA framework. Notably, the sharpness in the ~22.4 degree XRD feature for Ti-BEA-F is indicative of a high-degree of crystallinity, which is expected for Ti-BEA that is synthesized in fluoride media. All other Ti-BEA contain broader features that are indicative of internal defects that form upon dealumination and synthesis in hydroxide media.

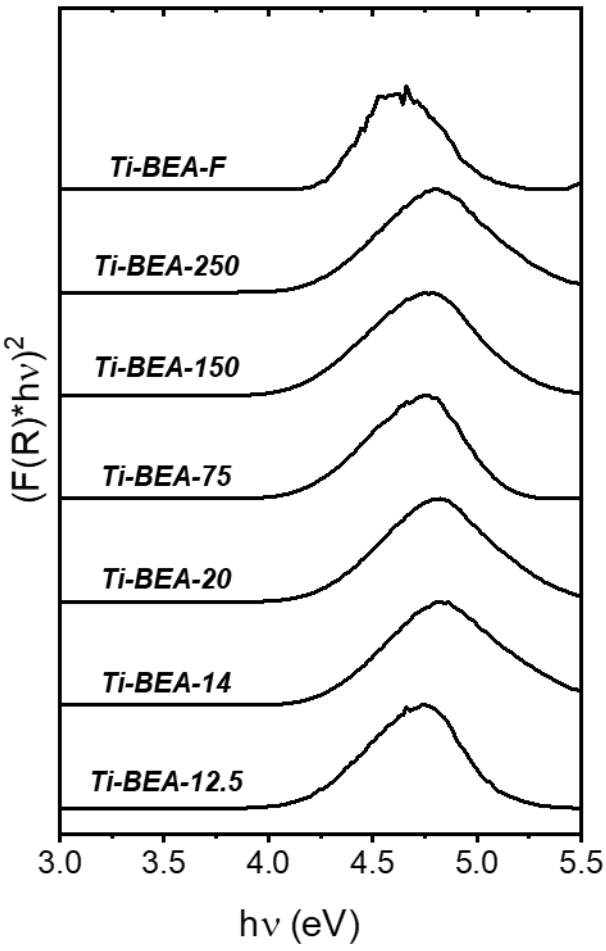

Figure F2. Tauc plots for all Ti-BEA used within this study. Diffuse-reflectance UV-vis spectra were collected under ambient conditions (~298 K). Ti-BEA were dehydrated in flowing air (100 cm^{-1} min^{-1}) for 6 h at 823 K prior to measurement. Tauc plots are normalized to the intensity of the feature at ~4.6 eV and are vertically offset for clarity.

Figure F2 shows that all Ti-BEA used within this study contain a single UV-vis absorbance feature around 4.6 eV. The leading edge (~4.2 – 4.5 eV) was fit using a line to extrapolate the x-intercept, which corresponds to the band gap of the materials. In all cases, the band gap (4.2 – 4.3 eV, Table 7.1) is significantly higher than that of bulk TiO_2 (~3.2 eV), which suggests that all Ti-BEA contain Ti atoms that are highly disperse and does not contain spectroscopically-observable fractions of bulk or oligomeric TiO_2.

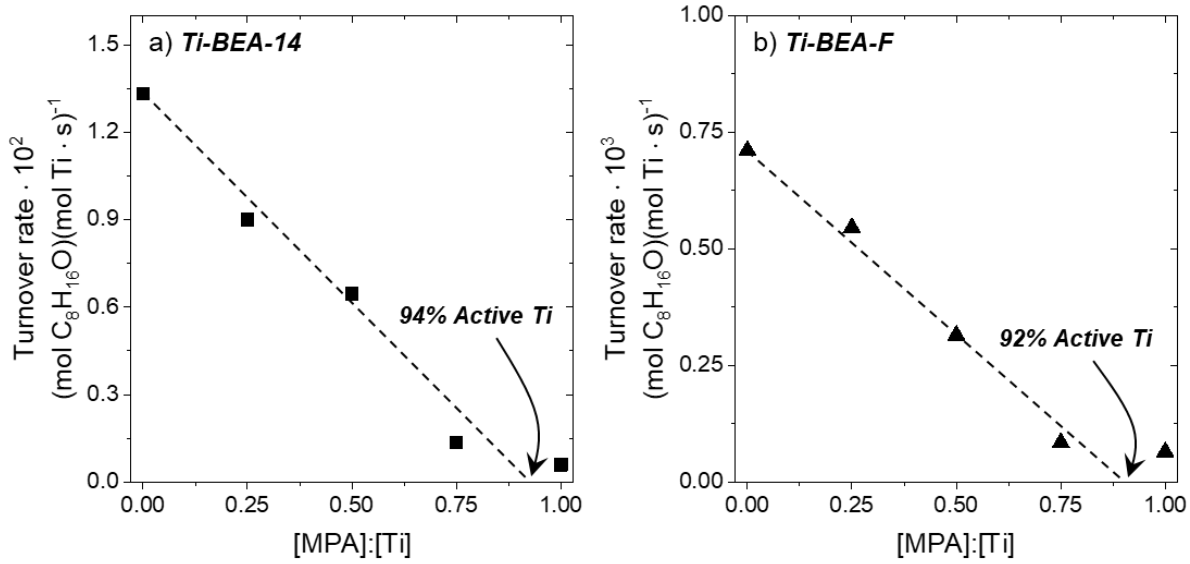

Figure F3. Turnover rates for $C_8H_{16}O$ formation as a function of methylphosphonic acid to Ti ratio ([MPA]:[Ti]; 0.01 M C_8H_{16}, 0.01 M H_2O_2) over (a) Ti-BEA-14 and (b) Ti-BEA-F. The dashed lines represent linear regression fits with the y-intercept set to the turnover rate in the absence of the MPA titrant.

Figure F3 shows representative plots for the turnover rate of C_8H_{16} epoxidation as a function of the ratio of MPA titrant to Ti atoms within Ti-BEA. For all Ti-BEA, the turnover rates for epoxidation decrease linearly with [MPA]:[Ti], which suggests that all active sites are catalytically equivalent within a given Ti-BEA. The x-axis intercept, where the turnover rates are extrapolated to zero is used as the amount of *active* Ti in each Ti-BEA for the epoxidation kinetics in section 7.3.4.

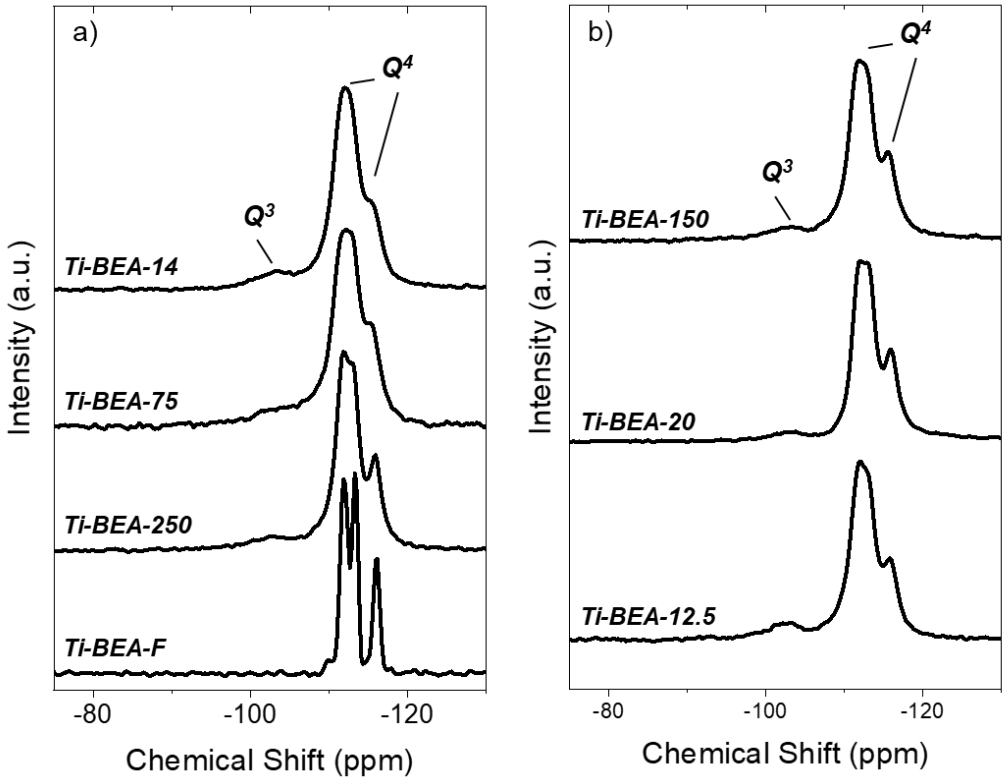

Figure F4. ^{29}Si direct polarization MAS-NMR of (a) Ti-BEA-14, Ti-BEA-75, Ti-BEA-250, and Ti-BEA-F and (b) Ti-BEA-12.5, Ti-BEA-20, and Ti-BEA-150. Spectra were obtained at ambient conditions (~298 K). Ti-BEA-X were dehydrated in flowing air (100 cm^3 min^{-1}) for 6 h at 823 K prior to measurement. Spectra are vertically offset for clarity.

Figure F4 shows ^{29}Si MAS-NMR spectra of all Ti-BEA contain distinct features at at -102 ppm and between 112 and 116 ppm, which correspond to Q^3 (i.e., $Si(OH)(OSi)_3$) and Q^4 (i.e. $Si(OSi)_4$) forms of Si atoms, respectively. The integrated area for the Q^3 sites relative to all ^{29}Si MAS-NMR features yields the fraction of Si atoms that possess a single hydroxyl moiety. The fraction of Q^3 (i.e., Φ_{NMR}) increases with the "hydrophilicity" of the materials. Notably, Ti-BEA-F does not contain any significant fraction of Q^3 sites, as this material was synthesized with the intention of creating a nearly defect-free pore structure. The splitting of the Q^4 sites (e.g., Ti-BEA-F, Ti-BEA-250) is indicative of a highly crystalline material, where this splitting represents contributions from the various crystallographically-distinct Si atoms within the BEA framework.

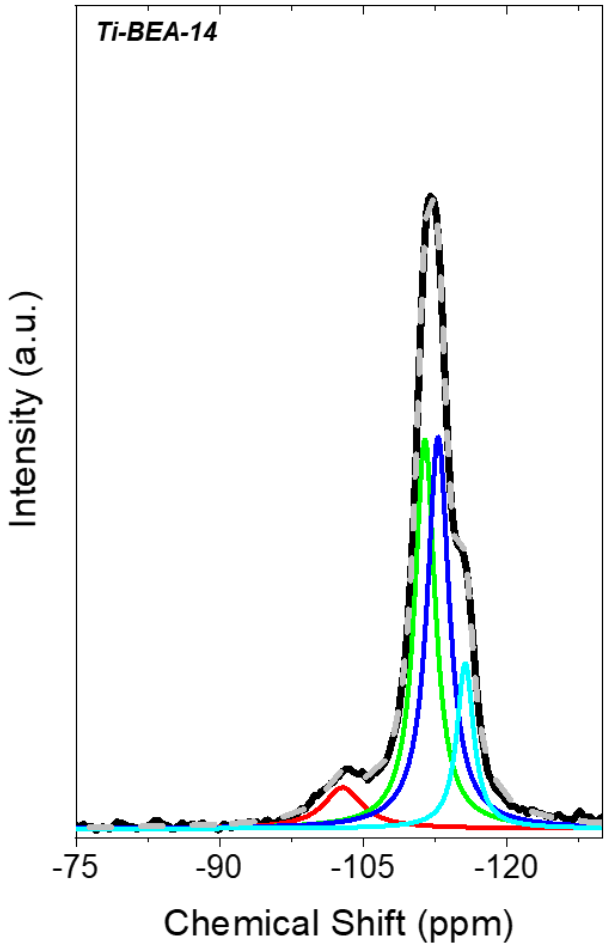

Figure F5. Example peak fitting procedure for ^{29}Si direct polarization MAS-NMR of Ti-BEA-12.5. The red curve represents NMR features attributed to Q^3 sites, while green, blue, and teal curves correspond to Q^4 sites; the gray curve represents the cumulative fit. Lorentzian curves were used for fitting procedure. Φ_{NMR} was estimated by dividing the area under the red curve by that of the gray curve.

Figure F5 shows an example peak-fitting procedure to quantify values of Φ_{NMR}. The red, green, blue, and teal peaks were fit with peak centers constrained at -102, -112, -113, and -116 ppm, based upon literature precedent for Q^3 sites[284-285] and the normal-splitting pattern of Q^4 sites.[386]

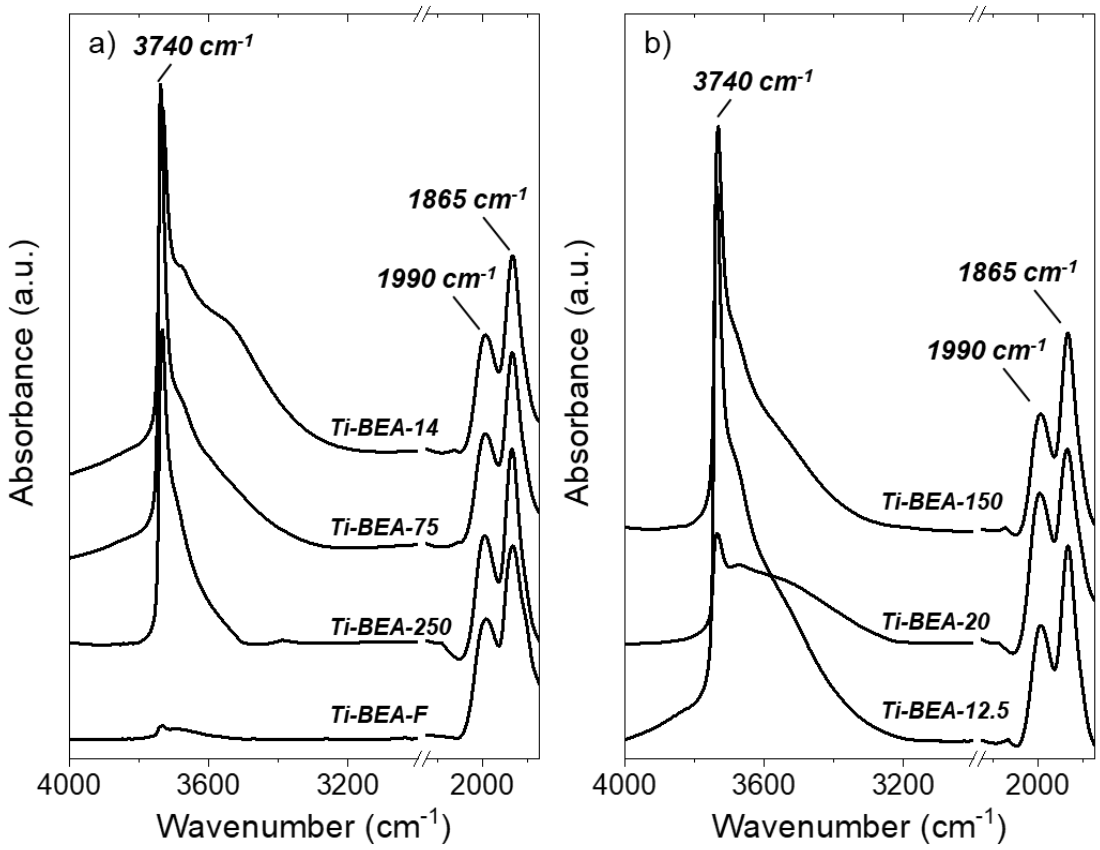

Figure F6. Infrared spectra of dehydrated (a) Ti-BEA-14, Ti-BEA-75, Ti-BEA-250, and Ti-BEA-F, and (b) Ti-BEA-12.5, Ti-BEA-20, and Ti-BEA-150. All Ti-BEA were dehydrated *in situ* under flowing He (50 cm^3 min^{-1}) for >2 h at 573 K prior to measurement. All spectra were normalized to an absorbance feature at 1865 cm^{-1} corresponding to ν(Si-O-Si) overtones (1865 and 1990 cm^{-1}), which is used as an internal standard for comparisons between the density of SiOH groups among Ti-BEA samples. Spectra are vertically offset for clarity.

Figure F6 shows the ν(O-H) and ν(Si-O-Si) overtone region of the infrared spectra of dehydrated Ti-BEA. The sharp absorbance feature at ~3740 cm^{-1} corresponds to isolated SiOH species that are not interacting via H-bonding with nearby H-bond donors or acceptors (i.e., other SiOH). The broadening within the ν(O-H) region is due to the H-bonding interactions of SiOH with other SiOH (i.e., $(SiOH)_4$) that cause a red shift in these vibrational modes.

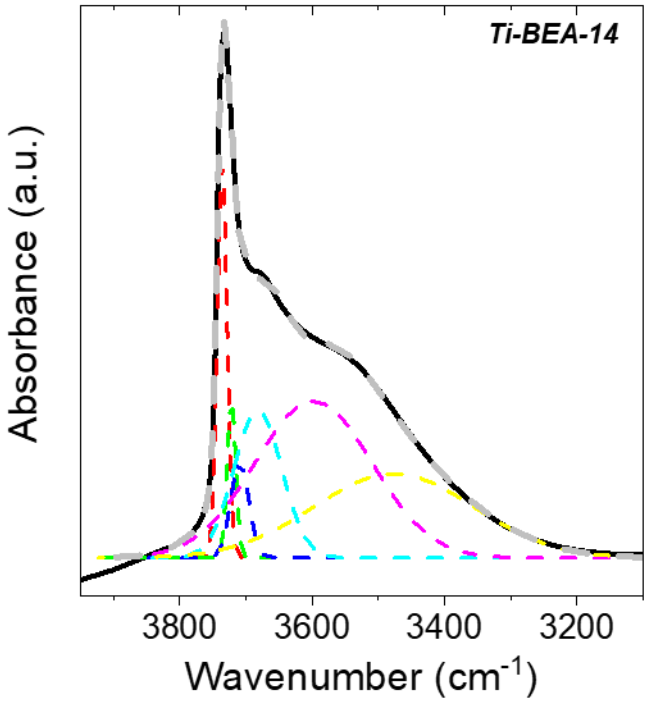

Figure F7. Infrared spectra of dehydrated Ti-BEA-14 that was treated in flowing He (50 cm^3 min^{-1}) for >2 h at 573 K prior to measurement. Gaussian curves were fit to the infrared spectra. Gray dashed curve represents cumulative fit of the six colored curves.

Six gaussian curves were chosen to peak fit the infrared spectra of dehydrated Ti-BEA so as to capture the curvature of the spectra and yield a R^2 value >0.995. Peak fits using three, four, and five curves were attempted and gave nearly identical results (i.e., values of Φ_{IR}). As such, six curves were chosen to fit all Ti-BEA to calculate values of Φ_{IR} (Table 7.1) and gave R^2 >0.995 in all cases.

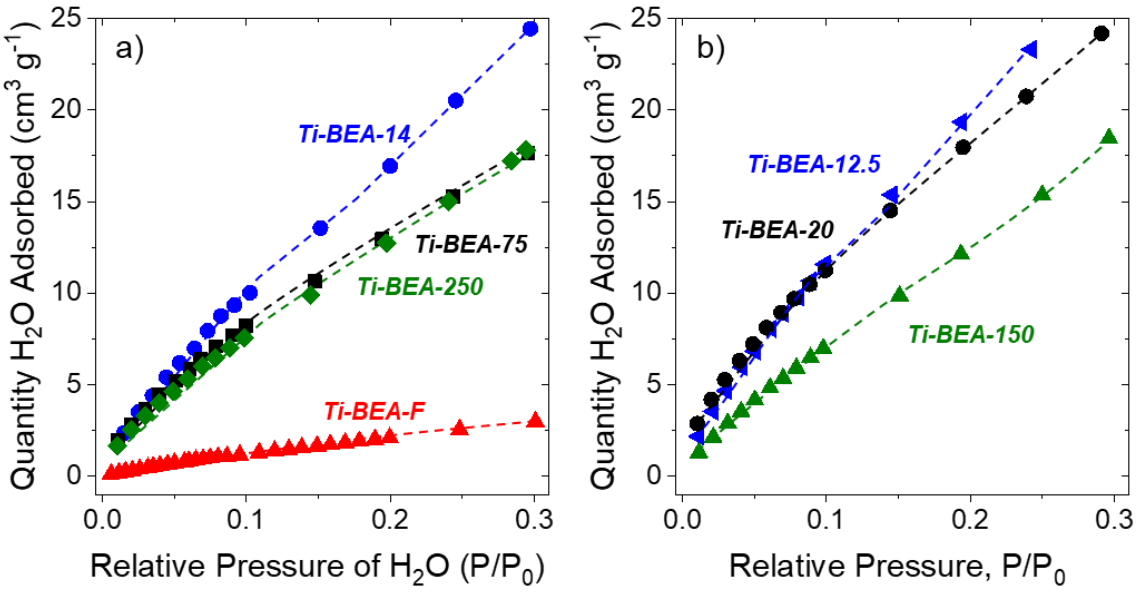

Figure F8. H_2O adsorption isotherms for (a) Ti-BEA-14 (●), Ti-BEA-75 (■), Ti-BEA-250 (♦), and Ti-BEA-F (▲) and (b) Ti-BEA-12.5 (◀), Ti-BEA-20 (●), and Ti-BEA-150 (▲) at 293 K. All Ti-BEA were degassed under vacuum ($<7 \cdot 10^{-4}$ kPa, 673 K) for 6 h prior to measurement. Dashed curves are intended to guide the eye.

Figure F8 shows H_2O uptake within Ti-BEA-F is much lower than all Ti-BEA synthesized by post-synthetic modification for $P/P_0 < 0.3$. This is because SiOH and $(SiOH)_4$ nucleate H_2O cluster formation, which precludes measurable differences in the uptake of H_2O among Ti-BEA that contain significant amounts of $(SiOH)_4$ (i.e., those synthesized by post-synthetic modification).

F.2. Adsorption of CD_3CN onto Lewis Acidic Ti atoms, SiOH sites, and Pore Walls

F.2.1. Peak Fitting of Infrared Spectra of CD_3CN Adsorbed to Ti-BEA-12.5 and van't Hoff Analysis

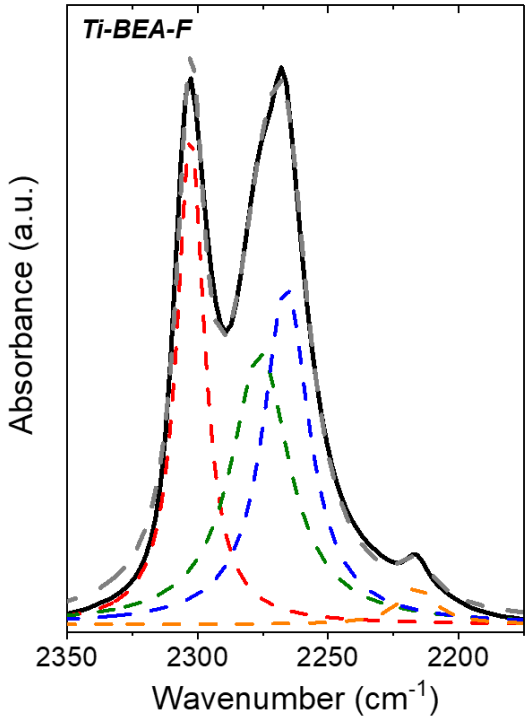

Figure F9. Example peak fitting of infrared spectra of CD_3CN adsorbed on Ti-BEA-F (2.4 kPa CD_3CN, 50 cm^3 min^{-1} He, 387 K). Color key: $\nu(C{\equiv}N)$ of CD_3CN coordinated to Ti atoms (red), SiOH atoms (green), and *BEA pore walls (blue); $\nu_{as}(CD_3)$ (orange); cumulative fit (gray). Lorentzian curves were used for the fitting procedure.

Figure F9 shows a representative peak-fitting procedure used to determine the areas of $\nu(C{\equiv}N)$ for CD_3CN bound to different types of adsorption sites (i.e., Ti, SiOH, and *BEA pore walls). Lorentzian curves were chosen, because gaussian fits (i.e., those used for Φ_{IR} analysis) did not yield R^2 values >0.98 when fitting the data. When fitting subsequent spectra (e.g., during the CD_3CN adsorption isotherm or isobar) the peak centers were fixed at 2302, 2274, 2263, and 2215 cm^{-1} for $\nu(C{\equiv}N)$ of CD_3CN coordinated to Ti atoms, SiOH atoms, and *BEA pore walls, and $\nu_{as}(CD_3)$, respectively.

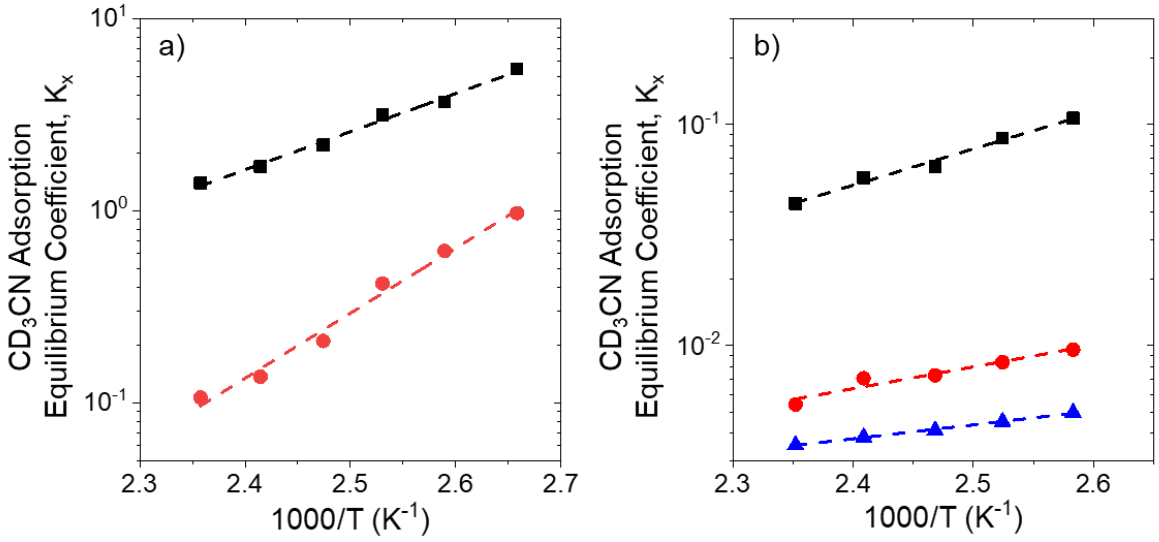

Figure F10. Equilibrium constants for the adsorption of CD_3CN to Ti atoms (■; ~2302 cm^{-1}), SiOH groups (●; ~2274 cm^{-1}), and *BEA pore walls (▲; ~2263 cm^{-1}) as a function of inverse temperature for (a) Ti-BEA-12.5, and for (b) Ti-BEA-F (0.46 kPa CD_3CN, ~101 kPa He, 373 – 423 K). Dashed lines represent fits of equation 7.6, whose slope and intercept are proportional to $\Delta H_{CD_3CN,x}$ and $\Delta S_{CD_3CN,x}$, respectively.

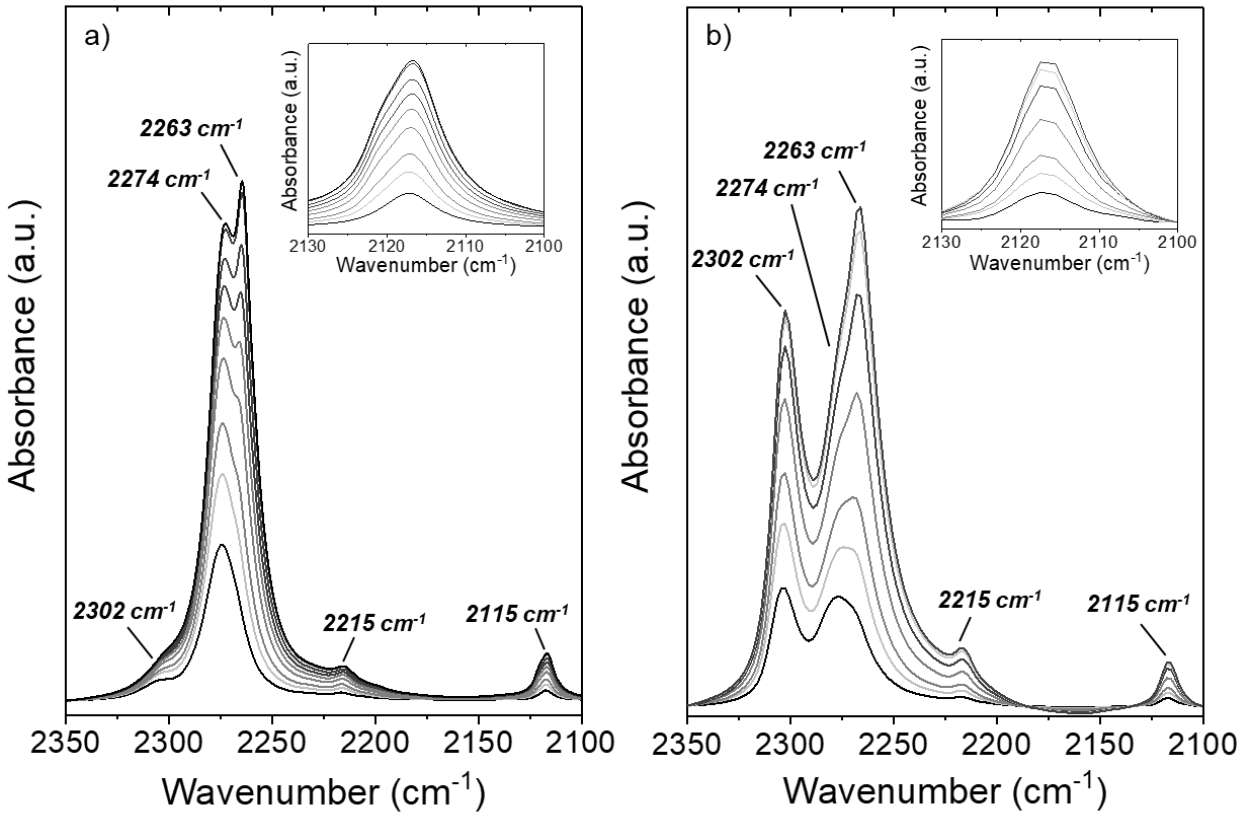

Figure F11. Infrared spectra of equilibrium coverages of adsorbed CD_3CN on (a) Ti-BEA-12.5 (0.46 – 6.95 kPa CD_3CN, 346 K), and (b) Ti-BEA-F (0.46 – 5.03 kPa CD_3CN, 387 K). The inset shows zoomed-in regions to clearly observe $\nu_s(CD_3)$.

Figure F11 shows infrared spectra of Ti-BEA-12.5 and Ti-BEA-F obtained *in situ* while contacting the catalysts with He streams containing CD_3CN. The insets of Figure F11 shows a zoomed-in region to clearly observe $\nu_s(CD_3)$, where there is clearly an overlapping feature that is blue shifted (i.e., to higher wavenumbers) on Ti-BEA-12.5 with increasing partial pressure of CD_3CN. The $\nu_s(CD_3)$ region on Ti-BEA-F, however, appears to be symmetric at all partial pressures of CD_3CN. Ti-BEA-12.5 contains silanols predominantly in the form of $(SiOH)_4$, which Ti-BEA-F contains silanols that are most-likely isolated and formed stochastically during crystallization. This suggests that as the partial pressure of CD_3CN is increased and the coverage over $(SiOH)_4$ on Ti-BEA-12.5 is increased, $\nu_s(CD_3)$ blue shifts as a result of the interaction between CD_3CN and $(SiOH)_4$. The interaction of the $-CD_3$ moiety with a Lewis basic function is known to cause a blue shift in $\delta_s(-CD_3)$,[314] while the interaction between a Lewis acid and the nitrile function (e.g., $Ti–NCCD_3$) does

not affect ν_s(-CD_3).[387] This suggests that the electropositive end of CD_3CN (i.e., -CD_3) is surrounded by an electronegative environment (e.g., interactions with the silanol nest).

F.2.2. Adsorption Entropies Estimated by Campbell *et al.'s* Model

Adsorption onto solid surfaces result in losses of entropy with respect to the gas-phase species, which primarily correspond to losses in translational and rotational forms of entropy. Campbell et al. have shown that the standard state entropies of adsorbed species ($S^0_{ads}(T)$) can be estimated to be proportional to the entropy of the gas-phase molecule[315] ($S^0_{gas}(T)$) by the relationship

$$S^0_{ads}(T) = 0.7 \cdot S^0_{gas}(T) - 3.3 \cdot R \quad \text{(F1)}$$

where T is the absolute temperature and R is the ideal gas constant. The standard entropy of gaseous CD_3CN at 350 K is near 257 J mol^{-1} K^{-1} (approximated from tabulated data for CH_3CN),[388] which suggests an entropic loss upon adsorption of ~114 J mol^{-1} K^{-1} based on equation S7 and the difference between values of $S^0_{gas}(T)$ and $S^0_{ads}(T)$. This estimate further suggests that the measured loss of entropy due to adsorption of CD_3CN onto $(SiOH)_4$ within Ti-BEA-12.5 (-150 ± 10 J mol^{-1} K^{-1}, Table 7.3) must result from additional interactions between CD_3CN and $(SiOH)_4$ that further constrain motion of this molecule upon adsorption to $(SiOH)_4$ nests.[315]

F.2.3. Partition Functions and Entropy Estimates for CD_3CN Molecules Bound to Ti and $(SiOH)_4$ Sites.

The two main contributors of vibrational entropy for CD_3CN molecules bound to Lewis acidic Ti atoms sites and $(SiOH)_4$ groups are frustrated translational and hindered rotational modes. The partition function used to describe frustrated translation ($q_{F,trans}$) for a bound surface species is given by

$$q_{F,trans} = \frac{e^{\left(\frac{-h\nu_{trans}}{2k_BT}\right)}}{1-e^{\left(\frac{-h\nu_{trans}}{2k_BT}\right)}} \quad \text{(F2)}$$

where h and k_B are Planck's and Boltzmann's constants, respectively, and ν_{trans} is the frequency for the frustrated translational vibration of the adsorbate,[389] which is modelled as a harmonic oscillation. The frequency of the vibration is calculated using
the relathionship

$$\nu_{trans} = \left(\frac{E_d}{2md_m{}^2}\right)^{1/2} \quad \text{(F3)}$$

where the depth of the potential (E_d) is taken to be the difference in enthalpy between CD_3CN at the adsorption site (i.e., Ti atom or $(SiOH)_4$ group) and CD_3CN physisorbed to the pore wall. This treatment provides a lower bound for the barrier to move CD_3CN from one site to the pore wall and subsequently to a distinct Ti atom or $(SiOH)_4$ group. The distance between sites (d_m; i.e., width of the energy well for frustrated translational movement) is approximated here as 4 Å and 1 Å for Lewis acidic Ti sites for SiOH sites, respectively). The mass (m) is that of the coordinated complex.

The two-dimensional hindered rotation partition function ($q_{H,rot}$) describes the rotation of a quasi-linear adsorbate (e.g., CD_3CN bound to Ti atoms) that resembles a cone in three-dimensional space.[390] This motion is represented by

$$q_{H,rot} = \left(\frac{4\pi^2 k_B T I_r}{\sigma^2 h^2}\right)^{1/2} e^{\left(\frac{-V_0}{2k_B T}\right)} J_0\left(\frac{iV_0}{2k_B T}\right) \quad \text{(F4)}$$

where σ is the periodicity of hindered rotation, assumed to be 40 degrees, I_r is the moment of rotational inertia

$$I_r = \sum_{i=1}^{l} m_i r_i^2 \quad \text{(F5)}$$

reflected by the mass (m_i) and distance (r_i) of each atom (i.e., N, C, and D; estimated from structural properties of CH_3CN)[391-392] from the center of rotation (i.e., the N atom), V_o is the rotational barrier height

$$V_0 = \frac{8\pi^2 \nu^2 I_r}{\sigma^2} \quad \text{(F6)}$$

where the vibrational frequency (ν) between the two adsorbing atoms (i.e., N and Ti; was estimated as 180 cm^{-1} based upon infrared spectra of CH_3CN bound to various transition-metal complexes),[393] and $J_0(x)$ is the Bessel's function of the first kind. The N atoms was chosen as the center of rotation in equation F5 to avoid overestimating the entropic contributions from hindered rotation that may overlap with frustrated translation. Partition functions describing both frustrated translational and hindered rotational modes (q_x) are related to entropies (S_x) by the Sackur-Tetrode equation[389]

$$S_x = Rln(q_x) + RT\left[\frac{\partial \ln(q_x)}{\partial T}\right] \quad \text{(F7)}$$

where x denotes the specific vibrational mode.

Equations F2, F4, and F7 allow for estimation of the entropic contributions resulting from frustrated translation and hindered rotation of CD_3CN molecules adsorbed on Ti and $(SiOH)_4$ sites. CD_3CN bound to $(SiOH)_4$ possess negligible contributions from hindered rotation, as these adsorption into these SiOH nests results in the loss of all three-dimensions of rotational entropy. Therefore, adsorption of CD_3CN onto $(SiOH)_4$ and Ti active sites (shown visually in Figure F12) are contain vibrational modes derived from frustrated translation, while the latter contains also contributions from hindered rotation. The entropies for CD_3CN bound to Ti and $(SiOH)_4$ sites (Table 7.1) are estimated, using the above analysis, to be 95 and 29 J mol^{-1} K^{-1}, respectively.

Table F1. Entropy Estimates for CD_3CN bound to $(SiOH)_4$ and Ti atoms at 350 K.

AdsorptionSite	S_{trans} (J mol^{-1} K^{-1})	S_{rot} (J mol^{-1} K^{-1})	$S_{trans} + S_{rot}$ (J mol^{-1} K^{-1})
Ti[a]	57	38	95
$(SiOH)_4$[a]	29	--	29
Si-O-Si[b]	120	135	255
Ti[b]	123	123	246
$(SiOH)_4$ (single CD_3CN)[b]	112	96	208
$(SiOH)_4$ (three CD_3CN)[b]	113	75	188

[a]Calculated using the Sackur-Tetrode equation. [b]Calculated by decomposing the transitional and rotational contributions of entropy from the DFT model. We note the large translational and rotational entropies predicted by the DFT model. We hypothesize there are due to the difficulty in exhaustively sampling all modes in a gas phase adsorbate, and instead focus on the relative change in translational and rotational entropies when adsorbed in Ti and $(SiOH)_4$.

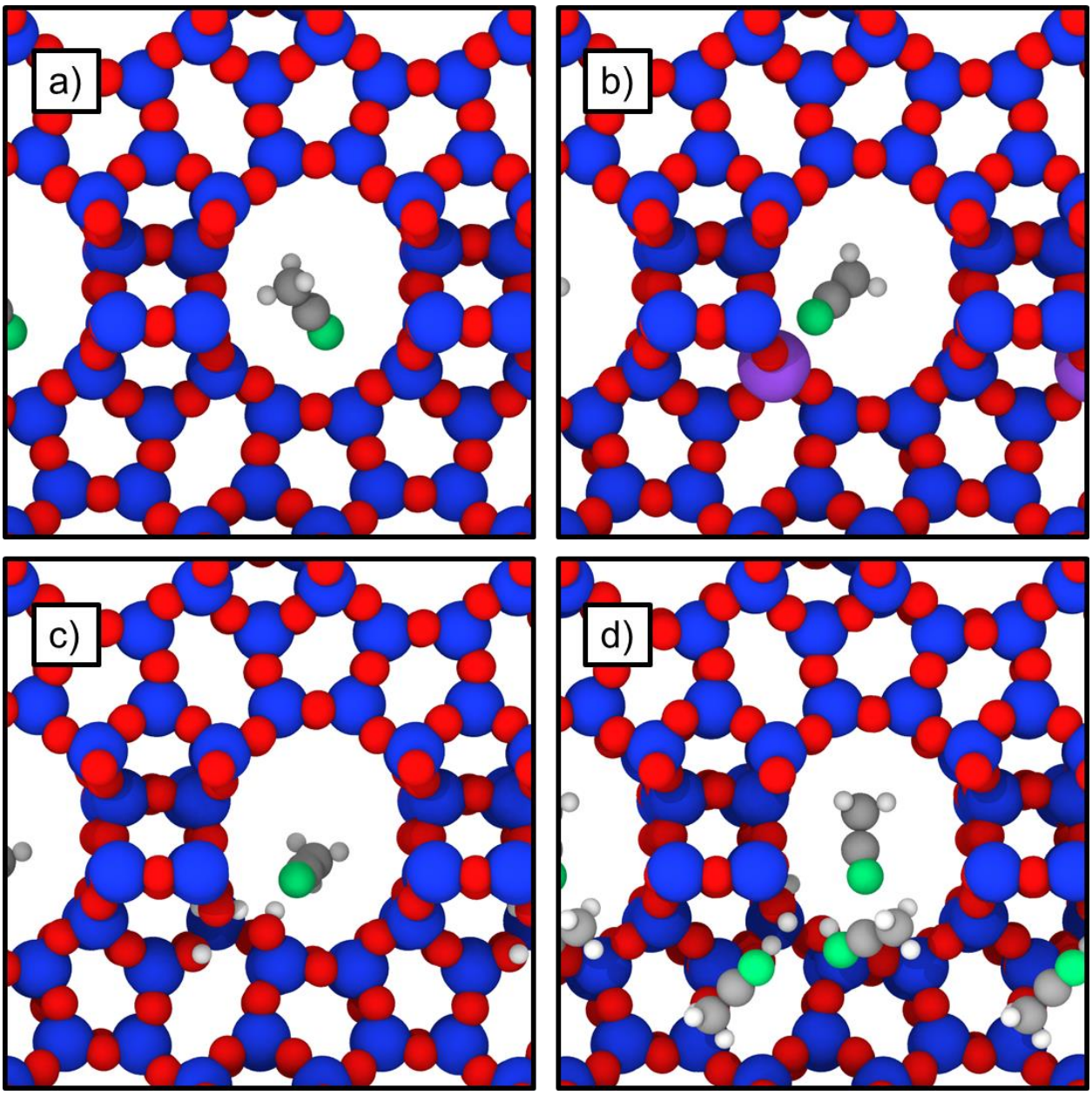

Figure F12. Representitive geometries from AIMD of interactions between a single CD_3CN adsorbed onto (a) Si-O-Si, (b) Ti, and (c) $(SiOH)_4$. Figure F12d represents the adsorption of three CD_3CN onto $(SiOH)_4$, where the CD_3CN on the bottom-left corner of the figure is interacting with the small side channel resulting from the vacancy within $(SiOH)_4$. Color scheme for atoms: hydrogen (white), carbon (gray), nitrogen (green), oxygen (red), silicon (blue), titanium (purple).

F.3. *In Situ* UV-vis Spectra of Ti-BEA Contacted with Solutions of H_2O_2

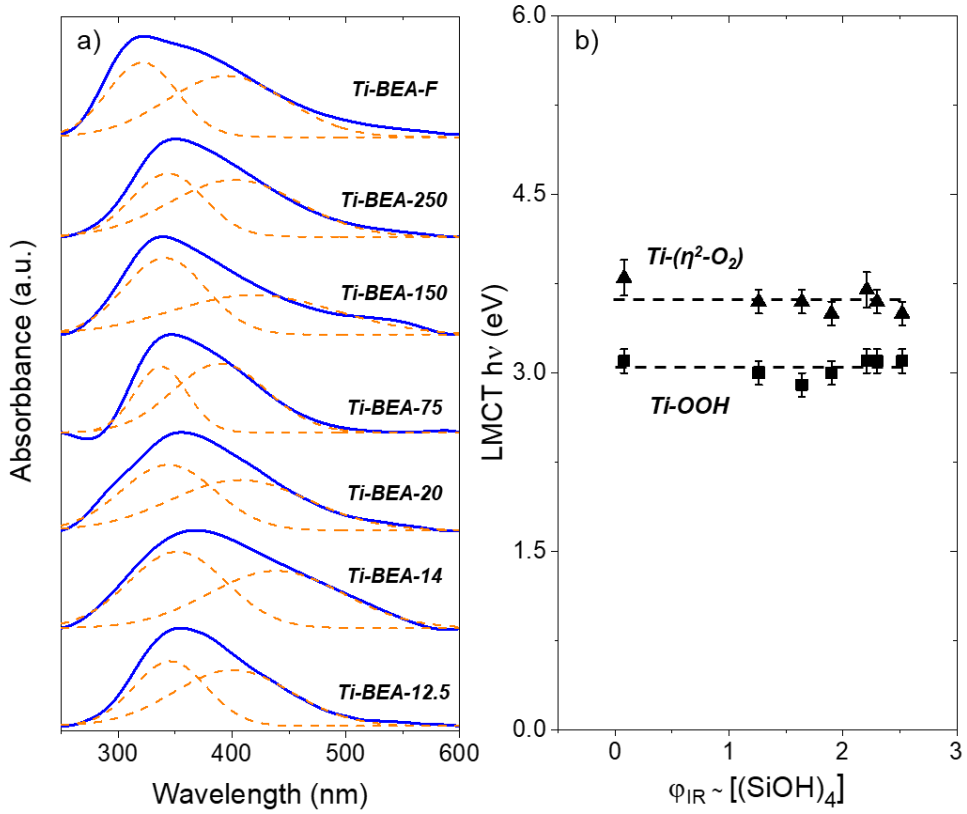

Figure F13. (a) UV-vis spectra of Ti-BEA obtained *in situ* under conditions that result in Ti-(η^2-O_2) (blue) and Ti-OOH (orange) saturated surfaces (0.01 M H_2O_2 in CH_3CN, 313 K; Section 3.4) and (b) ligand-to-metal charge transfer energies (LMCT hν) of Ti-OOH (■) and Ti-(η^2-O_2) (▲) species as a function of Φ_{IR}. Dashed curves in Figure F13a represents gaussian fits to UV-vis absorbance features and dashed lines in Figure F13b are intended to guide the eye. Spectra are normalized by their maximum absorbance and vertically offset for clarity.

Figure F13a shows UV-vis spectra obtained *in situ* when contacting Ti-BEA with solutions of H_2O_2 to visualize the absorbance features that form upon activation of H_2O_2. In all cases, the broad UV-vis feature (300 – 500 nm) contains two overlapping gaussian peaks that correspond to titanium hydroperoxo (Ti-OOH; higher wavelengths, lower energies) and peroxo (Ti-(η^2-O_2); lower wavelengths, higher energies) species. Figure F13b shows the ligand-to-metal charge transfer energies for Ti-OOH and Ti-(η^2-O_2) do not vary with Φ_{IR}, which suggests that the presence, proximity, and density of $(SiOH)_4$ within Ti-BEA do not significantly affect the electronic properties of the reactive species that form upon H_2O_2 activation.

F.4. Additional Kinetic Data and Derivation of Rate Expression for H_2O_2 Decomposition

F.4.1. C_8H_{16} Epoxidation Rates as a Function of [C_8H_{16}], [H_2O_2], and [H_2O] on Ti-BEA

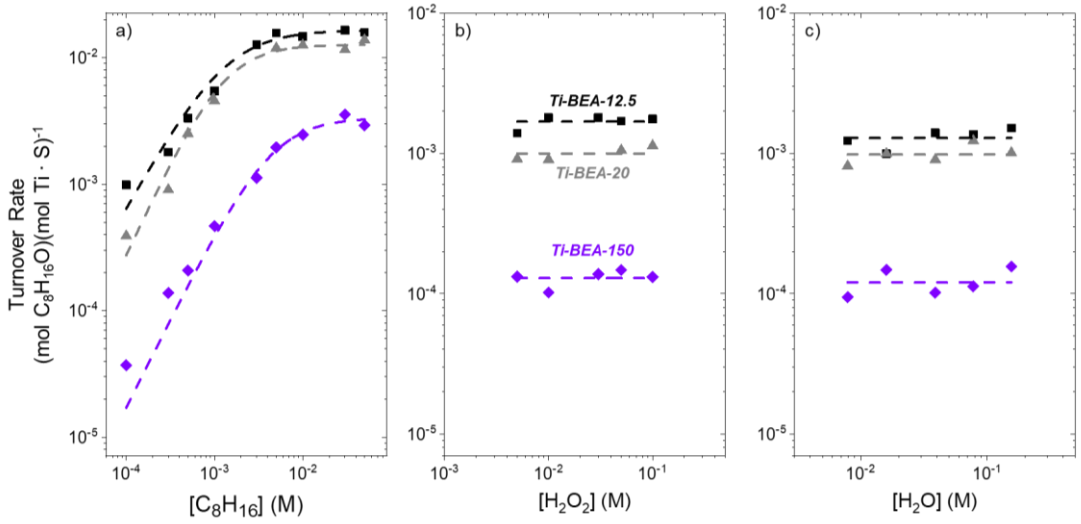

Figure F14. Turnover rates for the formation of $C_8H_{16}O$ as a function of the concentrations of (a) C_8H_{16} (0.01 M H_2O_2, 0.039 M H_2O), (b) H_2O_2 ($3 \cdot 10^{-4}$ M C_8H_{16}), and (c) H_2O ($3 \cdot 10^{-4}$ M C_8H_{16}, 0.01 M H_2O_2) on Ti-BEA-12.5 (■), Ti-BEA-20 (▲), and Ti-BEA-150 (♦) in CH_3CN at 313 K. Dashed lines represent least-squares regression fits of equation 7.8 (Figure F13a) and 7.9 (Figures F13b and F13c).

F.4.2. Derivation of the Rate Expression for H_2O_2 Decomposition

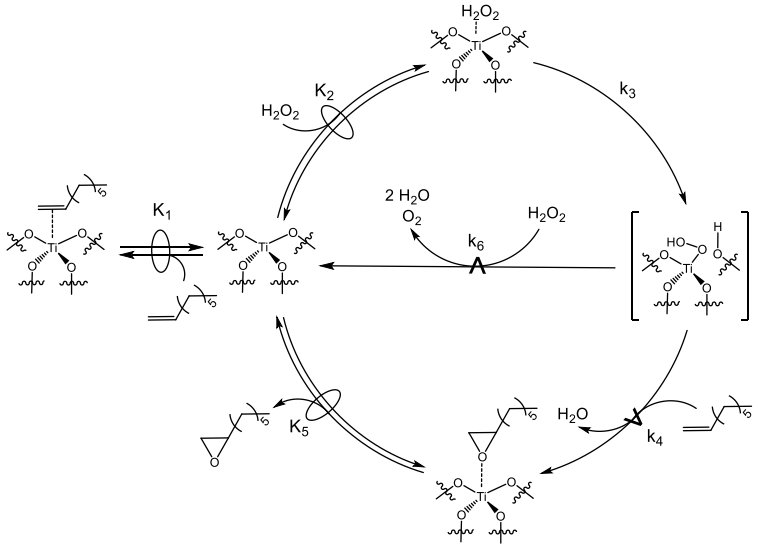

Scheme F1. Proposed Elementary Steps for C_8H_{16} Epoxidation and H_2O_2 Decomposition over Ti-BEA. The symbol ⇄ represents a quasi-equilibrated step, while ⇀ represents a kinetically relevant step. The Ti-OOH intermediate drawn are intended to represent the pool of Ti-OOH and Ti-(η^2-O_2) species that are present as shown by UV-vis (Figure 7.5).

Scheme 7.1 depicts a series of elementary steps that describe the measured effects of [C_8H_{16}], [H_2O_2], and [H_2O] on the rates of H_2O_2 decomposition. This catalytic cycle involves the quasi-equilibrated adsorption of C_8H_{16} (step 1) and H_2O_2 (step 2), and the irreversible activation of adsorbed H_2O_2 (step 3) to form Ti-(η^2-O_2) and Ti-OOH intermediates. Ti-OOH species (Section 7.3.3) then react with C_8H_{16} (step 4) or H_2O_2 (step 6) both of which react either from the fluid-phase directly (i.e., via an Eley-Rideal mechanism) or following coordination to a distinct site at which H_2O_2 does not activate (e.g., the pore wall or SiOH). These pathways form $C_8H_{16}O$, which then desorbs (step 5), or decomposition products (e.g., O_2 and H_2O), respectively. The reaction between Ti-OOH and H_2O_2 is kinetically relevant, which leads to rate for H_2O_2 decomposition (r_D)

$$r_D = k_6[H_2O_2][Ti-OOH] \tag{F8}$$

where [Ti-OOH] is the number of Ti-OOH intermediates and k_i is the rate constant for step "i" in Scheme F1. The application of the pseudo-steady state hypothesis on Ti-OOH and a site balance over all possible states of the Ti active site allows equation F8 to be restated as

$$\frac{r_D}{[L]} = \frac{\frac{k_3 k_6 K_2 [H_2O_2]^2}{k_4[C_8H_{16}]+k_6[H_2O_2]}}{1+K_1[C_8H_{16}]+K_2[H_2O_2]+\frac{k_3K_2[H_2O_2]}{k_4[C_8H_{16}]+k_6[H_2O_2]}+\frac{1}{K_5}[C_8H_{16}O]} \tag{F9}$$

where [L] is the total number of active sites and K_i is the equilibrium constant for step "i." The five terms in the denominator correspond to active metal atoms occupied by CH_3CN (i.e., the solvent), C_8H_{16}, H_2O_2, Ti-OOH, or $C_8H_{16}O$, respectively.

Reaction conditions that result in epoxidation turnover rates that are proportional to [C_8H_{16}] and invariant with [H_2O_2], result in surfaces that are saturated with Ti-OOH intermediates.[11, 54, 199, 275] When Ti-OOH is assumed to be the most abundant reactive intermediate (MARI), the term in the denominator of equation F9 that corresponds to the coverage of this surface species (i.e., the fourth term) dominates and yields a rate expression of the form

$$\frac{r_D}{[L]} = k_6[H_2O_2] \tag{F10}$$

F.4.3. Temperature Dependence of C_8H_{16} Epoxidation and H_2O_2 Decomposition Rates

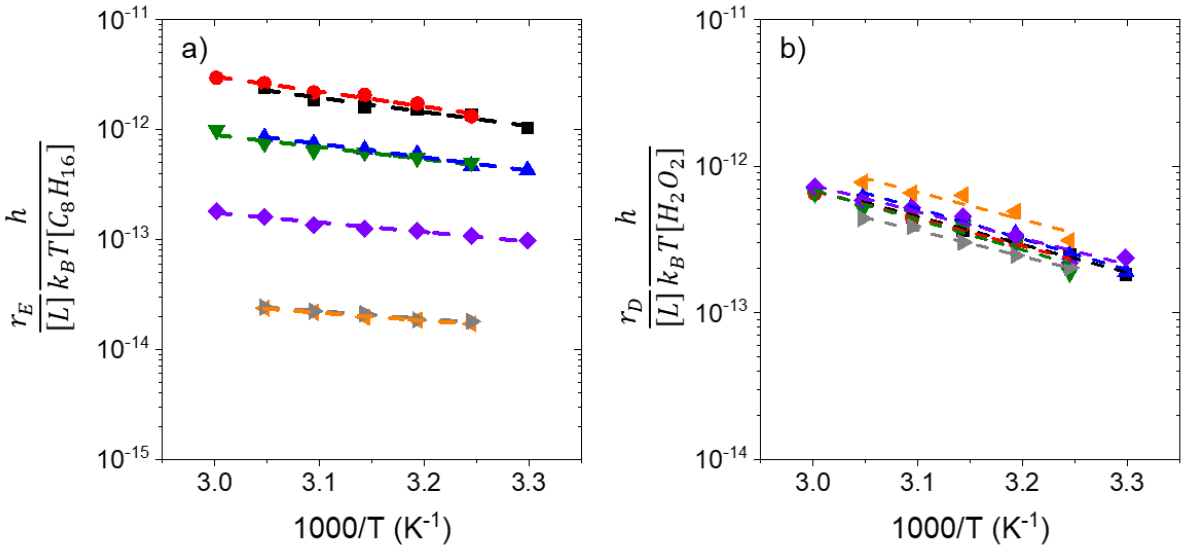

Figure F15. Turnover rates for (a) C_8H_{16} epoxidation and (b) H_2O_2 decomposition divided by $\frac{k_BT}{h}[C_8H_{16}]$ or $\frac{k_BT}{h}[H_2O_2]$ as a function of inverse temperature for Ti-BEA (0.1 mM C_8H_{16}, 0.01 M H_2O_2, in CH_3CN). Symbol key: Ti-BEA-12.5 (black ■); Ti-BEA-14 (red ●); Ti-BEA-20 (blue ▲); Ti-BEA-75 (green ▼); Ti-BEA-150 (purple ♦); Ti-BEA-250 (orange ◄); Ti-BEA-F (gray ►). Dashed lines represent fit of equations 7.14a and 7.14b, whose slopes are proportional to $\Delta H_{E,App}^{\ddagger}$ and $\Delta H_{D,App}^{\ddagger}$, and intercepts are proportional to $\Delta S_{E,App}^{\ddagger}$ and $\Delta S_{D,App}^{\ddagger}$, respectively.

F.5. Equilibrium Adsorption of C_8H_{16} onto Ti-BEA

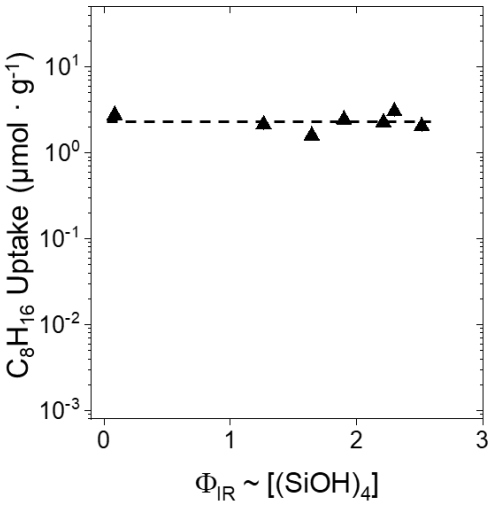

Figure F16. Uptake of C_8H_{16} into Ti-BEA as a function of Φ_{IR} in CH_3CN (0.1 mM C_8H_{16}, 0.039 M H_2O, 313 K). The span of the y-axis was chosen to facilitate comparisons with Figures 7a and 8. Dashed line is intended to guide the eye.

Figure F16 shows the uptake of C_8H_{16} into Ti-BEA under conditions that mimic the reaction solution (in the absence of H_2O_2), where the amount of C_8H_{16} adsorbed per mass of catalyst is assumed to be proportional to its intra-zeolitic concentration. The invariance in the uptake of C_8H_{16} (Figure F16) with Φ_{IR} suggests that the intra-zeolitic concentration of C_8H_{16} in proximity of active sites is not the cause of the difference in epoxidation rates among Ti-BEA. C_8H_{16} likely adsorbs to defect-free regions of the *BEA framework, which nucleate aliphatic-alkene cluster formation and results in nearly identical C_8H_{16} uptakes among Ti-BEA. Moreover, the rates of epoxidation are highest on hydrophilic Ti-BEA, which, on average, possess greater numbers of $(SiOH)_4$ near Ti active sites than their hydrophobic analogues. As such, it seems unlikely that the concentration of C_8H_{16} (i.e., a hydrophobic reactant) would be a factor of 100 greater near active sites in a hydrophilic environment.

APPENDIX G

Supplementary Information and Data for Chapter Eight

G.1. Catalyst Characterization

G.1.1. X-Ray Diffraction to Confirm Zeolite Framework

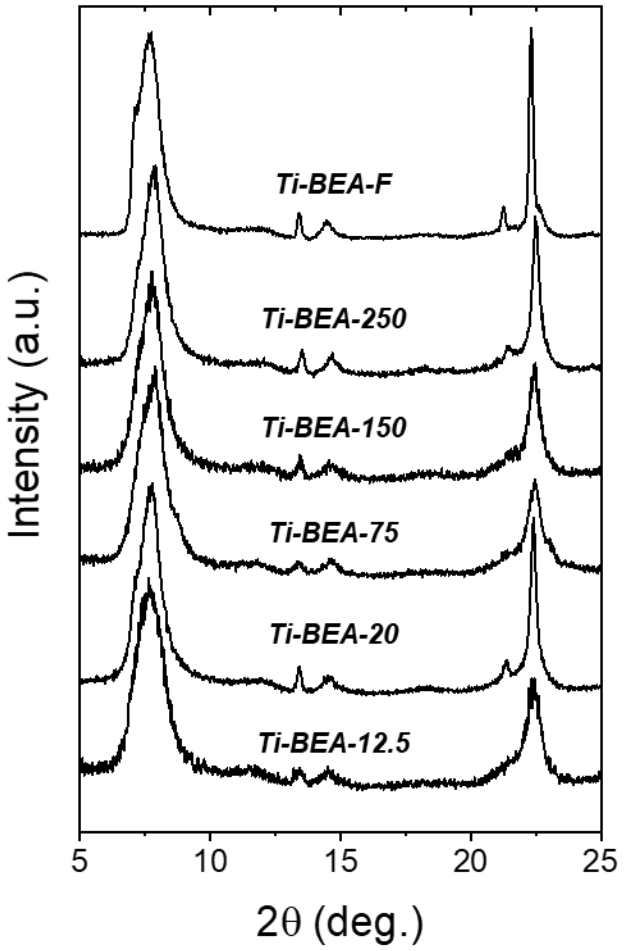

Figure G1. X-ray diffractograms for Ti-BEA used within this study. Diffractograms are vertically offset for clarity.

Figure G1 shows X-ray diffractograms for all Ti-BEA contain diffraction features that are characteristic of the *BEA framework. Notably the sharpness in the features within the diffractogram for Ti-BEA-F is indicative of the high crystallinity of this sample. All other Ti-BEA contain broadening within the diffractogram features that are associated with the presence of internal defects that form upon dealumination with HNO_3.

G.1.2. Diffuse Reflectance UV-Vis to Infer Dispersion of Ti Atoms

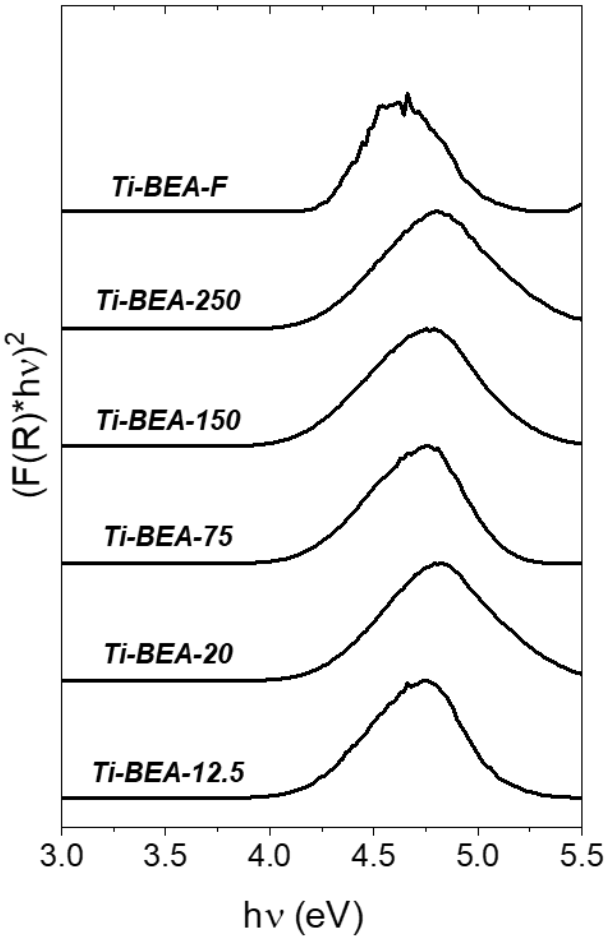

Figure G2. Tauc plots for all Ti-BEA used within this study. Spectra are normalized to the feature at ~4.6 eV and are vertically offset for clarity.

Figure G2 shows that all Ti-BEA contain a single UV-vis absorbance feature with a peak near 4.6 eV. The leading edge of this feature was used to determine the bandgap of each Ti-BEA. In all cases, the measured band gaps are similar (4.2 – 4.3 eV) and significantly greater than that of bulk TiO_2 (3.2 eV), which suggests that the Ti atoms in each of these materials is highly disperse and that these materials do not contain spectroscopically-observable bulk or oligomeric TiO_2.

G.1.3. Gas-Phase Infrared Characterization of Ti-BEA-X to Discriminate Differences in $(SiOH)_4$ Density

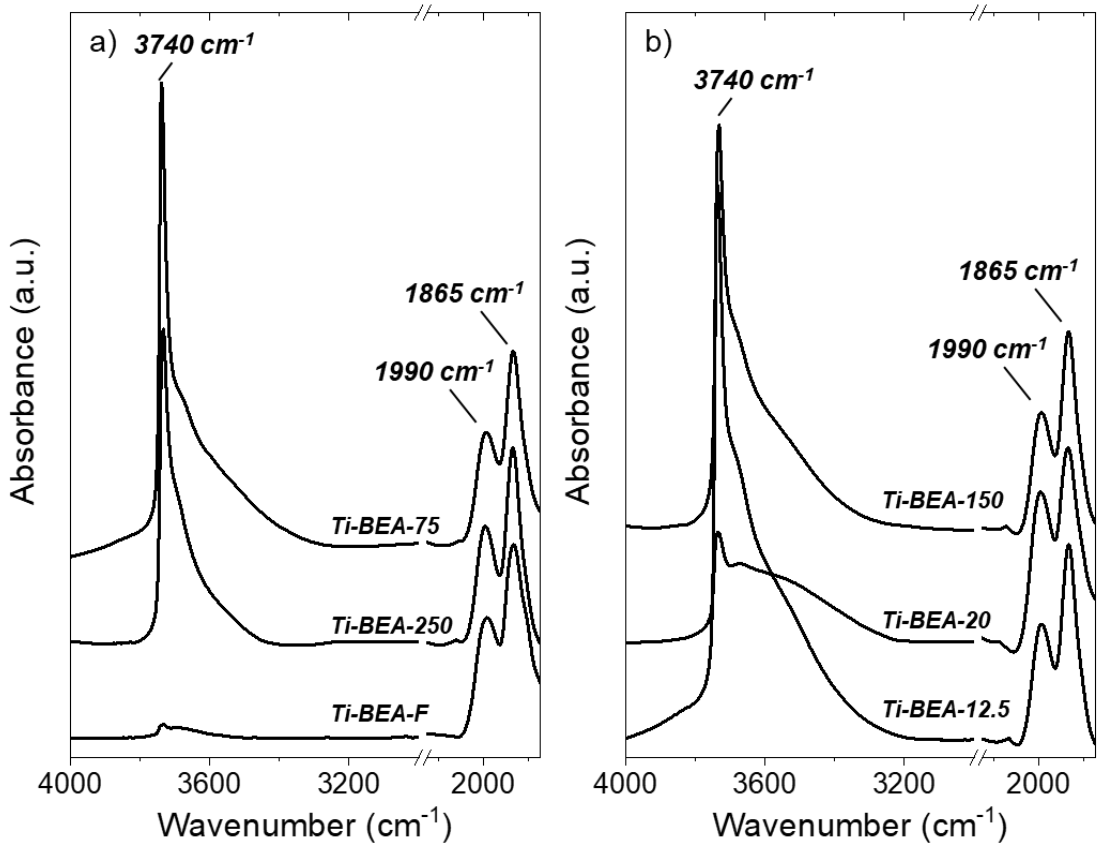

Figure G3. Infrared spectra of dehydrated (a) Ti-BEA-75, Ti-BEA-250, and Ti-BEA-F, and (b) Ti-BEA-12.5, Ti-BEA-20, and Ti-BEA-150. All Ti-BEA were dehydrated *in situ* under flowing He (50 cm^3 min^{-1}) for 3 h at 573 K prior to measurement. Spectra were normalized to the absorbance feature at 1865 cm^{-1} corresponding to ν(Si-O-Si) overtones (1865 and 1990 cm^{-1}), which is used as an internal standard for comparisons between the density of SiOH groups among Ti-BEA samples. Spectra are vertically offset for clarity.

Figure G3 shows the ν(O-H) and ν(Si-O-Si) overtone region of the infrared spectra of dehydrated Ti-BEA. The sharp absorbance feature at ~3740 cm^{-1} corresponds to isolated SiOH species that are not interacting via H-bonding with nearby H-bond donors or acceptors (i.e., other SiOH). The broadening within the ν(O-H) region is due to the H-bonding interactions of SiOH with other SiOH (i.e., $(SiOH)_4$) that cause a red shift in these vibrational modes.

Differences in the density of isolated SiOH and $(SiOH)_4$ groups on each material across the series of Ti-BEA are determined by normalizing spectra by the intensity of the ν(Si-O-Si) modes (i.e., assuming a constant density of framework Si-O-Si bonds) and deconvoluting the peaks

for SiOH (3740 cm^{-1}) and $(SiOH)_4$ groups (3300-3700 cm^{-1}). The ratios of the integrated areas (Φ_{IR}) for ν(O-H) of $(SiOH)_4$ ($A_{(SiOH)_4}$) to those for ν(Si-O-Si) ($A_{(Si-O-Si)}$) provide measures of the relative density of $(SiOH)_4$ for each Ti-BEA

$$\Phi_{IR} = \frac{A_{(SiOH)_4}}{A_{(Si-O-Si)}} \quad \text{(G1)}$$

Table S1 shows that values for Φ_{IR} decrease as the initial ratio of Si:Al increases in the parent BEA zeolites, which is consistent with the trends observed for the total number of Si atoms coordinated to -OH groups (shown by Φ_{NMR}). Φ_{IR}, as defined here, provides semi-quantitative measure for changes in the number of $(SiOH)_4$ groups that result from differences in synthesis protocols for a given zeolite framework.

Table G1. Relative Densities of Hydrogen-Bonded SiOH (Φ_{IR}) within Ti-BEA

Sample Name	Φ_{IR}
Ti-BEA-12.5	2.30
Ti-BEA-20	1.90
Ti-BEA-75	2.21
Ti-BEA-150	1.64
Ti-BEA-250	1.26
Ti-BEA-F	0.08

G.2. Isothermal Titration Calorimetry

G.2.1. Development of Single-Site Binding Model

Isothermal titration calorimetry has been widely used for studying enzymatic systems, which detail the thermodynamics of the binding configurations.[394-395] Here, we present a brief mathematical formulation of the single site binding model.

Consider the binding of a *n* ligands (e.g., $C_8H_{16}O$), *L*, with an adsorption site (e.g., Ti atoms), *M*,

$$nL + M \overset{K}{\leftrightarrow} ML_n \quad \text{(G2)}$$

where *K* is the equilibrium binding constant for the formation of the *ML* complex (i.e., *n* =1). The equilibrium binding constant is represented by

$$K = \frac{[ML]}{[M][L]} \tag{G3}$$

where the brackets ([]) denote liquid-phase concentrations. These liquid-phase concentrations are related to the total concentrations of each component loaded into the calorimeter cell (denoted with a subscript *T*) by a mass balance on each component

$$[M]_T = [M] + [ML] \tag{G4}$$

$$[L]_T = [L] + [ML] \tag{G5}$$

Equations S4 and S5 are then substituted into equation S3, so the equilibrium constant is equated to the total concentrations of the titrant and or the adsorption site. Values of *K* reflect changes in free energy ΔG_{Ads} (and by extension, enthalpies (ΔH_{Ads}) and entropies (ΔS_{Ads})) by

$$\Delta G_{Ads} = -RTln(K) = \Delta H_{Ads} - T\Delta S_{Ads} \tag{G6}$$

where *R* is the ideal gas constant and *T* is the absolute temperature in Kelvin.

Within a given ITC experiment, the dependent variable is the total amount of heat released per injection of the titrant ($\frac{dQ}{d[L]_T}$)

$$\frac{dQ}{d[L]_T} = V \sum_i \Delta H_{Ads,i} d[ML_i] \tag{G7}$$

where *V* is the volume of the sample cell, $\Delta H_{Ads,i}$ is the adsorption enthalpy for the formation of *ML*, and $d[ML_i]$ is the amount of the *ML* complex formed during the injection. Equation S7 is then combined with equations S3 – S5 to yield the full form of the single-site binding model that was used to fit the integrated heat data from the ITC experiments.

$$\frac{dQ}{d[L]_T} = \frac{1}{2} V \Delta H_{Ads} \left[1 - \frac{\frac{[L]_T}{[M]_T} + \frac{1}{K[M]_T} - n}{\sqrt{\left(\frac{[L]_T}{[M]_T}\right)^2 + \left(n + \frac{1}{K[M]_T}\right)^2 - 2\frac{[L]_T}{[M]_T}\left(n - \frac{1}{K[M]_T}\right)}} \right] \tag{G8}$$

G.2.2. Sample Dilution Curve to Correct Heats Released Upon Titration

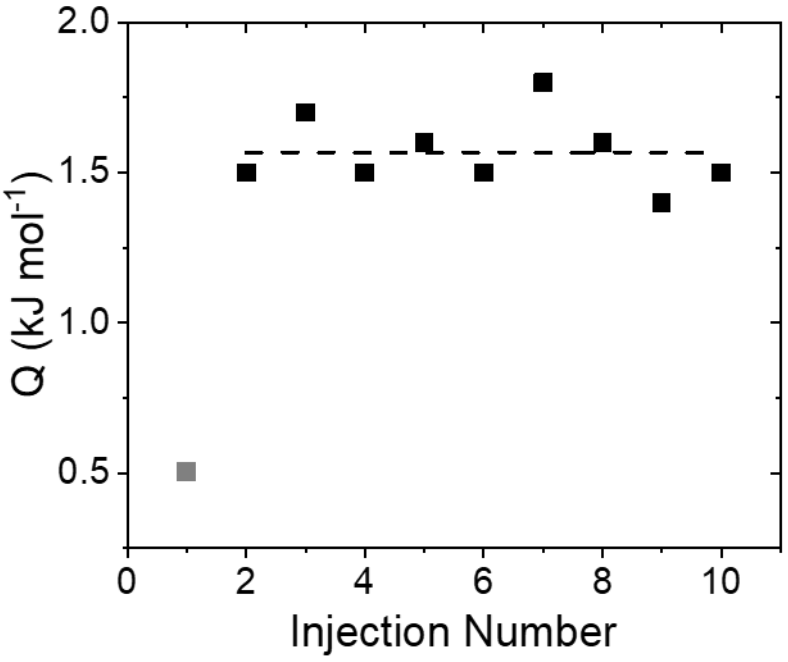

Figure G4. Heats released upon titration of $C_8H_{16}O$ (20 mM, 39 mM H_2O, in CH_3CN) into aqueous CH_3CN (39 mM H_2O) as a function of titration number at 313 K (250 rpm stirring). Each titration was 1 μL in volume. The transparent point was omitted from calculations of the heat of mixing due to common errors associated with early injections. The dashed line represents the heat of mixing that is associated with the dilution of $C_8H_{16}O$ into solutions of CH_3CN.

Figure G4 shows the heats released upon mixing of $C_8H_{16}O$ into CH_3CN (0.1 – 1.1 mM $C_8H_{16}O$). The constant value with successive titrations suggests that this value corresponds to the heat of infinite dilution, which is further supported by similar values obtained for more-dilute titration solutions of $C_8H_{16}O$. This heat of mixing was used to correct the isotherms for the titration of $C_8H_{16}O$ into Ti-BEA materials by adding this value to all heat values to correct for changes due to non-adsorption processes.

G.2.3. Schematic Depicting Sequential $C_8H_{16}O$ Titration of Ti Atoms within Ti-BEA-X

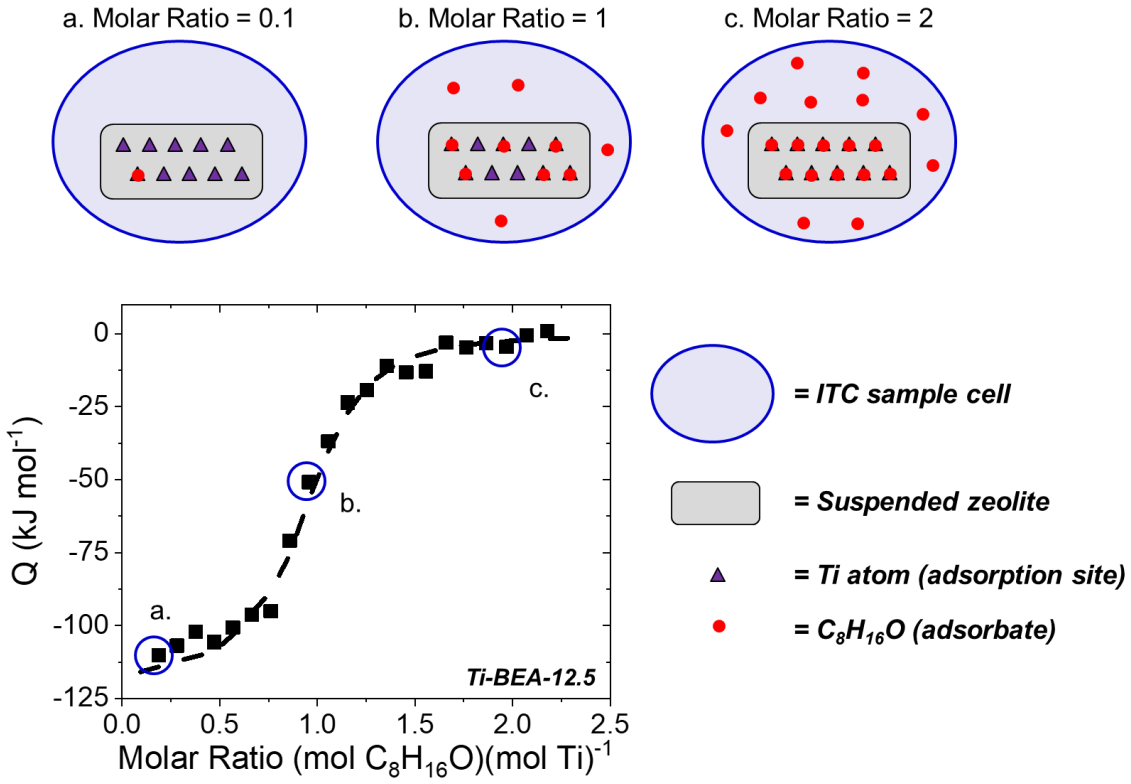

Scheme G1. Depiction of $C_8H_{16}O$ titration of Ti atoms within Ti-BEA-X at $C_8H_{16}O$:Ti molar ratios of a) 0.1, b) 1, and c) 2. These approximate molar ratios are indicated on a representative adsorption isotherm for the titration of Ti-BEA-12.5 with $C_8H_{16}O$ in CH_3CN (anhydrous) at 313 K. The dashed curve represents the fitting of a single-site binding model (Section G2.1). A legend is provided within the scheme to guide the reader in interpreting how $C_8H_{16}O$ binds to active sites.

Scheme G1 shows a visual representation for the titration of Ti atoms with $C_8H_{16}O$ with increasing amount of epoxide added to the system. At low molar ratios of $C_8H_{16}O$ to Ti (e.g., 0.1; Scheme G1a), all $C_8H_{16}O$ molecules that are introduced into the sample cell bind to Ti atoms, which is inferred from the large enthalpies of adsorption at low coverage (i.e., ΔH_{Ads} ~ -100 kJ mol^{-1}; Table 8.2). The inflection point in the adsorption isotherm indicates the stoichiometry in binding between the adsorbate and the adsorption site. In the limit of equimolar $C_8H_{16}O$ and Ti atoms (Scheme G1b), the partition between $C_8H_{16}O$ in the fluid phase and bound to Ti atoms is dictated by the free energy of adsorption. As the ratio of $C_8H_{16}O$ to Ti increases further (e.g., beyond a molar ratio of 2 for this system; Scheme G1c), each Ti atom present in BEA binds one

$C_8H_{16}O$ and the additional amounts of $C_8H_{16}O$ added to the cell remain in solution. This is shown by integrated heats released (per injection) that approach that of the heat of dilution.

G.3. Example Time- and Phase-Domain ATR-IR Spectra

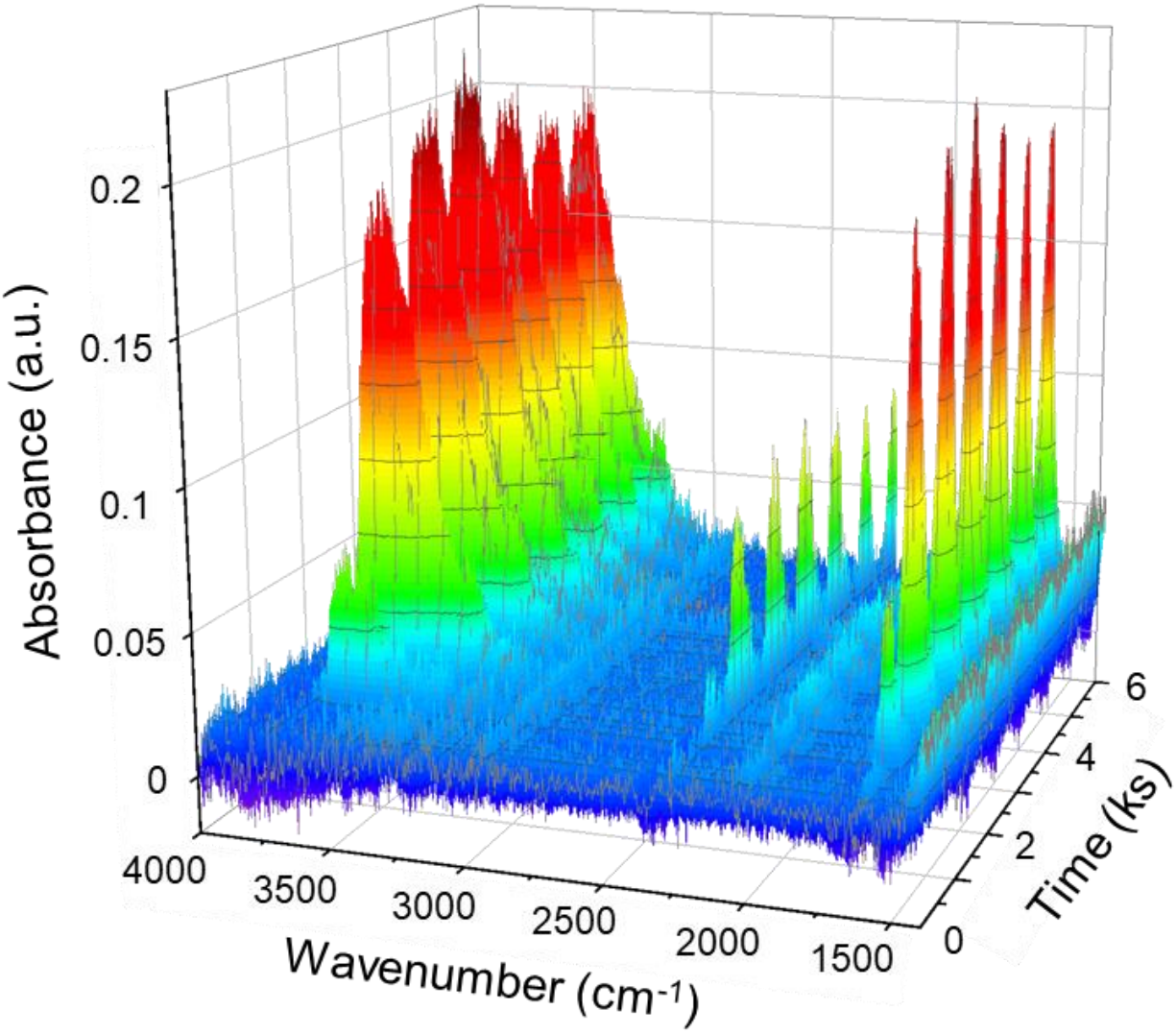

Figure G5. Representative time-resolved infrared spectra obtained in situ during the modulation of H_2O within CH_3CN over Ti-BEA-F (450 s period length, 313 K).

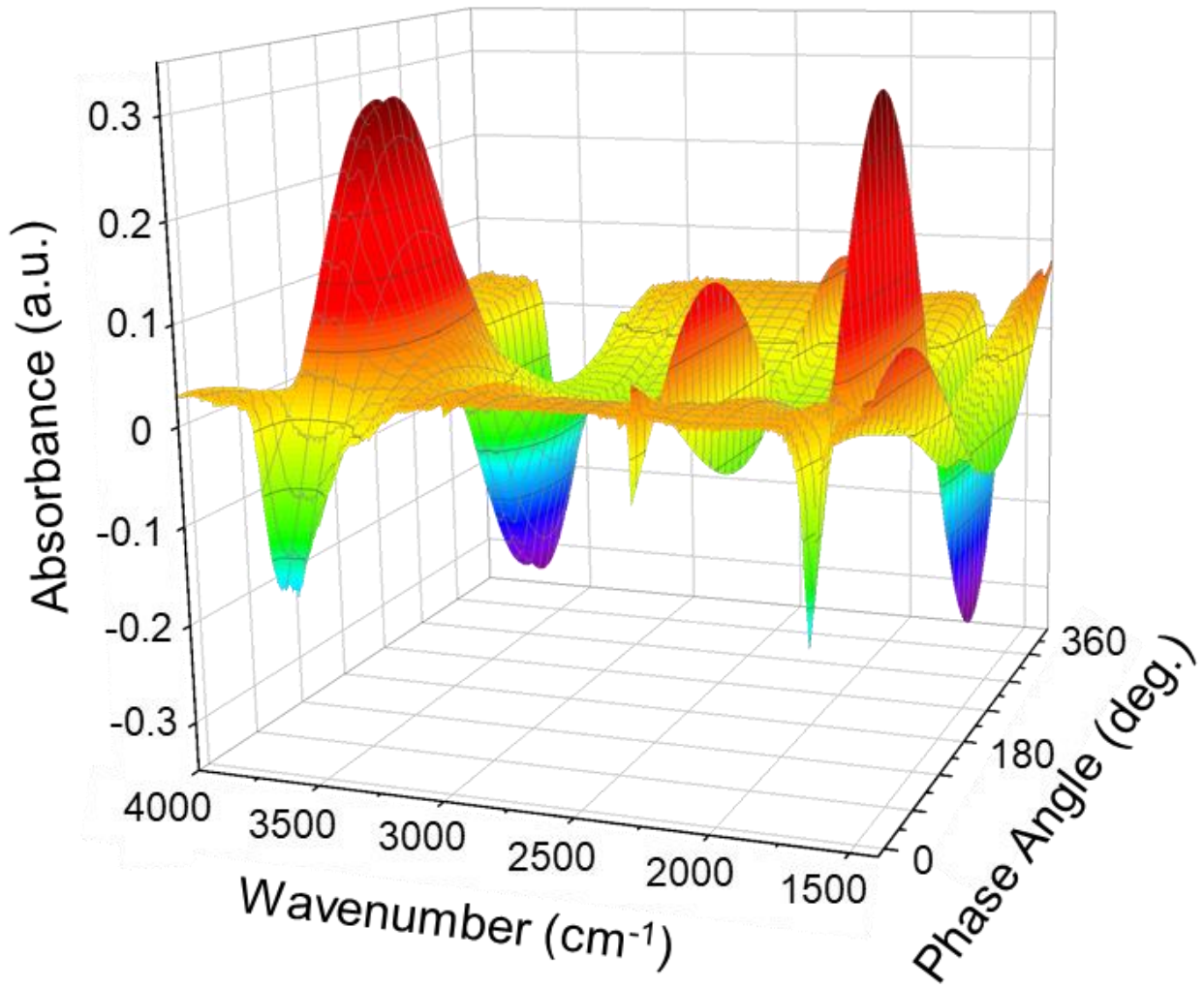

Figure G6. Phase-resolved infrared spectra that result from phase-sensitive detection of the time-resolved spectra in Figure G2.

G.4. Additional ATR-IR Data for H_2O within Ti-BEA-250

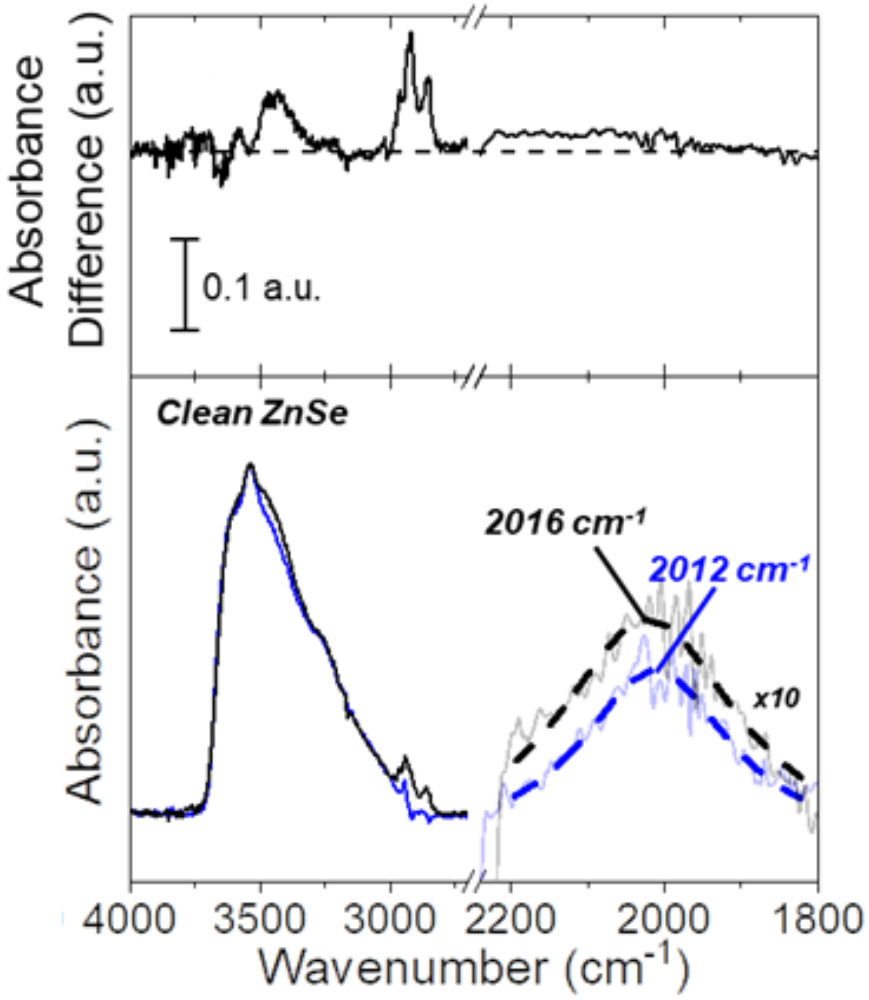

Figure G7. Infrared spectra obtained through multivariate analysis of modulation excitation experiments (Section 8.2.4) of H_2O in CH_3CN (0 – 5.5 M H_2O; blue) and in a solution of $C_8H_{16}O$ in CH_3CN (0.1 M $C_8H_{16}O$, 0 – 5.5 M H_2O; black) over a clean ZnSe internal reflection element. All spectra are normalized to the most-intense ν(O-H) feature (~3540 cm^{-1}) and have a resolution of 5 cm^{-1}. The region between 1800 – 2250 cm^{-1} have been scaled by the multiplier indicated. The dashed curves represent Lorentzian fits, which were used to quantify the peak center of the combination band. The top spectra is the difference spectra that represents that changes in the vibrational features for H_2O that result from the presence of $C_8H_{16}O$.

APPENDIX H

Supplementary Information and Data for Chapter Nine

H.1. Catalyst Characterization

H.1.1. X-Ray Diffraction

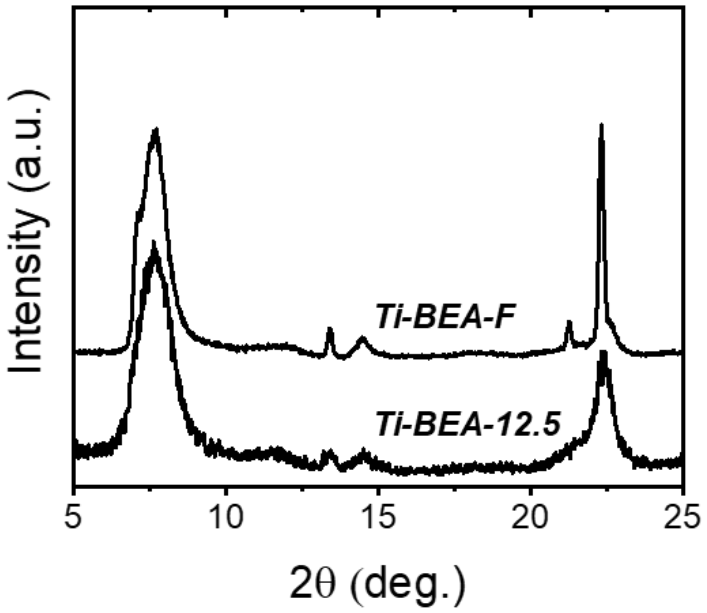

Figure H1. X-ray diffractograms for Ti-BEA-12.5 and Ti-BEA-F. Diffractograms are vertically offset for clarity.

Figure H1 shows X-ray diffractograms for Ti-BEA-12.5 and Ti-BEA-F contain distinct crystallographic features that are a hallmark of the *BEA framework. It should be noted that the sharpness in the 22.4 degree feature in Ti-BEA-F indicates a high degree of crystallinity. Ti-BEA-12.5 contains broad diffraction features that are indicative of internal defects that form upon dealumination and synthesis in hydroxide media.

H.1.2. Diffuse Reflectance UV-vis Spectra

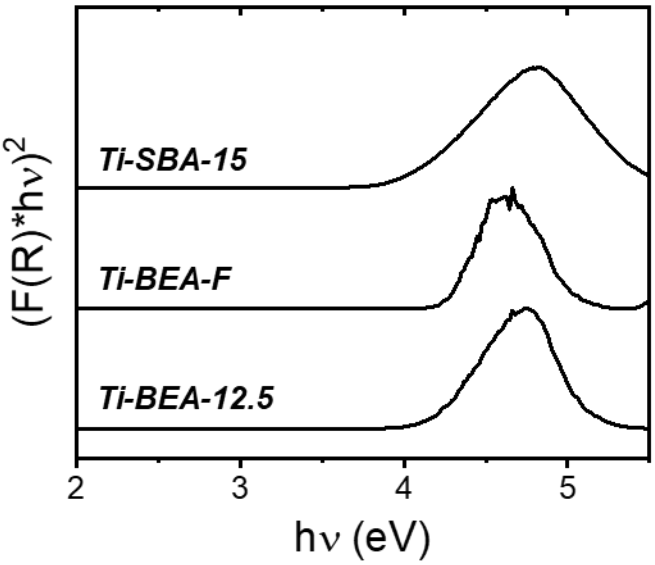

Figure H2. Tauc plots for Ti-BEA-12.5, Ti-BEA-F, and Ti-SBA-15. All plots were normalized to the most intense feature around 4.7 eV and are vertically offset for clarity.

Figure H2 shows that Ti-BEA-12.5, Ti-BEA-F, and Ti-SBA-15 contain a single UV-vis absorbance feature around 4.7 eV. The leading edge (~4.2 to 4.6 eV) was fit using a line to extrapolate the x intercept, which is equal to the band gap of the material.

H.1.3. Uptake of C_8H_{16} into Si-BEA-12.5 and SBA-15

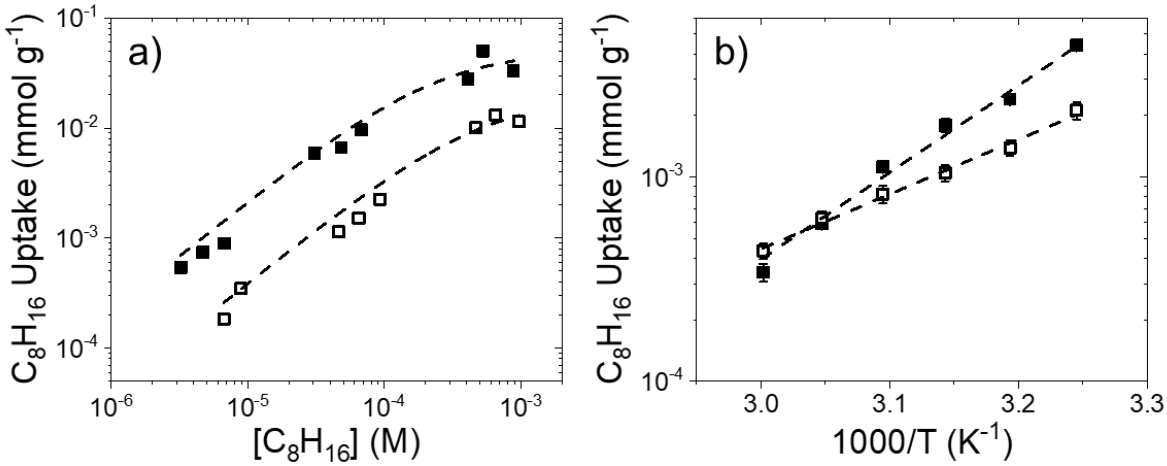

Figure H3. 1-Octene uptake (*per gram of solid*) into Si-BEA-12.5 (solid symbols) or SBA-15 (open symbols) as a (a) function of C_8H_{16} concentration at 313 K and (b) inverse temperature (0.05 mM C_8H_{16}) in CH_3CN. The dashed curves in panel (a) represent least regression fits of a Langmuir isotherm, while those in panel (b) are linear fits whose slopes are proportional to the enthalpy of C_8H_{16} adsorption (ΔH_{Ads}).

Figure H3 shows that C_8H_{16} uptake into Si-BEA-12.5 and SBA-15 is Langmuirian, where uptake is proportional to $[C_8H_{16}]$ at low concentrations of C_8H_{16} (<0.1 mM) and approaches saturation at high $[C_8H_{16}]$. Adsorption enthalpies for C_8H_{16} into these two porous materials was determined through van't Hoff analysis of C_8H_{16} uptake under conditions where C_8H_{16} uptake is proportional to $[C_8H_{16}]$.

H.2. *In Situ* UV-vis on Ti-SBA-15

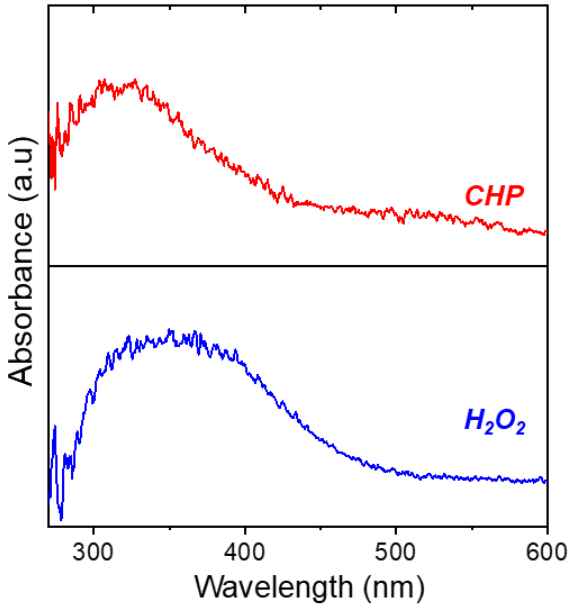

Figure H4. UV-vis difference spectra of H_2O_2- (bottom, 0.01 M H_2O_2, 0.039 M H_2O) and CHP-activated (top, 0.3 M CHP, 0.039 M H_2O) Ti-SBA-15 in CH_3CN at 313 K. In both cases, the background spectra is of Ti-SBA-15 in CH_3CN (0.039 M H_2O) at 313 K.

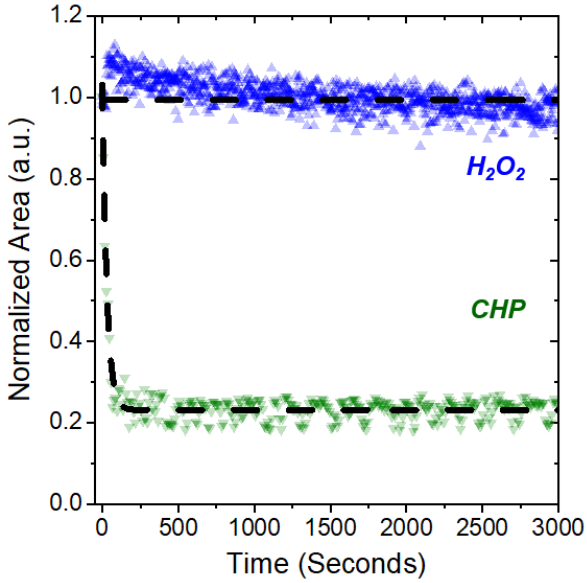

Figure H5. Areas for the LMCT bands of Ti-OOH (▲) and Ti-OOcumyl (▼) as a function of time as CH_3CN (0.039 M H_2O, 313 K) flowed over H_2O_2- or CHP-activated Ti-SBA-15, respectively. The dashed black curve for H_2O_2 is meant to guide the eye, while the curve for CHP represents an exponential decay fit with a decay constant (k_d) of $3.3 \cdot 10^{-2}$ s^{-1}. All areas were normalized to the initial area (i.e., at time = 0) before introduction of the oxidant-free CH_3CN solution.

H.3. Comparisons of Rates of C_8H_{16} Epoxidation and H_2O_2 Decomposition

Reaction conditions that result in turnover rates for C_8H_{16} epoxidation that are proportional to $[C_8H_{16}]$ and are independent of $[H_2O_2]$ (Section 9.3.2) are described by the following rate expression

$$\frac{r_E}{[L]} = k_4[C_8H_{16}] \quad \text{(H1)}$$

Equation H1 shows that extrapolation of the linear portion of Figures 9.3a and 9.3b allow us to estimate the value of $k_4[C_8H_{16}]$ under conditions where $C_8H_{16}O$ saturates Ti active sites. Similarly, the rates of H_2O_2 decomposition ($2.7 \cdot 10^{-3}$ (mol H_2O_2)(mol Ti $\cdot$ s)$^{-1}$) are equal to values of $k_6[H_2O_2]$.

Table H1. Calculated ratios of $k_4[C_8H_{16}]$:$k_6[H_2O_2]$ for Ti-BEA-12.5 (0.05 M C_8H_{16}) and Ti-SBA-15 (1 M C_8H_{16}) using interpolated values from Figures 9.3a and 9.3b and H_2O_2 decomposition rates.

Sample	$k_4[C_8H_{16}]$:$k_6[H_2O_2]$
Ti-BEA-12.5	11
Ti-SBA-15	8

Table S1 shows that under conditions where C_8H_{16} epoxidation rates are invariant with $[C_8H_{16}]$ (i.e., ~0.05 M on Ti-BEA-12.5 and 1 M on Ti-SBA-15) the ratio of $k_4[C_8H_{16}]$:$k_6[H_2O_2]$ are >>1, which allows for the simplification of equation 9.2a within the main text (Section 9.3.2).

Vita

Daniel Thomas Bregante was born on May 17th, 1993 in Berkeley, CA and grew up in Union City, CA. Daniel went through the New Haven Unified School District before returning to Berkeley for his undergraduate studies at the University of California, Berkeley. At Berkeley, Daniel graduated with a B.S. in Chemical Engineering with a minor in Chemistry. Daniel's first research experience was working with Professor Thomas Maimone in the Chemistry department on the total organic synthesis of complex natural products. In 2014, Daniel joined Professor Clayton Radke's group, where he worked on a variety of projects, including hydrogel synthesis, drug diffusion, tear-evaporation mass transfer models, and thermodynamic calculations for the properties of ultra-thin films. Upon graduation, Daniel completed an internship at Genentech Inc. in South San Francisco, where he developed assays to quantify the extent of peptide oxidation. In 2015, Daniel came to the cornfields, *ahem* Midwest, where he joined Professor David Flaherty's group at the University of Illinois at Urbana-Champaign for his Ph.D. studies. His dissertation focused on developing quantitative structure-function relationships for liquid-phase catalysis in microporous materials. Upon completion of his Ph.D., Daniel will complete his cross-continental journey and venture to the Massachusetts Institute of Technology for his postdoctoral studies, where he will work with Professor Yogesh Surendranath on developing methods to characterize electrocatalytic systems.

If you've made it this far, I commend you and wish you all the best.

-Daniel T. Bregante